Molecular Complexes of Manganese and Chromium as Catalysts for Energy Relevant Reactions: Understanding Reactivity and Mechanisms Through the Application of Electrochemical and Spectrochemical Techniques

Shelby Lane Hooe
Mechanicsville, VA

B.S., Chemistry, Gardner-Webb University, 2016

A Dissertation presented to the Graduate Faculty
of the University of Virginia in Candidacy for the Degree of Doctor of Philosophy

Department of Chemistry

University of Virginia
Date: May 17th, 2021

Abstract

The reduction of dioxygen (O_2) to water (H_2O) or hydrogen peroxide (H_2O_2) has importance in biological systems, oxidative functionalization reactions, and fuel cells. Herein, the synthesis and electrocatalytic reduction of dioxygen by a molecular manganese (III) complex with a tetradentate dianionic bipyridine-based ligand is described. This complex is competent for the reduction of dioxygen to H_2O_2 with 81±4% Faradaic efficiency. To understand the mechanism in greater deatil, spectrochemical stopped-flow and electrochemical techniques were employed to examine the catalytic rate law and kinetic reaction parameters. Under electrochemical conditions, the catalyst produces H_2O_2 by an *ECEC* mechanism, with a strong dependence on the pK_a of the proton donor. Under spectrochemical conditions, where the homogeneous reductant decamethylferrocene is used, H_2O_2 is instead produced via a disproportionation pathway, which does not show a strong acid dependence. Using this Mn-based electrocatalyst with *p*-benzoquinone (BQ) as an electron-proton transfer mediator (EPTM) precursor for oxygen reduction with 2,2,2-trifluoroethanol (TFE-OH) present as a weak Brønsted acid, quantitative selectivities for the four-electron/four proton reduction product H_2O are observed.

Alternatively, the electrocatalytic reduction of CO_2 by an earth abundant transition metal catalyst continues to represent an appealing method for addressing global climate change. Herein, a molecular chromium complex with a 2,2′-bipyridine-based ligand capable of selectively transforming CO_2 into CO with phenol as a sacrificial proton donor at turnover frequencies of $5.7 \pm 0.1\ s^{-1}$ with high Faradaic efficiency (96±8%) and low overpotential (110 mV) is described. Utilizing a mediator, dibenzothiophene-5,5-dioxide

(DBTD), can enhance the reactivity of this Cr complex and also enable new catalytic reactivity where the electrocatalytic reduction of CO_2 to CO can be carried out, by the Cr complex and DBTD, in the absence of an added proton donor. The catalytic mechanism was analyzed through chemical and electrochemical experiments, as well as through computational DFT analyses.

Copyright Information

Chapters 2, **3**, and **4** are modified versions of published work which have been reproduced in accordance with the American Chemical Society Journal Publishing Agreement. Proper citation for each chapter is given below and on the first page of each of the chapters within this thesis.

Chapter 2:
Hooe, S. L.; Rheingold, A. L.; Machan, C. W., *Journal of the American Chemical Society* **2018,** *140* (9), 3232-3241.

Chapter 3:
Hooe, S. L.; Machan, C. W., *Journal of the American Chemical Society* **2019,** *141* (10), 4379-4387.

Chapter 4:
Hooe, S. L.; Dressel, J. M.; Dickie, D. A.; Machan, C. W., *ACS Catalysis* **2020,** *10* (2), 1146-1151.

Chapter 5 contains material for upcoming publications and have been incorporated with consent of all current contributing authors. These authors include Emma N. Cook, Amelia G. Reid, and Charles W. Machan. The work in this chapter was published in preprint form and is available at https://doi.org/10.26434/chemrxiv.14156528.v1.

Chapters 6 contains material for upcoming publications and have been incorporated with consent of all current contributing authors. These authors include Juanjo J. Moreno, Emma N. Cook, Amelia G. Reid, and Charles W. Machan. The work in this chapter was published in preprint form and is available at https://doi.org/10.26434/chemrxiv.14165951.v1

Acknowledgements

Although several people can attest to the fact that I don’t always pronounce them or even use them correctly, I have always had a fascination with language, and in particular, with just words in general. We hear them, read them, and say them every single day, but taking the time to really consider the power that words have on a person’s perception, interpretation and even understanding has always been interesting to me. I am far from being able to brag about my communication abilities, but I have always tried to really dig in to all the possible meanings of a word so that I am able to understand all the different possible interpretations for how it can be perceived by myself and those around me. An acknowledgment can be defined as an action which demonstrates gratitude. However, it can also be defined as the acceptance of truth or existence of something. So, I guess both meanings of the word take precedence here because I have long accepted the truth that I would have never made it this far if it were not for the people who have most heavily influenced my life and I wish to acknowledge that fact and attempt to show all those individuals gratitude for their support in this section of my thesis. I also think it is crucial that I acknowledge first, that there are simply no words that can sufficiently express how thankful I am for all the people in my life who have helped me to become the person I am today. And while I am sure a few of the more influential people in my life just rolled their eyes thinking about how much further I have left to grow in life, let’s all just take a second and appreciate how far I have come these past five years. I don’t think we should ever forget that I was once the student walking around with a half-open camo backpack in dress shoes, wearing tall Nike socks, shorts, and a worn-out t-shirt with more holes than sleeves looking for the right classroom to walk in to and sit in the very back, closest to the exit. So, I think it is safe to say I have come along some type of way; both in style and organization at least.

To my roommates, teammates, and best friends from Gardner-Webb: thank you for never allowing me to miss a wedding, group text/call, or girl's weekend trip. Brooke Garrison, Jessica Fergusson (Fergie), Whitley Bowman (Whit), and Krista Chauvin (Gramz), you four are absolutely insane, wild, and always fun to be around. I don't think the five of us have ever been around each other without smiles on all our faces, laughing and having a good time. To Brooke, of course this excludes the time after that one bad home game where we sat in silence in my room that night while we ate our feelings splitting the extra-large pizza as we both tried to hide our tears. It really is crazy how in life you frequently end up looking back and laughing at those moments where you had once thought things were the worst they could ever be. We were freshman undergraduates in our first semester of college that night, Brooke, and little did we know how much more we were going to overcome together in the following years. Nonetheless, thank you four so much for continuing to remain close friends over the years and supporting me through graduate school.

To all the faculty and staff at Gardner-Webb who took part in my education during my undergraduate career, thank you for all your time and hard work. Transitioning to college was certainly not as easy as I had made it look at the time. Being only the second person within my entire extended family, alongside my older sister, to attend a four-year undergraduate institution, figuring out how balance athletics, academics, and the occasional work study when I could find the time quickly became a significant challenge early on. Without the help of all the teachers, tutors, and my disability specialists (Lauren Isom) I certainly would not have made it through.

To all the Machan Lab members, both past and present, thank you for continuing to include me as a member of the team over the years. To Asa Nichols, thank you for staying on this journey from start to finish alongside me over the years. A special shout out to the more rebellious type that made up the initial library/side office crew in the lab consisting of myself, Lauren Lieske, Jillian Turner, and Juan-José (Juanjo) Moreno-Diaz. Lauren, we went through some rough times together and we went through some times when maybe we had a little bit too much fun. Thank you for every hiking and brewery adventure you ever took me on. Words cannot describe the impact you had on making my time in graduate school more fun and enjoyable both in and out of the lab. Juanjo, thanks for coming into the Machan Lab and being my temporary big brother. You pushed me as a chemist to expand my skillset into computational chemistry; you always tried to make me see how talented I am and how I can make it as far on the success ladder as I wanted to go; and you had either a meme or gif to find sarcastic humor for literally every situation in life. You are both an amazing teacher and chemist, and words simply cannot describe how thankful I am for your friendship and getting to work with you while in graduate school.

To the younger generation Machan Lab members, thank you all for joining the party. Emma Cook, Amelia Reid, and Joe Kuehner, you three were awesome to work around. Joe, you are probably one of the smartest and most humble individuals I have ever met. You have a talent of combining superior intelligence and common sense that will guarantee your success no matter what do in life. Emma and Amelia, I have greatly enjoyed teaching and working with both of you over the years and I cannot thank you both enough for just being good individuals to work around. I know we call you two twins and so let's just acknowledge my use of the term "individuals" here. Regardless, you are both, in your own unique and individual ways of course, determined, stubborn, intelligent, and incredibly bright young women. Both of you will be champions of whatever you do and thank you both so very much for allowing me to be included in part of each of your journeys through graduate school.

To the superstar undergraduate student that I had the privilege of working with, Julia Dressel, thank you so much for working with me during your undergraduate career. I never saw myself as a good teacher or mentor. If anything, I think I more frequently saw myself as a bad example for other people in a lot of ways. However, the moment you came into our lab and demonstrated your determination and desire to learn I knew I needed to quickly figure out how to become a teacher/mentor that would stand by your side as you accomplished every goal you set out for yourself. Julia, you are so much smarter than you realize, you have a heart of gold, a determination to be admired, and you are humble beyond belief about it all. You are already an amazing person and scientist, and I am so excited to get to see all the things you will accomplish in the coming years. Thank you so much for letting me be included in your journey as you excelled through your undergraduate career.

To Spenser Simpson, Katy Wilson, Jeff Myers and Jacob Smith of the Harman Lab, thanks for being a lively crew and good lab neighbors over the years. To Xiaofan Jia and Bradley McKeown from the Gunnoe Lab, thanks for also being good lab neighbors and always being there to lend a hand or help me find a chemical over the years. To everyone else in the chemistry department at UVA, thank you for all the support you provided me with while in graduate school. To my committee members, Dr. Brent Gunnoe, Dr. Cassandra Fraser, Dr. Ian Harrison, and Dr. Gaurav Giri, thank you for serving on my committee and supporting me as I pursued this degree.

I have realized over the years that the people you work around have a big impact on your overall experience, but sometimes it takes even more interpersonal relationships to exist to have a real influence on who you are as a person. And if you know me at all you know my family is the biggest influence in my life. I am very fortunate to have gone to graduate school only an hour from home and I boldly admit that I took full advantage and even exploited that geographic utopian situation to the fullest extent. I can say for certainty that being able to drive an hour to my parents house for dinner on a bad day during the week, after a long tiring week in need of a weekend filled with sleeping and eating, or just because I wanted to get away was a big advantage that I would not have completed graduate school without. I have always believed I was the luckiest kid in the world to have parents that easily made Superman and Wonder Woman look subpar. Honestly, my parents are the coolest rockstars I have ever known. Together, they can handle any problem, achieve any goal, and conquer the world while still having time to throw a party before running out of daylight. My parents were the first ones to ever teach me what hard work was. I have watched both my parents work incredibly hard my entire life to make sure my sister and I find our passions in life while also learning to put our faith first, family second, and everything else third. I could not ask for a more loving and supportive family to be a part of in this life and I am incredibly thankful for them each and every day.

My mom, Sherry Hooe (aka Lady or Mimi), is my Lady. Mom, you made me dinners to take back to school every week for five years (to those of you judging me right now, leave me alone because I don't like to cook and I only eat stuff if it tastes good, is bad for me, or is any combination thereof), provided me with only rational insight to situations when I was an emotional cluster (of course no discussion is needed on the details or frequency here), and supported me through all the decisions I made over the years. You are the most determined woman I know and your relentless persistence on making sure your children have access to more than just a high school diploma has taught me the value of education, and how to never take it for granted. Lady, thank you so much for being the toughest momma bear out there and setting an example for how to kick down every door and road block that stands in the way of ones path to success and happiness in life.

My dad, Bill Hooe (aka Budd or Pop), is my Budd. Dad, thank you for just being there. I called you every morning around 6am while I walked to campus for the last five years and there was never a day when you didn't answer the phone after the first or second ring. On the phone, you were always perfectly content to be the talker or the listener depending on what I needed for the day. Whenever I sent a sporadic text letting you know I was on my way home (which you knew was code for "Shelby is all done and coming home with a full head of steam") you were always sure to have a drink and a snack ready for me as I made my way to the couch recliner where you gave me full control of the tv remote. Then, after I had a snack of course, you would always just sit and calmly listen while I vented, screamed, cursed, or threw stuff across the room releasing all my emotions and frustrations. Pop, the size of your heart, your strength, and your influence on my life is immeasurable. You are my father, my coach, my cheerleader, my support system, my friend, and my bestest Budd. Thank you for being the one who always understood me long before I ever understood myself.

To my sister, Samantha Hart (aka Manta) and my brother-in-law, Wally Hart, thank you both for always giving me a place to stay and feeding me when mom and dad were out of town. Manta, thank you for showing me that anything can be overcome in life, and that any accomplishment is within ones reach as long as they posses a relentless will to achieve. To my nephew Dawson, thank you for loving me way to much. I will never forget the night you came into this world. I remember pacing the hospital hallways with Pop for hours, while we anxiously awaited your arrival and found things to mess with in neighboring hospital areas when Mimi wasn’t looking. I remember when I first held you in my arms in the hospital that night and I could not believe that something so tiny could, in a single instant, take my heart by storm and instantly change/restructure every priority I had in my life. I’ll never forget driving back to school right after, at 4am in the morning, unable to stop the tears from streaming down my face. I thought there was something wrong with me, and it wasn’t until I was a couple miles from my apartment that I finally realized that this was the first time I ever cried from being so happy. Dawson, thank for entering my life when you did because it helped me structure my remaining time in graduate school and has been the driving force in helping me find the right career path for myself after graduate school. Also, thank you for picking me as your favorite person that you always want by your side. You love me so much more than I deserve and while that’s a lot of pressure for Aunt Shell, I will never want it any other way.

So now I guess there is just one last individual left to thank for helping me through graduate school. I think its important to point out here that the past five years of graduate school were actually the hardest years of my life thus far, but surprisingly not for any reasons which were related to school or lab. Working in lab was actually the part that was most often fun and kept me sane the past five years. While I have had to overcome a few of life's bigger challenges these past couple years, I can say with certainty that I am beyond blessed to have had someone in my life who supported me everyday, who mentored me as a person and as a chemist, who enthusiastically celebrated all my successes, who helped me identify all my failures and flaws in rationale, and who helped me grow as person more than I could have ever imagined the past five years of my life. To my PI, Charlie Machan, I don't even know where to begin. I know without a doubt there is no other PI at this university, nor in this world, who would have taken the time to handle me and get me through graduate school besides you. Anyone else would have not lasted six months with me before they would have been wise enough to kick me to the curb; I was simply a lot for anyone to handle. Of course I am a peach to work with now, but words simply cannot express how thankful I am that you were willing to take me on as a student in your lab and that you were relentlessly stubborn enough to not only get me through graduate school, but enable me to excel as a person both in and out of the lab far beyond any potential I had ever realized for myself. When I got here to UVA, I believed there was no chance I would be able to keep up and finish with any type of degree. To me (and probably a few others would agree) I was the least qualified, most poorly focused, and worst organized graduate student compared to probably any graduate student there ever was. I had a hard enough time spelling the word efficient, so my capacity to be any type of efficient had long been extinct in my mind. Similarly, I was stubborn in every possible way and let’s just say the thought of thinking through a decision before making one was very foreign to me at one time.

Charlie, in my opinion, you took on one of the biggest challenges any PI could take on for themselves, and that was mentoring me. You took on a student, whose most intelligent thought for the day once fell along the lines of something like what their next tattoo might be and turned them in to a successful chemist who now has the capacity to understand, and sometimes intelligently critique, the work of some of the brightest minds in science. You took on a student who never liked anybody and never wanted to talk to anybody and turned her in to someone who initiates the most intelligent conversation in the room. You took a student who didn’t have the capacity to learn and comprehend in a classroom and figured out how to get her to learn and understand in a capacity she never imagined for herself. You took an angry stubborn student who ignored all her emotions and showed her how to recognize her feelings and process them in a manner that kept her healthy and happy. You took a student who once never felt like they could “fit in” within this world of higher education and made her realize that she could excel as an intelligent mind in this sphere. You took on a student with no confidence in her abilities and showed her how to be not only a successful chemist, but a successful person as well. Charlie, you took me on as a student to mentor in your lab, and I am so happy you did. Thank you so much for helping me realize that I could become anything close to the person I am today. Your impact on my life cannot be measured on any scale and my mind is simply blown away every time I sit and think about how much of a positive influence you were able to input into my life in just five years’ time. Thank you so much for standing by my side and helping me overcome all of life’s challenges these past five years. I have never been as happy for any lasting period of time in my entire life than when working with you in your lab and I have truly loved every second of it. While I think you are a crazy person for sticking with me like you always have (no matter how hard I tried to push you away a couple times) I am forever thankful that you did. You are the coolest, nicest, most fun, energetic, intelligent, enthusiastic person I know and I am so thankful for this rock and roll party we have had these past couple years. You and your wife, Amanda, are truly amazing people, and I cannot wait to see where our journeys take each of us over the coming years.

Table of Contents

Chapter 3: Dioxygen Reduction to Hydrogen Peroxide by a Molecular Mn Complex-Mechanistic Divergence between Homogeneous and Heterogeneous Reductants

List of Abbreviations

Ar	argon
BDFE	bond dissociation free energy
Bpy	2,2’-bipyridine
BQ	*p*-benzoquinone
Co	cobalt
CO	carbon monoxide
CO_2	carbon dioxide
CO2RR	carbon dioxide reduction reaction
CPE	controlled potential electrolysis
Cp^*_2Fc	decamethylferrocene
CV	cyclic voltammetry
Cyclam	1,4,8,11-tetraazacyclotetradecane

DBTD	dibenzothiophene-5,5-dioxide
EPTM	electron-proton transfer mediator
Fc^+/Fc	ferrocenium/ferrocene
Fe	iron
F_5PhOH	pentaflourophenol
$F_5PhOH/F_5[PhO^-]TBA^+$	buffered pentaflourophenol
FOWA	foot of the wave analysis
HAT	hydrogen atom transfer
HOMO	high occupied molecular orbital
H_2O	water
H_2O_2	hydrogen peroxide
H_2Q	hydroquinone
IPCC	Intergovernmental Panel on Climate Change
KC_8	potassium intercalated graphite
KO_2	potassium superoxide
LUMO	lowest unoccupied molecular orbital
O_2	dioxygen
M	transition metal center
MeCN	acetonitrile
Mn	manganese
MnSOD	manganese superoxide dismutase
Ni	nickel
N,N-DMF	*N,N*-dimethylformamide

ORR	oxygen reduction reaction
PCET	proton-coupled electron transfer
PhOH	phenol
RDE	rotating disk electrochemistry
RM	redox mediator
RRDE	rotating ring disk electrochemistry
TBAPF$_6$	tetrabutylammonium hexafluorophosphate
TBACl	tetrabutylammonium chloride
^{tbu}dhbpy(H)$_2$	6,6′-di(3,5-di-*tert*-butyl-2-hydroxybenzene)-2,2′-bipyridine
[^{tbu}dhbpy]$^{2-}$	6,6′-di(3,5-di-*tert*-butyl-2-phenolate)-2,2′-bipyridine
TFEOH	2,2,2-triflouroethanol
THF	tetrahydrofuran
TOF	turnover frequency
TON	turnover number
TMP	tetramesitylporphyrin
TPP	tetraphenylporphyrin
TTBP	2,4,6-tri-*tert*-butylphenol
UNEP	United Nations Environment Programme
WMO	World Meteorological Organization
2-NO$_2$-PhOH	2-nitrophenol
4-CF$_3$-PhOH	4-trifluoromethylphenol

List of Figures

Figure 2.5.7. Plot of $E_{1/2}$ for Mn(^{tbu}dhbpy)Cl **1** against the log of the ratio of [PhO$^-$]/[PhOH] showing the the effects of fixed PhO$^-$ concentration with increasing PhOH concentration on $E_{1/2}$.

Figure 2.5.8. CVs of Mn(^{tbu}dhbpy)Cl **1** with buffered F_5PhOH.

Figure 2.5.9. Simulated catalytic Tafel plots comparing Mn(^{tbu}dhbpy)Cl **1** to literature values for O_2 to H_2O_2 reduction by molecular species.

Figure 2.6.10. A potential-p*K*$_a$ diagram for acids from p*K*$_a$ = 12.65 to 29.14.

Figure 2.7.11. UV−vis spectra of the as prepared chemically reduced [Mn(tbudhbpy)]^0 before and after the introduction of atmospheric air.

Figure S2.3.1. UV-vis serial dilution absorbance data obtained from Mn(^{tbu}dhbpy)Cl **1** in MeCN solution.

Figure S2.3.2. ^{1}H NMR of ^{tbu}dhbpy ligand.

Figure S2.3.3. ^{13}C{^{1}H} NMR of ^{tbu}dhbpy ligand.

Figure S2.3.4. ESI-MS of Mn(^{tbu}dhbpy)Cl **1**.

Figure S2.3.5. Kohn-Sham Orbital projections of the HOMO and LUMO of computational model Mn(dhbpy)Cl.

Figure S2.4.6. CV of Mn(^{tbu}dhbpy)Cl **1**, obtained under Ar saturation conditions.

Figure S2.4.7. Linear Fit of variable scan rate data from **Figure S2.4.6** demonstrating that Mn(^{tbu}dhbpy)Cl **1** shows a diffusion-limited current response.

Figure S2.4.8. Diagram showing the Nernstian voltage dependence of Mn(^{tbu}dhbpy)Cl **1** on the concentration of PhOH in MeCN at the first reduction under Ar saturation.

Figure S2.4.9. CVs of Mn(^{tbu}dhbpy)Cl **1**, obtained under Ar saturation conditions with 0.05 M TBACl with increasing scan rates.

Figure S2.4.10. Linear Fit of variable scan rate data from demonstrating that Mn(^{tbu}dhbpy)Cl **1** shows a diffusion-limited response with 0.05 M TBACl added.

Figure S2.4.11. CVs of Mn(^{tbu}dhbpy)Cl **1**, obtained under Ar saturation conditions and 0.05 M TBACl.

Figure S2.4.12. CVs of Mn(^{tbu}dhbpy)Cl 1, obtained under Ar saturation conditions comparing the effects of PhOH and TBACl separately.

Figure S2.4.13. CVs of Mn(^{tbu}dhbpy)Cl **1**, obtained under Ar saturation conditions and O_2 saturation conditions.

Figure S2.4.14. CVs showing O_2 and O_2 and PhOH control responses.

Figure S2.4.15. CVs of Mn(^{tbu}dhbpy)Cl **1**, obtained under O_2 saturation conditions with variable PhOH concentration.

Figure S2.4.16. Log-log plot from data obtained from CVs of Mn(^{tbu}dhbpy)Cl **1** (1 mM) with variable PhOH concentrations and O_2 saturation.

Figure S2.4.17. CVs of Mn(^{tbu}dhbpy)Cl **1**, obtained under variable O_2 concentration with 0.5 M PhOH.

Figure S2.4.18. Log-log plot from data obtained from CVs of Mn(^{tbu}dhbpy)Cl **1** (1 mM) under variable O_2 concentration conditions with 0.5 M PhOH.

Figure S2.4.19. CVs of Mn(^{tbu}dhbpy)Cl **1** at variable concentrations, obtained under O_2 saturation with 0.11 M PhOH.

Figure S2.4.20. Log-log plot from data obtained from CVs of Mn(^{tbu}dhbpy)Cl **1** under variable concentration conditions with 0.11 M PhOH and O_2 saturation.

Figure S2.4.21. CVs of Mn(^{tbu}dhbpy)Cl 1, obtained under O_2 saturation conditions comparing the effects of PhOH and TBACl.

Figure S2.4.22. Log-log plot from data obtained from CVs of Mn(^{tbu}dhbpy)Cl 1 (1 mM) at 0.5 M PhOH with variable TBACl concentration and O_2 saturation.

Figure S2.4.23. CVs of Mn(^{tbu}dhbpy)[OTf] (1 mM), obtained under O_2 saturation with variable PhOH concentrations.

Figure S2.4.24. Diagram showing the Nernstian voltage dependence of Mn(^{tbu}dhbpy)[OTf] on the concentration of PhOH in MeCN at the first reduction under Ar saturation.

Figure S2.4.25. CVs of Mn(^{tbu}dhbpy)[OTf] (1 mM), obtained under O_2 saturation with variable PhOH concentrations.

Figure S2.4.26. Log-log plot from data obtained from CVs of Mn(^{tbu}dhbpy)[OTf] (1 mM) with varied PhOH concentration under O_2 saturation conditions.

Figure S2.4.27. CVs of Mn(^{tbu}dhbpy)Cl **1**, obtained under O_2 saturation conditions with variable PhOH concentration (A) and a highlight of the phenolate oxidation feature (B).

Figure S2.4.28. CVs showing O_2 and O_2 and TFE control responses.

Figure S2.4.29. CVs of Mn(^{tbu}dhbpy)Cl **1**, obtained under Ar saturation with variable TFE concentrations.

Figure S2.4.30. Diagram showing the voltage dependence of Mn(^{tbu}dhbpy)Cl **1** at the first reduction on the log of the concentration of TFE under Ar saturation.

Figure S2.4.31. CVs of Mn(^{tbu}dhbpy)Cl **1**, obtained under O_2 saturation with variable TFE concentrations.

Figure S2.4.32. CVs of Mn(^{tbu}dhbpy)Cl **1**, obtained under O_2 saturation with variable TFE concentrations.

Figure S2.4.33. Log-log plot from data obtained from CVs of Mn(^{tbu}dhbpy)Cl **1** (1 mM) with variable TFE concentrations and O_2 saturation.

Figure S2.4.34. CVs of Mn(^{tbu}dhbpy)Cl **1**, obtained under variable O_2 concentrations with 3.0 M TFE.

Figure S2.4.35. Log-log plot from data obtained from CVs of Mn(^{tbu}dhbpy)Cl **1** (1 mM) with variable O_2 concentration and 3.0 M TFE.

Figure S2.4.36. CVs of Mn(^{tbu}dhbpy)Cl **1** at variable concentrations, obtained at O_2 saturation with 1.0 M TFE.

Figure S2.4.37. Log-log plot from data obtained from CVs of Mn(^{tbu}dhbpy)Cl **1** at variable concentrations, obtained at O_2 saturation with 1 M TFE.

Figure S2.4.38. CVs of Mn(^{tbu}dhbpy)Cl **1** (0.5 mM), obtained under Ar saturation with variable TFE concentrations.

Figure S2.4.39. Diagram showing the voltage dependence of Mn(^{tbu}dhbpy)Cl **1** at the first reduction on the log of the concentration of TFE under Ar saturation.

Figure S2.4.40. CVs of Mn(^{tbu}dhbpy)Cl **1** (0.5 mM), obtained under O_2 saturation with variable TFE concentrations.

Figure S2.4.41. Log-log plot from data obtained from CVs of Mn(^{tbu}dhbpy)Cl **1** (0.5 mM) with variable TFE concentrations and O_2 saturation.

Figure S2.4.42. CVs of Mn(^{tbu}dhbpy)Cl **1**, obtained under O_2 saturation with variable H_2O concentrations.

Figure S2.4.43. Linear Sweep Voltammograms of RRDE experiment Mn(^{tbu}dhbpy)Cl **1** at various rotation rates with 0.25 mM catalyst concentration and 0.6 M TFE concentration under argon saturation conditions; ring potential = 1.2 V vs Ag/AgCl.

Figure S2.4.44. Levich plot from data obtained from Linear Sweep Voltammograms of Mn(^{tbu}dhbpy)Cl **1** (0.25 mM) by RRDE with 0.6 M TFE under argon saturation conditions at various rotation rates.

Figure S2.4.45. Koutecky-Levich plot from data obtained from Linear Sweep Voltammograms of Mn(^{tbu}dhbpy)Cl **1** by RRDE with 0.6 M TFE under argon saturation conditions at various rotation rates.

Figure S2.4.46. Linear Sweep Voltammograms of RRDE experiment Mn(^{tbu}dhbpy)Cl **1** (0.25 mM) at various rotation rates with 0.6 M TFE concentration under O_2 saturation conditions; ring potential = 1.2 V vs Ag/AgCl.

Figure S2.4.47. Levich plot from data obtained from Linear Sweep Voltammograms of Mn(^{tbu}dhbpy)Cl **1** (0.25 mM) by RRDE with 0.6 M TFE under O_2 saturation conditions at various rotation rates.

Figure S2.4.48. Koutecky-Levich plot from data obtained from Linear Sweep Voltammograms of Mn(^{tbu}dhbpy)Cl **1** (0.25 mM) by RRDE with 0.6 M TFE under O_2 saturation conditions at various rotation rates.

Figure S2.4.49. Linear Sweep Voltammograms of RRDE experiment Mn(^{tbu}dhbpy)Cl **1** (0.25 mM) at various rotation rates with 0.45 M TFE concentration under argon saturation conditions; ring potential = 1.2 V vs Ag/AgCl.

Figure S2.4.50. Levich plot from data obtained from Linear Sweep Voltammograms of Mn(^{tbu}dhbpy)Cl **1** (0.25 mM) by RRDE with 0.45 M TFE under argon saturation conditions at various rotation rates.

Figure S2.4.51. Koutecky-Levich plot from data obtained from Linear Sweep Voltammograms of Mn(^{tbu}dhbpy)Cl **1** (0.25 mM) by RRDE with 0.45 M TFE under argon saturation conditions at various rotation rates.

Figure S2.4.52. Linear Sweep Voltammograms of RRDE experiments with Mn(^{tbu}dhbpy)Cl **1** (0.25 mM) at various rotation rates with 0.45 M TFE concentration under O_2 saturation conditions; ring potential = 1.2 V vs Ag/AgCl.

Figure S2.4.53. Levich plot from data obtained from Linear Sweep Voltammograms of Mn(^{tbu}dhbpy)Cl **1** (0.25 mM) by RRDE with 0.45 M TFE under O_2 saturation conditions at various rotation rates.

Figure S2.4.54. Koutecky-Levich plot from data obtained from Linear Sweep Voltammograms of Mn(^{tbu}dhbpy)Cl **1** (0.25 mM) by RRDE with 0.45 M TFE under O_2 saturation conditions at various rotation rates.

Figure S2.4.55. Linear Sweep Voltammograms of RDE experiment Mn(^{tbu}dhbpy)Cl **1** at various rotation rates under argon saturation.

Figure S2.4.56. Levich plot from data obtained from Linear Sweep Voltammograms of Mn(^{tbu}dhbpy)Cl **1** under argon saturation conditions at various rotation rates by RDE.

Figure S2.4.57. Koutecky-Levich plot from data obtained from Linear Sweep Voltammograms of Mn(^{tbu}dhbpy)Cl **1** under argon saturation conditions at various rotation rates by RDE.

Figure S2.4.58. Linear Sweep Voltammograms of RDE experiment Mn(^{tbu}dhbpy)Cl **1** at various rotation rates with 0.5 M PhOH under argon saturation.

Figure S2.4.59. Levich plot from data obtained from Linear Sweep Voltammograms of Mn(^{tbu}dhbpy)Cl **1** with 0.5 M PhOH under argon saturation conditions at various rotation rates by RDE.

Figure S2.4.60. Koutecky-Levich plot from data obtained from Linear Sweep Voltammograms of Mn(^{tbu}dhbpy)Cl **1** with 0.5 M PhOH under argon saturation conditions at various rotation rates by RDE.

Figure S2.4.61. Linear Sweep Voltammograms of RDE experiment Mn(^{tbu}dhbpy)Cl **1** at various rotation rates with 0.5 M PhOH under O_2 saturation.

Figure S2.4.62. Levich plot from data obtained from Linear Sweep Voltammograms of Mn(^{tbu}dhbpy)Cl **1** with 0.5 M PhOH under O_2 saturation conditions at various rotation rates by RDE.

Figure S2.4.63. Koutecky-Levich plot from data obtained from Linear Sweep Voltammograms of Mn(^{tbu}dhbpy)Cl **1** with 0.5 M PhOH under O_2 saturation conditions at various rotation rates by RDE.

Figure S2.5.64. Pourbaix diagram from data obtained from CVs of Mn(^{tbu}dhbpy)Cl **1** obtained under Ar saturation conditions comparing the effects of different buffered proton sources.

Figure S2.5.65. Mn(^{tbu}dhbpy)Cl **1** and Mn(^{tbu}dhbpy)[OTf] under Ar with 0.015 M TBA[PhO]; the $E_{1/2}$ values with are -0.84 V and -0.86 V vs Fc/Fc$^+$, respectively.

Figure S2.5.66. Mn(^{tbu}dhbpy)Cl **1** under Ar and Ar with 0.04 M PhOH buffer (TBA[PhO]/PhOH); the $E_{1/2}$ value with buffer is -0.73 V vs Fc/Fc$^+$.

Figure S2.5.67. Mn(^{tbu}dhbpy)[OTf] under Ar and Ar with 0.04 M PhOH buffer (TBA[PhO]/PhOH); the $E_{1/2}$ value with buffer is -0.72 V vs Fc/Fc$^+$, respectively.

Figure S2.5.68. CVs of Mn(^{tbu}dhbpy)Cl 1 (black) and Mn(^{tbu}dhbpy)[OTF] (red), obtained under Ar saturation conditions comparing the effects of PhOH Buffer.

Figure S2.5.69. CVs of Mn(^{tbu}dhbpy)Cl **1** showing the effect of TBA[PhO] titration to a fixed concentration of PhOH.

Figure S2.5.70. Plot of $E_{1/2}$ for Mn(^{tbu}dhbpy)Cl 1 against the log of the ratio of [PhO$^{–}$]/[PhOH] showing the the effects of fixed PhOH concentration with increasing PhO$^{–}$ concentration on $E_{1/2}$.

Figure S2.5.71. CVs of Mn(^{tbu}dhbpy)[OTf] showing the effect of PhOH titration to a fixed concentration of PhO$^{–}$.

Figure S2.5.72. Plot of $E_{1/2}$ for Mn(^{tbu}dhbpy)[OTf] against the log of the ratio of [PhO$^{–}$]/[PhOH] showing the the effects of fixed PhO$^{–}$ concentration with increasing PhOH concentration on $E_{1/2}$.

Figure S2.5.73. CVs of Mn(^{tbu}dhbpy)[OTf] showing the effect of TBA[PhO] titration to a fixed concentration of PhOH.

Figure S2.5.74. Plot of $E_{1/2}$ for Mn(^{tbu}dhbpy)[OTf] against the log of the ratio of [PhO$^{–}$]/[PhOH] showing the the effects of fixed PhOH concentration with increasing TBA[PhO] concentration on $E_{1/2}$.

Figure S2.5.75. CVs of Mn(^{tbu}dhbpy)Cl **1** with buffered PhOH under Ar saturation, Ar saturation with 0.0803 M PhOH buffer, and O_2 saturation with 0.0803 M PhOH buffer demonstrating minimal activity for oxygen reduction.

Figure S2.5.76. Selected CV traces with buffered F_5PhOH under Ar and O_2 saturation in comparison to the CV response of **1** Mn(^{tbu}dhbpy)Cl under Ar only.

Figure S2.5.77. Additional CV traces with buffered F_5PhOH under Ar saturation compared to **1** Mn(^{tbu}dhbpy)Cl under Ar saturation only.

Figure S2.5.78. Additional CV traces with buffered F_5PhOH under O_2 saturation compared to **1** Mn(^{tbu}dhbpy)Cl under Ar saturation only.

Figure S2.5.79. Relevant portions of the CV traces used for FOWA analysis with 11 mM buffered F_5PhOH under Ar and O_2 saturation with Mn(^{tbu}dhbpy)Cl **1** that have been adjusted to identical non-zero values in the pre-catalytic wave region.

Figure S2.5.80. Full and linear fit region used in foot-of-the-wave analysis of **1**.

Figure S2.5.81. Selected CV traces with buffered F_5PhOH under Ar and O_2 saturation in comparison to the CV response of [Mn(^{tbu}dhbpy)][OTf] under Ar only.

Figure S2.5.82. Selected CV traces with buffered F_5PhOH under Ar and O_2 saturation in comparison to the CV response of [Mn(^{tbu}dhbpy)][OTf] under Ar only.

Figure S2.5.83. Full and linear fit region used in foot-of-the-wave analysis of [Mn(^{tbu}dhbpy)][OTf].

Figure S2.6.84. CVs of Mn(^{tbu}dhbpy)Cl **1** used to potential-pKa diagram.

Figure S2.7.85. UV-vis spectra of the chemically reduced [Mn(^{tbu}dhbpy)]^0 after the introduction of atmospheric air overlaid with a normalized absorbance spectrum of the starting material **1** Mn(^{tbu}dhbpy)Cl.

Figure S2.7.86. Summary of stopped-flow spectrochemical experiments with [Mn(^{tbu}dhbpy)]^0 at 20.4°C in MeCN.

Figure S2.7.87. UV-vis spectra of the as chemically reduced [Mn(^{tbu}dhbpy)]^0 before and after the introduction of atmospheric air in MeCN in comparison to the starting material.

Figure S3.3.2. The calculated R_{fit}/η_{cat} from stopped-flow spectrochemical experiments with PhOH, Cp_2^*Fe and Mn(^{tbu}dhbpy)Cl with varying O_2 concentration at 25.5°C in MeCN.

Figure S3.3.3. The calculated k_{obs} from stopped-flow spectrochemical experiments with PhOH, O_2 and Cp_2^*Fe with varying Mn(^{tbu}dhbpy)Cl concentration at 25.5°C in MeCN.

Figure S3.3.4. The calculated k_{obs} from stopped-flow spectrochemical experiments with O_2, Cp_2^*Fe and Mn(^{tbu}dhbpy)Cl with varying PhOH concentration at 25.5°C in MeCN.

Figure S3.3.5. The calculated k_{obs} from stopped-flow spectrochemical experiments with 0.1 M $TBAPF_6$, O_2, Mn(^{tbu}dhbpy)Cl and PhOH with varying Cp_2^*Fe concentration at 25.5°C in MeCN.

Figure S3.3.6. The calculated R_{fit}/η_{cat} from stopped-flow spectrochemical experiments with 0.1 M $TBAPF_6$, Cp_2^*Fe, Mn(^{tbu}dhbpy)Cl and PhOH with varying O_2 concentration at 25.5°C in MeCN.

Figure S3.3.7. The calculated k_{obs} from stopped-flow spectrochemical experiments with 0.1 M $TBAPF_6$, O_2, Cp_2^*Fe and PhOH with varying Mn(^{tbu}dhbpy)Cl concentration at 25.5°C in MeCN.

Figure S3.3.8. The calculated k_{obs} from stopped-flow spectrochemical experiments with 0.1 M $TBAPF_6$, Cp_2^*Fe, Mn(^{tbu}dhbpy)Cl and O_2 with varying PhOH concentration at 25.5°C in MeCN.

Figure S3.3.9. Eyring plot of the stopped-flow data spectrochemical experiments with Mn(^{tbu}dhbpy)Cl in MeCN with PhOH.

Figure S3.3.10. Eyring plot of the stopped-flow data spectrochemical experiments with Mn(^{tbu}dhbpy)Cl with 0.1 M $TBAPF_6$ in MeCN with PhOH.

Figure S3.3.11. UV-Visible spectra for Ti(O)SO_4-based detection of varying H_2O_2 concentrations. Calibration curve from data.

Figure S3.3.12. UV-visible spectra for the detection of H_2O_2 from O_2 reduction using Cp_2*Fc as a chemical reductant and treatment with Ti(O)SO_4.

Figure S3.5.13. UV-visible spectra for the detection of H_2O_2 from O_2 reduction using Cp_2*Fc as a chemical reductant and treatment with Ti(O)SO_4.

Figure S3.5.14. UV-visible spectra for the detection of H_2O_2 from O_2 reduction using Cp_2*Fc as a chemical reductant and treatment with Ti(O)SO_4.

Figure S3.5.15. UV-visible spectra for the detection of H_2O_2 from O_2 reduction using Cp_2*Fc as a chemical reductant and treatment with Ti(O)SO_4.

Figure S3.4.16. Plot of E_p versus log (v) (mV/s), comparing buffered and unbuffered conditions under Ar saturation. Values from the aprotic response under O_2 also included.

Figure S3.4.17. CVs of Mn(^{tbu}dhbpy)Cl **1**, obtained under Ar saturation conditions with 10 mM F_5PhOH Buffer.

Figure S3.4.18. CVs of Mn(^{tbu}dhbpy)Cl **1**, obtained under O_2 saturation conditions with 10 mM F_5PhOH Buffer.

Figure S3.4.19. CVs of Mn(^{tbu}dhbpy)Cl **1**, obtained under Ar saturation conditions with 10 mM 2-NO_2-PhOH Buffer.

Figure S3.4.20. CVs of Mn(^{tbu}dhbpy)Cl **1**, obtained under O_2 saturation conditions with 10 mM 2-NO_2-PhOH Buffer.

Figure S3.4.21. CVs of Mn(^{tbu}dhbpy)Cl **1**, obtained under Ar saturation conditions with 10 mM 4-CF_3-PhOH Buffer.

Figure S3.4.22. CVs of Mn(^{tbu}dhbpy)Cl **1**, obtained under O_2 saturation conditions with 10 mM 4-CF_3-PhOH Buffer.

Figure S3.4.23. Plots of **(A)** TOF vs scan rate and **(B)** i_{cat}/i_p vs the inverse of the square root of the scan rate for Mn(^{tbu}dhbpy)Cl **1**, with F_5PhOH buffer, 2-NO_2-PhOH Buffer, and 4-CF_3-PhOH Buffer from data in **Figures S17-S21**.

Figure S3.5.24. The calculated k_{obs} from stopped-flow spectrochemical experiments with 0.1 M $TBAPF_6$, F_5PhOH Buffer, O_2 and Mn(^{tbu}dhbpy)Cl with varying Cp_2^*Fe concentration at 25.5°C in MeCN.

Figure S3.5.25. The calculated R_{fit}/η_{cat} from stopped-flow spectrochemical experiments with 0.1 M $TBAPF_6$, F_5PhOH Buffer, Cp_2^*Fe and Mn(^{tbu}dhbpy)Cl with varying O_2 concentration at 25.5°C in MeCN.

Figure S3.5.26. The calculated k_{obs} from stopped-flow spectrochemical experiments with 0.1 M $TBAPF_6$, F_5PhOH Buffer, O_2 and Cp_2^*Fe with varying Mn(^{tbu}dhbpy)Cl concentration at 25.5°C in MeCN.

Figure S3.5.27. The calculated k_{obs} from stopped-flow spectrochemical experiments with 0.1 M $TBAPF_6$, Mn(^{tbu}dhbpy)Cl, O_2 and Cp_2^*Fe with varying F_5PhOH Buffer concentration at 25.5°C in MeCN.

Figure S3.5.28. The calculated k_{obs} from stopped-flow spectrochemical experiments with 0.1 M $TBAPF_6$, 2-NO_2-PhOH Buffer, O_2 and Mn(^{tbu}dhbpy)Cl with varying Cp_2^*Fe concentration at 25.5°C in MeCN.

Figure S3.5.29. The calculated R_{fit}/η_{cat} from stopped-flow spectrochemical experiments with 0.1 M $TBAPF_6$, 2-NO_2-PhOH Buffer, Cp_2^*Fe and Mn(^{tbu}dhbpy)Cl with varying O_2 concentration at 25.5°C in MeCN.

Figure S3.5.30. The calculated k_{obs} from stopped-flow spectrochemical experiments with 0.1 M $TBAPF_6$, 2-NO_2-PhOH Buffer, O_2 and Cp_2^*Fe with varying Mn(^{tbu}dhbpy)Cl concentration at 25.5°C in MeCN.

Figure S3.5.31. The calculated k_{obs} from stopped-flow spectrochemical experiments with 0.1 M $TBAPF_6$, Mn(^{tbu}dhbpy)Cl, O_2 and Cp_2^*Fe with varying 2-NO_2-PhOH Buffer concentration at 25.5°C in MeCN.

Figure S3.5.32. The calculated k_{obs} from stopped-flow spectrochemical experiments with 0.1 M $TBAPF_6$, 4-CF_3-PhOH Buffer, O_2 and Mn(^{tbu}dhbpy)Cl with varying Cp_2^*Fe concentration at 25.5°C in MeCN.

Figure S3.5.33. The calculated $R_{\mathrm{fit}}/\eta_{\mathrm{cat}}$ from stopped-flow spectrochemical experiments with 0.1 M $TBAPF_6$, 4-CF_3-PhOH Buffer, Cp_2^*Fe and Mn(^{tbu}dhbpy)Cl with varying O_2 concentration at 25.5°C in MeCN.

Figure S3.5.34. The calculated k_{obs} from stopped-flow spectrochemical experiments with 0.1 M $TBAPF_6$, 4-CF_3-PhOH Buffer, O_2 and Cp_2^*Fe with varying Mn(^{tbu}dhbpy)Cl concentration at 25.5°C in MeCN.

Figure S3.5.35. The calculated k_{obs} from stopped-flow spectrochemical experiments with 0.1 M $TBAPF_6$, Mn(^{tbu}dhbpy)Cl, O_2 and Cp_2^*Fe with varying 4-CF_3-PhOH Buffer concentration at 25.5°C in MeCN.

Figure S3.5.36. Eyring plots of the stopped-flow data spectrochemical experiments with Mn(^{tbu}dhbpy)Cl with 0.1 M $TBAPF_6$ in MeCN with F_5PhOH buffer.

Figure S3.5.37. Eyring plots of the stopped-flow data spectrochemical experiments with Mn(^{tbu}dhbpy)Cl with 0.1 M $TBAPF_6$ in MeCN with 2-NO_2-PhOH buffer.

Figure S3.5.38. Eyring plots of the stopped-flow data spectrochemical experiments with Mn(^{tbu}dhbpy)Cl with 0.1 M TBAPF$_6$ in MeCN with 4-CF$_3$-PhOH buffer.

Figure S3.6.39. The calculated k_{obs} from stopped-flow spectrochemical experiments with 0.1 M TBAPF$_6$, TTBP, O$_2$ and Mn(^{tbu}dhbpy)Cl with varying Cp$_2^*$Fe concentration at 25.5°C in MeCN.

Figure S3.6.40. The calculated R$_{fit}$/η$_{cat}$ from stopped-flow spectrochemical experiments with 0.1 M TBAPF$_6$, TTBP, Cp$_2^*$Fe and Mn(^{tbu}dhbpy)Cl with varying O$_2$ concentration at 25.5°C in MeCN.

Figure S3.6.41. The calculated k_{obs} from stopped-flow spectrochemical experiments with 0.1 M TBAPF$_6$, TTBP, O$_2$ and Cp$_2^*$Fe with varying Mn(^{tbu}dhbpy)Cl concentration at 25.5°C in MeCN.

Figure S3.6.42. The calculated k_{obs} from stopped-flow spectrochemical experiments with 0.1 M TBAPF$_6$, Mn(^{tbu}dhbpy)Cl, O$_2$ and Cp$_2^*$Fe with varying TTBP concentration at 25.5°C in MeCN.

Figure S3.6.43. Eyring plots of the stopped-flow data spectrochemical experiments with Mn(^{tbu}dhbpy)Cl with 0.1 M TBAPF$_6$ in MeCN with TTBP.

Figure S3.6.44. Stopped-Flow CCD data of 2,4,6-tritertbutylphenol radical appearance over 1000 seconds.

Figure S3.6.45. Stopped-Flow data comparing the appearance of decamethylferricenium and 2,4,6-tritertbutylphenoxyl radical at 778 and 626 nm, respectively.

Figure S3.9.46. ^{1}H NMR 2-NO$_2$-PhOH Buffer; d_1-CDCl$_3$; 600 MHz Varian.

Figure S3.9.47. ^{1}H NMR F$_5$PhOH-PhOH Buffer; d_1-CDCl$_3$; 600 MHz Varian.

Figure S3.9.48. ^{1}H NMR 4-CF$_3$-PhOH Buffer; d_1-CDCl$_3$; 600 MHz Varian.

Figure S3.9.49. Stopped-flow data spectrochemical experiment sample series of five shots and the average of that series with Mn(^{tbu}dhbpy)Cl in MeCN.

Figure S3.9.50. Stopped-flow data spectrochemical experiment sample series of five shots and the average of that serieswith Mn(^{tbu}dhbpy)Cl in MeCN with 0.1 M TBAPF$_6$.

Figure S3.9.51. Stopped-flow data spectrochemical experiment sample series of five shots and the average of that series with Mn(^{tbu}dhbpy)Cl in MeCN.

Figure S3.9.52. Stopped-flow data spectrochemical experiment sample series of five shots and the average of that series with Mn(^{tbu}dhbpy)Cl in MeCN with 0.1 M TBAPF$_6$.

Figure S3.9.53. Stopped-flow data spectrochemical experiment sample series of five shots and the average of that series with Mn(^{tbu}dhbpy)Cl in MeCN with 0.1 M TBAPF$_6$.

Figure S3.9.54. Stopped-flow data spectrochemical experiment sample series of five shots and the average of that series with Mn(^{tbu}dhbpy)Cl in MeCN with 0.1 M TBAPF$_6$.

Figure S3.9.55. Stopped-flow data spectrochemical experiment sample series of five shots and the average of that series with Mn(^{tbu}dhbpy)Cl in MeCN with 0.1 M TBAPF$_6$.

Figure S3.9.56. Stopped-flow data spectrochemical experiment sample series of five shots and the average of that series with Mn(^{tbu}dhbpy)Cl in MeCN with 0.1 M TBAPF$_6$.

Figure S3.9.57. CVs of Mn(^{tbu}dhbpy)Cl **1**, obtained under Ar saturation conditions.

Figure S3.9.58. CVs of Mn(^{tbu}dhbpy)Cl **1**, obtained under O$_2$ saturation conditions. Conditions: 0.5 mM analyte; glassy carbon working electrode, glassy carbon counter electrode, Ag/AgCl pseudoreference electrode; varied scan rate; referenced to internal ferrocene standard.

Figure 4.3.1. Molecular structure of Cr(^{tbu}dhbpy)Cl(H$_2$O) **2**.

Figure S4.3.6. CVs of Cr(^{tbu}dhbpy)Cl(H_2O) at variable scan rates ranging from 25 to 5000 mV/s, obtained under Ar saturation conditions. Linear Fit of variable scan rate data from demonstrating that Cr(^{tbu}dhbpy)Cl(H_2O) shows a diffusion-limited current response.

Figure S4.3.7. CVs of Cr(^{tbu}dhbpy)Cl(H_2O) at variable scan rates ranging from 25 to 5000 mV/s, obtained under CO_2 saturation. Linear Fit of variable scan rate data from demonstrating that Cr(^{tbu}dhbpy)Cl(H_2O) shows a diffusion-limited current response.

Figure S4.3.8. CVs of Cr(^{tbu}dhbpy)Cl(H_2O), obtained under CO_2 saturation conditions with variable PhOH concentration. Log-log plot from data obtained from CVs of Cr(^{tbu}dhbpy)Cl(H_2O) (1.0 mM) with variable PhOH concentrations under CO_2 saturation.

Figure S4.3.9. CVs of Cr(^{tbu}dhbpy)Cl(H_2O) at variable concentrations, obtained under CO_2 saturation with 0.316 M PhOH. Log-log plot from data obtained from CVs of Cr(^{tbu}dhbpy)Cl(H_2O) under variable concentration conditions with 0.321 M PhOH under CO_2 saturation.

Figure S4.3.10. Current versus time trace from bulk electrolysis experiment. Charge passed versus time for the bulk electrolysis experiment.

Figure S4.3.11. GC calibration curve for the quantification of CO and H_2.

Figure S4.3.12. Results of rinse test bulk electrolysis post experiment shown in **Figure S4.3.10**. Current versus time trace from bulk electrolysis experiment. Charge passed versus time for the bulk electrolysis experiment.

Figure S4.3.13. Control bulk electrolysis without Cr(^{tbu}dhbpy)Cl(H_2O) present.

Figure S4.3.14. CVs from rinse test to check for possible adsorption from electrochemistry with Cr(^{tbu}dhbpy)Cl(H_2O).

Figure S4.3.15. CVs of the Cr(salen)Cl under various conditions for a comparative analysis to Cr(^{tbu}dhbpy)Cl(H_2O).

Figure S4.3.16. CVs of the Cr(bpy)$(CO)_4$ under various conditions for a comparative analysis to Cr(^{tbu}dhbpy)Cl(H_2O).

Figure S4.3.17. Current versus time trace from bulk electrolysis experiment. Charge passed versus time for the bulk electrolysis experiment.

Figure S4.3.18. Current versus time trace from bulk electrolysis experiment. Charge passed versus time for bulk electrolysis experiment.

Figure S4.3.19. CVs of Cr(^{tbu}dhbpy)Cl(H_2O) with 0.34 M PhOH at variable scan rates ranging from 25 to 5000 mV/s, obtained under Ar and CO_2 saturation conditions.

Figure S4.3.20. Plots of i_{cat}/i_p versus the inverse of the square root of the scan rate and TOF versus scan rate for Cr(^{tbu}dhbpy)Cl(H_2O), with 0.34 M PhOH from data in **Figure S4.3.19**.

Figure S4.3.21. CVs of Cr(^{tbu}dhbpy)Cl(H_2O) at variable scan rates ranging from 25 to 5000 mV/s, obtained under Ar saturation conditions with 40.3 mM TBACl both with and without 0.34 M PhOH.

Figure S4.3.22. Comparison of simulated and experimental CV data with 1.0 mM Cr(^{tbu}dhbpy)Cl(H_2O), obtained under CO_2 saturation conditions with 0.341 M PhOH concentration at scan rates of 50, 75, 200, and 300 mV/s.

Figure S4.3.23. Comparison of CVs under Ar and CO saturation conditions. Comparison of CVs under Ar and CO saturation conditions with 0.22 M PhOH.

Figure S4.4.24. Overlays of experimental versus simulated data of the second reduction of Cr(^{tbu}dhbpy)Cl(H_2O) with 0.157 M, 0.272 M, and 0.382 M PhOH under CO_2 saturation conditions.

Figure S4.3.25. Plot of log[k_2(s^{-1})] (apparent turnover frequency calculated from the simulated second-order rate constants) versus log[PhOH] from simulated data in **Figure S4.4.24**.

Figure S4.3.26. Control CV data. Comparison of CVs under Ar and Ar with PhOH. Comparison of CVs under CO_2 and CO_2 with PhOH.

Figure 5.2.1. Comparison of product selectivity in previous versus current work with Mn(^{tbu}dhbpy)Cl **1** to summarize the overall co-electrocatalytic effect of BQ.

Figure 5.3.2. CVs of TFEOH titration with 0.5 mM BQ obtained under Ar saturation conditions.

Figure 5.4.3. CVs comparing the effects of Mn(^{tbu}dhbpy)Cl **1**, TFEOH, and BQ.

Figure 5.5.4. The observed relationship between the concentration of added BQ and the reaction product as characterized by RRDE.

Figure S5.3.1. Coulometry experiment with 2.5 mM BQ in an MeCN solution under N_2 saturation conditions. The analyte solution volume was 25 mL, containing a total of 6.25 x 10^{-5} moles of BQ and passing a total of 9.7 C of charge.

Figure S5.3.2. ^{1}H NMR of an authentic BQ sample taken prior to coulometry experiment in **Figure S5.3.1** under an atmosphere of N_2.

Figure S5.3.3. ^{1}H NMR spectrum of an authentic $[BQ]^{2-}$ sample taken after coulometry experiment in **Figure S5.3.1** under an atmosphere of N_2.

Figure S5.3.4. CVs of TFEOH titration with 2.5 mM BQ obtained under Ar saturation conditions. Linear fit of -$E_{1/2}$ versus log[TFEOH (M)] for the two-electron BQ reduction feature observed between –0.75 and –0.86 V vs. Fc^+/Fc obtained from CV titration data.

Figure S5.3.5. CVs with 2.5 mM BQ with variable TFEOH concentration under Ar and O_2 saturation conditions.

Figure S5.4.6. Coulometry experiment with 2.5 mM BQ and 1.37 M TFEOH in an MeCN solution under N_2 saturation conditions.

Figure S5.4.7. ^1H NMR taken after coulometry experiment with 2.5 mM BQ and 1.37 M TFEOH under an atmosphere of N_2.

Figure S5.4.8. ^1H NMR taken of a solution with 2.5 mM H_2Q and 1.37 M TFEOH under an atmosphere of N_2.

Figure S5.4.9. Control ^1H NMR of BQ in CD_3CN under an N_2 atmosphere.

Figure S5.4.10. Control ^1H NMR of H_2Q in CD_3CN under an N_2 atmosphere.

Figure S5.4.11. Control ^1H NMR of quinhydrone in CD_3CN under an N_2 atmosphere.

Figure S5.4.12. Coulometry experiment with 2.6 mM BQ and 1.37 M acetic acid in an MeCN solution under N_2 saturation conditions.

Figure S5.4.13. ^1H NMR taken after coulometry experiment with 2.6 mM BQ and 1.37 M acetic acid under an atmosphere of N_2.

Figure S5.4.14. ^1H NMR taken of a solution with 2.5 mM H_2Q and 1.37 M acetic acid under an atmosphere of N_2.

Figure S5.4.15. CV data comparing the individual responses of 0.5 mM H_2Q and 0.5 mM BQ relative to when they are both present in situ.

Figure S5.4.16. CV data with 1.37 M TFEOH comparing the individual responses of 0.5 mM H_2Q and 0.5 mM BQ relative to when they are both present in situ.

Figure S5.4.17. CV data under argon saturation conditions comparing 0.5 mM BQ with 1.37 M TFEOH and 1.37 M acetic acid with the redox response of 0.5 mM H_2Q under aprotic conditions.

Figure S5.4.18. CV data under argon saturation conditions comparing 2.5 mM BQ with 1.37 M TFEOH and 1.37 M acetic acid with the redox response of 2.5 mM H_2Q under aprotic conditions.

Figure S5.5.19. CVs of TFEOH titration with 2.5 mM BQ obtained under Ar saturation conditions focusing on the one-electron BQ reduction feature at –1.69 V vs. Fc^+/Fc obtained from CV titration data.

Figure S5.6.20. CVs comparing 0.5 mM of Mn(^{tbu}dhbpy)Cl **1**, with 1.25 mM BQ both with and without 1.37 M TFEOH.

Figure S5.6.21. CVs comparing 0.5 mM of Mn(^{tbu}dhbpy)Cl **1**, with 2.5 mM BQ both with and without 1.37 M TFEOH under O_2 saturation conditions.

Figure S5.6.22. Overlay of ^{1}H NMR aromatic region from experiment with 2.5 mM H_2Q, 0.274 M TFEOH, and 0.5 mM Mn(^{tbu}dhbpy)Cl **1** in CD_3CN under an atmosphere of N_2 versus an atmosphere of air.

Figure S5.6.23. Overlay of ^{1}H NMR aromatic region from experiment with 2.5 mM H_2Q and 0.5 mM Mn(^{tbu}dhbpy)Cl **1** in CD_3CN under an atmosphere of N_2 versus an atmosphere of air.

Figure S5.6.24. Overlay of ^{1}H NMR aromatic region from experiment with 2.5 mM BQ, 0.274 M TFEOH, and 0.5 mM Mn(^{tbu}dhbpy)Cl **1** in CD_3CN under an atmosphere of N_2 versus an atmosphere of air.

Figure S5.6.25. Overlay of ^{1}H NMR aromatic region from experiment with 2.5 mM BQ and 0.5 mM Mn(^{tbu}dhbpy)Cl **1** in CD_3CN under an atmosphere of N_2 versus an atmosphere of air.

Figure S5.6.26. Overlay of ^{1}H NMR aromatic region from experiment with 0.5 mM H_2Q, 0.5 mM urea•H_2O_2, 0.274 M TFEOH in CD_3CN under an N_2 atmosphere with 0.5 mM Mn(^{tbu}dhbpy)Cl **1** present and in the absence of Mn(^{tbu}dhbpy)Cl **1**.

Figure S5.6.27. Aromatic region of control ^{1}H NMRs of 0.274 M TFEOH with 2.5 mM BQ versus 2.5 mM H_2Q in CD_3CN under an N_2 atmosphere.

Figure S5.7.28. CVs of 0.5 mM Mn(^{tbu}dhbpy)Cl **1**, and 0.5 mM BQ obtained under O_2 saturation conditions with variable TFEOH concentration.

Figure S5.7.29. CVs of 0.5 mM Mn(^{tbu}dhbpy)Cl **1**, and 2.5 mM BQ obtained under O_2 saturation conditions with variable TFEOH concentration.

Figure S5.7.30. CVs of 0.5 mM Mn(^{tbu}dhbpy)Cl **1**, and 1.37 M TFEOH obtained under O_2 saturation conditions with variable BQ concentration.

Figure S5.7.31. CVs of 0.5 mM Mn(^{tbu}dhbpy)Cl **1**, 0.5 mM BQ, and 1.37 M TFEOH with variable O_2 concentration.

Figure S5.7.32. CVs of 0.5 mM Mn(^{tbu}dhbpy)Cl **1**, 2.5 mM BQ, and 1.37 M TFEOH with variable O_2 concentration.

Figure S5.7.33. CVs with 1.37 M TFEOH under Ar and O_2 saturation conditions with variable Mn(^{tbu}dhbpy)Cl **1** and BQ concentration.

Figure S5.7.34. Control CVs of 2.5 mM BQ with 1.37 M TFEOH and 2.5 mM urea H_2O_2 under Ar saturation conditions to illustrate that no significant reactivity occurs between BQ and free H_2O_2 in the presence of a proton source.

Figure S5.8.35. Linear Sweep Voltammograms of RRDE experiment with 0.5 mM BQ and 1.37 M TFEOH at various rotation rates under Ar and O_2 saturation conditions; ring potential = 0.85 V vs Fc^+/Fc.

Figure S5.8.36. Levich plots from data obtained from Linear Sweep Voltammograms of BQ (0.5 mM) by RRDE with 1.37 M TFE under Ar and O_2 saturation conditions at various rotation rates; ring potential = 0.85 V vs Fc^+/Fc.

Figure S5.8.37. Koutecky-Levich plots from data obtained from Linear Sweep Voltammograms of BQ (0.5 mM) by RRDE with 1.37 M TFE under Ar and O_2 saturation conditions at various rotation rates; ring potential = 0.85 V vs Fc^+/Fc.

Figure S5.8.38. Linear Sweep Voltammograms of RRDE experiment with 0.5 mM BQ and 1.37 M TFEOH at various rotation rates under Ar and O_2 saturation conditions; ring potential = 0.4 V vs Fc^+/Fc.

Figure S5.8.39. Levich plots from data obtained from Linear Sweep Voltammograms of BQ (0.5 mM) by RRDE with 1.37 M TFE under Ar and O_2 saturation conditions at various rotation rates; ring potential = 0.4 V vs Fc^+/Fc.

Figure S5.8.40. Koutecky-Levich plots from data obtained from Linear Sweep Voltammograms of BQ (0.5 mM) by RRDE with 1.37 M TFE under Ar and O_2 saturation conditions at various rotation rates; ring potential = 0.4 V vs Fc^+/Fc.

Figure S5.8.41. Linear Sweep Voltammograms of RRDE experiment with 0.5 mM Mn(^{tbu}dhbpy)Cl **1** and 1.37 M TFEOH at various rotation rates under Ar and O_2 saturation conditions; ring potential = 0.85 V vs Fc^+/Fc.

Figure S5.8.42. Linear Sweep Voltammograms of RRDE experiment with 0.5 mM Mn(^{tbu}dhbpy)Cl **1**, 0.5 mM BQ and 1.37 M TFEOH at various rotation rates under Ar and O_2 saturation conditions; ring potential = 0.4 V vs Fc^+/Fc.

Figure S5.8.43. Levich plots from data obtained from Linear Sweep Voltammograms of 0.5 mM Mn(^{tbu}dhbpy)Cl **1** and 0.5 mM BQ by RRDE with 1.37 M TFE under Ar and O_2 saturation conditions at various rotation rates; ring potential = 0.4 V vs Fc^+/Fc.

Figure S5.8.44. Koutecky-Levich plots from data obtained from Linear Sweep Voltammograms of 0.5 mM Mn(^{tbu}dhbpy)Cl **1** and 0.5 mM BQ by RRDE with 1.37 M TFE under Ar and O_2 saturation conditions at various rotation rates; ring potential = 0.4 V vs Fc^+/Fc.

Figure S5.8.45. Linear Sweep Voltammograms of RRDE experiment with 0.5 mM Mn(^{tbu}dhbpy)Cl **1**, 0.5 mM BQ and 1.37 M TFEOH at various rotation rates under Ar and O_2 saturation conditions; ring potential = 0.85 V vs Fc^+/Fc.

Figure S5.8.46. Levich plots from data obtained from Linear Sweep Voltammograms of 0.5 mM Mn(^{tbu}dhbpy)Cl **1** and 0.5 mM BQ by RRDE with 1.37 M TFE under Ar and O_2 saturation conditions at various rotation rates; ring potential = 0.85 V vs Fc^+/Fc.

Figure S5.8.47. Koutecky-Levich plots from data obtained from Linear Sweep Voltammograms of 0.5 mM Mn(^{tbu}dhbpy)Cl **1** and 0.5 mM BQ by RRDE with 1.37 M TFE under Ar and O_2 saturation conditions at various rotation rates; ring potential = 0.85 V vs Fc^+/Fc.

Figure S5.8.48. Linear Sweep Voltammograms of RRDE experiment with 0.5 mM Mn(^{tbu}dhbpy)Cl **1**, 1.25 mM BQ and 1.37 M TFEOH at various rotation rates under Ar and O_2 saturation conditions; ring potential = 0.4 V vs Fc^+/Fc.

Figure S5.8.49. Levich plots from data obtained from Linear Sweep Voltammograms of 0.5 mM Mn(^{tbu}dhbpy)Cl **1** and 1.25 mM BQ by RRDE with 1.37 M TFE under Ar and O_2 saturation conditions at various rotation rates; ring potential = 0.4 V vs Fc^+/Fc.

Figure S5.8.50. Koutecky-Levich plots from data obtained from Linear Sweep Voltammograms of 0.5 mM Mn(^{tbu}dhbpy)Cl **1** and 1.25 mM BQ by RRDE with 1.37 M TFE under Ar and O_2 saturation conditions at various rotation rates; ring potential = 0.4 V vs Fc^+/Fc.

Figure S5.8.51. Linear Sweep Voltammograms of RRDE experiment with 0.5 mM Mn(^{tbu}dhbpy)Cl **1**, 1.25 mM BQ and 1.37 M TFEOH at various rotation rates under Ar and O_2 saturation conditions; ring potential = 0.85 V vs Fc^+/Fc.

Figure S5.8.52. Levich plots from data obtained from Linear Sweep Voltammograms of 0.5 mM Mn(^{tbu}dhbpy)Cl **1** and 1.25 mM BQ by RRDE with 1.37 M TFE under Ar and O_2 saturation conditions at various rotation rates; ring potential = 0.85 V vs Fc^+/Fc.

Figure S5.8.53. Koutecky-Levich plots from data obtained from Linear Sweep Voltammograms of 0.5 mM Mn(^{tbu}dhbpy)Cl **1** and 1.25 mM BQ by RRDE with 1.37 M TFE under Ar and O_2 saturation conditions at various rotation rates; ring potential = 0.85 V vs Fc^+/Fc.

Figure S5.8.54. Linear Sweep Voltammograms of RRDE experiment with 0.5 mM Mn(^{tbu}dhbpy)Cl **1**, 2.5 mM BQ and 1.37 M TFEOH at various rotation rates under Ar and O_2 saturation conditions; ring potential = 0.85 V vs Fc^+/Fc.

Figure S5.8.55. Levich plots from data obtained from Linear Sweep Voltammograms of 0.5 mM Mn(^{tbu}dhbpy)Cl **1** and 2.5 mM BQ by RRDE with 1.37 M TFE under Ar and O_2 saturation conditions at various rotation rates; ring potential = 0.85 V vs Fc^+/Fc.

Figure S5.8.56. Koutecky-Levich plots from data obtained from Linear Sweep Voltammograms of 0.5 mM Mn(^{tbu}dhbpy)Cl **1** and 2.5 mM BQ by RRDE with 1.37 M TFE under Ar and O_2 saturation conditions at various rotation rates; ring potential = 0.85 V vs Fc^+/Fc.

Figure S5.8.57. Linear Sweep Voltammograms of RRDE experiment with 0.5 mM Mn(^{tbu}dhbpy)Cl **1**, 2.5 mM BQ and 1.37 M TFEOH at various rotation rates under Ar and O_2 saturation conditions; ring potential = 0.4 V vs Fc^+/Fc.

Figure S5.8.58. Levich plots from data obtained from Linear Sweep Voltammograms of 0.5 mM Mn(^{tbu}dhbpy)Cl **1** and 2.5 mM BQ by RRDE with 1.37 M TFE under Ar and O_2 saturation conditions at various rotation rates; ring potential = 0.4 V vs Fc^+/Fc.

Figure S5.8.59. Koutecky-Levich plots from data obtained from Linear Sweep Voltammograms of 0.5 mM Mn(^{tbu}dhbpy)Cl **1** and 2.5 mM BQ by RRDE with 1.37 M TFE under Ar and O_2 saturation conditions at various rotation rates; ring potential = 0.4 V vs Fc^+/Fc.

Figure S5.11.60. Linear Sweep Voltammograms of RRDE experiment with 0.5 mM ferrocene at various rotation rates under Ar saturation conditions; ring potential = 0.85 V vs Fc^+/Fc.

Figure S5.11.61. Levich and Koutecky-Levich plots from data obtained from Linear Sweep Voltammograms of 0.5 mM ferrocene by RRDE under Ar saturation conditions at various rotation rates; ring potential = 0.85 V vs Fc^+/Fc.

Figure S6.3.1. CVs of 2.5 mM DBTD both with and without 0.1 M PhOH obtained under Ar and CO_2 saturation conditions.

Figure S6.3.2. Current versus time trace from bulk electrolysis experiment. Charge passed versus time for the bulk electrolysis experiment.

Figure S6.3.3. Current versus time trace from bulk electrolysis experiment. Charge passed versus time for the bulk electrolysis experiment.

Figure S6.3.4. CVs comparing the reactivity of Cr(^{tbu}dhbpy)Cl(H_2O) and DBTD under aprotic conditions.

Figure S6.3.5. Current versus time trace from bulk electrolysis experiment. Charge passed versus time for the bulk electrolysis experiment.

Figure S6.3.6. Current versus time trace from bulk electrolysis experiment. Charge passed versus time for the bulk electrolysis experiment.

Figure S6.3.7. Current versus time trace from bulk electrolysis experiment. Charge passed versus time for the bulk electrolysis experiment.

Figure S6.3.8. CVs evaluating the aprotic CO_2 reduction activity of Cr(^{tbu}dhbpy)Cl(H_2O) and decamethylcobaltocene Cp^*_2Co under aprotic conditions.

Figure S6.3.9. CVs evaluating the aprotic CO_2 reduction activity of Cr(^{tbu}dhbpy)Cl(H_2O) and dibenzothiophene-5-oxide (DBTMO).

Figure S6.3.10. $^{13}C\{^1H\}$ NMRs in D_2O for product analysis of bulk electrolysis solutions.

Figure S6.3.11. CVs of Cr(^{tbu}dhbpy)Cl(H_2O) at variable concentrations, obtained under CO_2 saturation with 2.5 mM DBTD.

Figure S6.3.12. CVs of DBTD at variable concentrations, obtained under CO_2 saturation with 1.0 mM Cr(^{tbu}dhbpy)Cl(H_2O).

List of Schemes

List of Tables

Chapter 1

Introduction

1.1 Global Climate Change and Increasing Energy Demands

Since 1890, when Samuel Langley and Frank Very first used infrared absorption to observe atmospheric carbon dioxide (CO_2) and water vapor, the effect of anthropogenic CO_2 emissions has gained increasing interest within the scientific community.[1] However, it was not until 1979, through the work of William Kellogg, that more accurate methods for analyzing the greenhouse effect were developed to provide concrete evidence of this phenomena.[2] Less than ten years later, in 1988, the World Meteorological Organization (WMO), in conjunction with the United Nations Environment Programme (UNEP), formed the Intergovernmental Panel on Climate Change (IPCC) which today continues to organize scientific data relevant to global climate change such that the multidimensional impact of climate change can be annually assessed and potential solutions can be presented. The analysis and documentation of data related to global climate change by the IPCC has since illustrated the severity of rising anthropogenic CO_2 emissions, which has indicated there is a growing need for the development of clean, renewable energy alternatives.[3]

Since the end of the industrial revolution, the concentration of greenhouse gases, such as CO_2, methane, and nitrous oxide, has consistently increased. The increasing concentrations of these gases within the earth's atmosphere has resulted in their absorption of heat that is reflected from the earth's surface. This heat then becomes trapped within the earth's atmosphere, which has resulted in a variety of environmental effects, such as rising global temperatures, ocean acidification, altering and more intense weather patterns, and rising sea levels.[4]

CO_2 is the most abundant anthropogenic greenhouse gas. Human activity has contributed to its rising atmospheric concentration through the combustion of coal, crude oil, and natural gas for energy production. The primary sources of energy production in the world arise from either materials, transportation, or electricity needs. Therefore, with the increasing global population causing greater energy demands, the need for cost-effective renewable energy alternatives is greater than it has ever been in earth's history.[4-5]

1.2 Addressing Energy Demands via Catalysis

Addressing global climate change requires the development of an alternative approach for supplying energy that is both sustainable and efficient.[6] One of the best examples of a system that is both efficient and sustainable can be found in biology. Photosynthesis is a biological process by which CO_2 and water are converted into glucose and O_2. In plants, photosynthesis is capable of converting light energy into chemical energy, supplying living organisms with the energy needed to carry out essential biological processes.[6-7] Therefore, photosynthesis represents an excellent example of a sustainable and efficient method for both the storage and supply of energy in the form of chemical bonds.[5-7]

Due to the intermittent supply of sunlight, captured electricity could be used to store energy in a manner analogous to photosynthesis. However, in order for the use of electricity to be considered a viable method, the energy required to drive the reaction of interest from reactants to products must be sufficiently low.[6] This can be achieved with a catalyst, which functions to lower the activation barrier of a given reaction. A viable electrocatalyst must be both selective, in terms of the product(s) produced from the supplied reactant(s), active, in terms of the rate at which it is able to turnover and selective enough to mitigate deleterious side reactions at the required operating potentials. Additionally, it is often desirable that a given electrocatalyst be robust, in terms of its ability to operate over extended time periods within a wide range of temperatures and pressures.[8]

An electrocatalyst can be either molecular, solubilized within a homogeneous solution with the substrate of interest, or heterogeneous, in a separate phase.[9] From a comparative standpoint, it is often the case that heterogeneous electrocatalysts surpass molecular electrocatalysts in the areas of activity and robustness. Conversely, molecular electrocatalysts are advantageous due to their selectivity and because the mechanistic pathway by which they carry out reactions can be more easily identified and characterized compared to heterogeneous electrocatalysts.[10-11] This can enable a more direct and systematic optimization of a given molecular electrocatalytic system. From a developmental standpoint, the comparison of heterogeneous versus molecular electrocatalytic systems can be perceived less so as an antagonistic relationship and more so as complementary approaches in the stepwise expansion of electrocatalytic systems. This implies that the development and systematic optimization of a molecular electrocatalytic system comes first. Once a thorough understanding and optimization of the molecular process has been carried out, it is then incorporated into a heterogeneous system that can then be further optimized.

Developing a molecular electrocatalytic system capable of meeting rising energy demands while also mitigating any negative environmental contribution can be done via two different generalized approaches. One approach is to create a carbon-neutral cycle where there is some constant source of electrical energy that, when applied to a catalyst, creates an active catalyst species. This active catalyst species can then react with CO_2 from the atmosphere to make fuels that can be used to supply energy. The use of these fuels for energy would then re-emit CO_2 back into the atmosphere through combustion and the "closed-loop" cycle would then continue; not reducing atmospheric CO_2 concentrations, but also not contributing to the continual rise of anthropogenic CO_2 concentrations (**Figure 1.2.1**).[12-13] In an ideal system, instead of giving off CO_2 from the combustion of fuels, this method would produce fuels in the form of value-added carbon-based products that are not then utilized directly for combustion processes by which CO_2 is a by-product.[13] This approach is convenient because it produces valuable products and directly contributes to decreasing the concentration of CO_2 in the atmosphere. The second approach is to employ a complementary clean energy source that does not utilize CO_2 in the atmosphere, but instead uses an alternative energy source that itself does not contribute to rising CO_2 concentrations in the atmosphere. An example if this would be a hydrogen fuel cell, where H_2 and O_2 react with a catalyst and convert in chemical bond energy to electrical energy. This approach is advantageous because the only products of this reaction are H_2O, electricity, and mild amounts of heat.[14]

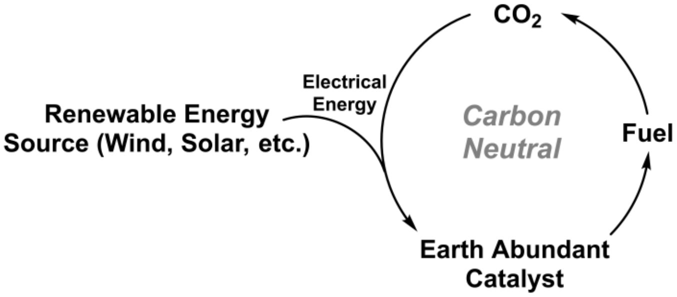

Figure 1.2.1. Schematic illustrating the "closed-loop" cycle approach to energy relevant electrocatalysis.

Herein, the focus is on the development of molecular inorganic electrocatalysts for energy-relevant redox reactions. The redox reactions of focus are the oxygen reduction reaction[15] (ORR) and the carbon dioxide reduction reaction[12] (CO2RR). Inorganic catalysts are ones by which an ionic metal center is coordinated to an organic ligand framework. Viable inorganic catalysts with earth abundant metal centers could be significant for meeting increasing energy demands in a sustainable manner. Therefore, possible points of systematic optimization lie in the realm of altering the metal center, the ligand framework, and the substrate environment to improve a desired molecular electrocatalytic process.

1.3 Background on Electrochemistry

In the energy relevant reactions of study, described in detail below, the common focal point is the transfer of electrons, and protons in most cases, as the reaction proceeds from reactants to products. Electrochemistry is a paramount method in the study of molecular inorganic electrocatalysts because it directly connects electricity to chemical processes. One of the fundamental advantages of electrochemistry lies in the ability to control the driving force for the transfer of an electron via an applied potential. The applied potential and electron transfer are carried out at an electrode. The electrode can be a variety of conducting materials, but herein glassy carbon is used due to its inherent inertness.[16-17] Below, **Figure 1.3.1** serves as a visual aid for understanding the overall process and goal of inorganic electrocatalysis involving a reduction reaction, when an electron is transferred to the catalyst from the electrode to generate an activated catalyst species that reacts with substrates to generate value-added products. Upon formation of the value-added products, the catalyst is re-oxidized through the transfer of electron(s) to the substrate, at which point it can be reduced by the electrode again to re-form the active catalyst species and repeat the process.

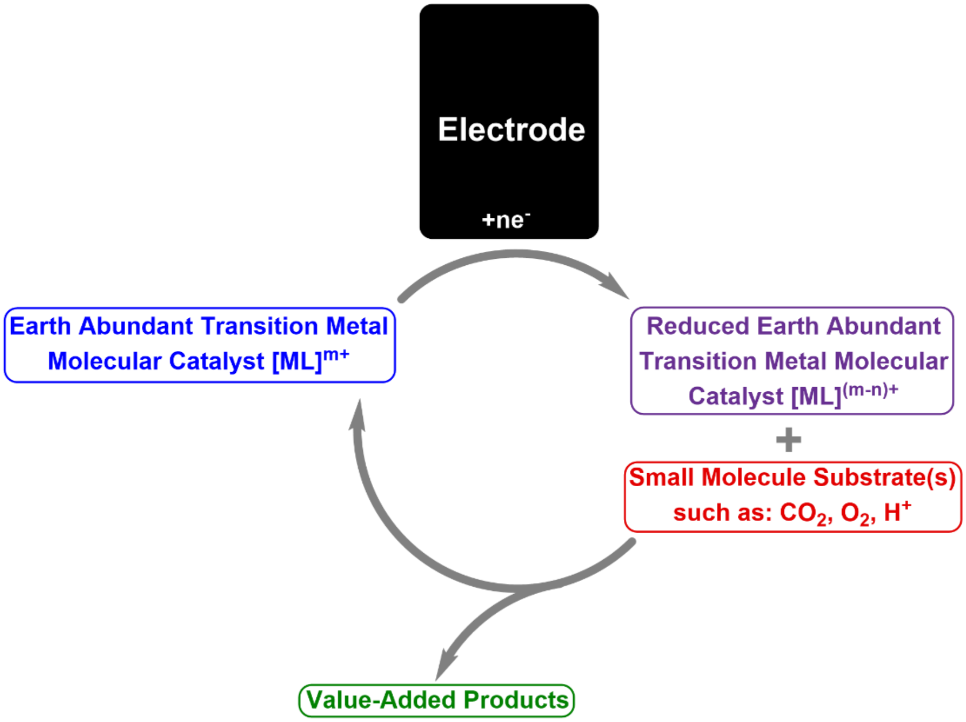

Figure 1.3.1. Schematic for understanding the overall process and goal of inorganic electrocatalysis herein involving a reduction reaction.

One of the most widely and conveniently used electrochemical techniques for studying a molecular species of interest is cyclic voltammetry. In cyclic voltammetry, current is measured while a potential region is swept as a function of time. The applied potential is analogous to energy being applied to a system, which is the electrochemical cell, and as the applied potential increases, the energy being applied to the system also increases. Once a sufficient amount of energy has been supplied to the system via an applied potential, an electron transfer process can occur, at the thin surface next to the electrode called the diffusion layer, which is observed as a response in current. The potential sweep and resulting current response is commonly analyzed as a cyclic voltammogram (CV). The electrochemical cell itself consists of a three-electrode setup: a working electrode where the reaction of interest is occurring, a reference electrode which functions as a reference to the applied potential, and a counter electrode that functions to complete the circuit and balance the current that is produced at the working electrode.[16-17]

This process can be understood by following the CV trace of ferrocene in **Figure 1.3.2** (*A*-*E*, purple). In a homogeneous solution of ferrocene, as the potential is swept from *A* to *C*, a peak in the anodic current is observed which corresponds to the one-electron oxidation of ferrocene to ferrocenium within the diffusion layer at the surface of the working electrode (**Figure 1.3.2**, gray). As the potential is swept from *A* to *B* the increase in current corresponds to the buildup of ferrocenium. At point *B* in the CV sweep, the concentration of ferrocenium has increased and concentration of ferrocene has decreased within the diffusion layer such that the current observed from *B* to *C* is that of the limited mass transport of ferrocene from the bulk solution. Point *C* is defined as the switching potential and as the potential is swept from *C* to *E* a peak in the cathodic current is observed which corresponds to the one-electron reduction of ferrocenium, built up in the diffusion layer, to ferrocene (**Figure 1.3.2**, red). As the potential is swept from *C* to *D* the increase in current corresponds to the buildup of ferrocene. At point *D* in the CV sweep, the concentration of ferrocene has increased and concentration of ferrocenium has decreased within the diffusion layer such that the current observed from *D* to *E* is that of the limited mass transport of any remaining ferrocenium from the bulk solution.[17]

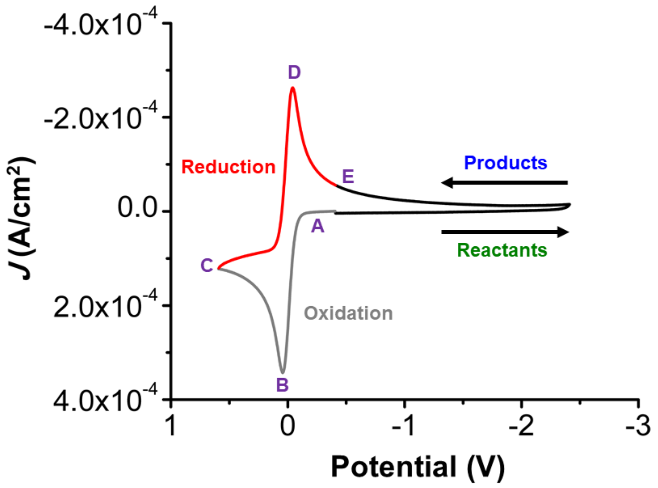

Figure 1.3.2. Sample CV trace of ferrocene for understanding cyclic voltammetry.

The applied potential required to observe the redox response of a given species is dictated by the Nernst equation (**equation 1.1**). The Nernst equation relates the standard potential ($E°$) of a species to the $E_{1/2}$ being experimentally observed within a given electrochemical cell setup (E). In reference to the CV of ferrocene in **Figure 1.3.2**, the $E_{1/2}$ would be determined be taking the potential at point *B* summed with the potential at point *D* and divided by two (E). The remainder of the Nernst equation includes the number of electrons transferred (n), the ideal gas constant (R), the temperature (T), Faraday's constant (F), and a constant (Q). The constant, Q, is the ratio of the concentration of the oxidized and reduced species being analyzed (**equation 1.2**). By convention, redox reactions are written as reductions.[17]

$$E = E° - \frac{RT}{nF} ln\,(Q) \qquad \textbf{(1.1)}$$

$$Q = \frac{[oxidized\ species]}{[reduced\ species]} = \frac{[products]}{[reactants]} \qquad \textbf{(1.2)}$$

In the Nernst equation, because the E is an equilibrium potential, the defined relationship enables the extrapolation of the effect that concentration changes and added substrate has on the equilibrium potential of a given redox process. For example, per the

Nernst equation, for an electrochemical reduction reaction of interest, a shift in the $E_{1/2}$ towards more positive potentials would indicate an equilibrium shift towards the products of a reaction. Conversely, a shift towards more negative potentials in a reduction reaction would indicate an equilibrium shift towards the reactants of a reaction.[9, 16-17]

Another valuable electrochemical technique that is commonly used when analyzing a molecular electrocatalyst is controlled potential electrolysis (CPE). In CPE, a constant potential is maintained, and current is measure over time. CPE of a bulk solution allows for the accumulation of products of an electrochemical reaction such that they can be identified and quantified. This is a valuable technique in electrocatalysis for determining the turnover number (TON) and faradaic efficiency (FE) of a catalyst during a define catalytic run as can be seen in equations **1.3** and **1.4**, respectively, where n is the number of electrons per mole of product.[18]

$$TON = \frac{moles\ of\ product}{moles\ of\ catalyst} \qquad (\mathbf{1.3})$$

$$FE = \frac{moles\ of\ product}{(moles\ of\ electrons/n)} * 100 \qquad (\mathbf{1.4})$$

Combining CPE with spectroscopic methods is another powerful tool for understanding reaction mechanisms. Spectroelectrochemical (SEC) methods allow for changes in electronic absorption bands to be observed with changes in applied potential. This is a useful technique particularly when dealing with complex reaction mixtures or when characterizing the direct synthesis of a reduced or oxidized species of interest.[11, 19-20]

1.4 The Oxygen Reduction Reaction

Processes that require the rapid and efficient utilization of dioxygen (O_2) are prevalent throughout numerous areas of biological chemistry. One example is hemoglobin and myoglobin in red blood cells. Due to the poor solubility of O_2 in aqueous solutions, the iron (Fe) atom present in hemoglobin and myoglobin proteins functions to bind O_2 in red blood cells to transport oxygen throughout the body in order to carry out additional physiological processes.[21] Another example are cytochrome P-450 enzymes, which also contain an inner heme, that carry out hydroxylation reactions in the body via dioxygen cleavage to produce water as a c0-product to the hydroxylated product.[22] Some additional biological processes relevant to understanding O_2 reactivity include the Mn-containing oxygen evolving complex of photosystem II[23] and the synthesis of ATP via complex IV of the electron transport chain.[24] Understanding the behavior of O_2 as a substrate, product, or a ligand in biological systems is often the starting point in the development of molecular electrocatalysts capable of carrying out the oxygen reduction reaction (ORR).

In the absence of a suitable proton donor, the one-electron reduction of O_2 produces superoxide ($O_2^{\bullet-}$) while the two-electron reduction of O_2 produces peroxide (O_2^{2-}). Since it is less activated, the superoxide anion can function as an oxidant or a reductant. For a molecular transition metal electrocatalyst, the metal center, ligand, and substrate environment directly affect the binding mode, oxidation state, and thus reactivity of the M-O_2 species that is formed. Under an aprotic O_2 atmosphere, M-O_2 binding can occur to form either an η^1-superoxo or η^2-peroxo (**Figure 1.4.1**). In the absence of sterically bulky ligand substituents, the formation of a η^1, η^1-cis or η^1, η^1-trans M_2-O_2

species is possible (**Figure 1.4.1**).[15, 25] Additional geometries for M-O_2 binding conformations exist,[26-29] but for simplicity of the work to be discussed the focus will be on catalysts that form monomeric metal-superoxo and/or metal-peroxo species.

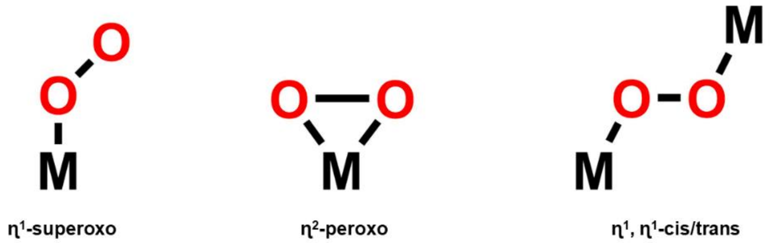

Figure 1.4.1. Examples of common M-O_2 binding conformations.

Under protic conditions, the reduction of O_2 to H_2O_2 occurs via a $2H^+/2e^-$ process. The reduction of O_2 to H_2O can occur via a $4H^+/4e^-$ process. A 2+2 mechanism is also possible in the reduction of O_2 to H_2O, where an initial reduction of O_2 to H_2O_2 occurs via a $2H^+/2e^-$ process and the H_2O_2 produced undergoes a subsequent $2H^+/2e^-$ reduction to make H_2O. Each of these different reduction processes occur at distinct thermodynamic potentials (**Table 1.4.1**).[15]

Table 1.4.1. Standard potentials for ORR pathways under aqueous conditions. Potentials referenced to the standard hydrogen electrode (SHE).[30]

ORR half-reaction	$E°_{(aqueous)}$(V vs. SHE)
$O_2\,(g) + 4H^+ + 4e^- \rightleftharpoons 2H_2O$	1.229
$O_2\,(g) + 2H^+ + 2e^- \rightleftharpoons H_2O_2$	0.695
$H_2O_2 + 2H^+ + 2e^- \rightleftharpoons 2H_2O$	1.763

The development of molecular electrocatalysts for the ORR is significant in the development of fuel cell technology[31] as well as in the industrial synthesis of hydrogen peroxide (H_2O_2).[32] Fuel cells represent a desirable alternative energy source because they directly convert chemical energy into electrical energy with greater efficiency than combunstion. Catalysts for sustainable hydrogen fuel cell technologies must be selective for H_2O over H_2O_2 due to the degradation processes fuel cell membranes undergo in the presence of H_2O_2.[31] Conversely, the current industrial method for the synthesis of hydrogen peroxide is the anthraquinone process, which is a multistep and energy intensive process where reducing equivalents are generated from coal. Therefore, one alternative to this industrial process lies in the development of ORR catalysts selective for the production of H_2O_2, such that a single-step synthetic method could be developed for industrial applications.[32]

1.5 Molecular Catalysts for the Oxygen Reduction Reaction

The pool of molecular electrocatalysts capable of reducing O_2 is large.[15] To date, heterogeneous platinum (Pt)-based electrocatalysts are the most active for industrial applications.[33] However, for the purposes described herein, the focus will be on molecular electrocatalysts for the ORR which contain earth abundant transition metal centers, such as Mn, Fe, and Co, and are known to proceed via monometallic mechanisms. As a result, this discussion will primarily focus on the recent and novel developments related to the reactivity of $[Mn(TPP)]^+$, $[Fe(TPP)]^+$, $[Co(TPP)]^0$, and derivatives thereof (where TPP = tetraphenylporphyrin); as well as a series of Co N_2O_2 complexes. Additional relevant work not discussed in this section is cited and/or discussed in the proceeding chapters related to the ORR.

One of the most extensive electrochemical kinetic analyses on Mn porphyrins was recently carried out by Nocera and coworkers.[34] In this study, manganese tetraphenylporphyrin and two xanthene-derived manganese hangman porphyrins were analyzed for their electrocatalytic ORR capabilities (**Figure 1.5.1A**). Initial studies began with Mn(TPP)Cl, where electrochemical analyses in acetonitrile (MeCN) determined that the $Mn^{III/II}$ redox couple (E° = 0.01 vs NHE) irreversibly reacted with O_2 under aprotic conditions. Upon the addition of a proton source of sufficient strength ($pK_{a(MeCN)}$ between 10.6 - 22.3), a catalytic S-shaped CV wave could be observed under O_2 saturation conditions indicative of catalysis occurring under kinetically limited conditions.[35] Product selectivity was determined via RRDE analyses which demonstrated that Mn(TPP)Cl selectively produced water, with the highest selectivity (98 ± 1 % for H_2O) observed using trifluoracetic acid as the proton source ($pK_{a(MeCN)}$ = 12.6). From additional CV data obtained with Mn(TPP)Cl under catalytic conditions, in combination with previous reports with metal porphyrins for ORR,[36-37] the authors proposed a mechanism for the observed reactivity, where the Mn^{II} intermediate can undergo a chemical reaction with O_2 and two equivalents of a proton source to form either a Mn^{III}-superoxide intermediate or a Mn^{IV}-peroxy intermediate which can be driven directly to the Mn^{III}-hydroperoxo intermediate in the presence of necessary proton donor equivalents (**Figure 1.5.1B**). Rate-determining cleavage of the O-O bond in the hydroperoxo intermediate results in the formation of a Mn^{V}-oxo intermediate which rapidly reacts to release water and return to the starting Mn^{III} species of the catalytic cycle.[34]

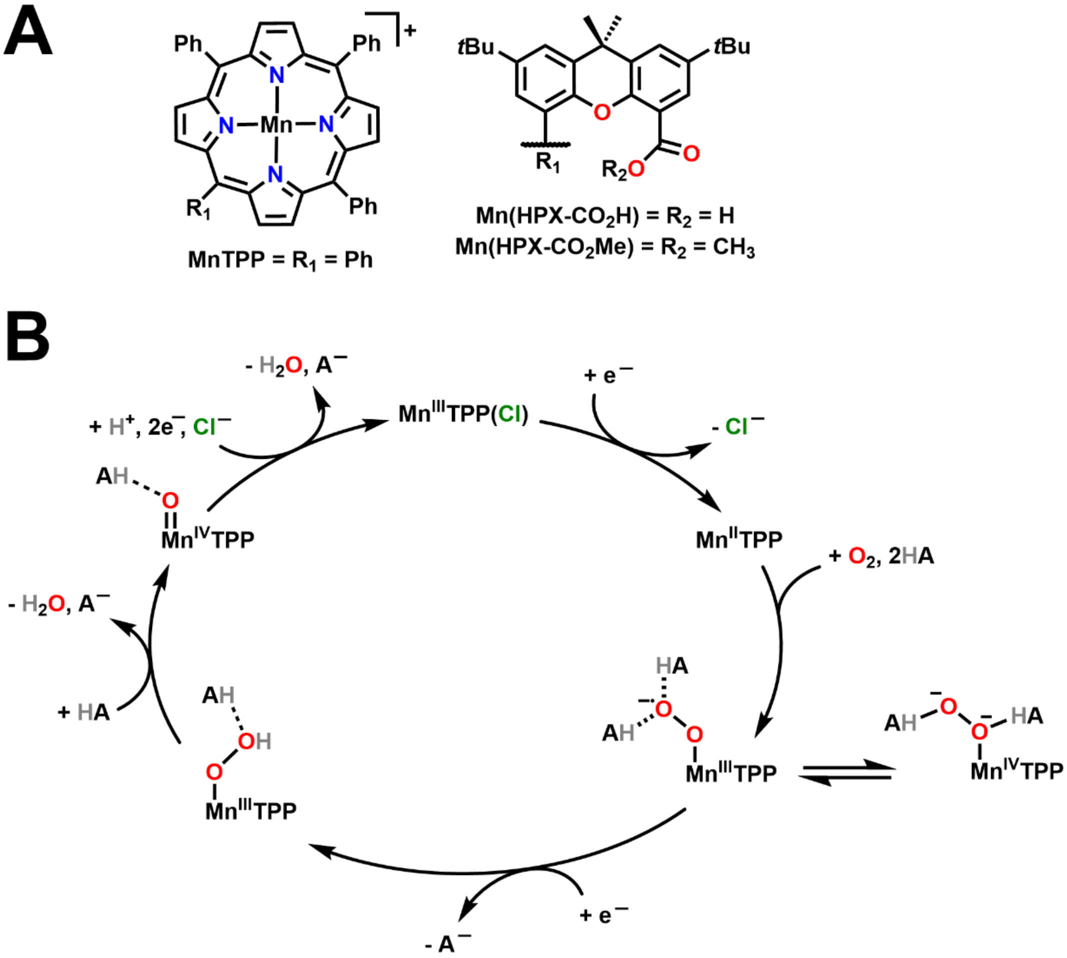

Figure 1.5.1. (**A**) Structure of manganese tetraphenylporphyrin (MnTPP) and two xanthene derived manganese hangman porphyrins ([Mn(HPX-CO_2H)] and [Mn(HPX-CO_2Me)]). All three complexes contain a chloride anion which is not shown. (**B**) Proposed mechanism for the electrocatalytic reduction of O_2 to H_2O by Mn(TPP); where HA represents a Brønsted acid.[34]

The novelty of this work from Nocera and coworkers arose from the ability to kinetically isolate the rate-determining O-O bond cleavage step, because the rate of formation of the Mn^{III}-superoxide was greater than the rate of O-O bond cleavage in the catalytic mechanism. Additionally, the authors also performed variable concentration CV analyses and developed Brønsted plots with the xanthene-derived manganese hangman porphyrin with ([Mn(HPX-CO_2H)]) and without ([Mn(HPX-CO_2Me)]) the ability to form an intramolecular H-bonding interaction. These results supported the proposed mechanism as well as demonstrated that the presence of secondary sphere effects where the complex which can form an intramolecular hydrogen bonding interaction (Mn(HPX-CO_2H)) directly lowered the observed reaction order from 2, observed for Mn(TPP)Cl and Mn(HPX-CO_2Me), to 1 with respect to proton donor.[34]

Changing metal centers but maintaining the same N4 porphyrin ligand coordination environment, Mayer and coworkers have published extensive studies on iron porphyrin derivatives for the ORR.[38-45] Previous studies on iron porphyrin derivatives have been carried out in both MeCN and *N,N*-dimethylformamide (*N,N*-DMF) with a variety of different proton donors of varying strength and these extensive studies have become model examples for how to identify and harness the effects of scaling relationships for a molecular electrocatalyst.[38, 40, 42-43] It is also worth pointing out that analysis of both the electrochemical and spectrochemical (utilizing decamethylferrocene (Cp_2*Fe) as a chemical reductant) reaction kinetics of $[Fe(TPP)]^+$ previously confirmed that the same mechanism was occurring under both experimental conditions.[44] The unique spectroscopic features of metal porphyrin complexes were significant in these studies because they enabled the monitoring of reaction intermediates. This has led to an extensive understanding of the catalytic mechanism of $[Fe(TPP)]^+$ for the ORR (**Figure 1.5.2**).[41]

For $[Fe(TPP)]^+$, the one-electron reduced $[Fe^{II}(TPP)]^0$ chemically reacts with O_2 to form an Fe^{III}-superoxide intermediate. Protonation of the Fe^{III}-superoxide has been identified as the rate-determining step of the reaction. Then, upon formation of the protonated superoxo intermediate, subsequent protonation of the distal oxygen followed by O-O bond cleavage occurs rapidly to form the Fe^{IV}-oxo species which reacts quickly to give off a second equivalent of H_2O.[41] Interestingly, a recent study by Mayer and coworkers with $[Fe(TMP)]^+$ (where TMP = tetramesitylporphyrin) suggests that protonation of the distal O atom of the Fe^{III}-hydroperoxo intermediate to produce H_2O versus the release of $[OOH]^–$ to form H_2O_2 is the key intermediate for determining catalyst selectivity.[39]

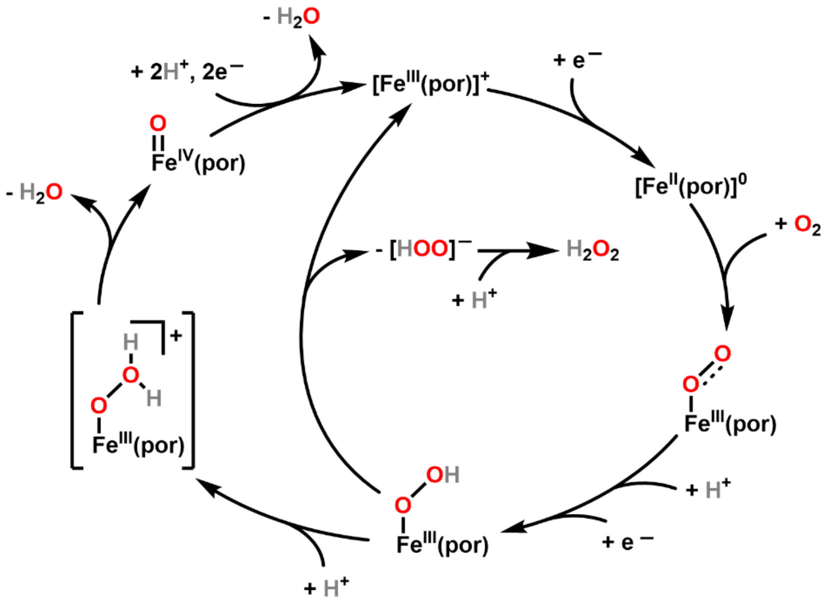

Figure 1.5.2. Proposed mechanism for the electrocatalytic reduction of O_2 to either H_2O or H_2O_2 by $[Fe(por)]^+$; where (por) = TPP, TMP, and any other porphyrin derivative thereof.[39, 41]

In comparison to the Mn and Fe porphyrins described above, Co complexes are unique as they have been reported to produce water while bypassing the high valent metal-oxo intermediates[46] commonly proposed for Mn and Fe systems that show selectivity for water.[34, 41] Recently, Stahl and coworkers have analyzed a wide variety of Co catalysts for ORR containing both N4 and N2O2 ligand frameworks.[46-49] There have been cases where Co catalysts for ORR are selective for H_2O_2 over water, and that the H_2O produced by Co catalysts often comes from disproportionation pathways due to catalyst instability in the presence of H_2O_2.[15, 50] However, Stahl and coworkers have illustrated the ability to thermodynamically bracket product selectivity with a Co porphyrin catalyst by combining the effects of pK_a and standard reduction potential.[46] The ability to thermodynamically control and eliminate the catalytic formation of specific products in the manner as reported by Stahl and coworkers, where potential/pK_a relationships can be used to determine selectivity for H_2O or H_2O_2 for a Co porphyrin catalyst system (**Figure 1.5.3**), is a very novel application of fundamental chemistry concepts and is an excellent example of how to understand and manipulate scaling relationships within a well-behaved system. Stahl and coworkers have since published additional work where they have established linear free energy relationships across a series of Co macrocycles.[49]

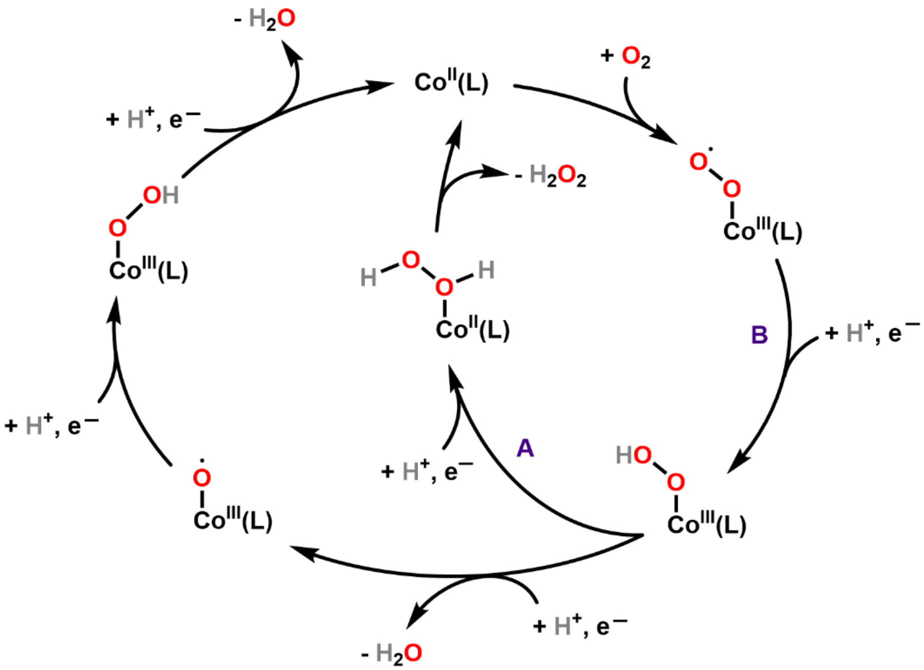

Figure 1.5.3. Generalized mechanism for Co ORR catalysts selective for either H_2O or H_2O_2; where L = any N4 macrocycle or N2O2 ligand framework.[46, 48]

Additional work by Stahl and coworkers has placed considerable attention on Co catalysts which possess an N2O2 ligand framework,[47-48] a unique feature specific to the experimental work to be described herein. Analyzing a series of Co ORR catalysts containing N4 and N2O2 ligand frameworks has provided an in-depth comparison of linear free energy relationships and general mechanistic trends between the two systems, specifically for the production of H_2O_2. For Co N2O2 ORR catalysts selective for the production of H_2O_2, the rate-limiting step has been suggested as proton transfer to the Co^{III}-hydroperoxo intermediate (**Figure 1.5.3**, step A). Interestingly, this is contrary to what has been reported for Co N4 macrocyclic catalysts, where PCET to form the Co^{III}-superoxide intermediate is rate-limiting (**Figure 1.5.3**, step B).[46, 48]

Both the $[Mn(TPP)]^+$ system discussed above and the $[Fe(TPP)]^+$ system show high selectivity for H_2O over H_2O_2 as the product. However, these two systems have distinct differences in their rate-determining steps. For $[Fe(TPP)]^+$, the rate determining step of the catalytic mechanism is the initial proton transfer to the Fe^{III}-superoxide intermediate, which is also the rate-limiting step for Co porphyrins that are selective for H_2O_2. Conversely, for $[Mn(TPP)]^+$, the rate-determining step of the catalytic mechanism was reported as O-O bond cleavage. Therefore, it goes without saying that for a molecular ORR catalyst, selectivity goes beyond just the metal center and nature of the rate-determining step. In addition to these factors, catalyst selectivity is likely additionally complicated by solvent effects, solution pK_a, and both the primary and secondary coordination sphere of the ligand framework. The studies described above serve as a limited overview of possible ORR pathways and how mechanistic insight can be obtained by understanding some of the most developed and well-known catalyst systems.

1.6 CO_2 Reduction Reaction

As stated above, the consumption of non-renewable fossil fuels has increased demand for the development of renewable energy resources and associated technologies. In particular, the reduction of carbon dioxide (CO_2) to carbon monoxide (CO) using renewable energy represents a potentially valuable pathway to the synthesis of liquid fuels via the Fischer-Tropsch process,[51] in the manufacturing of acetic acid,[52] and in hydroformylation reactions.[53]

As a small molecule, CO_2 is relatively inert; reduction of CO_2 to $CO_2^{\bullet-}$ occurs at –1.9 V versus NHE (**Table 1.6.1**). This high thermodynamic potential subsequently renders CO_2 as a challenging substrate for molecular electrocatalysts. The addition of protons significantly lowers the thermodynamic challenge of reducing CO_2.[12] Therefore, it is often the case that CO_2 reduction by a molecular electrocatalyst occurs under protic conditions via either a proton transfer pathway and/or a proton-coupled electron transfer pathway (PCET).[54]

Table 1.6.1. Standard potentials for CO2RR pathways under aqueous conditions at pH 7. Potentials referenced to the normal hydrogen electrode (NHE).[12, 55]

CO2RR half-reaction	$E°_{(aqueous)}$ in V vs NHE
$CO_2 + e^- \rightleftharpoons CO_2^-$	$E° = –1.9$ V
$CO_2 + 2H^+ + 2e^- \rightleftharpoons CO + H_2O$	$E° = –0.53$ V
$CO_2 + 2H^+ + 2e^- \rightleftharpoons HCO_2H$	$E° = –0.61$ V
$CO_2 + 4H^+ + 4e^- \rightleftharpoons HCOH + H_2O$	$E° = –0.48$ V
$CO_2 + 6H^+ + 6e^- \rightleftharpoons CH_3OH + H_2O$	$E° = –0.38$ V
$CO_2 + 8H^+ + 8e^- \rightleftharpoons CH_4 + 2H_2O$	$E° = –0.24$ V

In electrochemical CO_2 transformations, under protic conditions, by molecular transition metal catalysts two-electron reduced products are the most common, such as CO and H_2O or formate/formic acid ($HCOO^-$/HCOOH). There exist two possible pathways by which this type of CO_2 transformation process can occur. The first pathway is where the reduced metal center of the catalyst directly binds a CO_2 molecule (**Figure 1.6.1**, pathway 1). The binding of CO_2 to a reduced metal center can occur via three different mechanisms: (i) where the central carbon atom of the CO_2 molecule binds to the reduced metal center forming a M-C bond (**Figure 1.6.1**, pathway 3), (ii) where the reduced metal center forms an η^2 bond with the central carbon atom and one of the terminal oxygen atoms of the CO_2 molecule (**Figure 1.6.1**, pathway 4), and (iii) where one of the terminal oxygen atoms of the CO_2 molecule binds to the reduced metal center forming a M-O bond (**Figure 1.6.1**, pathway 5). It is often the case that both η^2 coordination and M-C bond formation leads to the formation of a metal hydroxycarbonyl intermediate (**Figure 1.6.1**, pathway 8), while formation of a M-O bond leads to the formation of a metal formato intermediate (**Figure 1.6.1**, pathway 9). The second possible pathway by which CO_2 transformation processes can occur is through the formation of a metal hydride (M-H) (**Figure 1.6.1**, pathway 2) which serves as the active species for promoting CO_2 insertion into the M-H bond to form either a metal hydroxycarbonyl (**Figure 1.6.1**, pathway 7) or metal formato (**Figure 1.6.1**, pathway 6) intermediate. It is frequently the case that a metal hydroxycarbonyl intermediate will lead to the formation of CO and a metal formato intermediate will lead to the formation of formate/formic acid. However, it is also important to note that aprotic CO_2 reduction is possible with a transition metal catalyst (**Figure 1.6.1**, pathway 10) and this occurs when a second CO_2 molecule serves as an O atom acceptor which leads to the formation of CO and carbonate ($[CO_3]^{2-}$).[20, 56]

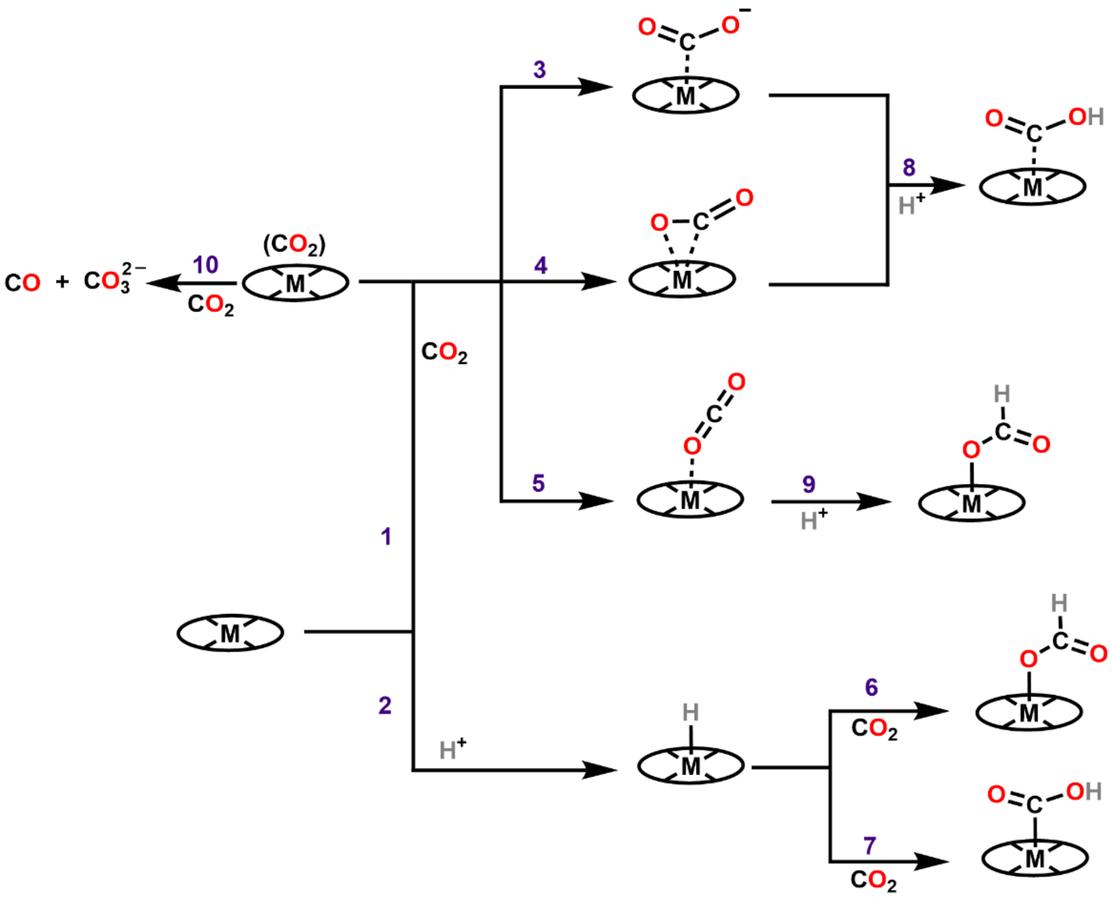

Figure 1.6.1. Different CO2RR mechanistic pathways.[56-57]

As discussed above, the binding and activation of CO_2 presents a high energy barrier which can be lowered by the addition of a proton source. Another barrier which can, and often does, serve as the rate-limiting step in the electrochemical reduction of CO_2 with an added proton donor by a transition metal catalyst is the formal cleavage of the C-O bond of the hydroxycarbonyl intermediate.[54] Therefore, the strength of the added proton donor can have a significant effect on the rate of CO2RR by a transition metal catalyst in the absence of a competing hydrogen evolution reaction. Similarly, it is well known that both the hydricity and pK_a of the metal hydride intermediate play key roles in the formate producing pathway for controlling formate production versus hydrogen evolution.[58-61] The final potential mechanistic barrier worth noting in the two-electron electrochemical conversion of CO_2 is the release of CO. It has previously been shown that transition metal center affinity for CO can significantly hinder the rate of CO release and can even lead to catalyst degradation processes.[62]

While the mechanistic description above for the two-electron electrochemical transformation of CO_2 mediated by a transition metal catalyst is heavily generalized, it does highlight the mechanistic complexity which must be considered when designing a molecular catalyst for CO2RR. Additionally, the above discussion suggests that the metal center, route of CO_2 activation, and proton donor strength are key points of control when attempting to identify and manipulate reaction kinetics and thermodynamics for the CO2RR. Not detailed above, but also relevant, is the role of ligand and secondary sphere effects, which have been shown to have a substantial impact in electrocatalytic systems for both CO2RR[63-64] and ORR.[47, 65]

1.7 Molecular Catalysts for the Reduction of CO_2

As was the case in the above sections, for the purposes described herein, the focus will be on molecular electrocatalysts which contain earth-abundant transition metal centers, such as Mn, Fe, and Ni, are well known to proceed primarily via a monometallic mechanism, and are selective for the production of CO, which is specifically relevant to the experimental work described herein. This section will provide a brief overview of some of the best molecular electrocatalytic systems with earth-abundant transition metals for CO_2 reduction to CO, which includes *meso*-substituted $[Fe(tetraphenylporphyrin)]^+$ complexes ($[Fe(TPP)]^+$), $Mn(bpy)(CO)_3Br$ (2,2′-bipyridine = bpy), and $[Ni(1,4,8,11\text{-}tetraazacyclotetradecane)]^{2+}$ ($[Ni(cyclam)]^{2+}$).[66] Additional relevant work not discussed in this section is cited and/or discussed in the proceeding chapters related to CO2RR.

It is known that [Fe(TPP)]$^{+}$[67-68] and derivatives thereof, currently represent a class of the most efficient and selective earth abundant molecular electrocatalysts for the reduction of CO_2 to CO, which has led to the extensive analysis and derivatization of the [Fe(TPP)]$^{+}$ system. Previous work by Savéant and coworkers demonstrated how to increase catalyst efficiency through the incorporation of both pendent protons and fluorine groups into the [Fe(TPP)]$^{+}$ system.[69] Warren and coworkers identified the significance of solvent effects between *N,N*-DMF and MeCN present in an [Fe(TPP)]$^{+}$-derived catalyst which contained a pendent proton source in the secondary coordination sphere.[70] Chang and coworkers have analyzed how the positional effects of an amide group in a series of [Fe(TPP)]$^{+}$ derivatives can effectively decrease overpotential and increase turnover frequency.[71] Nocera and coworkers studied a series of [Fe(TPP)]$^{+}$ derived hangman porphyrins containing either phenol, guanidinium, or sulfonic acid groups as an approach to lower the barrier for CO_2 activation, resulting in a stabilization effect for CO_2 binding.[63] Lastly, additional work by Savéant and coworkers have proven how that the addition of charged substituents onto the phenyl rings of [Fe(TPP)]$^{+}$ can not only break scaling relationships, but significantly enhance catalytic reactivity.[72] These studies mentioned above highlight only a few of the recent and novel studies that have been carried out on [Fe(TPP)]$^{+}$ and derivatives thereof for the electrocatalytic reduction of CO_2 to CO.

The proposed mechanism for CO_2 reduction to CO by [Fe(TPP)]$^{+}$ follows the generic mechanism described in the above section (**Figure 1.6.1**, pathway 1, 3, and 8). Upon formation of the Fe^{0} species, CO_2 binding occurs through the central carbon atom of the CO_2 molecule. The Fe^{I}-CO_2 species undergoes rapid protonation to form the Fe^{II}-hydroxycarbonyl intermediate by PCET. Subsequent protonation and cleavage of the C-

OH bond to release water has been proposed as the rate-determining step for the catalytic reaction, which is followed by release of CO from the metal carbonyl intermediate to then re-enter the catalytic cycle (**Figure 1.7.1**).[68]

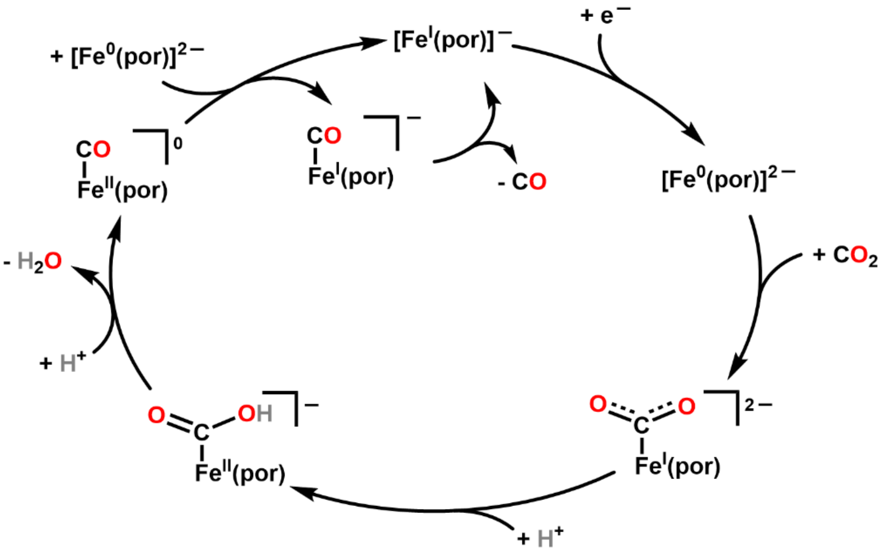

Figure 1.7.1. Mechanism for CO_2 reduction to CO by Fe[por]$^+$ catalysts; where (por) = TPP and any other porphyrin derivative thereof.[68]

Like [Fe(TPP)]$^+$, Mn(bpy)$(CO)_3$Br, and derivatives thereof, represent another class of earth-abundant CO2RR electrocatalysts selective for the production of CO in the presence of weak Brønsted acids.[73] There exist several distinct mechanistic features in the CO2RR mechanism of Mn(bpy)$(CO)_3$Br worth highlighting to compare with the more traditional mechanism for CO_2 reduction to CO, as seen with [Fe(TPP)]$^+$ (**Figure 1.7.1**). First, the one-electron reduced species of Mn(bpy)$(CO)_3$Br is susceptible to dimerization to form a $[Mn(bpy)(CO)_3]_2$ intermediate, which must be reduced for Mn-Mn cleavage to occur in order to bind and activate CO_2.[74] Substitution of CN for Br[75] and incorporation of bulky bipyridine ligands[76] have both been proven strategies which bypass dimerization. Notably, incorporation of Lewis acids with the bulky bipyridine derivatives enable aprotic CO_2 reduction to CO to occur at a lowered overpotential than occurs under protic conditions.[77] Second, previous computational work has shown that upon formation of the neutral Mn^I-hydroxycarbonyl intermediate, there exist two potential pathways by which CO2RR can take place to reach the product-bound Mn^0-$(CO)_4$ intermediate (**Figure 1.7.2**): either via an initial protonation followed by loss of H_2O and subsequent reduction ('*Protonation-First Pathway*'), or initial reduction to a Mn^0-hydroxycarbonyl intermediate followed by proton transfer and loss of H_2O ('*Reduction-First Pathway*').[78] Previous studies on a dimethoxyphenyl bipyridine derivative of $Mn(bpy)(CO)_3Br$ demonstrated that the selective pathway could be tuned by controlling the strength and concentration of the Brønsted acid.

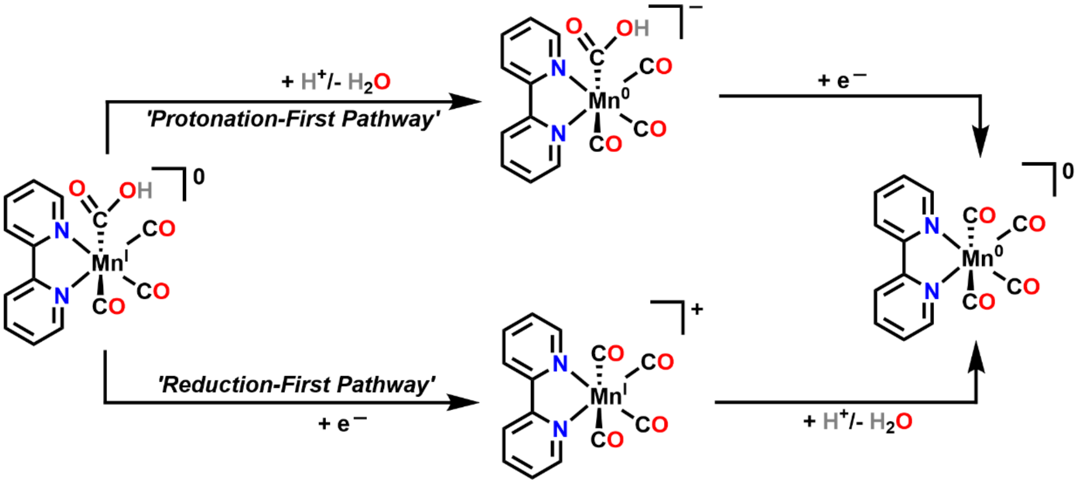

Figure 1.7.2. Comparison of protonation- versus reduction-first pathway for $Mn(bpy)(CO)_3Br$ for electrocatalytic CO2RR.[78]

Lastly, $[Ni(cyclam)]^{2+}$ represents one of the oldest molecular CO2RR catalysts still being studied to date, 40 years after its initial discovery.[79] Beyond a high efficiency and selectivity for CO, one of the more novel aspects of the $[Ni(cyclam)]^{2+}$ catalyst is its ability to operate in water[80-81] across a wide pH range.[82-83] There exist several possible isomers of the $[Ni(cyclam)]^{2+}$ catalyst, however computational studies have suggested the *trans I* isomer, where all four amine protons are cofacial, to be most catalytically active due to the lowered barrier for CO_2 activation that arises from the presence of adjacent H-bonding interactions between the amine protons and the metal-bound CO_2 intermediate.[84] These computational results were experimentally supported by the work of Kubiak *et al.* where systematically substituted methyl groups for the amine protons of the $[Ni(cyclam)]^{2+}$ catalyst resulted in decreased activity.[85] The rate-limiting step which has been proposed in CO_2 to CO conversion mechanisms by $[Ni(cyclam)]^{2+}$ has been CO release. This rate-limiting step also initiates a degradation pathway for $[Ni(cyclam)]^{2+}$, as CO accumulation can lead to the formation of $Ni(CO)_4$ under reducing conditions. However, additional work from Kubiak and coworkers has demonstrated the ability to utilize a simple CO scavenger in preparative scale electrolysis experiments, which has been show to extend the lifetime and long-term efficiency of the $[Ni(cyclam)]^{2+}$ catalyst.[62]

While $[Fe(TPP)]^{+}$, $Mn(bpy)(CO)_3Br$, and $[Ni(cyclam)]^{2+}$ do not represent an all-inclusive list of earth-abundant molecular electrocatalysts for CO_2 reduction to CO, these three catalysts systems are representative of foundational discoveries which has led to an abundance of systems derived from these catalyst platforms.[86]

1.8 Electrochemical Transformations with Organic Mediators

The reduction of O_2 to H_2O or H_2O_2 and the reduction of CO_2 to CO by molecular electrocatalysts requires the net transfer of multiple electrons and, in most cases, multiple protons to facilitate the reaction. The process by which living cells can break chemical bonds within energy-rich molecules in order to release energy is an exceptional example of how electrons and protons can be effectively transported within a synergistic system like the electron transport chain.[87] For example, nicotinamide adenine dinucleotide

(NAD^+/NADH) functions as an electron carrier in glycolysis and the Krebs cycle, where glucose is broken down into CO_2, H_2O, and heat.[87-88] Additionally, it has previously been shown that the electrochemically generated radical anion of phenazine, which is an aromatic nitrogen containing organic molecule, is able to bind CO_2 via an ECE type mechanism (where E represents an electron transfer step and C represents a chemical reaction step).[89] Therefore, given this reactivity, it is intriguing that there exists limited examples of co-catalytic mediators in molecular electrocatalytic O_2 or CO_2 reduction systems as a means to improve efficiency and/or alter selectivity (**Figure 1.8.1**).[90-91]

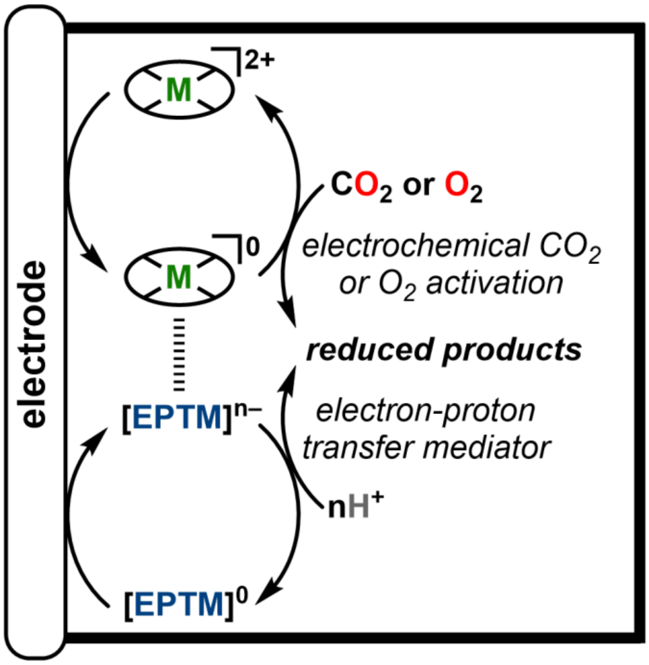

Figure 1.8.1. Illustration of a co-electrocatalytic process involving a redox mediator. RM = redox mediator; inner-sphere M = transition metal electrocatalyst.

In a previous study on Co(salophen) by Stahl and co-workers,[92] the catalytic mechanism for ORR utilizing hydroquinone (H_2Q) as an electron-proton transfer mediator (EPTM) was analyzed based on the use of these compounds in aerobic oxidation catalysis. These showed that a synergistic relationship existed between the Co(salophen) catalyst and *p*-hydroquinone which was generated via the electrocatalytic reduction of *p*-benzoquinone in the presence of acetic acid enabling the the selective conversion of O_2 to H_2O. A follow-up study on this system, expanded on previous results and correlated increased ORR rates with increasing H_2Q concentrations. Finally, Stahl and co-workers sought to increase the efficiency of this electrochemical ORR system by using an alternative quinone with a more positive reduction potential, thus reducing the overpotential. 2-Chlorobenzoquinone was found to show analogous reactivity with BQ at approximately 90 mV more positive potential by CV and CPE analyses. These results highlight how to increase the voltage efficiency of the reaction by changing the quinone functioning as the EPTM.[91]

A recent study by Chang and co-workers demonstrated the use of an EPTM in the electrochemical reduction of CO_2 to CO by $[Fe(TPP)]^+$. In this work, a series of NADH-inspired pyridine derivatives were used as EPTMs with $[Fe(TPP)]^+$ to increase the overall reaction rate, while maintaining selectivity for CO production. While the mechanistic analysis in this study is minimal, the authors were able to show the addition of a mediator with $[Fe(TPP)]^+$ directly increased catalyst TOF. This study, and the one described above, are excellent examples of how the addition of a mediator can enhance the efficiency and/or alter the selectivity in catalytic reactions which require the efficient and precise transfer of protons and electrons.

1.9 Outline of Research Chapters

The proceeding chapters will detail experimental work completed for a molecular manganese (Mn) system for ORR and a molecular chromium (Cr) system for CO_2

reduction. Both the Mn and Cr systems contain the same N2O2 ligand framework.[93-95] Chapters 2 and 3 focus on the Mn system for the catalytic reduction of O_2 to H_2O_2.[94-95] Chapter 2 contains detailed mechanistic findings of this electrocatalytic system as well as an in-depth potential-pK_a analysis via electrochemical methods.[94] Chapter 3 includes a follow-up study on this system where spectrochemical analyses, using decamethylferrocene as a chemical reductant, are carried out in parallel with electrochemical analyses to expand on the electrocatalytic studies detailed in Chapter 2. However, Chapter 3 identifies a divergence in mechanism, relative to the electrocatalytic mechanism reported in Chapter 2, which is dependent on the nature of electron transfer.[95]

Chapter 4 introduces a molecular Cr electrocatalyst capable of reducing CO_2 to CO. This system represents the first molecular Cr catalyst capable of carrying out this process quantitatively.[93] Chapter 5 and 6 incorporate the use of mediators into electrocatalytic systems. Chapter 5 demonstrates the use of *p*-benzoquinone with the Mn system, described in Chapter 2, to electrocatalytically reduce O_2 to H_2O selectively. This work provides evidence to further support the use of mediators for their ability to alter the selectivity of an electrocatalytic system. Chapter 6 describes the use of dibenzothiophene-5,5-dioxide (DBTD) to enhance the electrocatalytic reduction of CO_2 to CO by the Cr system reported in Chapter 4.

1.10 References:

1. Langley, S. P. a. V., Frank W., *The Temperature of the Moon, Memoir of the National Academy of Sciences*. 9th ed.; 1890; Vol. iv.
2. Kellogg, W. W., **1979,** *7*, 63-92.

3. IPCC *Global Warming of 1.5°C. An IPCC Special Report*; World Meterological Organization: Geneva, Switzerland, 2018.
4. Karl, T. R.; Trenberth, K. E., *Science* **2003,** *302*, 1719-1723.
5. Hammarström, L.; Hammes-Schiffer, S., *Acc. Chem. Research* **2009,** *42*, 1859-1860.
6. Kim, D.; Sakimoto, K. K.; Hong, D.; Yang, P., *Angew. Chem., Int. Ed.* **2015,** *54*, 3259-3266.
7. Hussain, A.; Arif, S. M.; Aslam, M., *Renew. Sust. Energ. Rev.* **2017,** *71*, 12-28.
8. DuBois, D. L., *Inorg. Chem.* **2014,** *53*, 3935-3960.
9. Sathrum, A. J.; Kubiak, C. P., *J. Phys. Chem. Lett.* **2011,** *2*, 2372-2379.
10. Corma, A.; Garcia, H., *Topics in Catalysis* **2008,** *48*, 8-31.
11. Machan, C. W.; Sampson, M. D.; Chabolla, S. A.; Dang, T.; Kubiak, C. P., *Organometallics* **2014,** *33*, 4550–4559.
12. Benson, E. E.; Kubiak, C. P.; Sathrum, A. J.; Smieja, J. M., *Chem. Soc. Rev.* **2009,** *38*, 89-99.
13. Finn, C.; Schnittger, S.; Yellowlees, L. J.; Love, J. B., *Chem. Comm.* **2012,** *48*, 1392-1399.
14. You, B.; Sun, Y., *Acc. Chem. Research* **2018,** *51*, 1571-1580.
15. Pegis, M. L.; Wise, C. F.; Martin, D. J.; Mayer, J. M., *Chem. Rev.* **2018,** *118*, 2340-2391.
16. Rountree, E. S.; McCarthy, B. D.; Eisenhart, T. T.; Dempsey, J. L., *Inorg. Chem.* **2014,** *53*, 9983-10002.

17. Elgrishi, N.; Rountree, K. J.; McCarthy, B. D.; Rountree, E. S.; Eisenhart, T. T.; Dempsey, J. L., *J. Chem. Ed.* **2018,** *95*, 197-206.
18. Costentin, C.; Drouet, S.; Robert, M.; Savéant, J.-M., *J. Am. Chem. Soc.* **2012,** *134*, 11235-11242.
19. Lee, K. J.; Elgrishi, N.; Kandemir, B.; Dempsey, J. L., *Nat. Rev. Chem.* **2017**, 0039.
20. Machan, C. W., *Current Opinion in Electrochemistry* **2019,** *15*, 42-49.
21. Abdu I. Alayash, R. P. P., and Robert E. Cashon, *Antioxidants & Redox Signaling* **2001,** *3*, 313-327.
22. Yoshikawa, S.; Shimada, A., *Chem. Rev.* **2015,** *115*, 1936-1989.
23. McEvoy, J. P.; Brudvig, G. W., *Chem. Rev.* **2006,** *106*, 4455-4483.
24. Mailloux, R. J., *Redox Biol.* **2015,** *4*, 381-398.
25. Machan, C. W., *ACS Catal.* **2020,** *10*, 2640-2655.
26. Niederhoffer, E. C.; Timmons, J. H.; Martell, A. E., *Chem. Rev.* **1984,** *84*, 137-203.
27. Zagal, J. H., *Coord. Chem. Rev.* **1992,** *119*, 89-136.
28. Elzing, A.; van der Putten, A.; Visscher, W.; Barendrecht, E., *Recueil des Travaux Chimiques des Pays-Bas* **1990,** *109*, 31-39.
29. Lee, Y.-M.; Hong, S.; Morimoto, Y.; Shin, W.; Fukuzumi, S.; Nam, W., *J. Am. Chem. Soc.* **2010,** *132*, 10668-10670.
30. Bratsch, S. G., *J. Phys. Chem. Ref. Data* **1989,** *18*, 1-21.
31. Firouzjaie, H. A.; Mustain, W. E., *ACS Catal.* **2020,** *10*, 225-234.
32. Campos-Martin, J. M.; Blanco-Brieva, G.; Fierro, J. L. G., *Angew. Chem., Int. Ed.* **2006,** *45*, 6962-6984.
33. Gasteiger, H. A.; Marković, N. M., *Science* **2009,** *324*, 48-49.

34. Passard, G.; Dogutan, D. K.; Qiu, M.; Costentin, C.; Nocera, D. G., *ACS Catal.* **2018,** *8*, 8671-8679.

35. Jean-Michel Savéant, C. C., *Elements of Molecular and Biomolecular Electrochemistry: An Electrochemical Approach to Electron Transfer Chemistry*. Wiley: 2019.

36. Collman, J. P.; Wagenknecht, P. S.; Hutchison, J. E., *Angew. Chem., Int. Ed.* **1994,** *33*, 1537-1554.

37. Chang, C. J.; Loh, Z.-H.; Shi, C.; Anson, F. C.; Nocera, D. G., *J. Am. Chem. Soc.* **2004,** *126*, 10013-10020.

38. Martin, D. J.; Wise, C. F.; Pegis, M. L.; Mayer, J. M., *Acc. Chem. Research* **2020**.

39. Brezny, A. C.; Johnson, S. I.; Raugei, S.; Mayer, J. M., *J. Am. Chem. Soc.* **2020,** *142*, 4108-4113.

40. Martin, D. J.; Mercado, B. Q.; Mayer, J. M., *Sci. Adv.* **2020,** *6*, eaaz3318.

41. Pegis, M. L.; Martin, D. J.; Wise, C. F.; Brezny, A. C.; Johnson, S. I.; Johnson, L. E.; Kumar, N.; Raugei, S.; Mayer, J. M., *J. Am. Chem. Soc.* **2019,** *141*, 8315-8326.

42. Pegis, M. L.; Wise, C. F.; Koronkiewicz, B.; Mayer, J. M., *J. Am. Chem. Soc.* **2017,** *139*, 11000-11003.

43. Pegis, M. L.; McKeown, B. A.; Kumar, N.; Lang, K.; Wasylenko, D. J.; Zhang, X. P.; Raugei, S.; Mayer, J. M., *ACS Cent. Sci.* **2016,** *2*, 850-856.

44. Wasylenko, D. J.; Rodríguez, C.; Pegis, M. L.; Mayer, J. M., *J. Am. Chem. Soc.* **2014,** *136*, 12544-12547.

45. Carver, C. T.; Matson, B. D.; Mayer, J. M., *J. Am. Chem. Soc.* **2012,** *134*, 5444-5447.

46. Wang, Y.-H.; Schneider, P. E.; Goldsmith, Z. K.; Mondal, B.; Hammes-Schiffer, S.; Stahl, S. S., *ACS Cent. Sci.* **2019,** *5*, 1024-1034.

47. Wang, Y.-H.; Pegis, M. L.; Mayer, J. M.; Stahl, S. S., *J. Am. Chem. Soc.* **2017,** *139*, 16458-16461.

48. Wang, Y.-H.; Goldsmith, Z. K.; Schneider, P. E.; Anson, C. W.; Gerken, J. B.; Ghosh, S.; Hammes-Schiffer, S.; Stahl, S. S., *J. Am. Chem. Soc.* **2018,** *140*, 10890-10899.

49. Wang, Y.-H.; Mondal, B.; Stahl, S. S., *ACS Catal.* **2020,** *10*, 12031-12039.

50. Fukuzumi, S.; Lee, Y.-M.; Nam, W., *ChemCatChem* **2018,** *10*, 9-28.

51. West, N. M.; Miller, A. J. M.; Labinger, J. A.; Bercaw, J. E., *Coord. Chem. Rev.* **2011,** *255*, 881-898.

52. Kalck, P.; Le Berre, C.; Serp, P., *Coord. Chem. Rev.* **2020,** *402*, 213078.

53. Hood, D. M.; Johnson, R. A.; Carpenter, A. E.; Younker, J. M.; Vinyard, D. J.; Stanley, G. G., *Science* **2020,** *367*, 542-548.

54. Costentin, C.; Drouet, S.; Passard, G.; Robert, M.; Saveant, J.-M., *J. Am. Chem. Soc.* **2013,** *135*, 9023-9031.

55. Qiao, J.; Liu, Y.; Hong, F.; Zhang, J., *Chem. Soc. Rev.* **2014,** *43*, 631-675.

56. Jiang, C.; Nichols, A. W.; Machan, C. W., *Dalton Trans.* **2019,** *48*, 9454-9468.

57. Wang, L.; Chen, W.; Zhang, D.; Du, Y.; Amal, R.; Qiao, S.; Wu, J.; Yin, Z., *Chem. Soc. Rev.* **2019,** *48*, 5310-5349.

58. Waldie, K. M.; Brunner, F. M.; Kubiak, C. P., *ACS Sustain. Chem. Eng.* **2018,** *6*, 6841-6848.

59. Ostericher, A. L.; Waldie, K. M.; Kubiak, C. P., *ACS Catal.* **2018,** *8*, 9596-9603.

60. DuBois, D. L.; Berning, D. E., *Appl.Organomet. Chem.* **2000,** *14*, 860-862.

61. Ostericher, A. L.; Porter, T. M.; Reineke, M. H.; Kubiak, C. P., *Dalton Trans.* **2019,** *48*, 15841-15848.

62. Froehlich, J. D.; Kubiak, C. P., *J. Am. Chem. Soc.* **2015,** *137*, 3565-3573.

63. Margarit, C. G.; Schnedermann, C.; Asimow, N. G.; Nocera, D. G., *Organometallics* **2019,** *38*, 1219-1223.

64. Nichols, A. W.; Machan, C. W., *Front. Chem.* **2019,** *7*, https://doi.org/10.3389/fchem.2019.00397.

65. McGuire Jr, R.; Dogutan, D. K.; Teets, T. S.; Suntivich, J.; Shao-Horn, Y.; Nocera, D. G., *Chem. Sci.* **2010,** *1*, 411-414.

66. Francke, R.; Schille, B.; Roemelt, M., *Chem. Rev.* **2018,** *118*, 4631-4701.

67. Hammouche, M.; Lexa, D.; Savéant, J. M.; Momenteau, M., *J. Electroanal. Chem. Interf. Electrochem.***1988,** *249*, 347-351.

68. Bhugun, I.; Lexa, D.; Savéant, J.-M., *J. Am. Chem. Soc.* **1996,** *118*, 1769-1776.

69. Costentin, C.; Passard, G.; Robert, M.; Savéant, J.-M., *Proc. Natl. Acad. Sci.* **2014,** *111*, 14990.

70. Sinha, S.; Warren, J. J., *Inorg. Chem.* **2018,** *57*, 12650-12656.

71. Nichols, Eva M.; Derrick, J. S.; Nistanaki, S. K.; Smith, P. T.; Chang, C. J., *Chem. Sci.* **2018,** *9*, 2952-2960.

72. Azcarate, I.; Costentin, C.; Robert, M.; Savéant, J.-M., *J. Am. Chem. Soc.* **2016,** *138*, 16639-16644.

73. Bourrez, M.; Molton, F.; Chardon-Noblat, S.; Deronzier, A., *Angew. Chem., Int. Ed.* **2011,** *50*, 9903-9906.

74. Grills, D. C.; Farrington, J. A.; Layne, B. H.; Lymar, S. V.; Mello, B. A.; Preses, J. M.; Wishart, J. F., *J. Am. Chem. Soc.* **2014,** *136*, 5563-5566.

75. Machan, C. W.; Stanton, C. J.; Vandezande, J. E.; Majetich, G. F.; Schaefer, H. F.; Kubiak, C. P.; Agarwal, J., *Inorg. Chem.* **2015,** *54*, 8849-8856.

76. Sampson, M. D.; Nguyen, A. D.; Grice, K. A.; Moore, C. E.; Rheingold, A. L.; Kubiak, C. P., *J. Am. Chem. Soc.* **2014,** *136*, 5460-5471.

77. Sampson, M. D.; Kubiak, C. P., *J. Am. Chem. Soc.* **2016,** *138*, 1386-1393.

78. Riplinger, C.; Sampson, M. D.; Ritzmann, A. M.; Kubiak, C. P.; Carter, E. A., *J. Am. Chem. Soc.* **2014,** *136*, 16285-16298.

79. Fisher, B. J.; Eisenberg, R., *J. Am. Chem. Soc.* **1980,** *102*, 7361-7363.

80. Kelly, C. A.; Blinn, E. L.; Camaioni, N.; D'Angelantonio, M.; Mulazzani, Q. G., *Inorg. Chem.* **1999,** *38*, 1579-1584.

81. Beley, M.; Collin, J.-P.; Ruppert, R.; Sauvage, J.-P., *Chem. Comm.* **1984**, 1315-1316.

82. Schneider, J.; Jia, H.; Kobiro, K.; Cabelli, D. E.; Muckerman, J. T.; Fujita, E., *Energy Environ. Sci.* **2012,** *5*, 9502-9510.

83. Neri, G.; Aldous, I. M.; Walsh, J. J.; Hardwick, L. J.; Cowan, A. J., *Chem. Sci.* **2016,** *7*, 1521-1526.

84. Song, J.; Klein, E. L.; Neese, F.; Ye, S., *Inorg. Chem.* **2014,** *53*, 7500-7507.

85. Froehlich, J. D.; Kubiak, C. P., *Inorg. Chem.* **2012,** *51*, 3932–3934.

86. Francke, R.; Schille, B.; Roemelt, M., *Chem. Rev.* **2018,** *118*, 4631-4701.

87. Kumari, A., Chapter 3 - Electron Transport Chain. In *Sweet Biochemistry*, Kumari, A., Ed. Academic Press: 2018; pp 13-16.

88. Sorci, L.; Kurnasov, O.; Rodionov, D. A.; Osterman, A. L., 7.08 - Genomics and Enzymology of NAD Biosynthesis. In *Comprehensive Natural Products II*, Liu, H.-W.; Mander, L., Eds. Elsevier: Oxford, 2010; pp 213-257.

89. Ogata, T.; Yamamoto, Y.; Wada, Y.; Murakoshi, K.; Kusaba, M.; Nakashima, N.; Ishida, A.; Takamuku, S.; Yanagida, S., *J. Phys. Chem.* **1995,** *99*, 11916-11922.

90. Smith, P. T.; Weng, S.; Chang, C. J., *Inorg. Chem.* **2020,** *59*, 9270-9278.

91. Anson, C. W.; Stahl, S. S., *J. Am. Chem. Soc.* **2017,** *139*, 18472-18475.

92. Anson, C. W.; Ghosh, S.; Hammes-Schiffer, S.; Stahl, S. S., *J. Am. Chem. Soc.* **2016,** *138*, 4186-4193.

93. Hooe, S. L.; Dressel, J. M.; Dickie, D. A.; Machan, C. W., *ACS Catal.* **2020,** *10*, 1146-1151.

94. Hooe, S. L.; Rheingold, A. L.; Machan, C. W., *J. Am. Chem. Soc.* **2018,** *140*, 3232-3241.

95. Hooe, S. L.; Machan, C. W., *J. Am. Chem. Soc.* **2019,** *141*, 4379-4387.

Chapter 2

Electrocatalytic Reduction of Dioxygen to Hydrogen Peroxide by a Molecular Manganese Complex with a Bipyridine-Containing Schiff Base Ligand

Reproduced with permission from Hooe, S. L.; Rheingold, A. L.; Machan, C. W., *Journal of the American Chemical Society* **2018,** *140* (9), 3232-3241. Copyright 2017 American Chemical Society.

Hooe, S. L.; Rheingold, A. L.; Machan, C. W., *Journal of the American Chemical Society* **2018,** *140* (9), 3232-3241. https://pubs.acs.org/doi/abs/10.1021/jacs.7b09027

2.1 Abstract

The synthesis and electrocatalytic reduction of dioxygen by a molecular manganese(III) complex with a tetradentate dianionic bipyridine-based ligand is reported. Electrochemical characterization indicates a Nernstian dependence on the added proton source for the reduction of Mn(III) to Mn(II). The resultant species is competent for the reduction of dioxygen to H_2O_2 with 81 ± 4% Faradaic efficiency. Mechanistic studies suggest that the catalytically active species has been generated through the interaction of the added proton donor and the parent Mn complex, resulting in the protonation of a coordinated phenolate moiety following the single-electron reduction, generating a neutral species with a vacant coordination site at the metal center. As a consequence, the active catalyst has a pendent proton source in close proximity to the active site for subsequent intramolecular reactions.

2.2 Introduction

The reduction of dioxygen (O_2) to water (H_2O) or hydrogen peroxide (H_2O_2) has importance in biological systems, oxidative functionalization reactions, and fuel cells.[1-3] Heterogeneous Pt electrodes are among the most efficient at catalyzing the oxygen reduction reaction (ORR), but natural metalloenzymes commonly use first-row transition metals to achieve analogous reactivity. Of the abiotic molecular species studied for the ORR, manganese (Mn), appears infrequently.[4-15] The molecular Mn complexes which have been shown to electrocatalytically reduce O_2 have either been porphyrins or porphyrin-derivatives and were examined under aqueous conditions while adsorbed to the electrode.[4-10, 15] It is conspicuous that molecular Mn species can have profound thermal reactivity with O_2,[1, 16-22] yet so few active homogeneous electrocatalytic systems have been identified.

The activity of Fe-, Co-, and Mn-based salens with O_2 is well-established and even used as a deliberate component in their synthesis.[23-26] Salicaldehyde-derived imines are not-ideal for use in ORR given their inherent instability: the condensation reaction to produce Schiff base salen-type ligands is in an equilibrium with H_2O, which can be a solvent, substrate, and product for the ORR. To address this deficiency, we were interested in a Schiff base ligand platform derived from 2,2′-bipyridine (bpy) obtained through synthetic modification at the 6,6′-positions with 2-hydroxybenzene moieties.[27-28] This ligand platform accesses a similar coordination environment to traditional salen-type ligands without relying on chemically/electrochemically reactive imine bonds as structural elements.

2.3 Synthesis and Characterization

Previous syntheses of bpy- or 1,10-phenanthroline-based ligands symmetrically functionalized with 2-hydroxybenzene moieties relied on low-yielding dearomatization reactions with alkyllithium reagents.[28-30] A significant improvement in overall reaction yield can be achieved through the use of a Suzuki-type cross-coupling reaction.[27, 31] Beginning from 2,4-di-*tert*-butyl-phenol, bromination in CH_2Cl_2 with Br_2 enabled the isolation of 2-bromo-4,6-di-*tert*-butyl-phenol in near quantitative yields. Treatment of the brominated intermediate with *n*-butyllithium, followed by $B(OMe)_3$, and a final acidic aqueous work-up was used to isolate the corresponding boronic acid. After a Pd-catalyzed cross-coupling reaction with 6,6′-dibromo-2,2′-bipyridine, 6,6′-di(3,5-di-*tert*-butyl-2-hydroxybenzene)-2,2′-bipyridine (^{tbu}dhbpy(H)$_2$) could be obtained. Metalation of (^{tbu}dhbpy(H)$_2$) to generate Mn(^{tbu}dhbpy)Cl **1** was achieved after 2 h under refluxing conditions in MeOH with manganese(II) acetate tetrahydrate, sparging with compressed air, and precipitation with saturated brine solution.

UV-vis (**Figure S2.3.1**) and NMR spectroscopies (**Figures S2.3.2-S2.3.3**), as well as ESI-MS (**Figure S2.3.4**) and microanalysis are consistent with the proposed structure of the ligand and the Mn complex shown in **Figure 2.3.1**. Evan's method measurements in acetonitrile (MeCN) exhibited a of μ_{eff} = 4.82 ± 0.03, consistent with a high-spin d^4 Mn(III) complex (**Table S2.3.1**).[32-33] Single crystals suitable for X-ray diffraction studies were grown by layering hexanes over a solution of **1** in THF. The molecular coordinates obtained from these X-ray data are also consistent with the proposed structure; Mn is fully chelated in a tetradentate fashion by ^{tbu}dhbpy with a chloride ligand in an axial coordination site and an overall distorted square pyramidal geometry at the metal center

(**Figure 2.3.1**). The UV-vis spectrum of **1** (**Figure S2.3.1**) in (MeCN) exhibits charge transfer bands in the visible region. The HOMO and LUMO orbitals are predicted to be primarily composed of unoccupied Mn δ orbitals and phenolate based π orbitals, respectively, by Kohn–Sham orbital projections (**Figure S2.3.5**).

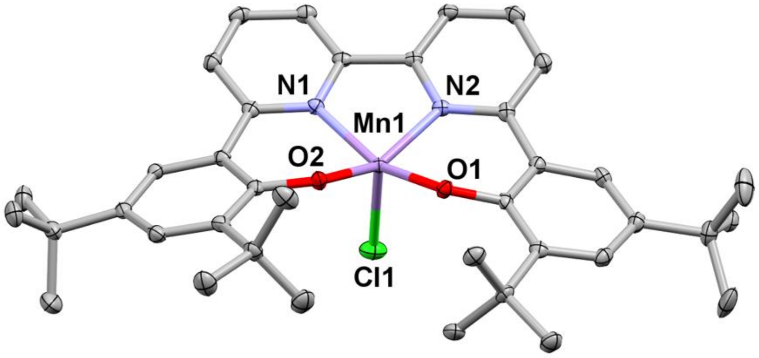

Figure 2.3.1. Molecular structure of Mn(^{tbu}dhbpy)Cl **1**, obtained from single-crystal X-ray diffraction studies. Blue = N, red = O, gray = C, green = Cl, purple = Mn; thermal ellipsoids at 50%, H atoms and a disordered occluded THF molecule omitted for clarity.

2.4 Electrochemical Studies with Non-Buffered Proton Sources

Cyclic voltammetry (CV) experiments were performed on **1** in a solution of 0.1 M tetrabutylammonium hexafluorophosphate ($TBAPF_6$) in MeCN (**Figures 2.4.3** and **S2.4.6**). At potentials negative of the ferricenium/ferrocene (Fc^+/Fc) reduction potential measured under experimental conditions, a single quasi-reversible feature is observed before -1.0 V. This wave is assigned to a $Mn^{III/II}$ reduction with $E_{1/2}$ = -0.63 V vs Fc^+/Fc (ΔE_p = 81 mV; ΔE_p(Fc) = 71 mV). Variable-scan rate studies show that the $Mn^{III/II}$ reduction is diffusion controlled at this reduction feature (**Figure S2.4.6-S2.4.7**).

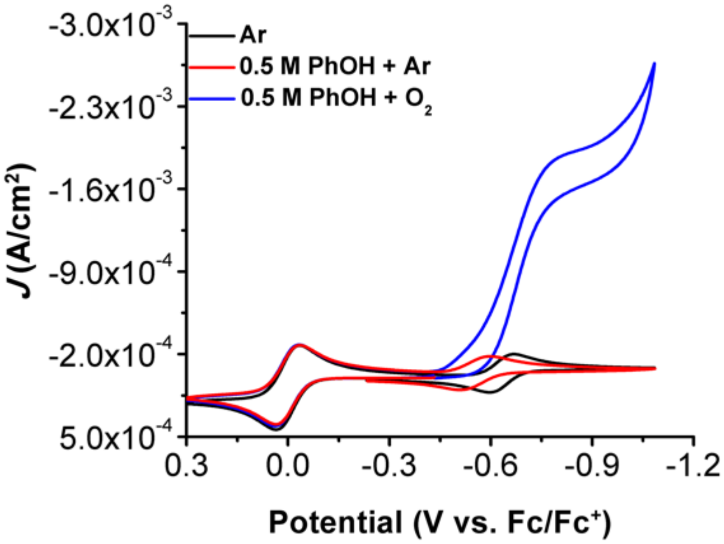

Figure 2.4.3. CVs of Mn(^{tbu}dhbpy)Cl **1**, obtained under Ar saturation conditions (black), Ar with 0.5 M PhOH (red), and 0.5 M PhOH under O_2 saturation (blue). Conditions: 1 mM analyte; glassy carbon working electrode, Pt wire counter electrode, Ag/AgCl pseudoreference electrode; scan rate 100 mV/s; referenced to internal ferrocene standard.

This reduction feature ($E_{1/2}$ = -0.63 V vs Fc^+/Fc) shows a proton donor-dependent voltage response; titrating phenol (PhOH) into solution shows a shift to more positive potentials (**Figure 2.4.4**). This Nernstian response was analyzed by plotting the $E_{1/2}$ against the log of PhOH concentration, which established a 1 [PhOH]/1 e- relationship through a slope of 70 mV/decade of PhOH concentration (**Figure S2.4.8**).[34-37]. Since the homogeneous electron transfer reaction involving **1** is fast enough to remain reversible under these conditions, we assign this response to an electrochemically driven proton transfer reaction. Given that the formation of a Mn–H species under these conditions would be unexpected, this is likely a proton transfer from a PhOH donor to a Mn-bound O atom acceptor to generate [Mn(^{tbu}dhbpy(H))Cl] (Species **2**, **Scheme 2.4.1**).

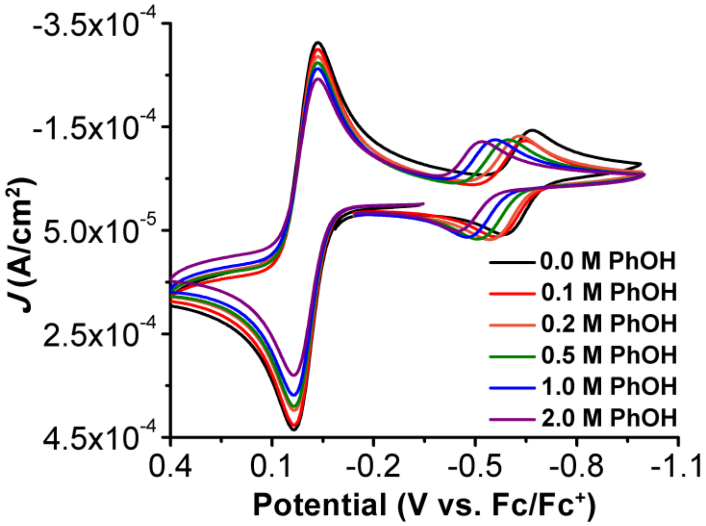

Figure 2.4.4. CVs of Mn(^{tbu}dhbpy)Cl **1**, obtained under Ar saturation conditions with variable PhOH concentration. Conditions: 1 mM analyte; glassy carbon working electrode, Pt wire counter electrode, Ag/AgCl pseudoreference electrode; scan rate 100 mV/s; referenced to internal ferrocene standard.

Titration of tetrabutylammonium chloride (TBACl) into a solution of **1** under Ar saturation in MeCN shows a minimal shift in the Mn$^{III/II}$ reduction feature (**Figures S2.4.9-S2.4.12**). With a fixed concentration of PhOH, titration of TBACl into solution under Ar saturation suppresses the shift to positive potentials, but not completely, implying that Cl$^-$ loss is part of the equilibrium following reduction but slow relative to the reduction-induced protonation reaction (**Figure 2.4.5**). ΔE_p remains in a range consistent with a one-electron process at all concentrations of added PhOH under these conditions when compared to Fc$^+$/Fc (**Table S2.4.2**).

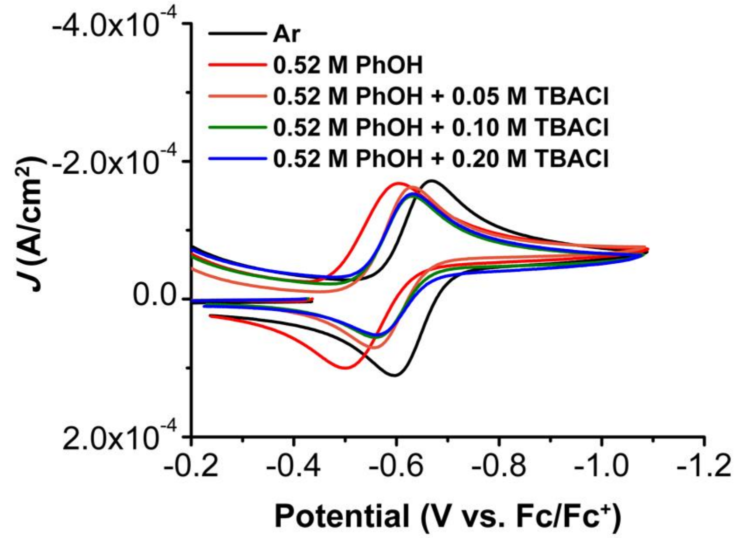

Figure 2.4.5. CVs of Mn(^{tbu}dhbpy)Cl **1**, obtained under Ar saturation conditions comparing the effects of fixed PhOH concentration and increasing TBACl concentration. Conditions: 1 mM analyte; glassy carbon working electrode, Pt wire counter electrode, Ag/AgCl pseudoreference electrode; 100 mV/s scan rate; referenced to internal ferrocene standard.

If these studies are instead conducted in the absence of PhOH under O_2 saturation, a slight change in the current response at the Mn$^{III/II}$ reduction feature occurs, suggesting a very slow binding interaction with O_2 under these conditions (**Figure S2.4.13**). Control experiments show that O_2 reduction by the glassy carbon electrode occurs at potentials ~650 mV more negative (**Figure S2.4.14**). If CV experiments are conducted with PhOH and O_2, however, a significant increase in current occurs at the Mn$^{III/II}$ reduction feature consistent with a catalytic response. Variable concentration studies under O_2 saturation (6.3 mM in MeCN[38]) established that the observed current reaches a peak at 0.5 M PhOH (**Figures 2.4.3** and **S2.4.15**). Before this saturation is reached, a log-log plot comparing the added PhOH concentration with observed current density suggests a first-order dependence (**Figure S2.4.16**). Similar studies with variable O_2 concentration and 0.5 M PhOH suggest a first-order dependence on O_2 (**Figures S2.4.17** and **S2.4.18**). Variable catalyst concentration studies with O_2 saturation and 0.11 M PhOH are consistent with a first-order dependence (**Figures S2.4.19** and **S2.4.20**). Given that product analysis by rotating ring-disk electrode (RRDE) experiments under these conditions suggest that the overall reaction is a $2H^+/2e^-$ reduction to H_2O_2, these data suggest a unimolecular activation of O_2 and a rate-limiting protonation/reduction step, *vide infra*.[13] Titration of TBACl into an MeCN solution with fixed PhOH concentration under O_2 saturation results in a suppression of catalytic current (**Figures S2.4.21-S2.4.22**), suggesting that Cl loss occurs upon O_2 binding and activation. Lastly, the abstraction of Cl^- from **1** with thallium(I) trifluoromethansulfonate [Tl(OTf)] results in a diminished Nernstian shift under Ar with PhOH titration, but comparable activity in the presence of O_2 (**Figures S2.4.23-S2.4.26**).

In order to quantify the overall efficiency of the catalytic reaction, it was necessary to repeat CV analysis with 2,2,2-trifluoroethanol (TFE-OH) as a proton source. As has been reported previously,[39] oxidation of the phenolate anions resulting from proton consumption in situ is observable on the CV timescale (**Figure S2.4.27**). Repeating the kinetic experiments described above with TFE-OH in the presence of O_2 established that a reaction with analogous kinetic parameters to the PhOH-based studies was occurring (**Figures S2.4.28-S2.4.41**). These data are in qualitative agreement with the predicted lower pK_a for TFE-OH (predicted pK_a (MeCN) = 35.4[40]; predicted value ignores homoconjugation) in comparison to PhOH (experimental pK_a (MeCN) = 29.14[41]). At low concentrations of TFE-OH, O_2 binding without catalytic current enhancement occurred on the CV timescale (**Figure S2.4.32**). Similar experimental effects were observed when H_2O, predicted to have an even higher pK_a than TFE-OH, was used as the sacrificial proton source (**Figure S2.4.42**).

RRDE experiments were performed with Mn(^{tbu}dhbpy)Cl **1** and TFE-OH to determine the current efficiency of O_2 reduction to H_2O_2. At concentrations of 0.25 mM **1** with 0.6 M TFE-OH under O_2 saturation, efficiencies of 81±4% are observed (**Figures S2.4.43-S2.4.54**). Using rotating disk electrode experiments, diffusion coefficients for the electroactive species at the $Mn^{III/II}$ feature were determined under all experimental conditions: Ar only 3.41×10^{-6} cm^2s^{-1}; Ar and 0.5 M PhOH 3.78×10^{-6} cm^2s^{-1}; O_2 and 0.5 M PhOH 4.21×10^{-6} cm^2s^{-1} (**Figures S2.4.55-S2.4.63**). These values do not suggest that a Mn–[μ^2-O–O]–Mn dimer is forming, consistent with the kinetic data on catalyst concentration detailed above.

2.5 Electrochemical Studies with Buffered Proton Sources

In an attempt to understand the proton donor-proton acceptor interaction further, buffered proton sources were analyzed by CV (**Figures S2.5.64**). The absence of a trend from these data is ascribed to side phenomena not related to proton activity, such as ligand exchange reactions with the anionic bases (**Figure S2.5.65-2.5.68**). In an attempt to interrogate the Nernstian relationship of proton donor and **1** further under buffered conditions, different ratios of tetrabutylammonium phenoxide and phenol were monitored by CV (**Figure 2.5.6**). When the ratio shifted towards higher PhOH concentration, a plot of $E_{1/2}$ against the log of the $[PhO^-]/[PhOH]$ exhibited a slope of 91 mV/decade (**Figure 2.5.7**). Titrating an excess of phenoxide under these conditions exhibited a slope of 54 mV/decade (**Figures S2.5.69-S2.5.70**). Although deviations from a Nernstian 1 substrate/1 e^- relationship are observed, the observed relationship is consistent with the concentration of proton donor relating to the $E_{1/2}$ for the reduction of **1**. Similar behavior is observed when the Cl-abstracted compound Mn(^{tbu}dhbpy)[OTf] is used (**Figure S2.5.71-S2.5.74**).

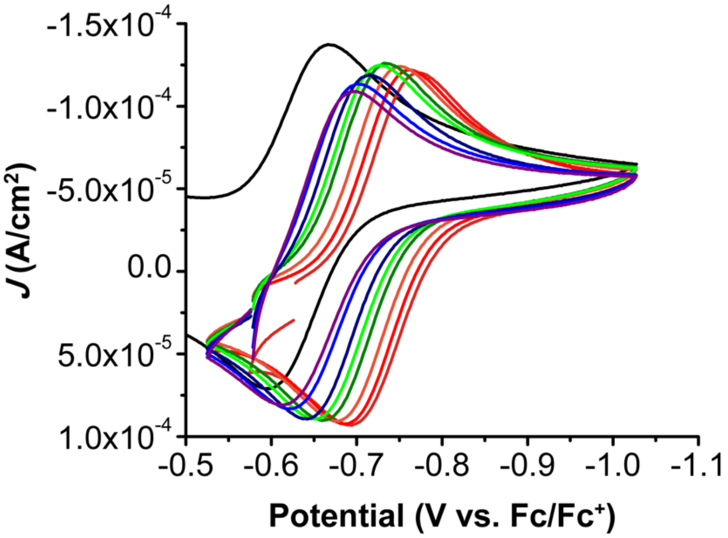

Figure 2.5.6. CVs of Mn(^{tbu}dhbpy)Cl **1**, obtained under Ar saturation conditions showing the the effects of fixed PhO$^-$ concentration with increasing PhOH concentration on $E_{1/2}$. Conditions: 1 mM Mn(^{tbu}dhbpy)Cl **1**; glassy carbon working electrode, glassy carbon counter electrode, Ag/AgCl pseudoreference electrode; 100 mV/s scan rate; referenced to internal ferrocene standard.

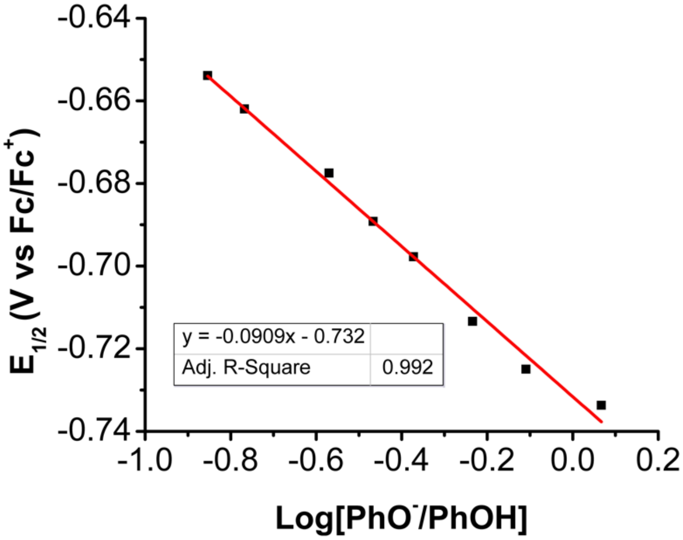

Figure 2.5.7. Plot of $E_{1/2}$ for Mn(^{tbu}dhbpy)Cl **1** against the log of the ratio of [PhO$^-$]/[PhOH] showing the effects of fixed PhO$^-$ concentration with increasing PhOH concentration on $E_{1/2}$.

In order to analyze this system using the foot-of-the-wave analysis (FOWA), selected experiments were repeated using the buffered pentafluorophenol (F_5PhOH/TBA[F_5PhO]) proton source, which should have a non-aqueous pH = pK_a = 20.11.[42] F_5PhOH was used as a proton source under buffered conditions because unsubstituted PhOH showed a minimal response, presumably due to the higher non-aqueous buffered pK_a(MeCN) (29.14; **Figure S2.5.75**). When the buffered proton source (F_5PhOH/TBA[F_5PhO]) was titrated into solution, maximal current was reached at a concentration of 11 mM (**Figures 2.5.8** and **S2.5.76-S2.5.78**). These data were used to determine apparent catalytic rates (k_{obs}) and maximal turnover frequencies (TOF_{max}) through FOWA (**Figures S2.5.79-S2.5.80**).[13-14, 43] For F_5PhOH/TBA[F_5PhO], TOF_{max} ($k_{obs}C_{substrate}$) = 3.13 x 10^4 s^{-1} and k_{obs} = 4.52 x 10^8 $M^{-1}s^{-1}$ ([Acid] = 11 mM; [O_2] = 6.3 mM). A simulated catalytic Tafel plot[44] comparing these catalysts to previous literature reports on catalysts which electrocatalytically produce H_2O_2 is shown below in **Figure 2.5.9**.[10, 45-48] When these buffered acid studies are repeated with [Mn(^{tbu}dhbpy)][OTf], k_{obs} decreases to 1.62 x 10^6 $M^{-2}s^{-1}$ as determined by comparable FOWA analysis (**Figure S2.5.81-S2.5.83**).

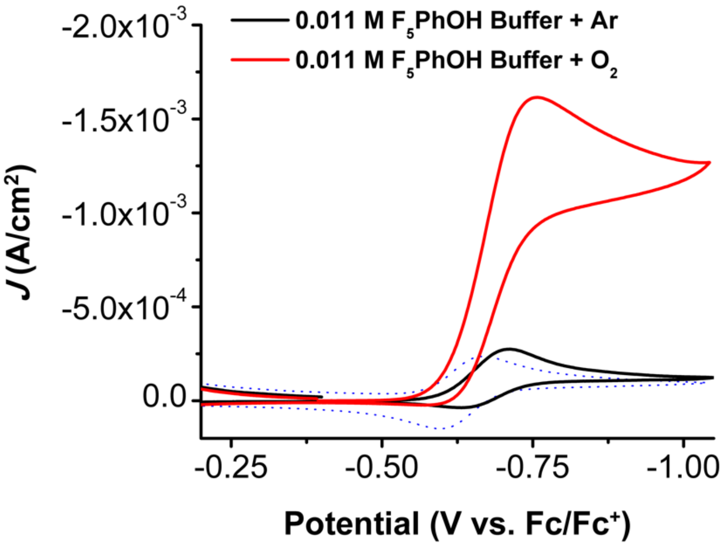

Figure 2.5.8. CVs of Mn(^{tbu}dhbpy)Cl **1**, obtained under Ar saturation conditions with 11 mM buffered F_5PhOH under Ar (black) and O_2 saturation (6.3 mM, red); aprotic conditions under Ar saturation are shown for reference (blue dotted line). Conditions: 1 mM analyte; glassy carbon working electrode, Pt wire counter electrode, Ag/AgCl pseudoreference electrode; scan rate 100 mV/s; referenced to internal ferrocene standard.

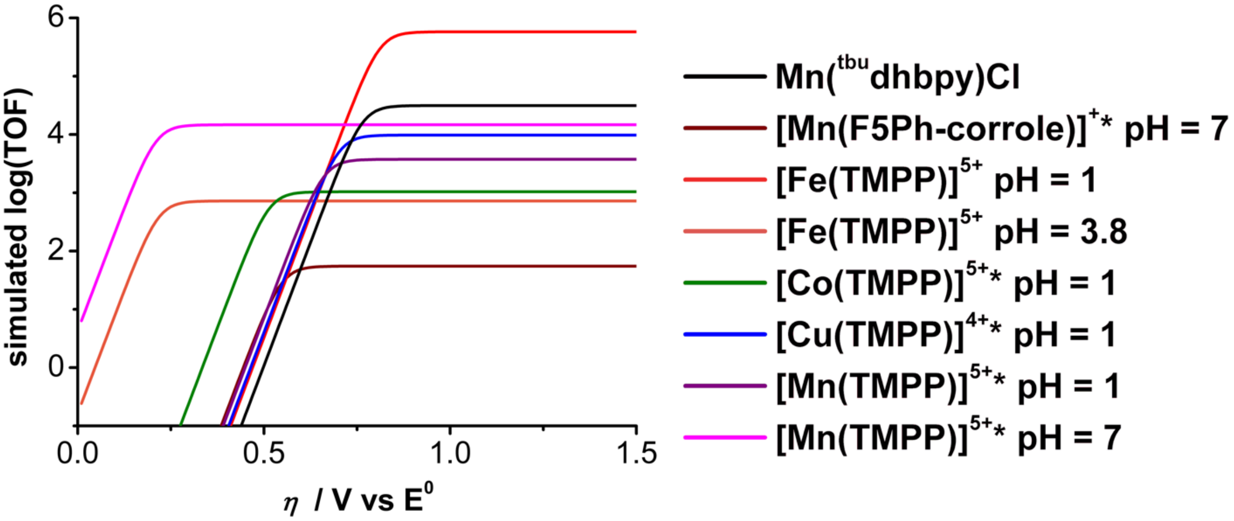

Figure 2.5.9. Simulated catalytic Tafel plots comparing Mn(^{tbu}dhbpy)Cl **1** to literature values for O_2 to H_2O_2 reduction by molecular species. The overpotential in V (η) refers to the difference between catalyst $E_{1/2}$ and the respective standard potentials E^0 for O_2/H_2O_2 under the experimental conditions reported (see Methods Section); TMPP = 5,10,15,20-tetrakis(*N*-methyl-pyridyl)porphyrin, * indicates an electrode surface-adsorbed catalyst.[10, 45-48]

2.6 Potential-pKa Analysis

Using the method of Dempsey *et al.*[36], further understanding of the relationship of the proton donor to the observed redox potential was obtained through a potential-pK_a relationship. Using 1:1 mixtures of acid with **1**, a potential-pK_a diagram was constructed to establish the relationship of $E_{1/2}$ to the acid pK_a (**Figures 2.6.10** and **S2.6.84**). This diagram obviates the need to define proton activity in a non-aqueous system, where ion pairs from dissociated acid are expected to exhibit drastically different properties than under aqueous conditions where solvation by water molecules can stabilize dissociation. Two distinct regions are observed in this diagram, a horizontal region from 29.14-20.11 pK_a and a slope of 32 mV/pK_a from 20.11-12.65 pK_a. Deviation from a Nernstian 1 pK_a/1 e^- relationship is observed, but the electrochemical response of **1** demonstrates a relationship between acid strength in MeCN and the thermodynamic reduction potential consistent with a proton donor-proton acceptor interaction.

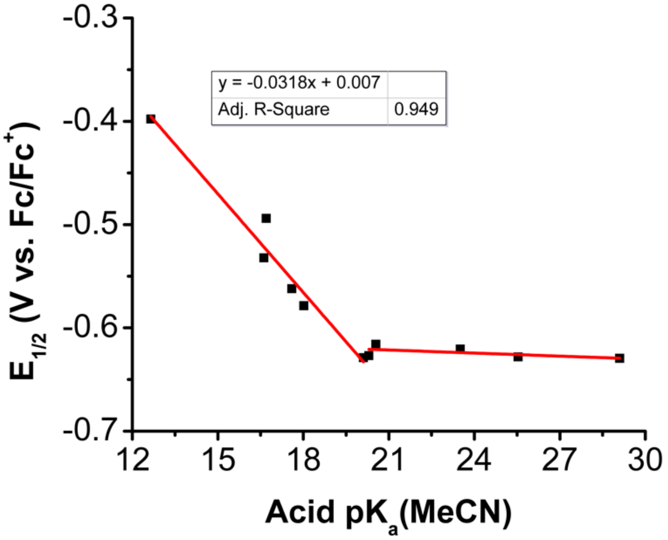

Figure 2.6.10. A potential-pK_a diagram for acids from pK_a = 12.65 to 29.14. Conditions: Ar saturation; 0.5 mM Mn(^{tbu}dhbpy)Cl **1**, 0.5 mM acid (**Figures S3.91**); glassy carbon working electrode, glassy carbon counter electrode, Ag/AgCl pseudoreference electrode; scan rate 100 mV/s; referenced to internal ferrocene standard. pK_a(MeCN): Phenol = 29.14; 4-CF_3-PhOH = 25.54; acetic acid = 23.51; perflouoro-*tert*-butanol = 20.55; 4-Br-benzoic acid = 20.3; F_5PhOH = 20.11; Cl_5PhOH = 18.02; 2,6-dichloro-benzoic acid = 17.6; salicylic acid = 16.7; 4-CF_3-F_4PhOH = 16.62; trifluoroacetic acid = 12.65.[42, 49-50]

2.7 Spectrochemical Studies

As a supplement to the electrochemical studies detailed above, a series of spectrochemical studies were undertaken to better understand the electrocatalytic activity of **1** toward O_2 reduction. Using potassium intercalated graphite (KC_8), chemical reductions were performed on a solution of **1** in tetrahydrofuran (THF; 2.3 mM). A distinct color change was observed and quantified by UV-vis absorbance spectroscopy; new λ_{max} were observed at 242, 324, and 365 nm (**Figure 2.7.11**). Evan's method measurements in THF and MeCN are consistent with a high-spin d^5 configuration (**Table S2.3.1**). Upon exposure to air, the sample appeared to revert to the color of the starting material, suggesting that a rapid reaction with oxygen had taken place; a charge transfer band consistent with the starting material is observed at λ_{max} 347 nm when the color change is quantified by UV-vis spectroscopy (**Figure S2.7.85**). In order to better understand this reaction, a series of stopped-flow experiments were used to determine relative rates of reaction between [Mn(^{tbu}dhbpy)]^0 and O_2.

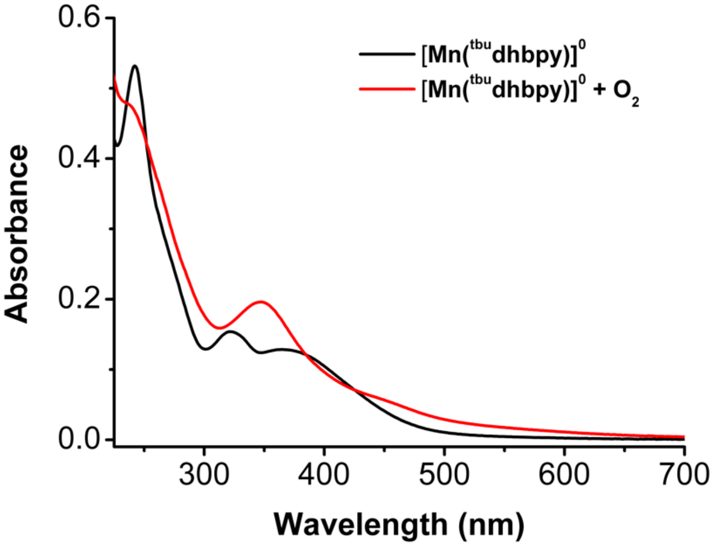

Figure 2.7.11. UV−vis spectra of the as prepared chemically reduced [Mn(^{tbu}dhbpy)]^0 before and after the introduction of air. Conditions: 2.3 mM starting concentration of **1** in THF; Omnicell, 0.2 mm spacer.

Removing the solvent from the as prepared THF solution of the chemically reduced [Mn(^{tbu}dhbpy)]^0 produced a yellow orange solid that was weighed and dissolved in anhydrous degassed MeCN to prepare an exact concentration prior to stopped-flow experiments. The reaction of the reduced Mn complex, [Mn(^{tbu}dhbpy)]^0, with O_2 was examined by monitoring the charge transfer bands at λ_{max} 345 nm. Fitting the resulting data from a single-mixing experiment with O_2 saturated MeCN suggested a $k_{obs}C_{substrate}$ of 3.17 s^{-1} at 20.4°C under nominally aprotic conditions (**Figure S2.7.86**).[13] An air exposure experiment with this MeCN solution was consistent with the product oxidized species being analogous to $[Mn(^{tbu}dhbpy)]^{1+}$ (**Figure S2.7.87**).

Subsequent experiments were conducted on the reactions between the likely product of this initial inner-sphere redox reaction, $O_2^{\bullet-}$, and the starting material **1**. An MeCN solution (5 mM) of solubilized potassium superoxide, KO_2, was prepared by combining equimolar amounts of 18-crown-6 and KO_2. Relative to the previous reaction, the superoxide radical reacts more readily with the Mn(III) center under these conditions, with a $k_{obs}C_{substrate}$ of 24.6 s^{-1} at 20.8°C (**Figure S2.7.88**). Kinetic and thermodynamic parameters of this reaction could be obtained through Van't Hoff and Eyring analyses across temperatures between 11.2 and 20.8°C (**Figures S2.7.88-S2.7.91** and **Table S2.7.4**). These showed that the reaction between superoxide and **1** is both favorable in the forward direction (ΔG_{298K} = -30.7 kcal/mol) and has a low activation barrier (E_a(298K) = 12.0 kcal/mol). These data suggest that upon O_2 activation through an inner-sphere reduction event, subsequent thermal steps are possible.

Isolating relevant substrate adduct species proved difficult, however. This can be explained in part by the utility of structural analogues of **1** as effective superoxide dismutase, catalase and peroxidase mimics.[27] This class of bipyridine-derived Schiff base Mn(III) complexes functions as both antioxidant and free radical scavengers; they are robust catalysts for converting $O_2^{\bullet-}$ rapidly to H_2O_2 in protic environments.[27] These properties are also the most plausible explanation for the incomplete mass balance, due to effective peroxidase mimicry, which consumes hydrogen peroxide in the presence of a proton source. Unfortunately, any competitive superoxide dismutase activity would be indistinguishable from a formal two-electron electrode-driven process in terms of current efficiency. Given the kinetic experiments detailed above, however, the electrochemical mechanism appears to be the dominant contributor to the observed catalytic response. Lastly, a qualitative activity test in MeCN with added H_2O_2 showed significant O_2 evolution from H_2O_2 disproportionation over 2 hours, suggesting a viable thermal pathway exists to explain the incomplete mass balance observed by RRDE (**Figure S2.7.92**).

2.8 Discussion and Proposed Mechanism

Based on these data, we can propose a mechanism for how the catalytic reaction is taking place (**Scheme 2.8.1**). Starting from **1**, a 1 PhOH/1 e^- step generates **2** (*i*), as determined by the slope of the plot constructed from the changes in $E_{1/2}$ versus the log of PhOH concentration under Ar saturation (70 mV/decade of concentration) and a potential-pK_a diagram demonstrating a Nernstian relationship between $E_{1/2}$ and pK_a(MeCN) between 12.65 and 20.11 (31 mV/pK_a(MeCN)). We propose that species **2** reacts rapidly with O_2 in a unimolecular fashion, resulting in the formation of the superoxide species **3** with chloride loss, based on the electrochemical kinetic and spectrochemical data above (*ii*). At this point, we believe that the rate-determining step of the reaction occurs, the reduction and intramolecular protonation of the superoxide adduct to generate a bound hydroperoxo species **4** (*iii*). Due to the presumed increase in effective concentration of proximal proton sources through ligand protonation, we propose that this proceeds via an intramolecular proton transfer reaction. DFT results qualitatively agree with this: the model of compound **3**, $[Mn(^{tbu}dhbpy(H))(\eta^1\text{-}O_2)]^+$, has an O–O distance of 1.207 Å, consistent with minimal bond activation.[51] If the computational model of compound **3** is reduced by a single electron to $[Mn(^{tbu}dhbpy(H))(\eta^1\text{-}O_2)]$ **3a**, the O–O bond length increases to 1.330 Å, suggestive of a superoxide species. Finally, in the model of **4**, [Mn(^{tbu}dhbpy)(η^1-O_2H)], (N.B. this is the presumptive product of an intramolecular proton transfer from the ligand to η^1-O_2 in **3a**; ΔG^0 = -20 kcal/mol) the O–O bond length is 1.461 Å, consistent with a metal-bound hydroperoxo.[51]

From product analysis by RRDE it is implied that the catalytic cycle primarily ends here with a final intramolecular protonation and H_2O_2 loss (81±4%), returning to **2** with further reduction in the presence of proton sources (*iv*). The incomplete mass balance implies that either the direct $4H^+/4e^-$ reduction to H_2O occurs slowly relative to the initial catalytic reaction, or that **1** is capable of catalyzing the disproportionation of two equivalents of H_2O_2 to 2 equiv of H_2O and one equiv of O_2. Given the spectrochemical results and literature precedent,[27] as well as our peroxidase activity test in MeCN, we favor the latter interpretation (*vi*). As noted above, Cl^- loss occurs slowly in the presence of proton sources under Ar saturation conditions, implying an off-cycle equilibrium exists (*v*). Interestingly, FOWA analysis and PhOH titration studies suggest that the Cl-abstracted species has lower activity and a diminished Nernstian response. We interpret this as Cl^- coordination helping to minimize charge with protonation in species **2**.

Scheme 2.8.1. Proposed catalytic cycle involving a cooperative metal-ligand redox-based protonation reaction. R = *tert*-butyl

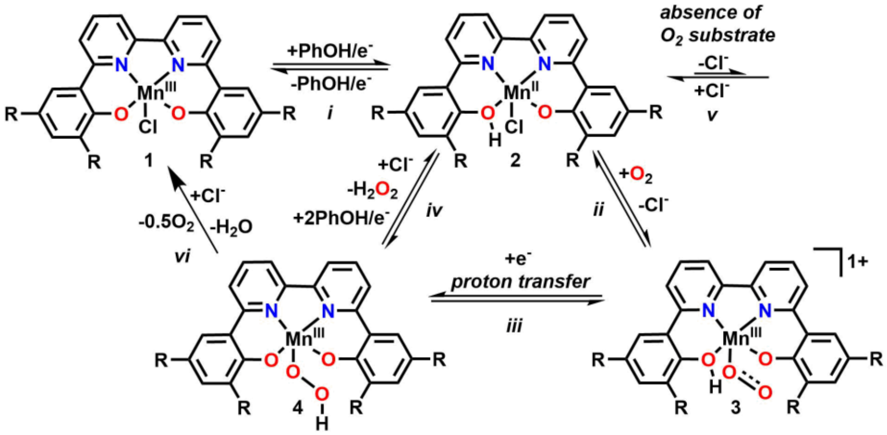

Cooperative metal-ligand activation of O_2 has been observed previously.[16, 52] The catalyst **1** reported here, however, exhibits Nernstian behavior with added proton sources that is assigned to a protonation reaction on the ligand framework upon a change in oxidation state at the metal center. However, this type of multi-site electron and proton transfer exhibits greater similarity to mechanisms proposed for hydrogen evolution reactions with dithiolene- and cobaloxime-based electrocatalysts.[53-57] Mn-based catechol complexes which invoke a mechanism involving ligand O atom and substrate H atom interactions have also been reported for similar O_2/H_2O_2 catalytic activity when using hydroxylamine as a proton and electron source.[58-59] This cooperative response in the presence of substrate is reminiscent of biological multisite electron and proton transfer mechanisms involving tyrosine residues.[60] We rationalize this in a qualitative way through the change in *d* orbital occupancy upon reduction, in the d^4 high-spin ground state, vacant *d* orbitals of appropriate π symmetry and energy are present to interact with the lone pairs of the O atoms of the ligand backbone. This is reflected in electronic structure predicted by the DFT and TD-DFT calculations detailed above. Upon reduction, a change in *d* orbital occupancy will diminish this interaction, increasing the basicity of the O atoms of the ligand. DFT calculations on the one electron-reduced model complex, $[Mn(^{tbu}dhbpy)Cl]^-$, predict that the HOMO is primarily metal-based and the HOMO-1 exhibits anti-bonding interactions between Mn and the O atoms (**Figure S2.8.93**). A comparison of Mulliken charges on the O atoms between $Mn(^{tbu}dhbpy)Cl$ and $[Mn(^{tbu}dhbpy)Cl]^-$ is also consistent with increased basicity; the relative negative charges shift from -0.56 to -0.65 upon single-electron reduction (**Tables S2.8.9 and S2.8.10**).

Mn(salen) complexes have been previously studied as superoxide dismutase mimics (MnSOD).[61] Although the ligand framework discussed here does not reconstruct the active site of MnSOD, the observed catalytic activity runs an ORR through all the proposed intermediates of the enzymatic cycle. MnSOD catalyzes either reaction (1) or (2) to the right as written when presented with a superoxide radical. In this catalyst system, the superoxide radical is instead formed by electrochemically produced Mn(II), which can be understood as the reverse of reaction (1). The electrode maintains the supply of Mn(II) in solution, which drives reaction (2) in the forward direction as written.

$$\mathrm{Mn(III)} + \mathrm{O_2}^{\bullet-} \rightleftharpoons \mathrm{Mn(II)} + \mathrm{O_2} \qquad (1)$$

$$\mathrm{Mn(II)} + 2\mathrm{H}^+ + \mathrm{O_2}^{\bullet-} \rightleftharpoons \mathrm{Mn(III)} + \mathrm{H_2O_2} \qquad (2)$$

2.9 Conclusion

These data suggest that Mn(^{tbu}dhbpy)Cl **1** is an active and selective molecular catalyst for the reduction of O_2 to H_2O_2. Notably, the catalytically active species has been generated through a net one electron/one proton reaction, yet the complex retains a vacant coordination site at the metal center. As a consequence, the active catalyst has a pendent proton sources in close proximity to the active site where substrate activation occurs. The change in metal oxidation state corresponding to substrate activation may favor rapid intramolecular proton transfer from the ligand, if it is assumed that the reversibility of the redox-driven ligand protonation reaction observed under Ar saturation occurs under catalytic conditions.[13-14]

2.10 Supporting Information

Materials and Methods

General

All chemicals and solvents (ACS or HPLC grade) were commercially available and used as received unless otherwise indicated. For all air-sensitive reactions and electrochemical experiments, solvents were obtained as anhydrous and air-free from a PPT Glass Contour Solvent Purification System. Gas cylinders were obtained from Praxair (Ar as 5.0; O_2 as 4.0) and passed through molecular sieves or Drierite prior to use. Gas mixing for variable concentration experiments was accomplished using a gas proportioning rotameter from Omega Engineering. NMR spectra were obtained on either a Varian 600 MHz or 500 MHz instrument and referenced to the residual solvent signal. UV-vis absorbance spectra were recorded on a Cary 60 from Agilent. GC experiments were performed using an Agilent 7890B Gas Chromatograph equipped with a thermal conductivity detector (TCD) using an Agilent J&W Select Permanent Gases/CO_2 column. Stopped-flow data were collected as single-mixing experiments on a CSF-61DX2 Stopped-Flow System from Hi-Tech Scientific. Temperature was controlled using a VWR Refrigerated Circulator with an ethylene glycol and water mixture. HRMS data were obtained by the Mass Spectrometry Lab at the University of Illinois at Urbana-Champaign and elemental analyses were performed by Midwest Laboratory. Unless otherwise noted, buffered acids were prepared by combining 2:1 ratios of acid to tetrabutylammonium hydroxide solutions (40%) in water or methanol, followed by extensive drying under vacuum. Analyses are summarized in the Supporting Information.

Synthetic Procedures

6,6'-di(3,5-di-tert-butyl-2-hydroxybenzene)-2,2'-bipyridine, ^{tbu}dhbpy(H)$_2$.

A Schlenk flask (200 mL) with stir bar was charged with 2,4-di-*tert*-butyl phenol (20.0 g, 97 mmol) and dry degassed CH_2Cl_2 (100 mL) under N_2 atmosphere. The resulting mixture was placed in a dry ice/acetone bath for 10 minutes. After this time, Br_2 (5.12 mL, 16.0 g, 0.10 mol) was added slowly via syringe. After this addition, the mixture was brought to room temperature and allowed to stir over the course of 2 h. At this time, the reaction was quenched with a saturated aqueous solution of $NaHCO_3$ (1 x 50 mL) and extracted before separating the organic and aqueous phases. The organic layer was washed with brine (1 x 50 mL) and the organic and aqueous phases separated. The combined organic phases were dried over $MgSO_4$ for 10 minutes before being filtered and the condensed under vacuum by rotary evaporator. The resulting yellow-orange solid was dissolved again in CH_2Cl_2 (100 mL) and basic alumina was added to the mixture (10 g) before the suspension was stirred vigorously for 10 m. This suspension was filtered through half-inch layers of silica gel over diatomaceous earth and washed with CH_2Cl_2 (2x75 mL) before being condensed under vacuum to reveal a pale yellow-orange solid, 2-bromo-4,6-di-*tert*-butyl-phenol. Yield (isolated) 27.1 g, 98% yield. ^{1}H NMR (d_2-CD_2Cl_2, 600 MHz): δ 7.35 (d, 1H, Ar*H*), 7.27 (d, 1H, Ar*H*), 1.41 (s, 9H, -C(CH_3)$_3$) 1.29 (s, 9H, -C(CH_3)$_3$). Elemental Analysis for $C_{14}H_{21}BrO$ Calc'd: C 58.95, H 7.42, N 0; Found: C 52.37, H 6.92, N 0.17. ESI-MS (m/z): Calc'd: 284.07758; found: 284.07723.

A Schlenk flask (500 mL) with stir bar was charged with 2-bromo-4,6-di*tert*-butyl-phenol (5 g, 0.0175 mol) and dry degassed diethyl ether (200 mL). The resulting solution was cooled to -78°C (dry ice/acetone bath) under N_2. *n*-Butyllithium (2.6 M in hexanes) was added slowly via syringe (16.1 mL, 0.042 mol), after which the solution allowed to warm to room temperature with vigorous stirring for 2 hours. After 2 h the solution was returned to -78°C, at which point trimethyl borate was added rapidly by syringe (3.15 mL, 0.0282 mmol) with vigorous stirring and the mixture left for 10 minutes before the ice bath was removed and the mixture left stirring overnight under N_2 (16 h). After this time, the flask was cooled to 0°C before quenching with HCl (25 mL, 2 M) and opened to air for 10 minutes. The suspension was extracted and the aqueous and organic layers separated. The aqueous layer was washed with CH_2Cl_2 (3x50 mL) after which all organic fractions were combined. The resulting solution was dried with $MgSO_4$ for 10 minutes, before the mixture was filtered to remove solid and the solvent was removed under reduced pressure to yield a yellow/orange oil, (3,5-ditert-butyl-2-hydroxy-phenyl)boronic acid, which was used without further purification. A round-bottom flask (500 mL) was charged with a stir bar and placed in a heating bath at room temperature. A suspension of 6,6'-dibromobipyridine (2.0 g, 6.37 mmol), toluene (250 mL), the unpurified (3,5-ditert-butyl-2-hydroxy-phenyl)boronic acid oil, MeOH (30 mL), 2 M Na_2CO_3 (60 mL), and $Pd(PPh_3)_4$ (5.0 mol. cat. %, 376 mg). The mixture was brought to reflux for 72 h under N_2 and then allowed to cool to room temperature before the layers were separated. The organic layer was washed with brine (1 x 50 mL) and the aqueous layer with dichloromethane (3 x 50 mL). The organic fractions were combined and dried with $MgSO_4$ for 10 minutes. The suspension was filtered and concentrate to dryness under reduced pressure. The yellow solid was recrystallized from toluene (10 mL) and washed with minimal hexanes (5 mL). Isolated yield: 2.28 g, 63%. ^{1}H NMR (d_2-CD_2Cl_2, 600 MHz): δ 8.10 (m, 6H, Ar*H*), 7.76 (d, 2H, Ar*H*), 7.45 (d, 2H, Ar*H*), 1.51 (s, 18H, -C(CH_3)$_3$), 1.38 (s, 18H, -C(CH_3)$_3$), ^{13}C[^{1}H] (d_2-CD_2Cl_2, 600 MHz) NMR δ 159.52 (Ar*C*), 157.09 (Ar*C*), 152.41 (Ar*C*), 140.85 (Ar*C*), 139.69 (Ar*C*), 138.05 (Ar*C*), 127.11 (Ar*C*), 121.90 (Ar*C*), 121.17 (Ar*C*), 119.30 (Ar*C*), 118.52 (Ar*C*), 35.81 (tbu*C*), 34.88 (tbu*C*), 31.91 (tbu*C*), 29.92 (tbu*C*). Elemental analysis for $C_{38}H_{48}N_2O_2$: calc'd: C: 80.81, H: 8.57 N: 4.96 found: C: 81.01 H: 9.11 N: 5.10. ESI-MS (m/z): calcd: 565.3716; found 565.3789

Mn(κ^4-N,N',O,O'-(6,6'-di(3,5-di-tert-butyl-2-hydroxybenzene)-2,2'-bipyridine))Cl, Mn(^{tbu}dhbpy)Cl, ***1****.*

A pear-shaped round-bottom flask (100 mL) was charged with a stir bar, methanol (50 mL) and ^{tbu}dhbpy(H)$_2$ (250 mg, 443 mmol). The resulting suspension was brought to reflux in air before Mn(OAc)$_2$•4H_2O (114 mg, 0.465 mmol) was added and the mixture refluxed for 1 h. During this time, the mixture became dark brown in color and was immediately quenched with saturated NaCl (50 mL). The brown suspension was filtered and the solidwashed with H_2O (2x5mL) before being dissolved in CH_2Cl_2, dried with $MgSO_4$, and condensed under reduced pressure. The isolated brown solid was then dissolved in MeCN (25 mL) and passed through a syringe filter with repeated washing (3x25 mL) before being condensed under reduced pressure. Yield, 72 mg 25%. Elemental Analysis for $C_{38}H_{46}ClMnN_2O_2$ Calc'd: C 69.88, H 7.10, N 4.29; Found: C 68.75, H 7.35, N 4.28. ESI-MS (m/z) [M–Cl]$^+$: Calc'd. 617.2940. Found: 617.2964.

Mn(κ^4-N,N',O,O'-(6,6'-di(3,5-di-tert-butyl-2-hydroxybenzene)-2,2'-bipyridine))[CF_3SO_3].

A pear-shaped round-bottom flask (50 mL) was charged with a stir bar under N_2 atmospheric conditions. Thallium trifluoromethanesulfonate (17.6 mg, 0.0498 mmol), Mn(^{tbu}dhbpy)Cl **1** (31 mg, 0.0475 mmol), and CH_2Cl_2 (10 mL) were added to the flask under an N_2 stream. The resulting suspension was left stirring under nitrogen for a 12 h. After this time, the reaction flask was sonicated until a dark cloudy solution was observed. The solution was then filtered through a porous glass frit which contained a half-inch of Celite. The Celite in the frit was then washed with additional CH_2Cl_2 (1x7 mL). The product was then condensed under reduced pressure until a dark oil was obtained and left in a vacuum desiccator for 24 hours to obtain the solid dark red-brown product. Isolated yield, 21 mg, 57.7%. ESI-MS (m/z) $[M–CF_3SO_3]^+$: Calc'd. 617.2940. Found: 617.2922.

Electrochemistry

All electroanalytical experiments were performed using a Metrohm Autolab PGSTAT302N potentiostat. Glassy carbon working (⌀ = 3 mm) and non-aqueous silver/silver chloride pseudoreference electrodes behind PTFE tips were obtained from CH Instruments. The pseudoreference electrodes were obtained by depositing chloride on bare silver wire in 10% HCl at oxidizing potentials and stored in a 0.1 M tetrabutylammonium hexafluorophosphate/acetonitrile solution in the dark prior to use. The counter electrode was Pt wire (Alfa Aesar, 99.95%, ⌀ = 0.5 mm) or a glassy carbon rod (⌀ = 3 mm) as indicated for individual experiments. All CV experiments were performed in a modified scintillation vial (20 mL volume) as a single-chamber cell with a cap modified with ports for all electrodes and a sparging needle. Tetrabutylammonium hexafluorophosphate was purified by recrystallization from ethanol and dried in a vacuum oven before being stored in a desiccator. All data were referenced to an internal ferrocene standard (ferrocinium/ferrocene reduction potential under stated conditions) unless otherwise specified. Rotating disk and rotating ring-disk electrode experiments were conducted using a Metrohm rotator with a Metrohm electrode consisting of a glassy carbon disk (⌀ = 5 mm) and a Pt ring.

Stopped-Flow Spectrochemical Methods.

Stopped-flow spectrochemical kinetics studies were performed with a CSF-61DX2 Stopped-Flow System from Hi-Tech Scientific with monitoring at a single wavelength using Kinetic Studio Software. All data fits were performed within the Kinetic Studio 4.0 Software Suite. Prior to experiments, dried and degassed MeCN was passed through all syringes and the cell block before reagents were loaded. In a typical experiment, SGE air-tight syringes with Luer lock valves would be charged with known concentrations of reagent under air-free conditions in a glovebox or immediately prepared and loaded using dry solvent from the solvent purification system. All concentrations are reported as syringe concentrations, which halve upon mixing in the cell block during an experiment. The Mn(^{tbu}dhpbpy)Cl, [Mn(^{tbu}dhpbpy)]^0, O_2, and [K(18-crown-6)+][O_2^-] MeCN solutions were prepared immediately prior to use. All data fits were taken from five-run averages using a second-order exponential with a linear component. For all experiments, pseudo-first order conditions were used: reagents were in ~100-fold excess of [Mn].

Computational Methods.

DFT calculations were performed on the Rivanna High-Performance Computing Cluster at the University of Virginia using ORCA 4.0.1.[62] Geometry optimizations were performed unrestricted with the B3LYP/G[63-67] functional and def2-TZVP[68-69] basis set with the RIJCOSX approximation[70], D3BJ dispersion correction[71-72], and CPCM[73] to model the MeCN solvent. Numerical frequency calculations at the same level of theory were performed to validate the optimized geometries as minima on the potential energy surface and to generate thermochemical data. TD-DFT calculations on the verified minimum were performed with def2-QZ2P basis sets[69] with nroots = 50, and maxdim = 10.

RDE Experiments

Conditions: performed under both argon and O_2 saturation conditions, 0.1 M $TBAPF_6$, 0.5 mM analyte, MeCN (50 mL), 0.5 M PhOH, glassy carbon disk electrode (5 mm diameter), Pt ring electrode, Pt wire counter electrode, Ag/AgCl pseudoreference electrode; scan rate 0.01 V/s.

The solution was sparged with argon until saturation was achieved and confirmed by CV. Then the analyte (0.5 mM) and 0.5 M PhOH were dissolved in the solution. A standard CV was taken of the solution to confirm the potential window to be used for the experiment (0 to -0.65 V). Linear Sweep Voltammograms (LSVs) were obtained for various rotation rates (between 200 and 2400 rpm) under the described conditions. Between each LSV, the electrode was polished on alumina and sonicated in ethanol. The cleaning procedure for the electrode was standardized by taking repeated LSVs at the same rotation rates to confirm repeated scans at the same rotation rate were exact overlays of one another. This same procedure was completed for O_2 saturation conditions, which were achieved by sparging the solution with O_2 for approximately 15 minutes.

Levich and Koutecky-Levich theory were applied to these experiments to calculate the diffusion coefficients for each of the conditions under which the experiment was run, argon and O_2 saturation. The slope of the Levich plot was obtained by plotting the square root of the angular rotation rate versus the limiting current at -0.55 V vs Ag/AgCl for both argon and O_2. The slope of these Levich plots were then used to calculate the diffusion coefficients under each of the experimental conditions, argon and O_2 saturation, using the following equation:

$$D = \sqrt{\left(\frac{slope}{0.620nFA\nu^{-1/6}C_0^*}\right)^3}$$

Where *D* is the diffusion coefficient, *slope* is the slope from the Levich plot, *n* is the number of electrons, *F* is Faraday's constant, *A* is the area of the electrode, ν is the kinematic viscosity of the solvent (0.0044 cm^2/s for MeCN) and C^*_0 is the concentration of O_2 at saturation in MeCN.

RRDE Collection Efficiency % Determination

Conditions: argon saturation, 0.1 M $TBAPF_6$, 0.25 mM Ferrocene, MeCN (50 mL), glassy carbon disk electrode (5 mm), Pt ring electrode, Pt wire counter electrode, Ag/AgCl pseudoreference electrode; scan rate 0.01 V/s.

To determine the collection efficiency of the rotating ring disk electrode (RRDE), an argon saturated MeCN solution (50 mL) of ferrocene (0.25 mM) was prepared with $TBAPF_6$ (0.1 M) as the supporting electrolyte. A standard CV was taken prior to the addition of ferrocene (0.25 mM) to ensure no air was present in the solution. Then a standard CV of ferrocene was obtained to determine the potential window (0.8 to 0 V vs Ag/AgCl) to use for determining the collection efficiency of the RRDE instrument. Once the potential window for ferrocene was verified by CV, the ring electrode potential was set at 0 V and LSVs for various rotation rates between 200 and 2400 rpm were obtained.

To calculate the collection efficiency of the RRDE, the ratio of the ring current to the disk current at each rotation rate was used to determine $N_{\text{empirical}}$ at each rotation rate. The $N_{\text{empirical}}$ value at reach rotation rate was then multiplied by a factor of 100 to determine the collection efficiency % at each rotation rate (~27%). A plot of the angular rotation rate versus the collection efficiency % verified that the collection efficiency was independent of rotation rate. Plots of rotation rate versus ring current and rotation rate versus disk current confirmed that the current produced was dependent on rotation rate.

$$collection\ effiency\ of\ Ferrocene = \frac{i_{ring\ corrected}}{i_{disk\ corrected}}$$

<u>RRDE Experiments (adapted[13])</u>

Conditions: performed under both argon and O_2 saturation conditions, 0.1 M $TBAPF_6$, 0.25 mM analyte, MeCN (50 mL), glassy carbon disk electrode (5 mm diameter), Pt ring electrode, Pt wire counter electrode, Ag/AgCl pseudoreference electrode; scan rate 0.01 V/s.

The solution was sparged with argon until saturation was achieved and confirmed by CV. The analyte (0.25 mM) was dissolved in solution and TFE (0.45 M and 0.6 M) was added via syringe. A standard CV was taken of the solution to confirm the potential window to be used for the experiment (0 to -0.65 V). The platinum ring was set to 1.2 V and the glassy carbon disk was set to 0 V. LSVs were obtained for various rotation rates (between 200 and 2400 rpm) under the described conditions. Between each LSV, the electrode was polished on alumina and sonicated in ethanol. The cleaning procedure for the electrode was standardized by taking repeated LSVs at the same rotation rates to confirm repeated scans at the same rotation rate were exact overlays of one another.

This same procedure was repeated for O_2 saturation conditions, which were achieved by sparging the solution with O_2 for approximately 15 minutes.

The difference between the amount of current produced at the disk under O_2 saturation conditions and the amount of current produced at the disk under argon saturation conditions was taken as the corrected disk current for O_2 saturation conditions ($i_{\text{disk corrected}}$) for each rotation rate. The difference between the amount of current produced at the ring under O_2 saturation conditions and the amount of current produced at the ring under argon saturation conditions was taken as the corrected ring current for O_2 saturation conditions ($i_{\text{ring corrected}}$) for each rotation rate.

To calculate the H_2O_2%, the $i_{\text{disk corrected}}$ was multiplied by the corresponding $N_{\text{empirical}}$ value for the specific rotation rate to determine the maximum amount of ring current for H_2O_2 production ($i_{\text{ring max}}$). The ratio of $i_{\text{ring corrected}}$ to $i_{\text{ring max}}$ was multiplied by a factor of 100 to determine the H_2O_2% generated at the ring across all measured rotation rates. Efficiencies of 82±3% and 81±4% were obtained for 0.45 M TFE and 0.6 M TFE, respectively.

$$\%H_2O_2 = (100)\frac{i_{ring\ corrected}}{i_{disk\ corrected}(collection\ efficency)}$$

Foot-of-the-Wave Analysis (FOWA) and Catalytic Tafel Plots (adapted[13])

For FOWA CVs were compared under Ar and O_2 saturation with the acid concentrations where maximum current was achieved for the buffered F5PhOH/TBA[F5PhO] acid. This plots i_c/i_p, where i_c is the catalytic current and i_p is the Faradaic current (this normalizes the plot with respect to electrode area, catalyst concentration, diffusion coefficient, and scan rate), on the y-axis against an x-axis with

1/(1+exp(f(E-E^0)), where $f = \frac{F}{RT}$, E is the applied potential, and E^0 is the $E_{1/2}$ of the reduction feature where catalysis occurs. From the slope of this plot, TOF$_{\text{max}}$ (TOF$_{\text{max}}$ = $k_{obs}C_{substrate}$) can be determined according to the following relationship:

$$\frac{i_c}{i_p} = \frac{2.24 n_{cat}^{\sigma} \sqrt{\frac{RT}{F\nu} k_{obs} C_{substrate}}}{1 + \exp\left[\frac{F}{RT}(E - E^0)\right]}$$

From RRDE analysis, 81±4% efficiency for H_2O_2, a value of n_{cat} = 2.38 could be calculated if the remaining current was assumed to be the $4H^+/4e^-$ reduction of O_2 to 2 H_2O. For these studies σ = 1 was used with the assumption that all electron transfer steps come directly from the electrode, setting this expression as the lower limit for TOF$_{\text{max}}$. The concentration for O_2 was assumed to be 6.3 mM at saturation.[38] The acids were assumed to be first order based on kinetic data for the rate-determining step. The remaining value, $\frac{RT}{F\nu}$ = 0.256796 s, could be calculated using constants under standard conditions and v = 0.1 Vs^{-1}. Fits were obtained to ~0.98, to represent a reasonable lower bound.

Catalytic Tafel plots for the catalysts reported here were simulated using the TOF$_{\text{max}}$ values determined from the FOWA. For the standard electrode potential of O_2 reduction to H_2O_2 in MeCN, a value of 0.356 V vs Fc/Fc$^+$ was used, under the assumption that an excess of protons exists, based on a reported value of 1.0 V vs NHE (corrected for Fc/Fc$^+$ = 0.644 V vs NHE).[44] For Mn($^{\text{tbu}}$dhbpy)Cl **1**, E^0: $E_{1/2}$(11 mM buffered F_5PhOH) = -0.672 V vs Fc/Fc$^+$. For the Mn(F5-Ph)corrole,[10] the authors reported an O_2 concentration of 0.26 mM and H_2O was assumed to be the proton source at pH = 7 with a concentration of 55.5 M. The catalytic wave was assumed to begin at the reported reduction with $E_{1/2}$ = -0.25 V vs Ag/AgCl (Ag/AgCl = 0.205 V vs NHE).[74] A value of 0.281 V vs NHE was used for the thermodynamic potential of O_2 reduction to H_2O_2 under aqueous conditions at pH = 7; 0.635 V vs NHE for pH = 1.[2]

Peroxidase Mimic Activity Test

Mn(^{tbu}dhbpy)Cl (15.6 mg) was dissolved in dry acetonitrile (20 mL) in a scintillation vial (1.2 mM solution) capped with a septum and sealed with electrical tape. The headspace was purged with nitrogen and a vent needle for 15 minutes. Then three “pre-injections” (1 mL) were taken from the solution headspace with an airtight syringe before any H_2O_2 was added. Aqueous H_2O_2 was then injected into the solution (0.015 mL injection; 9.8 M solution in water) of H_2O_2 was injected into the solution. Right after this addition of H_2O_2, a GC injection (1 mL) was taken of the headspace. After two additional injections over ~60 minutes, an additional aliquot of H_2O_2 (0.015 mL injection; 9.8 M solution in water) was injected into the solution and two subsequent GC injections were taken over ~60 minutes. These conditions were repeated without Mn(^{tbu}dhbpy)Cl for a control reaction. All the data were processed by subtracting the peak area associated with the largest peak area value observed for the three “pre-injections” from each of the experimental injections to correct for environmental contamination; the retention time of O_2 was verified with calibration injections.

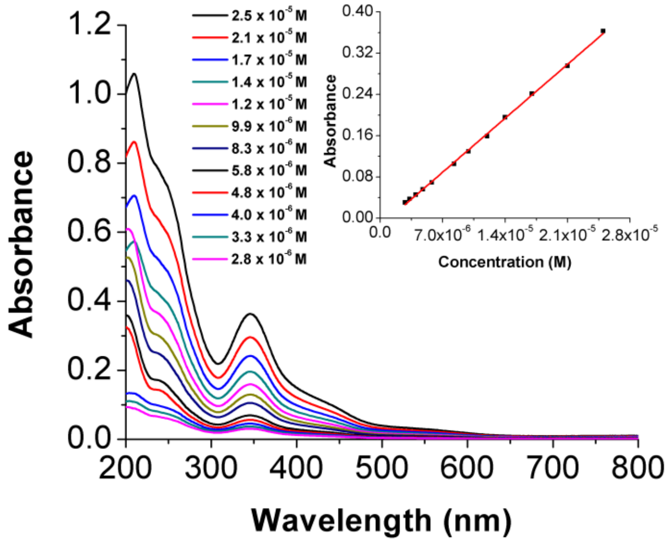

Figure S2.3.1. UV-vis serial dilution absorbance data obtained from Mn(^{tbu}dhbpy)Cl **1** in MeCN solution. Conditions: varying concentration; quartz cell with 1 cm pathlength. Inset: Plot of absorbance versus concentration (M) for Mn(^{tbu}dhbpy)Cl **1** in MeCN at 345 nm (14900 $M^{-1}cm^{-1}$); $R^2 = 0.999$. All: λ_{max} = 238 (31800 $M^{-1}cm^{-1}$), 345 (14900 $M^{-1}cm^{-1}$), 448 nm (3630 $M^{-1}cm^{-1}$), and 538 nm (1280 $M^{-1}cm^{-1}$).

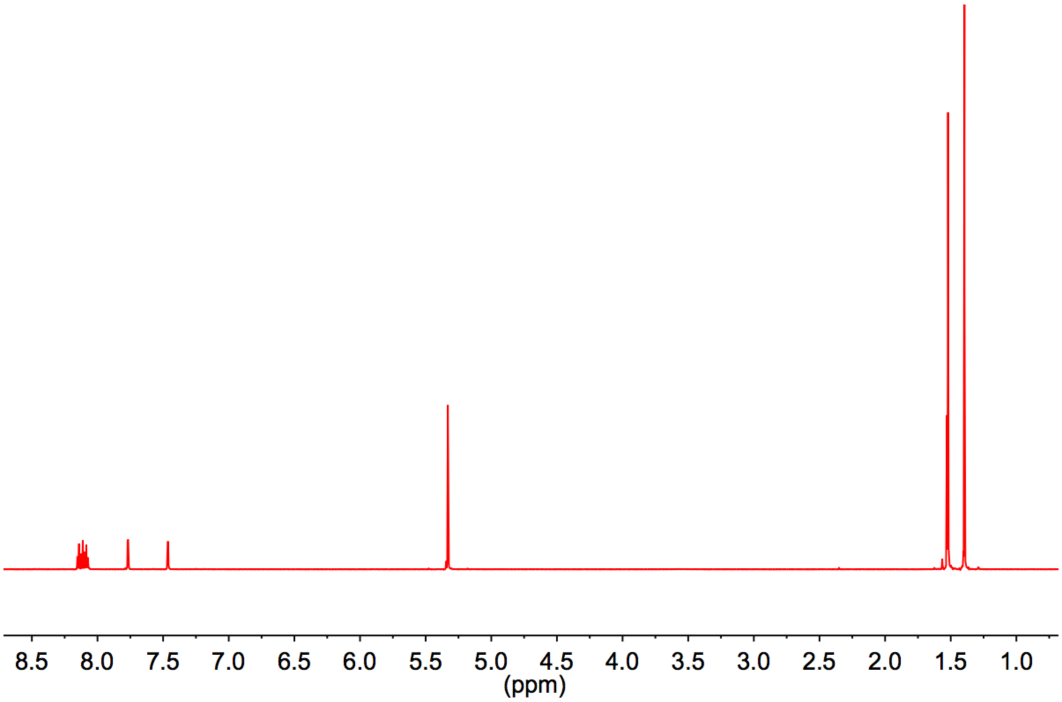

Figure S2.3.2. ^{1}H NMR of ^{tbu}dhbpy ligand; d_2-CD_2Cl_2; 600 MHz Varian.

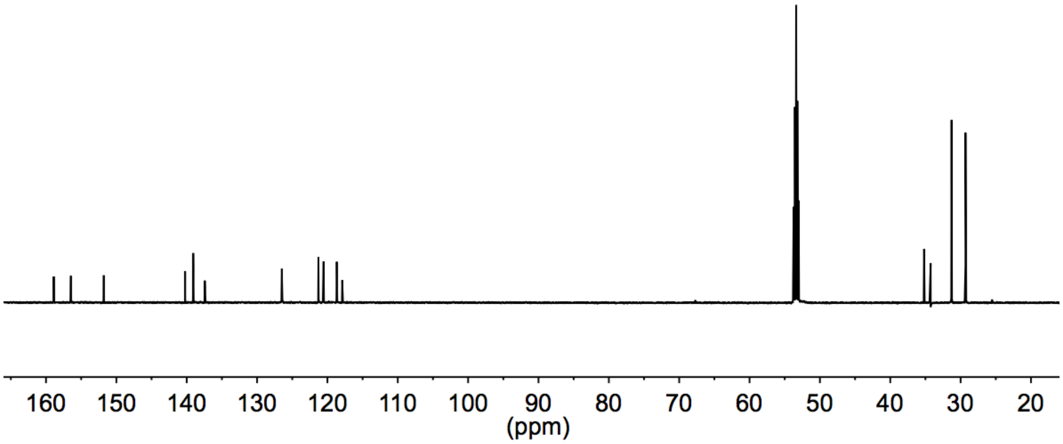

Figure S2.3.3. $^{13}C\{^{1}H\}$3. NMR of ^{tbu}dhbpy ligand; d_2-CD_2Cl_2; 600 MHz Varian.

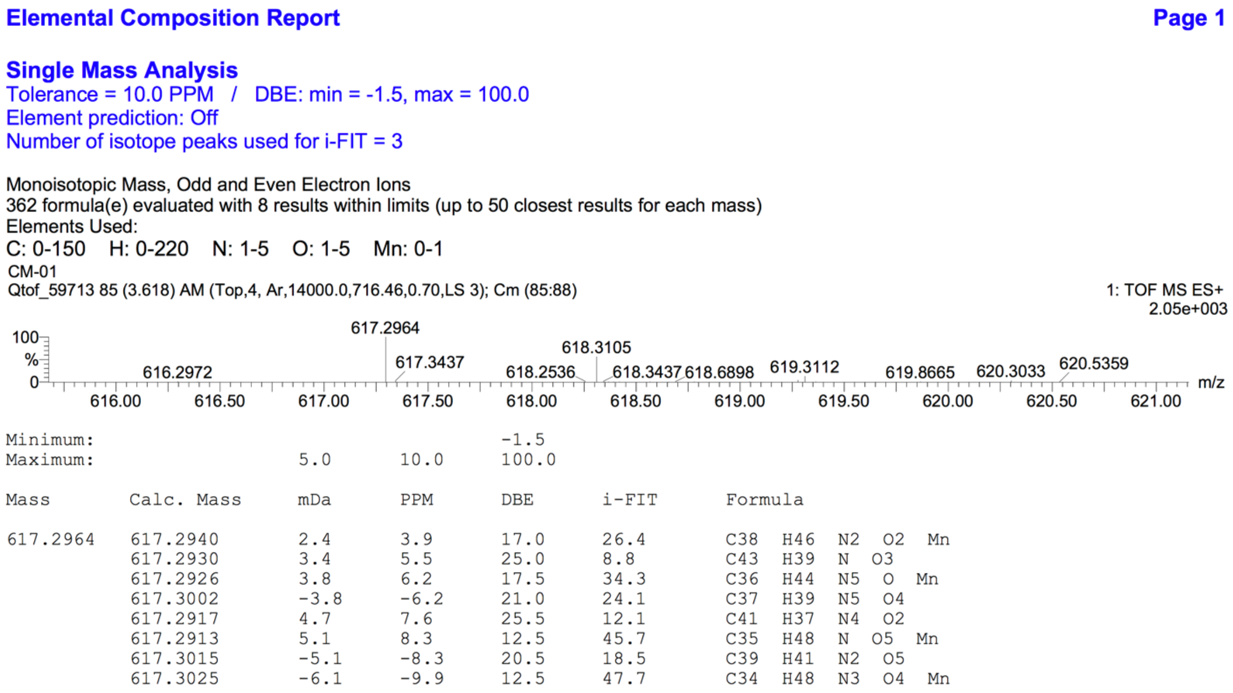

Elemental Composition Report **Page 1**

Single Mass Analysis
Tolerance = 10.0 PPM / DBE: min = -1.5, max = 100.0
Element prediction: Off
Number of isotope peaks used for i-FIT = 3

Monoisotopic Mass, Odd and Even Electron Ions
362 formula(e) evaluated with 8 results within limits (up to 50 closest results for each mass)
Elements Used:
C: 0-150 H: 0-220 N: 1-5 O: 1-5 Mn: 0-1
CM-01
Qtof_59713 85 (3.618) AM (Top,4, Ar,14000.0,716.46,0.70,LS 3); Cm (85:88)
1: TOF MS ES+
2.05e+003

```
Minimum:                                  -1.5
Maximum:                 5.0       10.0     100.0

Mass        Calc. Mass    mDa       PPM       DBE        i-FIT        Formula

617.2964    617.2940      2.4       3.9       17.0       26.4         C38  H46  N2  O2  Mn
            617.2930      3.4       5.5       25.0       8.8          C43  H39  N  O3
            617.2926      3.8       6.2       17.5       34.3         C36  H44  N5  O  Mn
            617.3002      -3.8      -6.2      21.0       24.1         C37  H39  N5  O4
            617.2917      4.7       7.6       25.5       12.1         C41  H37  N4  O2
            617.2913      5.1       8.3       12.5       45.7         C35  H48  N  O5  Mn
            617.3015      -5.1      -8.3      20.5       18.5         C39  H41  N2  O5
            617.3025      -6.1      -9.9      12.5       47.7         C34  H48  N3  O4  Mn
```

Figure S2.3.4. ESI-MS of Mn(^{tbu}dhbpy)Cl **1**.

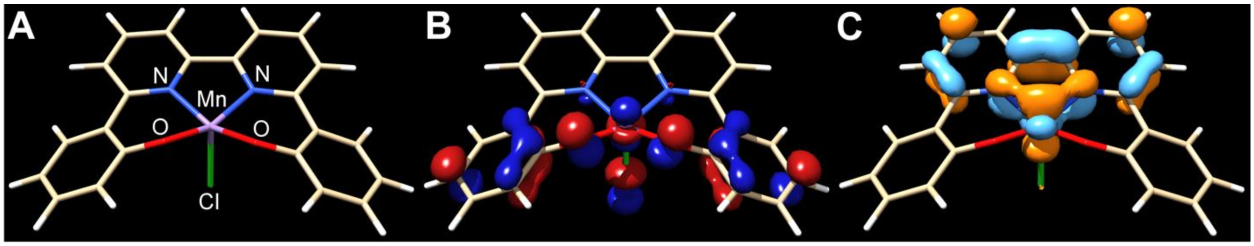

Figure S2.3.5. Kohn-Sham Orbital projections of the HOMO (B) and LUMO (C) of computational model Mn(dhbpy)Cl (A). B3LYP/G, CPCM(Acetonitrile), def2-TZVP, D3BJ, 2S+1 = 5; ORCA 4.0.1. Images created using Chimera and POVRAY.

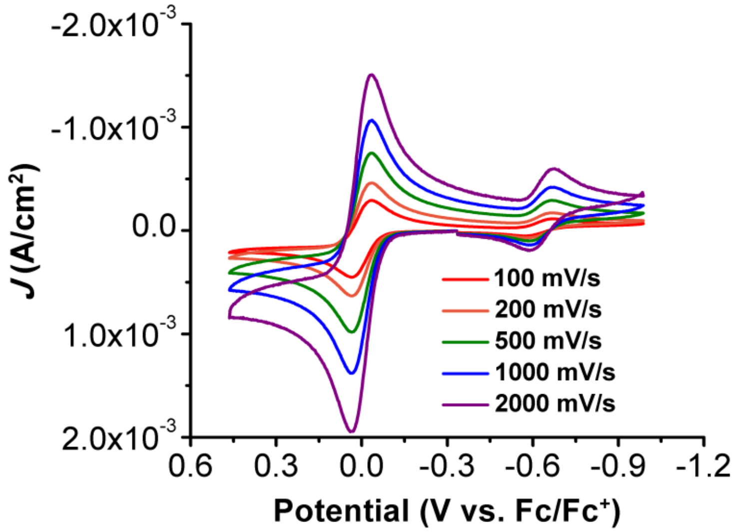

Figure S2.4.6. CV of Mn(^{tbu}dhbpy)Cl **1**, obtained under Ar saturation conditions. Conditions: 1 mM analyte; glassy carbon working electrode, Pt wire counter electrode, Ag/AgCl pseudoreference electrode; varied scan rate; referenced to internal ferrocene standard.

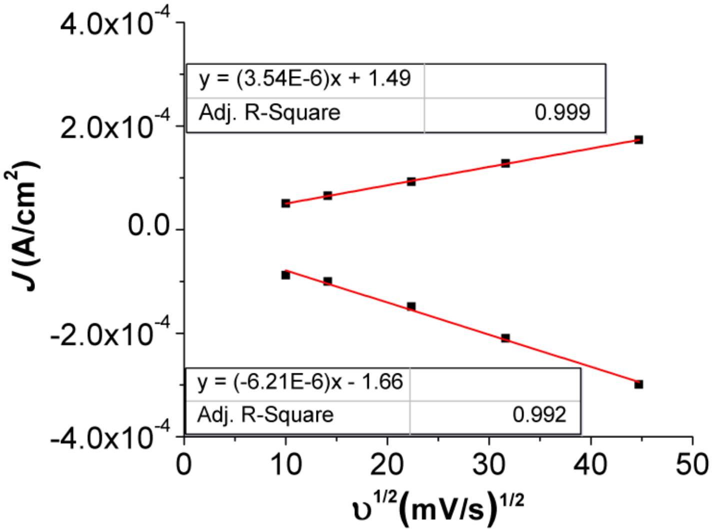

Figure S2.4.7. Linear Fit of variable scan rate data from **Figure S2.4.6** demonstrating that Mn(^{tbu}dhbpy)Cl **1** shows a diffusion-limited current response. Conditions: 1 mM analyte; glassy carbon working electrode, Pt wire counter electrode, Ag/AgCl pseudoreference electrode; varied scan rate; referenced to internal ferrocene standard.

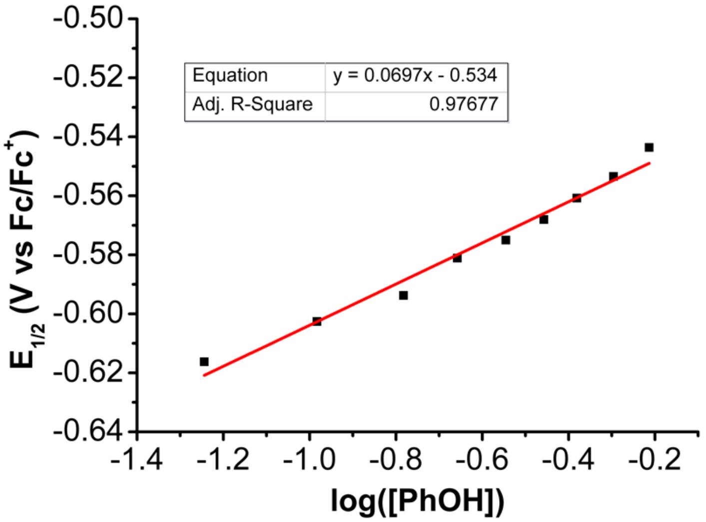

Figure S2.4.8. Diagram showing the Nernstian voltage dependence of Mn(^{tbu}dhbpy)Cl **1** on the concentration of PhOH in MeCN at the first reduction under Ar saturation (red). The slope of 70 mV/decade of PhOH concentration is consistent with a 1 [PhOH]/1 e$^-$ electrochemical reaction. Conditions: 1 mM **1**; 0.1 M TBAPF$_6$/MeCN; glassy carbon working electrode, Pt counter electrode, Ag/AgCl pseudoreference electrode; referenced to internal ferrocene standard.

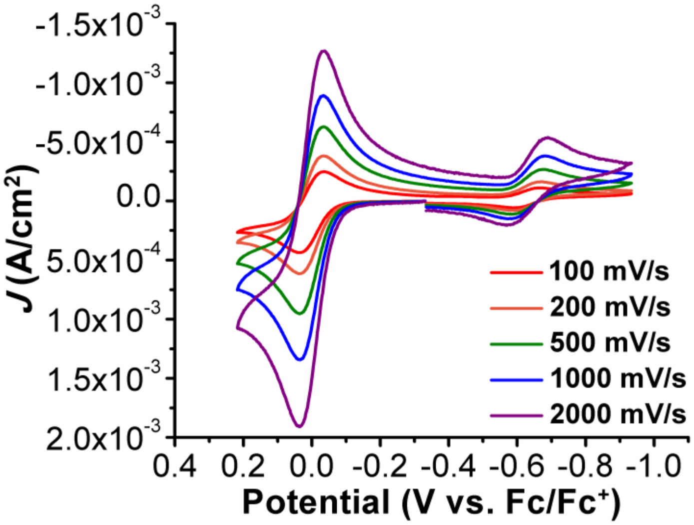

Figure S2.4.9. CVs of Mn(^{tbu}dhbpy)Cl 1, obtained under Ar saturation conditions with 0.05 M TBACl with increasing scan rates. Conditions: 1 mM analyte; glassy carbon working electrode, Pt wire counter electrode, Ag/AgCl pseudoreference electrode; varied scan rate; referenced to internal ferrocene standard.

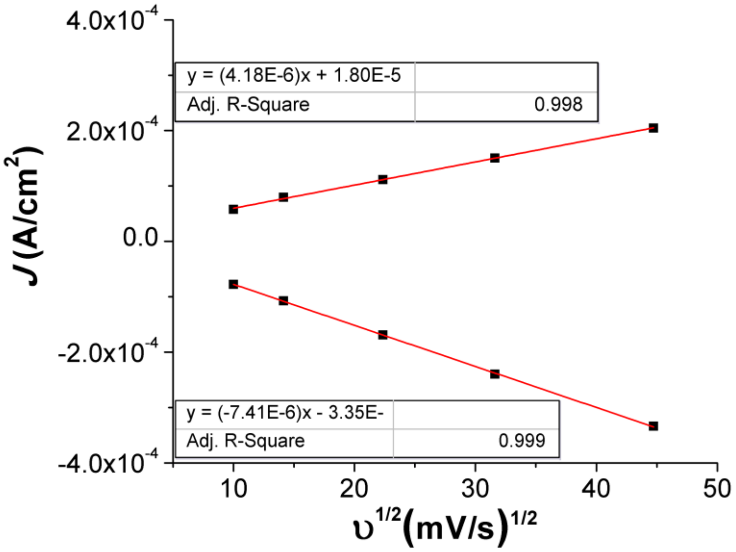

Figure S2.4.10. Linear Fit of variable scan rate data from Figure S9 demonstrating that Mn(^{tbu}dhbpy)Cl 1 shows a diffusion-limited response with 0.05 M TBACl added. Conditions: 1 mM analyte; glassy carbon working electrode, Pt wire counter electrode, Ag/AgCl pseudoreference electrode; varied scan rate; referenced to internal ferrocene standard.

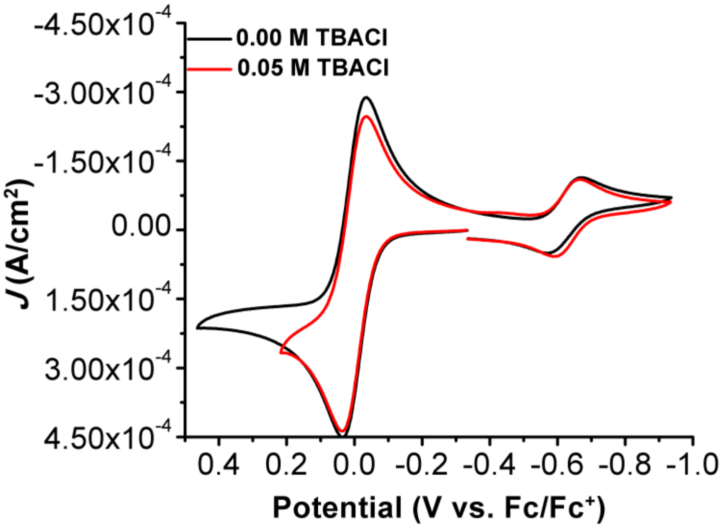

Figure S2.4.11. CVs of Mn(^{tbu}dhbpy)Cl 1, obtained under Ar saturation conditions (black) and 0.05 M TBACl (red). Conditions: 1 mM analyte; glassy carbon working electrode, Pt wire counter electrode, Ag/AgCl pseudoreference electrode; 100 mV/s scan rate; referenced to internal ferrocene standard.

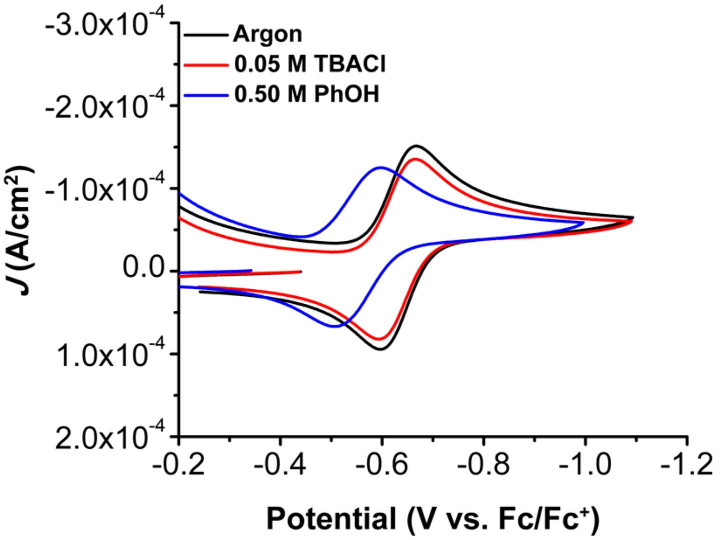

Figure S2.4.12. CVs of Mn(^{tbu}dhbpy)Cl 1, obtained under Ar saturation conditions comparing the effects of PhOH and TBACl separately. Conditions: 1 mM analyte; glassy carbon working electrode, Pt wire counter electrode, Ag/AgCl pseudoreference electrode; 100 mV/s scan rate; referenced to internal ferrocene standard.

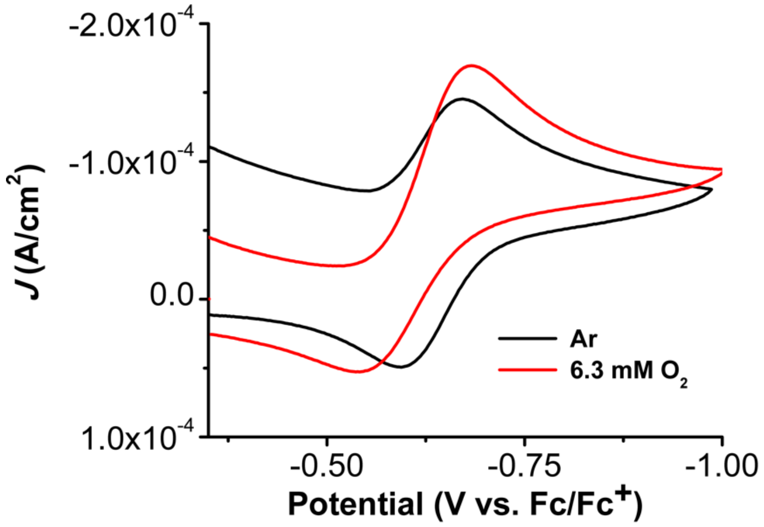

Figure S2.4.13. CVs of Mn(^{tbu}dhbpy)Cl **1**, obtained under Ar saturation conditions (black) and O_2 saturation conditions (red). Conditions: 1 mM analyte; glassy carbon working electrode, Pt wire counter electrode, Ag/AgCl pseudoreference electrode; scan rate 100 mV/s; referenced to internal ferrocene standard.

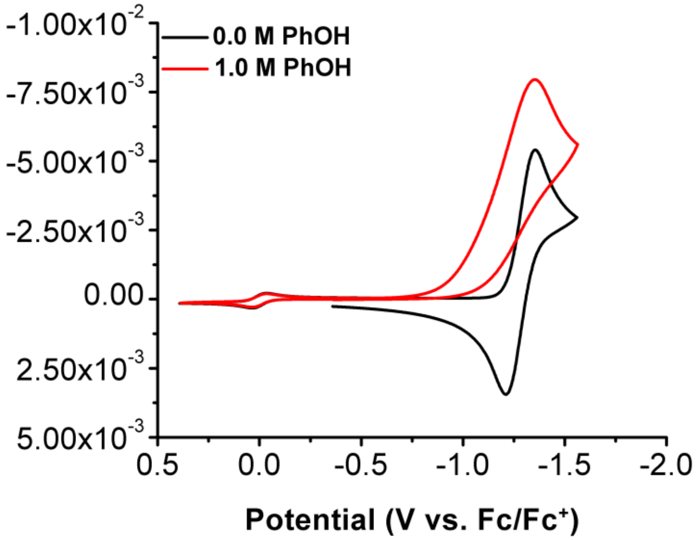

Figure S2.4.14. CVs showing O_2 and O_2 and PhOH control responses. Conditions: glassy carbon working electrode, Pt wire counter electrode, Ag/AgCl pseudoreference electrode; scan rate 100 mV/s; referenced to internal ferrocene standard.

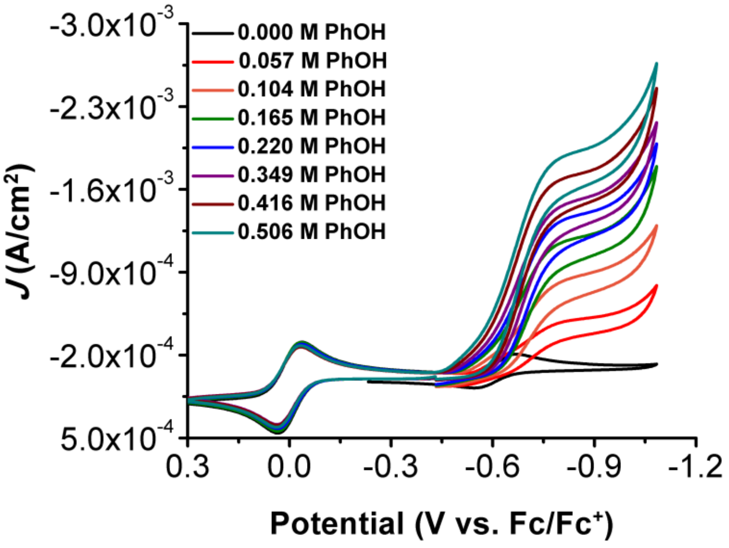

Figure S2.4.15. CVs of Mn(^{tbu}dhbpy)Cl **1**, obtained under O_2 saturation conditions with variable PhOH concentration. Conditions: 1 mM analyte; glassy carbon working electrode, Pt wire counter electrode, Ag/AgCl pseudoreference electrode; scan rate 100 mV/s; referenced to internal ferrocene standard.

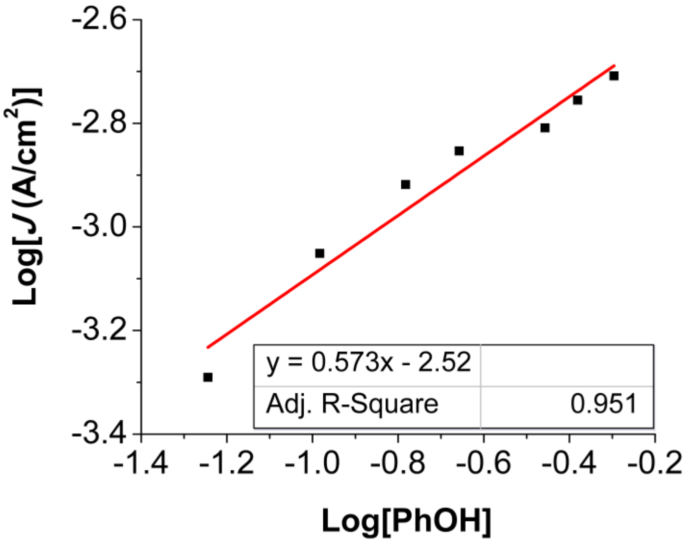

Figure S2.4.16. Log-log plot from data obtained from CVs of Mn(^{tbu}dhbpy)Cl **1** (1 mM) with variable PhOH concentrations and O_2 saturation. Adapted from Sathrum and Kubiak *J. Phys. Chem. Lett.* **2011**, *2*, 2372. *F* is Faraday's constant, *A* is the electrode area, [*Q*] is the substrate concentration, k_{cat} is the catalytic rate, *D* is the diffusion constant of the catalyst, [*cat*] is the concentration of the catalyst, and n_{cat} is the number of electrons involved in the catalytic process.

$$(1)\ \ i_{cat} = n_{cat} F A [cat] (D k_{cat} [Q]^{y})^{1/2}$$

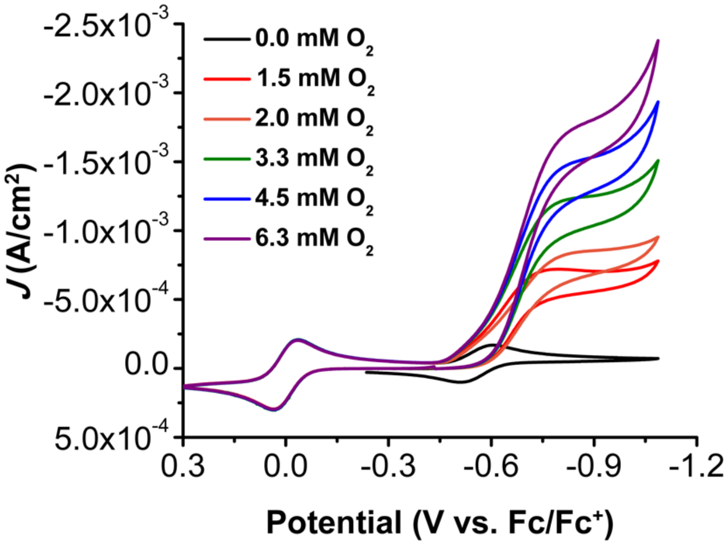

Figure S2.4.17. CVs of Mn(^{tbu}dhbpy)Cl **1**, obtained under variable O_2 concentration with 0.5 M PhOH. Conditions: 1 mM analyte; glassy carbon working electrode, Pt wire counter electrode, Ag/AgCl pseudoreference electrode; scan rate 100 mV/s; referenced to internal ferrocene standard.

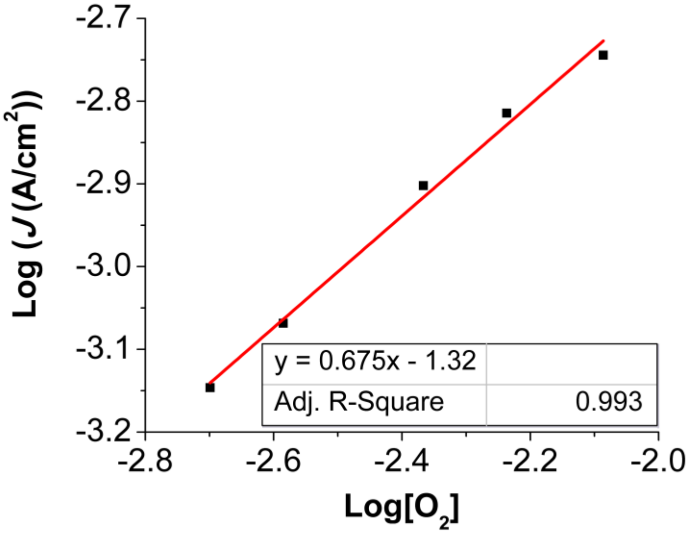

Figure S2.4.18. Log-log plot from data obtained from CVs of Mn(^{tbu}dhbpy)Cl **1** (1 mM) under variable O_2 concentration conditions with 0.5 M PhOH. The final data point has not been included in the fit because of the deviation from linearity consistent with saturation kinetics.

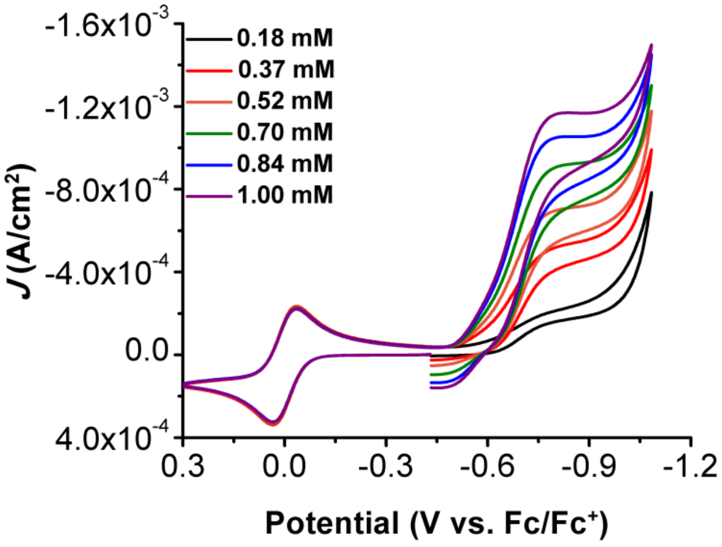

Figure S2.4.19. CVs of Mn(^{tbu}dhbpy)Cl **1** at variable concentrations, obtained under O_2 saturation with 0.11 M PhOH. Conditions: 1 mM analyte; glassy carbon working electrode, Pt wire counter electrode, Ag/AgCl pseudoreference electrode; scan rate 100 mV/s; referenced to internal ferrocene standard.

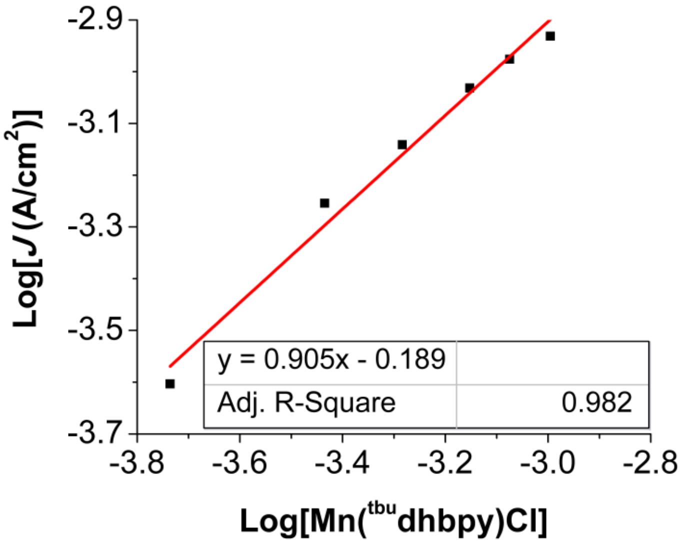

Figure S2.4.20. Log-log plot from data obtained from CVs of Mn(^{tbu}dhbpy)Cl **1** under variable concentration conditions with 0.11 M PhOH and O_2 saturation.

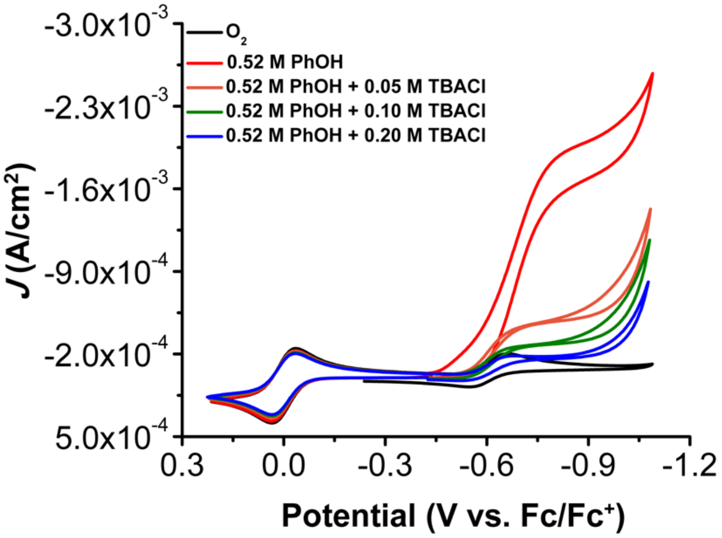

Figure S2.4.21. CVs of Mn(^{tbu}dhbpy)Cl 1, obtained under O_2 saturation conditions comparing the effects of PhOH and TBACl. Conditions: 1 mM analyte; glassy carbon working electrode, Pt wire counter electrode, Ag/AgCl pseudoreference electrode; 100 mV/s scan rate; referenced to internal ferrocene standard.

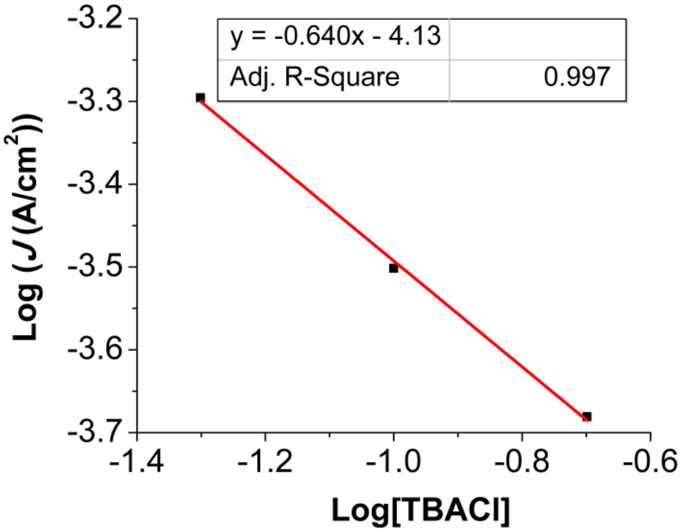

Figure S2.4.22. Log-log plot from data obtained from CVs of Mn(^{tbu}dhbpy)Cl 1 (1 mM) at 0.5 M PhOH with variable TBACl concentration and O_2 saturation.

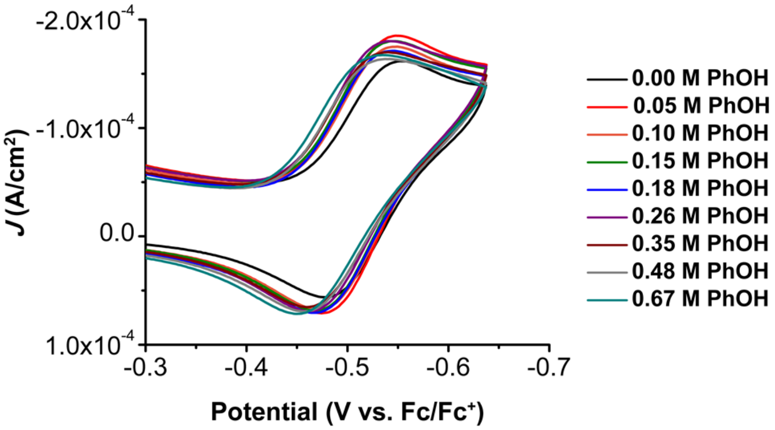

Figure S2.4.23. CVs of Mn(^{tbu}dhbpy)[OTf] (1 mM), obtained under O_2 saturation with variable PhOH concentrations. Conditions: 1 mM analyte; glassy carbon working electrode, Pt wire counter electrode, Ag/AgCl pseudoreference electrode; scan rate 100 mV/s; referenced to internal ferrocene standard.

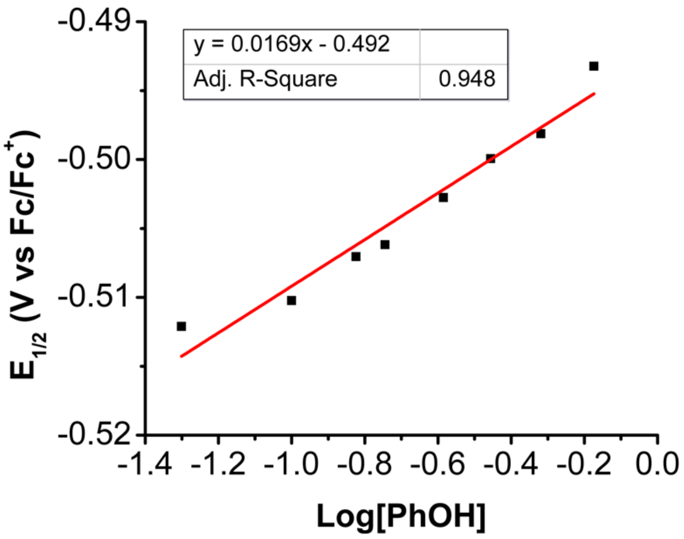

Figure S2.4.24. Diagram showing the Nernstian voltage dependence of Mn(^{tbu}dhbpy)[OTf] on the concentration of PhOH in MeCN at the first reduction under Ar saturation (red). The slope of 17 mV/decade concentration of PhOH is consistent with an approximately 1 [PhOH]/2 e^- electrochemical reaction. Conditions: 1 mM Mn(^{tbu}dhbpy)[OTf]; 0.1 M $TBAPF_6$/MeCN; glassy carbon working electrode, Pt counter electrode, Ag/AgCl pseudoreference electrode; referenced to internal ferrocene standard.

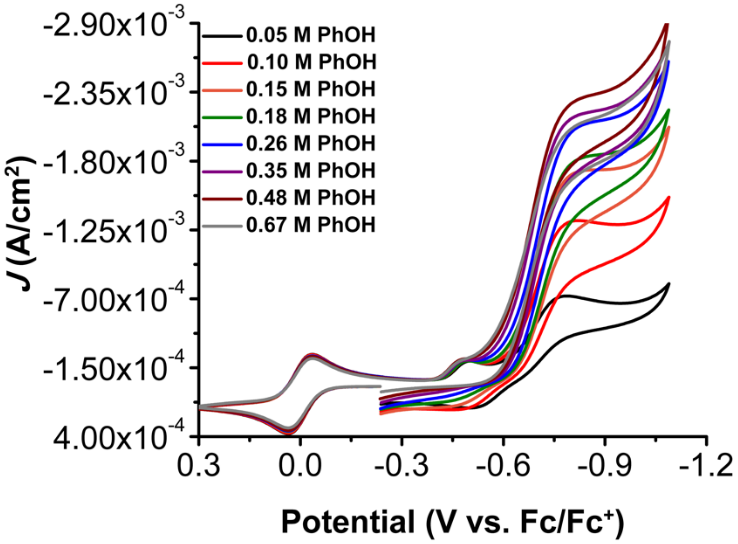

Figure S2.4.25. CVs of Mn(^{tbu}dhbpy)[OTf] (1 mM), obtained under O_2 saturation with variable PhOH concentrations. Conditions: 1 mM analyte; glassy carbon working electrode, Pt wire counter electrode, Ag/AgCl pseudoreference electrode; scan rate 100 mV/s; referenced to internal ferrocene standard.

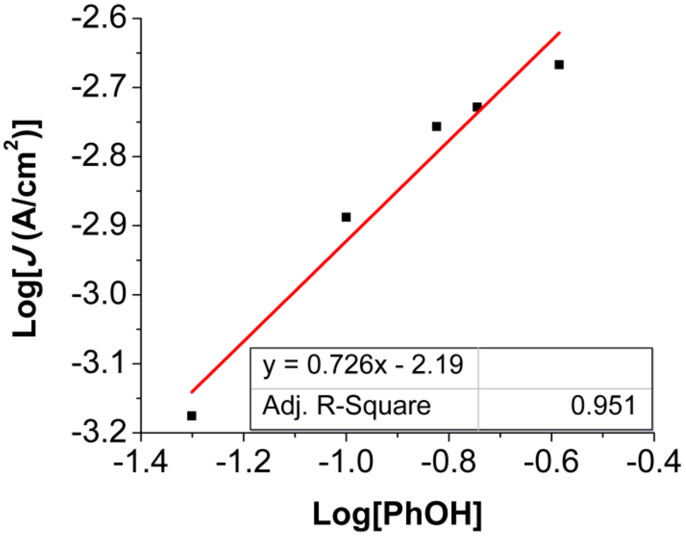

Figure S2.4.26. Log-log plot from data obtained from CVs of Mn(^{tbu}dhbpy)[OTf] (1 mM) with varied PhOH concentration under O_2 saturation conditions.

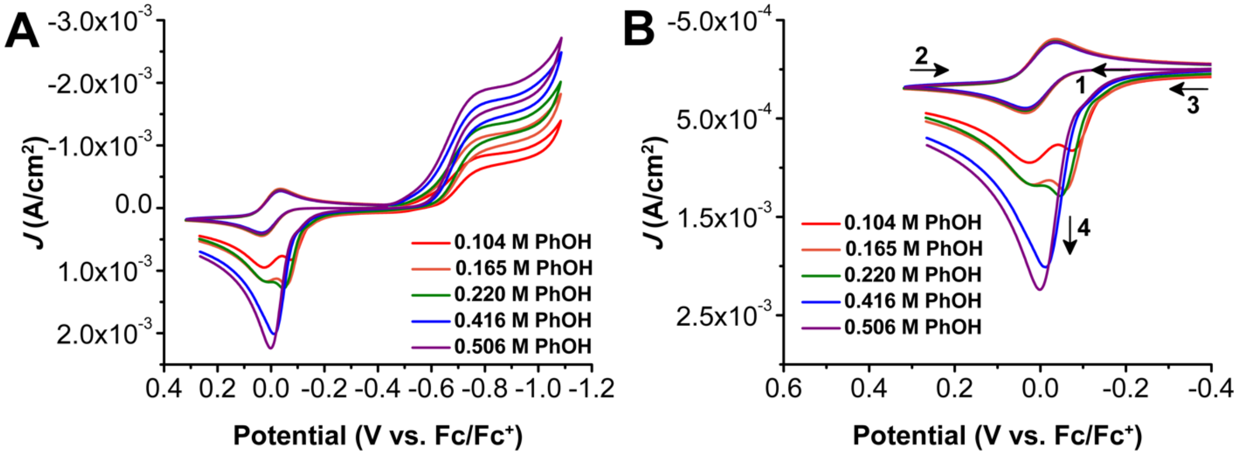

Figure S2.4.27. CVs of Mn(^{tbu}dhbpy)Cl **1**, obtained under O_2 saturation conditions with variable PhOH concentration (A) and a highlight of the phenolate oxidation feature (B). Conditions: 1 mM analyte; glassy carbon working electrode, Pt wire counter electrode, Ag/AgCl pseudoreference electrode; scan rate 100 mV/s; referenced to internal ferrocene standard. The CV sweep begins at -0.25 V (1), goes to 0.40 V (2), then -1.00 V (return at 3), then finishes at 0.40 V. The oxidation of phenolate ions is only observed upon returning to 0.40 V *after* the catalytic current occurs at -1.00 V (4); note the increase in current near Fc/Fc$^+$.

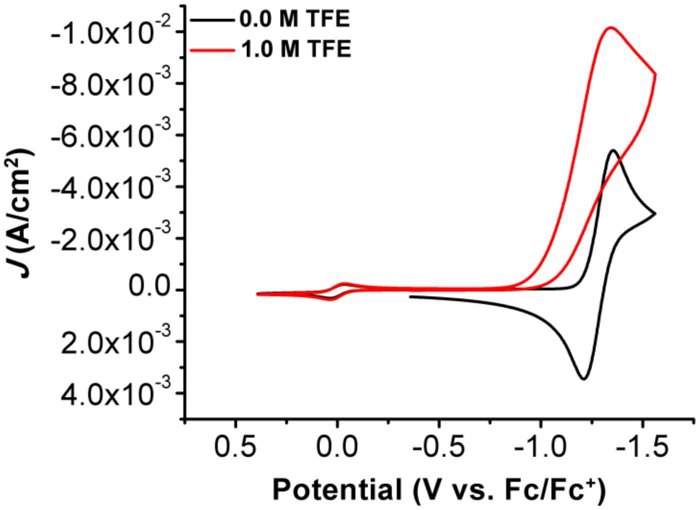

Figure S2.4.28. CVs showing O_2 and O_2 and TFE control responses. Conditions: glassy carbon working electrode, Pt wire counter electrode, Ag/AgCl pseudoreference electrode; scan rate 100 mV/s; referenced to internal ferrocene standard.

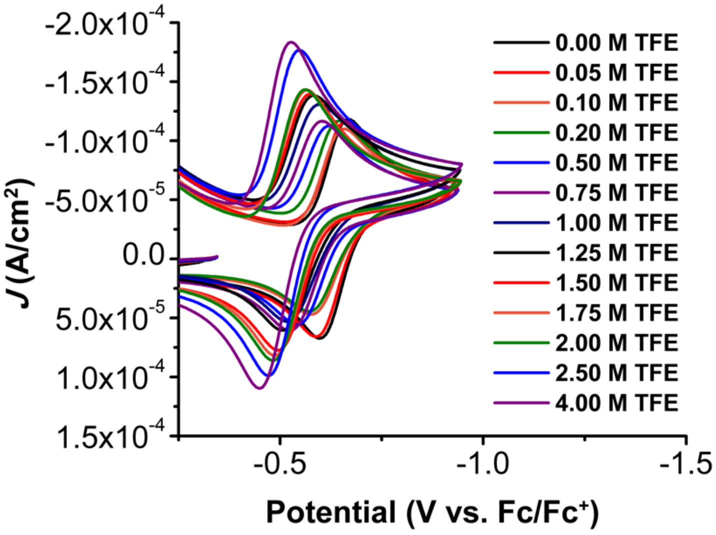

Figure S2.4.29. CVs of Mn(^{tbu}dhbpy)Cl **1**, obtained under Ar saturation with variable TFE concenrations. Conditions: 1 mM analyte; glassy carbon working electrode, Pt wire counter electrode, Ag/AgCl pseudoreference electrode; scan rate 100 mV/s; referenced to internal ferrocene standard.

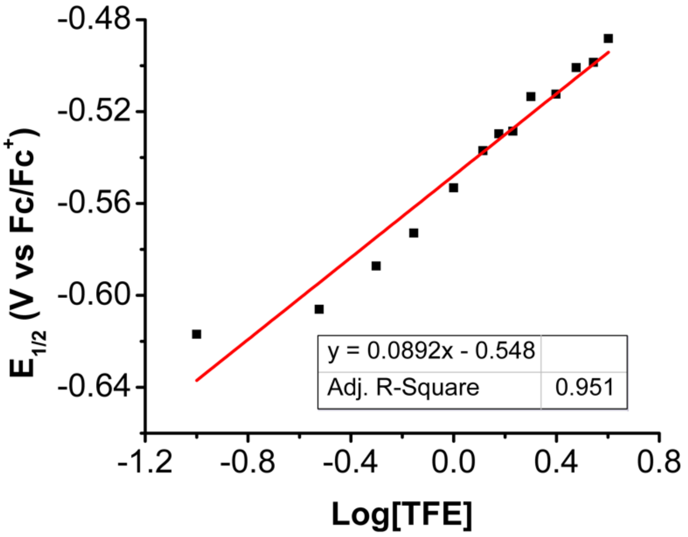

Figure S2.4.30. Diagram showing the voltage dependence of Mn(^{tbu}dhbpy)Cl **1** at the first reduction on the log of the concentration of TFE under Ar saturation (red). The slope of approximately 89 mV/decade of TFE concentration is consistent with a 1.5[TFE]/e$^-$ reaction. Conditions: 1 mM **1**; 0.1 M TBAPF$_6$/MeCN; glassy carbon working electrode, Pt counter electrode, Ag/AgCl pseudoreference electrode; referenced to internal ferrocene standard.

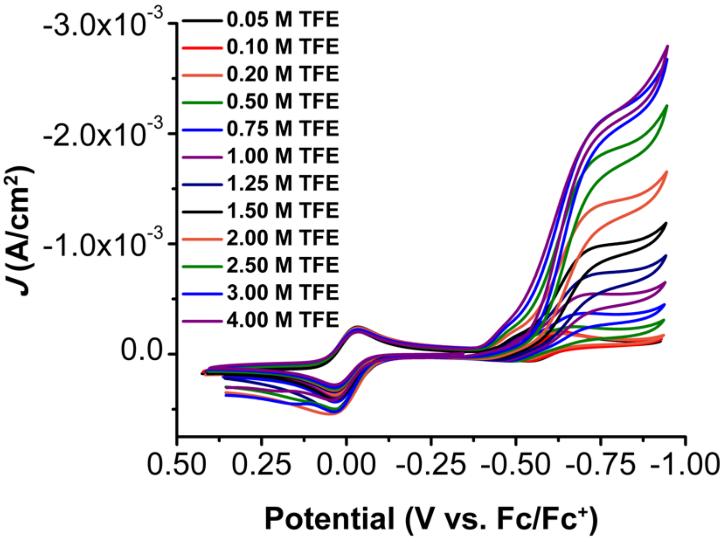

Figure S2.4.31. CVs of Mn(^{tbu}dhbpy)Cl **1**, obtained under O_2 saturation with variable TFE concenrations. Conditions: 1 mM analyte; glassy carbon working electrode, Pt wire counter electrode, Ag/AgCl pseudoreference electrode; scan rate 100 mV/s; referenced to internal ferrocene standard. After the catalytic wave, the CV continues again through the Fc/Fc$^+$ feature to show the absence of an oxidation feature similar to the one observed for PhOH.

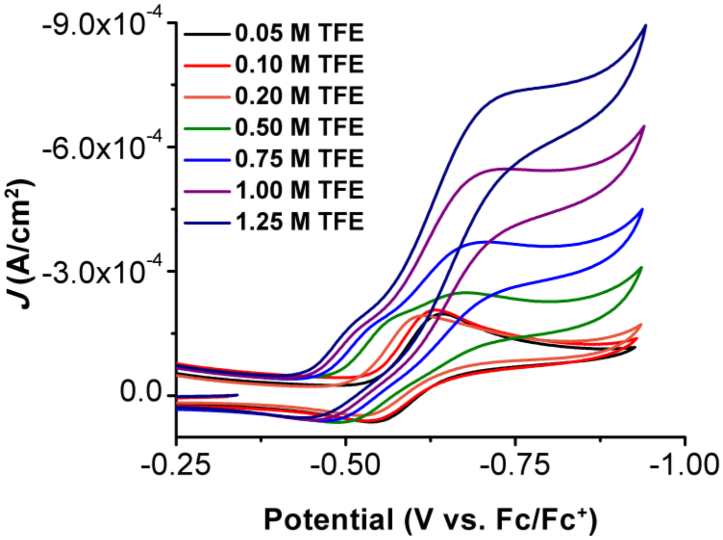

Figure S2.4.32. CVs of Mn(^{tbu}dhbpy)Cl **1**, obtained under O_2 saturation with variable TFE concenrations. Conditions: 1 mM analyte; glassy carbon working electrode, Pt wire counter electrode, Ag/AgCl pseudoreference electrode; scan rate 100 mV/s; referenced to internal ferrocene standard.

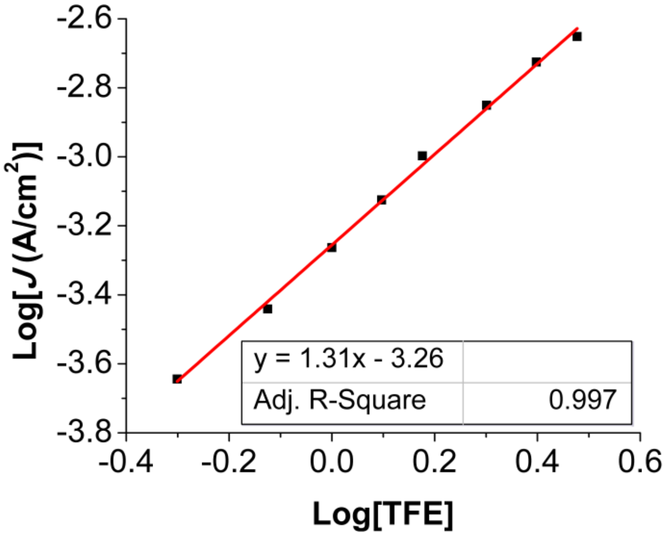

Figure S2.4.33. Log-log plot from data obtained from CVs of Mn(^{tbu}dhbpy)Cl **1** (1 mM) with variable TFE concentrations and O_2 saturation.

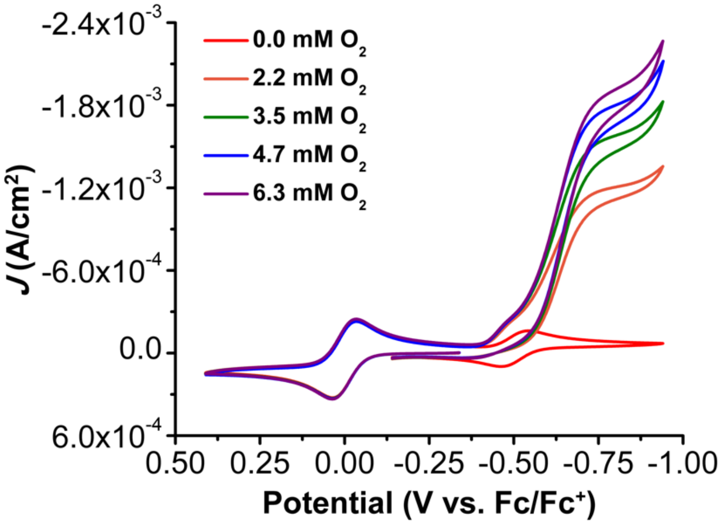

Figure S2.4.34. CVs of Mn(^{tbu}dhbpy)Cl **1**, obtained under variable O_2 concentrations with 3.0 M TFE. Conditions: 1 mM analyte; glassy carbon working electrode, Pt wire counter electrode, Ag/AgCl pseudoreference electrode; scan rate 100 mV/s; referenced to internal ferrocene standard.

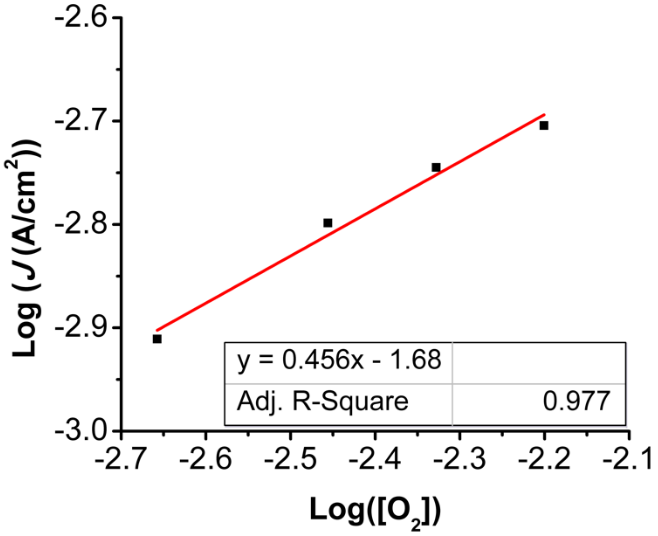

Figure S2.4.35. Log-log plot from data obtained from CVs of Mn(^{tbu}dhbpy)Cl **1** (1 mM) with variable O_2 concentration and 3.0 M TFE.

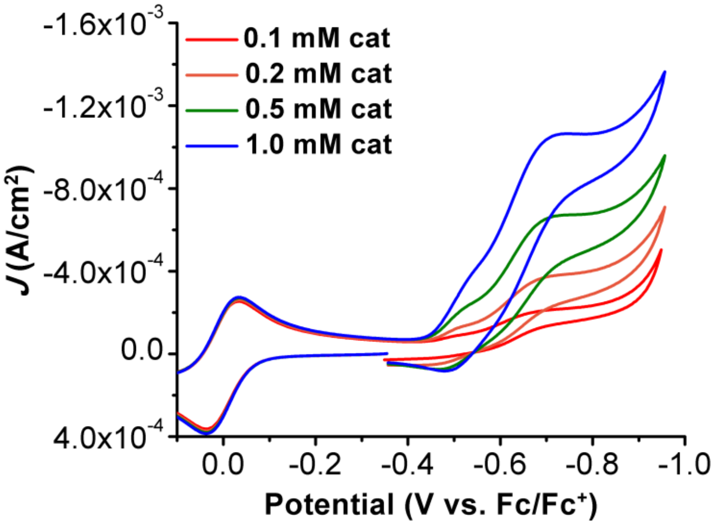

Figure S2.4.36. CVs of Mn(^{tbu}dhbpy)Cl **1** at variable concentrations, obtained at O_2 saturation with 1.0 M TFE. Conditions: glassy carbon working electrode, Pt wire counter electrode, Ag/AgCl pseudoreference electrode; scan rate 100 mV/s; referenced to internal ferrocene standard.

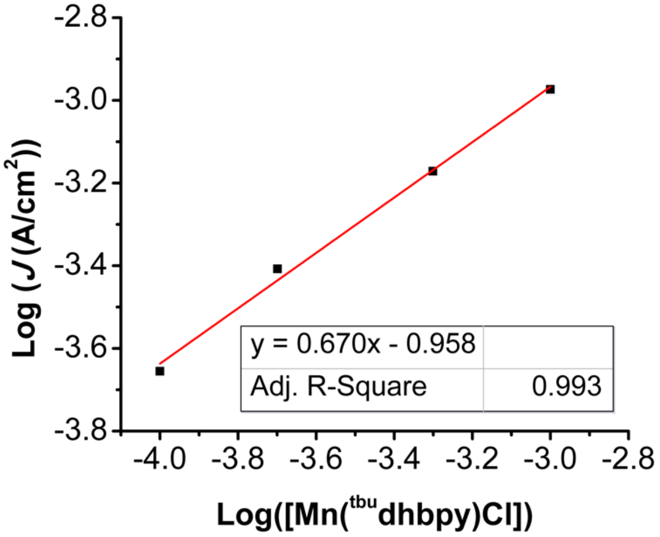

Figure S2.4.37. Log-log plot from data obtained from CVs of Mn(^{tbu}dhbpy)Cl **1** at variable concentrations, obtained at O_2 saturation with 1 M TFE.

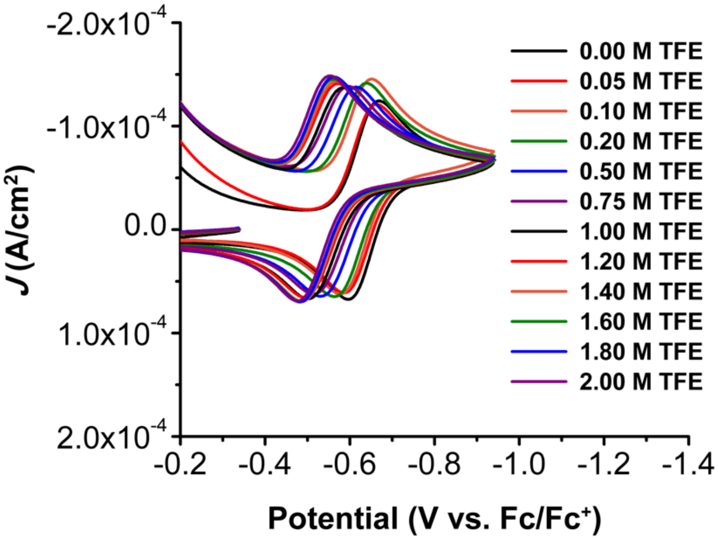

Figure S2.4.38. CVs of Mn(^{tbu}dhbpy)Cl **1** (0.5 mM), obtained under Ar saturation with variable TFE concenrations. Conditions: 0.5 mM analyte; glassy carbon working electrode, Pt wire counter electrode, Ag/AgCl pseudoreference electrode; scan rate 100 mV/s; referenced to internal ferrocene standard.

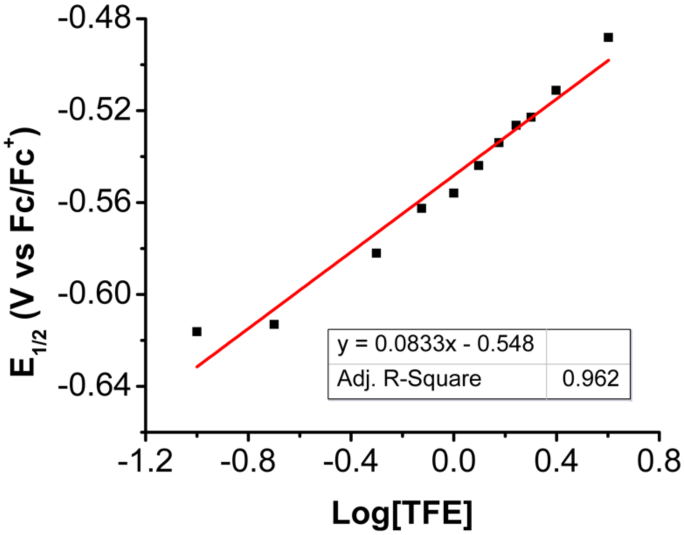

Figure S2.4.39. Diagram showing the voltage dependence of Mn(^{tbu}dhbpy)Cl **1** at the first reduction on the log of the concentration of TFE under Ar saturation. The slope of approximately 83 mV/decade of TFE concentration is consistent with a 1.5[TFE]/e$^-$ reaction. Conditions: 1 mM **1**; 0.1 M $TBAPF_6$/MeCN; glassy carbon working electrode, Pt counter electrode, Ag/AgCl pseudoreference electrode; referenced to internal ferrocene standard.

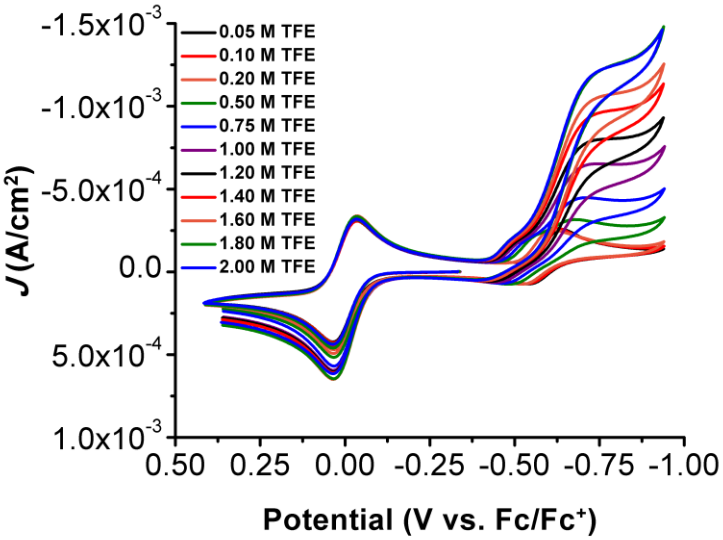

Figure S2.4.40. CVs of Mn(^{tbu}dhbpy)Cl **1** (0.5 mM), obtained under O_2 saturation with variable TFE concentrations. Conditions: 0.5 mM analyte; glassy carbon working electrode, Pt wire counter electrode, Ag/AgCl pseudoreference electrode; scan rate 100 mV/s; referenced to internal ferrocene standard.

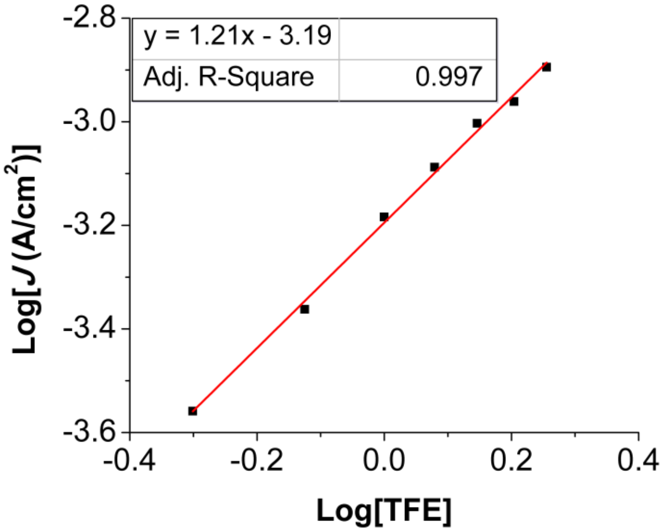

Figure S2.4.41. Log-log plot from data obtained from CVs of Mn(^{tbu}dhbpy)Cl **1** (0.5 mM) with variable TFE concentrations and O_2 saturation.

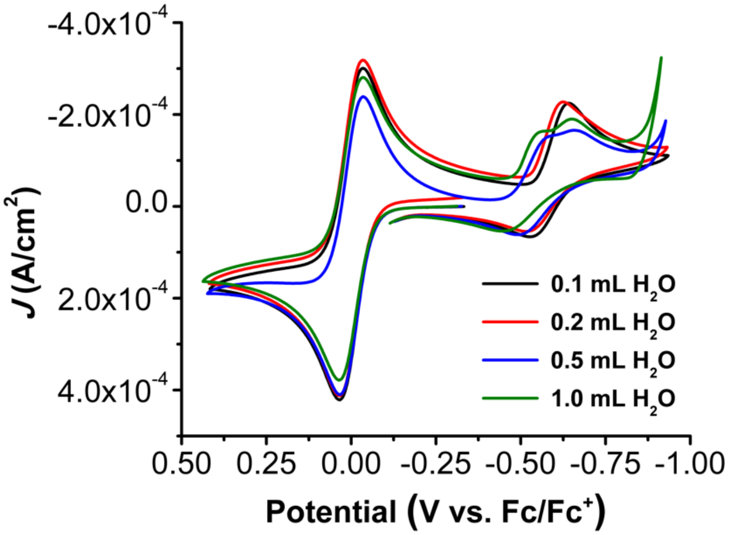

Figure S2.4.42. CVs of Mn(^{tbu}dhbpy)Cl **1**, obtained under O_2 saturation with variable H_2O concentrations. Conditions: 1 mM analyte; glassy carbon working electrode, Pt wire counter electrode, Ag/AgCl pseudoreference electrode; scan rate 100 mV/s; referenced to internal ferrocene standard.

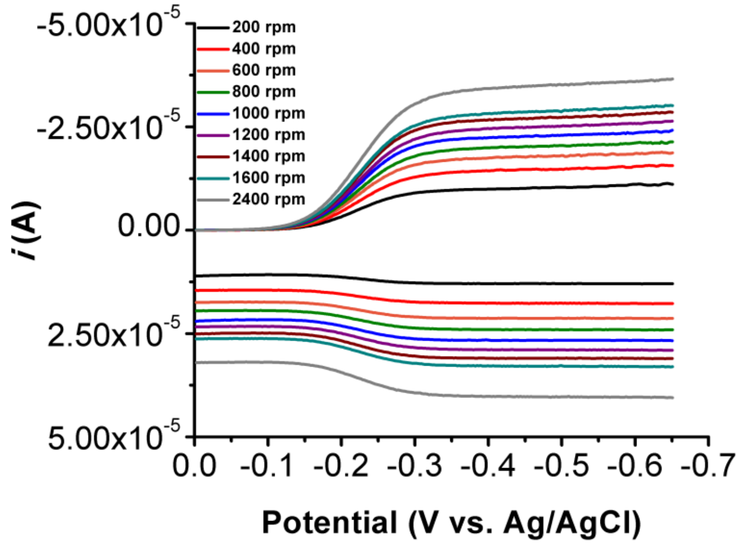

Figure S2.4.43. Linear Sweep Voltammograms of RRDE experiment Mn(^{tbu}dhbpy)Cl **1** at various rotation rates with 0.25 mM catalyst concentration and 0.6 M TFE concentration under argon saturation conditions; ring potential = 1.2 V vs Ag/AgCl. Conditions: 0.25 mM analyte; glassy carbon working electrode/Pt ring working electrode, Pt wire counter electrode, Ag/AgCl pseudoreference electrode; scan rate 0.01 V/s.

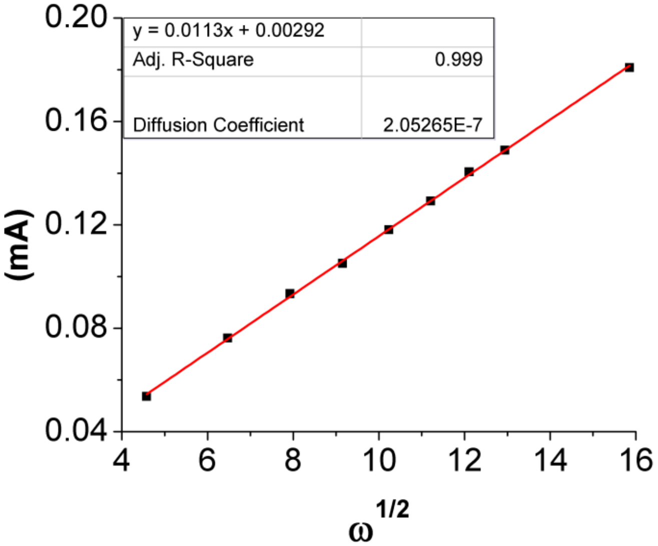

y = 0.0113x + 0.00292	
Adj. R-Square	0.999
Diffusion Coefficient	2.05265E-7

Figure S2.4.44. Levich plot from data obtained from Linear Sweep Voltammograms of Mn(^{tbu}dhbpy)Cl **1** (0.25 mM) by RRDE with 0.6 M TFE under argon saturation conditions at various rotation rates.

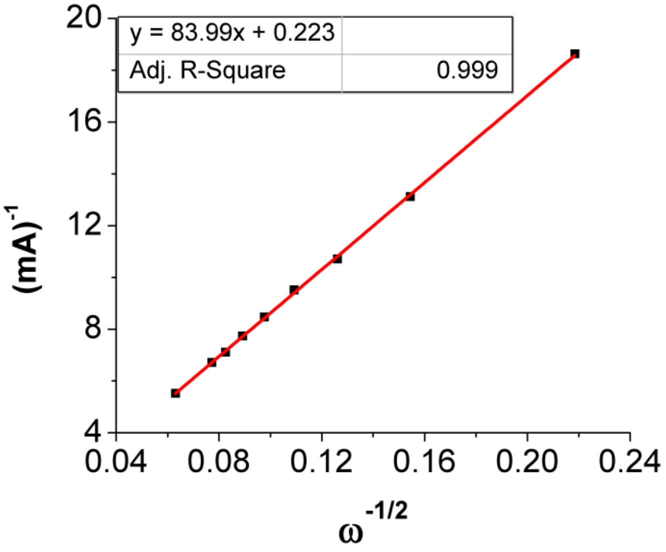

Figure S2.4.45. Koutecky-Levich plot from data obtained from Linear Sweep Voltammograms of Mn(^{tbu}dhbpy)Cl **1** by RRDE with 0.6 M TFE under argon saturation conditions at various rotation rates.

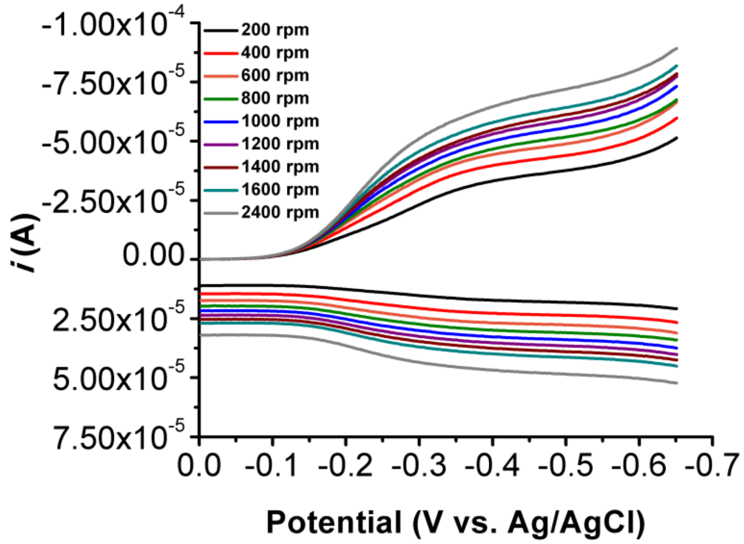

Figure S2.4.46. Linear Sweep Voltammograms of RRDE experiment Mn(^{tbu}dhbpy)Cl **1** (0.25 mM) at various rotation rates with 0.6 M TFE concentration under O_2 saturation conditions; ring potential = 1.2 V vs Ag/AgCl. Conditions: 0.25 mM analyte; glassy carbon working electrode/Pt ring working electrode, Pt wire counter electrode, Ag/AgCl pseudoreference electrode; scan rate 0.01 V/s. Current efficiency for H_2O_2 determined to be 81±4%.

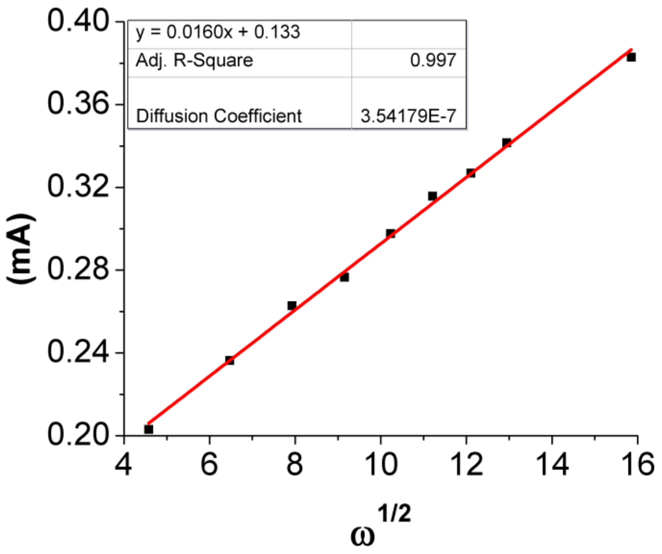

Figure S2.4.47. Levich plot from data obtained from Linear Sweep Voltammograms of Mn(^{tbu}dhbpy)Cl **1** (0.25 mM) by RRDE with 0.6 M TFE under O_2 saturation conditions at various rotation rates.

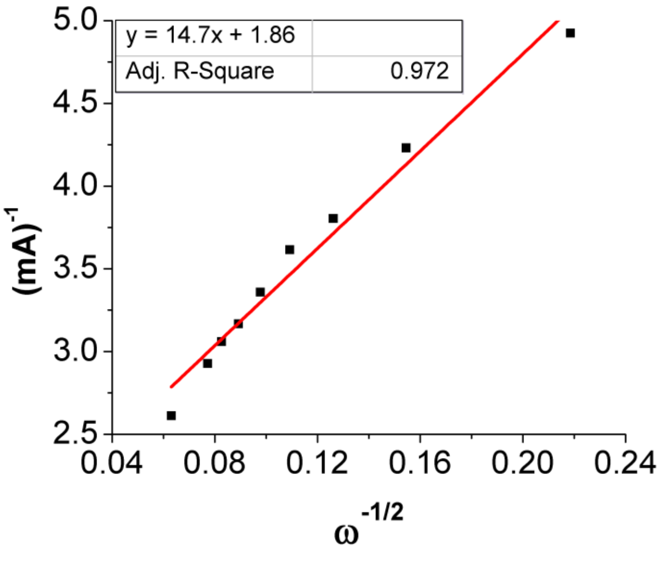

Figure S2.4.48. Koutecky-Levich plot from data obtained from Linear Sweep Voltammograms of Mn(^{tbu}dhbpy)Cl **1** (0.25 mM) by RRDE with 0.6 M TFE under O_2 saturation conditions at various rotation rates.

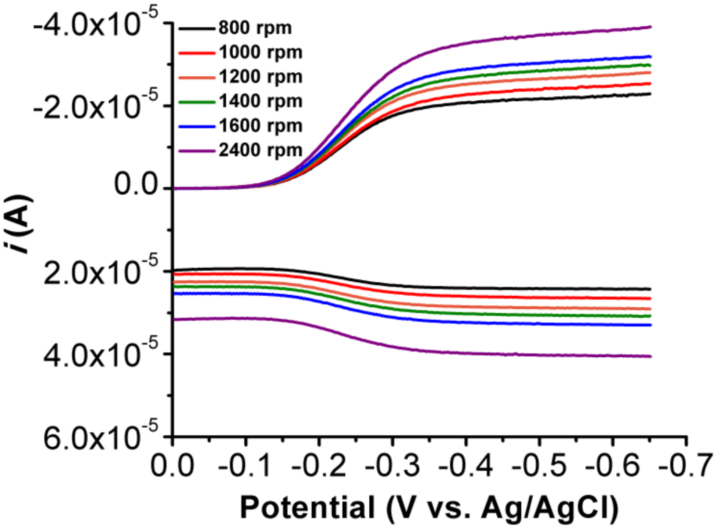

Figure S2.4.49. Linear Sweep Voltammograms of RRDE experiment Mn(^{tbu}dhbpy)Cl **1** (0.25 mM) at various rotation rates with 0.45 M TFE concentration under argon saturation conditions; ring potential = 1.2 V vs Ag/AgCl. Conditions: 0.25 mM analyte; glassy carbon working electrode/Pt ring working electrode, Pt wire counter electrode, Ag/AgCl pseudoreference electrode; scan rate 0.01 V/s.

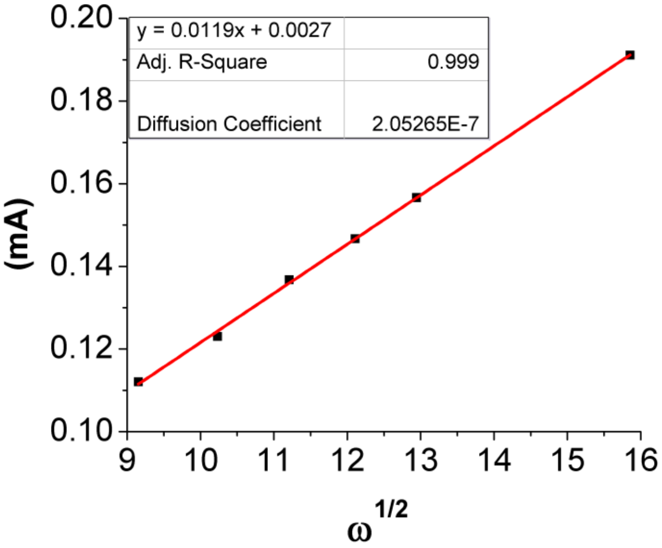

Figure S2.4.50. Levich plot from data obtained from Linear Sweep Voltammograms of Mn(^{tbu}dhbpy)Cl **1** (0.25 mM) by RRDE with 0.45 M TFE under argon saturation conditions at various rotation rates.

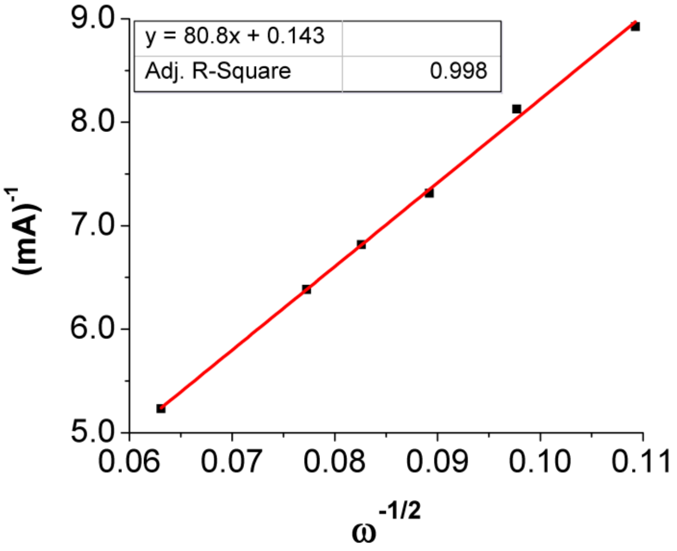

Figure S2.4.51. Koutecky-Levich plot from data obtained from Linear Sweep Voltammograms of Mn(^{tbu}dhbpy)Cl **1** (0.25 mM) by RRDE with 0.45 M TFE under argon saturation conditions at various rotation rates.

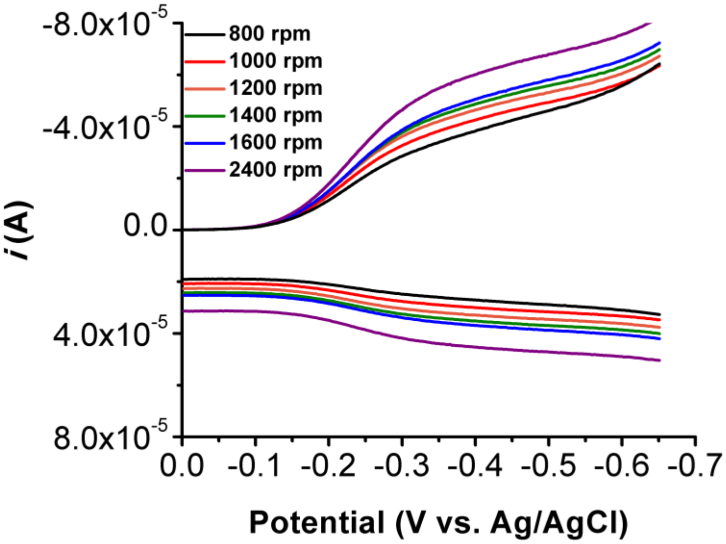

Figure S2.4.52. Linear Sweep Voltammograms of RRDE experiments with Mn(^{tbu}dhbpy)Cl **1** (0.25 mM) at various rotation rates with 0.45 M TFE concentration under O_2 saturation conditions; ring potential = 1.2 V vs Ag/AgCl. Conditions: 0.25 mM analyte; glassy carbon working electrode/Pt ring working electrode, Pt wire counter electrode, Ag/AgCl pseudoreference electrode; scan rate 0.01 V/s. Current efficiency for H_2O_2 determined to be 83±3%.

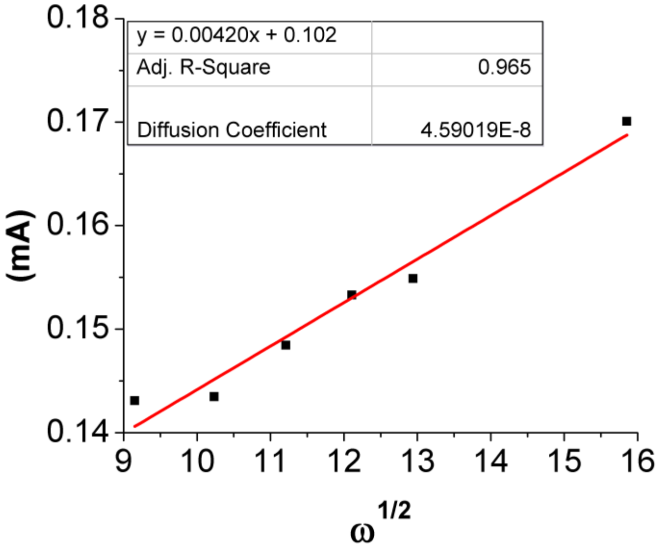

Figure S2.4.53. Levich plot from data obtained from Linear Sweep Voltammograms of Mn(^{tbu}dhbpy)Cl **1** (0.25 mM) by RRDE with 0.45 M TFE under O_2 saturation conditions at various rotation rates.

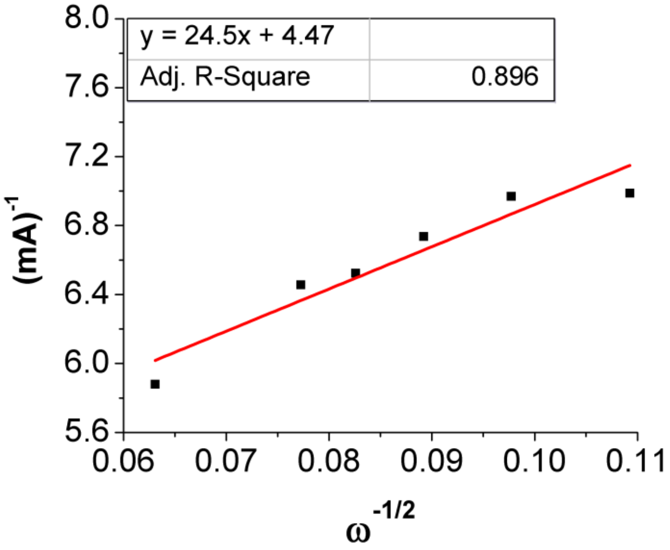

Figure S2.4.54. Koutecky-Levich plot from data obtained from Linear Sweep Voltammograms of Mn(^{tbu}dhbpy)Cl **1** (0.25 mM) by RRDE with 0.45 M TFE under O_2 saturation conditions at various rotation rates.

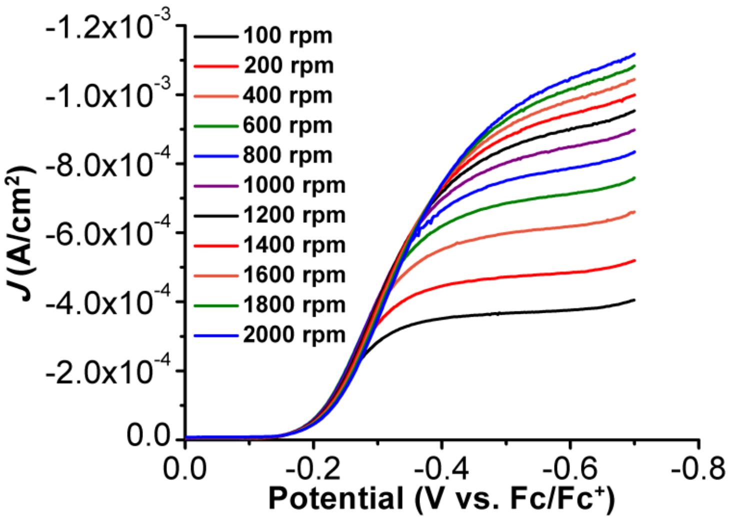

Figure S2.4.55. Linear Sweep Voltammograms of RDE experiment Mn(^{tbu}dhbpy)Cl **1** at various rotation rates under argon saturation. Conditions: 1 mM analyte; glassy carbon working electrode, Pt wire counter electrode, Ag/AgCl pseudoreference electrode; scan rate 0.01 V/s.

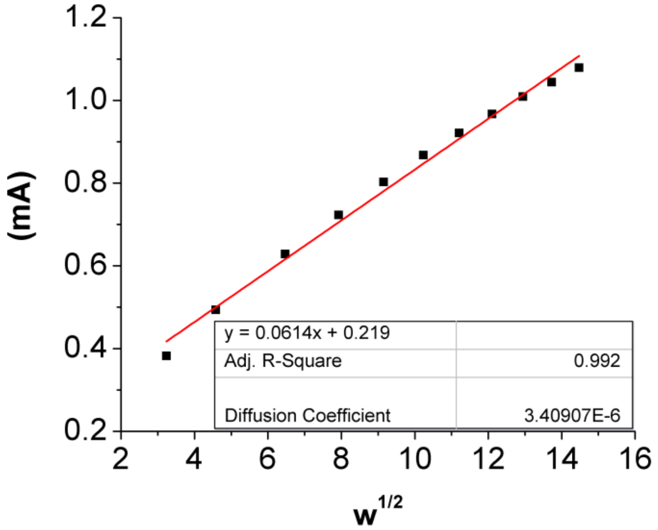

Figure S2.4.56. Levich plot from data obtained from Linear Sweep Voltammograms of Mn(^{tbu}dhbpy)Cl **1** under argon saturation conditions at various rotation rates by RDE. Conditions: 1 mM analyte; glassy carbon working electrode, Pt wire counter electrode, Ag/AgCl pseudoreference electrode; scan rate 0.01 V/s.

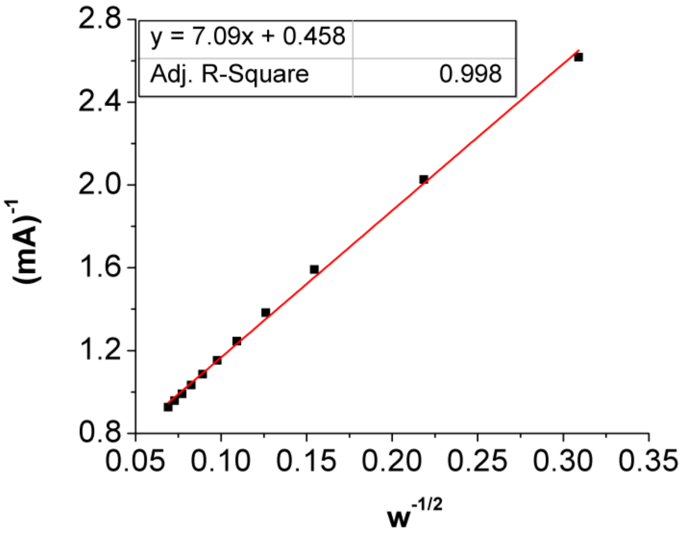

Figure S2.4.57. Koutecky-Levich plot from data obtained from Linear Sweep Voltammograms of Mn(^{tbu}dhbpy)Cl **1** under argon saturation conditions at various rotation rates by RDE. Conditions: 1 mM analyte; glassy carbon working electrode, Pt wire counter electrode, Ag/AgCl pseudoreference electrode; scan rate 0.01 V/s.

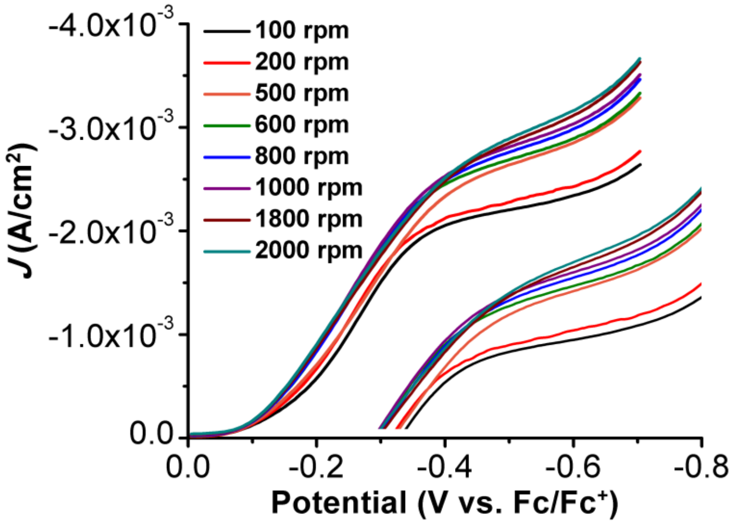

Figure S2.4.58. Linear Sweep Voltammograms of RDE experiment Mn(^{tbu}dhbpy)Cl **1** at various rotation rates with 0.5 M PhOH under argon saturation. Conditions: 1 mM analyte; glassy carbon working electrode, Pt wire counter electrode, Ag/AgCl pseudoreference electrode; scan rate 0.01 V/s. Figure inset contains the current plateau region of the LSV.

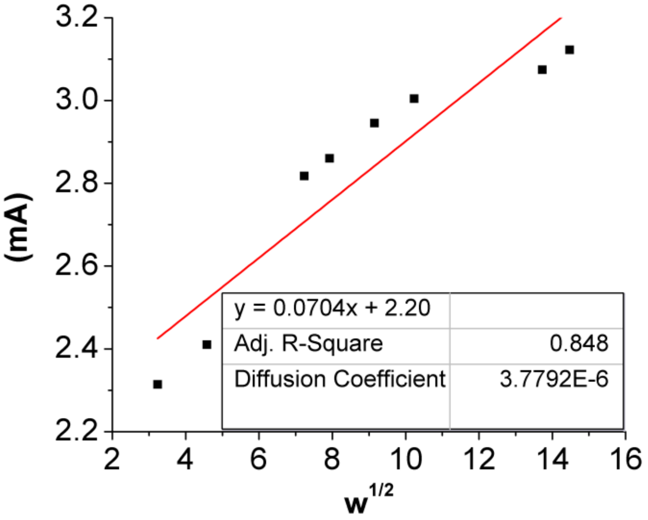

Figure S2.4.59. Levich plot from data obtained from Linear Sweep Voltammograms of Mn(^{tbu}dhbpy)Cl **1** with 0.5 M PhOH under argon saturation conditions at various rotation rates by RDE. Conditions: 1 mM analyte; glassy carbon working electrode, Pt wire counter electrode, Ag/AgCl pseudoreference electrode; scan rate 0.01 V/s.

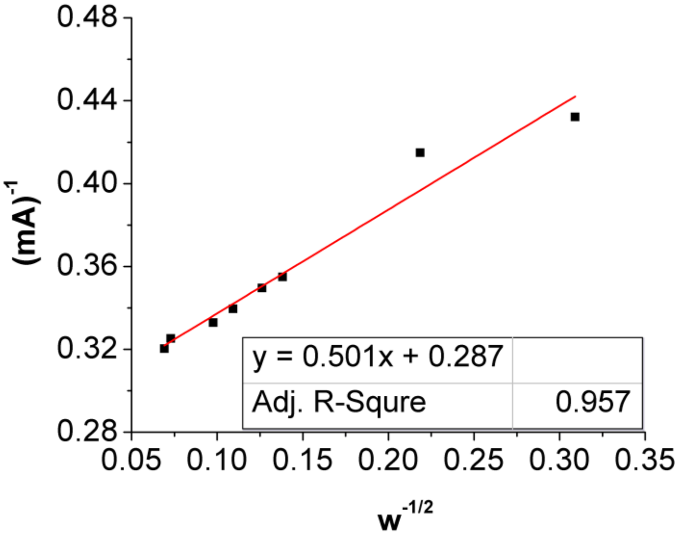

Figure S2.4.60. Koutecky-Levich plot from data obtained from Linear Sweep Voltammograms of Mn(^{tbu}dhbpy)Cl **1** with 0.5 M PhOH under argon saturation conditions at various rotation rates by RDE. Conditions: 1 mM analyte; glassy carbon working electrode, Pt wire counter electrode, Ag/AgCl pseudoreference electrode; scan rate 0.01 V/s.

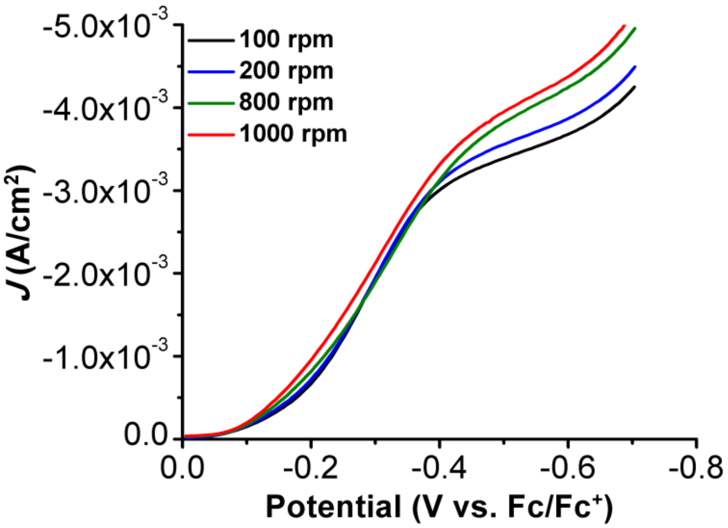

Figure S2.4.61. Linear Sweep Voltammograms of RDE experiment Mn(^{tbu}dhbpy)Cl **1** at various rotation rates with 0.5 M PhOH under O_2 saturation. Conditions: 1 mM analyte; glassy carbon working electrode, Pt wire counter electrode, Ag/AgCl pseudoreference electrode; scan rate 0.01 V/s.

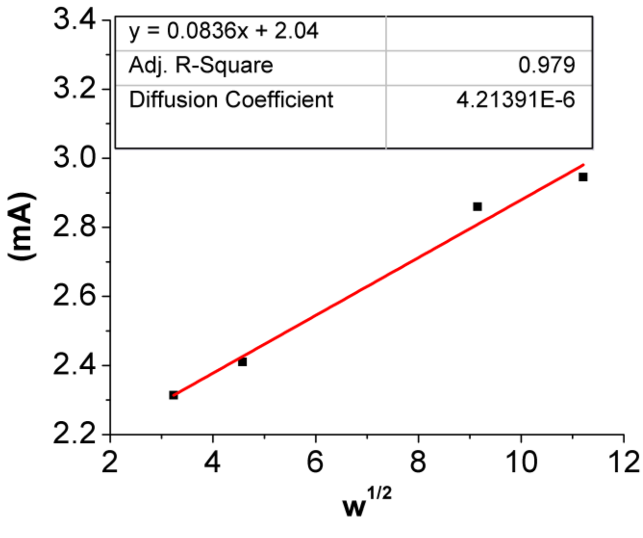

Figure S2.4.62. Levich plot from data obtained from Linear Sweep Voltammograms of Mn(^{tbu}dhbpy)Cl **1** with 0.5 M PhOH under O_2 saturation conditions at various rotation rates by RDE. Conditions: 1 mM analyte; glassy carbon working electrode, Pt wire counter electrode, Ag/AgCl pseudoreference electrode; scan rate 0.01 V/s.

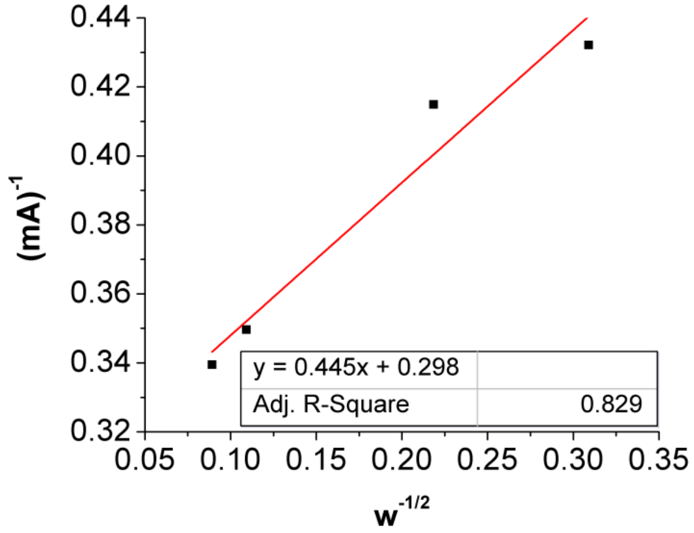

Figure S2.4.63. Koutecky-Levich plot from data obtained from Linear Sweep Voltammograms of Mn(^{tbu}dhbpy)Cl **1** with 0.5 M PhOH under O_2 saturation conditions at various rotation rates by RDE. Conditions: 1 mM analyte; glassy carbon working electrode, Pt wire counter electrode, Ag/AgCl pseudoreference electrode; scan rate 0.01 V/s.

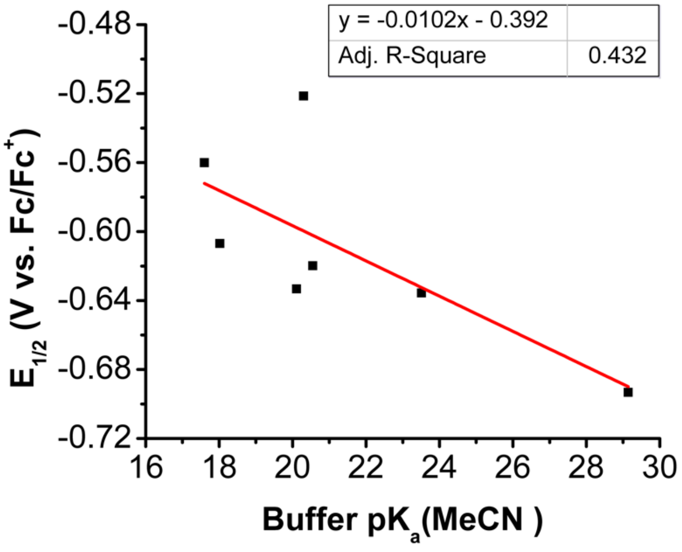

Figure S2.5.64. Pourbaix diagram from data obtained from CVs of Mn(^{tbu}dhbpy)Cl **1** obtained under Ar saturation conditions comparing the effects of different buffered proton sources. Buffered sources of phenol (pK_a = 29.14), acetic acid (23.51), 4-bromo-benzoic acid (20.3), perfluoro-tert-butanol (20.55), F_5PhOH (20.11), 2,6-dichloro-benzoic acid (17.6), and Cl_5PhOH (18.02) were prepared using a solution of tetrabutylammonium hydroxide (2:1) in water or methanol and extensive drying.

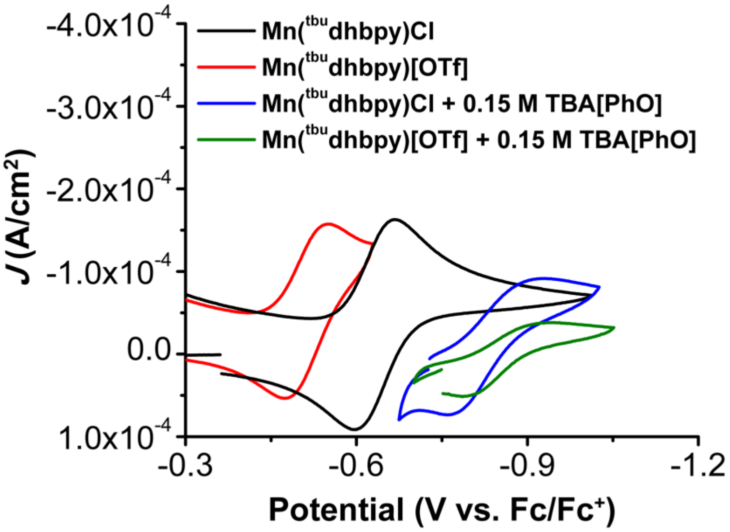

Figure S2.5.65. Mn(^{tbu}dhbpy)Cl **1** (blue) and Mn(^{tbu}dhbpy)[OTf] (green) under Ar with 0.015 M TBA[PhO]; the $E_{1/2}$ values with are -0.84 V and -0.86 V vs Fc/Fc$^+$, respectively. Conditions: 1 mM Mn(^{tbu}dhbpy)Cl **1**, 0.1 M TBAPF$_6$/MeCN; glassy carbon working electrode, glassy carbon counter electrode, Ag/AgCl pseudoreference electrode; 100 mV/s scan rate; referenced to internal Fc standard.

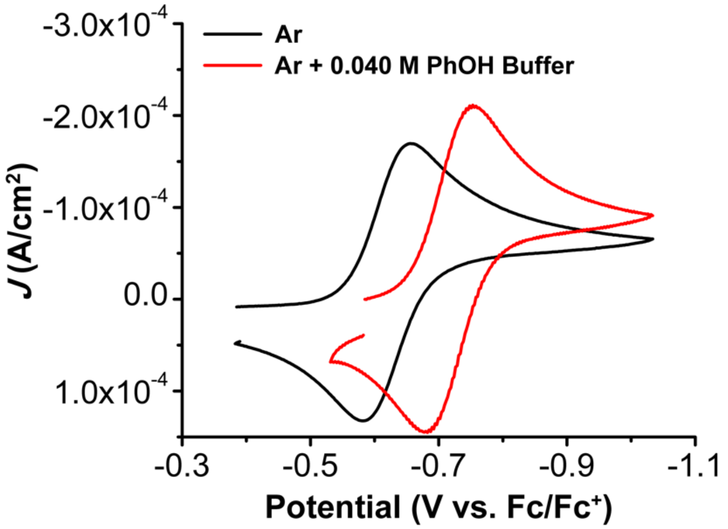

Figure S2.5.66. Mn(^{tbu}dhbpy)Cl **1** under Ar (black) and Ar with 0.04 M PhOH buffer (TBA[PhO]/PhOH; red); the $E_{1/2}$ value with buffer is -0.73 V vs Fc/Fc$^+$. Conditions: 1 mM Mn(^{tbu}dhbpy)Cl **1**, 0.1 M TBAPF$_6$/MeCN; glassy carbon working electrode, glassy carbon counter electrode, Ag/AgCl pseudoreference electrode; 100 mV/s scan rate; referenced to internal Fc standard.

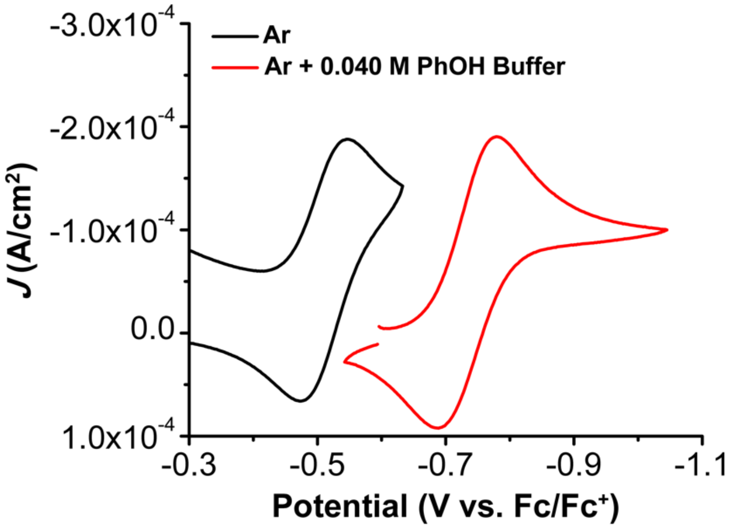

Figure S2.5.67. Mn(^{tbu}dhbpy)[OTf] under Ar (black) and Ar with 0.04 M PhOH buffer (TBA[PhO]/PhOH; red); the $E_{1/2}$ value with buffer is -0.72 V vs Fc/Fc$^+$, respectively. Conditions: 1 mM Mn(^{tbu}dhbpy)[OTf], 0.1 M TBAPF$_6$/MeCN; glassy carbon working electrode, glassy carbon counter electrode, Ag/AgCl pseudoreference electrode; 100 mV/s scan rate; referenced to internal Fc standard.

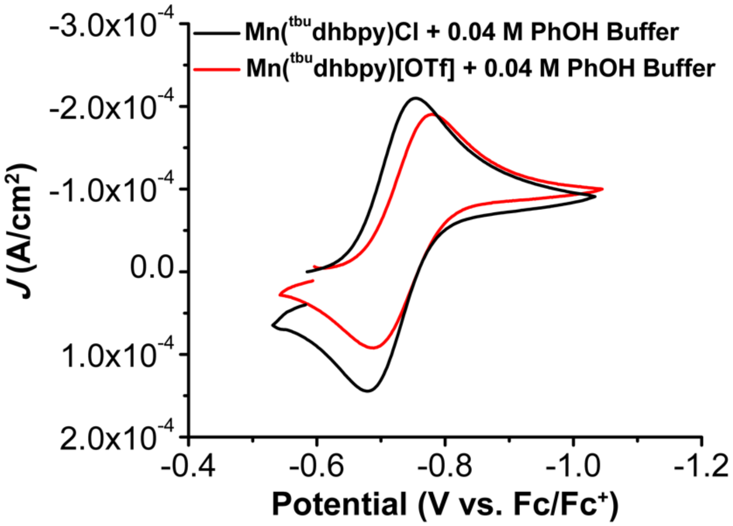

Figure S2.5.68. CVs of Mn(^{tbu}dhbpy)Cl 1 (black) and Mn(^{tbu}dhbpy)[OTF] (red), obtained under Ar saturation conditions comparing the effects of PhOH Buffer. Conditions: 1 mM analyte; glassy carbon working electrode, glassy carbon counter electrode, Ag/AgCl pseudoreference electrode; 100 mV/s scan rate; referenced to internal ferrocene standard.

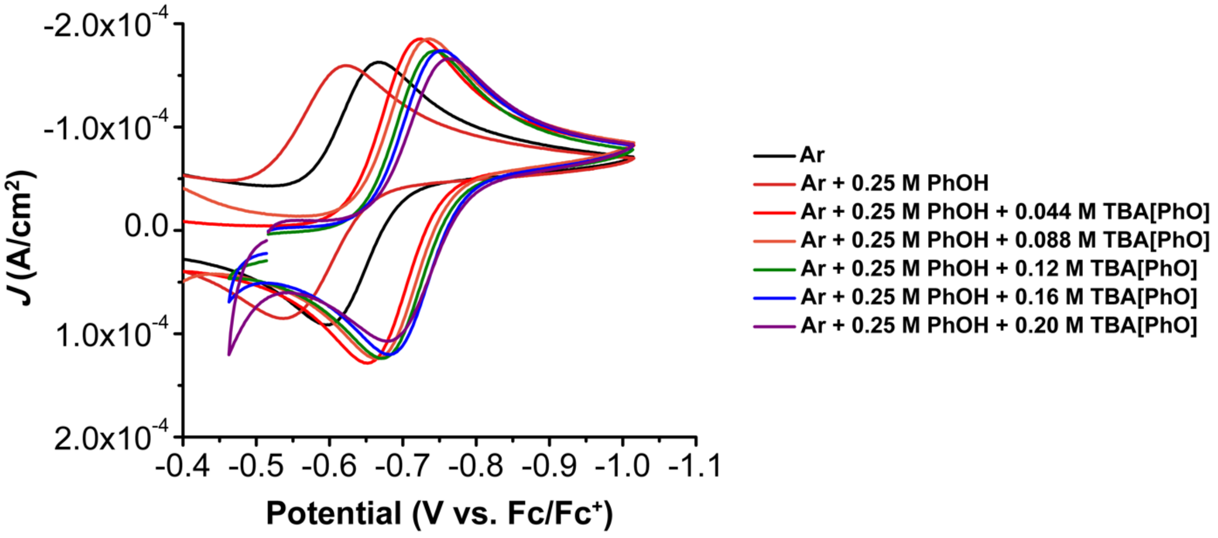

Figure S2.5.69. CVs of Mn(^{tbu}dhbpy)Cl **1** showing the effect of TBA[PhO] titration to a fixed concentration of PhOH. Conditions: 1 mM Mn(^{tbu}dhbpy)Cl **1** in MeCN/0.1 M TBAPF$_6$; glassy carbon working electrode, glassy carbon counter electrode, Ag/AgCl pseudoreference electrode; 100 mV/s scan rate; referenced to internal Fc standard.

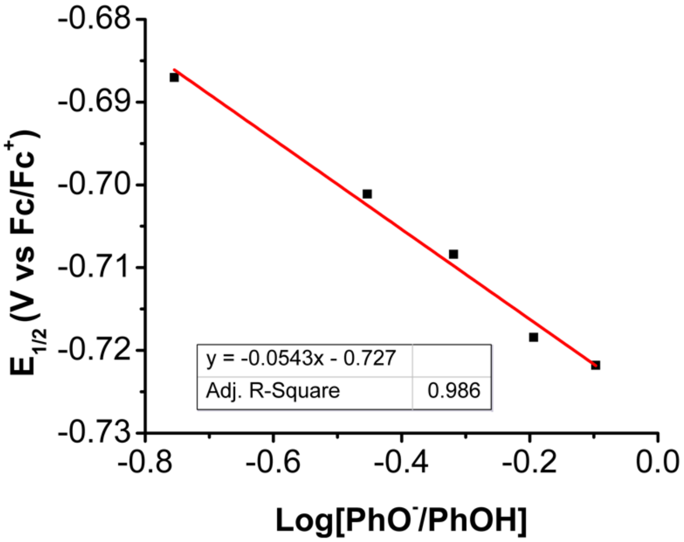

Figure S2.5.70. Plot of E$_{1/2}$ for Mn(^{tbu}dhbpy)Cl 1 against the log of the ratio of [PhO$^-$]/[PhOH] showing the the effects of fixed PhOH concentration with increasing PhO$^-$ concentration on E$_{1/2}$. Conditions: 1 mM Mn(^{tbu}dhbpy)Cl 1; glassy carbon working electrode, glassy carbon counter electrode, Ag/AgCl pseudoreference electrode; 100 mV/s scan rate; referenced to internal ferrocene standard.

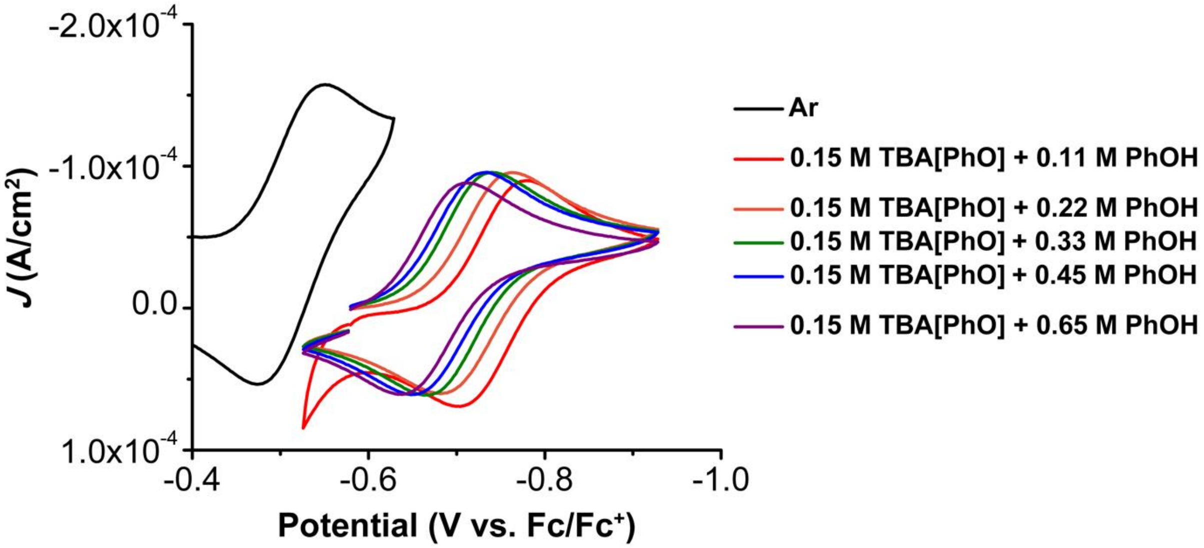

Figure S2.5.71. CVs of Mn(^{tbu}dhbpy)[OTf] showing the effect of PhOH titration to a fixed concentration of PhO$^-$. Conditions: 1 mM Mn(^{tbu}dhbpy)[OTf] in MeCN/0.1 M TBAPF$_6$; glassy carbon working electrode, glassy carbon counter electrode, Ag/AgCl pseudoreference electrode; 100 mV/s scan rate; referenced to internal Fc standard.

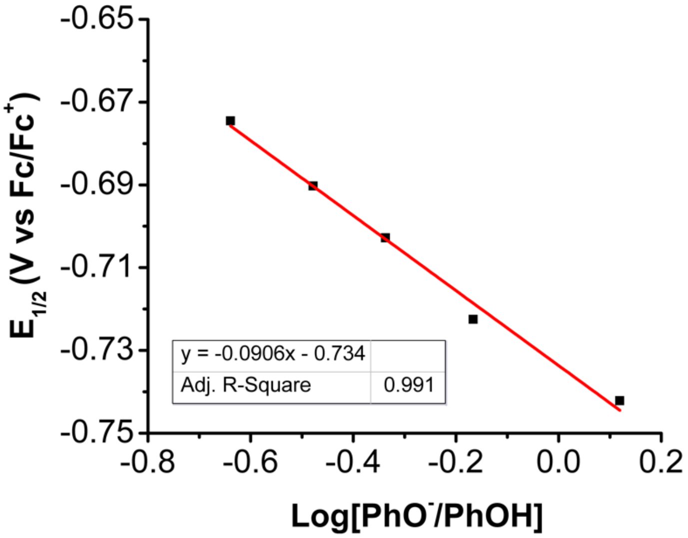

Figure S2.5.72. Plot of E$_{1/2}$ for Mn(^{tbu}dhbpy)[OTf] against the log of the ratio of [PhO$^-$]/[PhOH] showing the the effects of fixed PhO$^-$ concentration with increasing PhOH concentration on E$_{1/2}$. Conditions: 1 mM Mn(^{tbu}dhbpy)[OTf]; glassy carbon working electrode, glassy carbon counter electrode, Ag/AgCl pseudoreference electrode; 100 mV/s scan rate; referenced to internal ferrocene standard.

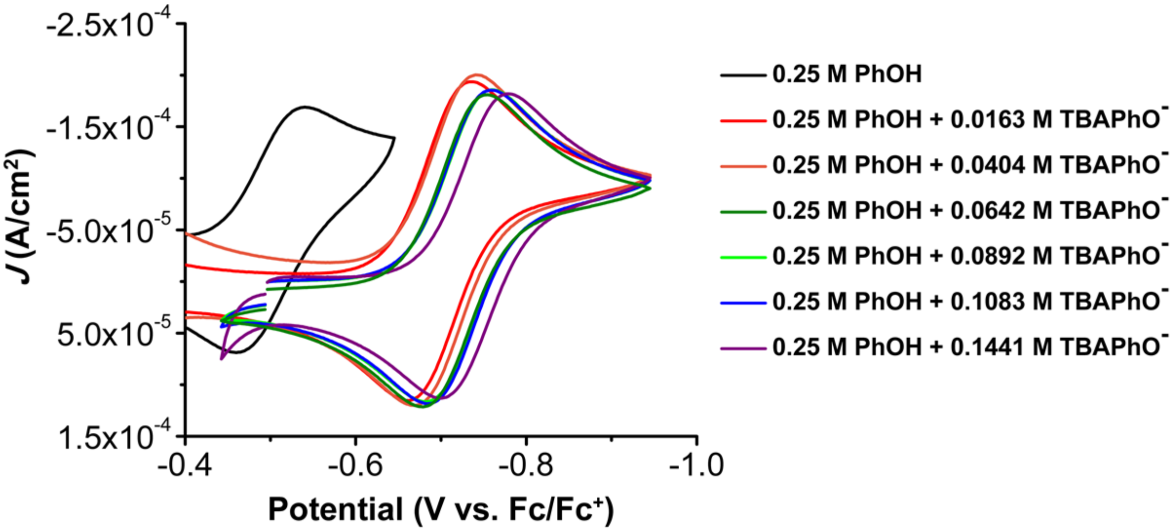

Figure S2.5.73. CVs of Mn(^{tbu}dhbpy)[OTf] showing the effect of TBA[PhO] titration to a fixed concentration of PhOH. Conditions: 1 mM Mn(^{tbu}dhbpy)[OTf] in MeCN/0.1 M TBAPF$_6$; glassy carbon working electrode, glassy carbon counter electrode, Ag/AgCl pseudoreference electrode; 100 mV/s scan rate; referenced to internal Fc standard.

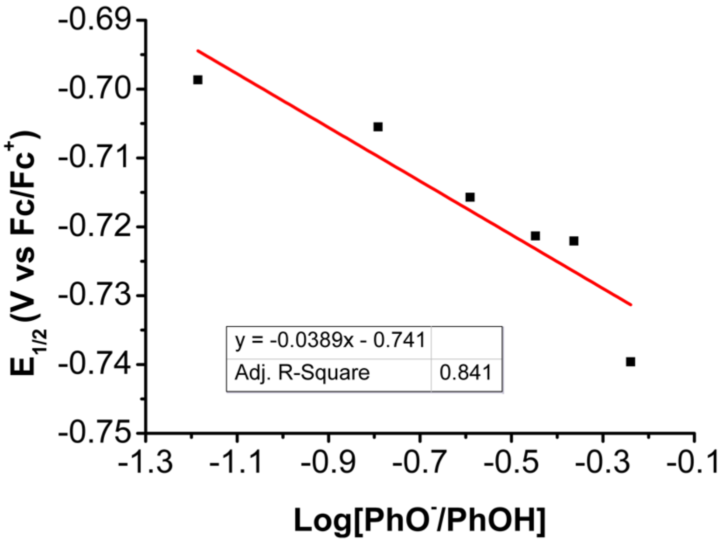

Figure S2.5.74. Plot of $E_{1/2}$ for Mn(^{tbu}dhbpy)[OTf] against the log of the ratio of [PhO^{-}]/[PhOH] showing the the effects of fixed PhOH concentration with increasing TBA[PhO] concentration on $E_{1/2}$. Conditions: 1 mM Mn(^{tbu}dhbpy)[OTf]; glassy carbon working electrode, glassy carbon counter electrode, Ag/AgCl pseudoreference electrode; 100 mV/s scan rate; referenced to internal ferrocene standard

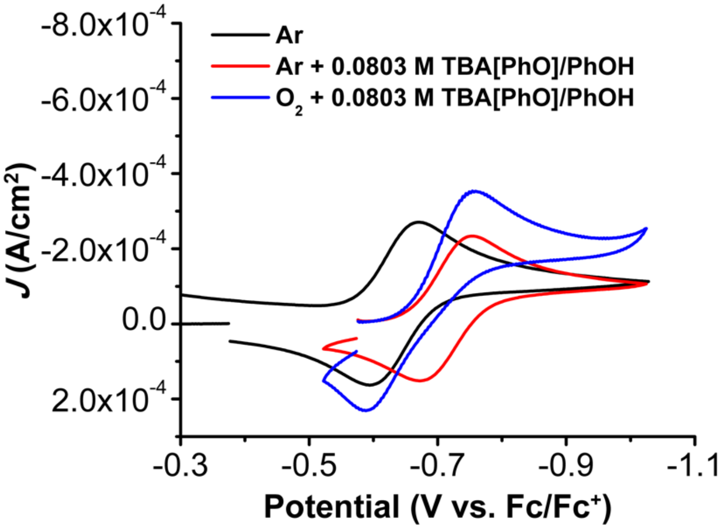

Figure S2.5.75. CVs of Mn(^{tbu}dhbpy)Cl **1** with buffered PhOH under Ar saturation (black), Ar saturation with 0.0803 M PhOH buffer (red), and O_2 saturation with 0.0803 M PhOH buffer (blue) demonstrating minimal activity for oxygen reduction. Conditions: 1 mM Mn(^{tbu}dhbpy)Cl **1**; glassy carbon working electrode, glassy carbon rod counter electrode, Ag/AgCl pseudoreference electrode; scan rate 0.1 V/s; referenced to internal ferrocene standard.

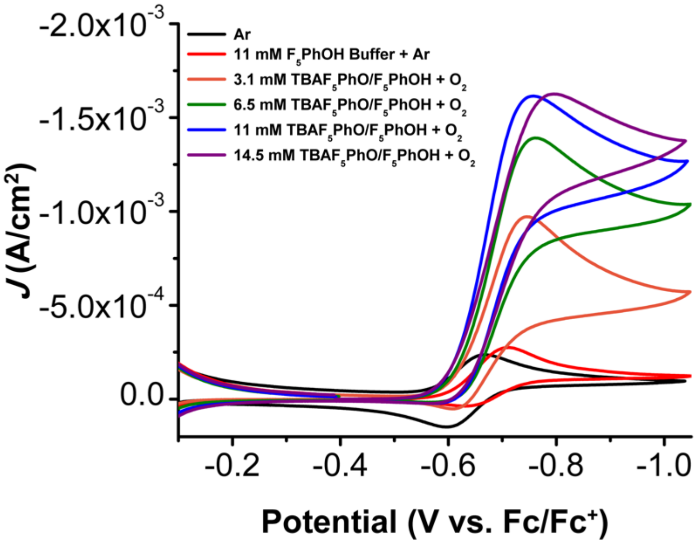

Figure S2.5.76. Selected CV traces with buffered F_5PhOH under Ar (red) and O_2 (orange to purple) saturation in comparison to the CV response of **1** Mn(^{tbu}dhbpy)Cl under Ar only (black). Conditions: 1 mM analyte; glassy carbon working electrode, glassy carbon rod counter electrode, Ag/AgCl pseudoreference electrode; scan rate 0.1 V/s; referenced to internal ferrocene standard.

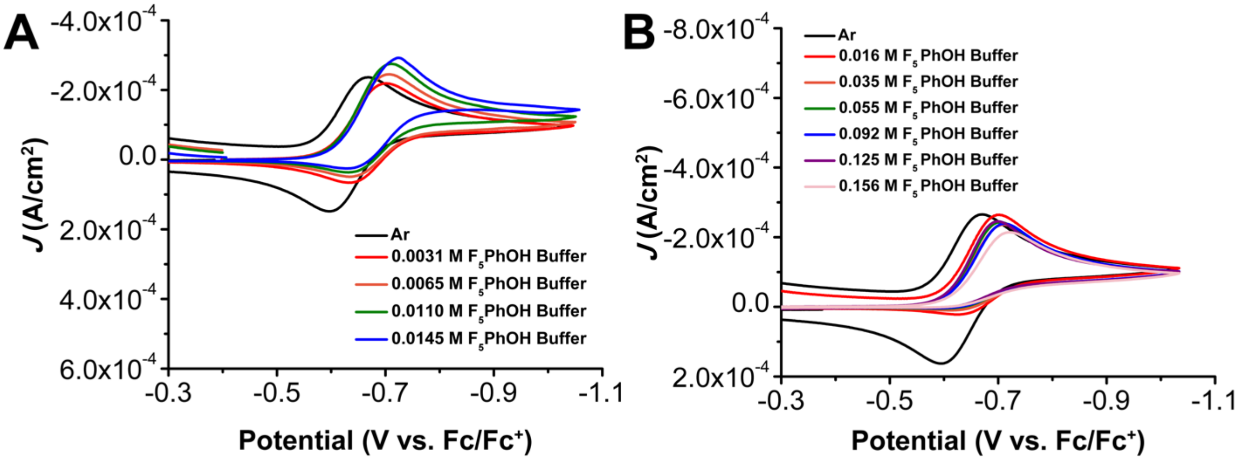

Figure S2.5.77. Additional CV traces with buffered F$_5$PhOH under Ar saturation compared to **1** Mn(^{tbu}dhbpy)Cl under Ar saturation only (black). Conditions: 1 mM analyte; glassy carbon working electrode, glassy carbon rod counter electrode, Ag/AgCl pseudoreference electrode; scan rate 0.1 V/s; referenced to internal ferrocene standard.

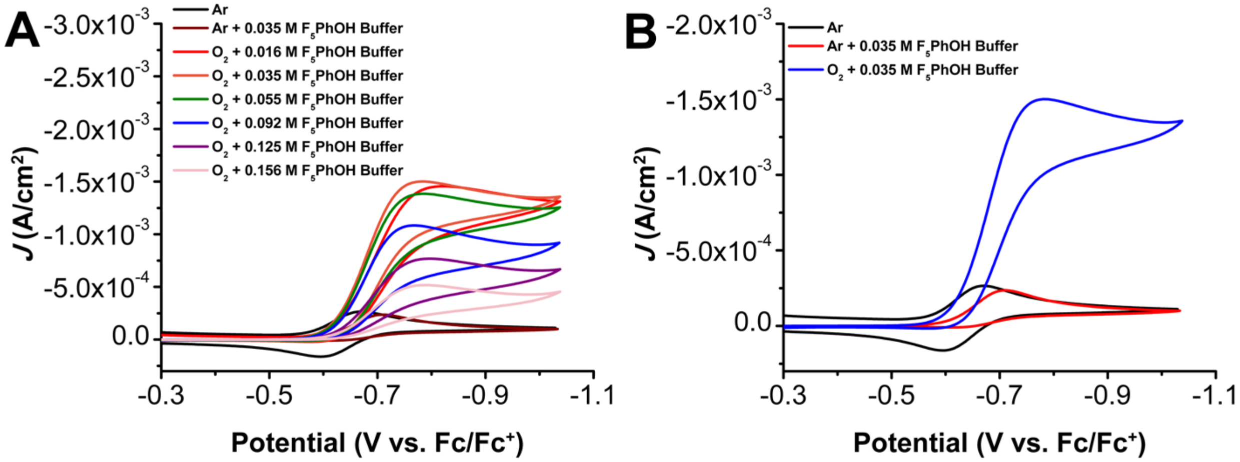

Figure S2.5.78. Additional CV traces with buffered F$_5$PhOH under O$_2$ saturation compared to **1** Mn(^{tbu}dhbpy)Cl under Ar saturation only (black). Conditions: 1 mM analyte; glassy carbon working electrode, glassy carbon rod counter electrode, Ag/AgCl pseudoreference electrode; scan rate 0.1 V/s; referenced to internal ferrocene standard.

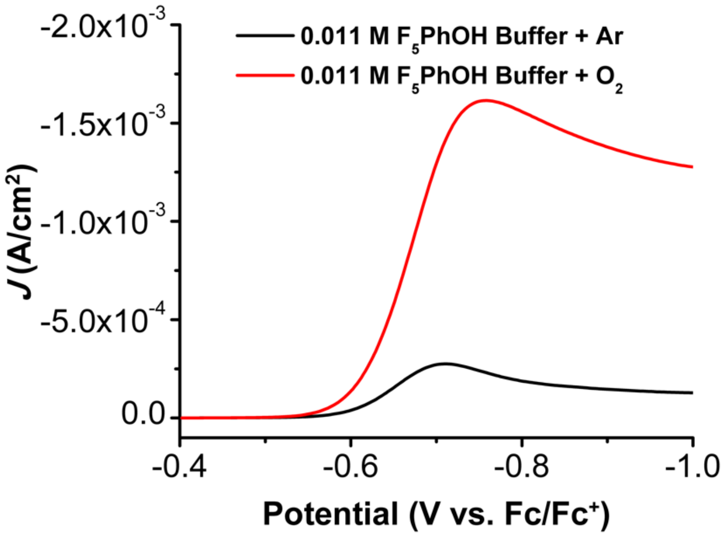

Figure S2.5.79. Relevant portions of the CV traces used for FOWA analysis with 11 mM buffered F_5PhOH under Ar (black) and O_2 (red) saturation with Mn(^{tbu}dhbpy)Cl **1** that have been adjusted to identical non-zero values in the pre-catalytic wave region. Conditions: 1 mM analyte; glassy carbon working electrode, glassy carbon rod counter electrode, Ag/AgCl pseudoreference electrode; scan rate 0.1 V/s; referenced to internal ferrocene standard.

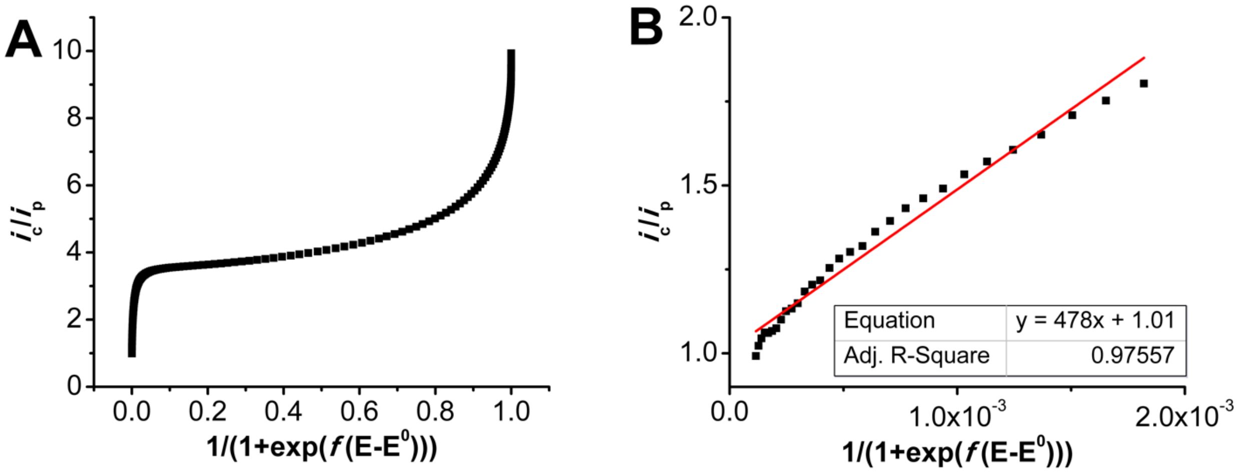

Figure S2.5.80. Full (A) and linear fit region (B) used in foot-of-the-wave analysis of **1**; i_c/i_p versus 1/(1+exp(f(E-E^0)) plots (where $f = \frac{F}{RT}$) to determine TOF$_{max}$ ($k_{obs}C_{substrate}$) according to the following relationship:

$$\frac{i_c}{i_p} = \frac{2.24 n_{cat}^{\sigma} \sqrt{\frac{RT}{F\nu} k_{obs} C_{substrate}}}{1 + \exp\left[\frac{F}{RT}(E - E^0)\right]}$$

where n_{cat}^{σ} = 2.38, σ = 1, $\frac{RT}{F\nu}$ = 0.256796 s; $E^0 = E_{1/2}$(11 mM $F_5PhOH/F_5PhO^-TBA^+$) = -0.672 V vs Fc/Fc$^+$.

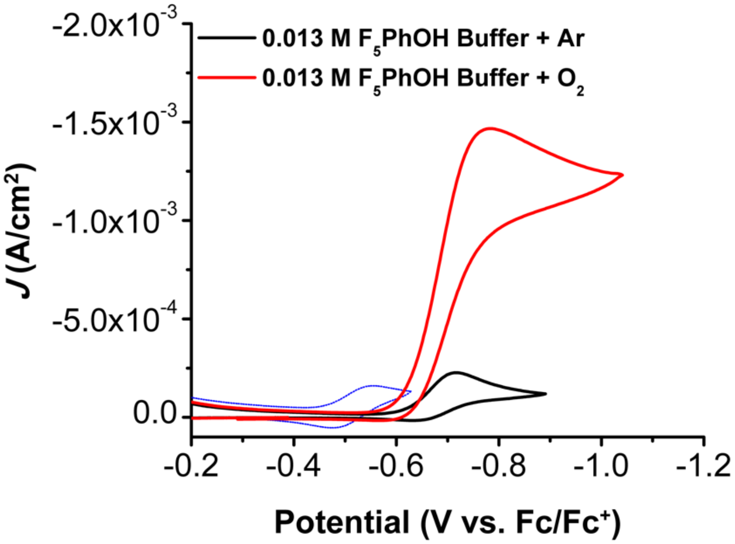

Figure S2.5.81. Selected CV traces with buffered F_5PhOH under Ar (red) and O_2 (orange to purple) saturation in comparison to the CV response of [Mn(^{tbu}dhbpy)][OTf] (blue dots) under Ar only. Conditions: 1 mM analyte; glassy carbon working electrode, glassy carbon rod counter electrode, Ag/AgCl pseudoreference electrode; scan rate 0.1 V/s. Referenced to internal ferrocene standard.

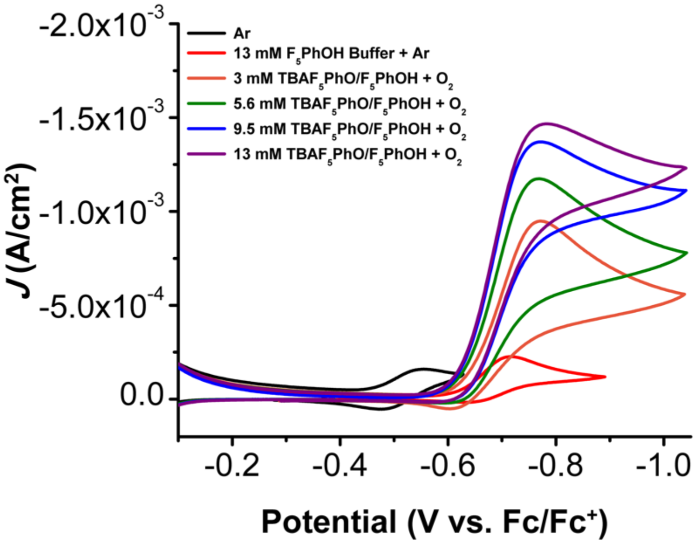

Figure S2.5.82. Selected CV traces with buffered F_5PhOH under Ar (red) and O_2 (orange to purple) saturation in comparison to the CV response of [Mn(^{tbu}dhbpy)][OTf] (black) under Ar only. Conditions: 1 mM analyte; glassy carbon working electrode, glassy carbon rod counter electrode, Ag/AgCl pseudoreference electrode; scan rate 0.1 V/s. Referenced to internal ferrocene standard.

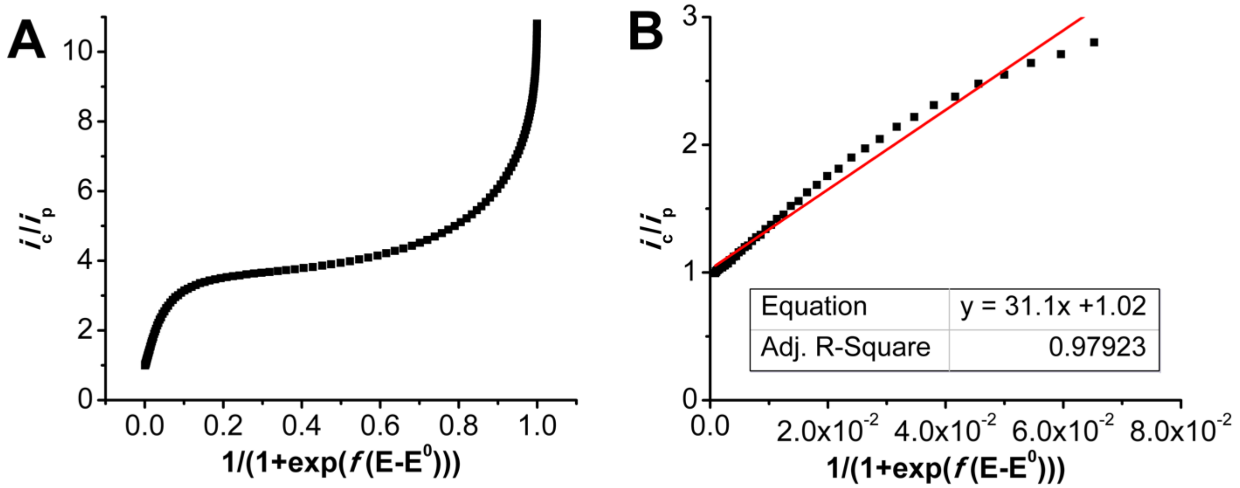

Figure S2.5.83. Full (A) and linear fit region (B) used in foot-of-the-wave analysis of [Mn(^{tbu}dhbpy)][OTf]; i_c/i_p versus 1/(1+exp(f(E-E^0)) plots (where $f = \frac{F}{RT}$) to determine TOF$_{max}$ ($k_{obs}C_{substrate}$) according to the following relationship: where n_{cat}^{σ} = 2.38, σ = 1, $\frac{RT}{F\nu}$ = 0.256796 s; E^0 = $E_{1/2}$(11 mM $F_5PhOH/F_5PhO^{-}TBA^{+}$) = -0.672 V vs Fc/Fc$^+$.

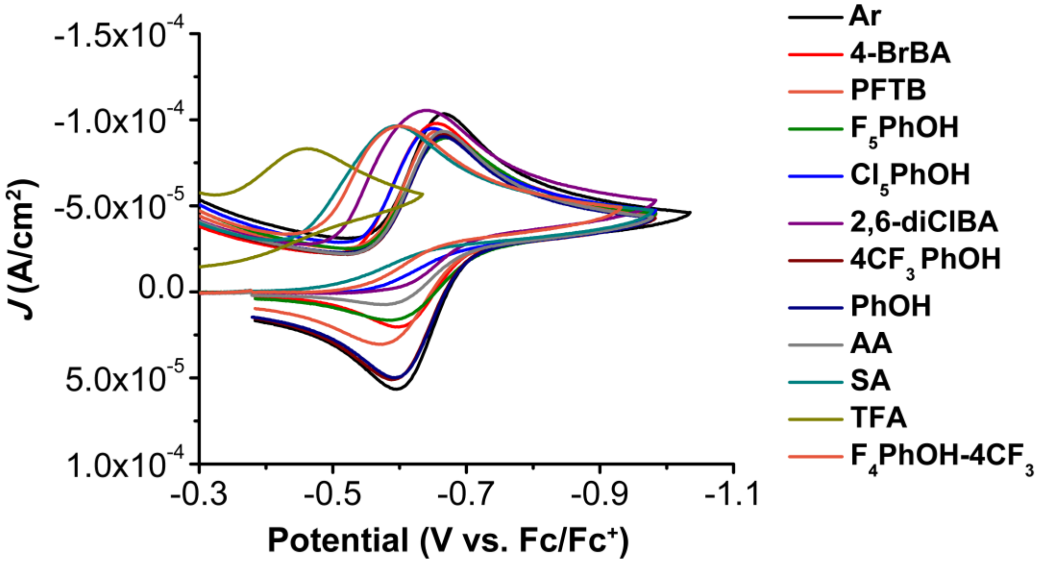

Figure S2.6.84. CVs of Mn(^{tbu}dhbpy)Cl **1** used to potential-pKa diagram. Reported values in MeCN were used, phenol(PhOH) = 29.14; 4-CF_3-PhOH = 25.54; acetic acid(AA) = 23.51; perflouoro-*tert*-butanol(PFTB) = 20.55; 4-Br-benzoic acid(4-BrBA) = 20.3; F_5PhOH = 20.11; Cl_5PhOH = 18.02; 2,6-diCl-benzoic acid(2,6-diClBA) = 17.6; salicylic acid(SA) = 16.7; F_4PhOH-4-CF_3 = 16.62; trifluoroacetic acid(TFA) = 12.65. Conditions: 0.5 mM Mn(^{tbu}dhbpy)Cl **1** and 0.5 mM added acid; glassy carbon working electrode, glassy carbon counter electrode, Ag/AgCl pseudoreference electrode; MeCN/0.1 M $TBAPF_6$; 100 mV/s scan rate; referenced to internal Fc standard. For all irreversible peaks, V at half-peak current height reported; all remained irreversible at 2 V/s.

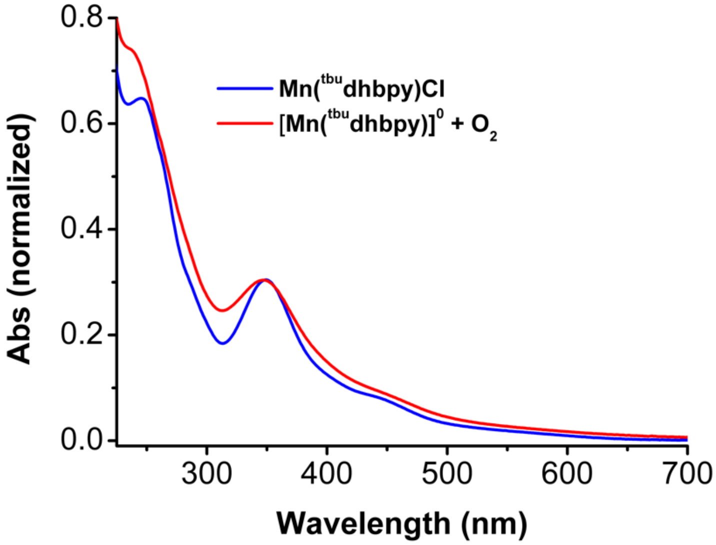

Figure S2.7.85. UV-vis spectra of the chemically reduced [Mn(^{tbu}dhbpy)]^0 after the introduction of atmospheric air overlaid with a normalized absorbance spectrum of the starting material 1 Mn(^{tbu}dhbpy)Cl. Conditions: 2.3 mM starting concentration of 1 in THF; Omnicell, 0.2 mm spacer.

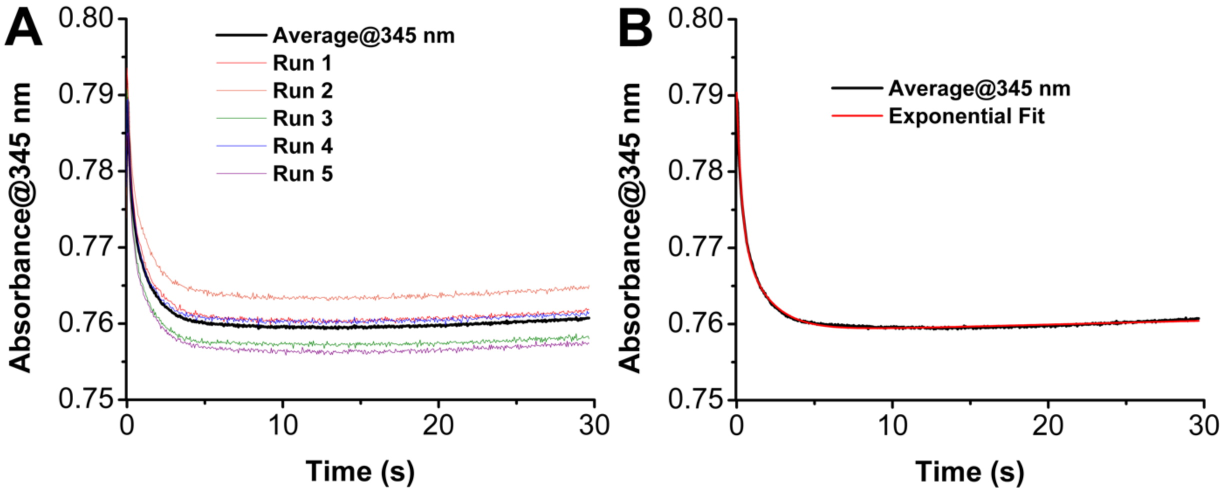

Figure S2.7.86. Summary of stopped-flow spectrochemical experiments with [Mn(^{tbu}dhbpy)]^0 at 20.4°C in MeCN. Data were fit using Kinetic Studio 4.0 (2 Exp + Mx + C); R^2 = 0.996. Syringe concentrations: [Mn(^{tbu}dhbpy)]^0 = 57 μM; [O_2] = 8.1 mM (Tsushima, M.; Tokuda, K.; Ohsaka, T. *Anal. Chem.* **1994**, *66*, 4551-4556).

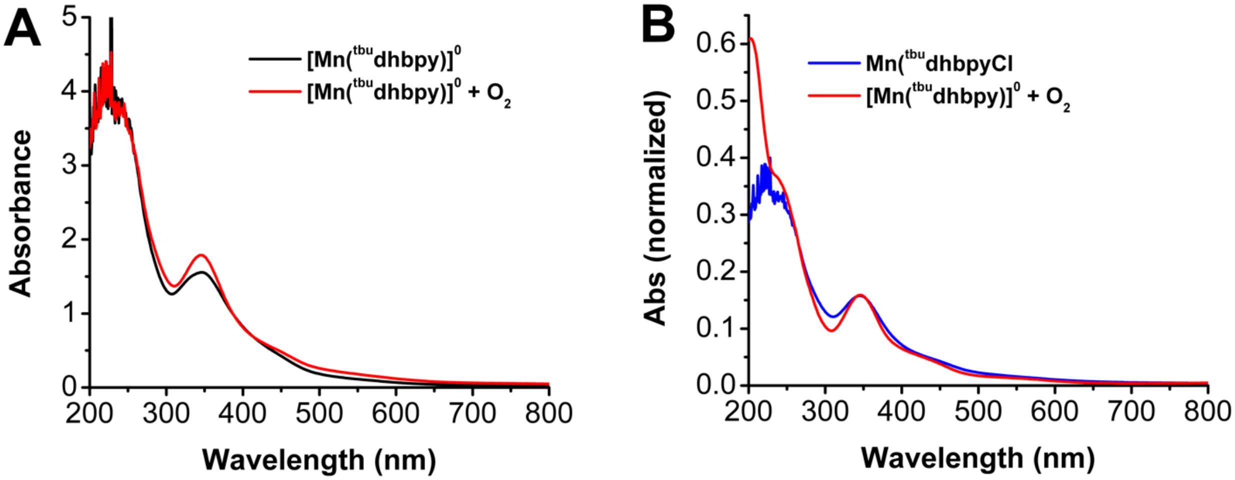

Figure S2.7.87. UV-vis spectra of the as chemically reduced [Mn(t^{bu}dhbpy)]^0 before and after the introduction of atmospheric air in MeCN (A) in comparison to the starting material (B). Conditions: MeCN, 1 cm pathlength.

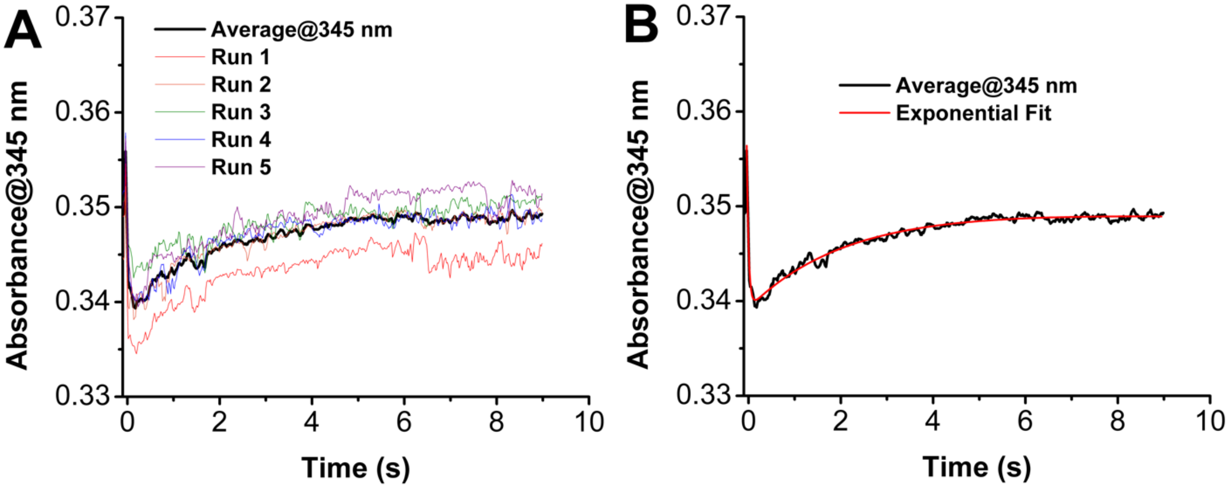

Figure S2.7.88. Summary of stopped-flow spectrochemical experiments with Mn(^{tbu}dhbpy)Cl and [K(18-crown-6)$^+$][O$_2^-$] at 20.8°C in MeCN. Data were fit using Kinetic Studio 4.0 (2 Exp + Mx + C); $R^2 = 0.912$. Syringe concentrations: Mn(^{tbu}dhbpy)Cl = 46 μM; [K(18-crown-6)$^+$][O$_2^-$] = 5 mM.

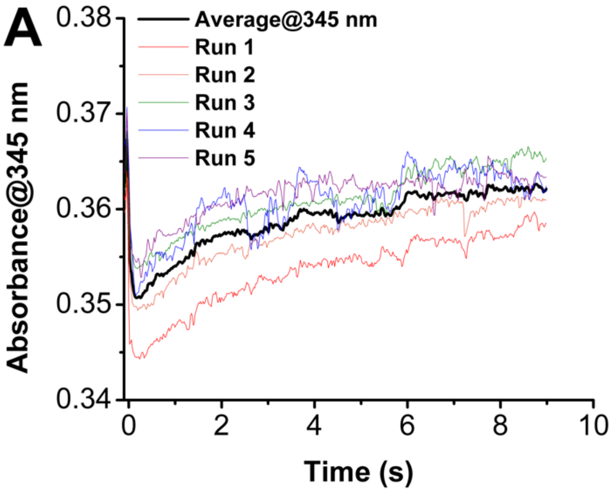

Figure S2.7.89. Summary of stopped-flow spectrochemical experiments with Mn(^{tbu}dhbpy)Cl and [K(18-crown-6)$^+$][O_2^-] at 16.2°C in MeCN. Data were fit using Kinetic Studio 4.0 (2 Exp + Mx + C); R^2 = 0.976. Syringe concentrations: Mn(^{tbu}dhbpy)Cl = 46 μM; [K(18-crown-6)$^+$][O_2^-] = 5 mM.

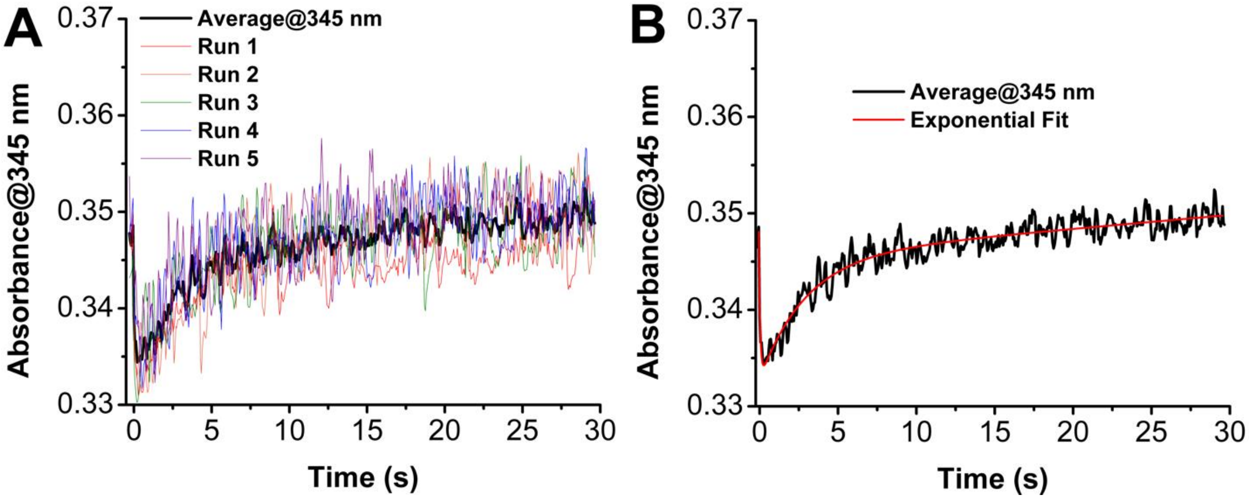

Figure S2.7.90. Summary of stopped-flow spectrochemical experiments with Mn(^{tbu}dhbpy)Cl and [K(18-crown-6)$^+$][O_2^-] at 11.2°C in MeCN. Data were fit using Kinetic Studio 4.0 (2 Exp + Mx + C) ; R^2 = 0.977. Syringe concentrations: Mn(^{tbu}dhbpy)Cl = 46 μM; [K(18-crown-6)$^+$][O_2^-] = 5 mM.

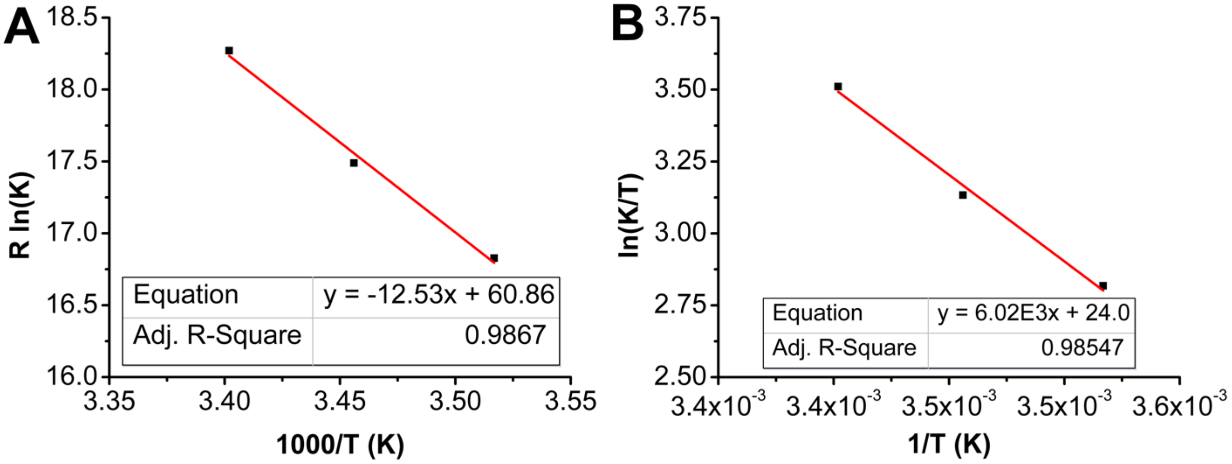

Figure S2.7.91. Van't Hoff (A) and Eyring (B) plots of the stopped-flow data spectrochemical experiments with Mn(^{tbu}dhbpy)Cl and [K(18-crown-6)$^+$][O_2^-].

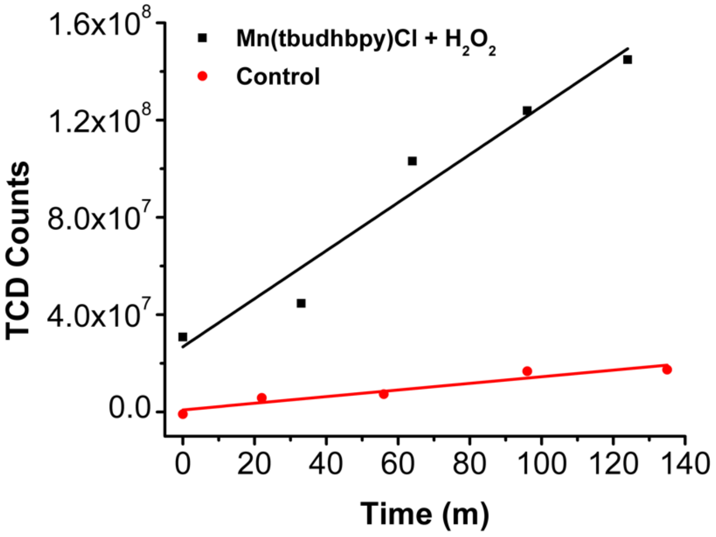

Figure S2.7.92. Peroxidase activity test with Mn(^{tbu}dhbpy)Cl (1.2 mM) and aqueous H_2O_2 (14.8 mM over two additions) in MeCN solution over ~120 minutes (black) and control reaction without added Mn(^{tbu}dhbpy)Cl (red). TCD is the thermal conductivity detector on the GC; the retention time of O_2 was verified by calibration samples.

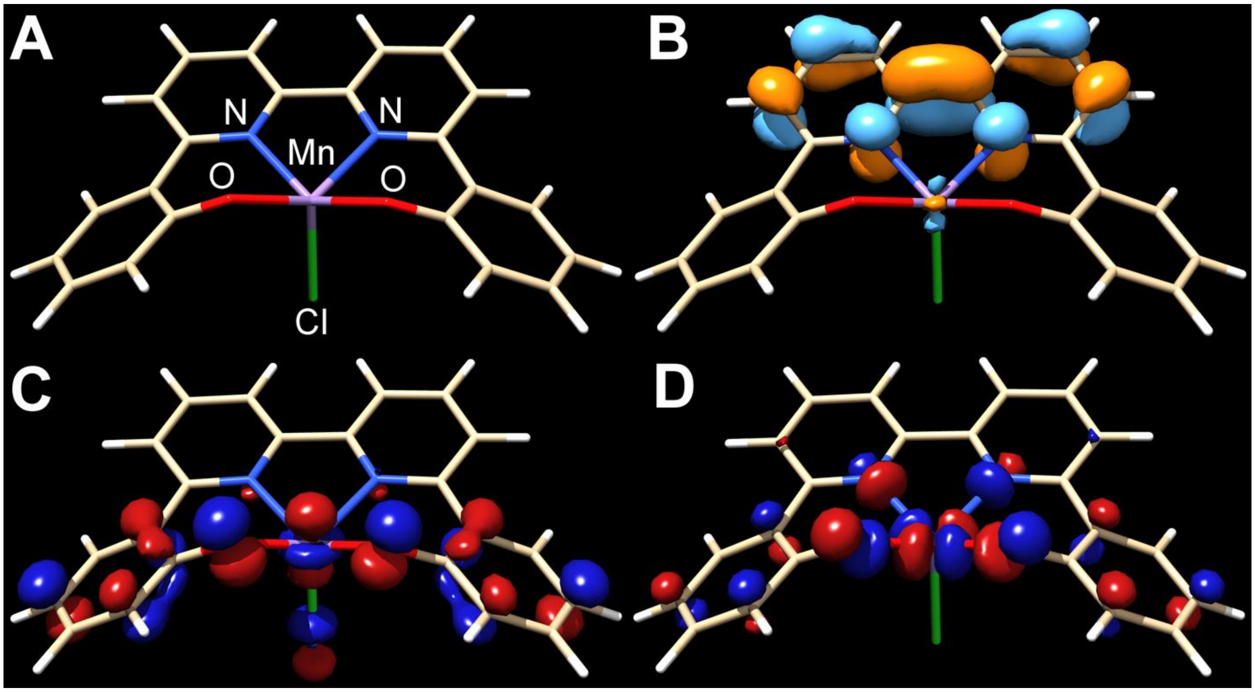

Figure S2.8.93. Kohn-Sham Orbital projections of the LUMO (B), HOMO-1 (C), and HOMO (D) of computational model [Mn(dhbpy)Cl]⁻ (A). B3LYP/G, CPCM(Acetonitrile), def2-TZVP, D3BJ, 2S+1 = 6; ORCA 4.0.1. Images created using Chimera and POVRAY.

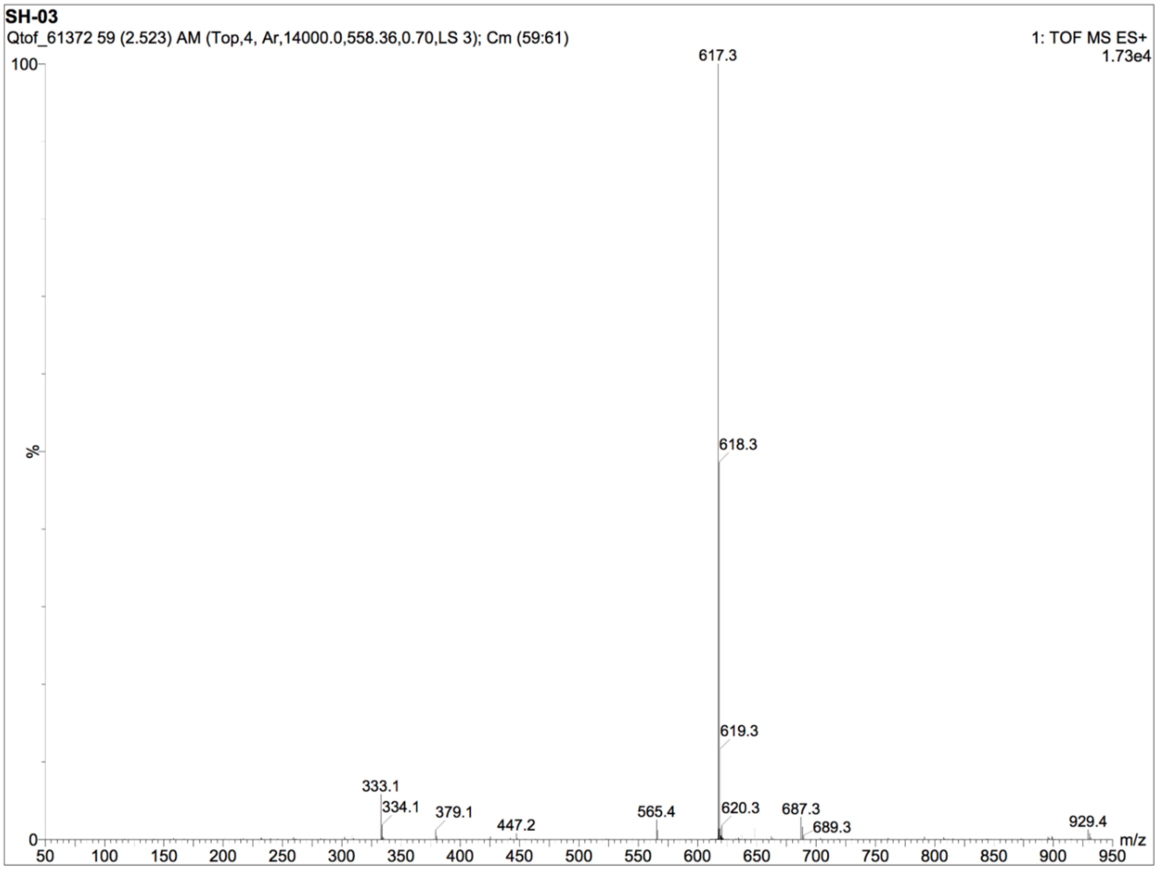

Elemental Composition Report **Page 1**

Single Mass Analysis
Tolerance = 10.0 PPM / DBE: min = -1.5, max = 100.0
Element prediction: Off
Number of isotope peaks used for i-FIT = 3

Monoisotopic Mass, Odd and Even Electron Ions
362 formula(e) evaluated with 7 results within limits (up to 50 closest results for each mass)
Elements Used:
C: 0-150 H: 0-220 N: 1-5 O: 1-5 Mn: 0-1

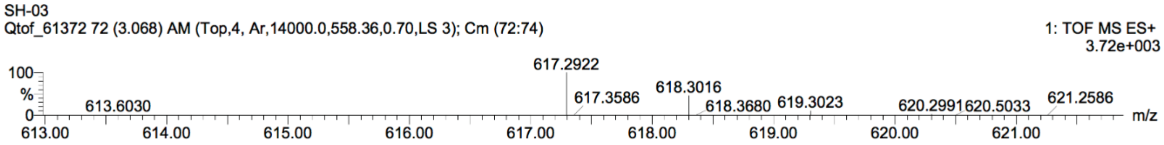

```
Minimum:                                    -1.5
Maximum:                   5.0      10.0    100.0

Mass        Calc. Mass     mDa      PPM     DBE      i-FIT      Formula

617.2922    617.2926       -0.4     -0.6    17.5     4.2        C36  H44  N5  O  Mn
            617.2917       0.5      0.8     25.5     4.9        C41  H37  N4  O2
            617.2930       -0.8     -1.3    25.0     10.0       C43  H39  N  O3
            617.2913       0.9      1.5     12.5     10.6       C35  H48  N  O5  Mn
            617.2940       -1.8     -2.9    17.0     1.3        C38  H46  N2  O2  Mn
            617.2900       2.2      3.6     13.0     18.2       C33  H46  N4  O4  Mn
            617.2890       3.2      5.2     21.0     2.8        C38  H39  N3  O5
```

Figure S2.10.94. ESI-MS characterization of Mn(^{tbu}dhbpy)[OTf].

Summary of Buffered Acid Characterization Data

$(NBu_4)^+F_5PhO^-/F_5PhOH$ Buffer.

A vial was charged with a stir bar and F_5PhOH (1.40 g, 7.63 mmol). Tetra-n-butyl ammonium hydroxide (40% w/v, 5.0 mL, 7.63 mmol) was added slowly with stirring, resulting in a clear solution. After 30 minutes, a second equivalent of F_5PhOH (1.40 g, 7.63 mmol) was added and stirred for an additional 30 minutes. A biphasic separation formed over this time and was subsequently chilled with vigorous stirring and sonicated to induce precipitation. The resulting white solid precipitate was isolated by filtration, washed with chilled de-ionized H_2O (3x5mL) and dried under vacuum for several days before use. Isolated yield, 4.32 g, 93% yield. ^1H NMR (d_2-CD_2Cl_2, 600 MHz): δ 10.59 (br s, 1H, ArO*H*), 3.15 (m, 8H, R_3NCH_2–), 1.60 (m, 8H, –CH_2–), 1.38 (m, 8H, –CH_2–), 1.28 (m, 12H, –CH_3). $^{19}F\{^1H\}$ NMR (d_2-CD_2Cl_2, 600 MHz): δ 52.29 (m), 48.72 (br s), 36.25 (br s). Elemental Analysis for $C_{28}H_{37}F_{10}NO_2$ Calc'd: C 55.17, H 6.12, N 2.30; Found: C 54.81, H 6.22, N 2.30.

All other buffered acids or tetrabutylammonium salts were prepared by combining 2:1 ratios of acid to tetrabutylammonium hydroxide solutions (40%) in water or methanol, followed by filtration and extensive drying under vacuum to yield hygroscopic solids of the formulation $(NBu_4)^+(A^-)[HA]$. TBA = $(NBu_4)^+$

Acetic Acid Buffer. ^1H NMR (d_2-CD_2Cl_2, 600 MHz): δ 3.84 (s, 3H, O*H*), 3.26 (m, 8H, TBA), 1.80 (s, 3H, -CH_3), 1.65 (m, 8H, TBA), 1.42 (m, 8H, TBA), 1.02 (m, 12H, TBA). Not a solid at room temperature, stored at -20 °C.

Benzoic Acid Buffer. ^{1}H NMR (d$_2$-CD$_2$Cl$_2$, 600 MHz): δ 8.06 (d, 4H, Ar*H*), 7.37 (m, 6H, Ar*H*), 6.70 (br, 1H, O*H*), 3.15 (m, 9H, TBA), 1.57 (m, 8H, TBA), 1.37 (m, 8H, TBA), 0.95 (m, 12H, TBA). Elemental Analysis for $C_{30}H_{47}NO_4$ Calc'd: C 74.19 H 9.75 N 2.88; Found: C 75.17 H 9.84 N 3.01.

$(NBu_4)^+$ Perflurotertbutoxide ^{1}H NMR (d$_2$-CD$_2$Cl$_2$, 600 MHz): δ 3.17 (m, 8H, TBA), 1.62 (m, 8H, TBA), 1.43 (m, 8H, TBA), 1.02 (m, 12H, TBA). Not a solid at room temperature, stored at -20 °C.

Phenol Buffer ^{1}H NMR (d$_2$-CD$_2$Cl$_2$, 600 MHz): δ 7.06 (m, 4H, Ar*H*), 6.81 (m, 4H, Ar*H*), 6.56 (m, 2H, Ar*H*), 5.32 (br, 1H, O*H*), 2.99 (m, 8H, TBA), 1.42 (m, 8H, TBA), 1.32 (m, 8H, TBA), 0.95 (m, 12H, TBA). Elemental Analysis for $C_{28}H_{47}NO_2$ Calc'd: C 78.27 H 11.03 N 3.26; Found: C 77.98 H 10.05 N 3.32.

$(NBu_4)^+$ Phenoxide ^{1}H NMR (d$_2$-CD$_2$Cl$_2$, 600 MHz): δ 7.02 (m, 2, Ar*H*), δ 6.71 (m, 2, Ar*H*), δ 6.45 (m, 1, Ar*H*), 3.12 (m, 8H, TBA), 1.56 (m, 8H, TBA), 1.39 (m, 8H, TBA), 0.99 (m, 12H, TBA). Elemental Analysis for $C_{22}H_{41}NO \cdot H_2O$ Calc'd: C 74.73 H 12.26 N 3.96; Found: C 72.02 H 11.61 N 3.63.

4-bromobenzoic acid buffer. ^{1}H NMR (d$_2$-CD$_2$Cl$_2$, 600 MHz): δ 7.22 (m, 4H, ArH), 7.11 (m, 4H, ArH), 3.23 (m, 8H, TBA), 1.63 (m, 8H, TBA), 1.41(m, 8H, TBA), 0.98 (m, 12H, TBA). Elemental Analysis for $C_{30}H_{45}Br_2NO_4$ Cacl'd: C 56.00 H 7.05 N 2.18; Found: C 53.82 H 6.59, N 1.92.

2,6-dichlorobenzoic acid buffer ^{1}H NMR (d$_2$-CD$_2$Cl$_2$, 600 MHz): δ 13.28 (br, 1H, O*H*), 7.92 (m, 4H, Ar*H*), 7.52 (m, 2H, Ar*H*), 3.17 (m, 8H, TBA), 1.62 (m, 8H, TBA), 1.43 (m, 8H, TBA), 1.02 (m, 12H, TBA). Elemental Analysis for $C_{30}H_{43}Cl_4NO_4$ Cacl'd: C 57.79, H 6.95, N 2.25; Found: C 57.87, H 7.16, N 2.30.

Pentachlorophenol buffer. ^{1}H NMR (d_2-CD_2Cl_2, 600 MHz): δ 4.86 (s, 1H, O*H*), 3.14 (m, 8H, TBA), 1.57 (m, 8H, TBA), 1.38 (m, 8H, TBA), 0.98 (m, 12H, TBA). Elemental Analysis for $C_{28}H_{37}Cl_{10}NO_2$ Cacl'd: C43.44 H 4.82 N 1.81; Found: C 49.74 H 6.07 N 2.44.

Table S2.3.1. Magnetic moment (μ_{eff}) determined by the Evan's method for Mn(^{tbu}dhbpy)Cl **1** and [Mn(^{tbu}dhbpy)]^0 in THF and MeCN. Samples were run in triplicate.

Solvent	**Avg. μ_{eff} Mn(^{tbu}dhbpy)Cl 1**	**Avg. μ_{eff} [Mn(^{tbu}dhbpy)]^0**
Tetrahydrofuran (THF)	5.1 (±0.1)	6.2 (±0.36)
Acetonitrile (MeCN)	4.82 (±0.03)	5.98 (±0.09)

Table S2.4.2. $E_{1/2}$ and ΔE_p as a function of PhOH concentration.

Added PhOH (M)	**$E_{1/2}$ (V)**	**ΔE_p (V)**
0.000	-0.63	-0.081
0.0559	-0.62	-0.096
0.100	-0.61	-0.086
0.200	-0.59	-0.089
0.216	-0.58	-0.082
0.266	-0.57	-0.086
0.369	-0.56	-0.091
0.424	-0.551	-0.090
0.480	-0.54	-0.085
0.533	-0.54	-0.089
1.00	-0.52	-0.083
2.00	-0.48	-0.073

Table S2.10.3. $E_{1/2}$ and ΔE_p as a function of TFE concentration.

Added TFE (M)	**$E_{1/2}$ (V)**	**ΔE_p (V)**
0.00	-0.63	-0.072
0.05	-0.63	-0.075
0.010	-0.62	-0.081
0.20	-0.61	-0.074
0.50	-0.58	-0.078
0.75	-0.56	-0.079
1.00	-0.560	-0.074
1.25	-0.54	-0.078
1.50	-0.54	-0.080
1.75	-0.53	-0.077
2.00	-0.52	-0.080
2.50	-0.51	-0.077
4.00	-0.49	-0.078

Table S2.7.4. Summary of Stopped-Flow Experiments.

Syringe 1	**Syringe 2**	**Temperature (°C)**	$k_{obs}[C_{sub}]$	k_{obs}
$[Mn(^{tbu}dhbpy)]^0$ 57 μM	O_2 8.1 mM	20.4	3.17 s^{-1}	783 s^{-1}
$Mn(^{tbu}dhbpy)Cl$ 46 μM	$[K(18\text{-crown-}6)^+][O_2]$ 5 mM	20.8	24.6 s^{-1}	9.84×10^3 s^{-1}
$Mn(^{tbu}dhbpy)Cl$ 46 μM	$[K(18\text{-crown-}6)^+][O_2]$ 5 mM	16.2	16.6 s^{-1}	6.64×10^3 s^{-1}
$Mn(^{tbu}dhbpy)Cl$ 46 μM	$[K(18\text{-crown-}6)^+][O_2]$ 5 mM	11.2	11.9 s^{-1}	4.76×10^3 s^{-1}

Table S2.10.5. Crystal data and structure refinement for **Mn(^{tbu}dhbpy)Cl 1**.

Identification code	CWM-001	
Empirical formula	C42 H54 Cl Mn N2 O3	
Formula weight	725.26	
Temperature	100.0 K	
Wavelength	0.71073 Å	
Crystal system	Triclinic	
Space group	P-1	
Unit cell dimensions	a = 9.4021(17) Å	α = 73.599(8)°.
	b = 12.198(3) Å	β = 80.485(11)°.
	c = 16.984(4) Å	γ = 88.031(8)°.
Volume	1842.8(7) Å^3	
Z	2	
Density (calculated)	1.307 Mg/m^3	
Absorption coefficient	0.472 mm^{-1}	
F(000)	772	
Crystal size	0.14 x 0.06 x 0.04 mm^3	
Theta range for data collection	1.740 to 25.978°.	
Index ranges	-11<=h<=8, -14<=k<=14, -20<=l<=19	
Reflections collected	26716	
Independent reflections	7142 [R(int) = 0.0469]	
Completeness to theta = 25.978°	98.8 %	
Absorption correction	Semi-empirical from equivalents	
Max. and min. transmission	0.2593 and 0.2319	
Refinement method	Full-matrix least-squares on F^2	
Data / restraints / parameters	7142 / 0 / 463	
Goodness-of-fit on F^2	1.025	

Final R indices [I>2sigma(I)]	R1 = 0.0427, wR2 = 0.0856
R indices (all data)	R1 = 0.0673, wR2 = 0.0955
Extinction coefficient	n/a
Largest diff. peak and hole	0.477 and -0.404 e.Å^{-3}

Table S2.10.6. Atomic coordinates (x 10^{4}) and equivalent isotropic displacement parameters (Å^{2}x 10^{3}) for **Mn(^{tbu}dhbpy)Cl 1**. U(eq) is defined as one third of the trace of the orthogonalized U^{ij} tensor.

	x	y	z	U(eq)
Mn(1)	7627(1)	5133(1)	6605(1)	12(1)
Cl(1)	5944(1)	6521(1)	6787(1)	24(1)
O(2)	9299(2)	5428(1)	6974(1)	15(1)
O(1)	7145(2)	3943(1)	7548(1)	14(1)
O(3)	12112(2)	9708(2)	3237(1)	40(1)
N(2)	6550(2)	4313(2)	6004(1)	12(1)
C(29)	5397(2)	2993(2)	8676(1)	14(1)
C(30)	5888(2)	3384(2)	7814(1)	13(1)
C(16)	10104(2)	6376(2)	6692(1)	14(1)
C(28)	4165(2)	2327(2)	8942(2)	16(1)
C(25)	5078(2)	3129(2)	7265(1)	14(1)
C(1)	9632(2)	6701(2)	5239(1)	14(1)
C(31)	6167(2)	3340(2)	9291(1)	16(1)
C(10)	5571(2)	3454(2)	6368(1)	14(1)
C(4)	8635(2)	5959(2)	4036(1)	16(1)
C(3)	9746(3)	6755(2)	3812(2)	18(1)
N(1)	8561(2)	5907(2)	5448(1)	12(1)
C(24)	9548(3)	5804(2)	8634(2)	27(1)
C(42)	12207(4)	10931(2)	2933(2)	43(1)
C(21)	11027(3)	5897(2)	8095(2)	17(1)
C(6)	6979(2)	4620(2)	5170(1)	13(1)
C(32)	5438(3)	2811(2)	10186(1)	22(1)
C(15)	10942(2)	6674(2)	7227(1)	15(1)
C(27)	3337(2)	2056(2)	8416(2)	17(1)
C(8)	5481(2)	3189(2)	5034(2)	18(1)
C(35)	2002(3)	1279(2)	8776(2)	22(1)
C(9)	5066(3)	2867(2)	5873(2)	17(1)
C(11)	10199(2)	7070(2)	5871(1)	13(1)
C(7)	6441(2)	4087(2)	4669(2)	16(1)
C(14)	11681(2)	7700(2)	6934(2)	17(1)
C(23)	11547(3)	4717(2)	8047(2)	26(1)
C(20)	13995(3)	9461(2)	6062(2)	24(1)
C(13)	11679(2)	8456(2)	6149(2)	15(1)
C(19)	11662(3)	10283(2)	6509(2)	30(1)
C(2)	10241(2)	7122(2)	4404(1)	16(1)
C(33)	7729(2)	2943(2)	9234(2)	19(1)
C(26)	3799(2)	2482(2)	7583(2)	17(1)
C(18)	12370(3)	10311(2)	5044(2)	22(1)
C(12)	10972(2)	8114(2)	5624(1)	14(1)

C(34)	6078(3)	4639(2)	9114(2)	20(1)
C(17)	12425(3)	9624(2)	5932(2)	18(1)
C(5)	8080(2)	5533(2)	4859(1)	14(1)
C(36)	856(3)	1548(2)	8222(2)	22(1)
C(38)	1309(3)	1404(3)	9621(2)	36(1)
C(22)	12092(3)	6348(2)	8520(2)	25(1)
C(37)	2494(3)	46(2)	8867(2)	39(1)
C(39)	12783(5)	9271(3)	2620(2)	59(1)
C(40)	13074(5)	10163(3)	1834(2)	68(1)
C(41)	13185(8)	11257(6)	2110(4)	42(2)
C(41A)	12253(9)	11128(6)	1990(4)	50(2)

Table S2.10.7. Bond lengths [Å] and angles [°] for **Mn(^{tbu}dhbpy)Cl 1**.

Mn(1)-Cl(1)	2.3274(8)	C(27)-C(35)	1.532(3)
Mn(1)-O(2)	1.8662(16)	C(27)-C(26)	1.363(3)
Mn(1)-O(1)	1.8356(15)	C(8)-H(8)	0.9500
Mn(1)-N(2)	2.0145(19)	C(8)-C(9)	1.360(3)
Mn(1)-N(1)	1.9905(19)	C(8)-C(7)	1.377(3)
O(2)-C(16)	1.329(3)	C(35)-C(36)	1.513(3)
O(1)-C(30)	1.330(3)	C(35)-C(38)	1.522(4)
O(3)-C(42)	1.434(3)	C(35)-C(37)	1.531(4)
O(3)-C(39)	1.361(4)	C(9)-H(9)	0.9500
N(2)-C(10)	1.356(3)	C(11)-C(12)	1.409(3)
N(2)-C(6)	1.353(3)	C(7)-H(7)	0.9500
C(29)-C(30)	1.408(3)	C(14)-H(14)	0.9500
C(29)-C(28)	1.375(3)	C(14)-C(13)	1.391(3)
C(29)-C(31)	1.520(3)	C(23)-H(23A)	0.9800
C(30)-C(25)	1.401(3)	C(23)-H(23B)	0.9800
C(16)-C(15)	1.421(3)	C(23)-H(23C)	0.9800
C(16)-C(11)	1.403(3)	C(20)-H(20A)	0.9800
C(28)-H(28)	0.9500	C(20)-H(20B)	0.9800
C(28)-C(27)	1.388(3)	C(20)-H(20C)	0.9800
C(25)-C(10)	1.459(3)	C(20)-C(17)	1.527(3)
C(25)-C(26)	1.403(3)	C(13)-C(12)	1.355(3)
C(1)-N(1)	1.355(3)	C(13)-C(17)	1.532(3)
C(1)-C(11)	1.455(3)	C(19)-H(19A)	0.9800
C(1)-C(2)	1.394(3)	C(19)-H(19B)	0.9800
C(31)-C(32)	1.526(3)	C(19)-H(19C)	0.9800
C(31)-C(33)	1.527(3)	C(19)-C(17)	1.515(3)
C(31)-C(34)	1.529(3)	C(2)-H(2)	0.9500
C(10)-C(9)	1.393(3)	C(33)-H(33A)	0.9800
C(4)-H(4)	0.9500	C(33)-H(33B)	0.9800
C(4)-C(3)	1.382(3)	C(33)-H(33C)	0.9800
C(4)-C(5)	1.365(3)	C(26)-H(26)	0.9500
C(3)-H(3)	0.9500	C(18)-H(18A)	0.9800
C(3)-C(2)	1.361(3)	C(18)-H(18B)	0.9800
N(1)-C(5)	1.355(3)	C(18)-H(18C)	0.9800
C(24)-H(24A)	0.9800	C(18)-C(17)	1.512(3)
C(24)-H(24B)	0.9800	C(12)-H(12)	0.9500
C(24)-H(24C)	0.9800	C(34)-H(34A)	0.9800
C(24)-C(21)	1.521(3)	C(34)-H(34B)	0.9800
C(42)-H(42A)	0.9900	C(34)-H(34C)	0.9800
C(42)-H(42B)	0.9900	C(36)-H(36A)	0.9800
C(42)-H(42C)	0.9900	C(36)-H(36B)	0.9800
C(42)-H(42D)	0.9900	C(36)-H(36C)	0.9800
C(42)-C(41)	1.498(7)	C(38)-H(38A)	0.9800
C(42)-C(41A)	1.544(8)	C(38)-H(38B)	0.9800
C(21)-C(15)	1.524(3)	C(38)-H(38C)	0.9800
C(21)-C(23)	1.524(3)	C(22)-H(22A)	0.9800
C(21)-C(22)	1.525(3)	C(22)-H(22B)	0.9800
C(6)-C(7)	1.371(3)	C(22)-H(22C)	0.9800
C(6)-C(5)	1.468(3)	C(37)-H(37A)	0.9800
C(32)-H(32A)	0.9800	C(37)-H(37B)	0.9800
C(32)-H(32B)	0.9800	C(37)-H(37C)	0.9800
C(32)-H(32C)	0.9800	C(39)-H(39A)	0.9900
C(15)-C(14)	1.375(3)	C(39)-H(39B)	0.9900

C(39)-C(40)	1.456(5)
C(40)-H(40A)	0.9900
C(40)-H(40B)	0.9900
C(40)-H(40C)	0.9900
C(40)-H(40D)	0.9900
C(40)-C(41)	1.547(8)
C(40)-C(41A)	1.449(8)
C(41)-H(41A)	0.9900
C(41)-H(41B)	0.9900
C(41A)-H(41C)	0.9900
C(41A)-H(41D)	0.9900

O(2)-Mn(1)-Cl(1)	108.33(5)
O(2)-Mn(1)-N(2)	151.65(7)
O(2)-Mn(1)-N(1)	88.48(7)
O(1)-Mn(1)-Cl(1)	103.47(5)
O(1)-Mn(1)-O(2)	90.67(7)
O(1)-Mn(1)-N(2)	88.23(7)
O(1)-Mn(1)-N(1)	156.96(7)
N(2)-Mn(1)-Cl(1)	99.45(6)
N(1)-Mn(1)-Cl(1)	98.63(6)
N(1)-Mn(1)-N(2)	81.77(8)
C(16)-O(2)-Mn(1)	126.89(14)
C(30)-O(1)-Mn(1)	127.20(14)
C(39)-O(3)-C(42)	107.9(2)
C(10)-N(2)-Mn(1)	125.71(15)
C(6)-N(2)-Mn(1)	113.74(15)
C(6)-N(2)-C(10)	120.30(19)
C(30)-C(29)-C(31)	121.0(2)
C(28)-C(29)-C(30)	117.8(2)
C(28)-C(29)-C(31)	121.1(2)
O(1)-C(30)-C(29)	118.7(2)
O(1)-C(30)-C(25)	122.0(2)
C(25)-C(30)-C(29)	119.3(2)
O(2)-C(16)-C(15)	119.3(2)
O(2)-C(16)-C(11)	122.0(2)
C(11)-C(16)-C(15)	118.7(2)
C(29)-C(28)-H(28)	117.8
C(29)-C(28)-C(27)	124.4(2)
C(27)-C(28)-H(28)	117.8
C(30)-C(25)-C(10)	121.8(2)
C(30)-C(25)-C(26)	119.5(2)
C(26)-C(25)-C(10)	118.6(2)
N(1)-C(1)-C(11)	121.2(2)
N(1)-C(1)-C(2)	118.7(2)
C(2)-C(1)-C(11)	120.0(2)
C(29)-C(31)-C(32)	111.40(19)
C(29)-C(31)-C(33)	111.60(19)
C(29)-C(31)-C(34)	107.89(19)
C(32)-C(31)-C(33)	106.79(19)
C(32)-C(31)-C(34)	107.7(2)
C(33)-C(31)-C(34)	111.4(2)
N(2)-C(10)-C(25)	120.9(2)
N(2)-C(10)-C(9)	118.8(2)
C(9)-C(10)-C(25)	120.3(2)
C(3)-C(4)-H(4)	120.6
C(5)-C(4)-H(4)	120.6
C(5)-C(4)-C(3)	118.7(2)
C(4)-C(3)-H(3)	120.0
C(2)-C(3)-C(4)	120.0(2)
C(2)-C(3)-H(3)	120.0
C(1)-N(1)-Mn(1)	125.04(15)
C(1)-N(1)-C(5)	120.86(19)
C(5)-N(1)-Mn(1)	114.03(15)
H(24A)-C(24)-H(24B)	109.5
H(24A)-C(24)-H(24C)	109.5
H(24B)-C(24)-H(24C)	109.5
C(21)-C(24)-H(24A)	109.5
C(21)-C(24)-H(24B)	109.5
C(21)-C(24)-H(24C)	109.5
O(3)-C(42)-H(42A)	109.9
O(3)-C(42)-H(42B)	109.9
O(3)-C(42)-H(42C)	111.4
O(3)-C(42)-H(42D)	111.4
O(3)-C(42)-C(41)	109.1(3)
O(3)-C(42)-C(41A)	101.9(4)
H(42A)-C(42)-H(42B)	108.3
H(42C)-C(42)-H(42D)	109.3
C(41)-C(42)-H(42A)	109.9
C(41)-C(42)-H(42B)	109.9
C(41A)-C(42)-H(42C)	111.4
C(41A)-C(42)-H(42D)	111.4
C(24)-C(21)-C(15)	109.5(2)
C(24)-C(21)-C(23)	110.2(2)
C(24)-C(21)-C(22)	108.1(2)
C(15)-C(21)-C(23)	110.2(2)
C(15)-C(21)-C(22)	112.3(2)
C(23)-C(21)-C(22)	106.5(2)
N(2)-C(6)-C(7)	121.7(2)
N(2)-C(6)-C(5)	114.8(2)
C(7)-C(6)-C(5)	123.6(2)
C(31)-C(32)-H(32A)	109.5
C(31)-C(32)-H(32B)	109.5
C(31)-C(32)-H(32C)	109.5
H(32A)-C(32)-H(32B)	109.5
H(32A)-C(32)-H(32C)	109.5
H(32B)-C(32)-H(32C)	109.5
C(16)-C(15)-C(21)	121.9(2)
C(14)-C(15)-C(16)	117.5(2)
C(14)-C(15)-C(21)	120.6(2)
C(28)-C(27)-C(35)	120.3(2)
C(26)-C(27)-C(28)	116.8(2)
C(26)-C(27)-C(35)	122.8(2)
C(9)-C(8)-H(8)	120.1
C(9)-C(8)-C(7)	119.8(2)
C(7)-C(8)-H(8)	120.1
C(36)-C(35)-C(27)	112.4(2)
C(36)-C(35)-C(38)	107.0(2)
C(36)-C(35)-C(37)	109.2(2)
C(38)-C(35)-C(27)	111.2(2)
C(38)-C(35)-C(37)	109.6(2)
C(37)-C(35)-C(27)	107.4(2)
C(10)-C(9)-H(9)	119.6
C(8)-C(9)-C(10)	120.7(2)

C(8)-C(9)-H(9)	119.6
C(16)-C(11)-C(1)	121.9(2)
C(16)-C(11)-C(12)	119.7(2)
C(12)-C(11)-C(1)	118.2(2)
C(6)-C(7)-C(8)	118.6(2)
C(6)-C(7)-H(7)	120.7
C(8)-C(7)-H(7)	120.7
C(15)-C(14)-H(14)	117.8
C(15)-C(14)-C(13)	124.5(2)
C(13)-C(14)-H(14)	117.8
C(21)-C(23)-H(23A)	109.5
C(21)-C(23)-H(23B)	109.5
C(21)-C(23)-H(23C)	109.5
H(23A)-C(23)-H(23B)	109.5
H(23A)-C(23)-H(23C)	109.5
H(23B)-C(23)-H(23C)	109.5
H(20A)-C(20)-H(20B)	109.5
H(20A)-C(20)-H(20C)	109.5
H(20B)-C(20)-H(20C)	109.5
C(17)-C(20)-H(20A)	109.5
C(17)-C(20)-H(20B)	109.5
C(17)-C(20)-H(20C)	109.5
C(14)-C(13)-C(17)	119.2(2)
C(12)-C(13)-C(14)	117.1(2)
C(12)-C(13)-C(17)	123.7(2)
H(19A)-C(19)-H(19B)	109.5
H(19A)-C(19)-H(19C)	109.5
H(19B)-C(19)-H(19C)	109.5
C(17)-C(19)-H(19A)	109.5
C(17)-C(19)-H(19B)	109.5
C(17)-C(19)-H(19C)	109.5
C(1)-C(2)-H(2)	119.8
C(3)-C(2)-C(1)	120.4(2)
C(3)-C(2)-H(2)	119.8
C(31)-C(33)-H(33A)	109.5
C(31)-C(33)-H(33B)	109.5
C(31)-C(33)-H(33C)	109.5
H(33A)-C(33)-H(33B)	109.5
H(33A)-C(33)-H(33C)	109.5
H(33B)-C(33)-H(33C)	109.5
C(25)-C(26)-H(26)	118.9
C(27)-C(26)-C(25)	122.1(2)
C(27)-C(26)-H(26)	118.9
H(18A)-C(18)-H(18B)	109.5
H(18A)-C(18)-H(18C)	109.5
H(18B)-C(18)-H(18C)	109.5
C(17)-C(18)-H(18A)	109.5
C(17)-C(18)-H(18B)	109.5
C(17)-C(18)-H(18C)	109.5
C(11)-C(12)-H(12)	119.0
C(13)-C(12)-C(11)	122.0(2)
C(13)-C(12)-H(12)	119.0
C(31)-C(34)-H(34A)	109.5
C(31)-C(34)-H(34B)	109.5
C(31)-C(34)-H(34C)	109.5
H(34A)-C(34)-H(34B)	109.5
H(34A)-C(34)-H(34C)	109.5
H(34B)-C(34)-H(34C)	109.5
C(20)-C(17)-C(13)	109.57(19)
C(19)-C(17)-C(20)	108.9(2)
C(19)-C(17)-C(13)	108.4(2)
C(18)-C(17)-C(20)	109.4(2)
C(18)-C(17)-C(13)	112.0(2)
C(18)-C(17)-C(19)	108.6(2)
C(4)-C(5)-C(6)	123.1(2)
N(1)-C(5)-C(4)	121.3(2)
N(1)-C(5)-C(6)	115.61(19)
C(35)-C(36)-H(36A)	109.5
C(35)-C(36)-H(36B)	109.5
C(35)-C(36)-H(36C)	109.5
H(36A)-C(36)-H(36B)	109.5
H(36A)-C(36)-H(36C)	109.5
H(36B)-C(36)-H(36C)	109.5
C(35)-C(38)-H(38A)	109.5
C(35)-C(38)-H(38B)	109.5
C(35)-C(38)-H(38C)	109.5
H(38A)-C(38)-H(38B)	109.5
H(38A)-C(38)-H(38C)	109.5
H(38B)-C(38)-H(38C)	109.5
C(21)-C(22)-H(22A)	109.5
C(21)-C(22)-H(22B)	109.5
C(21)-C(22)-H(22C)	109.5
H(22A)-C(22)-H(22B)	109.5
H(22A)-C(22)-H(22C)	109.5
H(22B)-C(22)-H(22C)	109.5
C(35)-C(37)-H(37A)	109.5
C(35)-C(37)-H(37B)	109.5
C(35)-C(37)-H(37C)	109.5
H(37A)-C(37)-H(37B)	109.5
H(37A)-C(37)-H(37C)	109.5
H(37B)-C(37)-H(37C)	109.5
O(3)-C(39)-H(39A)	109.5
O(3)-C(39)-H(39B)	109.5
O(3)-C(39)-C(40)	110.8(3)
H(39A)-C(39)-H(39B)	108.1
C(40)-C(39)-H(39A)	109.5
C(40)-C(39)-H(39B)	109.5
C(39)-C(40)-H(40A)	111.1
C(39)-C(40)-H(40B)	111.1
C(39)-C(40)-H(40C)	110.9
C(39)-C(40)-H(40D)	110.9
C(39)-C(40)-C(41)	103.1(4)
H(40A)-C(40)-H(40B)	109.1
H(40C)-C(40)-H(40D)	108.9
C(41)-C(40)-H(40A)	111.1
C(41)-C(40)-H(40B)	111.1
C(41A)-C(40)-C(39)	104.2(4)
C(41A)-C(40)-H(40C)	110.9
C(41A)-C(40)-H(40D)	110.9
C(42)-C(41)-C(40)	100.2(4)
C(42)-C(41)-H(41A)	111.7
C(42)-C(41)-H(41B)	111.7
C(40)-C(41)-H(41A)	111.7
C(40)-C(41)-H(41B)	111.7

H(41A)-C(41)-H(41B)	109.5
C(42)-C(41A)-H(41C)	111.2
C(42)-C(41A)-H(41D)	111.2
C(40)-C(41A)-C(42)	102.6(5)
C(40)-C(41A)-H(41C)	111.2
C(40)-C(41A)-H(41D)	111.2
H(41C)-C(41A)-H(41D)	109.2

Table S2.10.8. Anisotropic displacement parameters (Å^{2}x 10^3) for **Mn(^{tbu}dhbpy)Cl 1**. The anisotropic displacement factor exponent takes the form: $-2\pi^2[\, h^2\, a^{*2}U^{11} + \ldots + 2\, h\, k\, a^*\, b^*\, U^{12}\,]$

	U^{11}	U^{22}	U^{33}	U^{23}	U^{13}	U^{12}
Mn(1)	14(1)	13(1)	10(1)	-4(1)	-1(1)	-2(1)
Cl(1)	29(1)	24(1)	22(1)	-10(1)	-5(1)	8(1)
O(2)	19(1)	14(1)	11(1)	-2(1)	-4(1)	-5(1)
O(1)	13(1)	17(1)	11(1)	-3(1)	-1(1)	-2(1)
O(3)	56(1)	28(1)	29(1)	-3(1)	6(1)	3(1)
N(2)	13(1)	13(1)	11(1)	-4(1)	-3(1)	2(1)
C(29)	14(1)	13(1)	16(1)	-4(1)	-3(1)	3(1)
C(30)	12(1)	9(1)	17(1)	-4(1)	0(1)	0(1)
C(16)	13(1)	12(1)	17(1)	-6(1)	0(1)	1(1)
C(28)	18(1)	15(1)	13(1)	-1(1)	0(1)	1(1)
C(25)	15(1)	13(1)	14(1)	-4(1)	-1(1)	0(1)
C(1)	13(1)	12(1)	15(1)	-3(1)	-2(1)	2(1)
C(31)	18(1)	17(1)	11(1)	-3(1)	0(1)	-1(1)
C(10)	12(1)	12(1)	16(1)	-2(1)	-4(1)	1(1)
C(4)	19(1)	18(1)	12(1)	-4(1)	-5(1)	3(1)
C(3)	22(1)	18(1)	12(1)	-2(1)	-1(1)	3(1)
N(1)	13(1)	13(1)	12(1)	-4(1)	-3(1)	1(1)
C(24)	28(2)	36(2)	16(1)	-6(1)	-1(1)	-6(1)
C(42)	56(2)	26(2)	37(2)	-3(1)	12(2)	2(1)
C(21)	21(1)	18(1)	15(1)	-6(1)	-6(1)	-2(1)
C(6)	13(1)	13(1)	11(1)	-4(1)	-3(1)	4(1)
C(32)	22(1)	29(1)	14(1)	-6(1)	-1(1)	-3(1)
C(15)	17(1)	15(1)	14(1)	-6(1)	-2(1)	1(1)
C(27)	16(1)	14(1)	18(1)	-2(1)	0(1)	-1(1)
C(8)	17(1)	20(1)	20(1)	-10(1)	-6(1)	1(1)
C(35)	21(1)	20(1)	21(1)	0(1)	-1(1)	-6(1)
C(9)	17(1)	16(1)	19(1)	-5(1)	-4(1)	-2(1)
C(11)	12(1)	16(1)	14(1)	-7(1)	-2(1)	1(1)
C(7)	16(1)	20(1)	14(1)	-7(1)	-3(1)	2(1)
C(14)	17(1)	17(1)	18(1)	-8(1)	-3(1)	0(1)
C(23)	38(2)	21(1)	20(1)	-5(1)	-13(1)	1(1)
C(20)	21(1)	20(1)	30(2)	-6(1)	-5(1)	-6(1)
C(13)	12(1)	14(1)	19(1)	-7(1)	0(1)	0(1)
C(19)	34(2)	21(1)	36(2)	-14(1)	6(1)	-5(1)
C(2)	16(1)	15(1)	16(1)	-3(1)	-1(1)	0(1)
C(33)	19(1)	24(1)	14(1)	-4(1)	-4(1)	1(1)
C(26)	18(1)	14(1)	20(1)	-6(1)	-5(1)	-2(1)
C(18)	18(1)	16(1)	30(2)	-2(1)	-2(1)	-4(1)
C(12)	14(1)	14(1)	12(1)	-3(1)	1(1)	1(1)
C(34)	22(1)	22(1)	17(1)	-11(1)	0(1)	-1(1)
C(17)	18(1)	16(1)	23(1)	-9(1)	-1(1)	-3(1)
C(5)	14(1)	15(1)	13(1)	-6(1)	-4(1)	4(1)
C(36)	17(1)	22(1)	27(1)	-8(1)	2(1)	-5(1)
C(38)	26(2)	54(2)	22(2)	-3(1)	6(1)	-21(1)
C(22)	34(2)	25(1)	18(1)	-4(1)	-10(1)	-5(1)

C(37)	29(2)	18(1)	60(2)	5(1)	-7(2)	-6(1)
C(39)	91(3)	38(2)	46(2)	-19(2)	2(2)	10(2)
C(40)	80(3)	74(3)	42(2)	-17(2)	17(2)	-17(2)
C(41)	44(4)	42(4)	31(4)	-3(3)	9(3)	-11(4)
C(41A)	48(5)	36(4)	44(4)	11(3)	7(4)	6(4)

Table S2.10.9. Hydrogen coordinates (x 10^4) and isotropic displacement parameters ($Å^2$x 10 ^{3}) for **Mn(^{tbu}dhbpy)Cl 1**.

	x	y	z	U(eq)
H(28)	3861	2031	9524	20
H(4)	8265	5712	3626	19
H(3)	10165	7047	3244	21
H(24A)	9249	6561	8686	40
H(24B)	9595	5285	9186	40
H(24C)	8848	5506	8375	40
H(42A)	12592	11245	3333	52
H(42B)	11237	11250	2869	52
H(42C)	13093	11227	3050	52
H(42D)	11355	11293	3178	52
H(32A)	4433	3058	10253	32
H(32B)	5948	3059	10565	32
H(32C)	5464	1976	10313	32
H(8)	5110	2797	4700	21
H(9)	4425	2234	6125	21
H(7)	6725	4332	4082	19
H(14)	12230	7908	7293	20
H(23A)	11597	4226	8608	38
H(23B)	12505	4786	7706	38
H(23C)	10871	4380	7796	38
H(20A)	14032	9036	6641	35
H(20B)	14464	10210	5935	35
H(20C)	14497	9033	5692	35
H(19A)	11703	9853	7087	46
H(19B)	10652	10392	6430	46
H(19C)	12136	11029	6384	46
H(2)	11007	7668	4248	19
H(33A)	7752	2111	9339	29
H(33B)	8183	3159	9649	29
H(33C)	8256	3306	8677	29
H(26)	3238	2336	7206	20
H(18A)	12879	11042	4925	34
H(18B)	11362	10453	4968	34
H(18C)	12832	9884	4664	34
H(12)	10999	8592	5072	17
H(34A)	6522	5002	8538	29
H(34B)	6590	4886	9493	29
H(34C)	5064	4861	9197	29
H(36A)	543	2338	8159	33
H(36B)	30	1027	8473	33
H(36C)	1254	1452	7675	33
H(38A)	1951	1092	10028	54
H(38B)	387	985	9800	54
H(38C)	1144	2214	9580	54
H(22A)	11767	7089	8596	38
H(22B)	13047	6440	8173	38
H(22C)	12147	5805	9063	38
H(37A)	2943	-32	8322	58

H(37B)	1659	-473	9086	58
H(37C)	3195	-146	9251	58
H(39A)	12165	8668	2560	70
H(39B)	13702	8919	2769	70
H(40A)	12278	10215	1509	82
H(40B)	13987	10023	1495	82
H(40C)	14116	10354	1679	82
H(40D)	12749	9921	1382	82
H(41A)	14185	11404	2170	50
H(41B)	12831	11935	1718	50
H(41C)	11270	11124	1853	59
H(41D)	12743	11860	1666	59

Table S2.10.10. Caculated Mulliken charges for the model complex for Mn(dhbpy)Cl.

```
-------------------------------------------
MULLIKEN ATOMIC CHARGES AND SPIN POPULATIONS
-------------------------------------------
   0 Cl:   -0.637775    0.133925
   1 Mn:    0.634763    3.874990
   2 O :   -0.563173    0.027731
   3 O :   -0.561521    0.026758
   4 N :   -0.127625   -0.067216
   5 N :   -0.140650   -0.067174
   6 C :   -0.042610   -0.003803
   7 C :    0.383394    0.004886
   8 C :   -0.264671   -0.001570
   9 C :   -0.110224    0.002891
  10 H :    0.144770   -0.000068
  11 C :   -0.208438    0.000466
  12 C :   -0.189821    0.001557
  13 H :    0.150378    0.000013
  14 C :    0.217042    0.021170
  15 C :    0.269528    0.008115
  16 C :    0.224450    0.008903
  17 C :   -0.163206   -0.003828
  18 C :   -0.195236   -0.003571
  19 C :    0.221133    0.021678
  20 C :   -0.041640   -0.004237
  21 C :    0.387495    0.004886
  22 C :   -0.274698   -0.001608
  23 C :   -0.091360    0.002954
  24 H :    0.147393   -0.000075
  25 C :   -0.215648    0.000314
  26 C :   -0.199376    0.001751
  27 H :    0.148562    0.000011
  28 C :   -0.138852   -0.007227
  29 C :   -0.100096    0.012234
  30 C :   -0.117656    0.012663
  31 C :   -0.127941   -0.007421
  32 H :    0.167582   -0.000639
  33 H :    0.164107    0.000316
  34 H :    0.171477   -0.000168
  35 H :    0.158514   -0.000148
  36 H :    0.173887   -0.000656
  37 H :    0.169399    0.000330
  38 H :    0.134144    0.000537
  39 H :    0.153600   -0.000085
  40 H :    0.140150    0.000506
  41 H :    0.150453   -0.000090
Sum of atomic charges         :   -0.0000000
Sum of atomic spin populations:    4.0000000
```

Table S2.10.11. Caculated Mulliken charges for the model complex for [Mn(dhbpy)Cl]$^{-}$.

```
-------------------------------------------
MULLIKEN ATOMIC CHARGES AND SPIN POPULATIONS
-------------------------------------------
   0 Cl:   -0.728583    0.056829
   1 Mn:    0.758802    4.794762
   2 O :   -0.647434    0.030174
   3 O :   -0.648984    0.030194
   4 N :   -0.264013   -0.005752
   5 N :   -0.271864   -0.006593
   6 C :   -0.033594    0.000399
   7 C :    0.323025    0.006447
   8 C :   -0.266604    0.007120
   9 C :   -0.121818   -0.002258
  10 H :    0.132526    0.000319
  11 C :   -0.255029    0.009117
  12 C :   -0.180012   -0.003928
  13 H :    0.137063    0.000155
  14 C :    0.201563    0.015994
  15 C :    0.270558    0.007463
  16 C :    0.233135    0.009236
  17 C :   -0.176288    0.002462
  18 C :   -0.215924    0.002126
  19 C :    0.205221    0.015228
  20 C :   -0.036328    0.000086
  21 C :    0.372938    0.006679
  22 C :   -0.319682    0.007054
  23 C :   -0.099480   -0.002228
  24 H :    0.135533    0.000339
  25 C :   -0.261451    0.009044
  26 C :   -0.203384   -0.003877
  27 H :    0.139686    0.000165
  28 C :   -0.175677    0.002491
  29 C :   -0.111848    0.003498
  30 C :   -0.135559    0.003363
  31 C :   -0.174056    0.002871
  32 H :    0.153870   -0.000317
  33 H :    0.155102    0.000714
  34 H :    0.157589    0.000845
  35 H :    0.136951    0.000795
  36 H :    0.163742   -0.000320
  37 H :    0.158691    0.000707
  38 H :    0.107321   -0.000181
  39 H :    0.141824   -0.000524
  40 H :    0.106050   -0.000176
  41 H :    0.136426   -0.000519
Sum of atomic charges         :   -1.0000000
Sum of atomic spin populations:    5.0000000
```

Optimized Coordinates from DFT Calculations on Model Complex Mn(dhbpy)Cl.

Final Gibbs free enthalpy ... -2718.47538185 Hartrees

S = 2

Cl	-6.10195711162882	2.35533808810841	16.49467375600253
Mn	-3.89818974001652	2.21328978483382	17.44798906514088
O	-2.80140198202049	2.79474728722458	16.05186916078504
O	-3.73996437296707	3.84154298729586	18.34783076292856
N	-3.49760858899556	0.30153251676075	16.93766716519651
N	-4.38483124071602	1.31526535789143	19.18926560989270
C	-3.02663111973830	0.87347894522686	14.61087581390453
C	-2.85978439943717	2.26272928729860	14.83740619853535
C	-2.71721660952728	3.12015055872739	13.73445057724886
C	-2.77106955521215	2.63630806157774	12.44172491934674
H	-2.66863294300524	3.32030197555711	11.60889974262775
C	-2.97330367881879	1.27433365164429	12.20958134539685
C	-3.09120816439460	0.41485834724875	13.28406375279059
H	-3.26341845121593	-0.63529598647931	13.09521319995000
C	-3.09719987152353	-0.09237175134037	15.71093840098838
C	-3.60091508461179	-0.57678849327944	17.96458107491755
C	-4.09055307527826	-0.00722032435755	19.22819351573864
C	-4.27091528946002	-0.74838377007806	20.38027253442501
C	-3.28742432219008	-1.91237355412571	17.79957871160492
C	-4.88446042483298	1.95758101426815	20.26573769441146
C	-5.23620767617551	3.37787894124506	20.18204846252383
C	-4.63367921060034	4.24953271738698	19.24091907791644
C	-4.96641025592494	5.61339498599791	19.26632676981089
C	-5.89047196426531	6.10687583012764	20.16661474353069
H	-6.13925715629469	7.16053017966696	20.15589688298671
C	-6.51456230577548	5.24852526496296	21.07408624170850
C	-6.17984429159495	3.90847429541814	21.07778062798300
H	-6.67916199312054	3.24806762503591	21.77247407470401
C	-2.74156991476551	-1.43536955389088	15.51646091965853
C	-2.84019069363526	-2.33742280364753	16.55418433099834
C	-4.74950965438471	-0.10203390609509	21.51393557872492
C	-5.05302906422501	1.24151670699646	21.46012210199687
H	-2.56421708381119	-3.37168533878994	16.40192453241749
H	-2.36884547380689	-1.75546731020472	14.55724115367300
H	-3.38305169614280	-2.60900802357925	18.61720320348972
H	-4.04052993284802	-1.80143922843664	20.40294276929833
H	-4.87911762769601	-0.65091255294226	22.43655284485041
H	-5.40068117219469	1.75150125716599	22.34383912773689
H	-4.48206886083362	6.26275771954474	18.54893958119873
H	-7.25824465723978	5.62350094789469	21.76404948039186

H	-2.57225981151837	4.17432761615729	13.93155489494640
H	-3.04396047755572	0.89260764598227	11.20032459762149

Optimized Coordinates from DFT Calculations on Model Complex $[Mn(dhbpy)Cl]^-$.

Final Gibbs free enthalpy ... -2718.62391123 Hartrees

S = 5/2

Cl	-6.26180213865294	2.74778144233480	16.23596693089705
Mn	-4.09044821062247	2.44573342718422	17.25494429941493
O	-2.58597943788327	2.79196458054372	15.89518157056017
O	-3.70704720925311	4.02262201496944	18.51164652054564
N	-3.53506754811449	0.31673191715491	16.87139974259514
N	-4.44953440025437	1.35940059361168	19.17784329292390
C	-2.98594637400216	0.83201550755043	14.54630532646790
C	-2.70052146406918	2.22349499730404	14.72343595319249
C	-2.52236216044693	3.00324567076600	13.55468274813571
C	-2.66646064388988	2.47487648654779	12.28812920027837
H	-2.53674728051903	3.11349970547691	11.42229894488222
C	-2.99215063195577	1.12613486033128	12.12032038590494
C	-3.13664432172963	0.33132045485286	13.24274913653245
H	-3.39971691233431	-0.71026744633178	13.11162737050976
C	-3.08677317012519	-0.10851920565603	15.67528378302022
C	-3.64213193795886	-0.52707338824259	17.91181127884488
C	-4.12653697093672	0.05438711630198	19.19246854103082
C	-4.23258487023425	-0.70707219399092	20.34990209632898
C	-3.31010846212061	-1.87118548388326	17.79267711420319
C	-4.88746521232884	1.97762982442740	20.29088238894185
C	-5.25998273495188	3.40268807967459	20.25124653253365
C	-4.62128950661463	4.34793529675621	19.38750003816844
C	-5.00176977251131	5.70618203248711	19.51732039862399
C	-5.98120102680626	6.11621244908550	20.39872022963357
H	-6.25247130215893	7.16421365988183	20.45057724352898
C	-6.63329241551986	5.18346417887647	21.20979169937087
C	-6.25828194890966	3.85463095527961	21.12988149575640
H	-6.77179116236472	3.13237036451891	21.75119208313386
C	-2.71170958048945	-1.45241896501793	15.51358542825356
C	-2.83548910153534	-2.33014203821548	16.57128675232126
C	-4.66826555831246	-0.08686934558934	21.51294658263848
C	-4.98836645906939	1.25522087833207	21.49114096209545
H	-2.55026833455941	-3.36728176491040	16.45517150844343
H	-2.30869354905451	-1.79108646427713	14.57201496132885
H	-3.40467303307687	-2.54907293823173	18.62572705711291
H	-3.96928124589811	-1.75223946542130	20.35965989906521
H	-4.74291243392600	-0.65002087618896	22.43386837309026
H	-5.29494586594093	1.75430617093477	22.39716342812968

H	-4.49946113631213	6.42122659639300	18.87688344393261
H	-7.42037295373253	5.49025932921197	21.88585974610334
H	-2.28035852804538	4.05024524582609	13.69275970426388
H	-3.13264899277818	0.70863373934128	11.13237880726042

Optimized Coordinates from DFT Calculations on Model 3 Complex [Mn(dhbpy(H))(η^1-O_2)]$^+$.

Final Gibbs free enthalpy ... -2409.00396471 Hartrees

S = 3/2

Mn	-3.49891530376548	2.40000937753104	17.50435847328403
O	-2.03558295888115	2.61215145500576	15.87738528260695
O	-4.12546256172914	4.06817160639953	18.19902982936122
N	-3.40462275407458	0.34405809820548	16.89053254388160
N	-4.39738007072813	1.37356924591478	19.17967195855802
C	-2.93539383100958	0.83498263949090	14.54273211313777
C	-2.44781704334001	2.14302717092297	14.63898485948943
C	-2.35913863725949	2.97409646430280	13.53359071246047
C	-2.77300898392649	2.51476748134926	12.29222967270736
H	-2.70756277012828	3.16721660483726	11.43212289096732
C	-3.27673855789704	1.22475533709028	12.16373146811479
C	-3.35024231550023	0.40239490446456	13.27559577589012
H	-3.75469469994911	-0.59439924821128	13.17357702658857
C	-3.02729134306277	-0.10663143516143	15.67965537152656
C	-3.58424170847707	-0.51154760049402	17.91869696067583
C	-4.05822867719322	0.06803250206246	19.20281829856053
C	-4.15465532495231	-0.68272043638169	20.36148415339333
C	-3.35604037304121	-1.87258521270263	17.76468944005129
C	-4.88195373724008	1.99810993687623	20.27152236488766
C	-5.33807200500573	3.40016313674320	20.20048922106123
C	-4.93237075389831	4.34142861490329	19.20676082681226
C	-5.40610401897489	5.66608820598793	19.30322184608771
C	-6.28099186499968	6.06191608967905	20.29242571532905
H	-6.63276960027836	7.08547702689687	20.32283607107517
C	-6.72022228582992	5.13599771099388	21.24077058335001
C	-6.24594014002395	3.84128765919714	21.18409012088231
H	-6.61373810285613	3.13341777793624	21.91217112518620
C	-2.76620287493164	-1.46261990879214	15.48149186721848
C	-2.92997047528527	-2.34561731260001	16.53341979553059
C	-4.59618631925757	-0.04875861399480	21.51748184722008
C	-4.95731261576741	1.28073779481160	21.47920897193090
H	-2.72969324700098	-3.39942244212637	16.39649680538153
H	-2.43053924101037	-1.81143103288726	14.51742336123272
H	-3.50874903431947	-2.55680230070281	18.58374628406359

H	-3.87471321644076	-1.72317209667455	20.38371966525082
H	-4.65096157892424	-0.59724040543483	22.44803594405404
H	-5.27729502803562	1.76993088227311	22.38419584331108
H	-5.06454956165452	6.36583936144281	18.55116457412015
H	-7.42770255867299	5.42128548725378	22.00753787522122
H	-1.96721210573608	3.97624179198430	13.65351517818752
H	-3.61576757044315	0.86269146959273	11.20322273961625
H	-1.58455116263697	3.46398935449153	15.77779072563721
O	-1.50528524254055	2.41893900370028	18.76416493912039
O	-1.49420311663830	2.70304288428379	19.93739466555779

Optimized Coordinates from DFT Calculations on Model 3a Complex $[Mn(dhbpy(H))(\eta^1\text{-}O_2)]$.

Final Gibbs free enthalpy ... -2409.17786972 Hartrees

S = 2

Mn	-2.98300004710169	2.41151076038914	17.84631753693059
O	-1.99299638585760	2.71464707770247	15.86640623199572
O	-3.85137533564064	4.11535236059711	18.35792162843799
N	-3.30961690025913	0.40438129933600	16.97601726720523
N	-4.31789139127185	1.40814595730681	19.23406950198017
C	-2.94254305361604	0.90642080456236	14.61627280775649
C	-2.49830322727805	2.23205371480450	14.67712253798571
C	-2.53203664179570	3.06126513496573	13.56481672061961
C	-3.02044584203230	2.58380369715105	12.35785672453513
H	-3.04914295119470	3.23746820324771	11.49640904064570
C	-3.47606442964584	1.27317375505981	12.26645518685503
C	-3.43220726454905	0.45417083729526	13.38314918812903
H	-3.80555900532203	-0.55774102541973	13.31395512647219
C	-2.94682975120860	-0.03567481899105	15.75934826377810
C	-3.48691584753517	-0.46599308834921	17.99007430801106
C	-4.01421057939561	0.09778080456983	19.26121750018511
C	-4.22018261566712	-0.66954748940393	20.39700953444808
C	-3.23644696020959	-1.82336373479221	17.82795044041810
C	-4.87924155547051	2.02592152542334	20.28909741531741
C	-5.32480893618790	3.42804273999481	20.16987534793657
C	-4.79871471207214	4.37007841474082	19.22733063750402
C	-5.32525303707773	5.68368839610569	19.25044122477050
C	-6.32860969889112	6.06501046387961	20.11525483526305
H	-6.70605151227250	7.07996614965597	20.08710474506404
C	-6.86317189766668	5.13946188363586	21.01458782437848
C	-6.35589199246070	3.85510485018352	21.02851819525250
H	-6.79546035311432	3.14074041207745	21.71053776494806
C	-2.65461971881597	-1.38434868586301	15.54861793524783
C	-2.79064074249675	-2.27795214790405	16.59706613171967

C	-4.73258624309987	-0.03944871048635	21.52524257191881
C	-5.06507856874401	1.29967980541179	21.47843782941219
H	-2.56331754258210	-3.32556631026635	16.45360840006932
H	-2.32384591136736	-1.72041833252767	14.57794819819658
H	-3.38318146130391	-2.51598783949010	18.64157130334535
H	-3.97657932373840	-1.71967192889882	20.42106457717924
H	-4.87201486027968	-0.59917039557653	22.44049590318353
H	-5.45376712487055	1.78488976260168	22.35933271956375
H	-4.90677030867740	6.38996685695747	18.54390036950377
H	-7.66819331363714	5.41439468301284	21.68281355730049
H	-2.17301080203266	4.07896128288102	13.65364394980967
H	-3.87117382346047	0.89321189508196	11.33448594207913
H	-1.57998842824438	3.57884045800967	15.72681425485632
O	-1.20593908466981	2.29816181940891	18.86197817314079
O	-0.96639619050344	1.04945773237987	19.25304643523103

Optimized Coordinates from DFT Calculations on Model 4 Complex [Mn(dhbpy(H))(η^1-O_2H)].

Final Gibbs free enthalpy ... -2409.20990602 Hartrees

S = 2

Mn	-3.27025993114024	2.27265495477764	17.74686667595036
O	-2.56064687358897	2.83928717253094	16.11066954232706
O	-4.75008581501885	3.47185409958872	17.75247695072460
N	-3.33640790863353	0.27942916911995	16.98609644273607
N	-4.17717885483506	1.29067701868723	19.26060621391309
C	-2.91476745065873	0.90403926707234	14.68493737850088
C	-2.76595341519398	2.29874220041548	14.91639244208063
C	-2.77245767135926	3.16649623412176	13.80918330394706
C	-2.93171714097577	2.69411513098144	12.52055906101156
H	-2.93681322102767	3.39086550542630	11.69180470928625
C	-3.09539242346326	1.32783902942157	12.28977864897687
C	-2.91206037356732	-0.08976074316466	15.76816571065882
C	-3.43265131493968	-0.60432384785762	17.99862177570415
C	-4.01136163387966	-0.05346609595378	19.23921213708888
C	-4.43671030419174	-0.83687148527045	20.29452519173073
C	-3.06203658652747	-1.92847027800904	17.83814165359094
C	-4.85546113622669	1.90975068307977	20.24660690899665
C	-5.13772409222257	3.34491292071490	20.14503450227636
C	-5.12993056799087	4.02709295807281	18.89493864863035
C	-5.56299393515091	5.36614282772871	18.85873285603318
C	-5.94438873533271	6.03280486139960	20.00519911308657
H	-6.25869627240049	7.06687088877730	19.94370409327716
C	-5.90833412726676	5.38238053151859	21.24143346527366
C	-5.51626219637597	4.06050736407205	21.29529638745470

H	-5.48792096779255	3.56733730023806	22.25650581044366
C	-2.50677327745049	-1.41649503293734	15.55864015133282
C	-2.57874629276872	-2.32616067506553	16.59576295253079
C	-5.08709595508939	-0.21811523439757	21.35763002753521
C	-5.32423371611089	1.13948846400519	21.32300553659079
H	-2.25704270036552	-3.34730635009356	16.44350022687478
H	-2.12242767031791	-1.71922444432340	14.59736874095886
H	-3.13468449473214	-2.63240945175071	18.65287926672808
H	-4.29409636922141	-1.90610378976171	20.28113015422867
H	-5.44090925933054	-0.80783730891999	22.19216146089011
H	-5.89356518319213	1.60494797444567	22.11098581265573
H	-5.56859106880474	5.86260515050349	17.89698832546366
H	-6.18376104661427	5.90441512807366	22.14733259083139
H	-2.64411892866258	4.22390372469481	14.00207981465764
O	-1.53949414766584	2.09186254575339	18.55630994196670
O	-1.71390871119202	2.94480481606576	19.72919431036770
C	-3.08159956918136	0.45803855000853	13.36362092942579
H	-3.24096038878465	0.95049037958716	11.28687768866234
H	-3.23174426183566	-0.59774712041375	13.18346999506169
H	-1.83907400891902	2.29794500703629	20.43996244953695

2.11 Acknowledgments

From the original publication of this work, all contributing authors thank Dr. Bradley A. McKeown for helpful discussion for the work described in **Chapter 1** of this thesis. All experiments in this chapter were carried out by S.L.H. and C.W.M. All computational work in this chapter was completed by C.W.M. The original publication was written by C.W.M. and S.L.H. Crystallography studies were carried out by A.L.R.

2.12 References:

1. Sahu, S.; Goldberg, D. P., *J. Am. Chem. Soc.* **2016,** *138*, 11410-11428.

2. Wood, P. M., *Biochem. J.* **1988,** *253*, 287-289.

3. Sono, M.; Roach, M. P.; Coulter, E. D.; Dawson, J. H., *Chem. Rev.* **1996,** *96*, 2841-2888.

4. Masa, J.; Ozoemena, K.; Schuhmann, W.; Zagal, J. H., *J. Porphyrins Phthalocyanines* **2012,** *16*, 761-784.

5. Zagal, J.; Páez, M.; Tanaka, A. A.; dos Santos, J. R.; Linkous, C. A., *J. Electroanal. Chem.* **1992,** *339*, 13-30.

6. Zagal, J. H.; Griveau, S.; Silva, J. F.; Nyokong, T.; Bedioui, F., *Coord. Chem. Rev.* **2010,** *254*, 2755-2791.

7. Zagal, J. H.; Javier Recio, F.; Gutierrez, C. A.; Zuñiga, C.; Páez, M. A.; Caro, C. A., *Electrochem. Comm.* **2014,** *41*, 24-26.

8. Flyagina, I. S.; Hughes, K. J.; Pourkashanian, M.; Ingham, D. B., *Int. J. Hydrogen Energ.* **2014,** *39*, 21538-21546.

9. Masa, J.; Schuhmann, W., *Chem. Eur. J.* **2013,** *19*, 9644-9654.

10. Schöfberger, W.; Faschinger, F.; Chattopadhyay, S.; Bhakta, S.; Mondal, B.; Elemans, J. A. A. W.; Müllegger, S.; Tebi, S.; Koch, R.; Klappenberger, F.; Paszkiewicz, M.; Barth, J. V.; Rauls, E.; Aldahhak, H.; Schmidt, W. G.; Dey, A., *Angew. Chem. Int. Ed.* **2016,** *55*, 2350-2355.

11. McGuire Jr, R.; Dogutan, D. K.; Teets, T. S.; Suntivich, J.; Shao-Horn, Y.; Nocera, D. G., *Chem. Sci.* **2010,** *1*, 411-414.

12. Passard, G.; Ullman, A. M.; Brodsky, C. N.; Nocera, D. G., *J. Am. Chem. Soc.* **2016,** *138*, 2925-2928.

13. Pegis, M. L.; McKeown, B. A.; Kumar, N.; Lang, K.; Wasylenko, D. J.; Zhang, X. P.; Raugei, S.; Mayer, J. M., *ACS Cent. Sci.* **2016,** *2*, 850-856.

14. Wasylenko, D. J.; Rodríguez, C.; Pegis, M. L.; Mayer, J. M., *J. Am. Chem. Soc.* **2014,** *136*, 12544-12547.

15. Nagao, K.; Hiroshi, S.; Tetsuo, O., *Chem. Lett.* **1985,** *14*, 1917-1920.

16. Gennari, M.; Brazzolotto, D.; Pécaut, J.; Cherrier, M. V.; Pollock, C. J.; DeBeer, S.; Retegan, M.; Pantazis, D. A.; Neese, F.; Rouzières, M.; Clérac, R.; Duboc, C., *J. Am. Chem. Soc.* **2015,** *137*, 8644-8653.

17. Coggins, M. K.; Sun, X.; Kwak, Y.; Solomon, E. I.; Rybak-Akimova, E.; Kovacs, J. A., *J. Am. Chem. Soc.* **2013,** *135*, 5631-5640.

18. Coggins, M. K.; Toledo, S.; Shaffer, E.; Kaminsky, W.; Shearer, J.; Kovacs, J. A., *Inorg. Chem.* **2012,** *51*, 6633-6644.

19. Gallo, E.; Solari, E.; Floriani, C.; Re, N.; Chiesi-Villa, A.; Rizzoli, C., *Angew. Chem. Int. Ed.* **1996,** *35*, 1981-1983.

20. Hong, S.; Lee, Y.-M.; Sankaralingam, M.; Vardhaman, A. K.; Park, Y. J.; Cho, K.-B.; Ogura, T.; Sarangi, R.; Fukuzumi, S.; Nam, W., *J. Am. Chem. Soc.* **2016,** *138*, 8523-8532.

21. Pecoraro, V. L.; Baldwin, M. J.; Gelasco, A., *Chem. Rev.* **1994,** *94*, 807-826.

22. Jung, J.; Liu, S.; Ohkubo, K.; Abu-Omar, M. M.; Fukuzumi, S., *Inorg. Chem.* **2015,** *54*, 4285-4291.

23. Bailes, R. H.; Calvin, M., *J. Am. Chem. Soc.* **1947,** *69*, 1886-1893.

24. Niswander, R. H.; Martell, A. E., *Inorg. Chem.* **1978,** *17*, 2341-2344.

25. Hanson, J., *J. Chem. Ed.* **2001,** *78*, 1266.

26. Cozzi, P. G., *Chem. Soc. Rev.* **2004,** *33*, 410-421.

27. Campbell, I. B.; Walker, A. L.; Box, P. C.; Giblin, G. M. P.; Tranter, G. E., Bipyridine manganese complexes. In *WO2000009512 A2*, Google Patents: 2000.

28. Arora, H.; Philouze, C.; Jarjayes, O.; Thomas, F., *Dalton Trans.* **2010,** *39*, 10088–10098.

29. Capdevielle, *New J. Chem.* **1994,** *18*, 519–524.

30. Pun, S.-N.; Chung, W.-H.; Lam, K.-M.; Guo, P.; Chan, P.-H.; Wong, K.-Y.; Che, C.-M.; Chen, T.-Y.; Peng, S.-M., *J. Chem. Soc., Dalton Trans.* **2002**, 575–583.

31. Schmittel, M.; Ganz, A.; Schenk, W. A.; Hagel, M., *Z. Naturforsch.* **1999,** *54b*, 559–564.

32. Bain, G. A.; Berry, J. F., *J. Chem. Ed.* **2008,** *85*, 532.

33. Piguet, C., *J. Chem. Ed.* **1997,** *74*, 815.

34. Horvath, S.; Fernandez, L. E.; Appel, A. M.; Hammes-Schiffer, S., *Inorg. Chem.* **2013,** *52*, 3643-3652.

35. Machan, C. W.; Sampson, M. D.; Kubiak, C. P., *J. Am. Chem. Soc.* **2015,** *137*, 8564-8571.

36. McCarthy, B. D.; Dempsey, J. L., *Inorg. Chem.* **2017,** *56*, 1225-1231.

37. Solis, B. H.; Hammes-Schiffer, S., *Inorg. Chem.* **2014,** *53*, 6427-6443.

38. Li, Q.; Batchelor-McAuley, C.; Lawrence, N. S.; Hartshorne, R. S.; Compton, R. G., *J. Electroanal. Chem.* **2013,** *688*, 328-335.

39. Andrieux, C. P.; Hapiot, P.; Saveant, J. M., *J. Am. Chem. Soc.* **1987,** *109*, 3768-3775.

40. Lam, Y. C.; Nielsen, R. J.; Gray, H. B.; Goddard, W. A., *ACS Catal.* **2015,** *5*, 2521-2528.

41. Raamat, E.; Kaupmees, K.; Ovsjannikov, G.; Trummal, A.; Kütt, A.; Saame, J.; Koppel, I.; Kaljurand, I.; Lipping, L.; Rodima, T.; Pihl, V.; Koppel, I. A.; Leito, I., *J. Phys. Org. Chem.* **2013,** *26*, 162-170.

42. Kütt, A.; Leito, I.; Kaljurand, I.; Sooväli, L.; Vlasov, V. M.; Yagupolskii, L. M.; Koppel, I. A., *J. Org. Chem.* **2006,** *71*, 2829-2838.

43. Costentin, C.; Drouet, S.; Robert, M.; Savéant, J.-M., *J. Am. Chem. Soc.* **2012,** *134*, 11235-11242.

44. Cofre, P.; Sawyer, D. T., *Inorg. Chem.* **1986,** *25*, 2089-2092.

45. Kobayashi, N.; Saiki, H.; Osa, T., *Chem. Lett.* **1985,** *14*, 1917-1920.

46. Costentin, C.; Dridi, H.; Savéant, J.-M., *J. Am. Chem. Soc.* **2015,** *137*, 13535-13544.

47. Bettelheim, A.; Kuwana, T., *Anal. Chem.* **1979,** *51*, 2257-2260.

48. Qinggang He, T. M., GiSuk Hwang and Tebello Nyokong, *Int. J. Electrochem. Sci.* **2012,** *7*, 7045-7064.

49. McCarthy, B. D.; Martin, D. J.; Rountree, E. S.; Ullman, A. C.; Dempsey, J. L., *Inorg. Chem.* **2014,** *53*, 8350-8361.

50. Eckert, F.; Leito, I.; Kaljurand, I.; Kütt, A.; Klamt, A.; Diedenhofen, M., *J. Comput. Chem.* **2009,** *30*, 799-810.

51. Holland, P. L., *Dalton Trans.* **2010,** *39*, 5415-5425.

52. Feller, M.; Ben-Ari, E.; Diskin-Posner, Y.; Carmieli, R.; Weiner, L.; Milstein, D., *J. Am. Chem. Soc.* **2015,** *137*, 4634-4637.

53. Solis, B. H.; Yu, Y.; Hammes-Schiffer, S., *Inorg. Chem.* **2013,** *52*, 6994-6999.

54. Kaeffer, N.; Chavarot-Kerlidou, M.; Artero, V., *Acc. Chem. Res.* **2015,** *48*, 1286-1295.

55. Downes, C. A.; Yoo, J. W.; Orchanian, N. M.; Haiges, R.; Marinescu, S. C., *Chem. Commun.* **2017,** *53*, 7306-7309.

56. Zarkadoulas, A.; Field, M. J.; Artero, V.; Mitsopoulou, C. A., *ChemCatChem* **2017,** *9*, 2308-2317.

57. Chen, J.; Sit, P. H. L., *J. Phys. Chem. A* **2017,** *121*, 3515-3525.

58. Evans, D. F.; Sheriff, T. S., *J. Chem. Soc., Chem. Commun.* **1985**, 1407-1408.

59. Sheriff, T. S., *J. Chem. Soc., Dalton Trans.* **1992**, 1051-1058.

60. Formosinho, S.; Barroso, M., *Proton-Coupled Electron Transfer*. The Royal Society of Chemistry: Cambridge, UK, 2012.

61. Perry, J. J. P.; Shin, D. S.; Getzoff, E. D.; Tainer, J. A., *BBA - Proteins and Proteomics* **2010,** *1804*, 245-262.

62. Neese, F., *Wiley Interdisciplinary Reviews: Computational Molecular Science* **2012,** *2*, 73-78.

63. Vosko, S. H.; Wilk, L.; Nusair, M., *Can. J. Phys.* **1980,** *58*, 1200-1211.

64. Lee, C.; Yang, W.; Parr, R. G., *Phys. Rev. B* **1988,** *37*, 785-789.

65. Becke, A. D., *J. Chem. Phys.* **1993,** *98*, 5648-5652.

66. Becke, A. D., *J. Chem. Phys.* **1993,** *98*, 1372-1377.

67. Stephens, P. J.; Devlin, F. J.; Chabalowski, C. F.; Frisch, M. J., *J. Phys. Chem.* **1994,** *98*, 11623-11627.

68. Schäfer, A.; Horn, H.; Ahlrichs, R., *J. Chem. Phys.* **1992,** *97*, 2571-2577.

69. Weigend, F.; Ahlrichs, R., *Phys. Chem. Chem. Phys.* **2005,** *7*, 3297-3305.

70. Izsák, R.; Neese, F., *J. Chem. Phys.* **2011,** *135*, 144105.

71. Grimme, S.; Antony, J.; Ehrlich, S.; Krieg, H., *J. Chem. Phys.* **2010,** *132*, 154104.

72. Grimme, S.; Ehrlich, S.; Goerigk, L., *J. Comput. Chem.* **2011,** *32*, 1456-1465.

73. Cossi, M.; Rega, N.; Scalmani, G.; Barone, V., *J. Comput. Chem.* **2003,** *24*, 669-681.

74. Sawyer, D. T.; Sobkowiak, A.; Roberts, J. L., *Electrochemistry for Chemists*. 2nd ed.; John Wiley & Sons, Inc.: New York, 1995.

Chapter 3

Dioxygen Reduction to Hydrogen Peroxide by a Molecular Mn Complex: Mechanistic Divergence Between Homogeneous and Heterogeneous Reductants

Reproduced with permission from Hooe, S. L.; Machan, C. W., *Journal of the American Chemical Society* **2019,** *141* (10), 4379-4387. Copyright 2019 American Chemical Society.

Hooe, S. L.; Machan, C. W., *Journal of the American Chemical Society* **2019,** *141* (10), 4379-4387. https://pubs.acs.org/doi/10.1021/jacs.8b13373

3.1 Abstract

The selective electrocatalytic reduction of dioxygen (O_2) to hydrogen peroxide (H_2O_2) could be an alternative to the anthraquinone process used industrially, as well as enable the on-demand production of a useful chemical oxidant, obviating the need for long-term storage. There are challenges associated with this, since the two proton/two electron reduction of H_2O_2 to two equivalents of water (H_2O) or disproportionation to O_2 and H_2O can be competing reactions. Recently, we reported a Mn(III) Schiff base-type complex, Mn(^{tbu}dhbpy)Cl, where 6,6′-di(3,5-di-*tert*-butyl-2-phenolate)-2,2′-bipyridine = [^{tbu}dhbpy]$^{2-}$, that is active for the electrocatalytic reduction of O_2 to H_2O_2 (ca. 80% selectivity). The less-than-quantitative selectivity could be attributed in part to a thermal disproportionation reaction of H_2O_2 to O_2 and H_2O. To understand the mechanism in greater detail, spectrochemical stopped-flow and electrochemical techniques were employed to examine the catalytic rate law and kinetic reaction parameters. Under electrochemical conditions, the catalyst produces H_2O_2 by an *ECCEC* mechanism with appreciable rates down to overpotentials of 20 mV and exhibits a catalytic response with a strong dependence on proton donor pK_a. Mechanistic studies suggest that under spectrochemical conditions, where the homogeneous reductant decamethylferrocene (Cp^*_2Fe) is used, H_2O_2 is instead produced via a disproportionation pathway, which does not show a strong acid dependence. These results demonstrate that differences in mechanistic pathways can occur for homogeneous catalysts in redox processes, dependent on whether an electrode or homogeneous reductant is used.

3.2 Introduction

Molecular manganese (Mn) compounds are known to have profound reactivity with dioxygen (O_2) in solution under relatively mild conditions.[1-8] The pool of reported homogeneous Mn-based electrocatalysts for O_2 reduction is limited relative to other first-row transition metals[9-22], with a noteworthy recent report by Nocera, Constentin and co-workers on Mn porphyrins in non-aqeuous conditions.[23] This is conspicuous, given the well-known functions of mononuclear non-heme Mn-dependent enzymes in mediating redox transformations with O_2.[24] A common feature for the catalytic behavior of non-heme active sites is a preference for hydrogen peroxide (H_2O_2; a two-electron/two-proton reduction product) over water (H_2O; a four-electron/four-proton reduction product). Specificity for H_2O_2 can be challenging to achieve for molecular catalysts: the four electron/four proton reduction of O_2 to H_2O can occur as a '2+2' mechanism with H_2O_2 as an intermediate, rather than a concerted $4H^+/4e^-$ transformation. The differentiation between a 2+2 mechanism and concerted H_2O_2 production is described in detail in the recent report on Mn(porphyrins) under non-aqueous conditions mentioned above.[23] It is also worth mentioning that Stahl, Mayer, Hammes-Schiffer and co-workers have published extensively on the mechanism and activity of molecular Schiff base cobalt compounds for the selective electrocatalytic reduction of O_2 to H_2O_2.[25-28]

In a recent report[29], we described the electrocatalytic behavior of Mn(^{tbu}dhbpy)Cl **1**, where 6,6′-di(3,5-di-*tert*-butyl-2-phenolate)-2,2′-bipyridine = [^{tbu}dhbpy]$^{2-}$, with respect to the reduction of O_2 to H_2O_2 (ca. 80% selectivity). In the presence of weak Brønsted acids like phenol (PhOH), 2,2,2-trifluoroethanol (TFE), and buffered pentafluorophenol (F_5PhOH), significant electrocatalytic activity was observed. The phrase 'buffered' here describes reaction conditions where equimolar concentrations of the phenolate anion and the phenol are used, such that the effects of homoconjugation in non-aqeuous solvents are mitigated. *Nota bene*, the electrochemical mechanism was characterized with a first-order dependence on proton donor, O_2 and catalyst concentrations. We noted through preliminary experiments with stopped-flow spectrochemical methods that rapid reactivity occured between the chemically prepared $[Mn(^{tbu}dhbpy)]^0$ (Mn(II) oxidation state) and O_2, as well as between $Mn(^{tbu}dhbpy)Cl$ (Mn(III) oxidation state) and potassium superoxide (solubilized in MeCN as $[K(18\text{-crown-}6)^+][O_2^{\bullet-}]$).

As a part of our ongoing exploration of the catalytic behavior of $Mn(^{tbu}dhbpy)Cl$ **1**, spectrochemical methods have been used to examine the proposed catalytic cycle using decamethylferrocene, Cp^*_2Fe, as a reductant. Variable-temperature methods were used to extract kinetic parameters through Eyring analysis. These results, along with new electrochemical experiments, suggest that the catalytic mechanism proceeds via different pathways under electrocatalytic conditions than with a chemical reducing agent. With Cp^*_2Fe as a reducing agent, superoxide disproportionation to generate H_2O_2 occurs in a manner that is independent of proton donor pK_a. By comparison, the pK_a dependence of the electrocatalytic rate constant (k_{cat}) is consistent with an *ECCEC* mechanism for H_2O_2 production where reduction of a Mn-superoxide intermediate is coupled to an exogenous protonation reaction.[30] Additional stopped-flow and electrochemical experiments examining the role of proton donor sterics are consistent with these interpretations. Thermochemical and DFT analyses suggest that while hydrogen atom transfer (HAT) mechanisms are energetically feasible under certain conditions, these pathways are inconsistent with experimental observations.

3.3 Stopped-Flow Spectrochemical Results with Un-Buffered Proton Donors

Variable concentration stopped-flow spectrochemical studies were initially used to characterize the reduction of O_2 to H_2O_2 by Mn(^{tbu}dhbpy)Cl **1** (**Figure 3.3.1**) with Cp^*_2Fe as a reducing agent and unbuffered PhOH as a proton donor (**Figures S3.3.1-S3.3.8**). These data were consistent with first order dependences on [PhOH], [O_2], and [catalyst]. Although the experimental results match our previously reported electrochemically derived kinetic parameters **Eq (3.3.1)**, further testing and thermochemical analysis suggests this reflects a different rate-determining step for a divergent reaction mechanism, *vide infra*.[29] These variable concentration studies were conducted in a range where changes in [Cp^*_2Fe] did not impact the observed catalytic rate constant (**Figure S3.3.1** and **S3.3.5**).[20-21] Similar third-order rate constants are obtained from these experiments (**Table 3.3.1**) and subsequent Eyring analyses suggest insignificant differences between experiments with and without constant ion concentration (**Table 3.3.1, Figures S3.3.9-S3.3.10**). The slight overall enthalpic barriers ($\Delta H^{\ddagger}$ = 7.82 kcal mol^{-1} and 6.85 kcal mol^{-1} for experimental conditions with no electrolyte and with 0.1 M $TBAPF_6$, respectively) equate to low reaction barriers (~3 kcal mol^{-1}) at room temperature with favorable entropic parameters. Catalytic H_2O_2 production with Cp^*_2Fe and unbuffered PhOH was verified using spectrophotometric methods (**Figures S3.3.11-S3.3.12**).[25]

$$rate = k_{cat}[catalyst]^1[acid]^1[O_2]^1 \qquad \textbf{Eq (3.3.1)}$$

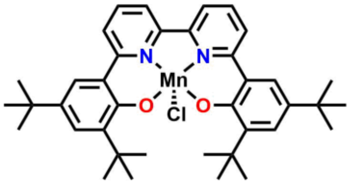

1

Figure 3.3.1. Structure of the Mn(^{tbu}dhbpy)Cl **1**, which shows catalytic activity for the reduction of O_2 to H_2O_2 in MeCN under reducing conditions in the presence of a proton donor.

Table 3.3.1. Catalytic rate constants (k_{cat}) and Eyring parameters for the Reduction of O_2 by Mn(^{tbu}dhbpy)Cl **1**, with Unbuffered PhOH as a Proton Donor.

Varied Substrate	**catalytic rate constant, k_{cat} ($M^{-2}s^{-1}$); no electrolyte**	**catalytic rate constant, k_{cat} ($M^{-2}s^{-1}$); 0.1 M $TBAPF_6$**	**Eyring Parameter**	**no electrolyte**	**0.1 M $TBAPF_6$**
PhOH	5.79 x 10^9	1.07 x 10^{10}	**ΔH‡ (kcal mol^{-1})**	7.82	6.85
Catalyst	2.10 x 10^{10}	1.97 x 10^{10}	**ΔS‡ (cal $mol^{-1}K^{-1}$)**	15.4	13.1
O_2	1.18 x 10^{10}	1.26 x 10^{10}	**ΔG‡ (kcal mol^{-1})**	3.25	2.94
Cp^*_2Fe	N.A.	N.A.			
Average	1.3 x 10^{10} (±0.4)	1.4 x 10^{10} (±0.4)			

* - all Gibbs free energy values calculated at 298 K.

3.4 Electrocatalytic Results with Buffered Proton Donors

Mayer and co-workers have detailed some important considerations relevant to studying ORR by homogeneous catalysts under non-aqueous conditions electro- and spectrochemically.[31] Their suggestions address two practical concerns: (1) homoconjugation of proton donors in non-aqueous solvents and (2) the exact value of the standard potential for ORR through its Nernstian relationship with the reaction equilibrium constant, K_{eq}. In our previous report[29], buffered F_5PhOH (where equimolar amounts of F_5PhO^- and F_5PhOH are present in solution) was used to determine the electrochemical rate constants, but we were intrigued by the necessity of using F_5PhOH (pK_a(MeCN) = 20.11[32]) under buffered conditions to achieve similar electrocatalytic behavior to that observed for unbuffered PhOH (pK_a(MeCN) = 29.14[33]). We also noted in our original report that minimal electrocatalytic activity was observed using buffered PhOH. This result is unsurprising: calculating the standard potential of ORR with buffered PhOH using **Eq (3.4.2)** shows that the catalyst ($E_{1/2}$ = -0.63 V vs Fc^+/Fc) is at 0.42 V *under*potential for O_2 reduction to H_2O_2 in these conditions (E^0 = -1.05 V vs Fc^+/Fc). Under non-buffered conditions, however, the significant homoconjugation equilibrium constant for PhOH in MeCN (log $K_f(AHA^-)_{MeCN}$ = 4.2)[31] will have a profound effect on lowering the effective pK_a of the proton donor, enabling catalytic current.

$$O_{2(g)} + 2HA_{(MeCN)} + 2e^- \rightleftharpoons H_2O_{2(MeCN)} + 2A^-$$

$$E^0 = [0.68 - 0.0592\mathrm{p}K_{\mathrm{a(MeCN)}}(HA)] \qquad \textbf{Eq (3.4.2)}$$

The pK_a values of a variety of phenol derivatives have been reported, so it is straightforward to identify a proton donor to test at the approximate point of zero overpotential for **1**. Considering **Eq (3.4.2)**, the electrocatalytic reduction of O_2 to H_2O_2 will occur with zero overpotential at ~pK_a(MeCN) = 23 for a catalyst with $E_{1/2}$ = ~-0.68 V vs Fc^+/Fc.[31] For consistency with acid type and a relevant pK_a range in MeCN, we used a series of phenol-derived proton donors, which are anionic when deprotonated. Using buffered solutions of F_5PhOH, 2-nitrophenol (2-NO_2-PhOH), and 4-trifluoromethylphenol (4-CF_3-PhOH), reaction conditions are obtained where the electrocatalyst is operating at 160 mV overpotential, 20 mV overpotential, and 80 mV underpotential, respectively, for the reduction of O_2 to H_2O_2 (**Table 3.4.2**).

Although the trend in the observed $E_{1/2}$ redox potential with respect to buffered proton donor pK_a approximately follows that expected for the redox-induced protonation of the ligand O atom we described previously[29], we note that a competing equilibrium association reaction between the anionic phenolate and **1** is likely under buffered conditions. Shifts in the observed $E_{1/2}$ value and quasi-reversibility of the Mn(III)/(II) reduction can then be attributed in part to presumptive displacement of the axial chloride ligand (**Table 3.4.2**). There is a statistically significant shift in the charge transfer coefficient α between the nominally aprotic redox response and the three proton-buffered conditions under Ar, suggesting an increased symmetry of the conversion coefficient between electrical and chemical energy (**Table S3.4.1**).[34] Further analysis of the logarithmic relationship between scan rate and the peak reduction potential under Ar saturation with the buffered proton donors suggests that an *EC* process also contributes to the quasi-reversibility of the Mn(III)/(II) reduction (**Figure S3.4.16**).[35-36]

Table 3.4.2. Tabulated experimental and thermochemical values for Mn(^{tbu}dhbpy)Cl **1**.

Buffered Proton Donor	**pK_a(MeCN)**	**ORR Standard Potential**	**ΔΔG at Standard Potential^C**	**$E_{1/2}$(catalyst)^D**	**Overpotential (ORR – $E_{1/2}$)^E**	**TOF (s^{-1})^F**	**catalytic rate constant, k_{cat} ($M^{-2}s^{-1}$)^G**
F_5PhOH	20.11^A	-0.51 V	-7.55 kcal mol^{-1}	-0.67 V	160 mV	17.4	2.76 x 10^5
2-NO_2-PhOH	22.85^A	-0.67 V	-0.859 kcal mol^{-1}	-0.69 V	20 mV	7.82	1.24 x 10^5
4-CF_3-PhOH	24.9^B	-0.79 V	3.87 kcal mol^{-1}	-0.71 V	-80 mV	-	-

^{A} – ref.[32]; ^{B} – ref.[37]; ^{C} – calculated using ΔΔG = -nF(ΔΔE), where ΔΔE = overpotential; ^{D} – determined in the presence of 10 mM buffered proton donor under Ar saturation conditions with 0.5 mM **1**; ^{E} – positive values represent an overpotential, negative values represent an underpotential, ^{F} – TOF obtained from $\frac{i_{cat}}{i_p}$ @ 1 V/s, see **Figures S3.4.23**. ^{G} – TOF/([O_2][acid]).

One way to compare these data is to calculate the relative Gibbs Free Energy at a given electrocatalytic potential, ΔΔG, using the ORR overpotential determined for *each individual set of experimental conditions*. This ΔΔG value represents the thermodynamic driving force for catalysis at the $E_{1/2}$ potential of the catalyst in the presence of the different buffered proton donors. When the buffered conditions are compared, an 11.4 kcal mol^{-1} difference is expected in the reaction driving force between F_5PhOH and 4-CF_3-PhOH at the respective $E_{1/2}$(catalyst). By using the known relationship of ΔG to ΔK_{eq}, this equates to a difference in the expected electrochemical equilibrium constant $\Delta\Delta K_{eq}$ of ~10^8 at 298 K.

Cyclic voltammetry (CV) experiments were performed with 10 mM of the buffered proton donor and 0.5 mM **1** in MeCN with 0.1 M $TBAPF_6$ as the electrolyte (**Figures S3.4.17-S3.4.22**). Under Ar saturation conditions, slight differences were observed in the Mn(III)/(II) reduction potential, which we ascribe to a combination of phenolate ion coordination to the Mn metal center and the protonation of the ligand O atoms, *vide supra* (**Figure 3.4.2A**).[29, 38] Under O_2 saturation conditions (6.3 mM in MeCN)[39] catalytic responses are observed with buffered F_5PhOH and 2-NO_2-PhOH (**Figure 3.4.2B**). Consistent with a kinetically limited catalytic response, the $\frac{i_{cat}}{i_p}$ ratio shows a linear scan rate dependence above 1 V/s for both conditions (**Figure S3.4.23**). Conversely, the observed current response is significantly diminished with buffered 4-CF_3-PhOH (**Figure 3.4.2B**), which is predicted to be at 80 mV of underpotential with respect to the standard reduction potential of O_2 to H_2O_2 (counterthermodynamic conditions). Using these data, a change in the electrocatalytic rate constant proportional to the thermochemical analysis above is observed: greater electrochemical driving force equates to greater TOF and therefore greater catalytic rate constant k_{cat} values (**Figure S3.4.23; Table 3.4.2**).[20] We propose that an *ECCEC* mechanism is occurring under electrocatalytic conditions, **Eq (3.4.3)-(3.4.7)**, where E_2^0 is at a more negative potential than E_1^0.[29-30] In these and the following equations, *L* = $[^{tbu}dhbpy]^{2-}$, *ROH* is a generic proton donor, and *(H)* is the association of a proton donor to the ligand framework, either as a protonation event or as a hydrogen-bonding interaction between the proton donor and the ligand O atom of the reduced Mn(II) species. In the latter case, proton transfer would occur from the resultant adduct.

$$[Mn^{III}(L)Cl]^0 + e^- \rightleftharpoons [Mn^{II}(L)Cl]^- \qquad E_1^0 \qquad \textbf{Eq (3.4.3)}$$

$$[Mn^{II}(L)Cl]^- + ROH \rightarrow [Mn^{II}(L(H))Cl]^0 + RO^- \qquad k_1 \qquad \textbf{Eq (3.4.4)}$$

$$[Mn^{II}(L(H))Cl]^0 + O_2 \rightarrow [Mn^{III}\big(L(H)\big)(O_2^{\bullet -})]^+ + Cl^- \qquad k_2 \qquad \textbf{Eq (3.4.5)}$$

$$[Mn^{III}\big(L(H)\big)(O_2^{\bullet -})]^+ + e^- \rightleftharpoons [Mn^{II}\big(L(H)\big)(O_2^{\bullet -})]^0 \qquad E_2^0 \qquad \textbf{Eq (3.4.6)}$$

$$[Mn^{II}\big(L(H)\big)(O_2^{\bullet -})]^0 + ROH \rightarrow [Mn^{III}(L)]^+ + H_2O_2 + RO^- \qquad k_3 \qquad \textbf{Eq (3.4.7)}$$

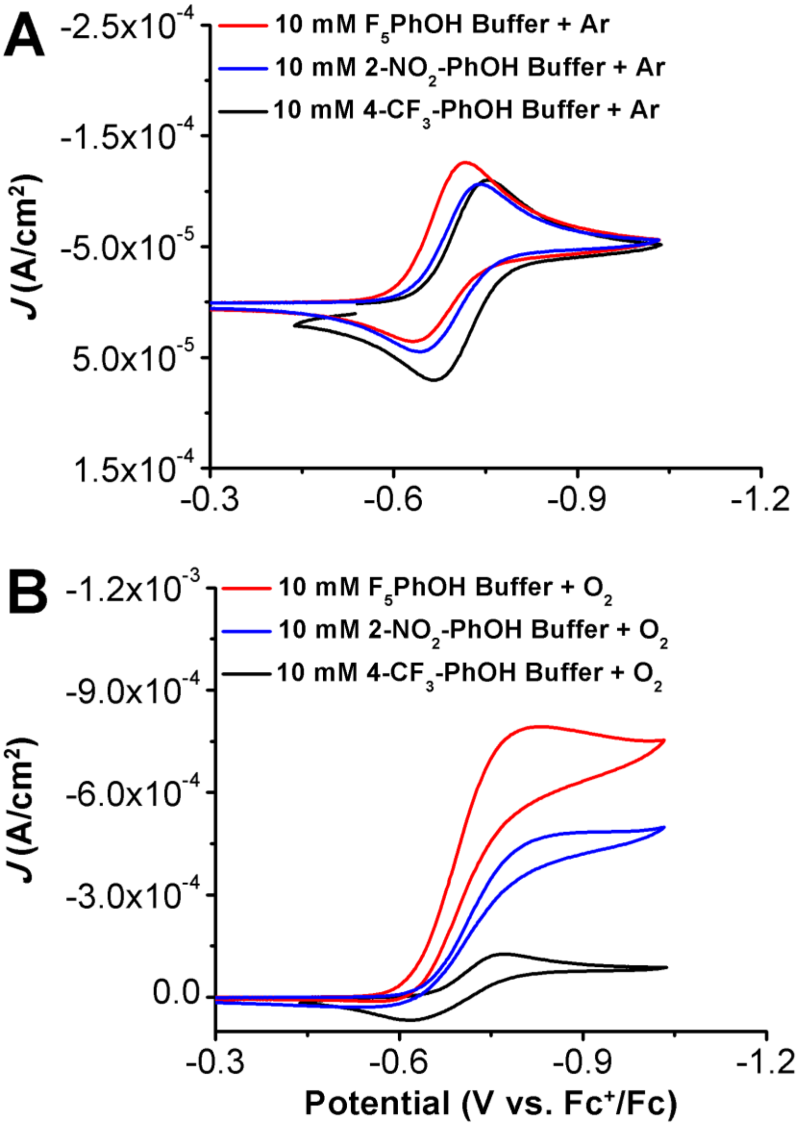

Figure 3.4.2. (A) CV response of Mn(^{tbu}dhbpy)Cl **1** under Ar saturation conditions with 10 mM of buffered F_5PhOH (red), 2-NO_2-PhOH (blue), and 4-CF_3-PhOH (black); **(B)** CV response of Mn(^{tbu}dhbpy)Cl **1** under O_2 saturation conditions (6.3 mM) with 10 mM of buffered F_5PhOH (red), 2-NO_2-PhOH (blue), and 4-CF_3-PhOH (black). Conditions: 0.5 mM **1**, 0.1 M $TBAPF_6$/MeCN; glassy carbon working electrode, glass carbon counter electrode, Ag/AgCl pseudoreference electrode, scan rate 100 mV/s; referenced to internal ferrocene standard.

3.5 Stopped-Flow Spectrochemical Results with Buffered Proton Donors

To understand the apparent relationship between pK_a(MeCN) of the buffered proton donor and the observed electrocatalytic response in greater detail, stopped-flow spectrochemical studies were conducted using Cp^*_2Fe as a reductant. Results were again obtained at variable temperatures and with varied concentrations of catalyst, reductant, and O_2 (**Figures S3.5.24-S3.5.38**). The use of increased buffer concentrations was observed to have a suppressive effect (**Figures S3.5.27, S3.5.31, S3.5.35**). The final experimental conditions were chosen where the reaction showed no dependence on Cp^*_2Fe (**Figures S3.5.24, S3.5.28,** and **S3.5.32**) and first-order dependence on catalyst and O_2 to compare with the previous results (**Figures S3.5.25-S3.5.26, S3.5.29-S3.5.30, S3.5.33-S3.5.34**). Unexpectedly, the observed third-order catalytic rate constants, k_{cat}, were within error of one another *for all three buffered proton donors* (**Table 3.5.3** and **Table S3.5.2**). This is in contrast to the electrochemical studies described above, where the observed catalytic current, which is related to the electrocatalytic rate constant, differs significantly between systems operating at over- and underpotentials with respect to the standard potential for the reduction of O_2 to H_2O_2. The absence of a pK_a effect on the catalytic rate constants suggests that a different mechanism is operative with a homogeneous reductant than under electrocatalytic conditions.

Table 3.5.3. ORR Standard Potentials, Spectrochemically Derived Catalytic Rate Constants, Calculated O–H BDFEs and Catalyst $E_{1/2}$ with 10 mM Buffered Proton Donor.

Proton Donor	**$BDFE_{MeCN}$(O–H)^A**	**catalytic rate constant, k_{cat} ($M^{-2}s^{-1}$)^B**	**Effective BDFE (-0.51 V vs Fc^+/Fc)^C**	**Effective BDFE $E_{1/2}$(catalyst)^D**
F_5PhOH	83.7 kcal mol^{-1}	4 x 10^{12} (±1)	70.7 kcal mol^{-1}	66.9 kcal mol^{-1}
2-NO_2-PhOH	94.3 kcal mol^{-1}	4 x 10^{12} (±2)	74.4 kcal mol^{-1}	70.3 kcal mol^{-1}
4-CF_3-PhOH	91.5 kcal mol^{-1}	6.7 x 10^{12} (±0.9)	77.3 kcal mol^{-1}	72.7 kcal mol^{-1}

^{A} – ORCA 4.0.1, CPCM(MeCN), B3LYP/G, def2-TZVP; ^{B} – determined spectrochemically; ^{C} – BDFE calculated using Cp^*_2Fe as a reductant; ^{D} – BDFE calculated from catalyst $E_{1/2}$ in the presence of 10 mM buffered proton donor under Ar saturation conditions

Analysis of the variable temperature data through Eyring analysis (**Figures S3.5.36-S3.5.38**) showed that at standard conditions, there is a narrow distribution in the Gibbs free energy of the reaction barrier (**Table 3.5.4**). *No trend in kinetic parameters based on pK_a(MeCN) is apparent, suggesting that protonation reactions involving the proton donor* *do not dominate the reaction parameters for Mn superoxide formation*, **Eq (3.4.5)**. We note that further reduction of a metal-bound superoxide to peroxide is unlikely to occur rapidly with Cp*$_2$Fe as a reductant under these conditions.[40] However, H_2O_2 production with Cp$^*{}_2$Fe and buffered proton donors was verified using spectrophotometric methods (**Figures S3.5.13-S3.5.15**). Based on these data, we propose that the final step of the mechanism has shifted to a disproportionation of a Mn-bound superoxide species as summarized in **Eq (3.5.8)**. The kinetic analysis of the spectrochemical reaction, **Eq (3.3.1)**, suggests that k_4 is not the rate-determining step.

$$[Mn^{III}(L(H))(O_2^{\bullet-})]^+ \rightarrow Mn^{III}(L) + 0.5\ H_2O_2 + 0.5\ O_2 \qquad k_4 \qquad \textbf{Eq (3.5.8)}$$

Table 3.5.4. Eyring Parameters for O_2 reduction with buffered proton donors from spectrochemical experiments.

	F_5PhOH	**2-NO_2-PhOH**	**4-CF_3-PhOH**
pK_a(MeCN)	20.11[A]	22.85[A]	24.9[B]
ΔH‡ (kcal mol^{-1})	7.60	6.71	8.85
ΔS‡ (cal mol^{-1}K^{-1})	26.7	23.7	31.1
ΔG‡ (kcal mol^{-1})	-0.353	-0.348	-0.420

* - all Gibbs free energy values calculated at 298 K. [A] – ref.[32]; [B] – ref.[37]

A thermochemical analysis of the reaction conditions was also conducted to assess whether the reductant and proton donor combinations were facilitating proton-coupled electron transfer (PCET) reactions under these conditions (**Table 3.5.3**). BDFE values were calculated for the three proton donors using DFT methods and effective BDFE for reductant/proton donor pairs were calculated using **Eq (3.5.9)**, where C_G = 54.9 kcal mol^{-1} in MeCN.[33]

$$BDFE_{MeCN}(X-H) = 1.37\mathrm{p}K_\mathrm{a} + 23.06E^0 + C_G \qquad \textbf{Eq (3.5.9)}$$

DFT calculations on the OO–H BDFE for hydroperoxide bound to the Mn(III) catalyst, (Mn^{III}(^{tbu}dhbpy)(OO–H)), were predicted to range from 73.7 to 76.4 kcal mol^{-1} (value is dependent on product spin state and O_2 coordination mode, see SI). Based on these values, HAT involving the proton donors (O–H BDFEs > 83 kcal mol^{-1}; **Table 3.5.3**) and Mn-bound superoxide is not a thermodynamically favored reaction pathway. HAT reactions were found to not the dominant contributor to catalytic activity in spectrochemical experiments with TTBP as a $H^{\bullet}$ source, *vide infra*. For a PCET pathway, all proton donor/reductant combinations are viable, if it is assumed that a negligible difference exists between the largest calculated OO–H BDFE of 76.4 kcal mol^{-1} and the derived value of 77.3 kcal mol^{-1} determined for buffered 4-CF_3-PhOH (pK_a(MeCN) = 24.9) when Cp^*_2Fe is the reductant. Under the most conservative assumption, however, the reaction would be at best isoergic, requiring that the final protonation step and release of hydrogen peroxide be thermodynamically favorable for catalytic turnover to occur. The near identical catalytic rate constants obtained experimentally suggest that this thermochemical relationship does not define O–H bond formation in the Mn-bound hydroperoxide with Cp^*_2Fe as the reductant.

3.6 Electrochemical and Stopped-Flow Results with a Sterically Hindered Proton Donor

The results discussed to this point suggest a difference in mechanism between electrocatalytic experiments and catalytic experiments with a homogeneous reductant. To probe this divergence further on the basis of steric parameters and proton donor bond-dissociation free energy (BDFE), we repeated the unbuffered acid experiments with 2,4,6-tri-*tert*-butylphenol (TTBP) (**Figures S3.6.39-S3.6.43**), which has a similar pK_a(MeCN) to

PhOH (28 and 29.14, respectively)[33, 41], but a significantly different steric profile. The O–H BDFE of TTBP is also weaker than PhOH by 8-9 kcal mol^{-1} and hydrogen atom transfer (HAT) from TTBP produces a radical with a diagnostic electronic absorbance spectrum.[33, 42] If HAT contributed to the overall mechanism, it would be possible to observe spectroscopically during stopped-flow experiments with TTBP, **Eq (3.5.10)**. By monitoring the appearance of the 2,4,6-tri-*tert*-butylphenoxyl radical at 626 nm (**Figures S3.6.44-S3.6.45**), the observed rate of O_2 reduction, k_{obs}, corresponding to the HAT pathway was determined to be 1.41 s^{-1}. By comparison, the rate of O_2 reduction as determined by the appearance of $[Cp^*_2Fe]^+$ at 778 nm under the same conditions was ~870 times faster at similar concentrations of TTBP (k_{obs} = 1.22 x 10^3 s^{-1}), indicating a minimal contribution of HAT reactivity by TTBP, **Eq (3.6.10)**.

$$[Mn^{III}(L(H))(O_2^{\bullet -})]^+ + ROH \rightarrow Mn^{III}(L)(O_2H) + RO^\bullet \qquad \textbf{Eq (3.6.10)}$$

Consistent with the results for buffered proton donors discussed above, spectrochemical rapid-mixing experiments using TTBP yielded third-order rate constants with remarkable agreement with the unbuffered PhOH data in MeCN with 0.1 M $TBAPF_6$ (**Table 3.6.5** and **Table S3.6.3**). Similar kinetic parameters were also obtained by Eyring analysis (**Table 3.6.5**), suggesting the absence of a steric effect in catalytic H_2O_2 formation under these conditions.

Table 3.6.5. Catalytic rate constants and Eyring parameters for the Reduction of O_2 by Mn(^{tbu}dhbpy)Cl, **1**, with Unbuffered TTBP as a Proton Donor.

Varied Substrate	**Catalytic rate constant, k_{cat} ($M^{-2}s^{-1}$); 0.1 M TBAPF$_6$**	**Eyring Parameter**	**0.1 M TBAPF$_6$**
TTBP	2.06 x 10^9	**ΔH‡ (kcal mol^{-1})**	8.34
Catalyst	1.26 x 10^{10}	**ΔS‡ (cal mol^{-1}K^{-1})**	18.2
O_2	1.06 x 10^{10}	**ΔG‡ (kcal mol^{-1})**	2.91
Cp$^*_2$Fe	N.A.		
Average	8.4 x 10^9 (±5)		

* - all Gibbs free energy values calculated at 298 K.

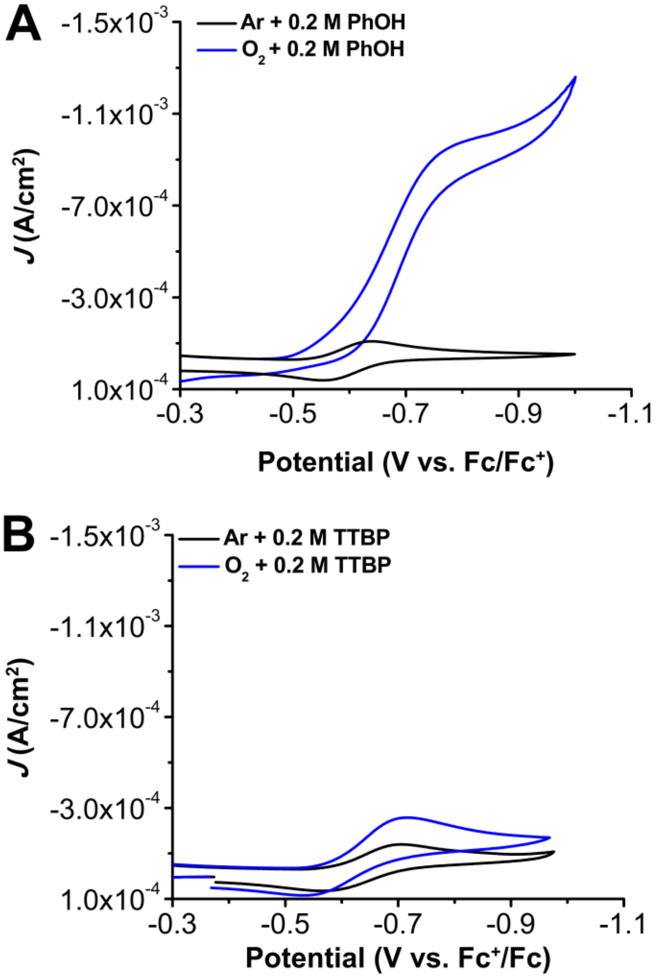

Figure 3.6.3. (A) CV response of Mn(^{tbu}dhbpy)Cl **1** under Ar (black) and O_2 (blue) saturation conditions with 0.2 M of PhOH **(B)** CV response of Mn(^{tbu}dhbpy)Cl **1** under Ar (black) and O_2 (blue) saturation conditions with 0.2 M of TTBP. Conditions: 1 mM **1**, 0.1 M TBAPF$_6$/MeCN; glassy carbon working electrode, glass carbon counter electrode, Ag/AgCl pseudoreference electrode, scan rate 100 mV/s; referenced to internal ferrocene standard.

CV experiments were also undertaken with unbuffered TTBP to compare with the spectrochemical results discussed above. It is worth noting that the steric constraints of TTBP inhibit its ability to homoconjugate and form hydrogen-bonding interactions.[43] In unbuffered solutions it cannot be discounted that the effective $pK_a(MeCN)$ of PhOH and TTBP are significantly different because of an unquantified difference in $K_f(AHA^-)_{MeCN}$. Simply, the data obtained by CV shows an inhibition of electrocatalytic current when TTBP (**Figure 3.6.3B**) is substituted for PhOH (**Figure 3.6.3A**) under otherwise identical conditions. At a minimum, this result is consistent with a difference in mechanism between the chemical and electrochemical reactions. The most straightforward explanation is that the rate of superoxide disproportionation **Eq (3.5.8)** is significant only when homogeneous reductants are used. This can be summarized as the difference between the diffusion-limited response of catalyst and homogeneous reductants in comparison to the *ECCEC* mechanism **Eq (3.4.3)-(3.4.7)** possible in the electrode double-layer.

3.7 Discussion of Proposed Mechanism

These data allow us to propose complete catalytic cycles for the reaction when driven either chemically or electrochemically, with a point of divergence following the formation of the superoxide adduct $[Mn^{III}(L(H)(O_2^{\bullet-})]^+$, **Figure 3.7.4**. In both cases, E_1^0, the initial one-electron reduction of **1**, generates a five-coordinate anionic intermediate, $[Mn^{III}(L)Cl]^-$. Subsequent protonation (k_1) and O_2 binding with chloride loss (k_2) generates the superoxide intermediate species common to both cycles, $[Mn^{III}(L(H)(O_2^{\bullet-})]^+$. The mechanistic data presented here and that we have reported previously,[29] indicate that the electrochemical catalytic cycle conforms to an overall *ECCEC* mechanism, where E_1^0 is at more positive (less reducing) potentials than E_2^0. Consistent with this, abstracting the chloride ligand from **1** and testing proton donors with higher p*K*a's revealed a pre-wave feature to the catalytic wave which is assigned to the formation of $[Mn^{III}(L(H)(O_2^{\bullet-})]^+$.[29] Following the E_2^0 reduction, a subsequent concerted protonation and electron transfer reaction k_3 generates H_2O_2; mass balance is achieved through a proton transfer reaction from the protonated Mn-bound O atom. Based on these data, k_3 represents the rate-determining step of the catalytic reaction and is the source of the observed p*K*a dependence, given the proposed role of the exogeneous proton donor in this step.

Conversely, the homogeneous reaction, where reducing equivalents are provided by Cp^*_2Fe, shows no p*K*a dependence. We ascribe this to the difference in E_1^0 and E_2^0: the reducing power of Cp^*_2Fe is invariant over the course of the reaction, meaning that the driving force for electron transfer from Cp^*_2Fe to the catalyst diminishes from E_1^0 to E_2^0. Under electrochemical conditions, conversely, the timescale of the CV experiment means that suitable potentials to drive the overall *ECCEC* reaction are quickly attained following the formation of $[Mn^{III}(L(H)(O_2^{\bullet-})]^+$, since the driving force for electron transfer is variable during the experiment. In the presence of Cp^*_2Fe, however, a disproportionation mechanism k_4 occurs (**Figure 3.7.4**). The mechanistic data reported here do not suggest that this is the rate-determining step, instead, the kinetic parameters suggest that k_2 **Eq(3.4.5)**, the O_2 binding step, is rate-determining since no p*K*a or $[Cp^*_2Fe]$ dependence is observed.

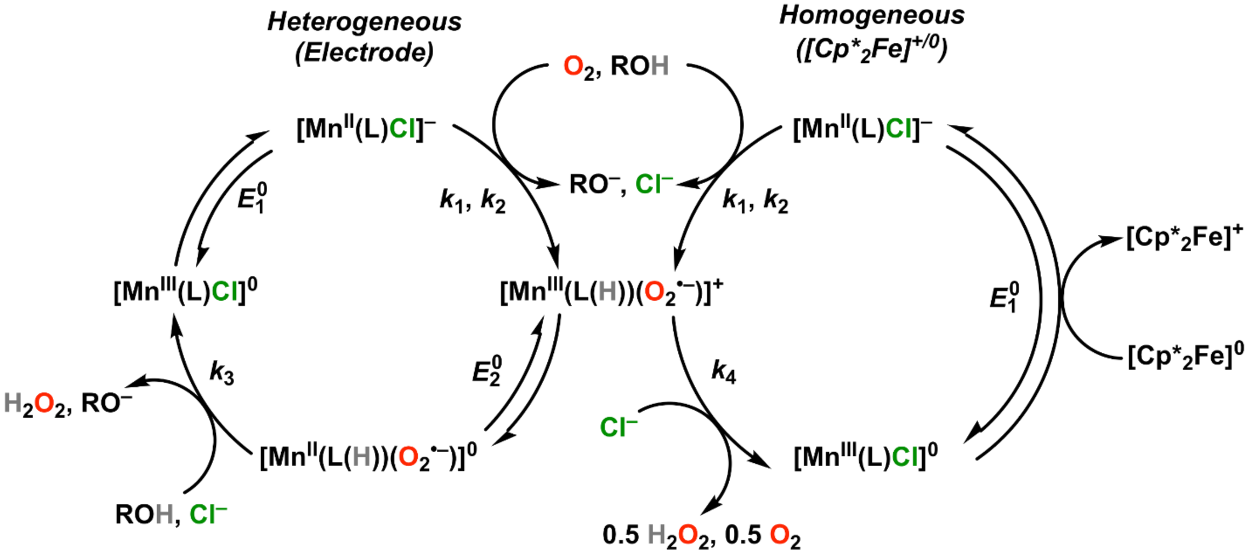

Figure 3.7.4. Proposed complete catalytic cycles for O_2 reduction driven by the electrode (heterogeneous) and driven by $Cp^*{}_2Fe$ (homogeneous); L = ^{tbu}dhbpy^{2-} and ROH = a generic proton donor.

3.8 Conclusion

In examining the kinetic and thermodynamic parameters of the ORR to H_2O_2 by **1**, we have encountered a mechanistic difference between catalytic systems driven via an electrode and that using $Cp^*{}_2Fe$ as a homogeneous reductant. In rapid-mixing spectrochemical studies, third-order rate constants were found to be nearly identical using buffered acids with pK_a(MeCN) ranging from ~20-25. Conversely, in electrocatalytic studies, catalysis occurs with a strong pK_a(MeCN) dependence and is generally consistent with a $2e^-/2H^+$ *ECCEC* pathway down to overpotentials of 20 mV. The absence of these pK_a(MeCN) effects on the experimentally observed catalytic response with $Cp^*{}_2Fe$ as a homogeneous reductant suggest that a disproportionation reaction pathway is occuring. The observation of divergent mechanisms for O_2 reduction when driven by homogeneous or heterogeneous reduction suggest that different reaction pathways can occur based on the choice of reductant when a reaction has multiple electrochemical reaction steps with different formal reduction potentials. Based on these results, further optimization of the ligand platform and reaction conditions to harness these effects and further isolate the point of divergence are currently underway.

3.9 Supporting Information

Materials and Methods

General.

All chemicals and solvents (ACS or HPLC grade) were commercially available and used as received unless otherwise indicated. Mn(^{tbu}dhbpy)Cl was prepared according to our previous report.[29] For all air-sensitive reactions and electrochemical experiments, HPLC-grade solvents were obtained as anhydrous and air-free from a PPT Glass Contour Solvent Purification System. Gas cylinders were obtained from Praxair (Ar as 5.0; O_2 as 4.0) and passed through activated molecular sieves prior to use. Gas mixing for variable concentration experiments was accomplished using a gas proportioning rotameter from Omega Engineering. UV-vis absorbance spectra were obtained on a Cary 60 from Agilent. HRMS data were obtained by the Mass Spectrometry Lab at the University of Illinois at Urbana-Champaign and elemental analyses were performed by Midwest Microlab. An Anton-Parr Multiwave Pro SOLV, NXF-8 microwave reactor was used for microwave syntheses.

Buffered Acid Synthesis.

All the buffered acids were synthesized in over 90% yield and characterized by ^{1}H NMR (**Figures S3.9.46-S3.9.48**) and elemental analysis.

General Experimental Procedure for TBA Buffered Acid Synthesis. A scintillation vial with threaded cap was charged with a stir bar under an N_2 atmosphere with one equivalent of acid. Tetra-*n*-butyl ammonium hydroxide (40% w/v, 5.0 mL, 7.63 mmol) was added with continuous stirring at room temperature. After 30 minutes, a second equivalent of acid was added and the solution was subsequently stirred for an additional hour. A biphasic separation formed and was chilled rapidly with liquid nitrogen (LN_2). Alternating between the cooling and sonication (approximately 1 minute LN_2 followed by 30 seconds of sonication) induced precipitation of a solid that was isolated by filtration. The isolated solid was washed with ice-cold deionized water (~30 mL) and dried overnight under high vacuum in a drying chamber. For acids with poor solubility in tetra-*n*-butyl ammonium hydroxide solution, some additional heating (up to 75 C°) was applied during synthesis to obtain the desired product.

Synthesis of 2-NO_2-PhOH Buffer. The orange-colored product was hygroscopic and was stored either in a glovebox or in a dessicator under active vacuum. Elemental Analysis for $C_{28}H_{45}N_3O_6$ Calc'd: C 64.71 H 8.73 N 8.09; Found: C 63.68 H 8.42 N 7.99. ^{1}H NMR (**Figure S3.9.46**) (*d*$_1$-$CDCl_3$, 600 MHz): δ 7.89 (m, 2H, ArH), 7.23 (m, 2H, ArH), 6.93 (m, 2H, ArH), 6.44 (m, 2H, ArH), 5.16 (br s, 1H, ArOH), 3.17 (m, 8H, R_3NCH_2–), 1.55 (m, 8H, –CH_2–), 1.34 (m, 8H, –CH_2–), 0.93 (m, 12H, –CH_3).

Synthesis of F_5PhOH Buffer. The white, solid product was both light and hygroscopic, so it was stored in the dark in either a glovebox or vaccum dessicator. Elemental Analysis for $C_{28}H_{37}F_{10}NO_2$ Calc'd: C 55.17 H 6.12 N 2.30; Found: C 54.81 H 6.22 N 2.30. ^{1}H NMR (**Figure S3.9.47**) (*d*$_1$-$CDCl_3$, 600 MHz): δ 14.54 (br s, 1H, ArOH), 3.13 (m, 8H, R_3NCH_2–), 1.56 (m, 8H, –CH_2–), 1.33 (m, 8H, –CH_2–), 0.91 (m, 12H, –CH_3).

Synthesis of 4-CF_3-PhOH Buffer. The light yellow product was hygroscopic, so it was stored either in a glovebox or vaccum dessicator. Elemental Analysis for $C_{30}H_{45}F_6NO_2$

Calc'd: C 63.70 H 8.02 N 2.48; Found: C 63.92 H 8.25 N 2.23. ^{1}H NMR (**Figure S3.9.48**) (d_1-$CDCl_3$, 600 MHz): δ 7.21 (m, 4H, ArH), 6.72 (m, 4H, ArH), 4.74 (s, 1H, ArOH), 2.82 (m, 8H, R_3NCH_2–), 1.31 (m, 8H, –CH_2–), 1.21 (m, 8H, –CH_2–), 0.85 (m, 12H, –CH_3).

Electrochemistry.

All electroanalytical experiments were performed using a Metrohm Autolab PGSTAT302N potentiostat. Glassy carbon working (⌀ = 3 mm) and non-aqueous silver/silver chloride pseudoreference electrodes behind PTFE tips were obtained from CH Instruments. The pseudoreference electrodes were obtained by depositing chloride on bare silver wire in 10% HCl at oxidizing potentials and stored in a 0.1 M tetrabutylammonium hexafluorophosphate/acetonitrile solution in the dark prior to use. The counter electrode was a glassy carbon rod (⌀ = 3 mm). All CV experiments were performed in a modified scintillation vial (20 mL volume) as a single-chamber cell with a cap modified with ports for all electrodes and a sparging needle. Tetrabutylammonium hexafluorophosphate ($TBAPF_6$) was purified by recrystallization from ethanol and dried in a vacuum oven before being stored in a desiccator. All data were referenced to an internal ferrocene standard (ferricenium/ferrocene reduction potential under stated conditions) unless otherwise specified. All voltammograms were corrected for internal resistance.

Computational Methods.

DFT calculations were performed on the Rivanna High-Performance Computing Cluster at the University of Virginia using ORCA 4.0.1.[44] Geometry optimizations were performed unrestricted with the B3LYP/G[45-49] functional and def2-TZVP[50-51] basis set with the RIJCOSX approximation[52], D3BJ dispersion correction[53-54], and CPCM[55] to model the MeCN solvent. Numerical frequency calculations at the same level of theory were performed to validate the optimized geometries as minima on the potential energy surface and to generate thermochemical data.

Stopped-Flow Spectrochemical Methods.

Stopped-flow rapid-mixing spectrochemical studies were performed with a CSF-61DX2 Stopped-Flow System from Hi-Tech Scientific with monitoring at a single wavelength using Kinetic Studio Software. All data fits were performed within the Kinetic Studio 4.0 Software Suite. Representative five-run datasets and corresponding averages are shown in **Figures S3.9.49-S3.9.56**. Prior to experiments, dried and degassed MeCN was passed through all syringes and the cell block before reagents were loaded. In a typical experiment, SGE air-tight syringes with Luer lock valves would be charged with known concentrations of reagent under air-free conditions in a glovebox or immediately prepared and loaded using solvent from the solvent purification system. All concentrations are reported as syringe concentrations, which halve upon mixing in the cell block during an experiment. The Mn(^{tbu}dhpbpy)Cl **1**, O_2, and proton donor-containing MeCN solutions were prepared immediately prior to use. All data fits were taken from five-run averages using a first-order exponential with a linear component. Linear fits were used for all catalytic rate constant values and averages of linear fit data from the individual variable concentration experiments were used to obtain standard deviations.

Previously we determined that under O_2 atmosphere in the presence of a proton source, the Mn(^{tbu}dhbpy)Cl **1** mediated an overall third-order catalytic reaction for the reduction of O_2.[29] The overall rate expression for the reaction was found to be:

$$k_{obs} = k_{cat}[O_2]^1[H^+]^1[catalyst]^1$$

Where k_{cat} is the catalytic rate constant (k_{cat} = 4.52 x 10^8 $M^{-2}s^{-1}$ from foot-of-the-wave analysis with 11 mM buffered pentafluorophenol as the proton donor), [O_2] is the concentration of oxygen, [H^+] is the proton donor and [*catalyst*] is the concentration of Mn($^{\text{tbu}}$dhbpy)Cl **1**.

Decamethylferrocene (Cp^*_2Fe) was found to be a suitable reductant for the Mn($^{\text{tbu}}$dhbpy)Cl **1**. Cp^*_2Fe in its oxidized form, decamethylferricenium ($[Cp^*_2Fe]^+$), displays a peak absorbance at 778 nm that was used to monitor the reaction in all the stopped-flow analyses. A two-syringe mixing experiment was used for all the stopped-flow studies described below. One syringe contained a solution of a known amount of Cp^*_2Fe in acetonitrile (MeCN). The second syringe contained a solution of the catalyst, O_2, and a proton source in MeCN. The mixing time was adjusted such that a plateau in the absorbance for $[Cp^*_2Fe]^+$ with respect to time could be observed.

For the spectrochemical reaction conditions, k_{obs} can be defined as:

$$k_{obs} = \frac{R_{fit}}{n_{cat} \ \times [O_2]}$$

where R_{fit} is the value obtained from fitting the data to a first exponential and n_{cat} is the number of electrons of Cp^*_2Fe per O_2 consumed (2.38 in the presence of a proton donor based on previous electrochemical experiments[29]). Thus, the change in the concentration of $[Cp^*_2Fe]^+$ can be determined from *R*. Dividing the change in $[Cp^*_2Fe]^+$ concentration by the value obtained from multipling the concentration of O_2 and n_{cat} is equal to the observed rate for O_2 reduction (k_{obs}) *as long as the concentration of O_2 is kept within a range where the reaction remains rate limiting with respect to O_2*.

If these conditions are met, an overall third-order rate law for the reaction described above is achieved that can be written as:

$$k_{obs} = k_{cat}[H^{+}]^{1}[catalyst]^{1}$$

This third-order rate law applies as long as the reaction remains independent of the concentration of $Cp^{*}_{2}Fe$ and rate limiting in the concentration of O_2. Therefore, initial studies began by attempting to find conditions where the observed rate (k_{obs}) varied linearly with increasing substrate concentration for all of the aboved described substrates except $Cp^{*}_{2}Fe$; the rate was determined to be invariant with respect to $[Cp^{*}_{2}Fe]$ in the presence and absence of tetrabutylammonium hexaflurophosphate ($TBAPF_6$) electrolyte.

By plotting k_{obs} versus the concentration of the experimentally varied substrate, the rate of the chemical reaction can be calculated.For instance, when the substrate being varied was O_2, the value of k_{obs} is equal to the R value obtained from fitting the data to a first exponential divided by n_{cat}. Rearranging the rate expression for calculating k_{cat} under these conditions becomes

$$\mathrm{k_{cat}} = \frac{\mathrm{slope}}{[\mathrm{catalyst}][\mathrm{H}^{+}]}$$

where [catalyst] and $[H^{+}]$ are fixed values experimentally. Similar expressions for varied [catalyst] and $[H^{+}]$ are readily obtained in an analogous manner.

Variable-Temperature Methods Summary.

Keeping the concentrations of the various substrates constant while varying the temperature enables the determination of the kinetic parameters for the reaction of interest using the Eyring equation. The Eyring equation can be used to calculate the thermodynamic values for the transition state of a reaction. The Eyring equation can be written as

$$ln\frac{k_{cat}}{T} = \frac{-\Delta H^{\ddagger}}{R}\left(\frac{1}{T}\right) + ln\frac{k_B}{h} + \frac{\Delta S^{\ddagger}}{R}$$

where R is the ideal gas constant, T is temperature, k_B is Boltzman's constant, h is Plank's constant, $\Delta H^{\ddagger}$ is the enthalpy, and $\Delta S^{\ddagger}$ is the entropy of the transition state. Plotting ln (k_{cat}/T) versus $1/T$ the entropy of the transition state of a reaction can be determined using the following equation

$$\Delta S^{\ddagger} = \left[(y - intercept) - \ln\left(\frac{k_B}{h}\right)\right] R$$

The enthalpy for the transition state of the reaction can be determined from the slope where

$$slope = \frac{-\Delta H^{\ddagger}}{R}$$

Using the Eyring equation above, along with obtaining k_{cat} values at varying temperatures, the values for entropy and enthalpy for the transition state can be determined. Using these values for enthalpy and entropy, the free energy of the transition state can then be calculated at any temperature.

H_2O_2 Calibration Curve.

Preparation of 0.1 M $Ti(O)SO_4$ Solution. Prepared from a modified procedure,[56] $Ti(O)SO_4$ (3.998 g, 25 mmol) was added to a 2.0 M solution of sulfuric acid (26.65 mL H_2SO_4 in 250 mL DI water) was made. The $Ti(O)SO_4$ had to be gently heated in order to completely dissolve all the solid.

Preparation of H_2O_2 Stock Solution. Urea hydrogen peroxide (25.1 mg) was dissolved in MeCN 30 mL to make a 3.22 mM solution. This solution served as the stock solution of hydrogen peroxide for the calibration curve.

Experimental Procedure for Calibration Curve. The solutions of varying H_2O_2 concentration were prepared from a modified procedure.[25] A total of eight concentrations were prepared to create a calibration curve for the quantification of hydrogen peroxide. Each solution was 10 mL of total volume with varying amounts of the hydrogen peroxide stock solution and MeCN. Of each 10 mL solution, 2 mL were used for the extraction. The extraction consisted of 2 mL of the calibration curve solution (described above), 5 mL of DI water, and 10 mL of DCM. The solution was extracted and 3 mL of the aqueous layer was put into the UV-Vis cuvette and then 0.1 mL of the $Ti(O)SO_4$ solution was added to the cuvette for each UV-Vis sample.

H_2O_2 Quantification Method.

The quantification of H_2O_2 was carried out following a previously reported procedure.[25] Each solution was 15 mL of MeCN in total volume with catalyst (Mn(^{tbu}dhbpy)Cl **1**), 0.1 M $TBAPF_6$, and an added proton donor. Each 15 mL solution was saturated with air for 12 minutes. This was a time course experiment and the time was started upon the addition of decamethylferrocene to the saturated solution. Data points were taken at various time points and each data point involved the removal to 2 mL of the 15 mL solution described above, to be used for extraction. The extraction consisted of 2 mL solution (described above), 5 mL of DI water, and 10 mL of DCM. The solution was extracted and 3 mL of the aqueous layer was put into the UV-Vis cuvette and then 0.1 mL of the $Ti(O)SO_4$ solution (described above) was added to the cuvette and a UV-Vis was taken of the sample. For each reaction solution, a background spectrum was also taken without the addition of the $Ti(O)SO_4$ solution.

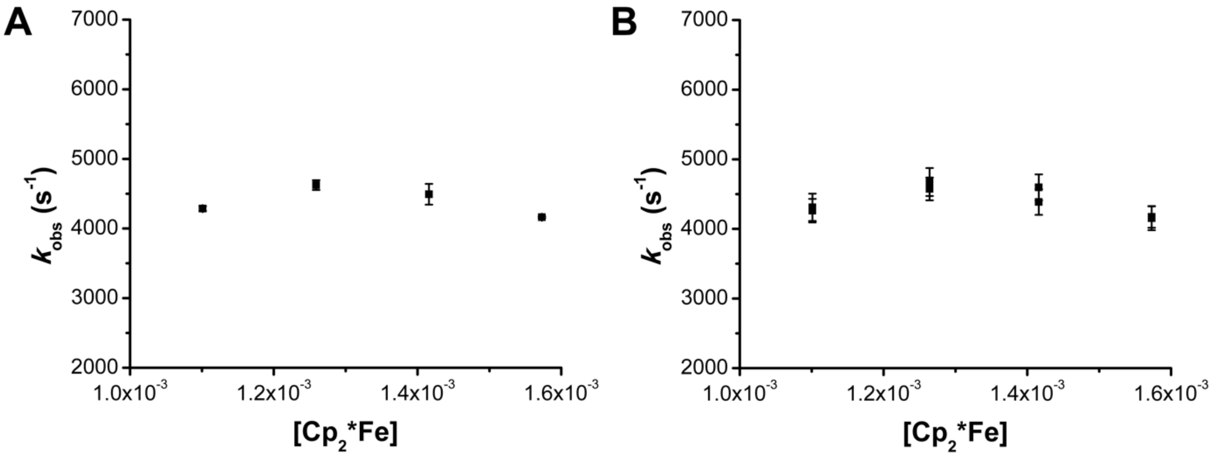

Figure S3.3.1. The calculated k_{obs} from stopped-flow spectrochemical experiments with PhOH, O_2 and Mn(^{tbu}dhbpy)Cl with varying Cp_2^*Fe concentration at 25.5°C in MeCN. Data were fit using Kinetic Studio 4.0 (1 Exp + Mx + C). Syringe concentrations: PhOH = 7.63 x 10^{-3} M; Mn(^{tbu}dhbpy)Cl = 4.91 x 10^{-5} M; O_2 = 9.64 x 10^{-4} M. Graph (A) represents all the series collected and the individual fits for each, while graph (B) represents the average of all the data points from graph (A).

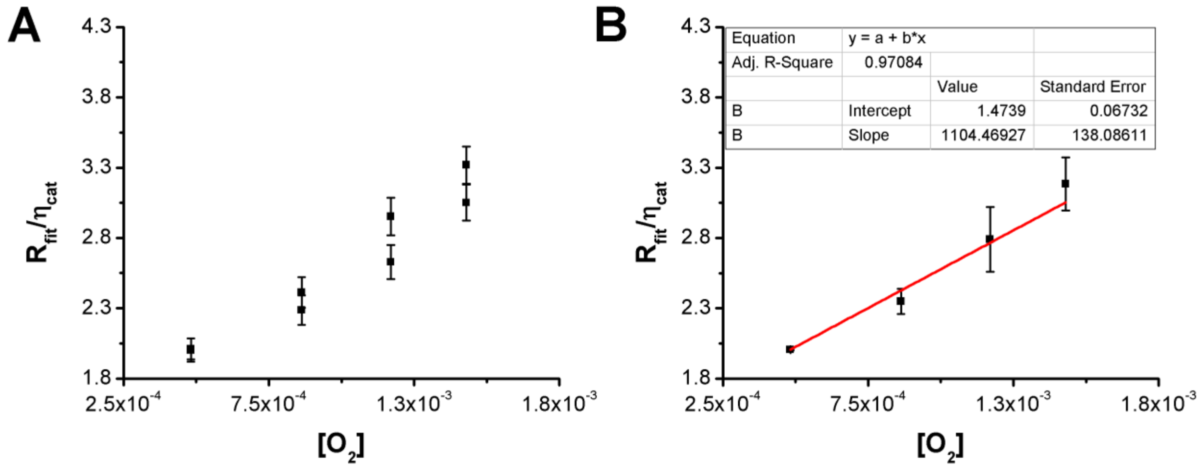

Equation	y = a + b*x		
Adj. R-Square	0.97084		
		Value	Standard Error
B	Intercept	1.4739	0.06732
B	Slope	1104.46927	138.08611

Figure S3.3.2. The calculated R_{fit}/η_{cat} from stopped-flow spectrochemical experiments with PhOH, Cp_2^*Fe and Mn(^{tbu}dhbpy)Cl with varying O_2 concentration at 25.5°C in MeCN. Data were fit using Kinetic Studio 4.0 (1 Exp + Mx + C). Syringe concentrations: PhOH = 7.63 x 10^{-3} M; Mn(^{tbu}dhbpy)Cl = 4.91 x 10^{-5} M; Cp_2^*Fe = 3.15 x 10^{-3} M. Graph (A) represents all the series collected and the individual fits for each, while graph (B) represents the average of all the data points from graph (A).

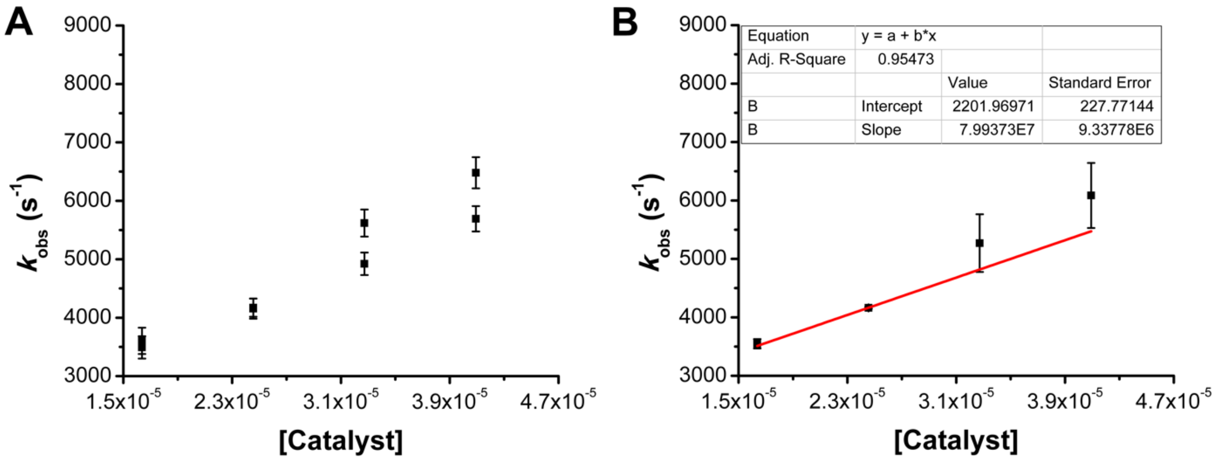

Equation	y = a + b*x		
Adj. R-Square	0.95473		
		Value	Standard Error
B	Intercept	2201.96971	227.77144
B	Slope	7.99373E7	9.33778E6

Figure S3.3.3. The calculated k_{obs} from stopped-flow spectrochemical experiments with PhOH, O_2 and Cp_2^*Fe with varying Mn(^{tbu}dhbpy)Cl concentration at 25.5°C in MeCN. Data were fit using Kinetic Studio 4.0 (1 Exp + Mx + C). Syringe concentrations: PhOH = 7.63 x 10^{-3} M; Cp_2^*Fe = 3.15 x 10^{-3} M; O_2 = 9.64 x 10^{-4} M. Graph (A) represents all the series collected and the individual fits for each, while graph (B) represents the average of all the data points from graph (A).

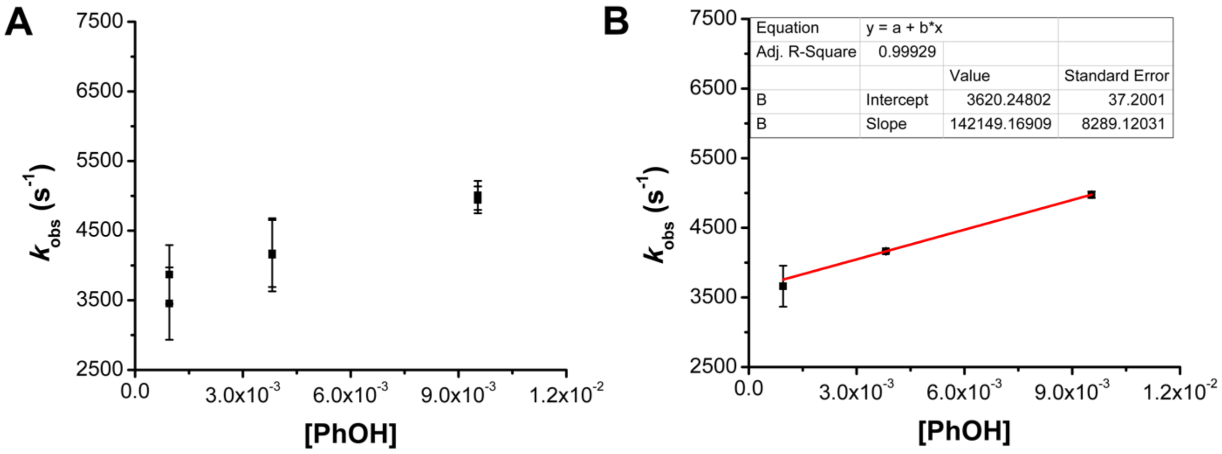

Equation	y = a + b*x		
Adj. R-Square	0.99929		
		Value	Standard Error
B	Intercept	3620.24802	37.2001
B	Slope	142149.16909	8289.12031

Figure S3.3.4. The calculated k_{obs} from stopped-flow spectrochemical experiments with O_2, Cp_2^*Fe and Mn(^{tbu}dhbpy)Cl with varying PhOH concentration at 25.5°C in MeCN. Data were fit using Kinetic Studio 4.0 (1 Exp + Mx + C). Syringe concentrations: O_2 = 9.64 x 10^{-4} M; Mn(^{tbu}dhbpy)Cl = 4.91 x 10^{-5} M; Cp_2^*Fe = 3.15 x 10^{-3} M. Graph (A) represents all the series collected and the individual fits for each, while graph (B) represents the average of all the data points from graph (A).

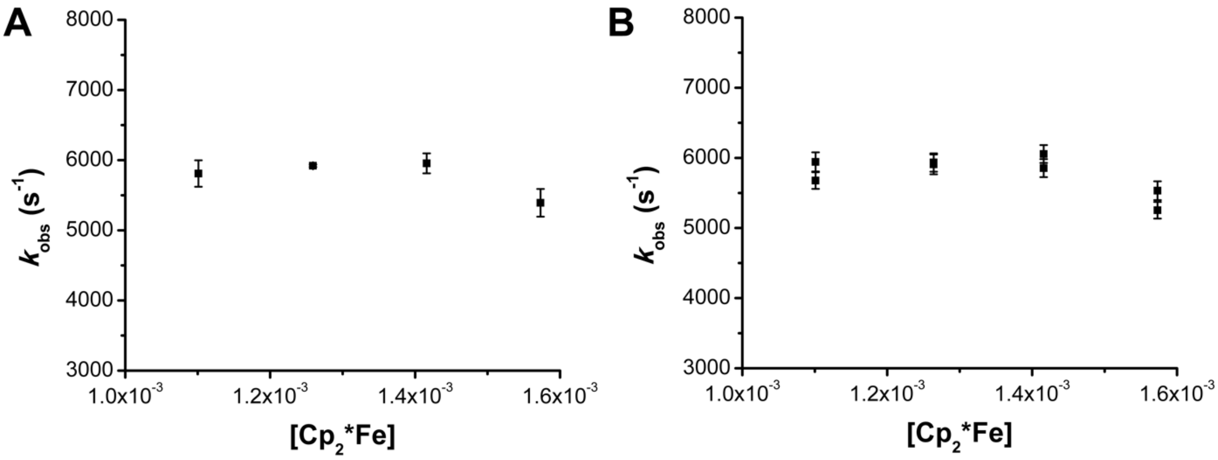

Figure S3.3.5. The calculated k_{obs} from stopped-flow spectrochemical experiments with 0.1 M $TBAPF_6$, O_2, Mn(^{tbu}dhbpy)Cl and PhOH with varying Cp_2^*Fe concentration at 25.5°C in MeCN. Data were fit using Kinetic Studio 4.0 (1 Exp + Mx + C). Syringe concentrations: O_2 = 7.30 x 10^{-4} M; PhOH = 7.82 x 10^{-3} M; Mn(^{tbu}dhbpy)Cl = 4.91 x 10^{-5} M. Graph (A) represents all the series collected and the individual fits for each, while graph (B) represents the average of all the data points from graph (A).

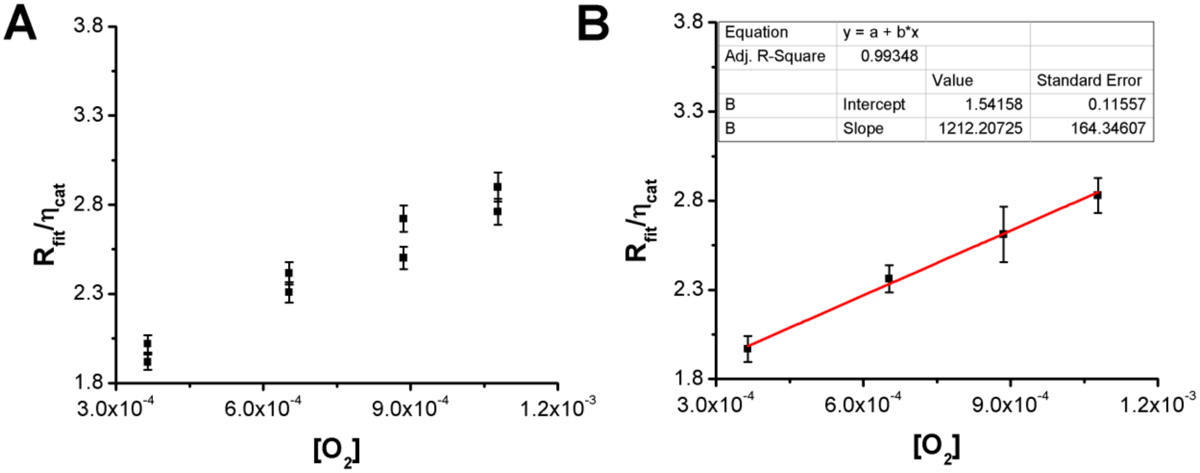

Equation	y = a + b*x		
Adj. R-Square	0.99348		
		Value	Standard Error
B	Intercept	1.54158	0.11557
B	Slope	1212.20725	164.34607

Figure S3.3.6. The calculated R_{fit}/η_{cat} from stopped-flow spectrochemical experiments with 0.1 M $TBAPF_6$, Cp_2^*Fe, Mn(^{tbu}dhbpy)Cl and PhOH with varying O_2 concentration at 25.5°C in MeCN. Data were fit using Kinetic Studio 4.0 (1 Exp + Mx + C). Syringe concentrations: Cp_2^*Fe = 3.03 x 10^{-3} M; PhOH = 7.82 x 10^{-3} M; Mn(^{tbu}dhbpy)Cl = 4.91 x 10^{-5} M. Graph (A) represents all the series collected and the individual fits for each, while graph (B) represents the average of all the data points from graph (A).

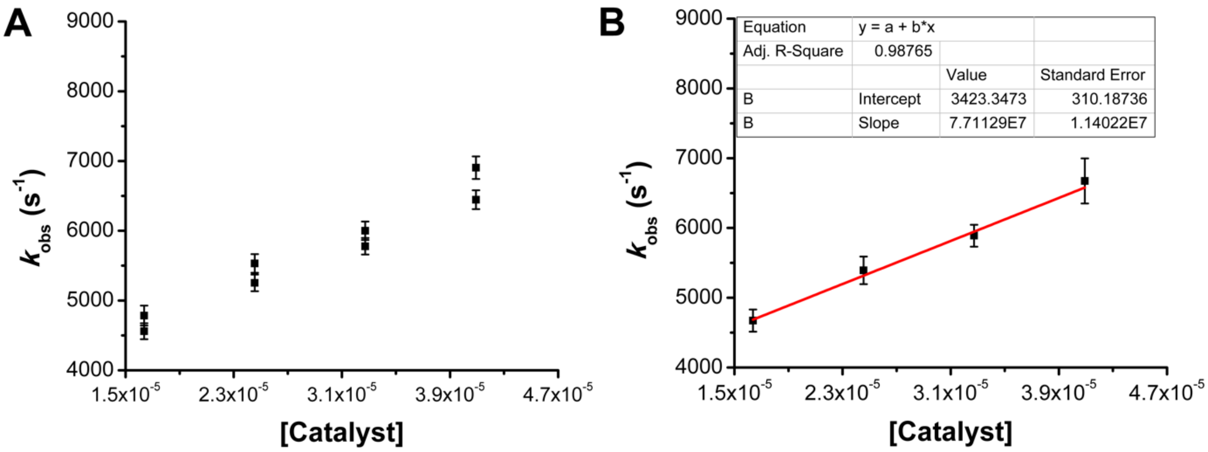

Equation	y = a + b*x		
Adj. R-Square	0.98765		
		Value	Standard Error
B	Intercept	3423.3473	310.18736
B	Slope	7.71129E7	1.14022E7

Figure S3.3.7. The calculated k_{obs} from stopped-flow spectrochemical experiments with 0.1 M TBAPF$_6$, O$_2$, Cp$_2^*$Fe and PhOH with varying Mn(^{tbu}dhbpy)Cl concentration at 25.5°C in MeCN. Data were fit using Kinetic Studio 4.0 (1 Exp + Mx + C). Syringe concentrations: O$_2$ = 7.30 x 10^{-4} M; PhOH = 7.82 x 10^{-3} M; Cp$_2^*$Fe = 3.03 x 10^{-3} M. Graph (A) represents all the series collected and the individual fits for each, while graph (B) represents the average of all the data points from graph (A).

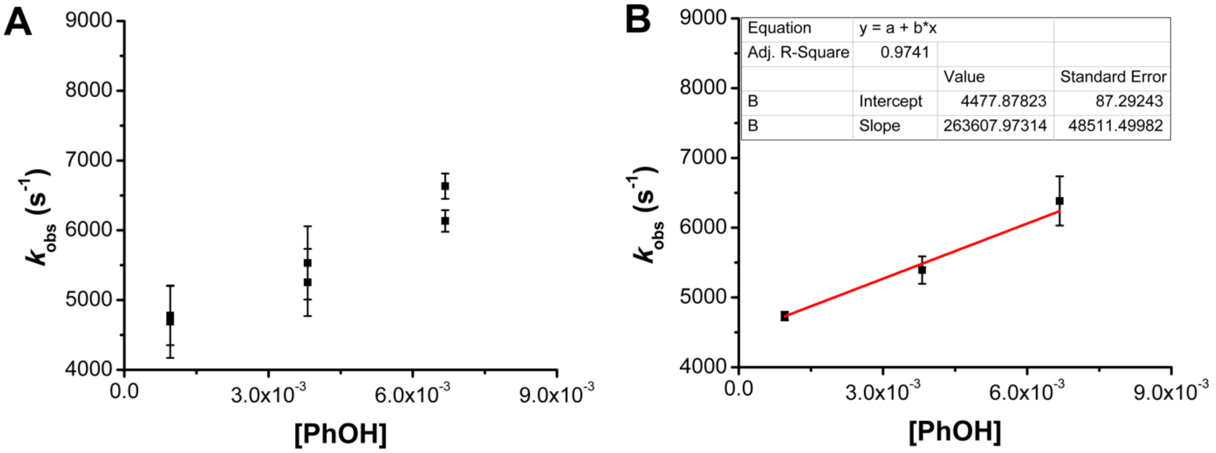

Equation	y = a + b*x		
Adj. R-Square	0.9741		
		Value	Standard Error
B	Intercept	4477.87823	87.29243
B	Slope	263607.97314	48511.49982

Figure S3.3.8. The calculated k_{obs} from stopped-flow spectrochemical experiments with 0.1 M TBAPF$_6$, Cp$_2^*$Fe, Mn(^{tbu}dhbpy)Cl and O$_2$ with varying PhOH concentration at 25.5°C in MeCN. Data were fit using Kinetic Studio 4.0 (1 Exp + Mx + C). Syringe concentrations: Cp$_2^*$Fe = 3.03 x 10^{-3} M; O$_2$ = 7.30 x 10^{-4} M; Mn(^{tbu}dhbpy)Cl = 4.91 x 10^{-5} M. Graph (A) represents all the series collected and the individual fits for each, while graph (B) represents the average of all the data points from graph (A).

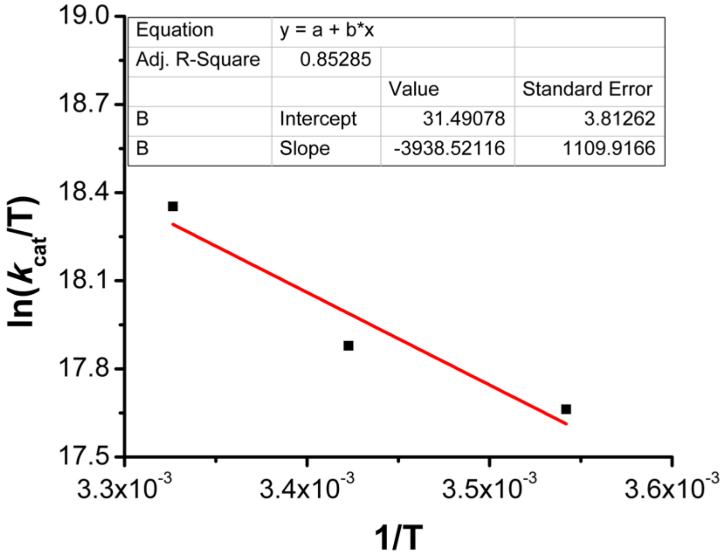

Equation	y = a + b*x		
Adj. R-Square	0.85285		
		Value	Standard Error
B	Intercept	31.49078	3.81262
B	Slope	-3938.52116	1109.9166

Figure S3.3.9. Eyring plot of the stopped-flow data spectrochemical experiments with Mn(^{tbu}dhbpy)Cl in MeCN with PhOH. Data were fit using Kinetic Studio 4.0 (1 Exp + Mx + C). Syringe concentrations: Mn(^{tbu}dhbpy)Cl = 5.55 x 10^{-5} M; O_2 = 9.64 x 10^{-4} M; Cp_2^*Fe = 3.10 x 10^{-3} M; PhOH = 8.05 x 10^{-3} M.

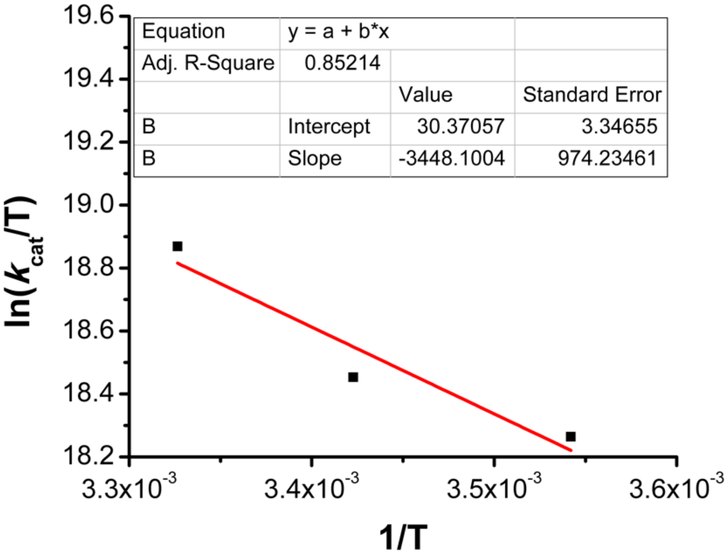

Equation	y = a + b*x		
Adj. R-Square	0.85214		
		Value	Standard Error
B	Intercept	30.37057	3.34655
B	Slope	-3448.1004	974.23461

Figure S3.3.10. Eyring plot of the stopped-flow data spectrochemical experiments with Mn(^{tbu}dhbpy)Cl with 0.1 M $TBAPF_6$ in MeCN with PhOH. Data were fit using Kinetic Studio 4.0 (1 Exp + Mx + C). Syringe concentrations: Mn(^{tbu}dhbpy)Cl = 5.17 x 10^{-5} M; O_2 = 7.30 x 10^{-4} M; Cp_2^*Fe = 3.01 x 10^{-3} M; PhOH = 7.78 x 10^{-3} M

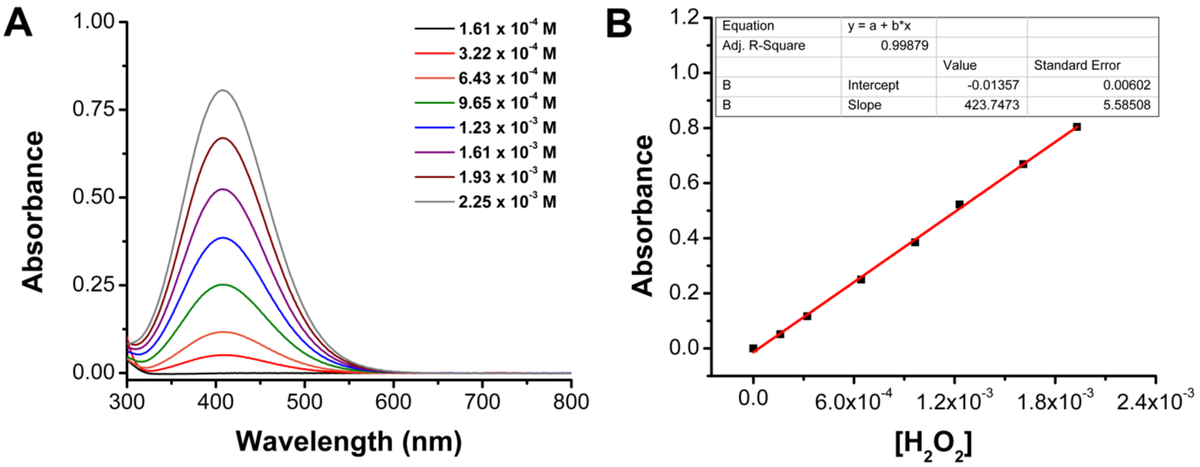

Figure S3.3.11. (**A**) UV-Visible spectra for Ti(O)SO_4-based detection of varying H_2O_2 concentrations. (**B**) Calibration curve from data in (**A**).

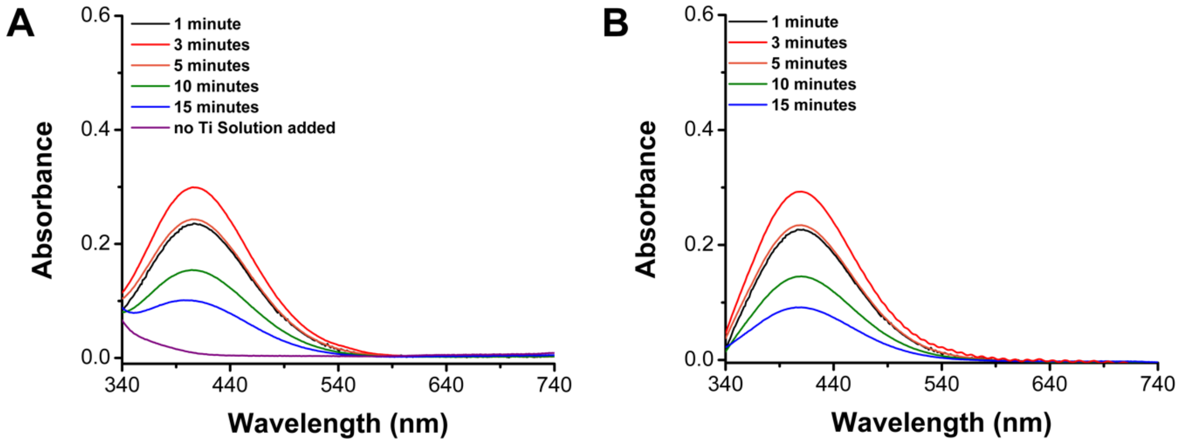

Figure S3.3.12. (**A**) UV-visible spectra for the detection of H_2O_2 from O_2 reduction using Cp_2*Fc as a chemical reductant and treatment with Ti(O)SO_4. (**B**) Data from (**A**) plotted with background subtracted without Ti(O)SO_4 solution addition. Concentrations of reaction solution in MeCN: Cp_2^*Fe = 6.13 x 10^{-3} M; Mn(^{tbu}dhbpy)Cl = 4.29 x 10^{-4} M; PhOH = 0.765 M. Maximum H_2O_2 concentration detected is 7.23 x 10^{-4} M.

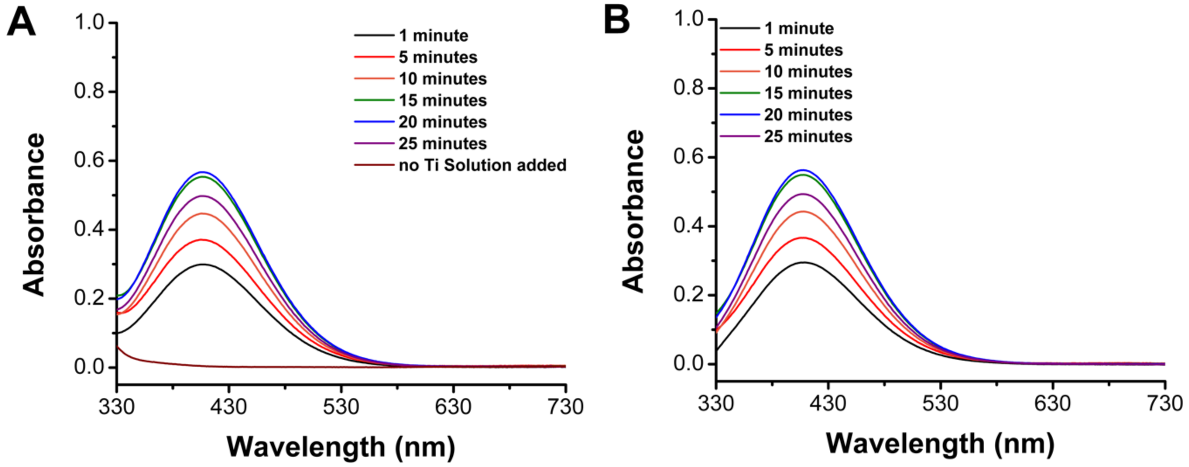

Figure S3.5.13. (**A**) UV-visible spectra for the detection of H_2O_2 from O_2 reduction using Cp_2*Fc as a chemical reductant and treatment with Ti(O)SO_4. (**B**) Data from (**A**) plotted with background subtracted without Ti(O)SO_4 solution addition. Concentrations of reaction solution in MeCN: Cp_2^*Fe = 6.48 x 10^{-3} M; Mn(^{tbu}dhbpy)Cl = 5.10 x 10^{-4} M; F_5PhOH Buffer = 6.13 x 10^{-3} M. Maximum H_2O_2 concentration detected is 1.36 x 10^{-3} M.

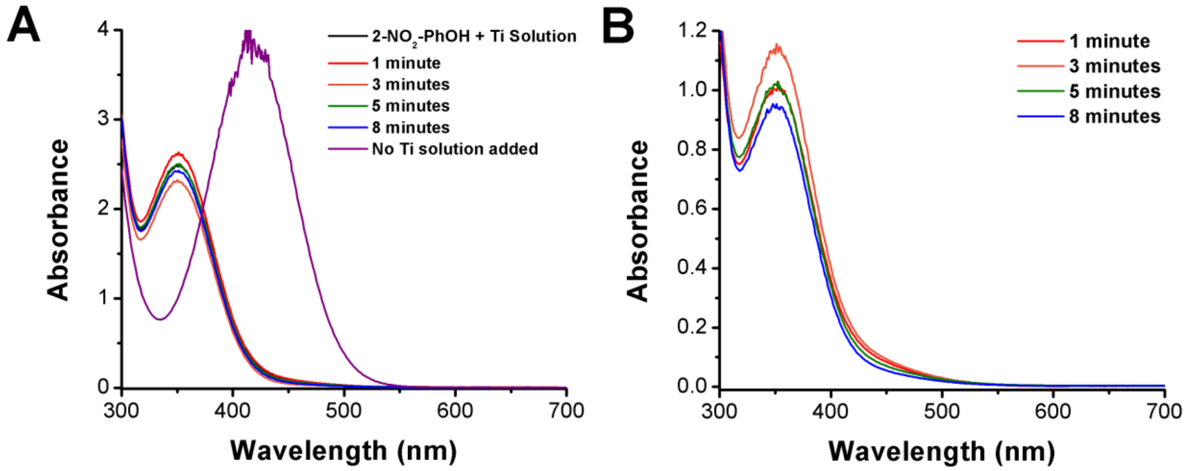

Figure S3.5.14. (**A**) UV-visible spectra for the detection of H_2O_2 from O_2 reduction using Cp_2*Fc as a chemical reductant and treatment with Ti(O)SO_4. (**B**) Data from (**A**) plotted with background subtracted without Ti(O)SO_4 solution addition. Concentrations of reaction solution in MeCN: Cp_2^*Fe = 8.73 x 10^{-3} M; Mn(^{tbu}dhbpy)Cl = 5.62 x 10^{-4} M; 2-NO_2-PhOH Buffer = 5.55 x 10^{-3} M. Maximum H_2O_2 concentration detected is 2.70 x 10^{-3} M.

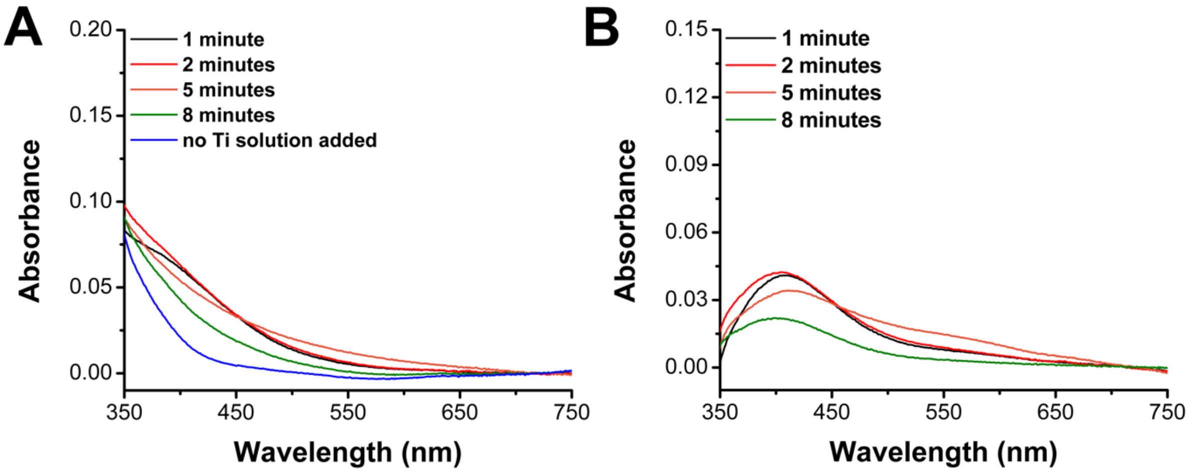

Figure S3.5.15. (**A**) UV-visible spectra for the detection of H_2O_2 from O_2 reduction using Cp_2*Fc as a chemical reductant and treatment with Ti(O)SO_4. (**B**) Data from (**A**) plotted with background subtracted without Ti(O)SO_4 solution addition. Concentrations of reaction solution in MeCN: $Cp_2^*Fe = 6.13 \times 10^{-3}$ M; $\mathrm{Mn(^{tbu}dhbpy)Cl} = 5.10 \times 10^{-4}$ M; 4-CF_3-PhOH = 6.73×10^{-3} M. Maximum H_2O_2 concentration detected is 4.19×10^{-5} M.

Table S3.4.1. Charge transfer coefficients, α, obtained from CV analysis.[57-58]

	Scan Rate (mV s^{-1})	Transfer Coefficient, α	Average	Standard Deviation
F_5PhOH Buffer	100	-0.767		
	200	-0.746		
	500	-0.690		
	1000	-0.656	-0.715	0.0508
2-NO_2-PhOH Buffer	100	-0.729		
	200	-0.722		
	500	-0.703		
	1000	-0.649	-0.701	0.0364
4-CF_3-PhOH	100	-0.778		
	200	-0.743		
	500	-0.719		
	1000	-0.690	-0.732	0.0370
Catalyst Only	100	-0.778		
	200	-0.875		
	500	-0.901		
	1000	-0.875	-0.857	0.0543
Ferrocene	100	-0.835		
	200	-0.757		
	500	-0.787		
	1000	-0.771	-0.787	0.0339

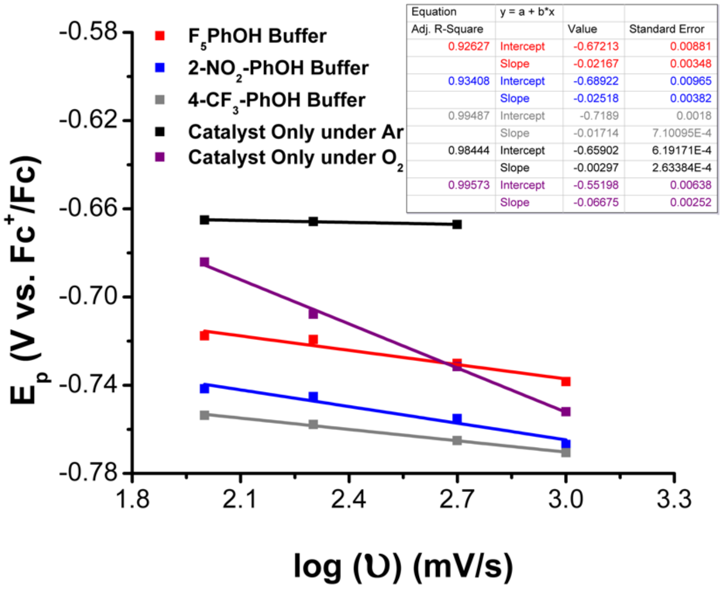

Figure S3.4.16. Plot of E$_p$ versus log (v) (mV/s), comparing buffered and unbuffered conditions under Ar saturation. Values from the aprotic response under O$_2$ also included.

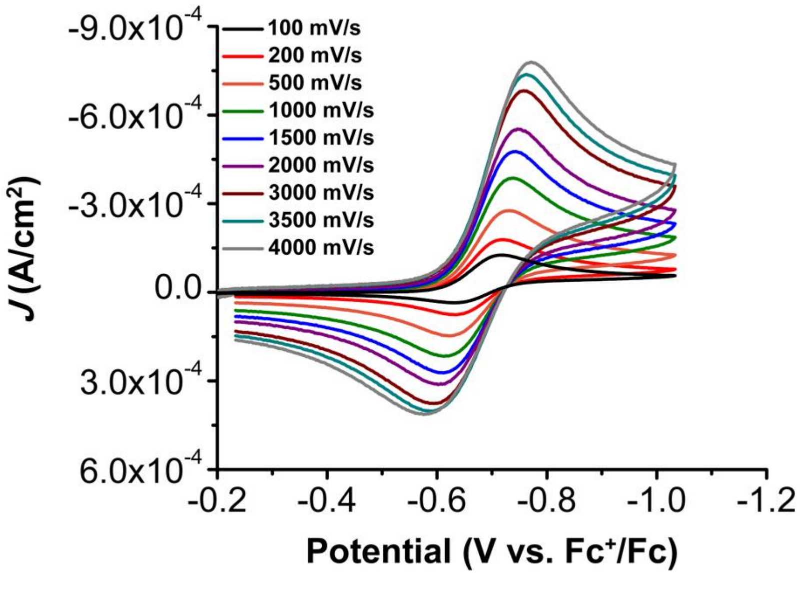

Figure S3.4.17. CVs of Mn(^{tbu}dhbpy)Cl **1**, obtained under Ar saturation conditions with 10 mM F$_5$PhOH Buffer. Conditions: 0.5 mM analyte; glassy carbon working electrode, glassy carbon counter electrode, Ag/AgCl pseudoreference electrode; varied scan rate; referenced to internal ferrocene standard.

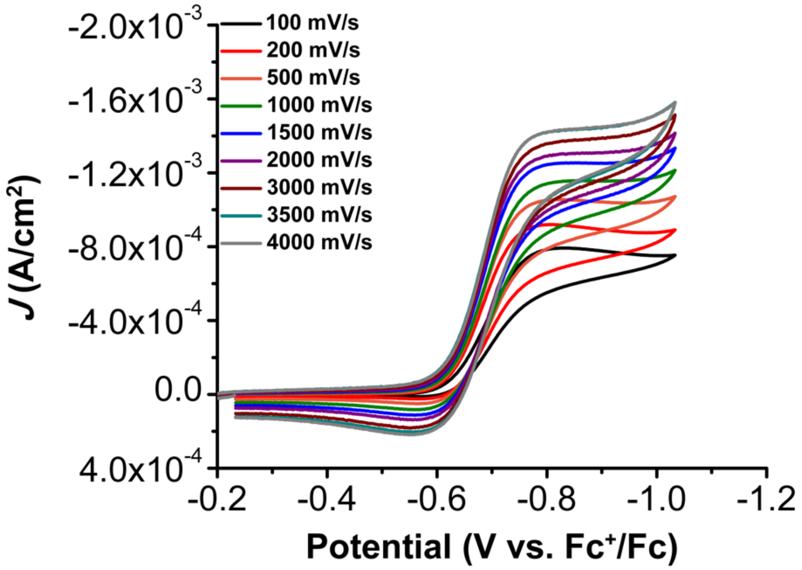

Figure S3.4.18. CVs of Mn(^{tbu}dhbpy)Cl **1**, obtained under O_2 saturation conditions with 10 mM F_5PhOH Buffer. Conditions: 0.5 mM analyte; glassy carbon working electrode, glassy carbon counter electrode, Ag/AgCl pseudoreference electrode; varied scan rate; referenced to internal ferrocene standard.

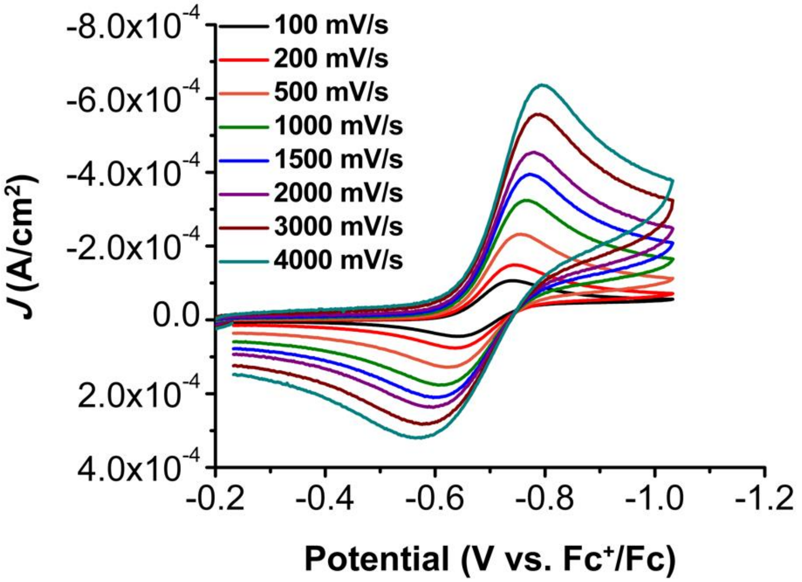

Figure S3.4.19. CVs of Mn(^{tbu}dhbpy)Cl **1**, obtained under Ar saturation conditions with 10 mM 2-NO_2-PhOH Buffer. Conditions: 0.5 mM analyte; glassy carbon working electrode, glassy carbon counter electrode, Ag/AgCl pseudoreference electrode; varied scan rate; referenced to internal ferrocene standard.

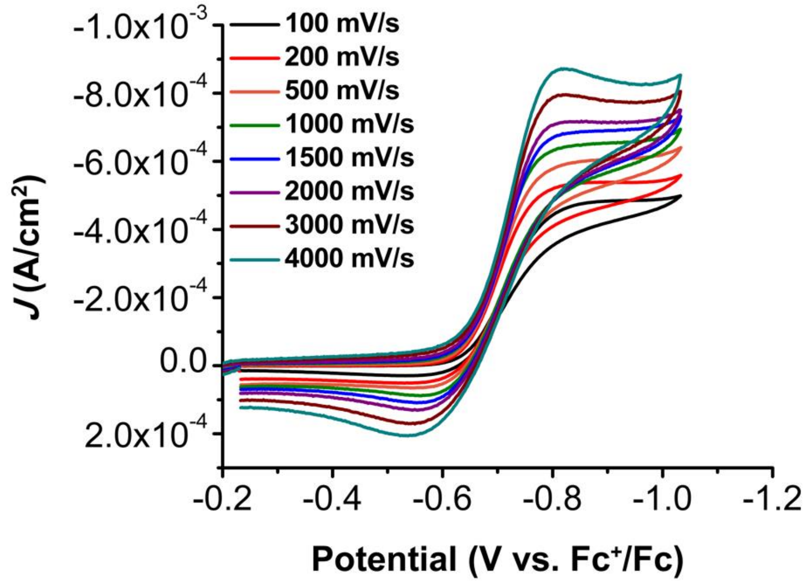

Figure S3.4.20. CVs of Mn(^{tbu}dhbpy)Cl **1**, obtained under O_2 saturation conditions with 10 mM 2-NO_2-PhOH Buffer. Conditions: 0.5 mM analyte; glassy carbon working electrode, glassy carbon counter electrode, Ag/AgCl pseudoreference electrode; varied scan rate; referenced to internal ferrocene standard.

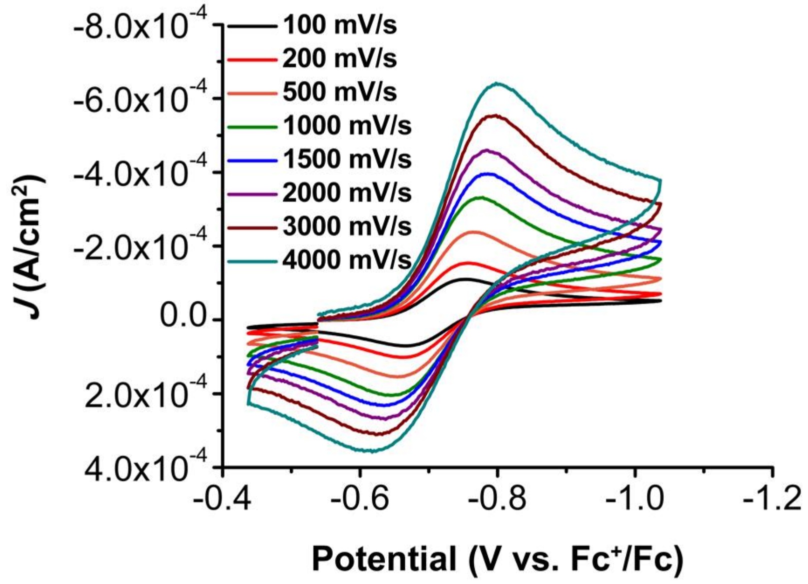

Figure S3.4.21. CVs of Mn(^{tbu}dhbpy)Cl **1**, obtained under Ar saturation conditions with 10 mM 4-CF_3-PhOH Buffer. Conditions: 0.5 mM analyte; glassy carbon working electrode, glassy carbon counter electrode, Ag/AgCl pseudoreference electrode; varied scan rate; referenced to internal ferrocene standard.

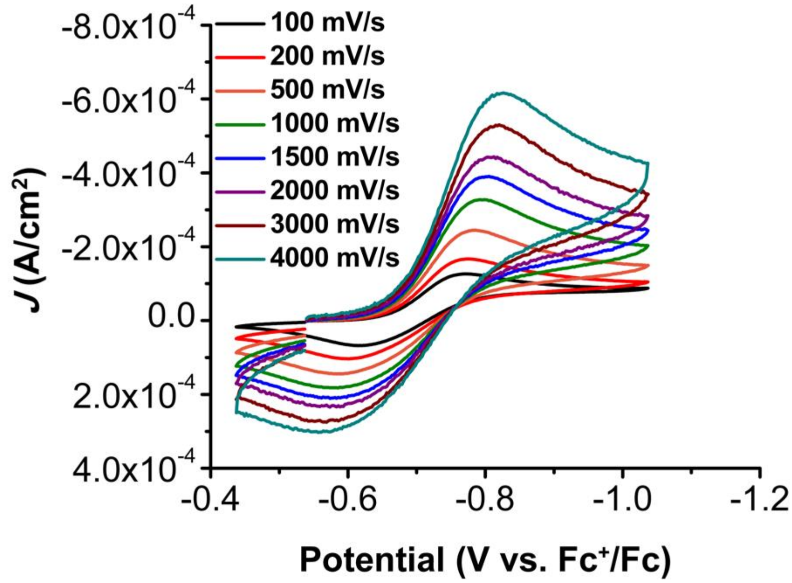

Figure S3.4.22. CVs of Mn(^{tbu}dhbpy)Cl **1**, obtained under O_2 saturation conditions with 10 mM 4-CF_3-PhOH Buffer. Conditions: 0.5 mM analyte; glassy carbon working electrode, glassy carbon counter electrode, Ag/AgCl pseudoreference electrode; varied scan rate; referenced to internal ferrocene standard.

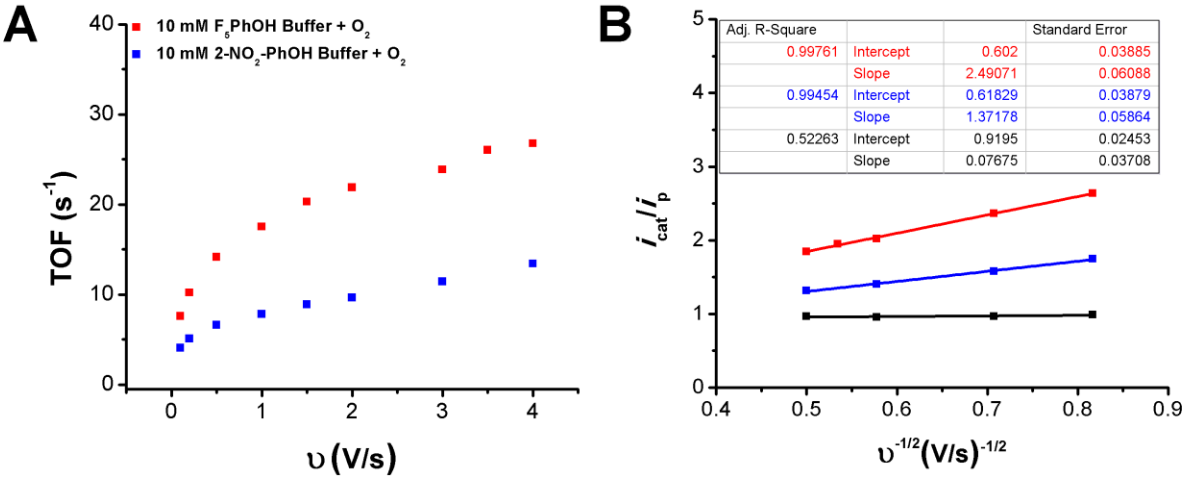

Adj. R-Square			Standard Error
0.99761	Intercept	0.602	0.03885
	Slope	2.49071	0.06088
0.99454	Intercept	0.61829	0.03879
	Slope	1.37178	0.05864
0.52263	Intercept	0.9195	0.02453
	Slope	0.07675	0.03708

Figure S3.4.23. Plots of **(A)** TOF vs scan rate and **(B)** i_{cat}/i_p vs the inverse of the square root of the scan rate for Mn(^{tbu}dhbpy)Cl **1**, with F_5PhOH buffer (red), 2-NO_2-PhOH Buffer (blue), and 4-CF_3-PhOH Buffer (black) from data in **Figures S17-S21**.

Calculation of TOF_{max} (adapted[59])

$$TOF_{max} = 0.1992\frac{n_p^3}{n_{cat}^2}\frac{F\nu}{RT}\left(\frac{i_{cat}}{i_p}\right)^2$$

Where n_p^3 is the number of electron transferred under faradaic conditions, n_{cat}^2 is the number of electrons transferred under catalytic conditions, R is the ideal gas constant, F is Faraday's constant, ν is the scan rate, T is temperature, i_{cat} is the catalytic current, and i_p is the faradaic current.

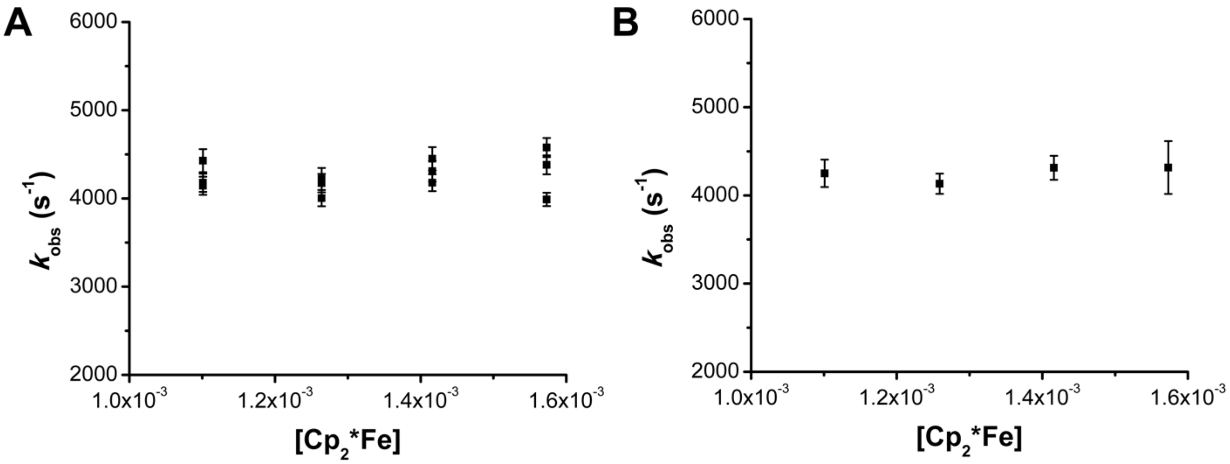

Figure S3.5.24. The calculated k_{obs} from stopped-flow spectrochemical experiments with 0.1 M $TBAPF_6$, F_5PhOH Buffer, O_2 and Mn(^{tbu}dhbpy)Cl with varying Cp_2^*Fe concentration at 25.5°C in MeCN. Data were fit using Kinetic Studio 4.0 (1 Exp + Mx + C). Syringe concentrations: Mn(^{tbu}dhbpy)Cl = 4.99 x 10^{-5} M; F_5PhOH Buffer = 2.46 x 10^{-5} M; O_2 = 7.30 x 10^{-4} M. Graph (A) represents all the series collected and the individual fits for each, while graph (B) represents the average of all the data points from graph (A).

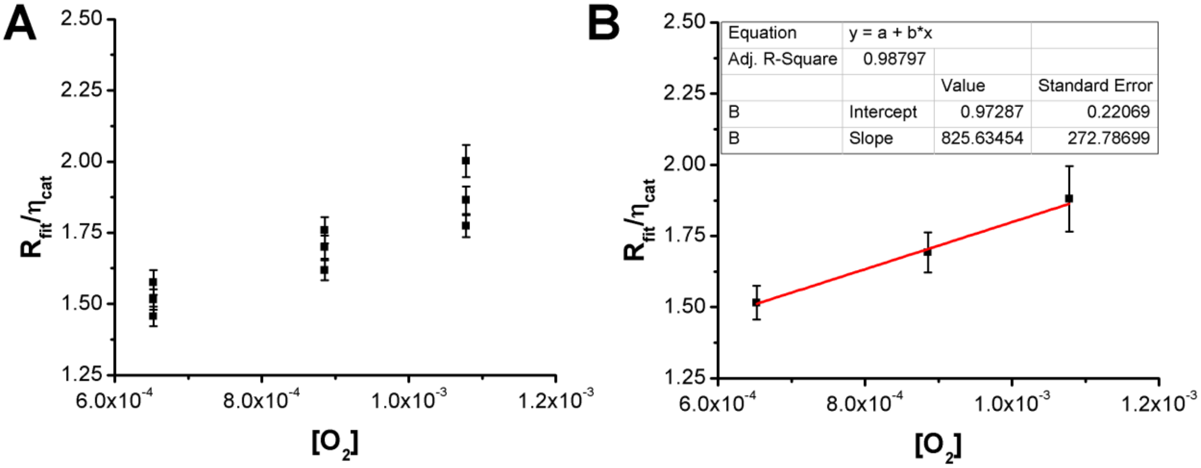

Equation	y = a + b*x		
Adj. R-Square	0.98797		
		Value	Standard Error
B	Intercept	0.97287	0.22069
B	Slope	825.63454	272.78699

Figure S3.5.25. The calculated R_{fit}/η_{cat} from stopped-flow spectrochemical experiments with 0.1 M $TBAPF_6$, F_5PhOH Buffer, Cp_2^*Fe and Mn(^{tbu}dhbpy)Cl with varying O_2 concentration at 25.5°C in MeCN. Data were fit using Kinetic Studio 4.0 (1 Exp + Mx + C). Syringe concentrations: Mn(^{tbu}dhbpy)Cl = 4.99 x 10^{-5} M; F_5PhOH Buffer = 2.46 x 10^{-5} M; Cp_2^*Fe = 3.13 x 10^{-3} M. Graph (A) represents all the series collected and the individual fits for each, while graph (B) represents the average of all the data points from graph (A).

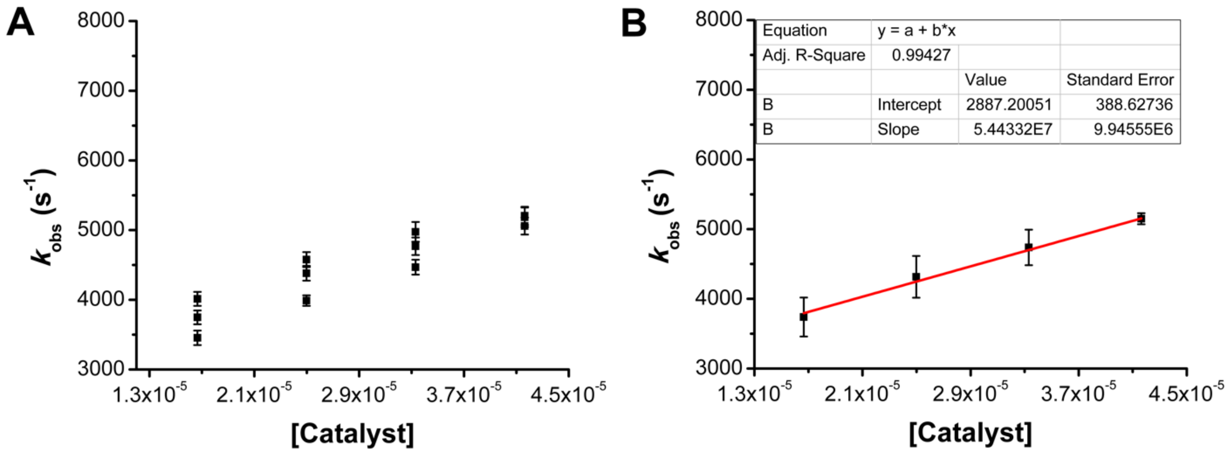

Figure S3.5.26. The calculated k_{obs} from stopped-flow spectrochemical experiments with 0.1 M TBAPF$_6$, F$_5$PhOH Buffer, O$_2$ and Cp$_2^*$Fe with varying Mn(^{tbu}dhbpy)Cl concentration at 25.5°C in MeCN. Data were fit using Kinetic Studio 4.0 (1 Exp + Mx + C). Syringe concentrations: Cp$_2^*$Fe = 3.13 x 10^{-3} M; F$_5$PhOH Buffer = 2.46 x 10^{-5} M; O$_2$ = 7.30 x 10^{-4} M. Graph (A) represents all the series collected and the individual fits for each, while graph (B) represents the average of all the data points from graph (A).

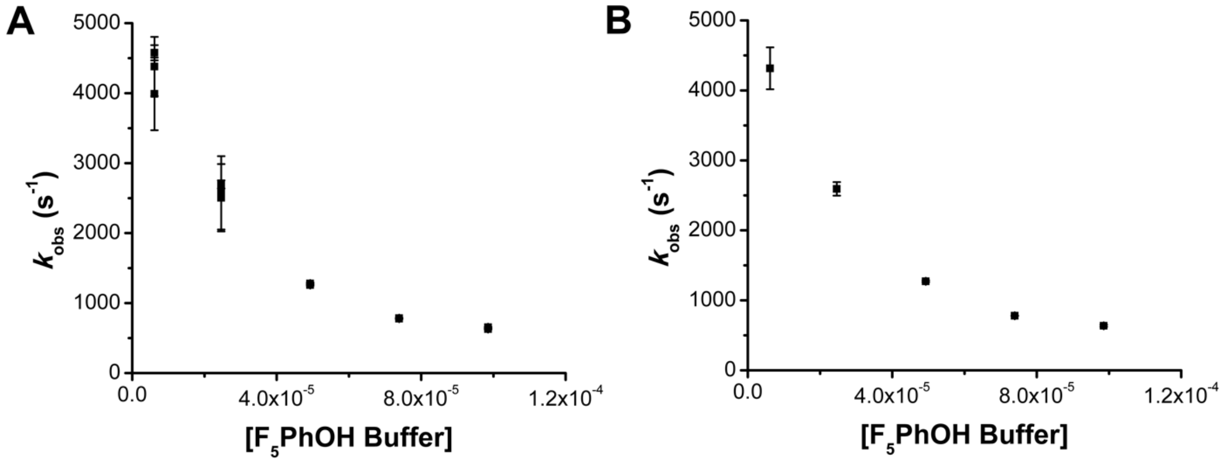

Figure S3.5.27. The calculated k_{obs} from stopped-flow spectrochemical experiments with 0.1 M TBAPF$_6$, Mn(^{tbu}dhbpy)Cl, O$_2$ and Cp$_2^*$Fe with varying F$_5$PhOH Buffer concentration at 25.5°C in MeCN. Data were fit using Kinetic Studio 4.0 (1 Exp + Mx + C). Syringe concentrations: Cp$_2^*$Fe = 3.13 x 10^{-3} M; Mn(^{tbu}dhbpy)Cl = 4.99 x 10^{-5} M; O$_2$ = 7.30 x 10^{-4} M. Graph (A) represents all the series collected and the individual fits for each, while graph (B) represents the average of all the data points from graph (A).

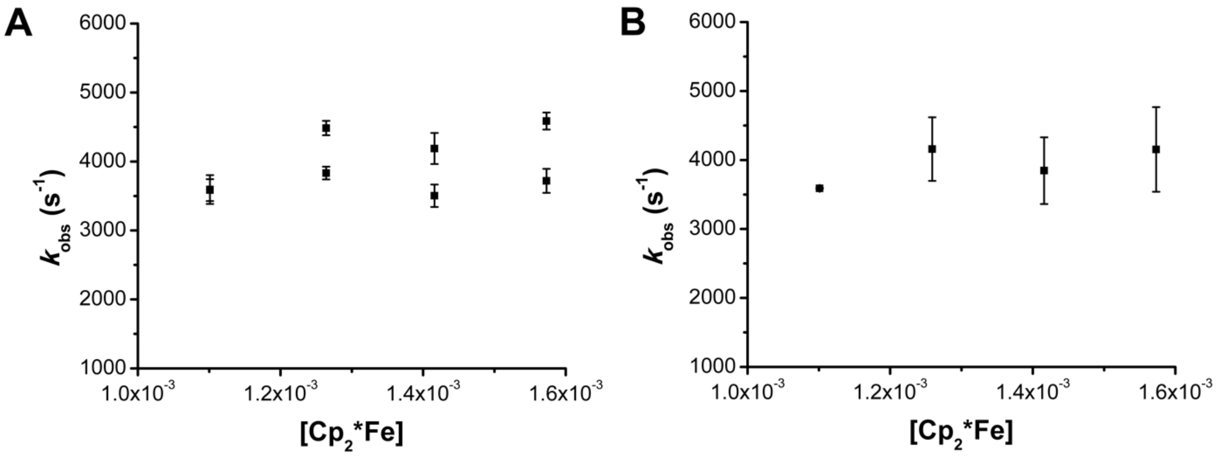

Figure S3.5.28. The calculated k_{obs} from stopped-flow spectrochemical experiments with 0.1 M TBAPF$_6$, 2-NO$_2$-PhOH Buffer, O$_2$ and Mn(^{tbu}dhbpy)Cl with varying Cp$_2^*$Fe concentration at 25.5°C in MeCN. Data were fit using Kinetic Studio 4.0 (1 Exp + Mx + C). Syringe concentrations: Mn(^{tbu}dhbpy)Cl = 4.99 x 10^{-5} M; 2-NO$_2$-PhOH Buffer = 2.89 x 10^{-5} M; O$_2$ = 7.30 x 10^{-4} M. Graph (A) represents all the series collected and the individual fits for each, while graph (B) represents the average of all the data points from graph (A).

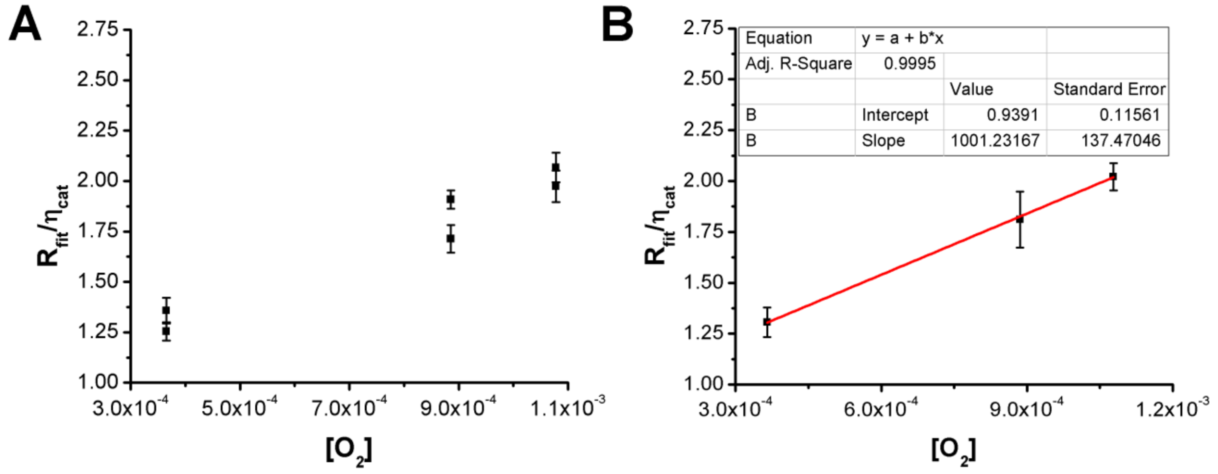

Equation	y = a + b*x		
Adj. R-Square	0.9995		
		Value	Standard Error
B	Intercept	0.9391	0.11561
B	Slope	1001.23167	137.47046

Figure S3.5.29. The calculated R$_{fit}$/η$_{cat}$ from stopped-flow spectrochemical experiments with 0.1 M TBAPF$_6$, 2-NO$_2$-PhOH Buffer, Cp$_2^*$Fe and Mn(^{tbu}dhbpy)Cl with varying O$_2$ concentration at 25.5°C in MeCN. Data were fit using Kinetic Studio 4.0 (1 Exp + Mx + C). Syringe concentrations: Mn(^{tbu}dhbpy)Cl = 4.99 x 10^{-5} M; 2-NO$_2$-PhOH Buffer = 2.89 x 10^{-5} M; Cp$_2^*$Fe = 3.07 x 10^{-3} M. Graph (A) represents all the series collected and the individual fits for each, while graph (B) represents the average of all the data points from graph (A).

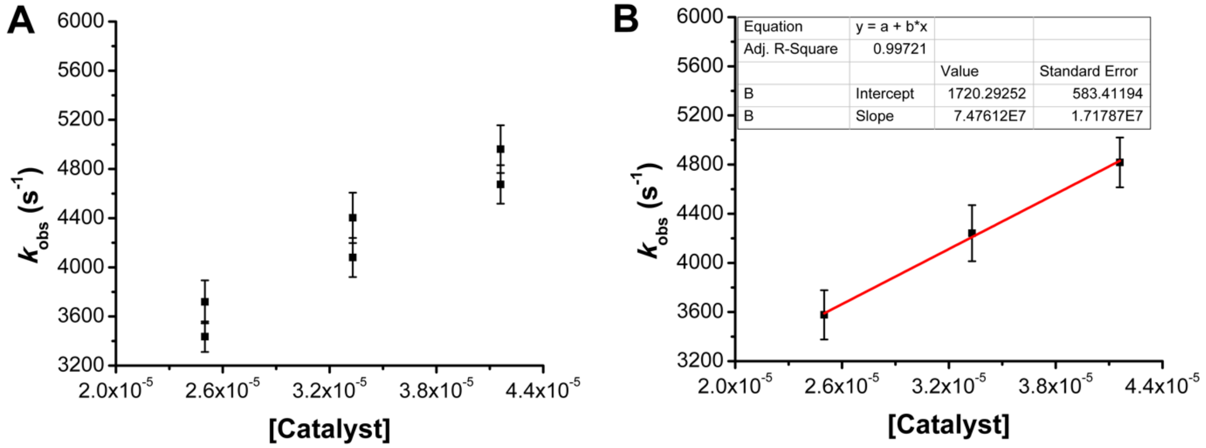

Figure S3.5.30. The calculated k_{obs} from stopped-flow spectrochemical experiments with 0.1 M TBAPF$_6$, 2-NO$_2$-PhOH Buffer, O$_2$ and Cp$_2^*$Fe with varying Mn(^{tbu}dhbpy)Cl concentration at 25.5°C in MeCN. Data were fit using Kinetic Studio 4.0 (1 Exp + Mx + C). Syringe concentrations: Cp$_2^*$Fe = 3.07 x 10^{-3} M; 2-NO$_2$-PhOH Buffer = 2.89 x 10^{-5} M; O$_2$ = 7.30 x 10^{-4} M. Graph (A) represents all the series collected and the individual fits for each, while graph (B) represents the average of all the data points from graph (A).

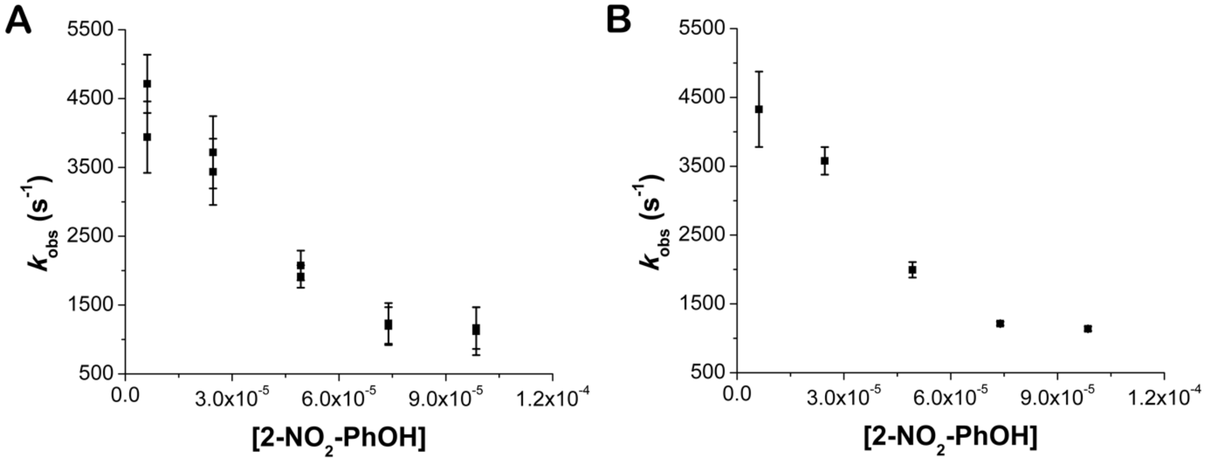

Figure S3.5.31. The calculated k_{obs} from stopped-flow spectrochemical experiments with 0.1 M TBAPF$_6$, Mn(^{tbu}dhbpy)Cl, O$_2$ and Cp$_2^*$Fe with varying 2-NO$_2$-PhOH Buffer concentration at 25.5°C in MeCN. Data were fit using Kinetic Studio 4.0 (1 Exp + Mx + C). Syringe concentrations: Cp$_2^*$Fe = 3.07 x 10^{-3} M; Mn(^{tbu}dhbpy)Cl = 4.99 x 10^{-5} M; O$_2$ = 7.30 x 10^{-4} M. Graph (A) represents all the series collected and the individual fits for each, while graph (B) represents the average of all the data points from graph (A).

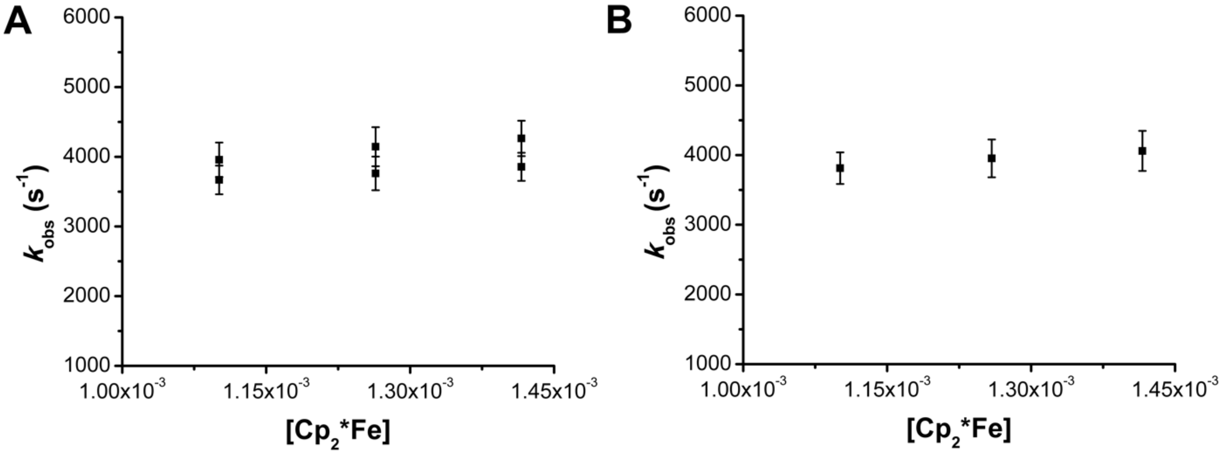

Figure S3.5.32. The calculated k_{obs} from stopped-flow spectrochemical experiments with 0.1 M TBAPF$_6$, 4-CF$_3$-PhOH Buffer, O$_2$ and Mn(^{tbu}dhbpy)Cl with varying Cp$_2$*Fe concentration at 25.5°C in MeCN. Data were fit using Kinetic Studio 4.0 (1 Exp + Mx + C). Syringe concentrations: Mn(^{tbu}dhbpy)Cl = 4.74 x 10^{-5} M; 4-CF$_3$-PhOH Buffer = 2.26 x 10^{-5} M; O$_2$ = 7.30 x 10^{-4} M. Graph (A) represents all the series collected and the individual fits for each, while graph (B) represents the average of all the data points from graph (A).

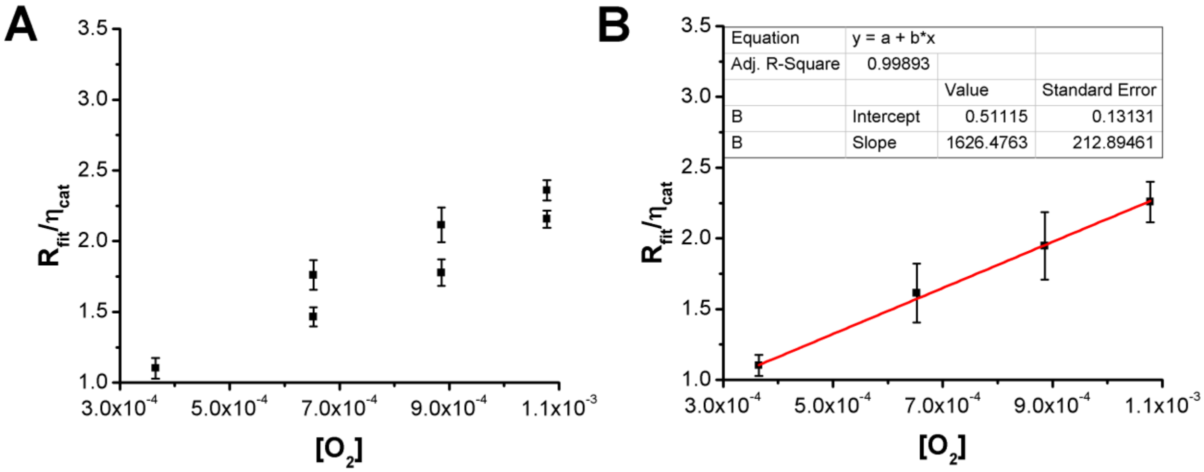

Equation	y = a + b*x		
Adj. R-Square	0.99893		
		Value	Standard Error
B	Intercept	0.51115	0.13131
B	Slope	1626.4763	212.89461

Figure S3.5.33. The calculated R$_{fit}$/η$_{cat}$ from stopped-flow spectrochemical experiments with 0.1 M TBAPF$_6$, 4-CF$_3$-PhOH Buffer, Cp$_2$*Fe and Mn(^{tbu}dhbpy)Cl with varying O$_2$ concentration at 25.5°C in MeCN. Data were fit using Kinetic Studio 4.0 (1 Exp + Mx + C). Syringe concentrations: Mn(^{tbu}dhbpy)Cl = 4.74 x 10^{-5} M; 4-CF$_3$-PhOH Buffer = 2.26 x 10^{-5} M; Cp$_2$*Fe = 3.04 x 10^{-3} M. Graph (A) represents all the series collected and the individual fits for each, while graph (B) represents the average of all the data points from graph (A).

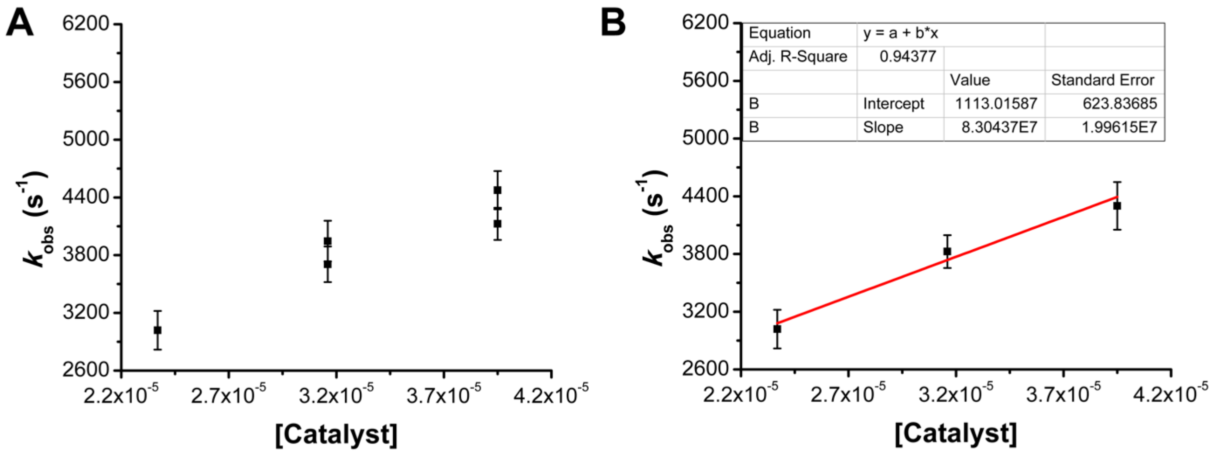

Figure S3.5.34. The calculated k_{obs} from stopped-flow spectrochemical experiments with 0.1 M TBAPF$_6$, 4-CF$_3$-PhOH Buffer, O$_2$ and Cp$_2^*$Fe with varying Mn(^{tbu}dhbpy)Cl concentration at 25.5°C in MeCN. Data were fit using Kinetic Studio 4.0 (1 Exp + Mx + C). Syringe concentrations: Cp$_2^*$Fe = 3.04 x 10^{-3} M; 4-CF$_3$-PhOH Buffer = 2.26 x 10^{-5} M; O$_2$ = 7.30 x 10^{-4} M. Graph (A) represents all the series collected and the individual fits for each, while graph (B) represents the average of all the data points from graph (A).

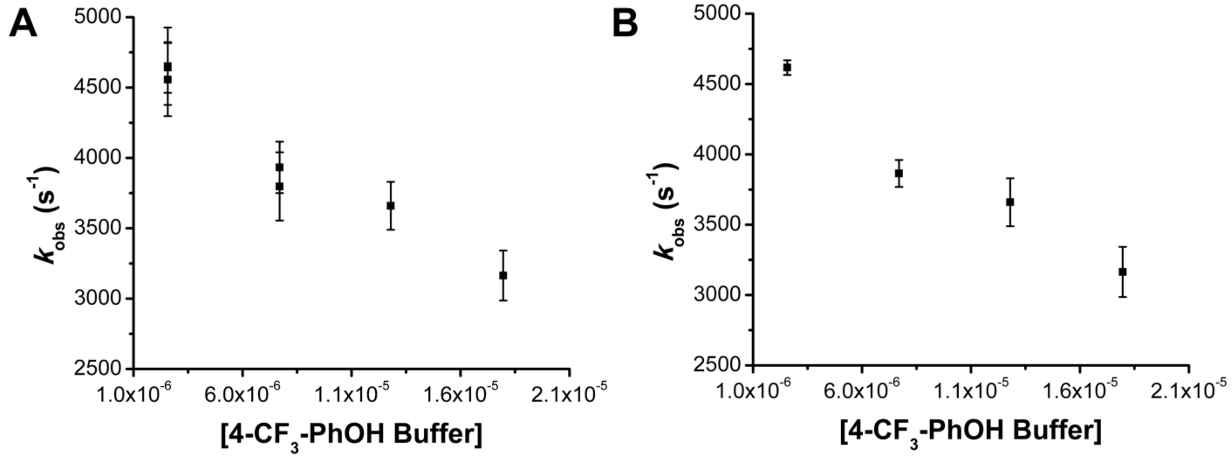

Figure S3.5.35. The calculated k_{obs} from stopped-flow spectrochemical experiments with 0.1 M TBAPF$_6$, Mn(^{tbu}dhbpy)Cl, O$_2$ and Cp$_2^*$Fe with varying 4-CF$_3$-PhOH Buffer concentration at 25.5°C in MeCN. Data were fit using Kinetic Studio 4.0 (1 Exp + Mx + C). Syringe concentrations: Cp$_2^*$Fe = 3.04 x 10^{-3} M; Mn(^{tbu}dhbpy)Cl = 4.74 x 10^{-5} M; O$_2$ = 7.30 x 10^{-4} M. Graph (A) represents all the series collected and the individual fits for each, while graph (B) represents the average of all the data points from graph (A).

Table S3.5.2. Third order rate constants obtained from spectrochemical experiments with 0.1 M $TBAPF_6$. H^+ corresponds to the proton donor indicated in the column heading.

Varied Substrate	F_5PhOH Buffer k_{cat} ($M^{-2}s^{-1}$)	$2\text{-}NO_2\text{-}PhOH$; k_{cat} ($M^{-2}s^{-1}$)	$4\text{-}CF_3\text{-}PhOH$; k_{cat} ($M^{-2}s^{-1}$)
H^+	N.A.	N.A.	N.A.
Catalyst	4.43×10^{12}	5.17×10^{12}	7.35×10^{12}
O_2	2.69×10^{12}	2.78×10^{12}	6.07×10^{12}
Cp^*_2Fe	N.A.	N.A.	N.A.
Average	4×10^{12} (±1)	4.0×10^{12} (±0.2)	6.7×10^{12} (±0.9)

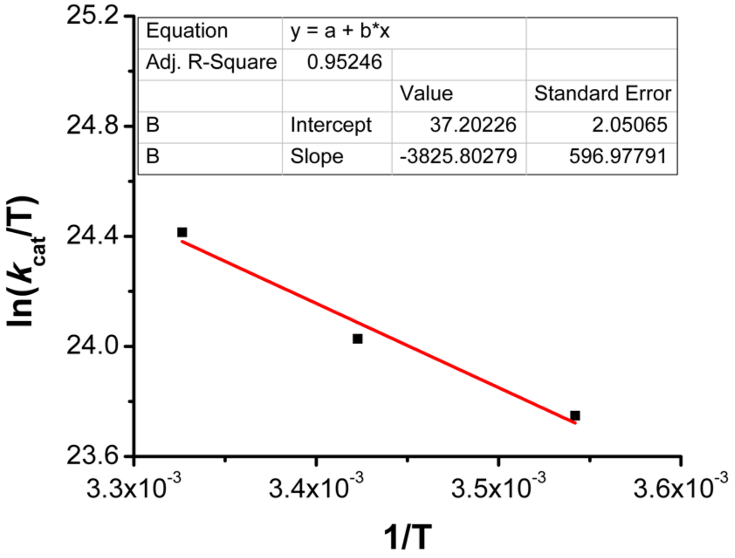

Equation	y = a + b*x		
Adj. R-Square	0.95246		
		Value	Standard Error
B	Intercept	37.20226	2.05065
B	Slope	-3825.80279	596.97791

Figure S3.5.36. Eyring plots of the stopped-flow data spectrochemical experiments with $Mn(^{tbu}dhbpy)Cl$ with 0.1 M $TBAPF_6$ in MeCN with F_5PhOH buffer. Data were fit using Kinetic Studio 4.0 (1 Exp + Mx + C). Syringe concentrations: $Mn(^{tbu}dhbpy)Cl = 5.17 \times 10^{-5}$ M; $O_2 = 7.30 \times 10^{-4}$ M; $Cp_2^*Fe = 3.01 \times 10^{-3}$ M; F_5PhOH buffer $= 2.18 \times 10^{-5}$ M.

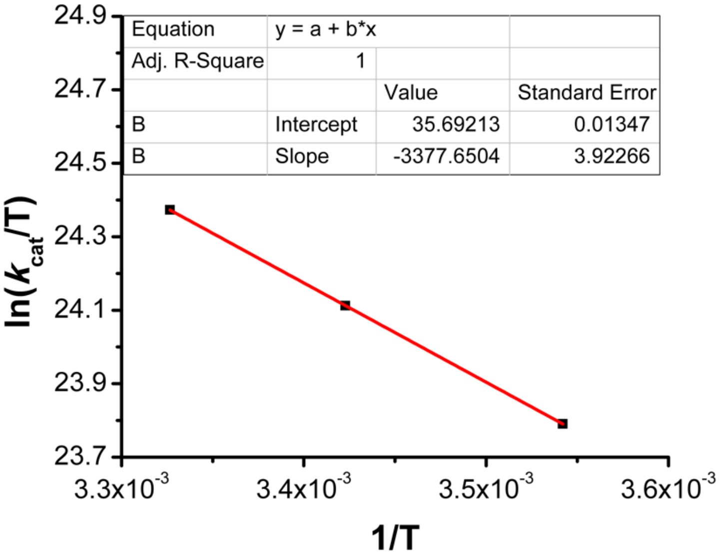

Figure S3.5.37. Eyring plots of the stopped-flow data spectrochemical experiments with Mn(^{tbu}dhbpy)Cl with 0.1 M TBAPF$_6$ in MeCN with 2-NO$_2$-PhOH buffer. Data were fit using Kinetic Studio 4.0 (1 Exp + Mx + C). Syringe concentrations: Mn(^{tbu}dhbpy)Cl = 5.36 x 10^{-5} M; O$_2$ = 7.30 x 10^{-4} M; Cp$_2^*$Fe = 3.31 x 10^{-3} M; 2-NO$_2$-PhOH buffer = 1.73 x 10^{-5} M.

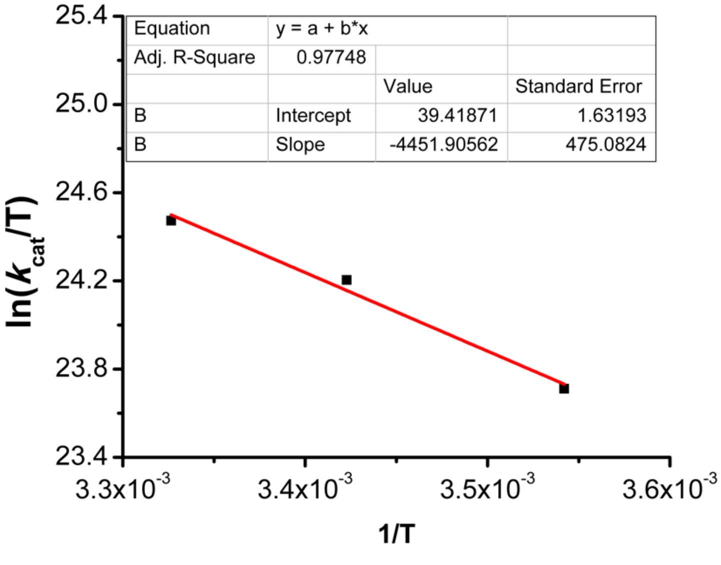

Figure S3.5.38. Eyring plots of the stopped-flow data spectrochemical experiments with Mn(^{tbu}dhbpy)Cl with 0.1 M TBAPF$_6$ in MeCN with 4-CF$_3$-PhOH buffer. Data were fit using Kinetic Studio 4.0 (1 Exp + Mx + C). Syringe concentrations: Mn(^{tbu}dhbpy)Cl = 5.36 x 10^{-5} M; O$_2$ = 7.30 x 10^{-4} M; Cp$_2^*$Fe = 3.31 x 10^{-3} M; 4-CF$_3$-PhOH buffer = 1.86 x 10^{-5} M.

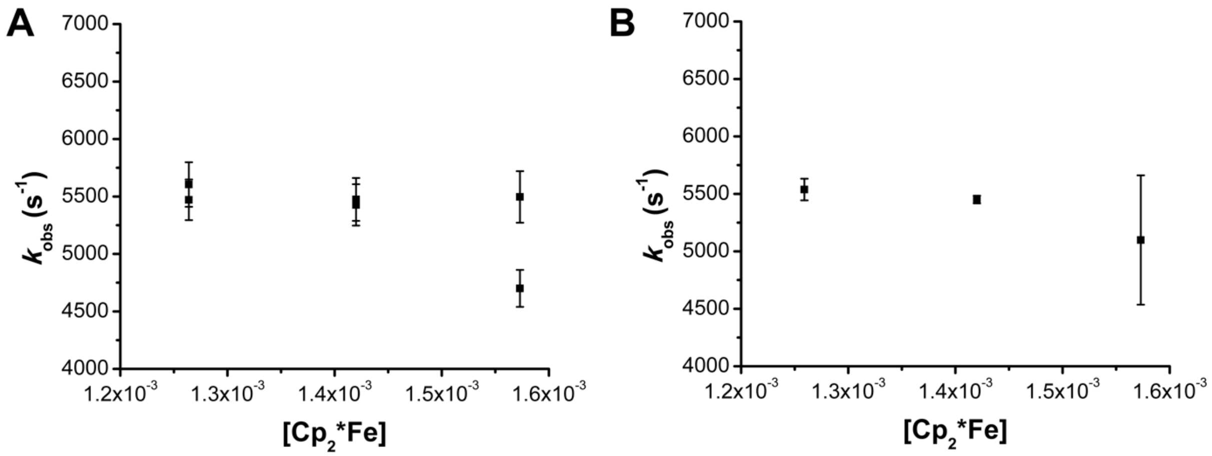

Figure S3.6.39. The calculated k_{obs} from stopped-flow spectrochemical experiments with 0.1 M $TBAPF_6$, TTBP, O_2 and Mn(^{tbu}dhbpy)Cl with varying Cp_2^*Fe concentration at 25.5°C in MeCN. Data were fit using Kinetic Studio 4.0 (1 Exp + Mx + C). Syringe concentrations: Mn(^{tbu}dhbpy)Cl = 4.96 x 10^{-5} M; TTBP = 7.30 x 10^{-3} M; O_2 = 7.30 x 10^{-4} M. Graph (A) represents all the series collected and the individual fits for each, while graph (B) represents the average of all the data points from graph (A).

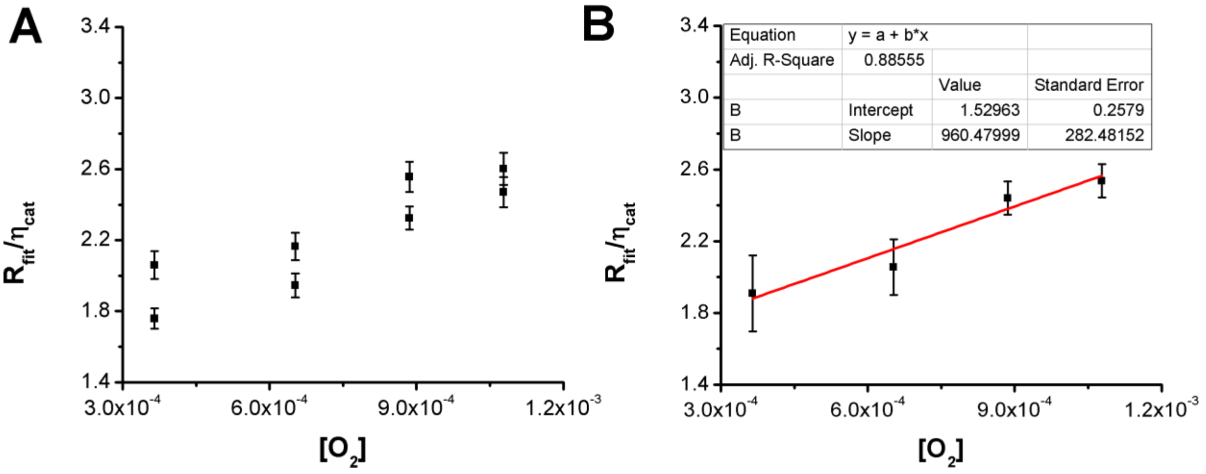

Equation	y = a + b*x		
Adj. R-Square	0.88555		
		Value	Standard Error
B	Intercept	1.52963	0.2579
B	Slope	960.47999	282.48152

Figure S3.6.40. The calculated R_{fit}/η_{cat} from stopped-flow spectrochemical experiments with 0.1 M $TBAPF_6$, TTBP, Cp_2^*Fe and Mn(^{tbu}dhbpy)Cl with varying O_2 concentration at 25.5°C in MeCN. Data were fit using Kinetic Studio 4.0 (1 Exp + Mx + C). Syringe concentrations: Mn(^{tbu}dhbpy)Cl = 4.96 x 10^{-5} M; TTBP = 7.30 x 10^{-3} M; Cp_2^*Fe = 3.00 x 10^{-3} M. Graph (A) represents all the series collected and the individual fits for each, while graph (B) represents the average of all the data points from graph (A).

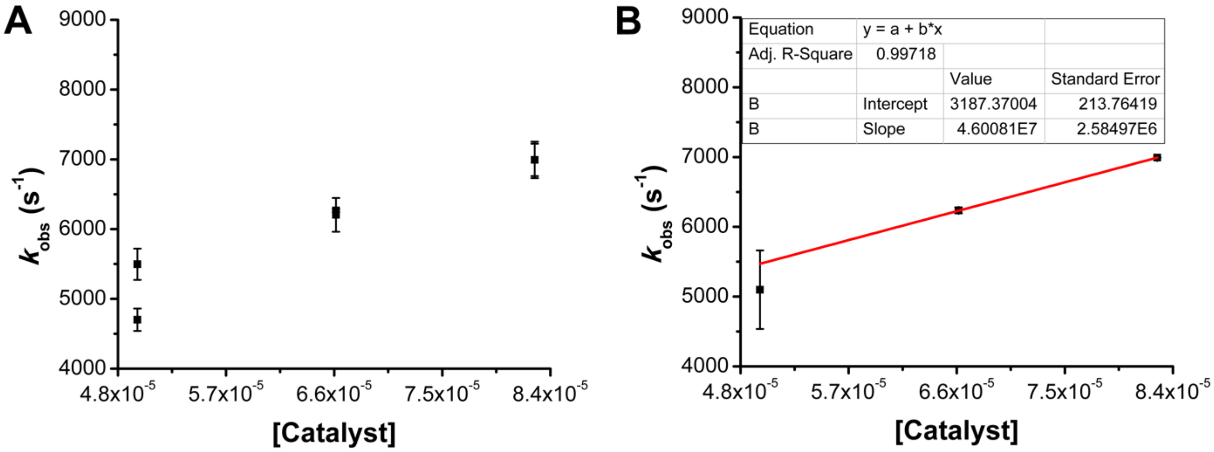

Figure S3.6.41. The calculated k_{obs} from stopped-flow spectrochemical experiments with 0.1 M TBAPF$_6$, TTBP, O$_2$ and Cp$_2^*$Fe with varying Mn(^{tbu}dhbpy)Cl concentration at 25.5°C in MeCN. Data were fit using Kinetic Studio 4.0 (1 Exp + Mx + C). Syringe concentrations: Cp$_2^*$Fe = 3.00 x 10^{-3} M; TTBP = 7.30 x 10^{-3} M; O$_2$ = 7.30 x 10^{-4} M. Graph (A) represents all the series collected and the individual fits for each, while graph (B) represents the average of all the data points from graph (A).

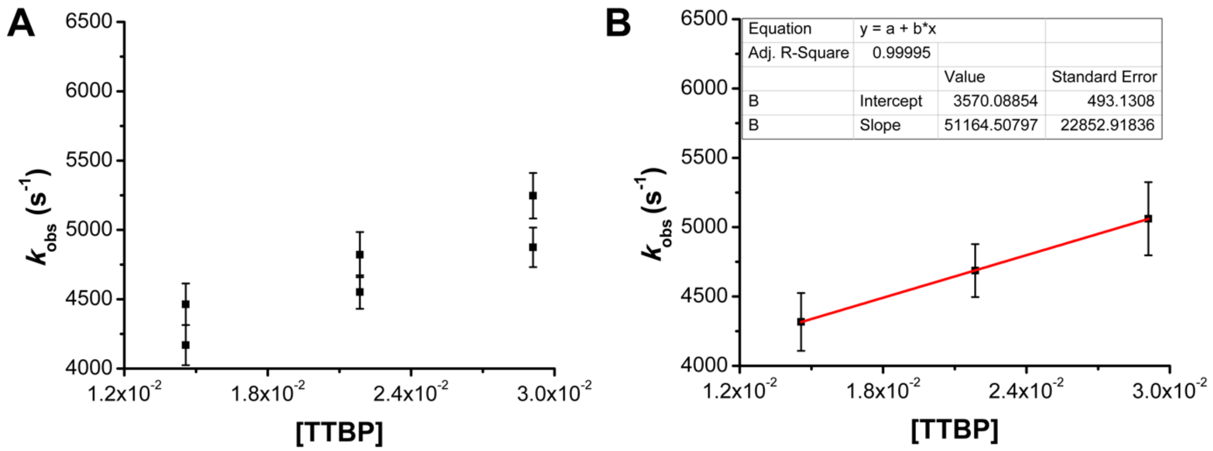

Figure S3.6.42. The calculated k_{obs} from stopped-flow spectrochemical experiments with 0.1 M TBAPF$_6$, Mn(^{tbu}dhbpy)Cl, O$_2$ and Cp$_2^*$Fe with varying TTBP concentration at 25.5°C in MeCN. Data were fit using Kinetic Studio 4.0 (1 Exp + Mx + C). Syringe concentrations: Cp$_2^*$Fe = 3.00 x 10^{-3} M; Mn(^{tbu}dhbpy)Cl = 4.96 x 10^{-5} M; O$_2$ = 7.30 x 10^{-4} M. Graph (A) represents all the series collected and the individual fits for each, while graph (B) represents the average of all the data points from graph (A).

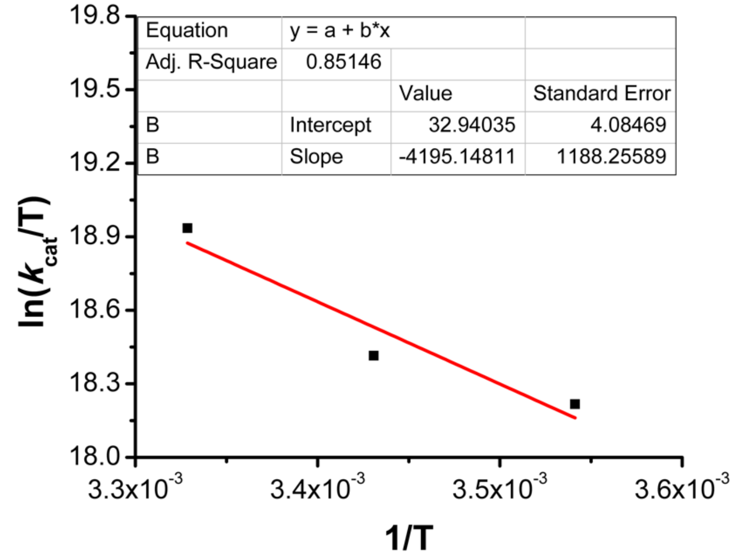

Figure S3.6.43. Eyring plots of the stopped-flow data spectrochemical experiments with Mn(^{tbu}dhbpy)Cl with 0.1 M TBAPF$_6$ in MeCN with TTBP. Data were fit using Kinetic Studio 4.0 (1 Exp + Mx + C). Syringe concentrations: Mn(^{tbu}dhbpy)Cl = 6.62 x 10^{-5} M; O$_2$ = 7.30 x 10^{-4} M; Cp$_2^*$Fe = 3.00 x 10^{-3} M; TTBP = 7.30 x 10^{-3} M.

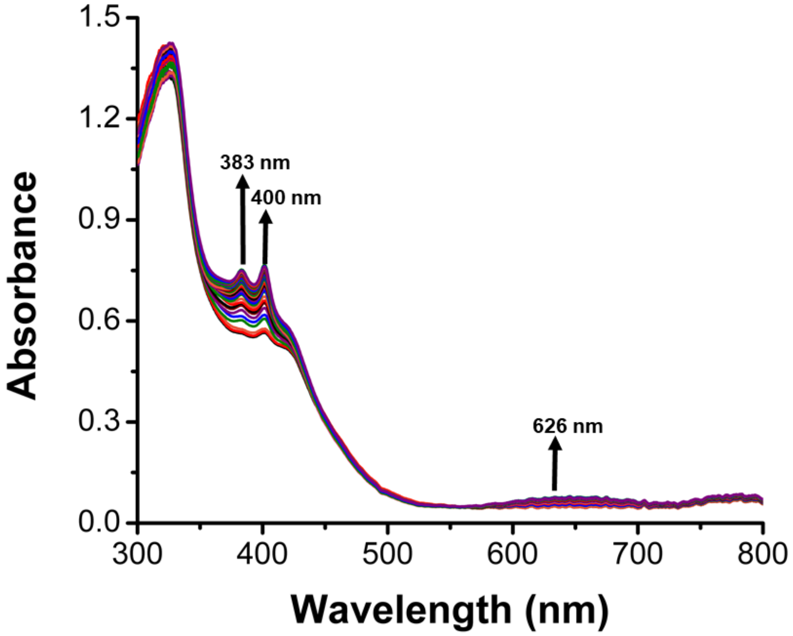

Figure S3.6.44. Stopped-Flow CCD data of 2,4,6-tritertbutylphenol radical appearance over 1000 seconds. Syringe concentrations: Mn(^{tbu}dhbpy)Cl = 4.85 x 10^{-5} M; O$_2$ = 1.77 x 10^{-3} M; Cp$_2^*$Fe = 3.22 x 10^{-3} M; 2,4,6-tritertbutylphenol = 3.40 x 10^{-2} M.

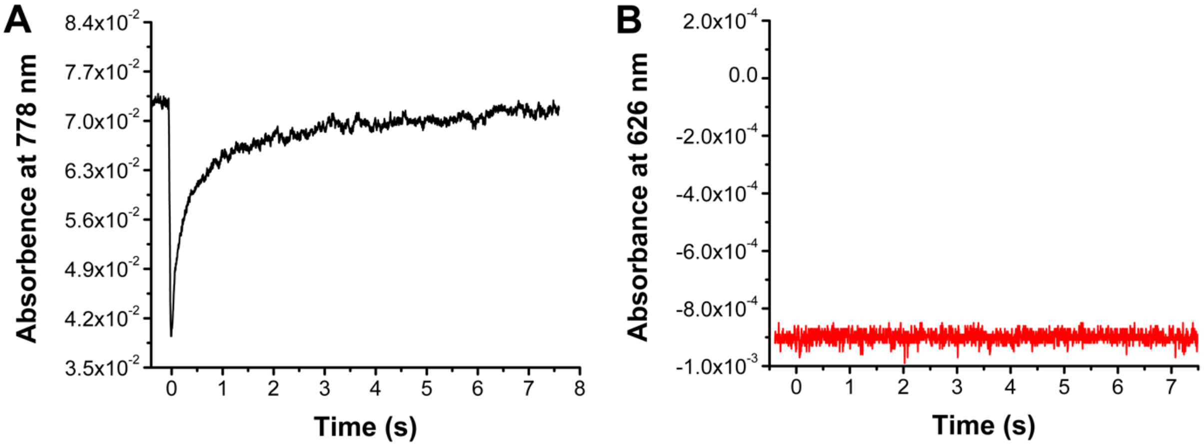

Figure S3.6.45. Stopped-Flow data comparing the appearance of **(A)** decamethylferricenium (black) and **(B)** 2,4,6-tritertbutylphenoxyl radical (red) at 778 and 626 nm, respectively. Syringe concentrations: Mn(^{tbu}dhbpy)Cl = 4.42 x 10^{-4} M; O_2 = 1.77 x 10^{-3} M; Cp_2^*Fe = 3.96 x 10^{-3} M; 2,4,6-tritertbutylphenol = 3.40 x 10^{-2} M.

Table S3.6.3. Third order rate constants obtained from spectrochemical experiments with 0.1 M $TBAPF_6$. H^+ corresponds to the proton donor indicated in the column heading.

Varied Substrate	Catalyst + PhOH k_{cat} ($M^{-2}s^{-1}$)	Catalyst + TTBP k_{cat} ($M^{-2}s^{-1}$)
H^+	1.07 x 10^{10}	2.06 x 10^9
Catalyst	1.97 x 10^{10}	1.26 x 10^{10}
O_2	1.26 x 10^{10}	1.06 x 10^{10}
Cp^*_2Fe	N.A.	N.A.
Average	1.4 x 10^{10} (±0.5)	8.4 x 10^9 (±5)

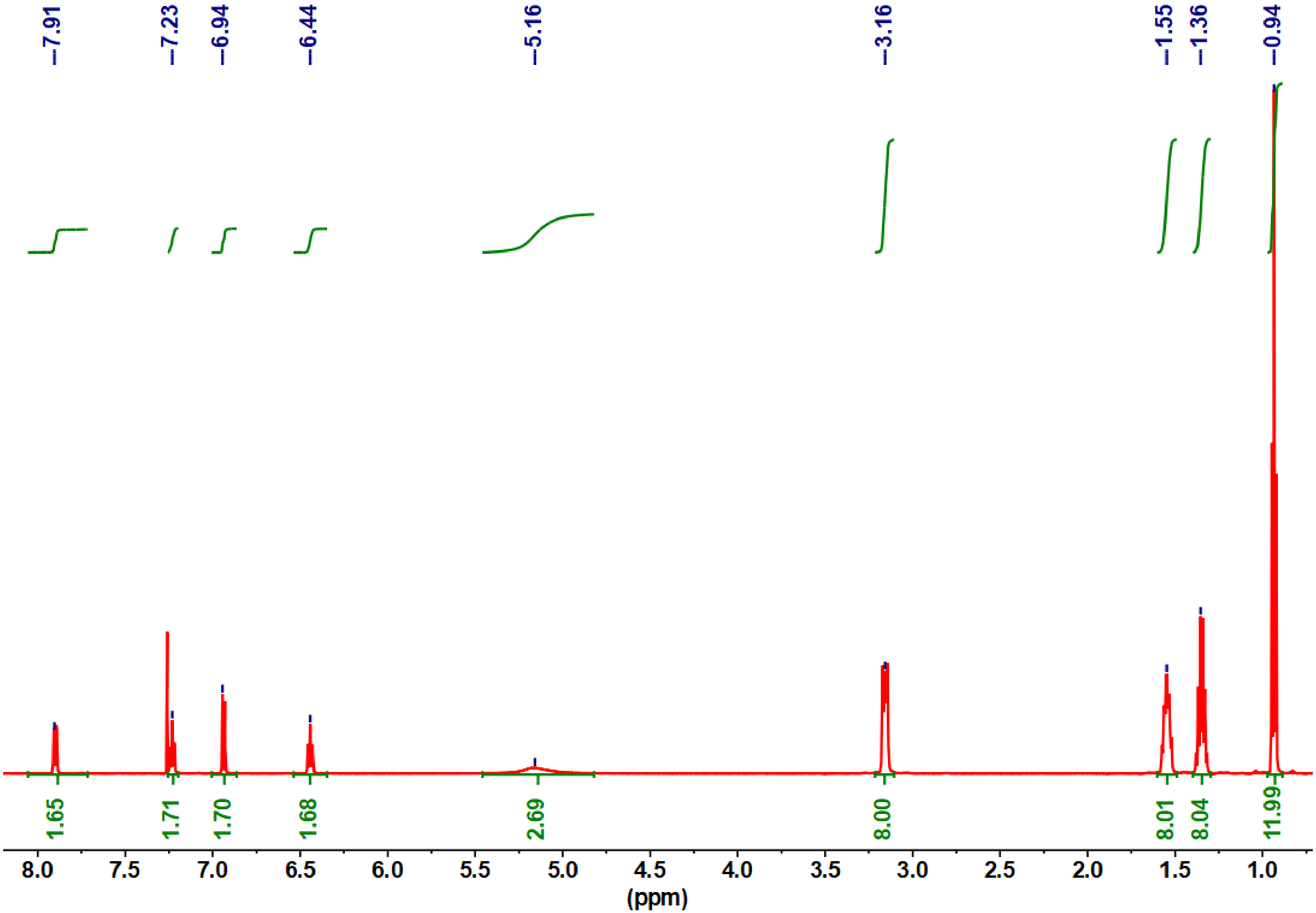

Figure S3.9.46. ^{1}H NMR 2-NO$_2$-PhOH Buffer; *d$_1$*-CDCl$_3$; 600 MHz Varian.

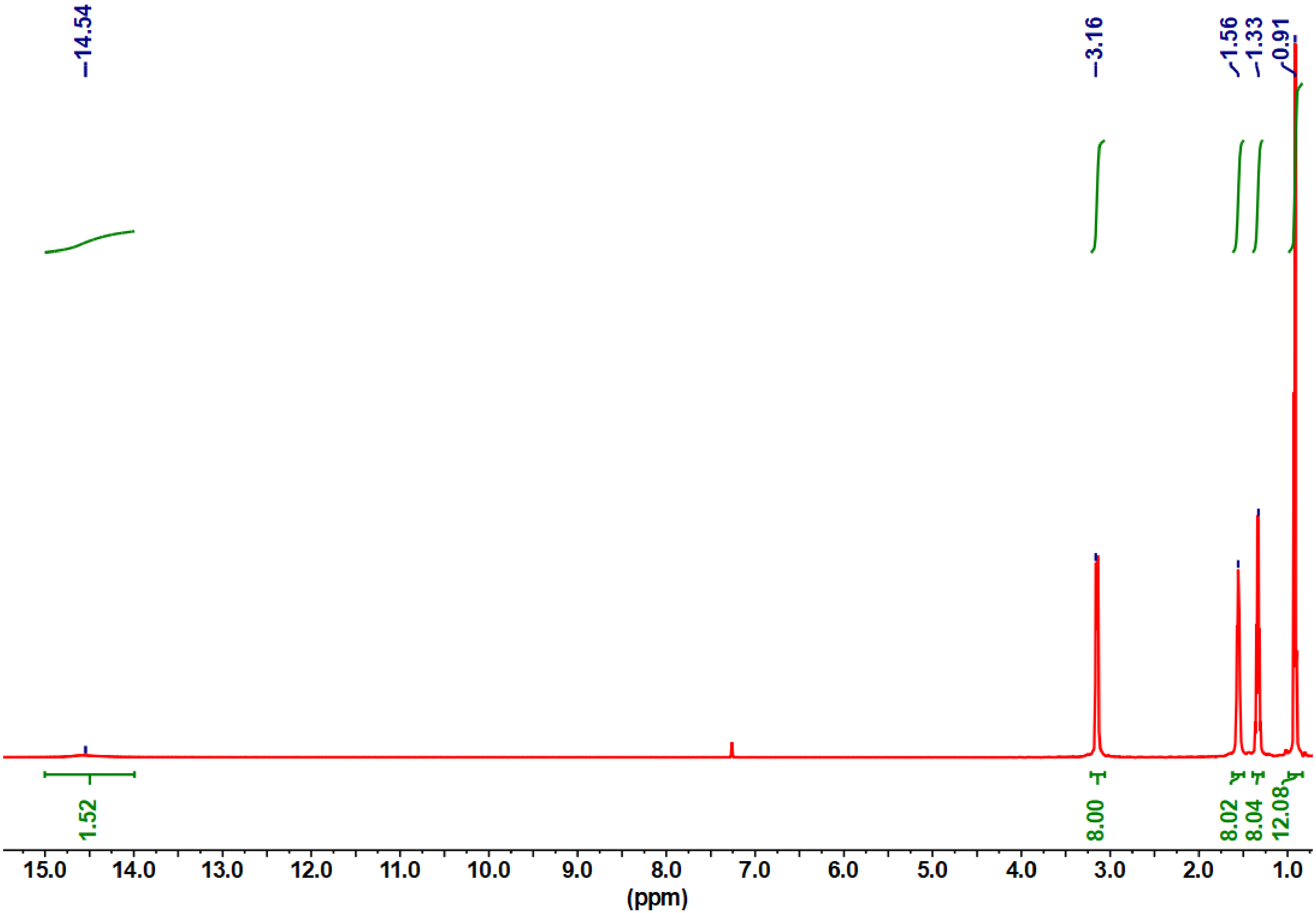

Figure S3.9.47. ^1H NMR F_5PhOH-PhOH Buffer; *d*$_1$-$CDCl_3$; 600 MHz Varian.

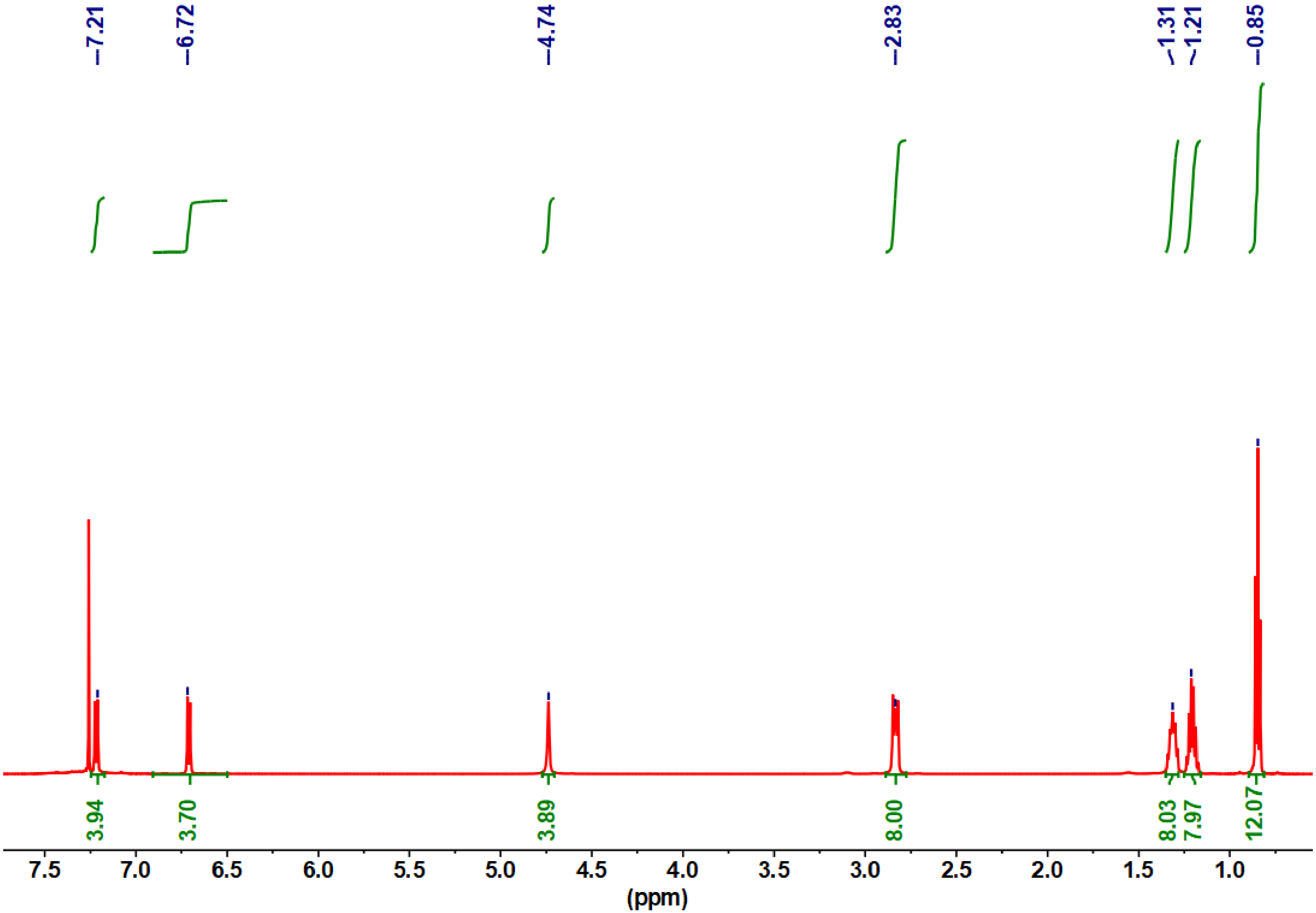

Figure S3.9.48. ^{1}H NMR 4-CF_3-PhOH Buffer; *d_1*-$CDCl_3$; 600 MHz Varian.

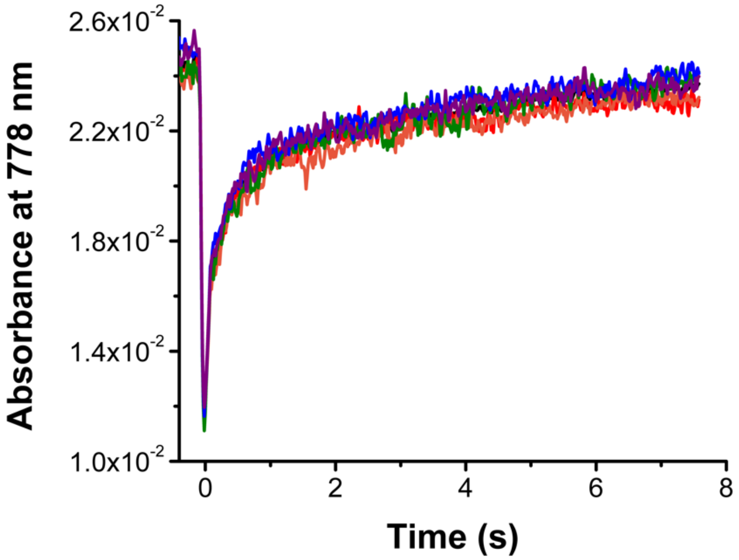

Figure S3.9.49. Stopped-flow data spectrochemical experiment sample series of five shots (black, red, orange, green, and blue) and the average of that series (purple) with Mn(^{tbu}dhbpy)Cl in MeCN. Syringe concentrations: Mn(^{tbu}dhbpy)Cl = 8.03×10^{-5} M; O_2 = 9.64×10^{-4} M; Cp_2^*Fe = 3.16×10^{-3} M.

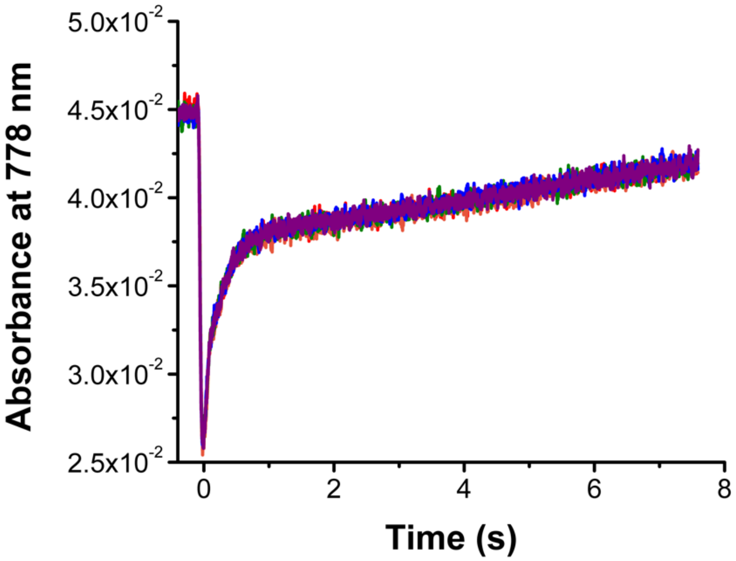

Figure S3.9.50. Stopped-flow data spectrochemical experiment sample series of five shots (black, red, orange, green, and blue) and the average of that series (purple) with Mn(^{tbu}dhbpy)Cl in MeCN with 0.1 M $TBAPF_6$. Syringe concentrations: Mn(^{tbu}dhbpy)Cl = 6.43×10^{-5} M; O_2 = 7.30×10^{-4} M; Cp_2^*Fe = 3.10×10^{-3} M.

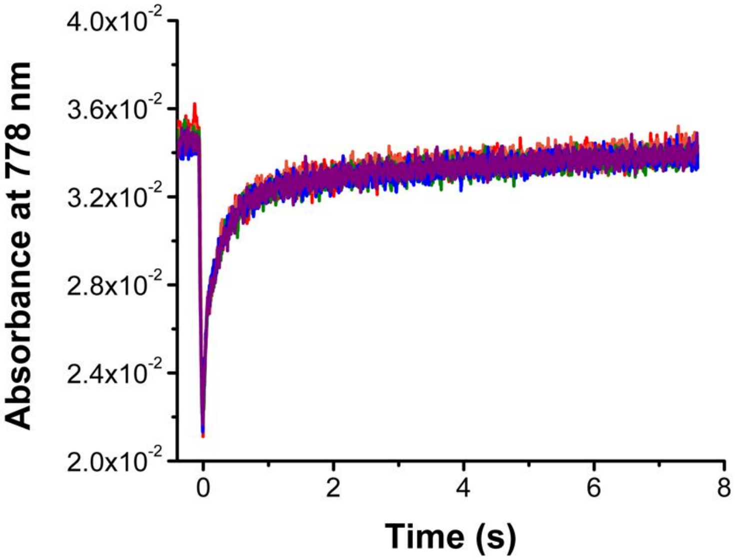

Figure S3.9.51. Stopped-flow data spectrochemical experiment sample series of five shots (black, red, orange, green, and blue) and the average of that series (purple) with Mn(^{tbu}dhbpy)Cl in MeCN. Syringe concentrations: Mn(^{tbu}dhbpy)Cl = 8.18 x 10^{-5} M; O_2 = 9.64 x 10^{-4} M; PhOH = 7.62 x 10^{-3} M; Cp_2^*Fe = 3.15 x 10^{-3} M.

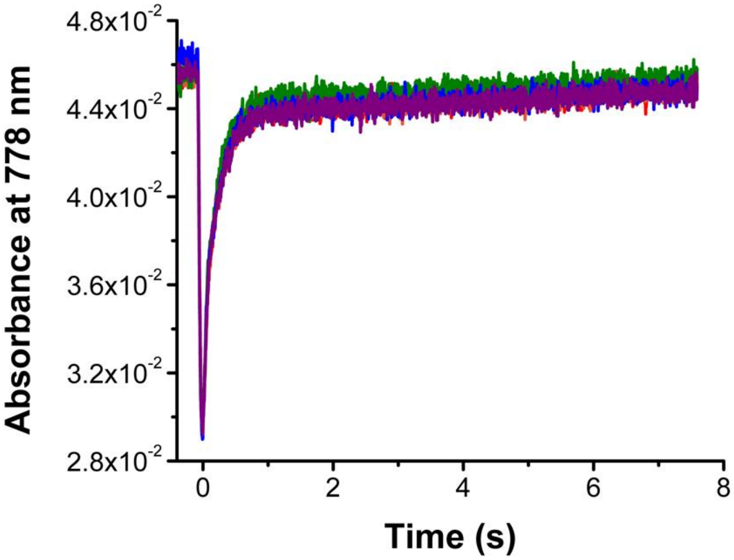

Figure S3.9.52. Stopped-flow data spectrochemical experiment sample series of five shots (black, red, orange, green, and blue) and the average of that series (purple) with Mn(^{tbu}dhbpy)Cl in MeCN with 0.1 M $TBAPF_6$. Syringe concentrations: Mn(^{tbu}dhbpy)Cl = 8.18 x 10^{-5} M; PhOH = 7.81 x 10^{-3} M; O_2 = 7.30 x 10^{-4} M; Cp_2^*Fe = 3.10 x 10^{-3} M.

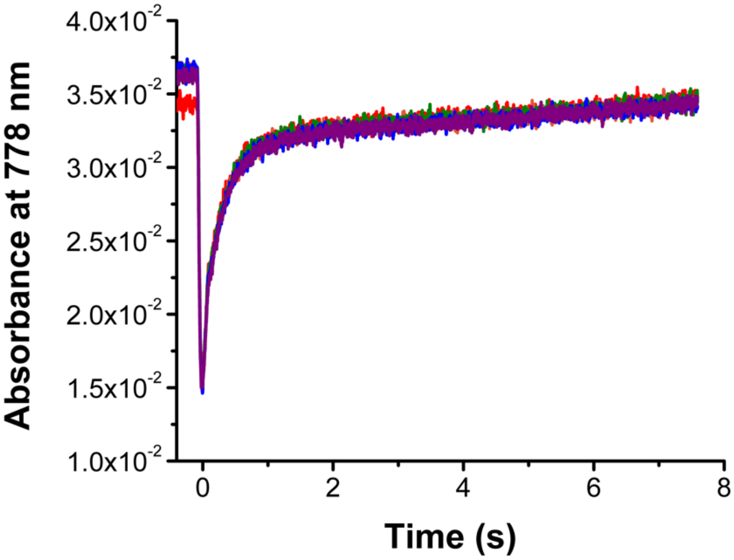

Figure S3.9.53. Stopped-flow data spectrochemical experiment sample series of five shots (black, red, orange, green, and blue) and the average of that series (purple) with Mn(^{tbu}dhbpy)Cl in MeCN with 0.1 M TBAPF$_6$. Syringe concentrations: Mn(^{tbu}dhbpy)Cl = 8.32 x 10^{-5} M; F$_5$PhOH Buffer = 2.46 x 10^{-5} M; O$_2$ = 7.30 x 10^{-4} M; Cp$_2^*$Fe = 3.10 x 10^{-3} M.

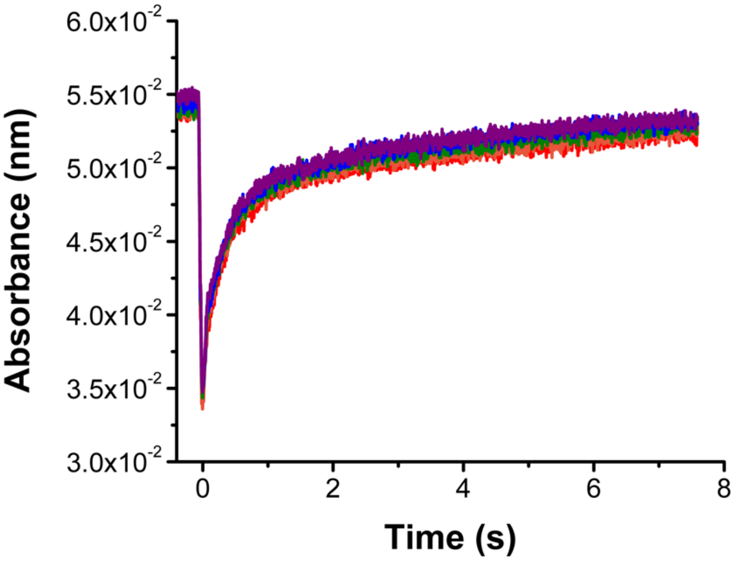

Figure S3.9.54. Stopped-flow data spectrochemical experiment sample series of five shots (black, red, orange, green, and blue) and the average of that series (purple) with Mn(^{tbu}dhbpy)Cl in MeCN with 0.1 M TBAPF$_6$. Syringe concentrations: Mn(^{tbu}dhbpy)Cl = 8.33 x 10^{-5} M; 2-NO$_2$-PhOH = 2.89 x 10^{-5} M; O$_2$ = 7.30 x 10^{-4} M; Cp$_2^*$Fe = 3.06 x 10^{-3} M.

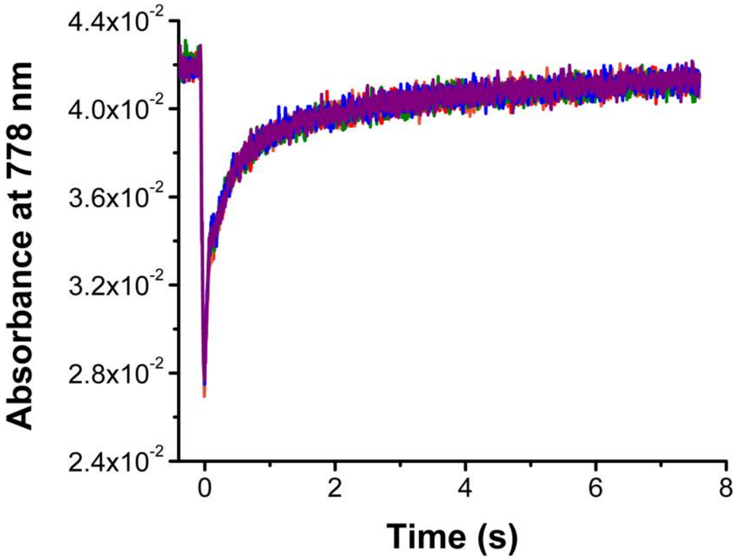

Figure S3.9.55. Stopped-flow data spectrochemical experiment sample series of five shots (black, red, orange, green, and blue) and the average of that series (purple) with Mn(^{tbu}dhbpy)Cl in MeCN with 0.1 M TBAPF$_6$. Syringe concentrations: Mn(^{tbu}dhbpy)Cl = 4.74 x 10^{-5} M; 4-CF$_3$-PhOH = 2.65 x 10^{-5} M; O$_2$ = 2.16 x 10^{-3} M; Cp$_2^*$Fe = 3.15 x 10^{-3} M.

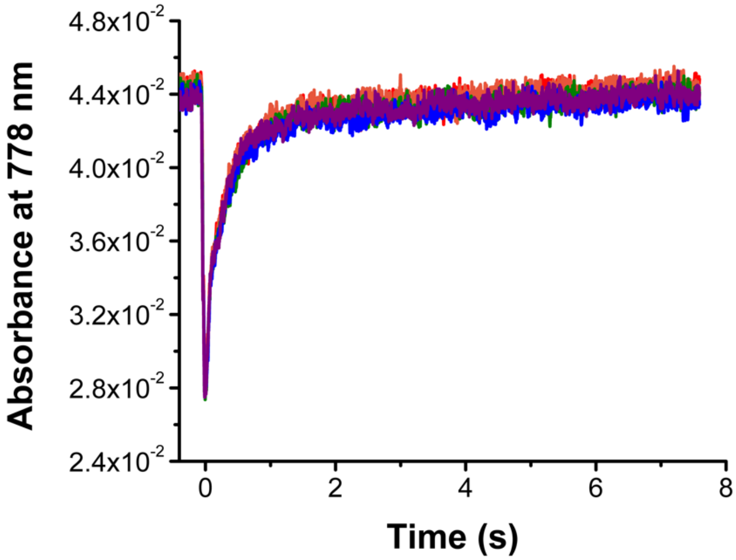

Figure S3.9.56. Stopped-flow data spectrochemical experiment sample series of five shots (black, red, orange, green, and blue) and the average of that series (purple) with Mn(^{tbu}dhbpy)Cl in MeCN with 0.1 M TBAPF$_6$. Syringe concentrations: Mn(^{tbu}dhbpy)Cl = 6.62 x 10^{-5} M; TTBP = 7.44 x 10^{-3} M; O$_2$ = 7.30 x 10^{-4} M; Cp$_2^*$Fe = 3.00 x 10^{-3} M.

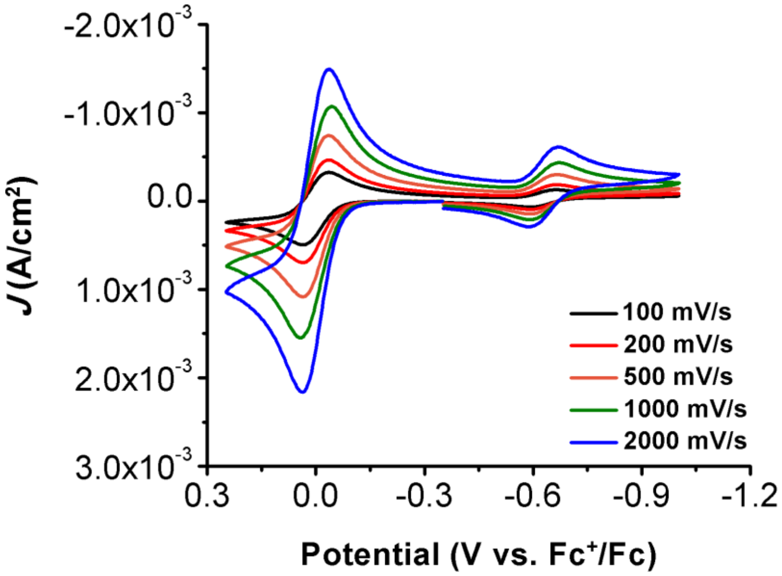

Figure S3.9.57. CVs of Mn(^{tbu}dhbpy)Cl **1**, obtained under Ar saturation conditions. Conditions: 0.5 mM analyte; glassy carbon working electrode, glassy carbon counter electrode, Ag/AgCl pseudoreference electrode; varied scan rate; referenced to internal ferrocene standard.

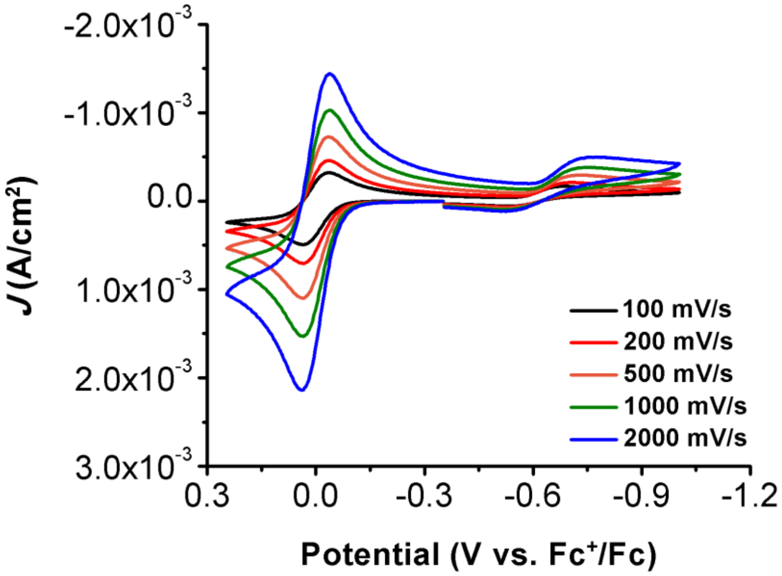

Figure S3.9.58. CVs of Mn(^{tbu}dhbpy)Cl **1**, obtained under O_2 saturation conditions. Conditions: 0.5 mM analyte; glassy carbon working electrode, glassy carbon counter electrode, Ag/AgCl pseudoreference electrode; varied scan rate; referenced to internal ferrocene standard.

Computational Summary

Table S3.9.4. Single point energies used in BDFE determinations (1 eH = 627.509 kcal mol^{-1}). Although full values are shown for completeness, only three significant figures are used for any calculated BDFEs reported in the manuscript. Performed with ORCA 4.0.1; unrestricted with the B3LYP/G functional; def2-TZVP basis set; RIJCOSX approximation; D3BJ dispersion correction, and CPCM to model the MeCN solvent. Numerical frequency calculations at the same level of theory were performed to validate the optimized geometries as minima on the potential energy surface and to generate thermochemical data.

Compound	Spin State (2*S*+1)	Gibbs Free Enthalpy (eH)	Gibbs Free Enthalpy (kcal mol^{-1})
$H^{\bullet}$	2	-0.49712	-311.9472741
PhOH	1	-307.5477039	-192988.9521
$PhO^{\bullet}$	2	-306.9116133	-192589.7995
F_5PhOH	1	-803.9606995	-504492.5746
$F_5PhO^{\bullet}$	2	-803.3302092	-504096.9363
2-NO_2-PhOH	1	-512.1519946	-321379.986
2-NO_2-$PhO^{\bullet}$	2	-511.5045476	-320973.7072
4-CF_3-PhOH	1	-644.7520695	-404587.7264
4-CF_3-$PhO^{\bullet}$	2	-644.1091693	-404184.3007
$[Mn(^{tbu}dhbpy)(H)(\eta_1\text{-}O_2)]^+$ *up* (ref. 1)	4	-2409.003965	-1511671.669
$[Mn(^{tbu}dhbpy)(H)(\eta_2\text{-}O_2)]^+$ *down*	4	-2409.017185	-1511679.965
$[Mn(^{tbu}dhbpy)(H)(\eta_2\text{-}O_2)]^+$ *down*	6	-2409.016763	-1511679.7
$[Mn(^{tbu}dhbpy)(\eta_1\text{-}O_2)]^{+\bullet}$	5	-2408.401596	-1511293.677
$[Mn(^{tbu}dhbpy)(\eta_1\text{-}O_2H)]$	5	-2409.211905	-1511802.154
$[Mn(^{tbu}dhbpy)(\eta_1\text{-}O_2)]^{\bullet}$	4	-2408.592966	-1511413.764
$[Mn(^{tbu}dhbpy)(\eta_2\text{-}O_2)]^{\bullet}$	6	-2408.597285	-1511416.474
$[Mn(^{tbu}dhbpy)(\eta_1\text{-}O_2H)]^+$ (ref. 1)	4	-2409.026242	-1511685.648
$[Mn(^{tbu}dhbpy)(\eta_2\text{-}O_2H)]^+$	6	-2409.008879	-1511674.753

In our computational studies on the proposed mechanisms, we discovered that there several minima with slight energetic differences in some cases between η_2- and η_1-O_2 binding modes to the Mn metal center and different conformations of the phenolate moieties relative to the plane of the bipyridine ring. These results are included for completeness and a range of values for relevant O–H BDFEs are reported in the manuscript. Ref. 1 – Hooe, S.L.; Rheingold, A.L.; Machan, C.W. *J. Am. Chem. Soc.* **2018**, *140*, 3232-3241

Coordinates

PhOH

C	-2.391252	0.485617	0.000851
C	-2.367141	-0.903394	0.000180
C	-1.157491	-1.593436	-0.000308
C	0.034716	-0.876345	0.000152
C	0.024375	0.514054	0.000782
C	-1.191468	1.194393	0.000905
O	-1.259341	2.558905	0.000272
H	-0.367435	2.930610	-0.002944
H	-3.328014	1.027770	0.000576
H	-3.302323	-1.449004	-0.000543
H	-1.144738	-2.675464	-0.001189
H	0.983164	-1.398401	0.000050
H	0.953337	1.072404	0.001218

$PhO^\bullet$

C	-2.427073	0.477768	0.003650
C	-2.392880	-0.892237	0.000475
C	-1.162658	-1.575701	-0.002016
C	0.047509	-0.858457	0.000302
C	0.041518	0.511424	0.001970
C	-1.202729	1.242381	0.001011
O	-1.215152	2.494074	-0.004412
H	-3.358708	1.029087	0.003575
H	-3.316594	-1.454658	-0.001862
H	-1.147192	-2.656495	-0.005847
H	0.987922	-1.392685	0.000830
H	0.955788	1.091119	0.004324

F_5PhOH

C	-2.376446	0.503405	-0.000319
C	-2.362266	-0.881627	-0.000385
C	-1.158348	-1.569238	0.000138
C	0.030741	-0.857559	0.000120
C	0.004506	0.525886	-0.000161
C	-1.192235	1.236298	0.000019
O	-1.250137	2.583016	0.001754
H	-0.356729	2.957354	-0.000494
F	-3.552689	1.145896	-0.000136
F	-3.515837	-1.557592	-0.000399
F	-1.145053	-2.907115	0.000554
F	1.200934	-1.503855	0.000324
F	1.159939	1.212841	-0.001015

$F_5PhO^\bullet$

C	-2.423486	0.491125	-0.000198
C	-2.393467	-0.874617	-0.000076

C	-1.159437	-1.542024	-0.000126
C	0.050711	-0.832169	0.000111
C	0.032562	0.533821	0.000509
C	-1.208972	1.288590	-0.000149
O	-1.230054	2.527701	-0.000740
F	-3.582829	1.131032	0.000304
F	-3.512695	-1.594372	0.000447
F	-1.137228	-2.860555	-0.000370
F	1.194977	-1.511624	-0.000237
F	1.168557	1.214132	0.000525

2-NO_2-PhOH

C	-2.333980	0.527453	-0.000823
C	-2.300222	-0.851501	-0.000221
C	-1.082378	-1.544664	0.000758
C	0.097594	-0.838185	0.000579
C	0.074628	0.562373	-0.000066
C	-1.148645	1.270164	-0.000379
O	-1.243370	2.602562	-0.000047
H	-0.326910	2.960247	0.003121
H	-3.271003	1.067280	-0.001683
H	-3.231646	-1.402240	-0.000658
H	-1.067601	-2.625372	0.001472
H	1.051728	-1.341983	0.001056
N	1.328457	1.262225	-0.000962
O	2.374490	0.631479	-0.002569
O	1.315809	2.508612	0.000422

2-NO_2-PhO$^\bullet$

C	-2.370882	0.502591	0.009176
C	-2.329198	-0.866116	-0.006513
C	-1.093739	-1.524204	-0.013666
C	0.107158	-0.794780	-0.005003
C	0.094317	0.573863	0.003585
C	-1.168304	1.320453	0.019626
O	-1.265685	2.556915	0.052878
H	-3.306912	1.044391	0.020054
H	-3.245137	-1.441024	-0.011359
H	-1.050558	-2.604260	-0.027611
H	1.051317	-1.317026	-0.015601
N	1.387222	1.257507	-0.004120
O	2.395910	0.572683	0.140558
O	1.415410	2.467836	-0.162004

4-CF_3-PhOH

C	-2.396755	0.625358	0.001076
C	-2.386699	-0.760503	0.001084
C	-1.178993	-1.452077	0.000906
C	0.023966	-0.747500	0.001078
C	0.020959	0.636166	0.000924
C	-1.192393	1.326438	0.000670

O	-1.249761	2.682596	-0.000858
H	-0.357011	3.053805	-0.003990
H	-3.330724	1.170693	0.000387
H	-3.323459	-1.299124	0.000686
C	-1.139590	-2.944354	-0.000544
H	0.967283	-1.277641	0.001200
H	0.954353	1.185088	0.000753
F	-2.365487	-3.504609	-0.001594
F	-0.485841	-3.445418	1.080827
F	-0.485057	-3.442827	-1.082606

4-CF$_3$-PhO$^\bullet$

C	-2.428773	0.610486	0.012864
C	-2.410237	-0.759956	0.009505
C	-1.184604	-1.440425	-0.007209
C	0.037312	-0.740463	-0.019462
C	0.041916	0.625590	-0.015914
C	-1.198683	1.369766	0.001724
O	-1.206073	2.621773	0.011564
H	-3.360021	1.159612	0.023592
H	-3.334925	-1.317852	0.018044
C	-1.138927	-2.944120	0.001007
H	0.969668	-1.288597	-0.031367
H	0.965961	1.186812	-0.022614
F	-2.358497	-3.501225	-0.073894
F	-0.554564	-3.407717	1.127358
F	-0.415834	-3.418486	-1.035198

[Mn(^{tbu}dhbpy)(H)(η_1-O_2)]$^+$ *up* (ref. 1)

Mn	-3.498915	2.400009	17.504358
O	-2.035583	2.612151	15.877385
O	-4.125463	4.068172	18.199030
N	-3.404623	0.344058	16.890533
N	-4.397380	1.373569	19.179672
C	-2.935394	0.834983	14.542732
C	-2.447817	2.143027	14.638985
C	-2.359139	2.974096	13.533591
C	-2.773009	2.514767	12.292230
H	-2.707563	3.167217	11.432123
C	-3.276739	1.224755	12.163731
C	-3.350242	0.402395	13.275596
H	-3.754695	-0.594399	13.173577
C	-3.027291	-0.106631	15.679655
C	-3.584242	-0.511548	17.918697
C	-4.058229	0.068033	19.202818
C	-4.154655	-0.682720	20.361484
C	-3.356040	-1.872585	17.764689
C	-4.881954	1.998110	20.271522
C	-5.338072	3.400163	20.200489
C	-4.932371	4.341429	19.206761
C	-5.406104	5.666088	19.303222
C	-6.280992	6.061916	20.292426
H	-6.632770	7.085477	20.322836
C	-6.720222	5.135998	21.240771
C	-6.245940	3.841288	21.184090
H	-6.613738	3.133418	21.912171
C	-2.766203	-1.462620	15.481492
C	-2.929970	-2.345617	16.533420
C	-4.596186	-0.048759	21.517482
C	-4.957313	1.280738	21.479209
H	-2.729693	-3.399422	16.396497
H	-2.430539	-1.811431	14.517423
H	-3.508749	-2.556802	18.583746
H	-3.874713	-1.723172	20.383720
H	-4.650962	-0.597240	22.448036
H	-5.277295	1.769931	22.384196
H	-5.064550	6.365839	18.551165
H	-7.427703	5.421285	22.007538
H	-1.967212	3.976242	13.653515
H	-3.615768	0.862691	11.203223
H	-1.584551	3.463989	15.777791
O	-1.505285	2.418939	18.764165
O	-1.494203	2.703043	19.937395

[Mn(^{tbu}dhbpy)(H)(η_2-O_2)]$^+$ *down* 2S+1=4

O	-5.878339	3.224967	17.104052
Mn	-4.284795	2.139843	17.233606
O	-3.366494	2.856284	15.804552

O	-3.460746	3.749381	18.635468
N	-3.579093	0.314494	16.832772
N	-4.576429	1.300034	19.074210
C	-3.084034	0.854825	14.488858
C	-3.228379	2.258271	14.624444
C	-3.195044	3.074342	13.484309
C	-3.036715	2.529090	12.226170
H	-3.015304	3.176312	11.359056
C	-2.920909	1.146084	12.074175
C	-2.944697	0.333348	13.189015
H	-2.879651	-0.735251	13.048396
C	-3.073169	-0.061139	15.634666
C	-3.653081	-0.551038	17.878426
C	-4.239498	-0.009975	19.114264
C	-4.419775	-0.757822	20.265209
C	-3.191007	-1.845914	17.765997
C	-5.029132	1.936796	20.172801
C	-5.281376	3.387417	20.133323
C	-4.476218	4.275011	19.407129
C	-4.693852	5.643183	19.440507
C	-5.740002	6.154111	20.194713
H	-5.913419	7.221829	20.211375
C	-6.565615	5.295712	20.914549
C	-6.329651	3.931791	20.885821
H	-6.978346	3.266372	21.438387
C	-2.547768	-1.357553	15.511255
C	-2.612940	-2.241423	16.564773
C	-4.933558	-0.131717	21.392068
C	-5.222800	1.219263	21.354274
H	-2.212525	-3.239910	16.459956
H	-2.077323	-1.658334	14.590278
H	-3.263981	-2.533309	18.593358
H	-4.156841	-1.802935	20.292503
H	-5.079375	-0.693086	22.304387
H	-5.566357	1.732342	22.239023
H	-4.048053	6.297412	18.867865
H	-7.391412	5.688186	21.491525
H	-3.298469	4.142085	13.625430
H	-2.822010	0.708233	11.090566
O	-6.442646	2.206097	16.506247
H	-2.943682	4.458237	18.224397

$[Mn(^{tbu}dhbpy)(H)(\eta_2\text{-}O_2)]^+$ *down* 2S+1=6

O	-5.842673	3.230923	17.032614
Mn	-4.182890	2.149564	17.264602
O	-3.245720	2.842312	15.853842
O	-3.466420	3.771757	18.627809
N	-3.556096	0.311632	16.844310
N	-4.536725	1.304118	19.083136
C	-3.090584	0.856902	14.498948

C	-3.172084	2.261955	14.657325
C	-3.139660	3.093629	13.529961
C	-3.041877	2.559354	12.260344
H	-3.020643	3.217273	11.401395
C	-2.986424	1.175370	12.086607
C	-3.009560	0.347136	13.190661
H	-2.991153	-0.721584	13.036013
C	-3.082179	-0.069256	15.636153
C	-3.633002	-0.555281	17.887709
C	-4.203557	-0.007274	19.126820
C	-4.386703	-0.752094	20.279062
C	-3.201309	-1.859767	17.761709
C	-5.006538	1.940636	20.174330
C	-5.282308	3.387095	20.125329
C	-4.494270	4.284572	19.394180
C	-4.734683	5.648498	19.417136
C	-5.789919	6.146144	20.167762
H	-5.982106	7.210649	20.177337
C	-6.600267	5.277947	20.892937
C	-6.340597	3.918043	20.873454
H	-6.978478	3.245715	21.430106
C	-2.593038	-1.377230	15.495539
C	-2.656858	-2.263543	16.547717
C	-4.904377	-0.123037	21.402367
C	-5.202652	1.225661	21.356961
H	-2.283006	-3.270967	16.430909
H	-2.151088	-1.684278	14.562390
H	-3.277333	-2.549611	18.586851
H	-4.124585	-1.797383	20.308853
H	-5.050916	-0.681161	22.316543
H	-5.556758	1.739260	22.236999
H	-4.099758	6.309624	18.840378
H	-7.433273	5.659368	21.466899
H	-3.193561	4.162653	13.688065
H	-2.934574	0.748754	11.094499
O	-6.241330	2.102855	16.478194
H	-2.952975	4.485013	18.219401

$[\mathrm{Mn}(^{tbu}\mathrm{dhbpy})(\eta_1\text{-}\mathrm{O}_2)]^{+\bullet}$

Mn	-3.678882	2.250940	17.561146
O	-2.995542	2.884905	15.991630
O	-3.921331	3.914039	18.276155
N	-3.445460	0.362417	16.970071
N	-4.352420	1.374432	19.218701
C	-3.051811	0.901213	14.612574
C	-3.006120	2.303240	14.792662
C	-2.945519	3.145409	13.673999
C	-2.960452	2.625776	12.394487
H	-2.921891	3.293838	11.543990
C	-3.039814	1.245795	12.200987

C	-3.079968	0.406395	13.295656
H	-3.164046	-0.657237	13.128460
C	-3.067999	-0.040102	15.733892
C	-3.539624	-0.517356	18.004430
C	-4.040713	0.050088	19.263861
C	-4.218401	-0.688453	20.414078
C	-3.210797	-1.846514	17.846118
C	-4.897730	2.007432	20.283894
C	-5.303324	3.411231	20.193197
C	-4.792124	4.291246	19.211600
C	-5.186854	5.636005	19.211271
C	-6.096943	6.107323	20.137030
H	-6.398510	7.146322	20.111631
C	-6.636872	5.241914	21.089974
C	-6.237022	3.921079	21.113802
H	-6.679476	3.260005	21.844121
C	-2.699140	-1.382030	15.552217
C	-2.767472	-2.274015	16.598776
C	-4.726641	-0.047489	21.539272
C	-5.068197	1.284753	21.474585
H	-2.477420	-3.304891	16.452020
H	-2.340479	-1.711236	14.591420
H	-3.292602	-2.539015	18.668430
H	-3.966011	-1.736001	20.443840
H	-4.853692	-0.594888	22.462792
H	-5.447633	1.783222	22.350797
H	-4.764845	6.286526	18.457131
H	-7.369024	5.596575	21.802343
H	-2.894281	4.212301	13.846133
H	-3.076784	0.832081	11.202806
O	-1.411700	2.149463	18.536107
O	-1.069960	1.290142	19.309309

[Mn(^{tbu}dhbpy)(η_1-O_2H)]

O	-5.673848	2.584616	16.606664
Mn	-3.875944	2.237901	17.415202
O	-2.663034	2.771123	16.065920
O	-3.754582	3.874217	18.310920
N	-3.522556	0.319588	16.907125
N	-4.392223	1.334456	19.158456
C	-3.064804	0.909421	14.588721
C	-2.801420	2.281732	14.841221
C	-2.661582	3.153278	13.747453
C	-2.814408	2.703720	12.449658
H	-2.717290	3.400849	11.626994
C	-3.111035	1.362609	12.198418
C	-3.223273	0.484946	13.259466
H	-3.466868	-0.549670	13.061949
C	-3.144699	-0.072533	15.674287

C	-3.632547	-0.561774	17.928113
C	-4.101299	0.012191	19.198907
C	-4.269712	-0.725247	20.355814
C	-3.349024	-1.903270	17.748400
C	-4.888368	1.978322	20.234101
C	-5.258643	3.394370	20.137108
C	-4.666446	4.268796	19.190572
C	-5.029325	5.625955	19.199898
C	-5.971024	6.109406	20.087476
H	-6.242700	7.157164	20.062697
C	-6.582424	5.247909	21.000394
C	-6.219509	3.915124	21.020189
H	-6.709992	3.251367	21.718377
C	-2.827038	-1.420519	15.459580
C	-2.932260	-2.328871	16.492745
C	-4.734963	-0.073594	21.491927
C	-5.043232	1.269372	21.434422
H	-2.685271	-3.368653	16.328046
H	-2.479629	-1.739396	14.489994
H	-3.449537	-2.604289	18.561892
H	-4.040086	-1.778584	20.379393
H	-4.853546	-0.617947	22.418728
H	-5.385909	1.783089	22.318111
H	-4.553631	6.278218	18.479190
H	-7.339003	5.613822	21.681174
H	-2.441978	4.192266	13.955876
H	-3.258356	1.012016	11.186160
O	-6.093617	1.544443	15.665511
H	-5.698986	1.846970	14.835059

$[\mathrm{Mn}(^{tbu}\mathrm{dhbpy})(\eta_1\text{-}\mathrm{O}_2)]^{\bullet}$ 2S+1=4

O	-5.687730	2.538140	16.633261
Mn	-3.828445	2.223837	17.439286
O	-2.680420	2.777133	16.066878
O	-3.735265	3.865838	18.319630
N	-3.487817	0.309826	16.919974
N	-4.365169	1.325011	19.169977
C	-3.017358	0.893148	14.598900
C	-2.785774	2.270547	14.842898
C	-2.632056	3.137409	13.748939
C	-2.743022	2.676157	12.451113
H	-2.634728	3.368244	11.625657
C	-3.010476	1.328236	12.204336
C	-3.135166	0.457204	13.269103
H	-3.357496	-0.581974	13.071502
C	-3.106995	-0.083112	15.687389
C	-3.602213	-0.572143	17.941736
C	-4.074568	0.001724	19.210670
C	-4.247182	-0.734836	20.366803
C	-3.320112	-1.913211	17.764735

C	-4.867270	1.969239	20.243600
C	-5.240702	3.383625	20.144509
C	-4.650435	4.258407	19.197995
C	-5.017856	5.613762	19.201494
C	-5.962196	6.096071	20.086683
H	-6.237676	7.142673	20.058976
C	-6.571374	5.234632	21.001391
C	-6.204617	3.903327	21.025389
H	-6.694687	3.239743	21.723922
C	-2.789887	-1.433109	15.477611
C	-2.899218	-2.340024	16.510438
C	-4.717227	-0.083016	21.501006
C	-5.026725	1.259466	21.442555
H	-2.651884	-3.379948	16.347377
H	-2.437876	-1.754686	14.510858
H	-3.424043	-2.613413	18.578397
H	-4.017394	-1.788036	20.391660
H	-4.838884	-0.627475	22.427294
H	-5.373814	1.772474	22.324862
H	-4.543236	6.265362	18.479601
H	-7.330069	5.599685	21.680212
H	-2.434751	4.181155	13.955858
H	-3.125207	0.966696	11.191687
O	-6.096079	1.631772	15.761743

$[\mathrm{Mn}(^{tbu}\mathrm{dhbpy})(\eta_2\text{-}\mathrm{O}_2)]^{\bullet}$ 2S+1=6

O	-5.901046	2.991960	16.767310
Mn	-3.968734	2.224293	17.399005
O	-2.987508	2.852402	15.943477
O	-3.636210	3.790624	18.413796
N	-3.479933	0.316869	16.891869
N	-4.455270	1.303866	19.124332
C	-3.020413	0.874579	14.558101
C	-2.982225	2.279060	14.747608
C	-2.900635	3.116565	13.621768
C	-2.890125	2.598112	12.341969
H	-2.836364	3.267123	11.492522
C	-2.964807	1.217793	12.145229
C	-3.023849	0.380450	13.241711
H	-3.100194	-0.685009	13.076947
C	-3.035504	-0.071975	15.679494
C	-3.578711	-0.561140	17.918965
C	-4.139820	-0.013048	19.162509
C	-4.359135	-0.766725	20.300693
C	-3.194812	-1.882134	17.776697
C	-4.980386	1.935991	20.194760
C	-5.272532	3.369820	20.128206
C	-4.550193	4.233196	19.263342
C	-4.797507	5.615601	19.329246

C	-5.754474	6.130954	20.182109
H	-5.937936	7.198164	20.198505
C	-6.496766	5.280757	21.005624
C	-6.244298	3.922777	20.978267
H	-6.827903	3.267670	21.610437
C	-2.597916	-1.394539	15.510932
C	-2.679886	-2.292692	16.553664
C	-4.900778	-0.139929	21.416740
C	-5.204428	1.204373	21.369438
H	-2.343708	-3.311583	16.420772
H	-2.180800	-1.703840	14.566599
H	-3.285429	-2.576852	18.596523
H	-4.114461	-1.816440	20.325312
H	-5.069940	-0.702688	22.324441
H	-5.586992	1.704674	22.244637
H	-4.224810	6.261395	18.676330
H	-7.265213	5.677178	21.655331
H	-2.853246	4.184371	13.792668
H	-2.982872	0.803813	11.146376
O	-5.997331	1.699724	16.503646

[Mn(^{tbu}dhbpy)(η_1-O_2H)]$^+$ 2S+1=4 (ref. 1)

Mn	-4.229483	2.048472	17.399605
O	-4.478831	2.380459	15.623167
O	-5.383928	3.370537	17.900042
N	-3.603093	0.197423	16.938951
N	-4.461190	1.200549	19.199655
C	-2.891626	0.833170	14.694398
C	-3.588793	2.064476	14.683637
C	-3.374959	2.980671	13.644863
C	-2.476038	2.697364	12.634939
H	-2.315210	3.416467	11.842366
C	-1.765070	1.495262	12.646184
C	-3.117328	-0.172425	15.734108
C	-3.761971	-0.701362	17.942275
C	-4.239158	-0.139240	19.209810
C	-4.443699	-0.888735	20.350555
C	-3.469139	-2.038024	17.757735
C	-4.876417	1.852116	20.309747
C	-5.081759	3.300198	20.280669
C	-5.346467	3.991697	19.073943
C	-5.598311	5.370776	19.096934
C	-5.566540	6.067435	20.287608
H	-5.755207	7.132859	20.292394
C	-5.274300	5.401944	21.481384
C	-5.043313	4.039676	21.472045
H	-4.801769	3.543507	22.400296
C	-2.837368	-1.525820	15.504770
C	-3.015069	-2.451430	16.510749

C	-4.898300	-0.245606	21.495990
C	-5.114657	1.115234	21.477372
H	-2.802553	-3.495998	16.330874
H	-2.500378	-1.842409	14.531355
H	-3.596969	-2.747549	18.559702
H	-4.261321	-1.951385	20.352195
H	-5.088171	-0.812790	22.396439
H	-5.490655	1.615138	22.354902
H	-5.808286	5.864677	18.158277
H	-5.221910	5.949192	22.412438
H	-3.928231	3.909521	13.663316
O	-2.521636	2.773776	17.580118
O	-2.396056	3.579049	18.712987
C	-1.976714	0.581097	13.661253
H	-1.043665	1.279474	11.870113
H	-1.404571	-0.335004	13.669074
H	-2.000931	2.983571	19.375154

[Mn(^{tbu}dhbpy)(η_2-O_2H)]$^+$ 2S+1=6

O	-5.847619	3.145102	17.114309
Mn	-4.243695	2.152638	17.240042
O	-3.359462	2.841855	15.772578
O	-3.576768	3.824056	18.540748
N	-3.509382	0.311838	16.841208
N	-4.582792	1.278582	19.043472
C	-3.020471	0.825724	14.493892
C	-3.216874	2.225411	14.605377
C	-3.225766	3.017754	13.446841
C	-3.055519	2.454120	12.198407
H	-3.066940	3.083911	11.318247
C	-2.883944	1.074113	12.072483
C	-2.867653	0.284039	13.203747
H	-2.761398	-0.783889	13.084096
C	-2.979960	-0.067032	15.655925
C	-3.584043	-0.551030	17.887458
C	-4.228757	-0.021110	19.098340
C	-4.456383	-0.777370	20.240582
C	-3.081439	-1.832573	17.801765
C	-5.107207	1.902805	20.116198
C	-5.337384	3.353639	20.088569
C	-4.432211	4.247311	19.363623
C	-4.551731	5.668300	19.584218
C	-5.561625	6.177277	20.348011
H	-5.672552	7.245951	20.471327
C	-6.475566	5.304335	20.968250
C	-6.340612	3.916779	20.849235
H	-7.046332	3.281350	21.365151
C	-2.409701	-1.348300	15.555755
C	-2.462544	-2.221581	16.617872
C	-5.043129	-0.166930	21.335923

C	-5.354405	1.181451	21.283852
H	-2.026672	-3.206991	16.533002
H	-1.917138	-1.644522	14.644887
H	-3.152985	-2.514024	18.634392
H	-4.177222	-1.817968	20.277330
H	-5.232059	-0.732841	22.237228
H	-5.752172	1.684095	22.151324
H	-3.842080	6.301599	19.069887
H	-7.286876	5.707040	21.558624
H	-3.370305	4.083319	13.567177
H	-2.774288	0.621224	11.096805
O	-6.386135	2.116135	16.231689
H	-6.363825	2.549318	15.362464

3.10 Acknowledgments

The authors thank the University of Virginia for generous funding and ARCS for maintenance and support with the Rivanna High-Performance Cluster.

3.11 References:

1. Sahu, S.; Goldberg, D. P., *J. Am. Chem. Soc.* **2016,** *138*, 11410-11428.
2. Gennari, M.; Brazzolotto, D.; Pécaut, J.; Cherrier, M. V.; Pollock, C. J.; DeBeer, S.; Retegan, M.; Pantazis, D. A.; Neese, F.; Rouzières, M.; Clérac, R.; Duboc, C., *J. Am. Chem. Soc.* **2015,** *137*, 8644-8653.
3. Coggins, M. K.; Sun, X.; Kwak, Y.; Solomon, E. I.; Rybak-Akimova, E.; Kovacs, J. A., *J. Am. Chem. Soc.* **2013,** *135*, 5631-5640.
4. Coggins, M. K.; Toledo, S.; Shaffer, E.; Kaminsky, W.; Shearer, J.; Kovacs, J. A., *Inorg. Chem.* **2012,** *51*, 6633-6644.
5. Gallo, E.; Solari, E.; Floriani, C.; Re, N.; Chiesi-Villa, A.; Rizzoli, C., *Angew. Chem. Int. Ed.* **1996,** *35*, 1981-1983.
6. Hong, S.; Lee, Y.-M.; Sankaralingam, M.; Vardhaman, A. K.; Park, Y. J.; Cho, K.-B.; Ogura, T.; Sarangi, R.; Fukuzumi, S.; Nam, W., *J. Am. Chem. Soc.* **2016,** *138*, 8523-8532.

7. Jung, J.; Liu, S.; Ohkubo, K.; Abu-Omar, M. M.; Fukuzumi, S., *Inorg. Chem.* **2015,** *54*, 4285-4291.

8. Ching, H. Y. V.; Anxolabéhère-Mallart, E.; Colmer, H. E.; Costentin, C.; Dorlet, P.; Jackson, T. A.; Policar, C.; Robert, M., *Chem. Sci.* **2014,** *5*, 2304-2310.

9. Baglia, R. A.; Zaragoza, J. P. T.; Goldberg, D. P., *Chem. Rev.* **2017,** *117*, 13320-13352.

10. Balamurugan, M.; Saravanan, N.; Ha, H.; Lee, Y. H.; Nam, K. T. J. N. C., *Nano Convergence* **2018,** *5*, 18.

11. Masa, J.; Ozoemena, K.; Schuhmann, W.; Zagal, J. H., *J. Porphyr. Phthalocyanines* **2012,** *16*, 761-784.

12. Zagal, J.; Páez, M.; Tanaka, A. A.; dos Santos, J. R.; Linkous, C. A., *J. Electroanal. Chem.* **1992,** *339*, 13-30.

13. Zagal, J. H.; Griveau, S.; Silva, J. F.; Nyokong, T.; Bedioui, F., *Coord. Chem. Rev.* **2010,** *254*, 2755-2791.

14. Zagal, J. H.; Javier Recio, F.; Gutierrez, C. A.; Zuñiga, C.; Páez, M. A.; Caro, C. A., *Electrochem. Commun.* **2014,** *41*, 24-26.

15. Flyagina, I. S.; Hughes, K. J.; Pourkashanian, M.; Ingham, D. B., *Int. J. Hydrogen Energ.* **2014,** *39*, 21538-21546.

16. Masa, J.; Schuhmann, W., *Chem. Eur. J.* **2013,** *19*, 9644-9654.

17. Schöfberger, W.; Faschinger, F.; Chattopadhyay, S.; Bhakta, S.; Mondal, B.; Elemans, J. A. A. W.; Müllegger, S.; Tebi, S.; Koch, R.; Klappenberger, F.; Paszkiewicz, M.; Barth, J. V.; Rauls, E.; Aldahhak, H.; Schmidt, W. G.; Dey, A., *Angew. Chem. Int. Ed.* **2016,** *55*, 2350-2355.

18. McGuire Jr, R.; Dogutan, D. K.; Teets, T. S.; Suntivich, J.; Shao-Horn, Y.; Nocera, D. G., *Chem. Sci.* **2010,** *1*, 411-414.

19. Passard, G.; Ullman, A. M.; Brodsky, C. N.; Nocera, D. G., *J. Am. Chem. Soc.* **2016,** *138*, 2925-2928.

20. Pegis, M. L.; McKeown, B. A.; Kumar, N.; Lang, K.; Wasylenko, D. J.; Zhang, X. P.; Raugei, S.; Mayer, J. M., *ACS Cent. Sci.* **2016,** *2*, 850-856.

21. Wasylenko, D. J.; Rodríguez, C.; Pegis, M. L.; Mayer, J. M., *J. Am. Chem. Soc.* **2014,** *136*, 12544-12547.

22. Nagao, K.; Hiroshi, S.; Tetsuo, O., *Chem. Lett.* **1985,** *14*, 1917-1920.

23. Passard, G.; Dogutan, D. K.; Qiu, M.; Costentin, C.; Nocera, D. G., *ACS Catal.* **2018**.

24. Law, N. A.; Caudle, M. T.; Pecoraro, V. L., *Advances in Inorganic Chemistry: Manganese Redox Enzymes and Model Systems: Properties, Structures, and Reactivity*. 1999; Vol. 46.

25. Anson, C. W.; Stahl, S. S., *J. Am. Chem. Soc.* **2017,** *139*, 18472-18475.

26. Wang, Y.-H.; Pegis, M. L.; Mayer, J. M.; Stahl, S. S., *J. Am. Chem. Soc.* **2017,** *139*, 16458-16461.

27. Anson, C. W.; Ghosh, S.; Hammes-Schiffer, S.; Stahl, S. S., *J. Am. Chem. Soc.* **2016,** *138*, 4186-4193.

28. Solis, B. H.; Hammes-Schiffer, S., *Inorg. Chem.* **2014,** *53*, 6427-6443.

29. Hooe, S. L.; Rheingold, A. L.; Machan, C. W., *J. Am. Chem. Soc.* **2018,** *140*, 3232-3241.

30. Costentin, C.; Savéant, J.-M., *Chem. Electro. Chem.* **2014,** *1*, 1226-1236.

31. Pegis, M. L.; Wise, C. F.; Martin, D. J.; Mayer, J. M., *Chem. Rev.* **2018,** *118*, 2340-2391.

32. Kütt, A.; Leito, I.; Kaljurand, I.; Sooväli, L.; Vlasov, V. M.; Yagupolskii, L. M.; Koppel, I. A., *J. Org. Chem.* **2006,** *71*, 2829-2838.

33. Warren, J. J.; Tronic, T. A.; Mayer, J. M., *Chem. Rev.* **2010,** *110*, 6961-7001.

34. Bockris, J. O. M.; Nagy, Z., *J. Chem. Ed.* **1973,** *50*, 839.

35. Elgrishi, N.; Kurtz, D. A.; Dempsey, J. L., *J. Am. Chem. Soc.* **2017,** *139*, 239-244.

36. Savéant, J.-M., *Elements of molecular and biomolecular electrochemistry: an electrochemical approach to electron transfer chemistry*. John Wiley & Sons, Inc.: Hoboken, NJ, 2006.

37. Roy, K.; Popelier, P. L. A., *J. Phys. Org. Chem.* **2009,** *22*, 186-196.

38. Bard, A. J.; Faulkner, L. R., *Electrochemical Methods: Fundamentals and Applications*. 2nd ed.; John Wiley & Sons, Inc.: Hoboken, NJ, 2001.

39. Li, Q.; Batchelor-McAuley, C.; Lawrence, N. S.; Hartshorne, R. S.; Compton, R. G., *J. Electroanal. Chem.* **2013,** *688*, 328-335.

40. Oliveira, R.; Zouari, W.; Herrero, C.; Banse, F.; Schöllhorn, B.; Fave, C.; Anxolabéhère-Mallart, E., *Inorg. Chem.* **2016,** *55*, 12204-12210.

41. McCarthy, B. D.; Martin, D. J.; Rountree, E. S.; Ullman, A. C.; Dempsey, J. L., *Inorg. Chem.* **2014,** *53*, 8350-8361.

42. Manner, V. W.; Markle, T. F.; Freudenthal, J. H.; Roth, J. P.; Mayer, J. M., *Chem. Commun.* **2008**, 256-258.

43. Harlow, G. A.; Bruss, D. B., *Anal. Chem.* **1958,** *30*, 1833-1836.

44. Neese, F., *WIREs Comput. Mol. Sci.* **2012,** *2*, 73-78.

45. Vosko, S. H.; Wilk, L.; Nusair, M., *Can. J. Phys.* **1980,** *58*, 1200-1211.

46. Lee, C.; Yang, W.; Parr, R. G., *Phys. Rev. B* **1988,** *37*, 785-789.

47. Becke, A. D., *J. Chem. Phys.* **1993,** *98*, 5648-5652.

48. Becke, A. D., *J. Chem. Phys.* **1993,** *98*, 1372-1377.

49. Stephens, P. J.; Devlin, F. J.; Chabalowski, C. F.; Frisch, M. J., *J. Phys. Chem.* **1994,** *98*, 11623-11627.

50. Schäfer, A.; Horn, H.; Ahlrichs, R., *J. Chem. Phys.* **1992,** *97*, 2571-2577.

51. Weigend, F.; Ahlrichs, R., *Phys. Chem. Chem. Phys.* **2005,** *7*, 3297-3305.

52. Izsák, R.; Neese, F., *J. Chem. Phys.* **2011,** *135*, 144105.

53. Grimme, S.; Antony, J.; Ehrlich, S.; Krieg, H., *J. Chem. Phys.* **2010,** *132*, 154104.

54. Grimme, S.; Ehrlich, S.; Goerigk, L., *J. Comput. Chem.* **2011,** *32*, 1456-1465.

55. Cossi, M.; Rega, N.; Scalmani, G.; Barone, V., *J. Comput. Chem.* **2003,** *24*, 669-681.

56. Deadman, B. J.; Hellgardt, K.; Hii, K. K., *React. Chem. Eng.* **2017,** *2*, 462-466.

57. Muhammad, H.; Tahiri, I. A.; Muhammad, M.; Masood, Z.; Versiani, M. A.; Khaliq, O.; Latif, M.; Hanif, M., *J. Electroanal. Chem.* **2016,** *775*, 157-162.

58. Nicholson, R. S.; Shain, I., *Anal.Chemistry* **1964,** *36*, 706-723.

59. Franco, F.; Pinto, M. F.; Royo, B.; Lloret-Fillol, J., *Angew. Chem. Int. Ed.* **2018,** *57*, 4603-4606.

Chapter 4

Highly Efficient Electrocatalytic Reduction of CO_2 to CO by a Molecular Chromium Complex

Reproduced with permission from Hooe, S. L.; Dressel, J. M.; Dickie, D. A.; Machan, C. W., *ACS Catalysis* **2020,** *10* (2), 1146-1151. Copyright 2019 American Chemical Society.

Hooe, S. L.; Dressel, J. M.; Dickie, D. A.; Machan, C. W., *ACS Catalysis* **2020,** *10* (2), 1146-1151. https://pubs.acs.org/doi/abs/10.1021/acscatal.9b04687

4.1 Abstract

Earth-abundant transition metal catalysts capable of reducing CO_2 to useful products have become an attractive approach to meet increasing energy demands and address concerns of rising CO_2 emissions. Group 6 molecular compounds remain underexplored in this context relative to other transition metals. Here, we present a molecular chromium complex with a 2,2′-bipyridine-based ligand capable of selectively transforming CO_2 into CO with phenol as a sacrificial proton donor at turnover frequencies of 5.7±0.1 s^{-1} with high Faradaic efficiency (96±8%) and low overpotential (110 mV). To achieve the reported catalytic activity, the parent Cr(III) species is reduced by two electron equivalents, suggesting a d^5 active species configuration. Although previous results have suggested that low valent species from the Cr/Mo/W triad are non-privileged for CO_2 reduction in synthetic molecular systems, the results presented here suggest reactivity analogous to late transition metals is possible with early transition metals.

4.2 Introduction:

Rising anthropogenic carbon dioxide (CO_2) emissions and atmospheric concentrations continue to drive interest in utilizing renewable energy sources to designate this combustion byproduct as a C_1 synthon.[1, 2] In particular, the electrocatalytic reduction of CO_2 into carbon monoxide (CO) is one potential solution, as CO can be a feedstock for light alkanes in a renewable energy-based Fischer-Tropsch process, if the required H_2 can be generated directly from H_2O.[3, 4] Although molecular electrocatalysts for the selective reduction of CO_2 to CO can contain expensive transition metals such as Pd,[5] Ru,[6] and Re,[7] recent developments have focused on earth abundant transition metals such as Mn,[8, 9] Fe,[10] Co,[11] and Ni.[12] It is intriguing that, despite the known role of Mo in the activity of formate[13, 14] and carbon monoxide[15] dehydrogenase enzymes, there has been relatively minimal success in the development of active and selective CO_2 reduction electrocatalysts utilizing the Cr/Mo/W triad.[16-22] A d^6 electron configuration is generally thought to be non-privileged for electrocatalysis under current molecular electrocatalyst 'design principles', since the frontier molecular orbitals with sufficient d_{z^2} character and reducing power that are thought to be essential for catalytic activity are easier to access with later transition metals containing redox-active ligands.[23, 24]

Kubiak and co-workers showed that Mo and W(bpy-*t*Bu)$(CO)_4$ catalysts, where (bpy-*t*Bu) is 4,4′-di-*tert*-butyl-2,2′-bipyridine, have electrochemical activity at reducing potentials under CO_2 saturation conditions; the W derivative was reported to have quantitative Faradaic efficiency for CO (FE_{CO}).[16] In a subsequent study, Hartl and co-workers described the voltametric response of unfunctionalized bpy analogues of Cr-, Mo-, and W-based tetracarbonyl cores, on Au electrodes,[22] but did not report FE_{CO}.[20] An additional report by Grice and Saucedo described a catalytic response from $M(CO)_6$ (M = Cr, Mo, W) complexes under reducing conditions, but the FE_{CO} was only reported for Mo.[21] Mo and W catalysts have limited additional reports for electrocatalytic CO_2 reduction.[25, 26]

Herein, we report what is, to our knowledge, the only known Cr homogeneous electrocatalyst with quantitative current efficiencies for the reduction of CO_2 to CO and H_2O.[17, 20, 21] At catalytic overpotentials of 110 mV, FE_{CO} of 96±8% are observed over 15.0 turnovers, with negligible H_2 production (<1%). Here, turnover is defined as the passing of charge corresponding to two electron equivalents per catalyst molecule in solution. This unprecedented activity and selectivity are enabled by the unique properties of the ligand framework, which contains a 2,2′-bipyridine backbone with two phenolate moieties. It is worth noting that the observed activity of the reduced Cr catalyst described here is in contrast to the generally accepted 'design principles' which have guided catalyst development for CO_2 reduction over the past 40 years: the selection bias of continued optimization on initial successes has incorrectly suggested that highly reduced mid-to-late transition metals are privileged as molecular electrocatalysts for CO_2 reduction.[23]

4.3 Results and Discussion

The ligand precursor 6,6′-di(3,5-di-*tert*-butyl-2-hydroxybenzene)-2,2′-bipyridine, (^{tbu}dhbpy(H)$_2$) was synthesized by a modified method from our previously reported procedure (see **4.5 Supporting Information** (**4.5 SI**)).[27] Metalation of (^{tbu}dhbpy(H)$_2$) to generate Cr(^{tbu}dhbpy)Cl(H_2O) (**2**) was achieved at room temperature by stirring overnight (^{tbu}dhbpy(H)$_2$) with one equivalent of chromium(**II**) dichloride in tetrahydrofuran (THF) under an inert atmosphere, followed by exposure to air (**SI**). The purified product was characterized by UV-vis (**Figure S4.3.1**), NMR (**Table S4.3.1**), ESI-MS (**Figure S4.3.2**), microanalysis (**4.5 SI**), and single crystal X-ray diffraction (XRD) studies (**Figure 4.3.1**). Crystals suitable for XRD studies were grown via room temperature evaporation of a concentrated solution of **2** in a mixture of dichloromethane and acetonitrile (MeCN) (**Figure 4.3.1**).

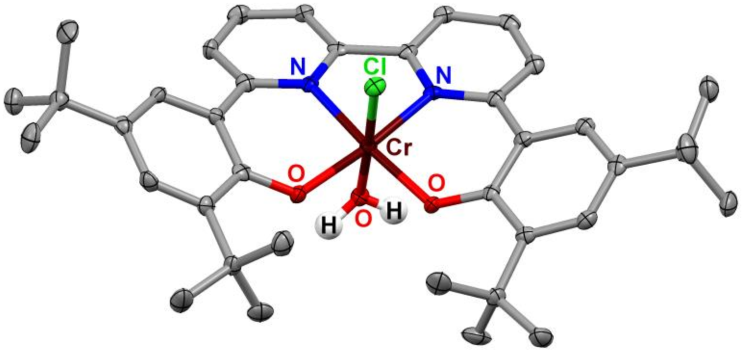

Figure 4.3.1. Molecular structure of Cr(^{tbu}dhbpy)Cl(H_2O) (**2**), obtained from single-crystal X-ray diffraction studies. Blue = N, red = O, gray = C, green = Cl, maroon = Cr, white = H atoms of bound water molecule; thermal ellipsoids at 50%; ligand H atoms and occluded MeCN molecule omitted for clarity; hydrogen atoms of the Cr-bound water molecule were located in the diffraction map and refined isotropically.

Cyclic voltammetry (CV) experiments were performed on Cr(^{tbu}dhbpy)Cl(H_2O) (**1**) in dimethylformamide (DMF) with 0.1 M tetrabutylammonium hexafluorophosphate ($TBAPF_6$) as the supporting electrolyte. Under argon (Ar) saturation conditions, three redox features are observed with E_p = –1.66 V, E_p = –1.78 V, and $E_{1/2}$ = –1.95 V versus the ferrocenium/ferrocene (Fc^+/Fc) reduction potential (**Figure 4.3.2**, black). Under CO_2 saturation conditions in the presence of a proton source, catalysis for CO_2 reduction mediated by **2** was observed at the third redox feature, $E_{1/2}$ = –1.95 V versus Fc^+/Fc, *vide infra* (**Figure 4.3.2**, green). Using TBACl as a source of excess anions, the dissociation of Cl^- upon electrochemical reduction of **2** was analyzed (**Figures S4.3.3** and **S4.3.4**).

Under Ar saturation conditions, the addition of TBACl causes a shift towards more negative potentials at the first redox feature (**Figure S4.3.3A**); interestingly, this shift is less significant under identical conditions in the presence of phenol (PhOH) (**Figure S4.3.3B**). These results are similar to that observed under CO_2 (**Figure S4.3.4A**). This suggests that the first two redox features are related to one another and that the feature at more positive potentials is likely to be a solvento species resulting from an equilibrium chloride displacement reaction. Additionally, only 1.9 equivalents of charge were passed at a potential of –2.3 V versus Fc^+/Fc during a coulometry experiment with **2** under an inert atmosphere (**Figure S4.3.5**). This suggests that the active catalyst species of **2** is generated via a two-electron reduction. Consistent with this, variable scan rate dependence studies show a coalescence of the first and second reduction waves at scan rates ≥ 2000 mV/s (**Figure S4.3.6**). Therefore, we ascribe the existence of these first two waves as representing end-states of a chloride dissociation equilibrium involving the parent Cr(III) species.

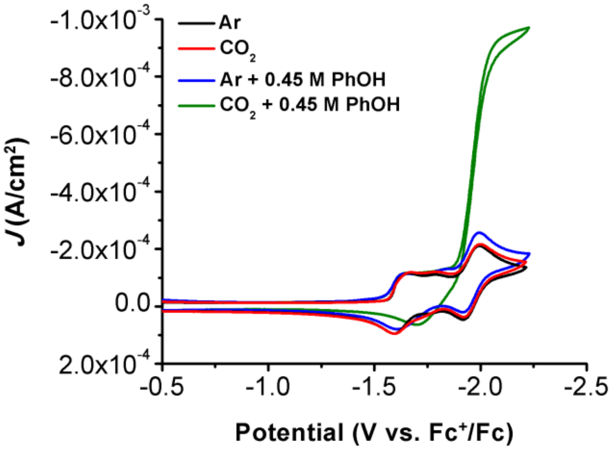

Figure 4.3.2. Comparison of CVs under Ar and CO_2 saturation conditions with and without 0.45 M PhOH. Conditions: 1.0 mM analyte in 0.1 M $TBAPF_6$/DMF; glassy carbon working electrode, glassy carbon rod counter electrode, Ag/AgCl pseudoreference electrode; referenced to Fc^+/Fc internal standard; 100 mV/s scan rate.

Upon the addition of phenol (PhOH) as a proton donor under Ar saturation conditions, only minor shifts in potential and changes in current are observed (**Figure 4.3.2**, blue). In previous studies, we have shown that this ligand framework undergoes a multisite proton-coupled electron transfer reaction under reducing conditions with an added proton donor, where reduction of Mn and Fe metal centers causes protonation of the metal-coordinated O atoms.[27-29] Unlike the previous cases, no clear Nernstian dependence on the concentration of added proton donor is observed, suggesting that formal protonation of the Cr-bound O atoms is not occurring to the extent which it was previously observed for related Fe and Mn derivatives.[27-29] There are, however, changes in the CV response consistent with an interaction between the added PhOH and the reduced Cr species, which we tentatively assign as the result of a non-covalent interaction between the proton donor and the reduced catalyst.[30, 31]

Under CO_2 saturation conditions without PhOH present, minimal changes are observed in the CV compared to under Ar saturation conditions (**Figure 4.3.2**, red). Variable scan rate studies under both Ar (**Figure S4.3.6**) and CO_2 (**Figure S4.3.7**) saturation demonstrate that the third, reversible reduction feature at $E_{1/2} = -1.95$ V versus Fc^+/Fc is diffusion controlled, indicative of a homogeneous electrochemical response (**Figures S4.3.6** and **S4.3.7**). Under CO_2 saturation conditions with added PhOH, a large increase in current is observed at the third reduction feature in the form of an irreversible wave with a distinct plateau (**Figure 4.3.2**, green). In order to probe the electrochemical reaction taking place and develop a catalytic rate expression, variable concentration studies were performed under these conditions. By titrating PhOH into a CO_2 saturated solution of **2**, the logarithmic relationship between the increase in current and the PhOH concentration can be used to determine the order for the reaction with respect to the proton donor (**Figure S4.3.8**).[32] Similar studies were done varying the concentration of CO_2 (**Figure 4.3.3**) and the concentration of catalyst (**Figure S4.3.9**). The electrochemical reaction under these conditions was found to have a first-order concentration dependence with respect to PhOH (**Figure S4.3.8**), complex **2** (**Figure S4.3.9**), and CO_2 (**Figure 4.3.3**).[32]

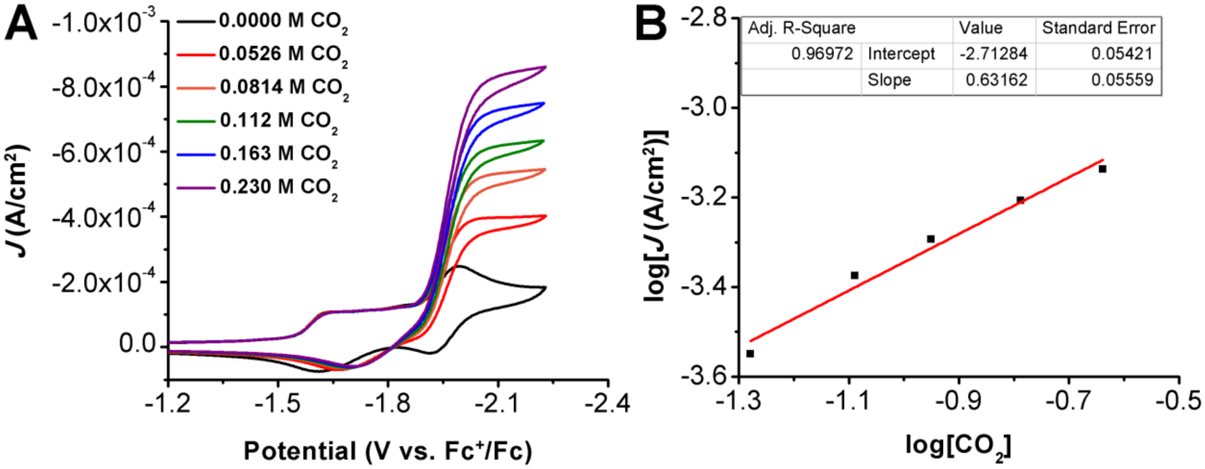

Figure 4.3.3. (**A**) CVs of Cr(^{tbu}dhbpy)Cl(H_2O) **2** obtained under variable CO_2 concentration with 0.36 M PhOH. Conditions: 1.0 mM analyte with 0.1 M $TBAPF_6$/DMF; glassy carbon working electrode, glassy carbon counter electrode, Ag/AgCl pseudoreference electrode; 100 mV/s scan rate; referenced to internal ferrocene standard. (**B**) Log-log plot from data obtained from CVs of Cr(^{tbu}dhbpy)Cl(H_2O) **1** (1.0 mM) under variable CO_2 concentration conditions with 0.36 M PhOH.

CPE was performed at –2.1 V vs Fc^+/Fc with 0.62 M PhOH under CO_2 saturation conditions (**Figure S4.3.10**). Gaseous products were assessed by GC to quantify the amount of product produced (**Figure S4.3.11**). The results of this experiment (**Table S4.3.2**) showed that **2** was capable of reducing CO_2 to CO under these conditions with 96±8% FE_{CO} over 15.0 turnovers (turnover represents two electron equivalents of charge passed for each equivalent of **2** in solution). As a control for catalyst degradation producing a catalytically active species, the working electrode from this experiment was rinsed with DMF and air-dried. Subsequently, the electrolysis chamber was prepared again with the catalyst omitted under otherwise analogous conditions. Compared to the CPE experiment with **1** present, approximately 22-fold less current was observed at –2.1 V vs Fc^+/Fc with analogous PhOH and CO_2 concentrations; the observed amounts of CO were below the detection limit of the instrument and H_2 was observed with a FE_{H2} of 4±3% (**Figure S4.3.12**). The data obtained from this 'rinse test' were comparable in terms of charge passed and products produced to that obtained in an additional control CPE experiment in the absence of **2** with a freshly polished electrode under CO_2 saturation conditions with added PhOH (**Figure S4.3.13**). These data are consistent with the proposal that **2** is a pre-catalyst for a molecular catalytic response. In parallel, results from a CV rinse test showed no apparent adsorption onto the electrode surface during catalytic CV experiments in the presence of **2** (**Figure S4.3.14**).

The electrocatalytic performance observed for **2**, FE_{CO} (96±8%) and low overpotential (110 mV), represent a profound advancement over the known molecular Cr electrocatalysts for CO_2 reduction.[16, 18, 20-22, 24-26] In order to further demonstrate this, we prepared partial structural analogues $Cr(bpy)(CO)_4$[33] and the Cr salen complex *N,N'*-bis(3,5-di-tert-butylsalicylidene)-1,2-cyclohexanediaminochromium(III) chloride (mixture of *R,R* and *S,S* isomers), Cr(salen)Cl,[34] for a comparative study (**Figure 4.3.4**, **See 4.5 SI**). CV experiments under Ar saturation conditions with the Cr(salen)Cl complex showed four irreversible redox features with E_p = –2.18, E_p = –2.46 V, E_p = –2.59 V, and E_p = –2.95 V vs. Fc^+/Fc (**Figure S4.3.15**, black). The $Cr(bpy)(CO)_4$ complex exhibited two redox features, one reversible with $E_{1/2}$ = –2.03 and one irreversible with E_p = –2.64 V vs. Fc^+/Fc (**Figure S4.3.16**, black). Under CO_2 saturation conditions, a slight increase in current is observed for the Cr(salen)Cl in the absence of a sacrificial proton donor (**Figure S4.3.15**, red). Upon the addition of PhOH under both Ar and CO_2 saturation conditions, minimal current changes are observed with Cr(salen)Cl present; a shift towards positive potentials is observed under both Ar and CO_2 saturation conditions for the first two reduction features (**Figure S4.3.15**).

Under CO_2 saturation conditions, CVs of the Cr(bpy)$(CO)_4$ complex demonstrate minimal reactivity in comparison to the experiments conducted with Ar present (**Figure S4.3.16**). Interestingly, upon the addition of PhOH under CO_2 saturation conditions, increases in current are observed (**Figure S4.3.16**, blue). However, the Cr(bpy)$(CO)_4$ complex shows current increases under both Ar and CO_2 saturation conditions with PhOH present, suggesting limited selectivity for CO_2 (**Figure S4.3.16**). Less than quantitative amounts of CO and H_2 were detected in CPE experiments performed to assess the possibility of catalytic CO_2 reduction with the Cr(salen)Cl (**Figure S4.3.17**) and Cr(bpy)$(CO)_4$ (**Figure S4.3.18**) complexes and both appeared to degrade over time during the electrolysis (**Table S4.3.3**). The described CPE results and CV comparison (**Figure 4.3.4A**) of the three Cr complexes (**Figure 4.3.4B-D**) suggest that **2** displays unique redox and electrocatalytic activity for CO_2 reduction compared to the Cr(salen)Cl and the Cr(bpy)$(CO)_4$.

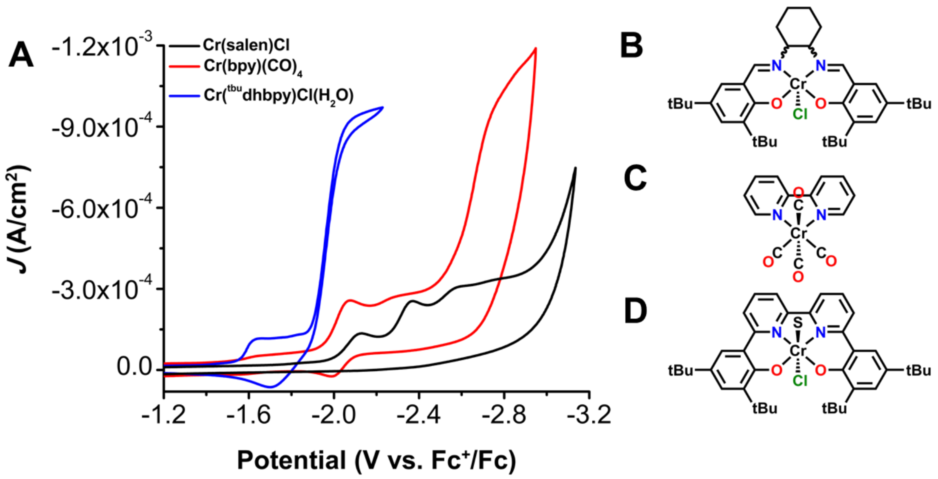

Figure 4.3.4. (**A**) Comparison of CVs for different Cr complexes under CO_2 saturation conditions: 0.22 M PhOH (black) with the Cr(salen)Cl complex (**B**), 1.32 M PhOH (red) with the $Cr(bpy)(CO)_4$ complex (**C**), and 0.34 M PhOH (blue) with **2** (**D)**, where S is a solvento adduct of water or DMF. Conditions: 1.0 mM analyte in 0.1 M $TBAPF_6$/DMF; glassy carbon working electrode, glassy carbon rod counter electrode, Ag/AgCl pseudoreference electrode; referenced to Fc^+/Fc from either ferrocene or decamethylferrocene internal standard; 100 mV/s scan rate.

Variable scan rate methods were used to establish where the catalytic reaction becomes independent of scan rate for **2** (**Figures S4.3.19**, **S4.3.20** and **Table S4.3.4**).[35] CV data obtained at scan rates from 25 mV/s to 5000 mV/s under catalytic conditions showed that a scan rate-independent regime is achieved between 200 mV/s to 1000 mV/s. Using the ratio of i_{cat}/i_p from data taken at identical scan rates to calculate the TOF_{MAX} values across this range provided an average TOF_{MAX} of 5.7 ± 0.1 s^{-1} at a catalytic overpotential of 110 mV (**See Figure S4.3.20 for determination of TOF_{MAX}**).

CO_2 reduction mechanisms which produce CO could have two possible rate-defining steps: (*i*) CO_2 binding and (*ii*) C–OH bond cleavage.[23, 24] Overwhelmingly, mechanistic proposals for molecular catalysts center on C–OH bond cleavage as the rate-determining step because of the kinetic constraints imposed by heavy atom bond cleavage.[23, 24] Given that the Cr(III) catalyst is activated by only two overall electron equivalents to a putative *d*^{5} state, we were interested in excluding the possibility of CO_2 binding as the rate-determining step. Combined with experimental data of the diffusion coefficient from variable scan rate studies of **2** (**Figure S4.3.21**), digital CV simulations were used to fit experimental catalytic data from 50 to 300 mV/s. According to this analysis, the overall reaction follows an *ECEC* (*E* – electrochemical step; *C* – chemical step) mechanism, where reduction and chemical steps follow one another in sequence. The complete proposed cycle from the singly reduced [Cr(^{tbu}dhbpy)][AH]^0 state, where [HA] indicates a non-covalent interaction between the PhOH and the ligand (L) O atoms of the neutral Cr pre-catalyst, is summarized below, (**eq (4.3.1)-(4.3.5), Figure 4.3.5**). Given the low electron count at the Cr center for this complex, we cannot exclude many of these species as being mono or di-solvento DMF adducts: these are given speculative speciation assignments in **Figure 4.3.5**.

$$[[Cr(L)][AH]]^0 + e^- \overset{E_1^0}{\rightleftharpoons} [[Cr(L)][AH]]^- \quad \textbf{(4.3.1)}$$

$$[Cr(L)][\mathrm{AH}]^- + CO_2 \overset{k_1}{\rightarrow} [Cr(L)(CO_2H)]^0 + A^- \quad \textbf{(4.3.2)}$$

$$[Cr(L)(CO_2H)]^0 + e^- \overset{E_2^0}{\rightleftharpoons} [Cr(L)(CO_2H)]^- \quad \textbf{(4.3.3)}$$

$$[Cr(L)(CO_2H)]^- + AH \overset{k_2}{\rightarrow} [Cr(L)(CO)]^0 + A^- + H_2O \quad \textbf{(4.3.4)}$$

$$[Cr(L)(CO)]^0 + AH \overset{k_3}{\rightarrow} [[Cr(L)][AH]]^0 + CO \quad \textbf{(4.3.5)}$$

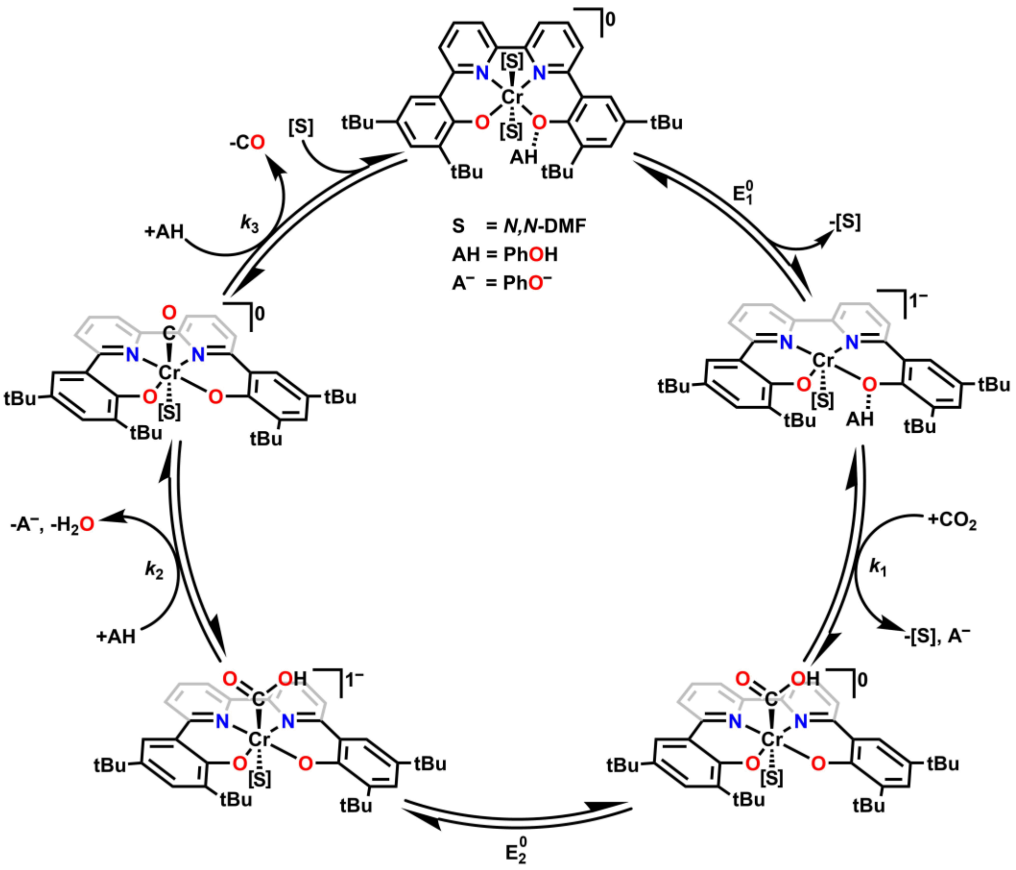

Figure 4.3.5. Proposed mechanistic cycle for the reduction of CO_2 by **2** in DMF with PhOH as the proton donor; [S] indicate possible but speculative assignments for DMF solvento species that were not considered in the CV simulations.

To further explore the validity of this mechanistic proposal, digital CV simulation was used to model the catalytic waveforms at a series of scan rates from 50 to 300 mV/s simultaneously for an averaged comparison with the experimentally obtained data (**Figure 4.3.6**, **S4.3.22** and **Table S4.3.5**). For simplicity, only the final reduction wave, from which the catalytic response originates, was modeled (**4.5 SI**). Importantly, modeling the catalytic wave across five separate scan rates was consistent with the experimentally observed TOF_{MAX} arising from k_2, the C–OH bond cleavage step: 6.8 s^{-1} compared to 5.7 ± 0.1 s^{-1} for the experimental TOF_{MAX} (**Figure 4.3.6**). Alternate mechanistic simulations following an *ECCE*-type mechanism were consistent with k_1 as the rate-determining step, but predicted that CO release from the Cr center was not favored, with a K_{eq} of 7.3 x 10^{-3}. This mechanism could be excluded as a possibility based on the experimental observation that no Nernstian voltammetric response indicative of an equilibrium CO binding reaction was observed experimentally at any relevant reduction feature of **2** (**Figure S4.3.23**).

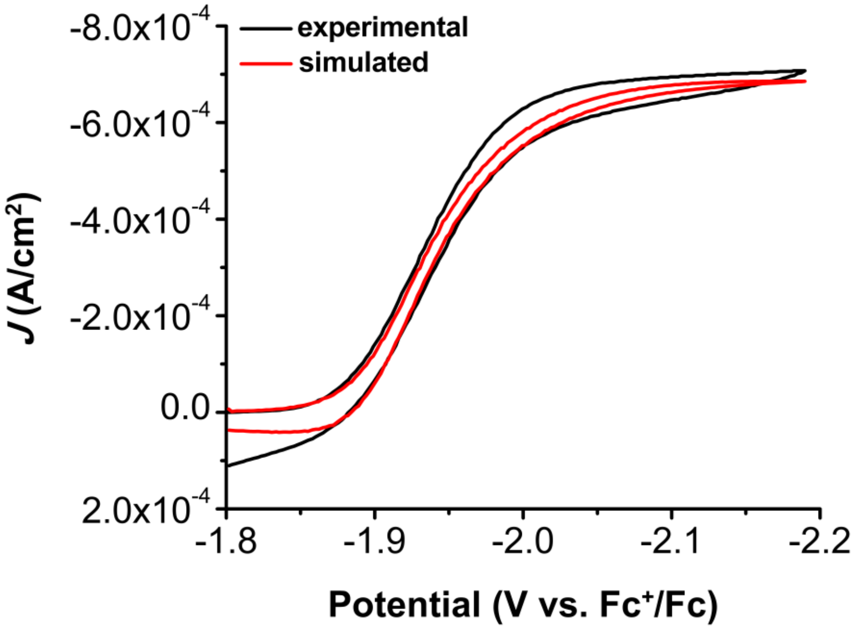

Figure 4.3.6. Comparison of simulated (red) and experimental (black) CV with 1.0 mM Cr(^{tbu}dhbpy)Cl(H_2O) **2**, obtained under CO_2 saturation conditions with 0.341 M PhOH concentration at 100 mV/s. Conditions: 0.1 M $TBAPF_6$/DMF; glassy carbon working electrode, glassy carbon counter electrode, Ag/AgCl pseudoreference electrode; referenced to internal ferrocene standard.

Using the reaction parameters obtained from this, additional CV simulations were used to assess the data on the concentration dependence of the catalytic current discussed above. Simulating the second-order rate constant for k_2 across different PhOH concentrations produced values which validated the assignment of first-order concentration dependence of the catalytic current on PhOH (**Figure S4.3.25**): a linear slope of 1.01 was obtained from a plot comparing log([PhOH]) against log(k_2(s^{-1})) (**Figure S4.3.26**).[36]

4.4 Conclusion

We have established that **1** is active and selective as a molecular catalyst for the electrochemical reduction of CO_2 to CO with excellent stability. To our knowledge, no prior study of electrocatalytic behavior for a molecular Cr species has achieved the performance reported here. Although the observed turnover frequency of 5.7 ± 0.1 s^{-1} is modest relative to other molecular electrocatalysts, such as those based on $[Fe(tetraphenylporphyrin)]^+$ and $M(bpy)(CO)_3X$ (where M = Re or Mn; X = Br or Cl),[9, 37-40] we believe that with further study the activity of this Cr-based catalyst can be improved. Because of their intermediate *d*-electron count, Group 6 metals are commonly thought of as poor candidates for developing molecular electrocatalysts for CO_2 reduction; to this point, all catalyst reports have invoked negative valency or reduction of the ligand framework by multiple electron equivalents to achieve a catalytic response for the Cr/Mo/W triad.[16-23, 25, 26] A key aspect appears to be the low electron count achieved at Cr during catalyst activation (d^5) facilitating rapid CO release, which is indirectly observed by the absence of interactions between CO and the reduced Cr species observed experimentally in control CVs (**Figure S4.4.24**). We also note with interest that this *d* electron count assumes minimal participation of the bpy backbone, which is unlikely to be rigorously true, and we are currently attempting to further elucidate the electronic structure of the active species. The unique catalytic response of this molecular Cr complex represents an entry point into active and selective transition metal electrocatalysts from Group 6 and earlier, which to this point have been extremely rare.[10, 24, 37-41]

4.5 Supporting Information

Materials and Methods

General

All chemicals and solvents (ACS or HPLC grade) were commercially available and used as received unless otherwise indicated. For all air-sensitive reactions and electrochemical experiments, solvents were obtained as anhydrous and air-free from a PPT Glass Contour Solvent Purification System; ferrocene was purified by sublimation. Gas cylinders were obtained from Praxair (Ar as 5.0; CO_2 as 4.0) and passed through molecular sieves or Drierite prior to use. Gas mixing for variable concentration experiments was accomplished using a gas proportioning rotameter from Omega Engineering. NMR spectra were obtained on either a Varian 600 MHz or 500 MHz instrument and referenced to the residual solvent signal. Microwave reactions were carried out using an Anton-Parr Multiwave Pro SOLV, NXF-8 microwave reactor. UV-vis absorbance spectra were recorded on a Cary 60 from Agilent. GC experiments were performed using an Agilent 7890B Gas Chromatograph equipped with a thermal conductivity detector (TCD) using an Agilent J&W Select Permanent Gases/CO_2 column. HRMS data were obtained by the Mass Spectrometry Lab at the University of Illinois at Urbana-Champaign and elemental analyses were performed by Midwest Laboratory. CV data were simulated using DigiElch 8.

Electrochemistry

All electroanalytical experiments were performed using either a Metrohm Autolab PGSTAT302N Potentiostat or a Biologic SP-50 Potentiostat. Glassy carbon working (⌀ = 3 mm) and non-aqueous silver/silver chloride pseudoreference electrodes behind PTFE tips were obtained from CH Instruments. The pseudoreference electrodes were obtained by depositing chloride on bare silver wire in 10% HCl at oxidizing potentials and stored in a 0.1 M tetrabutylammonium hexafluorophosphate/DMF solution in the dark prior to use. The counter electrode was a glassy carbon rod (⌀ = 3 mm) as indicated for individual experiments. All CV experiments were performed in a modified scintillation vial (20 mL volume) as a single-chamber cell with a cap modified with ports for all electrodes and a sparging needle. Tetrabutylammonium hexafluorophosphate was purified by recrystallization from ethanol and dried in a vacuum oven before being stored in a desiccator. All data were referenced to an internal ferrocene standard (ferrocenium/ferrocene reduction potential under stated conditions) unless otherwise specified.

Bulk Electrolysis

Bulk electrolysis experiments were performed in a glass Pine H-cell with two compartments separated by a glass frit. A 60 mL stock solution of DMF with 0.1 M $TBAPF_6$ was prepared for each bulk electrolysis experiment. Approximately 25 mL of the stock solution was added to each half of the H-cell. One side of the H-cell contained the $Cr(^{tbu}dhbpy)Cl(H_2O)$ **2** catalyst, any additional substrate, such as PhOH, and a glassy carbon rod working electrode. The other side of the H-cell contained approximately 0.075 M ferrocene as a sacrificial reductant along with a graphite rod counter electrode and a Ag/AgCl pseudoreference electrode. The electrolysis experiment was referenced by taking a CV of the side of the H-cell that contained the ferrocene solution. The H-cell was sealed with two septa that were connected by a piece of PTFE tubing which aided to maintain equal pressure between each half of the cell during the electrolysis. Before starting the electrolysis experiment, both sides of the H-cell were sparged with the desired gas for 20 minutes and the sealed cell was allowed to equilibrate for 30 minutes. The resistance between the two halves of the H-cell was measured using the i-interrupt procedure available in the NOVA software provided by Metrohm.

Bulk Electrolysis Product Analysis

During bulk electrolysis experiments, 250 μL GC injections of the headspace were periodically taken for the detection and quantification of any gaseous products produced. After each bulk electrolysis experiment, the total volume of solution was measured and the solution containing the $Cr(^{tbu}dhbpy)Cl(H_2O)$ **2** catalyst in the H-cell was separated. The total volume of the sealed H-cell was also measured to account for the total headspace volume for accurate quantification of gaseous products. A calibration curve (**Figure S4.3.11**) for CO and H_2 was made in the H-cell from an experimental setup with identical volumes of DMF in 0.1 M $TBAPF_6$ as was carried out during experiments with $Cr(^{tbu}dhbpy)Cl(H_2O)$ **2**. Known volumes of CO and H_2 were injected into the cell with stirring and 250 μL injections of the H-cell headspace was taken for GC injections. The limit of detection (LOD) and limit of quantitation (LOQ) for CO and H_2 in the GC were determined from 7 consecutive injections at the lowest observable concentrations of each gaseous product respectively.[42] For CO, the LOD was determined to be 5.77 x 10^{-7} moles and the LOQ was determined to be 1.92 x 10^{-6} moles. For H_2, the LOD was determined to be 4.55 x 10^{-6} moles and the LOQ was determined to be 1.52 x 10^{-5} moles.

Single crystal X-ray diffraction

A suitable single crystal of **2** was coated with Paratone oil and mounted on a MiTeGen MicroLoop. The X-ray intensity data were measured on a Bruker Kappa APEXII Duo system equipped with a fine-focus sealed tube (Mo K_α, λ = 0.71073 Å) and a graphite monochromator. The frames were integrated with the Bruker SAINT software package [a] using a narrow-frame algorithm. Data were corrected for absorption effects using the Multi-Scan method (SADABS).[a] The structure was solved and refined using the Bruker SHELXTL software package[b] within APEX3[a] and OLEX2.[c] Non-hydrogen atoms were refined anisotropically. The O-H hydrogen atom was located in the diffraction map and refined isotropically. All other hydrogen atoms were placed in geometrically calculated positions with $U_{iso} = 1.2U_{equiv}$ of the parent atom ($U_{iso} = 1.5U_{equiv}$ for methyl).

[a] Bruker **2012**. *Saint; SADABS; APEX3*. Bruker AXS Inc., Madison, Wisconsin, USA.

[b] Sheldrick, G. M., SHELXT-Integrated Space-Group and Crystal-Structure Determination. *Acta Cryst.* **2015**, A**71**, 3-8.

[c] Dolomanov, O. V.; Bourhis, L. J.; Gildea, R. J.; Howard, J. A. K.; Puschmann, H., OLEX2: A Complete Structure Solution, Refinement and Analysis Program. *J. Appl. Cryst.* **2009**, **42**, 339-341.

Synthesis of 6,6'-di(3,5-di-tert-butyl-2-hydroxybenzene)-2,2'-bipyridine (^{tbu}dhbpy(H)$_2$)

The synthesis of (^{tbu}dhbpy(H)$_2$) was carried out as previously reported[27, 28] with one modification: the final Suzuki-Miyaura style cross-coupling reaction was carried out under microwave conditions. The microwave conditions were set to heat the reaction mixture to 170 °C as fast as possible and then held at that temperature for 90 minutes.

*Synthesis of Cr(^{tbu}dhbpy)Cl(H_2O) (**1**)*

Metalation of (^{tbu}dhbpy(H)$_2$) with Cr(III) to generate Cr(^{tbu}dhbpy)Cl(H_2O) (**1**) was achieved by stirring (^{tbu}dhbpy(H)$_2$) (0.250 g, 0.443 mmol) with one equivalent of chromium(II) dichloride (0.0544 g, 0.443 mmol) in tetrahydrofuran (THF) under an inert atmosphere overnight. Following exposure to air, the reaction mixture was condensed under reduced pressure. The resulting residue was dissolved in dichloromethane (DCM) and washed with brine (3 x 50 mL) and saturated ammonium chloride (6 x 50 mL). The organic layer was condensed under reduced pressure, dissolved in a minimal amount of MeCN (5 mL), and filtered to remove any remaining ligand impurity. The filtrate was then condensed and the isolated red solid was washed with deionized water (150 mL) and boiling hexanes (100 mL). 26% isolated yield. Elemental analysis for $C_{38}H_{48}ClCrN_2O_3$ calc'd: C 68.30, H 7.24, N 4.19; found: C 67.95, H 7.20, N 4.35.

Evans Method Characterization of Cr(^{tbu}dhbpy)Cl(H_2O)

The spin state of the Cr(^{tbu}dhbpy)Cl(H_2O) catalyst was characterized as a Cr(III) species via Evans' Method.[43, 44] Three capillary inserts were made with a 50% v/v mixture of *N*,*N*-DMF and *N*,*N*-DMF-d_7. Each insert was flame sealed, and then placed in an NMR tube. Then 5.6 mg of **2** was dissolve in 2.5 mL of *N*,*N*-DMF. Approximately 0.6 mL of the solution of **2** was added to each of the three NMR tubes containing a flame sealed insert. ^{1}H NMR spectra with 64 scans were then taken using a 600 MHz Varian NMR Spectrometer. The results of this experiment, which was run in triplicate, can be seen in **Table S4.3.1**. The average μ_{eff} was 3.73±0.12.

Synthesis of N,N'-bis(3,5-di-tert-butylsalicylidene)-1,2-cyclohexanediaminochromium(III) chloride (Cr(salen)Cl)

The Cr(salen)Cl complex was prepared similar to reported procedures.[34] The salen ligand[45] (0.250 g, 0.457 mmol; mixture of *R,R* and *S,S* isomers) was dissolved in 50 mL of THF. Chromium(II) dichloride (0.0562 g , 0.457 mmol) was added and the solution was stirred at room temperature overnight under an inert atmosphere. The solution was then exposed to air and condensed down. The brown solid was dissolved in DCM and washed with brine (3 x 50 mL) and saturated ammonium chloride (5 x 50 mL) The organic layer was then condensed and washed with pentanes to obtain the brown purified product. The purified product that was isolated in 49% yield. Elemental analysis for $C_{36}H_{52}ClCrN_2O_2$ calc'd: C 68.39, H 8.29, N 4.43; found: C 67.96, H 8.17, N 4.44.

Synthesis of Cr(bpy)(CO)$_4$

The light sensitive Cr(bpy)(CO)$_4$ was synthesized similarly to previous reports.[33] Cr(CO)$_6$ (0.900 g, 0.409 mmol) precursor and 2,2′-bipyridine (0.639 g, 0.409 mmol) were dissolved in toluene and refluxed overnight (12 h). The toluene solution was filtered while still warm and the solid material was washed with hexanes (100 mL) to obtain a dark red product in 27% yield. Elemental analysis for $C_{14}H_8CrN_2O_4$ calc'd: C 52.51, H 2.52, N 8.75; found: C 52.34, H 2.40, N 8.75.

Calculation of Overpotential

The calculation of overpotential for **2** was performed according to reported methods.[46] The following equation was used for the determination of the reaction standard potential in V with respect to the Fc^+/Fc couple:

$$E_{CO2/CO} = 0.73\,V - 0.059(pK_a)$$

The pK_a for PhOH in DMF is reported as 18.8[47]:

$$E_{CO2/CO}(PhOH) = -1.84\,V\ vs\ Fc^+/Fc$$

The $E_{cat/2}$ determined experimentally for **2** is –1.95 V vs Fc^+/Fc; the overpotential is:

$$\eta = \left|E_{cat/2} - E_{CO2/CO}\right| = |-1.95\,V - (-1.84\,V)| = 110\,mV$$

This assumes no contribution from homoconjugation of the acid and that the equimolar quantities of water introduced with the catalyst (as well as adventitious H_2O concentration) do not contribute significantly to the formation of carbonic acid, pK_a(DMF) 7.37.[48] Control CVs with CO_2 and the Cr compound under nominally aprotic conditions do not show appreciable activity.

*We note that the homoconjugation constant for PhOH in DMF has been reported as $7.0 \times 10^3\ M^{-1}$.[49] Therefore, we indicate that the described overpotential calculated above for PhOH is a lower limit approximation as homoconjugation could change the effective pK_a of PhOH.

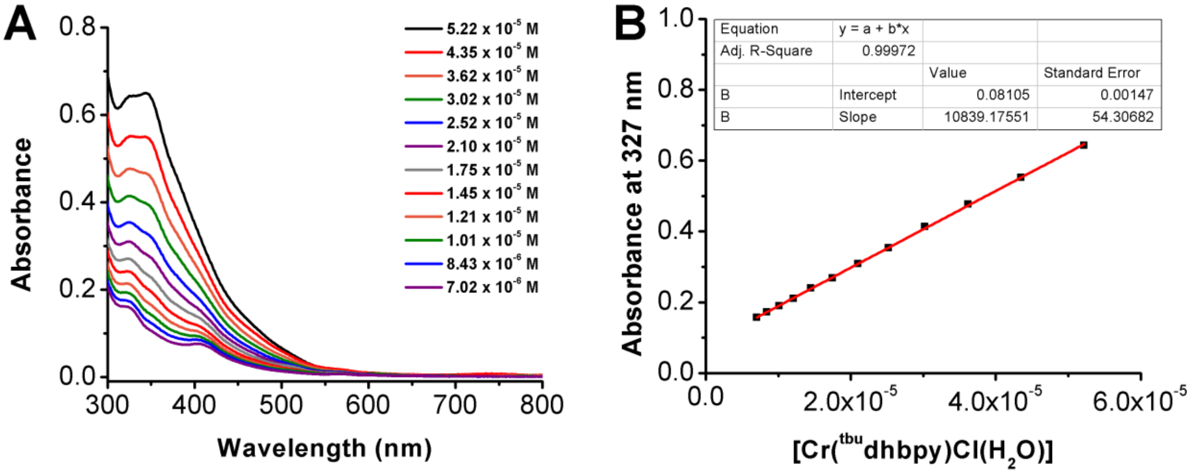

Figure S4.3.1. (**A**) UV-vis serial dilution absorbance data obtained from Cr(^{tbu}dhbpy)Cl(H_2O) **2** in a DMF solution. Conditions: varying concentration; quartz cell with 1 cm pathlength. (**B**) Plot of absorbance versus concentration (M) for Cr(^{tbu}dhbpy)Cl(H_2O) **2** in DMF at 327 nm (10800 M^{-1} cm^{-1}); R^2 = 0.999. All: λ_{max} = 343 nm (11900 M^{-1} cm^{-1}) and 404 nm (5750 M^{-1} cm^{-1}).

Table S4.3.1. Evans' method results for Cr(^{tbu}dhbpy)Cl(H_2O) **2** in DMF.[43, 44]

Trial	Chemical Shift (ppm)	Chemical Shift (Hz)	Total Magnetic Moment (emu mol^{-1})	Paramagnetic Moment (emu mol^{-1})	μ_{eff} (Bohr Magnetons)
1	0.0820	49.2	0.00568	5.69 x 10^{-3}	3.68
2	0.0800	48.0	0.00554	5.55 x 10^{-3}	3.64
3	0.0900	54.0	0.00624	6.25 x 10^{-3}	3.86

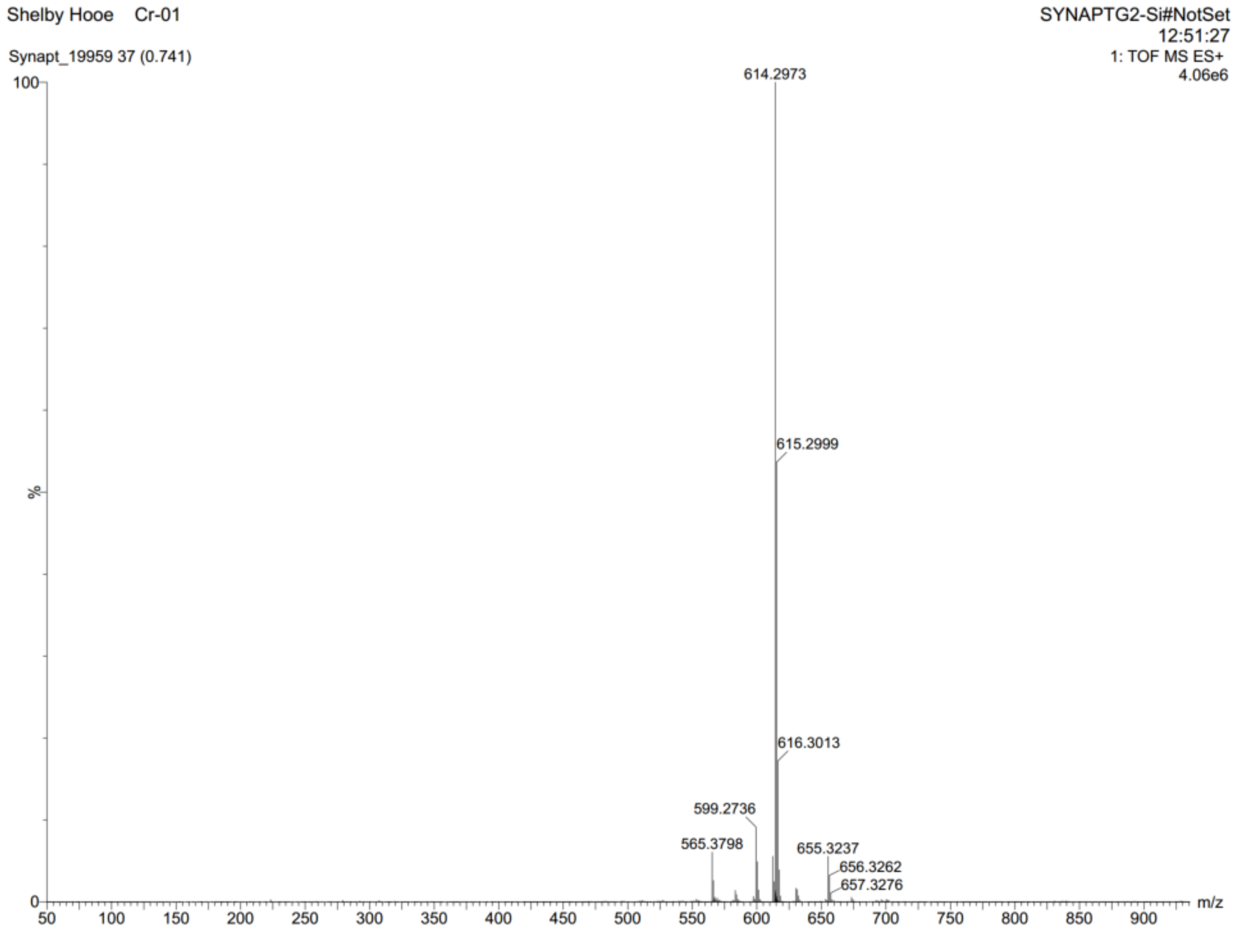

Single Mass Analysis
Tolerance = 5.0 PPM / DBE: min = -50.0, max = 100.0
Element prediction: Off
Number of isotope peaks used for i-FIT = 9

Monoisotopic Mass, Odd and Even Electron Ions
198 formula(e) evaluated with 2 results within limits (up to 10 best isotopic matches for each mass)
Elements Used:
C: 0-90 H: 0-130 N: 0-2 O: 0-2 Cr: 0-1

```
Minimum:                                -50.0
Maximum:                5.0      5.0    100.0

Mass        Calc. Mass  mDa      PPM     DBE     i-FIT    Norm    Conf(%) Formula

614.2973    614.2964    0.9      1.5     17.0    1238.5   0.000   100.00  C38 H46 N2 O2 Cr
            614.2974    -0.1     -0.2    30.0    1256.6   18.125  0.00    C48 H38
```

Figure S4.3.2. ESI-MS characterization of Cr(^{tbu}dhbpy)Cl(H_2O) **2**.

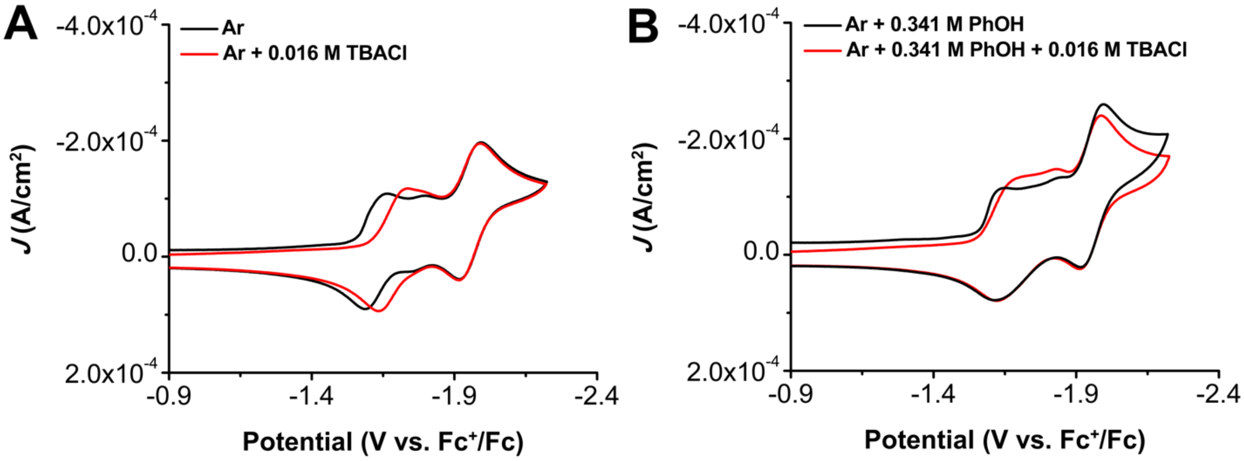

Figure S4.3.3. CVs of Cr(^{tbu}dhbpy)Cl(H_2O) **2** under Ar saturation conditions examining the effect of TBACl under aprotic (**A**) and protic conditions (**B**). Conditions: 1.0 mM analyte, 0.1 M $TBAPF_6$/DMF; glassy carbon working electrode, glassy carbon counter electrode, Ag/AgCl pseudoreference electrode; 100 mV/s scan rate; referenced to internal ferrocene standard.

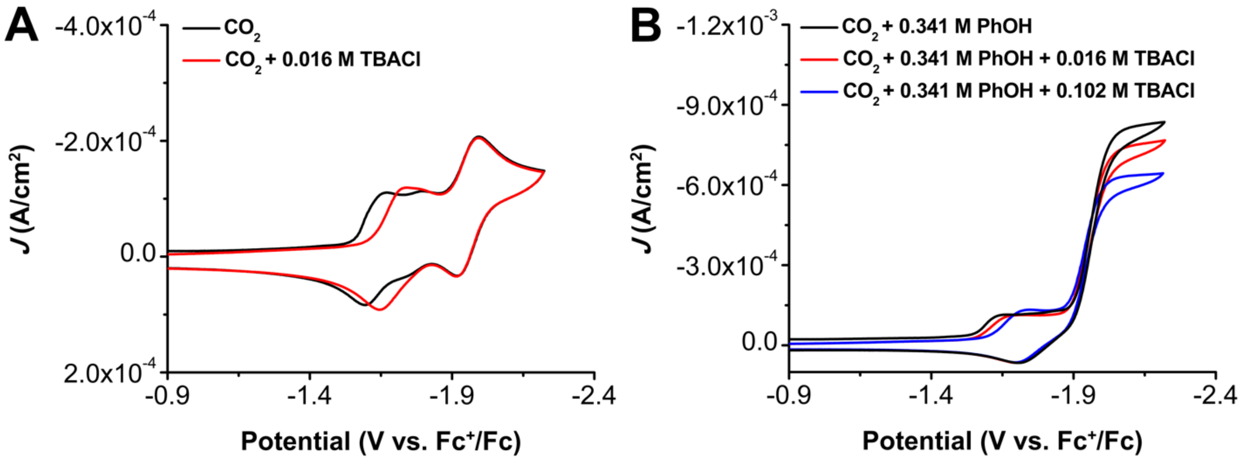

Figure S4.3.4. CVs of Cr(^{tbu}dhbpy)Cl(H_2O) **2** under CO_2 saturation conditions examining the effect of TBACl under aprotic (**A**) and protic conditions (**B**). Conditions: 1.0 mM analyte, 0.1 M $TBAPF_6$/DMF; glassy carbon working electrode, glassy carbon counter electrode, Ag/AgCl pseudoreference electrode; 100 mV/s scan rate; referenced to internal ferrocene standard.

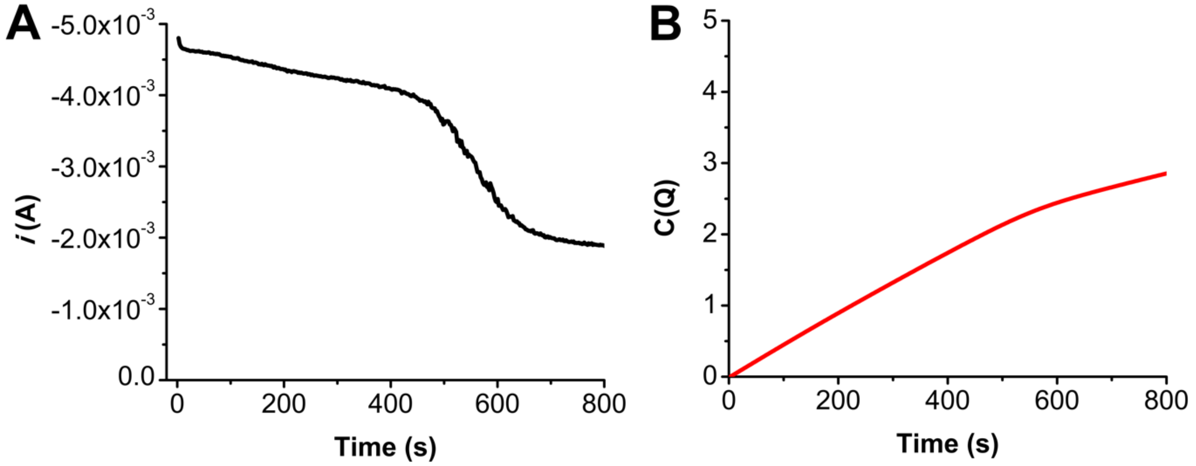

Figure S4.3.5. Results of coulometry experiment to determine the number of electrons transferred in the faradaic reaction. **(A)** Current versus time trace from bulk electrolysis experiment. (**B**) Charge passed versus time for the coulometry experiment shown in (**A**). Conditions were 0.56 mM Cr(^{tbu}dhbpy)Cl(H_2O) 2 under an N_2 atmosphere at –2.3 V vs Fc^+/Fc in 0.1 M $TBAPF_6$/DMF; working electrode was carbon cloth, counter electrode was carbon cloth, and the reference was a nonaqueous Ag/AgCl pseudoreference electrode; 0.075 M Fc was used as sacrificial oxidant.

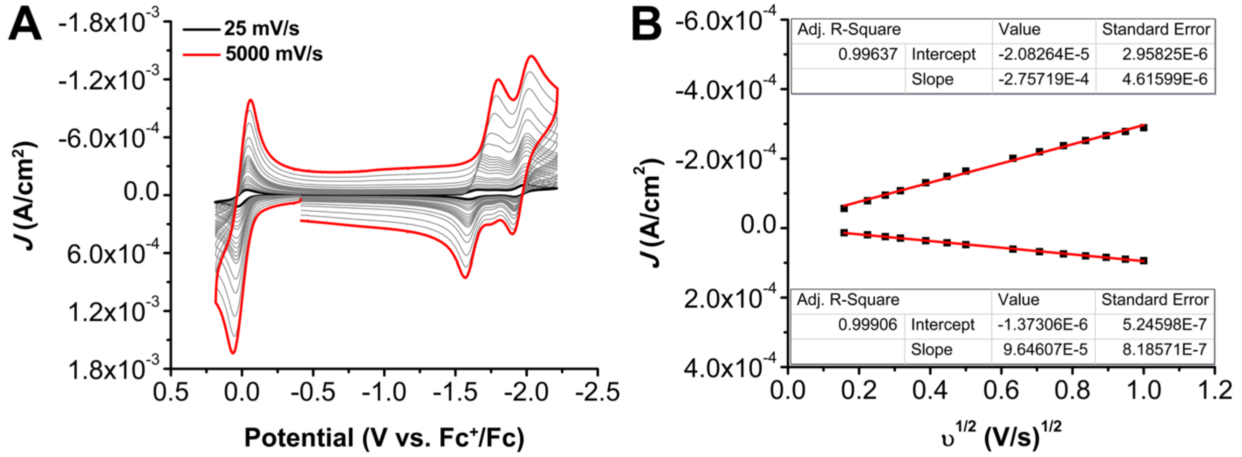

Adj. R-Square		Value	Standard Error
0.99637	Intercept	-2.08264E-5	2.95825E-6
	Slope	-2.75719E-4	4.61599E-6

Adj. R-Square		Value	Standard Error
0.99906	Intercept	-1.37306E-6	5.24598E-7
	Slope	9.64607E-5	8.18571E-7

Figure S4.3.6. (**A**) CVs of Cr(^{tbu}dhbpy)Cl(H_2O) **2** at variable scan rates ranging from 25 (black) to 5000 (red) mV/s, obtained under Ar saturation conditions. (**B**) Linear Fit of variable scan rate data from (**A**) demonstrating that Cr(^{tbu}dhbpy)Cl(H_2O) **2** shows a diffusion-limited current response. The data in (**B**) was obtained from the reversible redox feature at -1.95 V vs Fc^+/Fc. Conditions: 1.0 mM analyte, 0.1 M $TBAPF_6$/DMF; glassy carbon working electrode, glassy carbon counter electrode, Ag/AgCl pseudoreference electrode; varied scan rate; referenced to internal ferrocene standard.

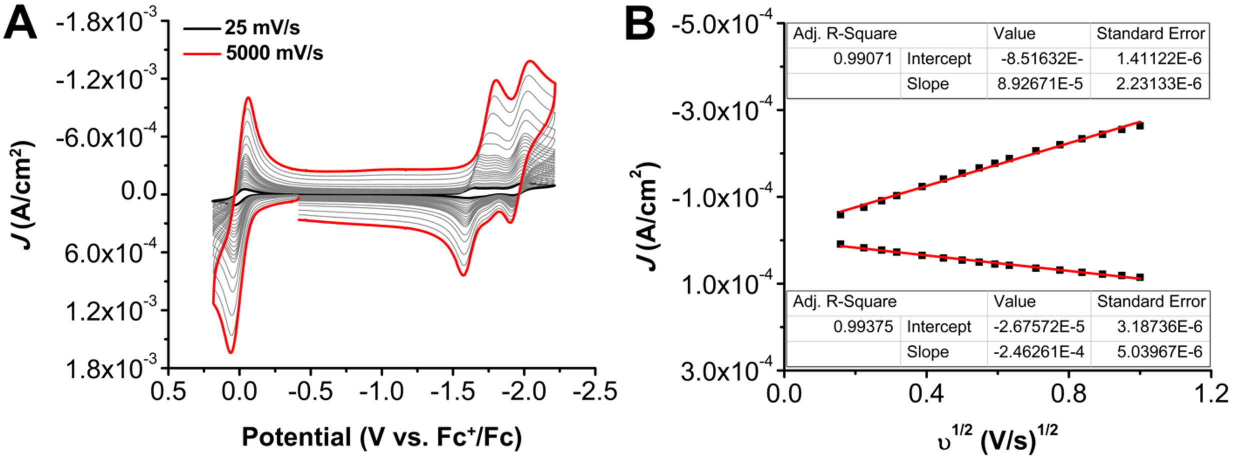

Adj. R-Square		Value	Standard Error
0.99071	Intercept	-8.51632E-	1.41122E-6
	Slope	8.92671E-5	2.23133E-6

Adj. R-Square		Value	Standard Error
0.99375	Intercept	-2.67572E-5	3.18736E-6
	Slope	-2.46261E-4	5.03967E-6

Figure S4.3.7. (**A**) CVs of Cr(^{tbu}dhbpy)Cl(H_2O) **2** at variable scan rates ranging from 25 (black) to 5000 (red) mV/s, obtained under CO_2 saturation. (**B**) Linear Fit of variable scan rate data from (**A**) demonstrating that Cr(^{tbu}dhbpy)Cl(H_2O) **2** shows a diffusion-limited current response. The data in (**B**) was obtained from the reversible redox feature at –1.95 V vs Fc$^+$/Fc. Conditions: 1.0 mM analyte, 0.1 M $TBAPF_6$/DMF; glassy carbon working electrode, glassy carbon counter electrode, Ag/AgCl pseudoreference electrode; varied scan rate; referenced to internal ferrocene standard.

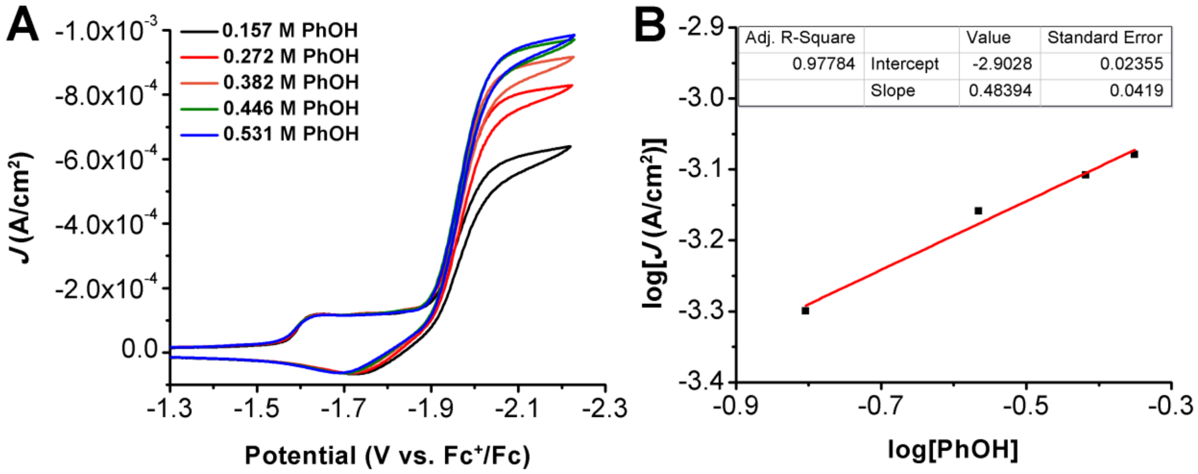

Figure S4.3.8. (**A**) CVs of Cr(^{tbu}dhbpy)Cl(H_2O) **2**, obtained under CO_2 saturation conditions with variable PhOH concentration. Conditions: 1.0 mM analyte, 0.1 M $TBAPF_6$/DMF; glassy carbon working electrode, glassy carbon counter electrode, Ag/AgCl pseudoreference electrode; 100 mV/s scan rate; referenced to internal ferrocene standard. (**B**) Log-log plot from data obtained from CVs of Cr(^{tbu}dhbpy)Cl(H_2O) **2** (1.0 mM) with variable PhOH concentrations under CO_2 saturation. For all variable concentration studies (**Figure 4.3.3, S4.3.8, S4.3.9**) analysis was adapted from Sathrum and Kubiak *J. Phys. Chem. Lett.* **2011**, 2, 2372.[32] F is Faraday's constant, A is the electrode area, [Q] is the substrate concentration, k_{cat} is the catalytic rate, D is the diffusion constant of the catalyst, [cat] is the concentration of the catalyst, and n_{cat} is the number of electrons involved in the catalytic process.

$$i_{cat} = n_{cat}FA[cat](Dk_{cat}[Q]^{y})^{1/2}$$

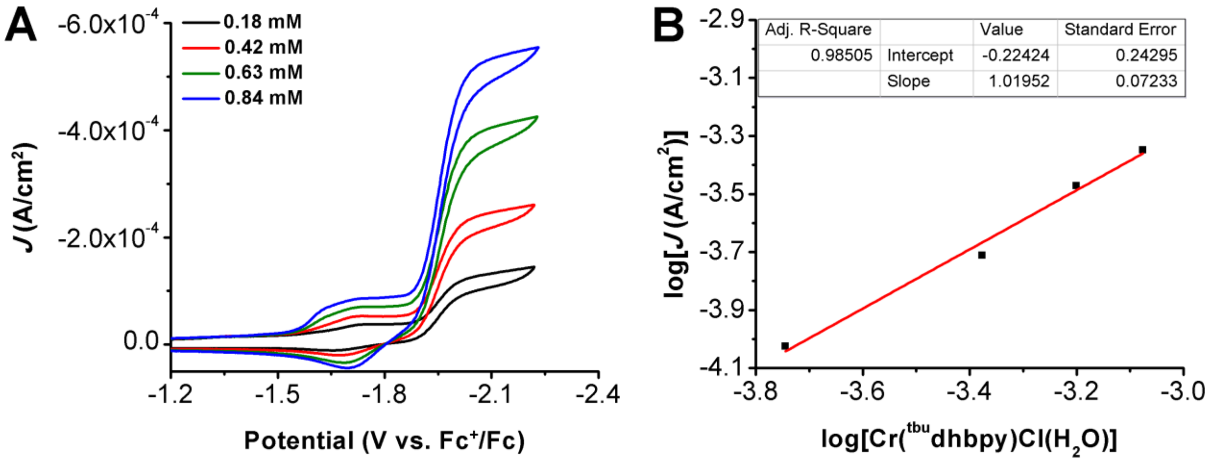

Figure S4.3.9. (**A**) CVs of $Cr(^{tbu}dhbpy)Cl(H_2O)$ **2** at variable concentrations, obtained under CO_2 saturation with 0.316 M PhOH. Conditions: 0.1 M $TBAPF_6$/DMF; glassy carbon working electrode, glassy carbon counter electrode, Ag/AgCl pseudoreference electrode; 100 mV/s scan rate; referenced to internal ferrocene standard. (**B**) Log-log plot from data obtained from CVs of $Cr(^{tbu}dhbpy)Cl(H_2O)$ **2** under variable concentration conditions with 0.321 M PhOH under CO_2 saturation.

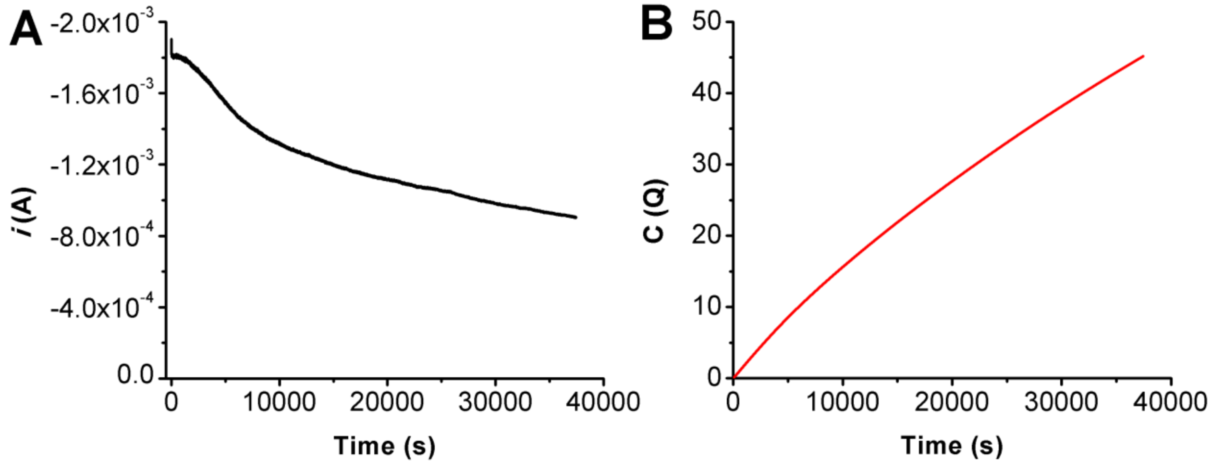

Figure S4.3.10. (**A**) Current versus time trace from bulk electrolysis experiment. (**B**) Charge passed versus time for the bulk electrolysis experiment shown in (**A**). Conditions were 0.58 mM $Cr(^{tbu}dhbpy)Cl(H_2O)$ **2**, 0.62 M PhOH, and under a CO_2 atmosphere at –2.1 V vs Fc^+/Fc in 0.1 M $TBAPF_6$/DMF; working electrode was a glassy carbon rod, counter electrode was a graphite rod, and the reference was a nonaqueous Ag/AgCl pseudoreference electrode; 0.075 M Fc was used as sacrificial oxidant.

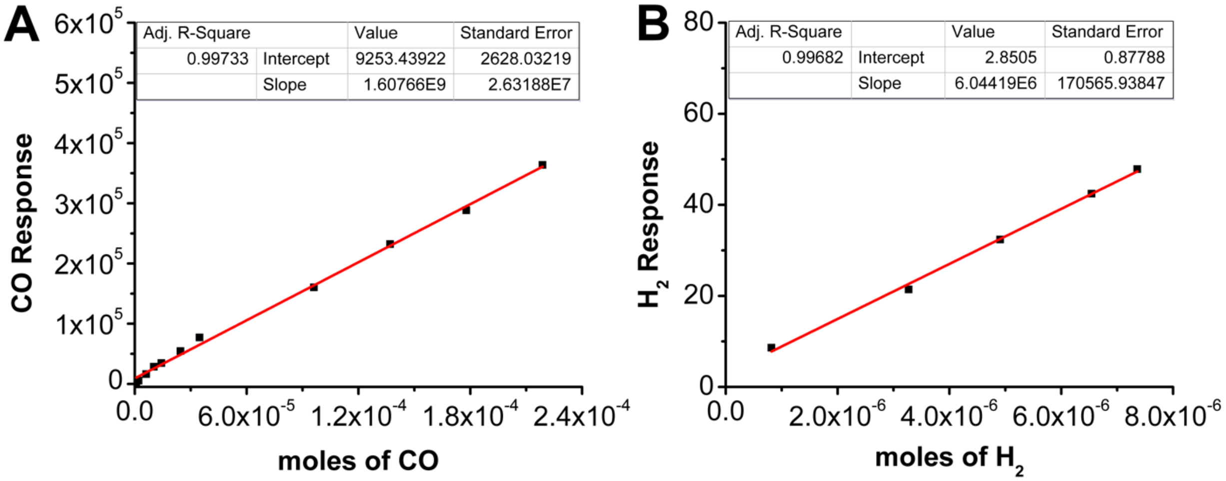

Figure S4.3.11. GC calibration curve for the quantification of (**A**) CO and (**B**) H_2.

Table S4.3.2. Results of CO quantification obtained from experiment shown in **Fig. S4.3.10**.

Time (s)	**Charge (coulombs)**	**moles (e-)**	**Moles of CO**	**FE$_{CO}$**
7750	12.57	1.30×10^{-4}	7.07×10^{-5}	108.58
10080	15.72	1.63×10^{-4}	8.25×10^{-5}	101.32
17420	24.7	2.56×10^{-4}	1.34×10^{-4}	103.15
21970	29.83	3.09×10^{-4}	1.47×10^{-4}	94.96
26880	35.03	3.63×10^{-4}	1.65×10^{-4}	90.84
31680	39.79	4.12×10^{-4}	1.85×10^{-4}	89.69
37440	45.17	4.68×10^{-4}	1.99×10^{-4}	85.02
37440	45.17	4.68×10^{-4}	2.26×10^{-4}	96.47
37440	45.17	4.68×10^{-4}	2.11×10^{-4}	90.29

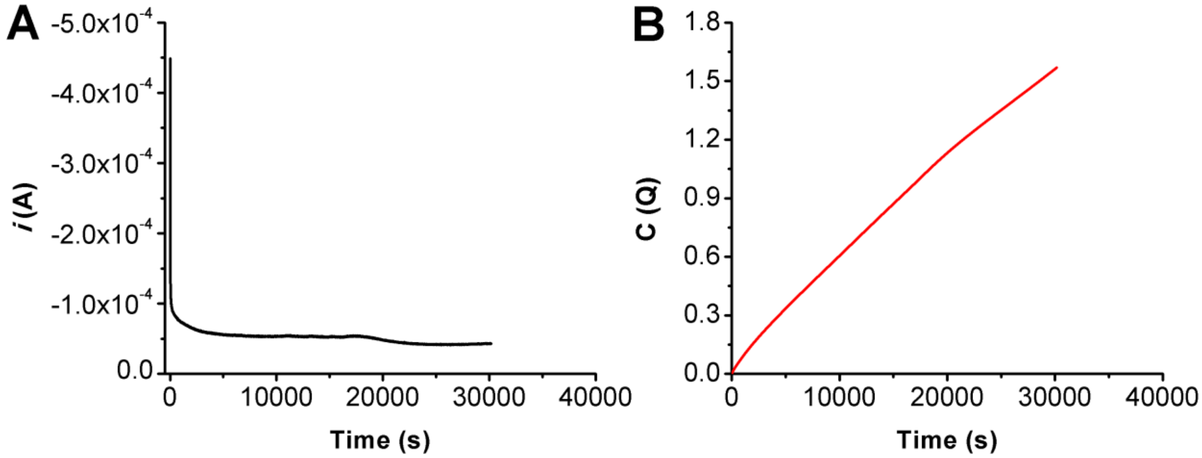

Figure S4.3.12. Results of rinse test bulk electrolysis post experiment shown in **Figure S4.3.10**. (**A**) Current versus time trace from bulk electrolysis experiment. (**B**) Charge passed versus time for the bulk electrolysis experiment shown in (**A**)**.** Conditions were 0.57 M PhOH under a CO_2 atmosphere at –2.1 V vs Fc^+/Fc in 0.1 M $TBAPF_6$/DMF; working electrode was a glassy carbon rod, counter electrode was a graphite rod, and the reference was a nonaqueous Ag/AgCl pseudoreference electrode; 0.075 M Fc was used as sacrificial oxidant.

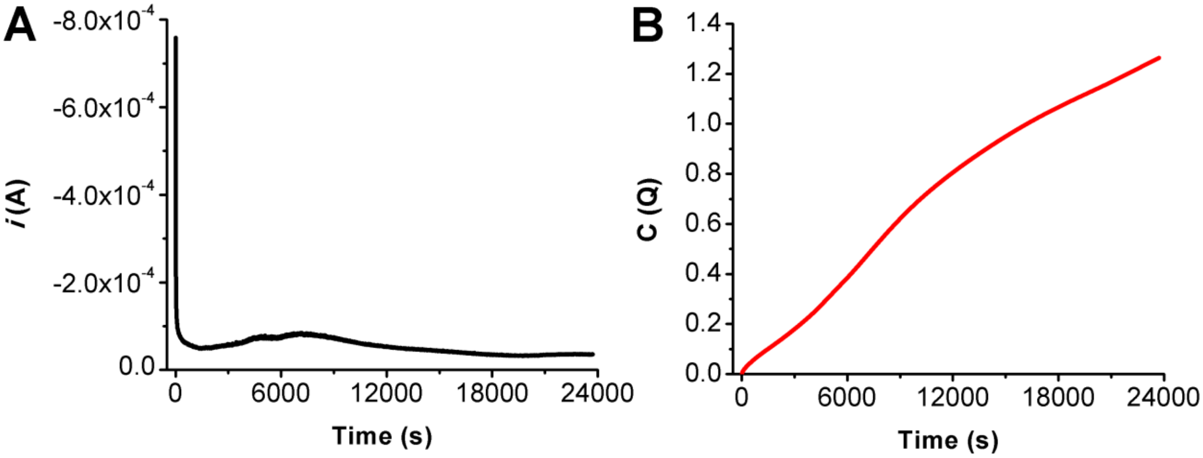

Figure S4.3.13. Control bulk electrolysis without **2** present. (**A**) Current versus time trace from bulk electrolysis experiment. (**B**) Charge passed versus time for the bulk electrolysis experiment shown in (**A**). Conditions were 0.64 M PhOH under a CO_2 atmosphere at –2.8 V vs Fc^+/Fc in 0.1 M $TBAPF_6$/DMF; working electrode was a glassy carbon rod, counter electrode was a graphite rod, and the reference was a nonaqueous Ag/AgCl pseudoreference electrode; 0.075 M Fc was used as sacrificial oxidant.

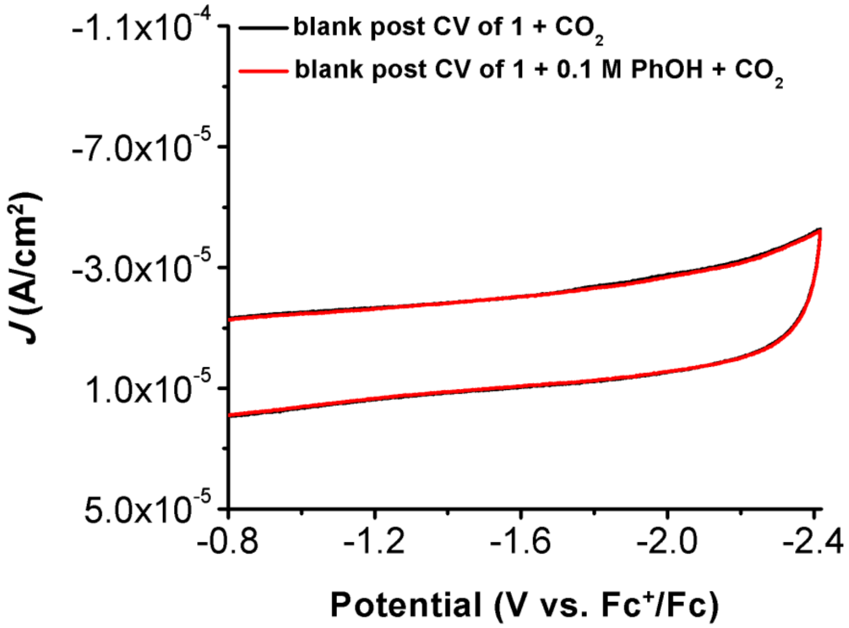

Figure S4.3.14. CVs from rinse test to check for possible adsorption from electrochemistry with Cr(^{tbu}dhbpy)Cl(H_2O) **2**. A 1.0 mM solution of **2** in DMF was prepared and CVs were taken under CO_2 saturation conditions with and without 0.1 M PhOH. After each of the described CVs, the electrodes were removed from the DMF solution containing **2**, lightly dried with a Kimwipe®, and immediately placed into a “blank solution”, which consisted of a DMF electrolyte solution under Ar saturation conditions. A CV was then immediately taken in attempt to detect any possible adsorption occurring by **2**. Conditions: 0.1 M $TBAPF_6$/DMF; glassy carbon working electrode, glassy carbon counter electrode, Ag/AgCl pseudoreference electrode; 100 mV/s scan rate; referenced to ferrocene standard.

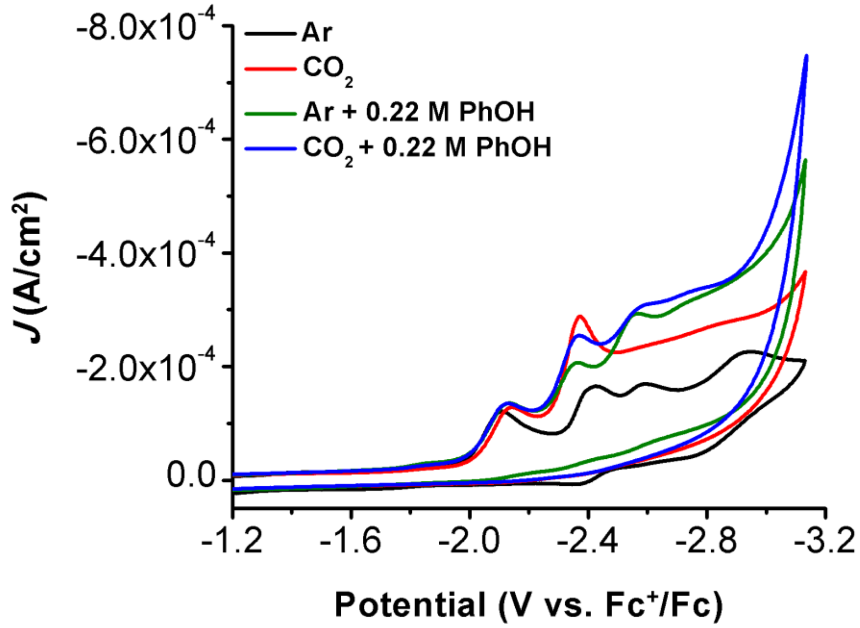

Figure S4.3.15. CVs of the Cr(salen)Cl under various conditions for a comparative analysis to **2**. Conditions: 1.0 mM analyte; 0.1 M TBAPF$_6$/DMF; glassy carbon working electrode, glassy carbon rod counter electrode, Ag/AgCl pseudoreference electrode; referenced to ferrocene internal standard; 100 mV/s scan rate.

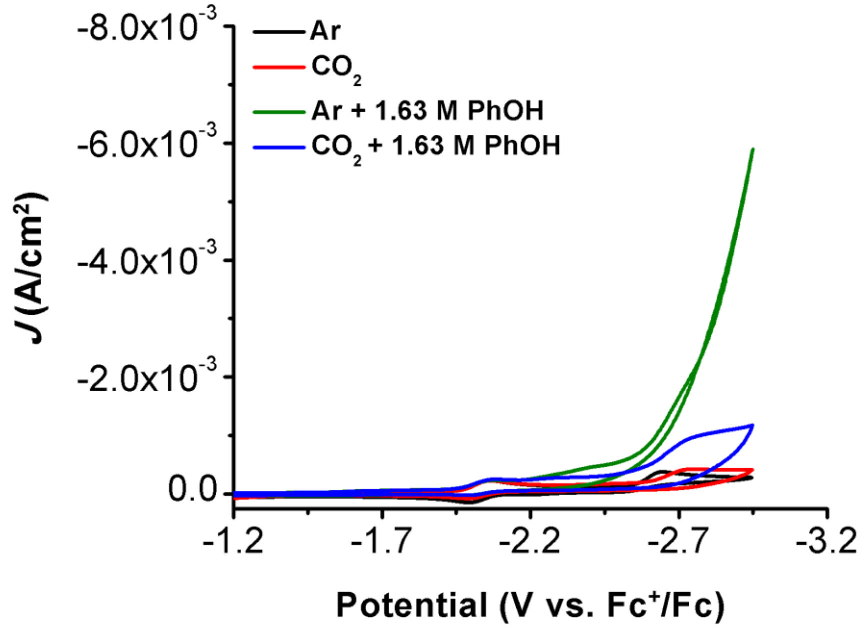

Figure S4.3.16. CVs of the Cr(bpy)(CO)$_4$ under various conditions for a comparative analysis to **2**. Conditions: 1.0 mM analyte; 0.1 M TBAPF$_6$/DMF; glassy carbon working electrode, glassy carbon rod counter electrode, Ag/AgCl pseudoreference electrode; referenced to ferrocene from internal decamethylferrocene standard; 100 mV/s scan rate.

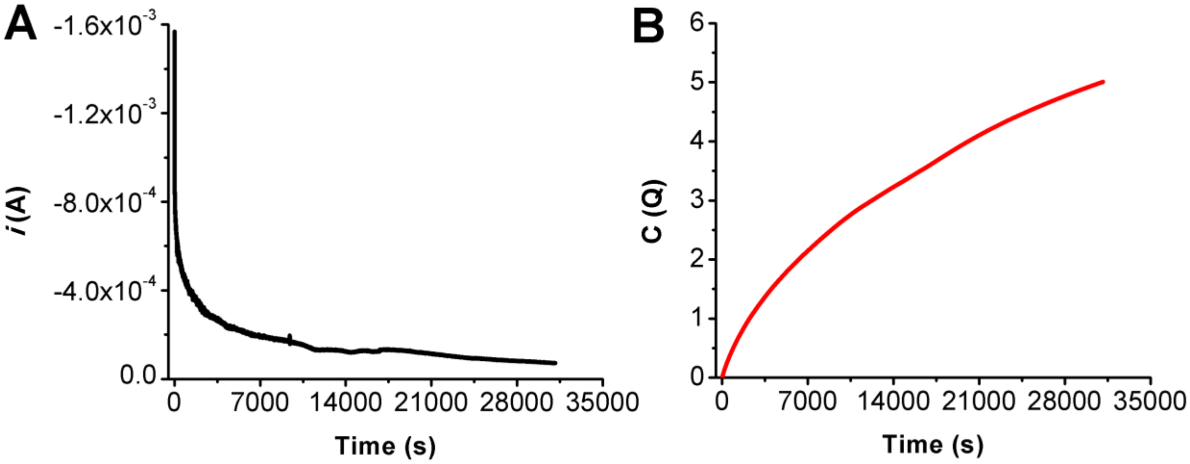

Figure S4.3.17. (**A**) Current versus time trace from bulk electrolysis experiment. (**B**) Charge passed versus time for the bulk electrolysis experiment shown in (**A**). Conditions were 0.66 mM Cr(salen)Cl, 0.63 M PhOH, and under a CO_2 atmosphere at –2.4 V vs Fc^+/Fc in 0.1 M $TBAPF_6$/DMF; working electrode was a glassy carbon rod, counter electrode was a graphite rod, and the reference was a nonaqueous Ag/AgCl pseudoreference electrode; 0.075 M Fc was used as sacrificial oxidant.

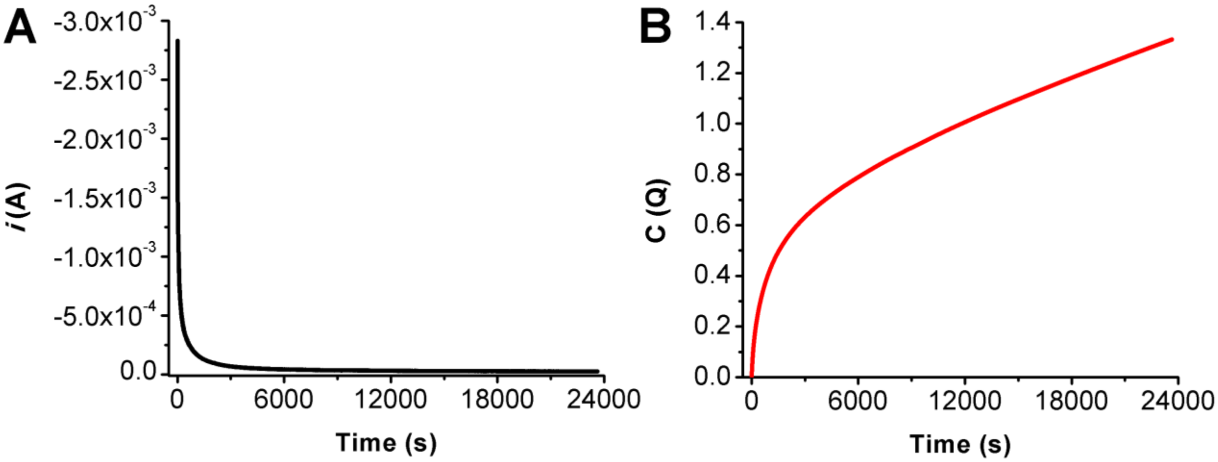

Figure S4.3.18. (**A**) Current versus time trace from bulk electrolysis experiment. (**B**) Charge passed versus time for bulk electrolysis experiment shown in (**A**). Conditions were 0.83 mM $Cr(bpy)(CO)_4$, 0.63 M PhOH, and under a CO_2 atmosphere at –2.8 V vs Fc^+/Fc in 0.1 M $TBAPF_6$/DMF; working electrode was a glassy carbon rod, counter electrode was a graphite rod, and the reference was a nonaqueous Ag/AgCl pseudoreference electrode; 0.075 M Fc was used as sacrificial oxidant.

Table S4.3.3. Comparison of the results of CO quantification obtained from CPE experiments shown in **Figure S4.3.10**, **S4.3.17**, and **S4.3.18**.

Catalyst	**[PhOH]**	**Applied Potential (V vs Fc^+/Fc)**	**Charge Passed (C)**	**Time (h)**	**Mol CO**	**FE_{CO}**	**Mol H_2**	**FE_{H_2}**
Cr(^{tbu}dhbpy)Cl(H_2O)[a]	0.62 M	–2.1	45.17	10.4	4.68 x 10^{-4}	96%	-[d]	<1%
Cr(salen)Cl[b]	0.63 M	–2.4	5.02	8.64	-[d]	<1%	-[d]	<1%
Cr(bpy)$(CO)_4$[c]	0.63 M	–2.8	1.33	6.57	-[d]	<1%	-[d]	<1%

* - electrolyses performed with [CO_2] = 0.23 M; [a] – 0.58 mM; [b] – 0.66 mM; [c] – 0.83 mM; [d] – below GC detection limit

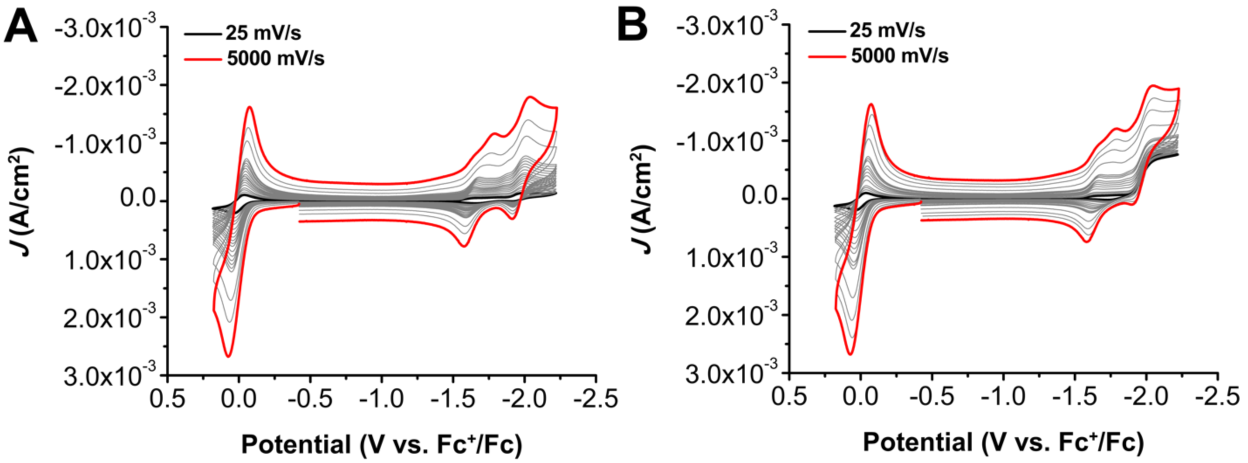

Figure S4.3.19. CVs of Cr(^{tbu}dhbpy)Cl(H_2O) **2** with 0.34 M PhOH at variable scan rates ranging from 25 (black) to 5000 (red) mV/s, obtained under Ar (**A**) and CO_2 (**B**) saturation conditions. Conditions: 1.0 mM analyte, 0.1 M $TBAPF_6$/DMF; glassy carbon working electrode, glassy carbon counter electrode, Ag/AgCl pseudoreference electrode; varied scan rate; referenced to internal ferrocene standard.

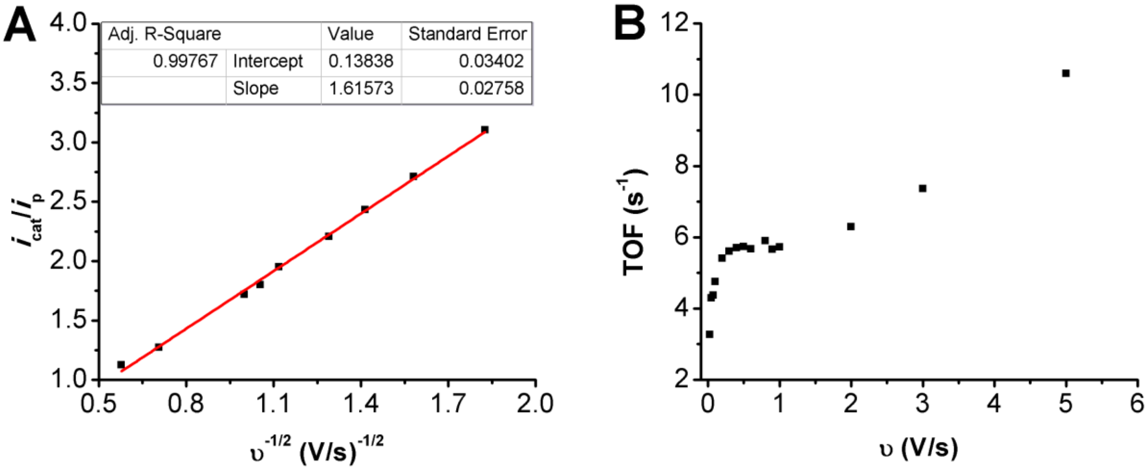

Figure S4.3.20. Plots of (**A**) i_{cat}/i_p versus the inverse of the square root of the scan rate and (**B**) TOF versus scan rate for Cr(^{tbu}dhbpy)Cl(H_2O) **2**, with 0.34 M PhOH from data in **Figure S4.3.19**.

Calculation of TOF_{max} (adapted)[35]

$$TOF_{max} = 0.1992\frac{n_p^3}{n_{cat}^2}\frac{F\nu}{RT}\left(\frac{i_{cat}}{i_p}\right)^2$$

Where n_p is the number of electrons transferred under faradaic conditions, n_{cat} is the number of electrons transferred under catalytic conditions, R is the ideal gas constant, F is Faraday's constant, ν is the scan rate, T is temperature, i_{cat} is the catalytic current, and i_p is the faradaic current.

Table S4.3.4. TOF and k_{cat} values determined from the i_{cat}/i_p method with variable scan rates in **Figure S4.3.19** and **S4.3.20**.

Scan Rate (V/s)	TOF_{max} (s^{-1})
0.025	3.27
0.05	4.30
0.075	4.37
0.1	4.75
0.2	5.40
0.3	5.61
0.4	5.70
0.5	5.73
0.6	5.67
0.8	5.90
0.9	5.66
1	5.73
2	6.29
3	7.36
5	10.6

Table S4.3.5. Table of simulated data for the proposed *ECEC* mechanism (**Figure 4.3.5**).

Charge-Transfer Reaction	**E^0 (V vs. Fc^+/Fc)**	**α/λ (eV)**	**k_s (cm/s)**
E_1^0	–1.97	0.5	0.01
E_2^0	–1.91	0.5	0.01
Chemical Reaction	**K_{eq}**	**k_f**	**k_b**
k_1	3.61	1.00 x 10^9 ($M^{-1}s^{-1}$)	2.77 x 10^8 ($M^{-1}s^{-1}$)
k_2	2.03 x 10^{-5}	20 ($M^{-1}s^{-1}$)	9.99 x 10^6 ($M^{-1}s^{-1}$)
k_3	8.50	1.00 x 10^9 (s^{-1})	1.18 x 10^8 ($M^{-1}s^{-1}$)

*Initial concentrations for simulation were 1.0 mM $[Cr(^{tbu}dhbpy(H))]^0$, 0.23 M CO_2, and 0.34 M PhOH. All other intermediate and product concentrations were set to 0.

*Diffusion coefficient for the catalyst was calculated from variable scan rate CV data with added TBACl (**Figure S4.3.21**) to minimize the effects of the chloride binding equilibrium on the electrochemical response, resulting in a value of 2.0 x 10^{-6} cm^2/s. All catalyst species were assumed to be identical.

*Alpha was set to 0.5 and k_s to 0.01 cm/s under the assumption that catalyst reduction occurred by a reversible Nernstian process that was not limited by electron transfer. The k_f values for k_1 and k_2 were fixed at the diffusion limit to prevent the simulation from selecting higher simulated rate constants, which occurred in unrestricted simulations.

*CO was assumed to have an identical diffusion coefficient to CO_2 (2.7 x 10^{-5} cm^2/s)[50]; PhO^- identical to PhOH (1.2 x 10^{-5} cm^2/s).[51]

*The best fits for the catalytic waveform at all scan rates (**Figures 4.3.6 and S4.3.22**) were obtained by setting the second-order rate constant k_f value for the k_2 term at 20 $M^{-1}s^{-1}$, leading to a predicted TOF_{MAX} of 6.8 s^{-1} (0.341 M PhOH concentration), compared to the experimental value of 5.7 ± 0.1 s^{-1}.

* All five experimental data sets (**Figure 4.3.6** in main text and **Figure S4.3.22**) from 50 to 300 mV/s, were fit simultaneously to produce averaged values

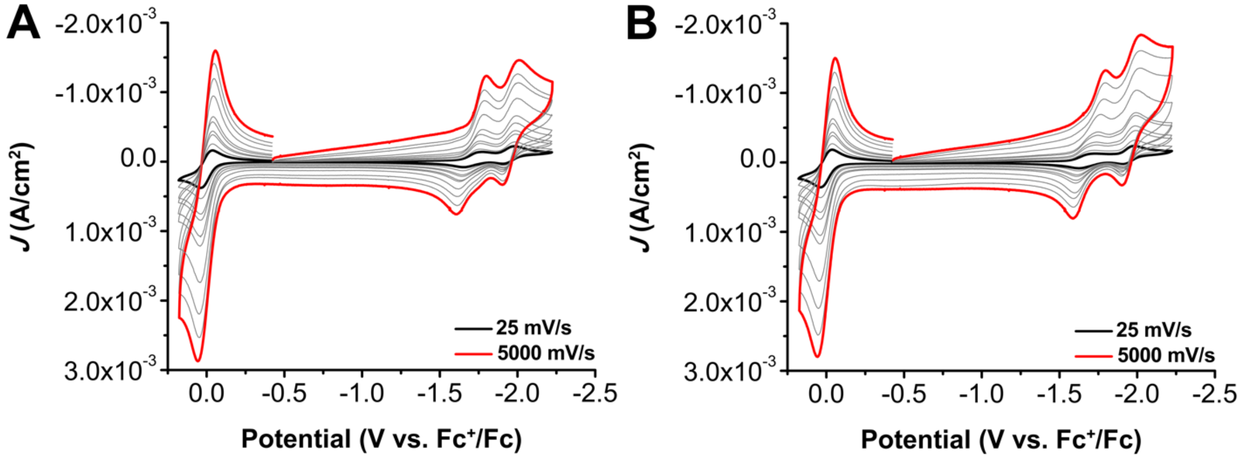

Figure S4.3.21. CVs of Cr(^{tbu}dhbpy)Cl(H_2O) **2** at variable scan rates ranging from 25 (black) to 5000 (red) mV/s, obtained under Ar saturation conditions with 40.3 mM TBACl both with (**A**) and without (**B**) 0.34 M PhOH. Conditions: 1.0 mM analyte, 0.1 M TBAPF$_6$/DMF; glassy carbon working electrode, glassy carbon counter electrode, Ag/AgCl pseudoreference electrode; varied scan rate; referenced to internal ferrocene standard.

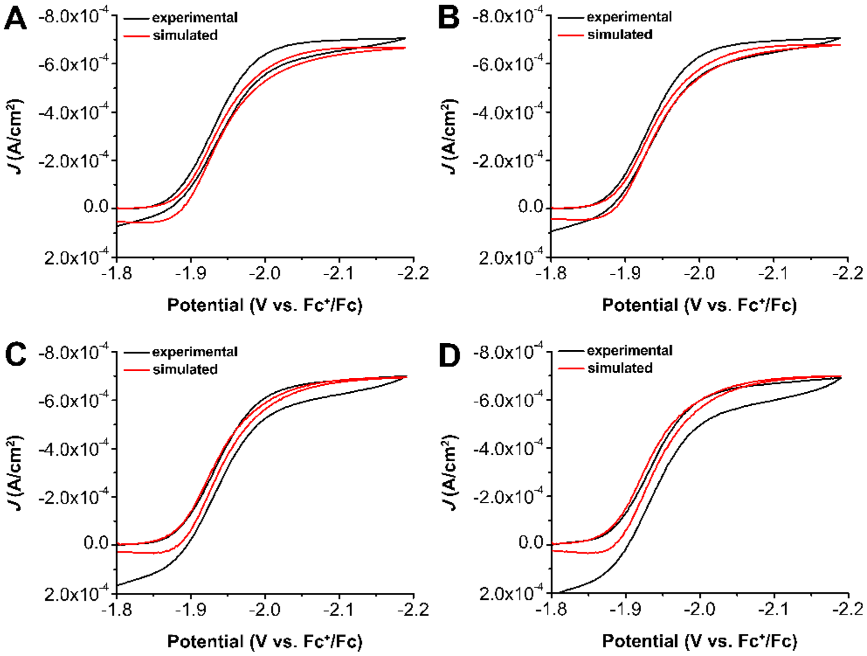

Figure S4.3.22. Comparison of simulated (red) and experimental (black) CV data with 1.0 mM Cr(^{tbu}dhbpy)Cl(H_2O) **2**, obtained under CO_2 saturation conditions with 0.341 M PhOH concentration at scan rates of 50 (**A**), 75 (**B**), 200 (**C**), and 300 mV/s (**D**). All five experimental data sets (including **Figure 4.3.6** in main text) from 50 to 300 mV/s, were fit simultaneously to produce averaged values. Conditions: 0.1 M $TBAPF_6$/DMF; glassy carbon working electrode, glassy carbon rod counter electrode, Ag/AgCl pseudoreference electrode; referenced to internal ferrocene standard.

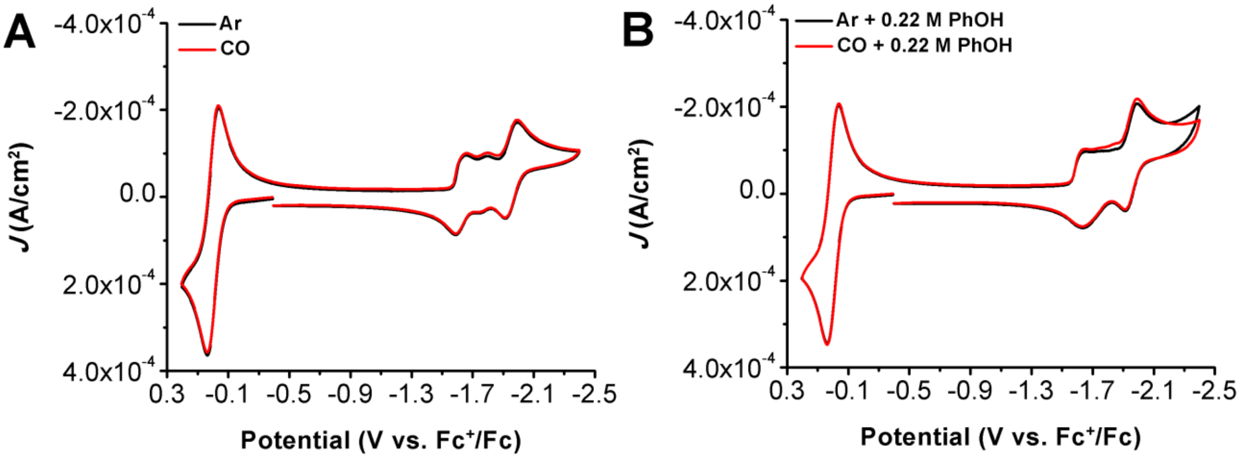

Figure S4.3.23. (**A**) Comparison of CVs under Ar (black) and CO (red) saturation conditions. (**B**) Comparison of CVs under Ar (black) and CO (red) saturation conditions with 0.22 M PhOH. Conditions: 1.0 mM analyte in 0.1 M TBAPF$_6$/DMF; glassy carbon working electrode, glassy carbon rod counter electrode, Ag/AgCl pseudoreference electrode; referenced to Fc$^+$/Fc internal standard; 100 mV/s scan rate.

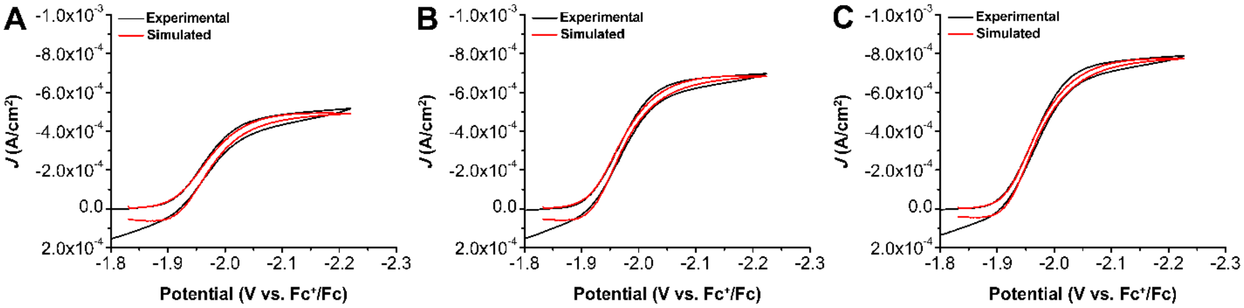

Figure S4.4.24. Overlays of experimental (black) versus simulated (red) data of the second reduction of **2** with 0.157 M (**A**), 0.272 M (**B**), and 0.382 M (**C**) PhOH under CO$_2$ saturation conditions. Conditions: 0.1 M TBAPF$_6$/DMF; glassy carbon working electrode, glassy carbon rod counter electrode, Ag/AgCl pseudoreference electrode; referenced to Fc$^+$/Fc internal standard; 100 mV/s scan rate.

*From the simulated data k_2 (M^{-1}s^{-1}) values of 23.87, 25.81, and 22.86 M were obtained for 0.157, 0.272, and 0.382 M PhOH, respectively, from which apparent TOFs for k_2 (s^{-1}) were calculated.

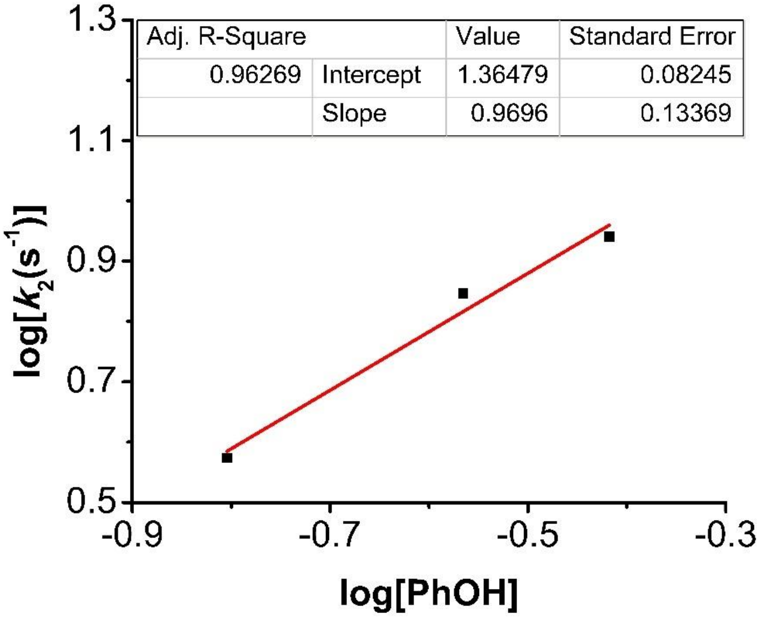

Figure S4.3.25. Plot of log[k_2(s^{-1})] (apparent turnover frequency calculated from the simulated second-order rate constants) versus log[PhOH] from simulated data in **Figure S4.4.24**.

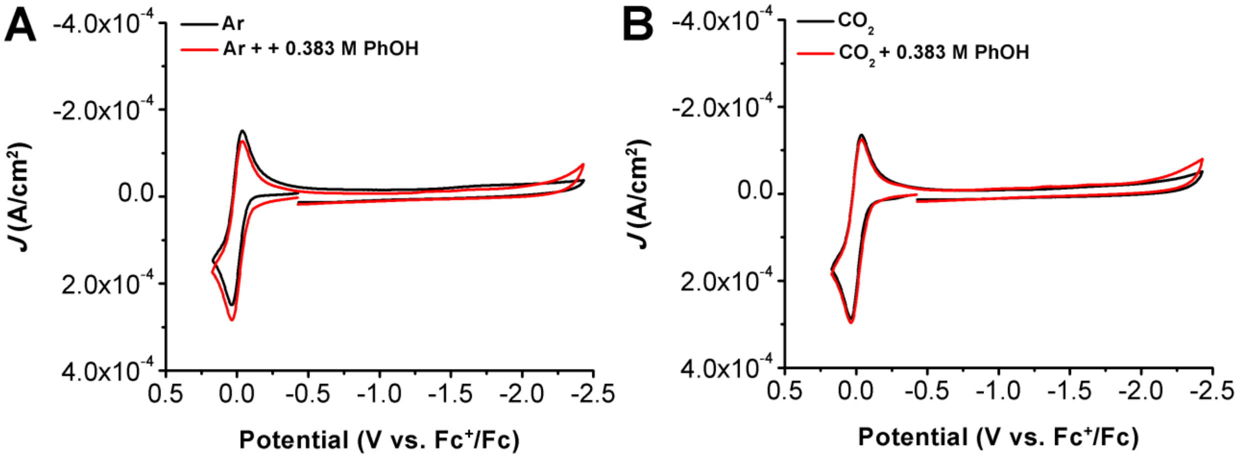

Figure S4.3.26. Control CV data. (**A**) Comparison of CVs under Ar (black) and Ar and PhOH (red). (**B**) Comparison of CVs under CO_2 (black) and CO_2 with PhOH (red). Conditions: 0.1 M $TBAPF_6$/DMF; glassy carbon working electrode, glassy carbon rod counter electrode, Ag/AgCl pseudoreference electrode; referenced to Fc^+/Fc internal standard; 100 mV/s scan rate.

Table S4.5.6. Crystal data and structure refinement for Cr(^{tbu}dhbpy)Cl(H_2O) **2**.

	2
Chemical formula	$C_{40}H_{51}ClCrN_3O_3$
Formula weight (g/mol)	709.29
Temperature (K)	100(2)
Crystal size (mm)	0.027 x 0.051 x 0.224
Crystal habit	yellow rod
Crystal system	triclinic
Space group	P -1
a (Å)	6.7438(15)
b (Å)	15.597(3)
c (Å)	19.696(4)
α (°)	68.339(6)
β (°)	81.912(6)
γ (°)	81.492(6)
Volume (Å^3)	1895.8(7)
Z	2
ρ_{calc} (g/cm^3)	1.243
μ (mm^{-1})	0.412
Theta range for data collection (°)	1.41 to 25.75
Index ranges	$-8 \le h \le 8$ $-19 \le k \le 18$ $-23 \le l \le 24$
Reflections collected	31094
Independent reflections	7223 [R_{int} = 0.1185]
Max. and min. transmission	0.9890 and 0.9130
Data / restraints / parameters	7223 / 0 / 454
Goodness-of-fit on F^2	1.006
R_1 [I>2σ(I)]	0.0561
wR_2 [all data]	0.1366

4.6 Acknowledgments: The authors thank Dr. Vagulejan Balasanthiran for providing the *N,N'*-bis(3,5-di-tert-butylsalicylidene)-1,2-cyclohexanediammine ligand as a mixture of *R,R* and *S,S* isomers. C.W.M. conceived and supervised the experiments; S.L.H. and J.M.D. conducted all experiments; D.A.D. collected and refined X-ray crystallographic data; C.W.M. and S.L.H. wrote the original published work.

4.7 References:

1. Ballivet-Tkatchenko, D.; Camy, S.; Condoret, J. S., Carbon Dioxide, a Solvent and Synthon for Green Chemistry. In *Environmental Chemistry: Green Chemistry and Pollutants in Ecosystems*, Lichtfouse, E.; Schwarzbauer, J.; Robert, D., Eds. Springer Berlin Heidelberg: Berlin, Heidelberg, 2005; pp 541-552.
2. IPCC *Global Warming of 1.5°C. An IPCC Special Report*; World Meterological Organization: Geneva, Switzerland, 2018.
3. Jacobs, G.; Davis, B. H., Chapter 5 Conversion of Biomass to Liquid Fuels and Chemicals via the Fischer–Tropsch Synthesis Route. In *Thermochemical Conversion of Biomass to Liquid Fuels and Chemicals*, The Royal Society of Chemistry: 2010; Vol. 1, pp 95-124.
4. Seh, Z. W.; Kibsgaard, J.; Dickens, C. F.; Chorkendorff, I.; Nørskov, J. K.; Jaramillo, T. F., *Science* **2017,** *355*, eaad4998.
5. Raebiger, J. W.; Turner, J. W.; Noll, B. C.; Curtis, C. J.; Miedaner, A.; Cox, B.; DuBois, D. L., *Organometallics* **2006,** *25*, 3345-3351.
6. Chen, Z.; Chen, C.; Weinberg, D. R.; Kang, P.; Concepcion, J. J.; Harrison, D. P.; Brookhart, M. S.; Meyer, T. J., *Chem. Comm.* **2011,** *47*, 12607-12609.
7. Wong, K.-Y.; Chung, W.-H.; Lau, C.-P., *J. Electroanal. Chem.* **1998,** *453*, 161-170.
8. Sampson, M. D.; Nguyen, A. D.; Grice, K. A.; Moore, C. E.; Rheingold, A. L.; Kubiak, C. P., *J. Am. Chem. Soc.* **2014,** *136*, 5460-5471.
9. Smieja, J. M.; Sampson, M. D.; Grice, K. A.; Benson, E. E.; Froehlich, J. D.; Kubiak, C. P., *Inorg. Chem.* **2013,** *52*, 2484-2491.
10. Azcarate, I.; Costentin, C.; Robert, M.; Savéant, J.-M., *J. Am. Chem. Soc.* **2016,** *138*, 16639-16644.

11. Cometto, C.; Chen, L.; Lo, P.-K.; Guo, Z.; Lau, K.-C.; Anxolabéhère-Mallart, E.; Fave, C.; Lau, T.-C.; Robert, M., *ACS Catal.* **2018,** *8*, 3411-3417.
12. Froehlich, J. D.; Kubiak, C. P., *Inorg. Chem.* **2012,** *51*, 3932-3934.
13. Reda, T.; Plugge, C. M.; Abram, N. J.; Hirst, J., **2008,** *105*, 10654-10658.
14. Leopoldini, M.; Chiodo, S. G.; Toscano, M.; Russo, N., **2008,** *14*, 8674-8681.
15. Dobbek, H.; Gremer, L.; Kiefersauer, R.; Huber, R.; Meyer, O., **2002,** *99*, 15971-15976.
16. Clark, M. L.; Grice, K. A.; Moore, C. E.; Rheingold, A. L.; Kubiak, C. P., *Chem. Sci.* **2014,** *5*, 1894-1900.
17. Ramos Sende, J. A.; Arana, C. R.; Hernandez, L.; Potts, K. T.; Keshevarz-K, M.; Abruna, H. D., *Inorg. Chem.* **1995,** *34*, 3339-3348.
18. Pickett, C. J.; Pletcher, D., *Dalton Trans.* **1976**, 749-752.
19. Maia, L. B.; Fonseca, L.; Moura, I.; Moura, J. J. G., *J. Am. Chem. Soc.* **2016,** *138*, 8834-8846.
20. Tory, J.; Setterfield-Price, B.; Dryfe, R. A. W.; Hartl, F., *ChemElectroChem* **2015,** *2*, 213-217.
21. Grice, K. A.; Saucedo, C., *Inorg. Chem.* **2016,** *55*, 6240-6246.
22. Neri, G.; Donaldson, P. M.; Cowan, A. J., *J. Am. Chem. Soc.* **2017,** *139*, 13791-13797.
23. Jiang, C.; Nichols, A. W.; Machan, C. W., *Dalton Trans.* **2019**.
24. Francke, R.; Schille, B.; Roemelt, M., *Chem. Rev.* **2018,** *118*, 4631-4701.
25. Franco, F.; Cometto, C.; Sordello, F.; Minero, C.; Nencini, L.; Fiedler, J.; Gobetto, R.; Nervi, C., *ChemElectroChem* **2015,** *2*, 1372-1379.

26. Sieh, D.; Lacy, D. C.; Peters, J. C.; Kubiak, C. P., **2015,** *21*, 8497-8503.

27. Hooe, S. L.; Rheingold, A. L.; Machan, C. W., *J. Am. Chem. Soc.* **2018,** *140*, 3232-3241.

28. Nichols, A. W.; Chatterjee, S.; Sabat, M.; Machan, C. W., *Inorg. Chem.* **2018,** *57*, 2111-2121.

29. Hooe, S. L.; Machan, C. W., *J. Am. Chem. Soc.* **2019,** *141*, 4379-4387.

30. Chapovetsky, A.; Do, T. H.; Haiges, R.; Takase, M. K.; Marinescu, S. C., *J. Am. Chem. Soc.* **2016,** *138*, 5765-5768.

31. Chapovetsky, A.; Welborn, M.; Luna, J. M.; Haiges, R.; Miller, T. F.; Marinescu, S. C., *ACS Cent. Sci.* **2018,** *4*, 397-404.

32. Sathrum, A. J.; Kubiak, C. P., *J. Phys. Chem. Lett.* **2011,** *2*, 2372-2379.

33. Stiddard, M. H. B., *J. Chem. Soc.* **1962**, 4712-4715.

34. Kanthimathi, M.; Nair, B. U.; Ramasami, T.; Shibahara, T., *Chem. Sci.* **1997,** *109*, 235-248.

35. Franco, F.; Pinto, M. F.; Royo, B.; Lloret-Fillol, J., *Angew. Chem. Int. Ed.* **2018,** *57*, 4603-4606.

36. Passard, G.; Dogutan, D. K.; Qiu, M.; Costentin, C.; Nocera, D. G., *ACS Catal.* **2018**.

37. Azcarate, I.; Costentin, C.; Robert, M.; Saveant, J. M., *J. Am. Chem. Soc.* **2016,** *138*, 16639-16644.

38. Costentin, C.; Passard, G.; Robert, M.; Savéant, J.-M., *Proc. Natl. Acad. Sci.* **2014,** *111*, 14990.

39. Riplinger, C.; Sampson, M. D.; Ritzmann, A. M.; Kubiak, C. P.; Carter, E. A., *J. Am. Chem. Soc.* **2014,** *136*, 16285-16298.

40. Sampson, M. D.; Kubiak, C. P., *J. Am. Chem. Soc.* **2016,** *138*, 1386-1393.

41. Rebelein, J. G.; Lee, C. C.; Hu, Y.; Ribbe, M. W., *Nature Comm.* **2016,** *7*, 13641.

42. Harris, D. C., *Quantitative Chemical Analysis*. 7th ed.; W.H. Freeman and Company: New York: 2007.

43. Grant, D. H., *J. Chem. Educ.* **1995,** *72*, 39.

44. Bain, G. A.; Berry, J. F., *J. Chem. Educ.* **2008,** *85*, 532.

45. Hanson, J., *J. Chem. Educ.* **2001,** *78*, 1266.

46. Pegis, M. L.; Wise, C. F.; Martin, D. J.; Mayer, J. M., *Chem. Rev.* **2018,** *118*, 2340-2391.

47. Pegis, M. L.; Roberts, J. A. S.; Wasylenko, D. J.; Mader, E. A.; Appel, A. M.; Mayer, J. M., *Inorg. Chem.* **2015,** *54*, 11883-11888.

48. Roy, S.; Sharma, B.; Pécaut, J.; Simon, P.; Fontecave, M.; Tran, P. D.; Derat, E.; Artero, V., *J. Am. Chem. Soc.* **2017,** *139*, 3685-3696.

49. Nielsen, M. F. H., Ole, *Acta Chemica Scandinavica* **1992**, 883-896.

50. Bhugun, I.; Lexa, D.; Savéant, J.-M., *J. Am. Chem. Soc.* **1996,** *118*, 1769-1776.

51. James, H. J.; Broman, R. F., *J. Phys. Chem.* **1971,** *75*, 4019-4024.

Chapter 5

Non-Covalent Assembly of Proton Donors and *p*-Benzoquinone Anions for Co-Electrocatalytic Reduction of Dioxygen

Chapter 5 contains material for upcoming publications and have been incorporated with consent of all current contributing authors. These authors include Emma N. Cook, Amelia G. Reid, and Charles W. Machan. The work in this chapter was published in preprint form and is available at https://doi.org/10.26434/chemrxiv.14156528.v1.

5.1 Abstract

The two-electron and two-proton p-hydroquinone/p-benzoquinone (H_2Q/BQ) redox couple has mechanistic parallels to the function of ubiquinone in the electron transport chain. This proton-dependent redox behavior has shown applicability in catalytic aerobic oxidation reactions, redox flow batteries, and co-electrocatalytic oxygen reduction. Under nominally aprotic conditions in non-aqueous solvents, BQ can be reduced by up to two electrons in separate electrochemically reversible reactions. With weak acids (AH) at high concentrations, potential inversion can occur due to favorable hydrogen-bonding interactions with the intermediate monoanion $[BQ(AH)_m]^{\bullet-}$. The solvation shell created by these interactions can mediate a second one-electron reduction coupled to proton transfer at more positive potentials ($[BQ(AH)_m]^{\bullet-} + nAH + e^- \rightleftharpoons [HBQ(AH)_{(m+n)-1}(A)]^{2-}$), resulting in an overall two electron reduction at a single potential. Here we show that the resultant hydrogen-bonded $[HBQ]^-$ adduct mediates the transfer of electrons and the proton donor 2,2,2-trifluoroethanol (TFEOH) to a Mn-based complex during the electrocatalytic reduction of dioxygen (O_2). The Mn electrocatalyst is selective for H_2O_2 with only TFEOH and O_2 present, however, with BQ present under otherwise analogous conditions, an electrogenerated $[HBQ(AH)_4(A)]^{2-}$ adduct (where AH = TFEOH) alters product selectivity to 96(±0.5)% H_2O in a co-electrocatalytic fashion. These results suggest that hydrogen-bonded $[HBQ]^-$ anions can function in an analogous co-electrocatalytic manner to H_2Q.

5.2 Introduction

The systematic optimization of molecular electrocatalysts requires an in-depth mechanistic understanding of the movement of electrons and protons to facilitate a reaction of interest.[1-3] Biological models, particularly the water splitting reaction of photosystem II[4-5] and complex IV in the electron transport chain,[6] are common inspiration for the development of molecular electrocatalytic systems for artificial photosynthesis, where proton (H^+) and electron ($e^–$) equivalents need to be efficiently directed.[7] Given the known role of tyrosine as a mediator of protons and electrons in the Mn-containing oxygen evolving complex of photosystem II,[4] there is considerable incentive to identify co-catalytic phenol/quinone derivatives to improve the activity and/or alter the selectivity of Mn-based electrocatalytic processes related to the interconversion of H_2O, H_2O_2, and O_2. To the best of our knowledge, no co-electrocatalytic systems have been reported with Mn and quinone derivatives,[8] although prior studies have noted that hydroquinones and aldehydes can drive partial O_2 reduction during chemical oxidations mediated by Mn complexes.[9-13]

It has been previously demonstrated that *p*-hydroquinone (H_2Q) can function as an electron–proton transfer mediator (EPTM) in the co-electrocatalytic reduction of O_2 to H_2O by a Co(salophen) compound.[14-15] In the co-electrocatalytic system, formal reduction and protonation of BQ to generate H_2Q is proposed to occur in *N,N*-dimethylformamide (DMF) solution with acetic acid (AcOH; pK_a(DMF) = 13[16]) as a proton donor. In this system, H_2Q is a discrete intermediate, which engages in the formal transfer of proton and electron equivalents to intermediate Co–O_2[H]$^{+/0}$ species. Importantly, the presence of the EPTM shifted product selectivity from H_2O_2 (91% efficiency under otherwise identical conditions with Co(salophen) and decamethylferrocene as the electron source) to H_2O (overall quantitative, thanks to thermal reactivity between H_2Q, Co(salophen), and O_2).[14]

The reduction chemistry of quinones in aprotic solvents is known to be highly dependent on solvent, added proton donor activity, and electrolyte.[17-22] Under aprotic conditions, sequential one-electron reduction events are generally observed. Depending on proton donor activity and hydrogen-bonding strength, potential inversion can occur, enabling a two-electron reduction at a single potential. Under these conditions with a neutral quinone ($[Q]^0$), the second electron transfer in the two-electron reduction (**Eq (5.2.2)**) is more facile than the first electron transfer (**Eq (5.2.1)**). When pK_a comparisons are available, they can fail to address the complex solvent mixtures which result at high concentrations of added weak proton donors,[22-27] which directly impact the stability of the BQ-based mono- and di-anions.[22, 28]

$$[Q]^0 + e^- \overset{E_1^0}{\rightleftharpoons} [Q]^{\cdot -} \qquad \textbf{Eq (5.2.1)}$$

$$[Q]^{\cdot -} + e^- \overset{E_2^0}{\rightleftharpoons} [Q]^{2-} \qquad \textbf{Eq (5.2.2)}$$

A pioneering study by Gupta and Linschitz[18] noted that at certain hydrogen-bonding interaction strengths between the proton donor and *para*-quinone radical anions $[Q]^{\bullet -}$ in MeCN, such an effective potential inversion was possible with weak acids (e.g. 2,2,2-trifluoroethanol, TFEOH), when the second reduction was accompanied by proton transfer in a solvated shell of proton donors ($[Q(AH)_m]^{\bullet -} + nAH + e^- \rightleftharpoons Q + [HQ(AH)_{(m+n)-1}(A)]^{2-}$); where AH is a proton donor and A^- is the conjugate base form of AH). The stabilization of the $[Q]^{\bullet -}$ and $[HQ]^-$ species, as well as the observation of electrochemical irreversibility at sufficient acid concentrations, were ascribed to the strong hydrogen-bonds formed between the anions and proton donors in solution facilitating at least one proton transfer to achieve potential inversion.[18] Notably, this effect was also observed by Evans and co-workers using an *ortho*-quinone derivative in MeCN with high concentrations of added TFEOH.[27]

We were interested in the possibility that hydrogen-bonded adducts of the form $[HBQ(AH)_{(m+n)-1}(A)]^{2–}$ could perform a similar function to H_2Q for co-electrocatalytic O_2 reduction. One advantage would be that $[HBQ(AH)_{(m+n)-1}(A)]^{2–}$ would be comprised of highly reversible interactions, minimizing the height of any new kinetic barriers in the co-electrocatalytic mechanism. A second advantage would be a thermodynamic one: reaction selectivity could be changed from H_2O_2 to H_2O, without requiring the use of a stronger proton donor and increasing the reaction overpotential. To the best of our knowledge, the use of hydrogen-bonded quinone anion adducts in an analogous role to their hydroquinone counterparts has only been applied to the study of quinone-based energy storage systems.[29]

Given the profound interest in Mn complexes as electrocatalysts for O_2 reduction[30-44] and the single report on the use of the BQ/H_2Q redox couple in tandem with a molecular electrocatalyst to facilitate O_2 reduction,[15] we sought to carry out a study on the co-electrocatalytic competency of hydrogen-bonded $[HBQ]^–$ anions using a Mn-based catalyst developed in our lab.[45-46] This molecular Mn complex, Mn(^{tbu}dhbpy)Cl **1**, where 6,6′-di(3,5-di-*tert*-butyl-2-phenolate)-2,2′-bipyridine = $[^{tbu}dhbpy]^{2–}$, is a competent catalyst for the selective reduction of O_2 to H_2O_2 (ca. 80% selectivity) in the presence of weak Brønsted acids (phenol derivatives and TFEOH). Based on our mechanistic studies, a Mn(III)-superoxide species was proposed to be the key intermediate.[45-46] Herein, we report the selective electrocatalytic reduction of O_2 to H_2O (96±0.5%) by a catalyst system comprised of Mn(^{tbu}dhbpy)Cl **1**, *p*-benzoquinone (BQ), and 2,2,2-trifluoroethanol (TFEOH) as a sacrificial proton donor. This notable change in selectivity is achieved through the addition of co-catalytic amounts of BQ as a redox and proton-donor mediator (**Figure 5.2.1**).

Mechanistic experiments suggest that a key component is the generation of hydrogen-bonded $[HBQ(AH)_{(m+n)-1}(A)]^{2-}$adducts *in situ*, which we propose serve an analogous function to H_2Q in transferring proton donors and electrons to Mn-$O_2[H]^{+/0}$ intermediates. The number of TFEOH equivalents is dependent on the concentration of BQ, ranging from 5.6 at 0.5 mM of BQ to 4.7 at an increased BQ concentration of 2.5 mM (**Figure 5.2.1**). Given that the solvation shell of the $[HBQ(AH)_{(m+n)-1}(A)]^{2-}$ adducts is by all definitions a non-ideal solvent, we consider that these data suggest the *average* structure in solution is best described as $[HBQ(TFEOH)_4(TFEO)]^{2-}$.

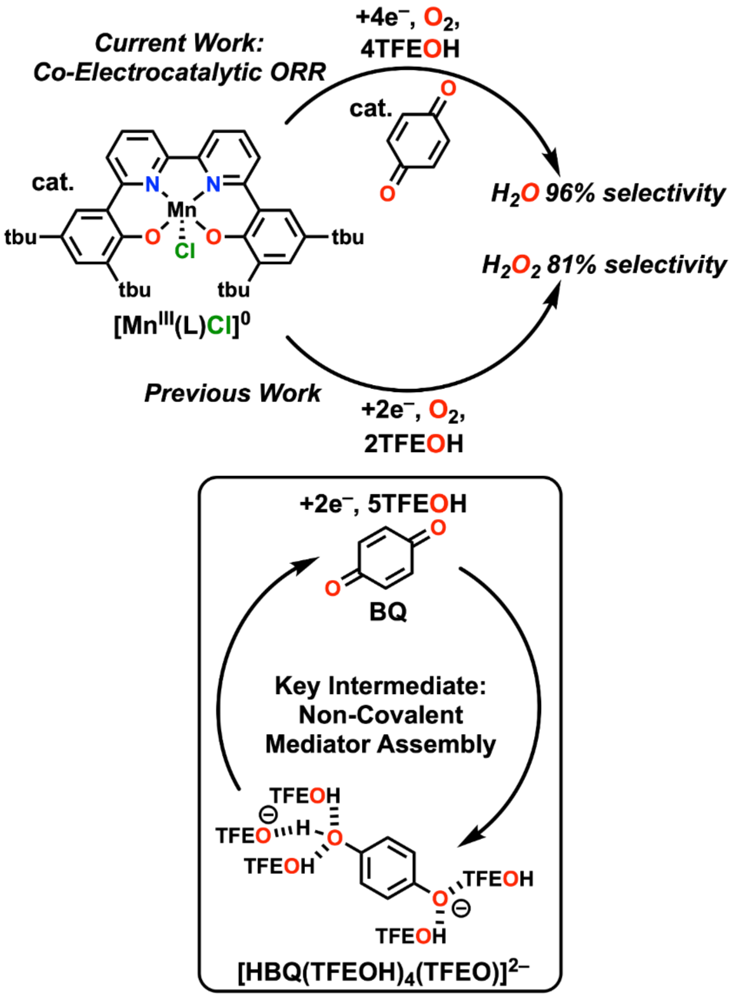

Figure 5.2.1. Comparison of product selectivity in previous versus current work with Mn(^{tbu}dhbpy)Cl **1** to summarize the overall co-electrocatalytic effect of BQ; L = ^{tbu}dhbpy^{2-}, TFEOH = 2,2,2-trifluoroethanol and [Mn^{III}(L)Cl]^0 = Mn(^{tbu}dhbpy)Cl **1**.

5.3 CV Analysis of BQ Reduction with TFEOH

Cyclic voltammetry (CV) experiments were carried out with 0.1 M tetrabutylammonium hexafluorophosphate (TBAPF$_6$) as supporting electrolyte in acetonitrile (MeCN) solution. Under argon (Ar) saturation conditions, BQ displays two reversible redox features with E$_{1/2}$ values of –0.89 V and –1.69 V versus the ferrocenium/ferrocene (Fc$^+$/Fc) redox couple (**Figure 5.3.2A**, black), consistent with previous reports.[18, 25] These reduction features are assigned to BQ/[BQ]$^{\bullet-}$ and [BQ]$^{\bullet-}$/[BQ]$^{2-}$, respectively. As has been observed previously, the second reduction feature shows a slightly diminished current response, consistent with previously proposed reactivity between the monoanion $[BQ]^{-}$ and the dianion $[BQ]^{2-}$.[18] Coulometry performed at –2.1 V versus Fc^{+}/Fc confirmed that these two redox features correspond to an overall two-electron reduction process under aprotic conditions (**Figure S5.3.1-S5.3.3**). These data are consistent with previous proposals of sequential one-electron $BQ/[BQ]^{\bullet-}$ and $[BQ]^{\bullet-}/[BQ]^{2-}$ proceses.[18]

Titrating increasing quantities of TFEOH into an Ar-saturated MeCN solution of 0.5 mM BQ resulted in the convergence of these two redox processes into a single irreversible redox feature at 1.37 M TFEOH (voltage at half-peak current –0.66 V vs Fc^{+}/Fc), which displayed an increased current response relative to those from the one-electron redox features under aprotic conditions (**Table S5.3.1**, **Figure 5.3.2A**, blue and black traces). The titration data at low [TFEOH] were consistent with the response observed for analogous experiments with 2.5 mM BQ, however the same degree of irreversibility was not observed at the higher BQ concentration (**Table S5.3.2** and **Figure S5.3.4**). Comparing CV titration data with BQ and TFEOH under Ar and O_2 did not reveal significant differences in the observed electrochemical response, indicating that the anionic species generated under these conditions does not interact with O_2 in a catalytic fashion on the CV timescale (**Figure S5.3.5**).

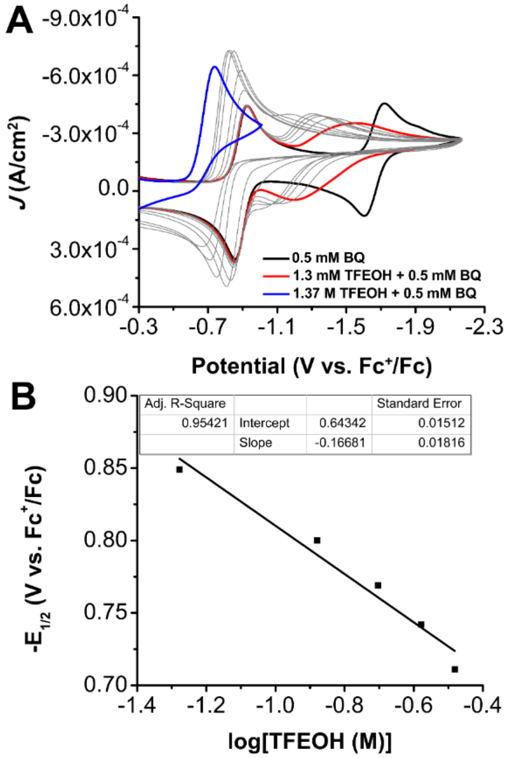

Figure 5.3.2. (**A**) CVs of TFEOH titration with 0.5 mM BQ obtained under Ar saturation conditions. (**B**) Linear fit of -$E_{1/2}$ versus log[TFEOH (M)] for the two-electron BQ/[BQ]$^{2-}$ reduction feature obtained from CV titration data in (**A**), using only reversible two-electron responses observed in the region from –0.85 to –0.70 V. Conditions: 0.1 M TBAPF$_6$/MeCN; glassy carbon working electrode, glassy carbon counter electrode, Ag/AgCl pseudoreference electrode; 100 mV/s scan rate; referenced to internal ferrocene standard.

5.4 Coulometric Analysis of BQ Reduction with TFEOH

Coulometry at –1.1 V versus Fc$^+$/Fc with 2.5 mM BQ and 0.13 M TFEOH suggests that with an added proton donor this single redox feature corresponds to a two-electron reduction (**Figure S5.4.6**). However, NMR analysis of the product of this reduction shows excellent agreement with authentic samples of H$_2$Q under analogous conditions (**Figures S5.4.7-S5.4.11**). Indeed, replicating these coulometry and control experiments with acetic acid (AcOH; pK_a = 23.5)[47], which is expected to be sufficiently acidic to directly generate H$_2$Q produce identical results (**Figures S5.4.12-S5.4.14**). Previous studies have shown that the disproportionation of $[HBQ]^{-}$ to a dianionic quinhydrone species $[H_2Q{\bullet}BQ]^{2-}$ occurs under these conditions (**Eq (5.4.3)**).[48] This assignment was based on a distinct NMR spectrum obtained for the quinhydrone dimer experimentally relative to H_2Q, which we do not observe. We emphasize that this observation is inconsistent with the reported pK_a of TFEOH (35.4), which should thermodynamically preclude it from protonating $[HQ]^{-}$ (pK_a H_2Q = 26.20) and suggests that additional thermal reactions are occurring. We note that the previously reported conditions[48] were aprotic, conducted with stoichiometric amounts of added base. Therefore, we propose that under our electrolysis conditions where 1.37 M TFEOH is present, a second thermal reaction occurs (**Eq (5.4.4)**), producing H_2Q.

$$2[HQ]^{-} \rightleftharpoons [H_2Q \bullet BQ]^{2-} \qquad \textbf{Eq (5.4.3)}$$

$$[H_2Q \bullet BQ]^{2-} + 2TFEOH \rightleftharpoons 2[H_2Q] + 2[TFEO]^{-} \qquad \textbf{Eq (5.4.4)}$$

Based on these observations, we next conducted CV experiments using BQ, H_2Q, AcOH and TFEOH to establish whether evidence of either **Eqs (5.4.3)** or **(5.4.4)** was apparent. If **Eq (5.4.3)** was relevant on the electrochemical timescale under these conditions, there should be a quantifiable difference in the reduction of BQ, with and without a stoichiometric amount of H_2Q present, consistent with a favorable equilibrium interaction ($K > 1$). Others have noted previously that much greater concentrations are required to observe this interaction, which resulted in diagnostic adsorption features in the observed CV response.[49] However, with and without 1.37 M TFEOH present, we observed no evidence of an analogous strong interaction during the reduction of BQ when H_2Q was present (**Figures S5.4.15-S5.4.16**), suggesting minimal speciation of the dianionic quinhydrone species $[H_2Q{\bullet}BQ]^{2-}$ with an excess of proton donor present. While the coulometry experiments demonstrate that this reaction does occur, the absence of an interaction between BQ and H_2Q under CV conditions suggests that the reaction summarized by **Eq (5.4.3)** is not relevant on that timescale. We also note that the reduction features of BQ with 1.37 M TFEOH present were approximately 0.36 V more negative than those with 1.37 M AcOH present, a trend which holds from 0.5 mM to 2.5 mM BQ (**Figures S5.4.17-S5.4.18**). These observations are consistent with the difference in proton donor activity and the expected thermodynamic favorability of $[HQ]^-$.

5.5 Quantification of TFEOH Binding During BQ Reduction

To better understand the speciation under electrochemical conditions, the relationship between the overall two-electron BQ redox response and TFEOH was analyzed by CV through TFEOH titration data under Ar saturation conditions according to the framework of Gupta and Linschitz (**Figures 5.3.2, S5.3.2** and **S5.5.19**; **Methods**).[18] At TFEOH concentrations where the two-electron BQ redox feature remains reversible, plotting the $-E_{1/2}$ of the two-electron BQ redox feature against log[TFEOH (M)] gives a slope consistent with a $2e^-$/5.6TFEOH redox process ([BQ] = 0.5 mM; **Figure 5.3.2B**). Based on prior reports,[18, 27] this suggests that the two-electron reduced BQ species is the result of a stabilized monoanionic H-bonded intermediate undergoing a second reduction, which is concerted with proton transfer in the non-covalent assembly **Eq (5.5.6)**.[18] Our observation of a two-electron redox response is consistent with the standard potential of **Eq (5.5.5)** occurring at more negative potentials than that of **Eq (5.5.6)**.

$$[BQ]^0 + mTFEOH + e^- \quad \overset{E_3^0}{\rightleftharpoons} \quad [BQ(TFEOH)_m]^- \qquad \textbf{Eq (5.5.5)}$$

$$[BQ(TFEOH)_m]^- + nTFEOH + e^- \quad \overset{E_4^0}{\rightleftharpoons}$$

$$[HBQ(TFEOH)_{(m+n)-1}(TFEO)]^{2-} \quad \mathbf{Eq\ (5.5.6)}$$

At higher concentrations of BQ (2.5 mM), comparable analysis of the two-electron BQ reduction feature shows that the average number of TFEOH molecules engaged in hydrogen-bonding interactions diminishes slightly to 4.7 (**Figure S5.3.4**). Analysis of K_{eq} for the equilibrium binding events depicted in **Eq (5.5.5)** and **Eq (5.5.6)**, produced values of 4.31 x 10^7 at 0.5 mM BQ and 2.31 x 10^6 at 2.5 mM BQ, comparable to those determined for other weak acids previously.[18] Note that as the reaction in **Eq (5.5.6)** shifts to increasingly positive potentials in comparison to **Eq (5.5.5)**, a disproportionation reaction to produce the same two-electron reduction product also becomes increasingly favorable (**see Methods**).

The experimental observation of irreversibility at high TFEOH concentrations, coupled with the multiple equivalents solvating the anionic species (**Figure 5.3.2**) suggest that formal proton transfer is occurring to some degree.[18, 27] It is worth noting that the non-ideality of the solvent system should support proton transfer reactions, where high concentrations of the TFEOH are expected to favorably solvate mono- and dianionic species.[22-25, 27, 50] As discussed above, previous computational studies estimate that TFEOH has insufficient proton activity to monoprotonate $[BQ]^{2-}$ ($[HBQ]^- \rightleftharpoons H^+ + [BQ]^{2-}$; p$K_a$(MeCN) = 40.96), but a second protonation is thermodynamically disfavored ($[H_2Q] \rightleftharpoons H^+ + [HBQ]^-$; p$K_a$(MeCN) = 26.20).[51] Therefore, we assign an average value of 5 to m+n in **Eq (5.5.6)**.

We emphasize that our data do not enable us to exclude the formal generation of H_2Q (presumably as a component of a dianionic quinhydrone[48-49]) following the predicted formation of $[HQ]^{-}$, based on reported pK_a values in MeCN. However, our control CV data do not demonstrate a strong interaction between BQ and H_2Q during reduction with or without TFEOH present, which would be consistent with a favorable K for the formation of the dianionic quinhydrone species $[H_2Q{\bullet}BQ]^{2-}$ under electrochemical conditions, **Eq (5.4.3)**. This dianionic quinhydrone species is proposed to be the intermediate to H_2Q formation, **Eq (5.4.4)**, which we observe in our electrolysis data with AcOH and TFEOH present. Therefore, we postulate that this thermal decomposition pathway occurs slowly on the CV timescale.

5.6 Co-Electrocatalytic Studies with Mn(^{tbu}dhbpy)Cl 1, BQ and TFEOH

As we reported in our initial study on **1**,[45] the addition of TFEOH under O_2 saturation conditions causes a catalytic increase in current (**Figure 5.6.3A**, red). Upon the addition of 0.5 mM BQ to a solution of **1** (1:1 ratio of **1**:BQ) and TFEOH (1.37 M) under O_2 saturation conditions, a shift towards more positive potentials and a multielectron irreversible wave consistent with catalysis is observed (**Figure 5.6.3B**, blue). Comparative electrochemical reaction conditions where Mn(^{tbu}dhbpy)Cl **1**, O_2, TFEOH, or BQ are omitted do not show analogous activity, indicating that an alternate electrochemical process is occurring when all four components are present. Importantly, these observations are consistent when greater concentrations of BQ (1.25 mM or 2.5 mM) are present (**Figures S5.6.20-S5.6.21**).

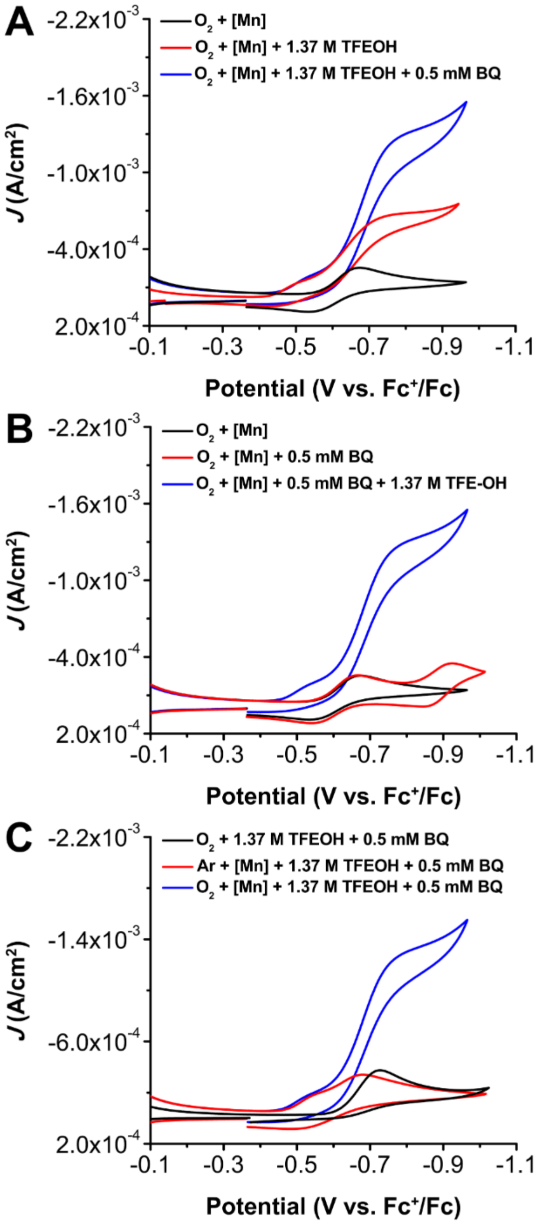

Figure 5.6.3. (**A**) CVs comparing 0.5 mM of Mn(^{tbu}dhbpy)Cl **1**, with 1.37 M TFEOH both with (blue) and without (red) 0.5 mM BQ. (**B**) CVs comparing 0.5 mM of Mn(^{tbu}dhbpy)Cl **1**, with 0.5 mM BQ both with (blue) and without (red) 1.37 M TFEOH under O_2 saturation conditions. (**C**) CVs comparing 0.5 mM Mn(^{tbu}dhbpy)Cl **1**, with 1.37 M TFEOH and 0.5 mM BQ under Ar (red) and O_2 (blue) saturation conditions compared to a control CV in the absence of Mn(^{tbu}dhbpy)Cl **1** (black). Conditions: 0.1 M TBAPF$_6$/MeCN; glassy carbon working electrode, glassy carbon counter electrode, Ag/AgCl pseudoreference electrode; 100 mV/s scan rate; referenced to internal ferrocene standard.

Notably, with **1**, 0.5 mM BQ, and 1.37 M TFEOH under Ar saturation conditions, a shift in the BQ reduction potential is observed (**Figure 5.6.3C**, comparing red and black).

Specifically, the BQ redox feature (0.5 mM) in the presence of 1.37 M TFEOH shifts to more positive potentials by 0.046 V when **1** (0.5 mM) is added. Based on this, we qualitatively interpret the positive shifts in the BQ reduction potential to be the result of an interaction between the hydrogen-bonded $[HBQ]^{-}$ monoanion and the one-electron reduced and monoprotonated product of **1**. However, due to the closeness of the of BQ and Mn reduction potentials (E_p = –0.60 V and –0.77 V vs. Fc^+/Fc with 0.2 M TFEOH, respectively) and their respective dependences on added TFEOH concentration, more rigorous quantification is not possible. We note that our previous studies have shown that the ligand framework of **1** is protonated upon Mn(III)/(II) reduction in the presence of added proton donor.[45-46] No shift is observed for the Mn(III)/(II) reduction because the reduced BQ species are not generated until more negative potentials.

We have established in our previous studies that the Mn catalyst binds O_2 to generate a Mn(III)-superoxide, which is reduced to a hydroperoxide with proton transfer at more negative potentials.[45-46] Since the potential for the reduction of this Mn(III)-superoxide intermediate overlaps with the reduction of BQ under these conditions, we propose that the observed co-electrocatalysis arises from an intramolecular reaction as summarized in **Eq (5.6.7)**.

$$2[HBQ(TFEOH)_4(TFEO)]^{2-} + [Mn^{III}\big(L(H)\big)(O_2^{\cdot -})]^0 \quad \rightleftharpoons$$

$$2[BQ]^0 + [Mn^{II}(L(H))]^0 + 4[TFEO]^- + 2H_2O + 6TFEOH \qquad \mathbf{Eq\ (5.6.7)}$$

We expect that $[HBQ(TFEOH)_4(TFEO)]^{2-}$ has comparable reducing power to H_2Q and note that H_2Q functions as a competent reductant of O_2 and H_2O_2 under experimental conditions with **1** present in control studies (**Figures S5.6.22-S5.6.27**).[9-13]

5.7 Kinetic Analysis of Co-Electrocatalytic Conditions

To understand the relative kinetic relationships of the reaction components, variable concentration studies were carried out via CV (**Figures S5.7.28-S5.7.33**). Although the complexity of the reaction mixture precludes assigning concentration dependencies to the observed catalytic current, these data are consistent with the proposed equilibrium interactions described above, as well as the dependence of co-electrocatalytic activity on the presence of **1**, BQ, TFEOH, and O_2. In these data, a pronounced anodic wave is observed in the CV response near the $[BQ]^0/[HBQ(TFEOH)_4(TFEO)]^{2-}$ feature on the return sweep under co-catalytic conditions when BQ is in excess of complex **1** (**Figure S5.7.29**). This waveform suggests a mismatch between the generation of $[HBQ(TFEOH)_m(TFEO)]^{2-}$ and its rate of reaction with the intermediate $[Mn\text{-}(L(H))O_2^{\bullet-}]^{+/0}$ species, where L = $^{tbu}dhbpy^{2-}$ and (L(H)) denotes formal protonation of the O atom of the ligand framework.[45] The resulting accumulation of unreacted $[HBQ(TFEOH)_4(TFEO)]^{2-}$ in the reaction-diffusion layer results in appreciable re-oxidation of $[HBQ(TFEOH)_4(TFEO)]^{2-}$ to $[BQ]^0$ (reverse of **Eq (5.5.6)** and **Eq (5.5.5)** as written). Control CV data with BQ, TFEOH and urea•H_2O_2 present in MeCN show minimal differences, suggesting that $[HBQ(TFEOH)_m(TFEO)]^{2-}$ is relatively stable in the presence of H_2O_2 on the CV timescale (**Figure S5.7.34**).

5.8 Determining Co-Electrocatalytic Product Selectivity

Rotating ring-disk electrode (RRDE) experiments were carried out to quantify the electrocatalytic production of H_2O_2 (see **Materials and Methods** for description). Control experiments with BQ and added TFEOH showed that the electrogenerated $[HBQ(TFEOH)_4(TFEO)]^{2-}$ decomposes to produce a small amount of H_2O_2 (10 (±23)%, (**Figures S5.8.35-S5.8.40**; **Table S5.8.3**). In CVs of BQ with TFEOH present under O_2 saturation there is no multielectron catalytic response at reducing potentials (e.g., **Figure 5.6.3**). We postulate that this discounts appreciable H_2O generation during the catalytic response, which would otherwise explain the less-than-quantitative ring current. The proposed instability is consistent with the observations of others.[29]

With **1** and 1.37 M TFEOH under O_2 saturation conditions, the system exhibited comparable selectivity for H_2O_2 compared to our previous report, 68 (±13)% (**Figure S5.8.41** and **Table S5.8.3**). Here, the use of greater concentrations of TFEOH than previously reported[45] resulted in a slight shift of the average product distribution, but was within error of the original report. Upon the addition of one equivalent of BQ relative to **1** under these conditions, the system showed selectivity for H_2O_2 within error of the BQ-free system (69(±0.3)%). An increased cathodic current response was observed, suggesting reaction rate enhancement under 1:1 co-electrocatalytic conditions (**Figures S5.8.42-S5.8.47**). At 2.5 equivalents of BQ (1.25 mM) relative to **1** (0.5 mM), the selectivity of the system shifted to H_2O as the major product with 55(±4)% efficiency (**Figures S5.8.48-53** and **Table S5.8.3**). Lastly, with five equivalents of BQ (2.5 mM) relative to **1** (0.5 mM), the selectivity of the system became 96 (±0.5)% selective for H_2O (**Figures S5.8.54-S5.8.59** and **Table S5.8.3**). Consistent with the role of added BQ in shifting product selectivity, the observed decreases in efficiency for H_2O_2 showed a linear relationship with respect to the concentration of added BQ (**Figure 5.8.4**).

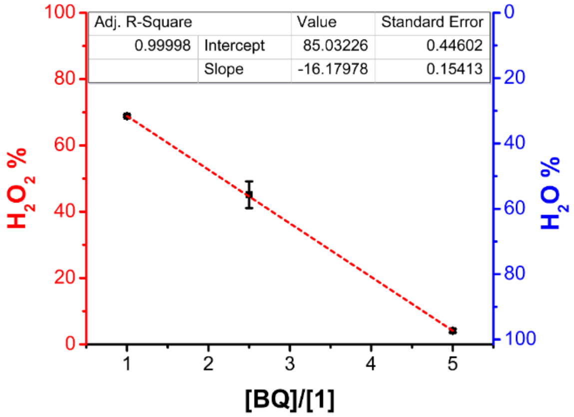

Figure 5.8.4. The observed relationship between the concentration of added BQ and the reaction product as characterized by RRDE at a rotation rate of 400 rpm. Conditions: 0.5 mM Mn(^{tbu}dhbpy)Cl **1**; 1.37 M TFEOH; 0.5, 1.25, or 5 mM BQ; 0.1 M $TBAPF_6$/MeCN.

5.9 Discussion

We have demonstrated that the selectivity for electrocatalytic O_2 reduction by Mn(^{tbu}dhbpy)Cl **1** with TFEOH as a proton donor can be altered from the $2H^+/2e^-$ product H_2O_2 to the $4H^+/4e^-$ product H_2O when BQ is added as a co-catalyst. Furthermore, current increases occur relative to the intrinsic performance of **1**, consistent with an enhanced rate of catalysis. Unlike the only previous report we are aware of,[15] this co-electrocatalytic effect leverages a non-covalent assembly between the added proton donor and redox mediator to achieve these improvements (**Figure 5.9.5**).

At high concentrations in MeCN, TFEOH acts to stabilize and solvate anionic quinone-derived species.[27] These solvent clusters assist thermodynamically favored monoprotonation of the intermediate $[BQ]^-$ species as a part of a proton-coupled electron transfer reaction to generate a stabilized $[HBQ]^-$ species. The concerted nature of this proton and electron transfer results in a standard potential which is more positive than the initial reduction, which is observed experimentally as an overall two-electron reduction feature.[22, 52] The reduction corresponding to the formation of the hydrogen-bond stabilized $[HBQ]^-$ is observed to shift to more positive potentials when **1** is present, suggesting a pre-equilibrium interaction between the two species.

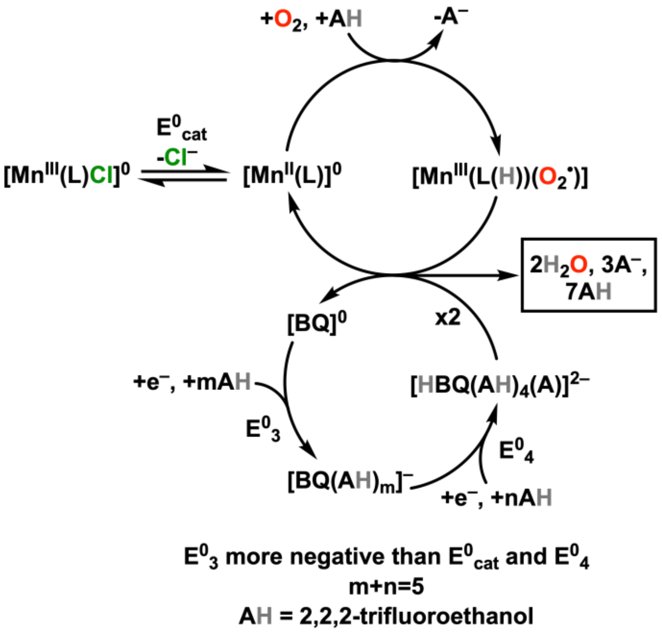

Figure 5.9.5. Proposed potential inversion mechanism for co-electrocatalytic O_2 reduction to water by $Mn(^{tbu}dhbpy)Cl$ **1** and BQ, where AH = TFEOH, m+n = 5, L = $[tbudhbpy]^{2-}$, and (L(H)) denotes formal protonation of the O atom of the ligand framework.

Based on our results, we propose that the hydrogen bond-stabilized $[HBQ]^-$ adduct serves as a redox mediator in these co-electrocatalytic reactions, delivering electrons and a single proton to $Mn\text{-}O_2[H]^{+/0}$ intermediates (**Figure 5.9.5**).15 In doing so, BQ also facilitates the net transfer of TFEOH to the Mn catalyst during the reaction. As $[HBQ]^-$ is oxidized to BQ, several equivalents of TFEOH are released from strong hydrogen-bonding interactions, allowing formal transfer to the Mn catalyst to occur. In the previously reported use of a BQ/H_2Q couple to achieve a co-electrocatalytic effect, separate hydrogen atom transfer and proton-coupled electron transfer steps from H_2Q were proposed to occur.[14-15] We note that in control experiments, significant reactivity was not observed between H_2O_2 and the hydrogen-bond stabilized $[HBQ]^-$; however, RRDE experiments suggest that it can generate small amounts of H_2O_2 from O_2. Our electrolysis studies show that the $[HBQ]^-$ anion is unstable under these conditions, decomposing to H_2Q in NMR studies. This implies that the previously reported dimerization to a quinhydrone dianion[48] can occur under these conditions, which we propose is an intermediate to H_2Q. However, CV experiments with equimolar amounts of BQ and H_2Q present do not show evidence of a strong equilibrium interaction during reduction, which was only observed previously at much larger ratios of H_2Q to BQ.[49]

5.10 Conclusions

These results suggest that energy transduction reactions analogous to those mediated by EPTMs are kinetically feasible by leveraging potential inversion phenomena from non-covalent effects, greatly expanding hypothetical reaction conditions. This suggests that an expanded range of weak proton donors can be used to achieve co-electrocatalytic changes in product distribution, enabling alternative strategies to optimize kinetic parameters of a co-electrocatalytic reaction without causing large increases in the overpotential of the reaction which occurs when using strong acids.

5.11 Supporting Information

Materials and Methods

General.

All chemicals and solvents (ACS or HPLC grade) were commercially available and used as received unless otherwise indicated. Mn(^{tbu}dhbpy)Cl **1** was prepared according to our previous report.[45] For all air-sensitive reactions and electrochemical experiments, HPLC-grade solvents were obtained as anhydrous and air-free from a PPT Glass Contour Solvent Purification System. Gas cylinders were obtained from Praxair (Ar as 5.0; O_2 as 4.0) and passed through the electrochemical working solvent with added molecular sieves prior to use. Gas mixing for variable concentration experiments was accomplished using a gas proportioning rotameter from Omega Engineering. UV-vis absorbance spectra were obtained on a Cary 60 from Agilent. An Anton-Parr Multiwave Pro SOLV, NXF-8 microwave reactor was used for microwave syntheses.

Electrochemistry.

All electroanalytical experiments were performed using a Metrohm Autolab PGSTAT302N potentiostat. Glassy carbon working (⌀ = 3 mm) and non-aqueous silver/silver chloride pseudoreference electrodes behind PTFE tips were obtained from CH Instruments. The pseudoreference electrodes were obtained by depositing chloride on bare silver wire in 10% HCl at oxidizing potentials and stored in a 0.1 M tetrabutylammonium hexafluorophosphate ($TBAPF_6$) acetonitrile solution in the dark prior to use. The counter electrode was a glassy carbon rod (⌀ = 3 mm). All CV experiments were performed in a modified scintillation vial (20 mL volume) as a single-chamber cell with a cap modified with ports for all electrodes and a sparging needle. Tetrabutylammonium hexafluorophosphate was purified by recrystallization from ethanol and dried in a vacuum oven before being stored in a desiccator. All data were referenced to an internal ferrocene standard (ferrocenium/ferrocene Fc^+/Fc reduction potential under stated conditions) unless otherwise specified; ferrocene was purified by sublimation prior to use. All voltammograms were corrected for internal resistance.

Rotating ring-disk electrode (RRDE) experiments were conducted using a Metrohm rotator with a Metrohm electrode consisting of a glassy carbon disk (⌀ = 5 mm) and a Pt ring. The average collection efficiency of the RRDE electrode was experimentally determined to be 25.5% using 0.5 mM ferrocene in 0.1 M $TBAPF_6$/MeCN. The counter electrode in the RRDE experiments was a glassy carbon rod (Type 2, ⌀ = 3 mm; Alfa Aesar) and the reference electrode was a non-aqueous Ag/AgCl reference electrode with a double-junction system from Metrohm. RRDE experiments were performed in a 50 mL graduated glass vessel from Metrohm as a single-chamber cell with adapted ports for all electrodes. All RRDE was referenced to an internal ferrocene standard.

Quantifying TFEOH Binding (adapted[18]).

To determine the average number of TFEOH equivalents involved in the overall two-electron BQ redox response from the CV titration data (**Figures 5.3.2** and **S5.3.4**), the slope of the $-E_{1/2}$ versus log[TFEOH (M)] was used in the concentration region where the feature remained reversible (–0.85 V to –0.70 V). The slope of this plot can be used to determine the number of TFEOH molecules *x* which associate to the $[BQ]^{2-}$ dianion, where *n* is the number of electrons involved (2), *F* is Faradays' constant (96485 $Cmol^{-1}$), *R* is the ideal gas constant ($JK^{-1}mol^{-1}$), *T* is temperature (K), **Eq (5.11.8)**.

$$(-slope) = 2.303\frac{nF}{xRT} \qquad \textbf{Eq (5.11.8)}$$

Using the linear fit equations obtained from the relevant regions of **Figures 5.3.2** and **S5.3.4**, averaged $E_{1/2}$ values (A and B) were determined for the respective representative concentration ranges and used to determine K_{eq} according to **Eq (5.11.9)** using Δ[TFEOH].

$$\exp\left(\frac{nF}{RT}\left(E^{B}_{1/2} - E^{A}_{1/2}\right)\right) = 1 + K_{eq}(\Delta[TFEOH])^{x} \qquad \textbf{Eq (5.11.9)}$$

Description of RRDE Quantification.

The collection efficiency was determined in the same manner as our previous reports[45] using 0.5 mM ferrocene (**Figure S5.11.60-S5.11.61**). Under conditions for which Levich behavior was observed, the difference between the amount of current produced at the disk under O_2 saturation and the amount of current produced at the disk under Ar saturation conditions was taken as the corrected disk current for O_2 saturation conditions ($I_{\text{disk corrected}}$) at each rotation rate. The difference between the amount of current produced at the ring under O_2 saturation conditions and the amount of current produced at the ring under Ar saturation conditions was taken as the corrected ring current for O_2 saturation conditions ($I_{\text{ring corrected}}$) at each rotation rate. To calculate the H_2O_2%, the $I_{\text{disk corrected}}$ was multiplied by the corresponding $N_{\text{empirical}}$ value for the specific rotation rate to determine the maximum amount of ring current for H_2O_2 production ($I_{\text{ring max}}$). The ratio of $I_{\text{ring corrected}}$ to $I_{\text{ring max}}$ was multiplied by a factor of 100 to determine the %H_2O_2 generated at the ring across all measured rotation rates (**Eq 5.11.10**).

$$\%H_2O_2 = (100)\frac{i_{ring\ corrected}}{i_{disk\ corrected}(N_{empirical})} \qquad \textbf{Eq (5.11.10)}$$

To ensure that ring current used above corresponded only to H_2O_2 oxidation, multi-segmented CV sweeps were obtained with 0.5 mM **1**, 1.37 M TFEOH, and 0.5 mM BQ under Ar and O_2 saturation conditions (**Figures S5.11.62 and S5.11.63**). Beginning from the resting potential, the voltage was swept to a switching potential of +1.1 vs Fc^+/Fc, then to a switching potential at –0.87 V vs Fc^+/Fc, followed by final switching potential of +1.05 V vs Fc^+/Fc before completing the sweep at the resting potential. As expected, data taken under Ar (**Figure S5.11.62**, black) display none of the expected oxidation features associated with H_2Q or quinhydrone oxidation (**Figures S5.11.64 and S5.11.65**). When catalytic potentials are swept, the return sweep shows anodic current increases at ~+0.4 V vs Fc^+/Fc, before the expected oxidation response of H_2O_2, suggestive of the re-oxidation of other reaction intermediates. To account for the background current unique to catalytic conditions, two sets of RRDE experiments were conducted with ring potentials of +0.85 V and +0.4 V vs Fc^+/Fc for the systems which exhibited Levich behavior: BQ and TFEOH (**Figures S5.8.35** and **S5.8.38**), 1:1 Mn to BQ with TFEOH (**Figures S5.8.42** and **S5.8.45**), 1:2.5 Mn to BQ with TFEOH (**Figures S5.8.48** and **S5.8.51**), and 1:5 Mn to BQ with TFEOH (**Figures S5.8.54** and **S5.8.57**). The raw disk current responses for both ring potentials were averaged at identical rotation rates to produce the required values for the analysis described in the preceeding paragraph. The difference between the ring currents at these two potentials under catalytic conditions was used for the H_2O_2 efficiency analysis to remove the current response from other reaction intermediates in the determination of $I_{\text{ring corrected}}$. CV traces obtained under co-electrocatalytic conditions using the working electrode of the RRDE electrode confirmed that minimal reversibility was present at a 2.5 mM concentration of BQ (**Figure S5.11.66**) with a larger working electrode. Data were compared at a single rotation rate (400 rpm; **Figure 5.8.4**) from the RRDE experiments with different ratios of **1**:BQ to minimize variability from the multiple equilibria involved in the overall reaction. To obtain an average and standard deviation at a rotation rate of 400 rpm, the current densities at 0.8 V, 0.85 V, and 0.9 V vs Fc^+/Fc were each used to calculate the $\%H_2O_2$.

Under conditions for which non-Levich behaviour was observed, with 0.5 mM **1** and 1.37 M TFEOH (**Figure S5.8.41**), the $\%H_2O_2$ was calculated using the method which has been previously established for similar systems which also display non-Levich behaviour (**Eq (5.11.11)**).[40, 42]

$$\%H_2O_2 = \frac{100\ x\ \frac{2i_{ring}}{N}}{i_{disk} + \frac{2i_{ring}}{N}} \qquad \textbf{Eq (5.11.11)}$$

Both the ring and disk currents used to calculate %H_2O_2 in **Eq (5.11.11)** were the raw O_2 currents determined by averaging the data from all the rotation rates at the catalyst $E_{1/2}$ (–0.63 V vs. Fc^+/Fc).

Disproportionation Mechanism.

As discussed in the main text, at high TFEOH concentrations, a two-electron reduction feature is observed. Since sequential one-electron reduction features are observed under aprotic conditions, this observation requires potential inversion. Under such conditions, it is worth noting that a disproportionation reaction **Eq (5.11.12)** becomes increasingly favorable as **Eq (5.4.4)** shifts increasingly positive of **Eq (5.4.3)**.[53] In this reaction, two equivalents of $[BQ(TFEOH)_m]^-$ disproportionate into one equivalent of $[BQ]^0$ and one equivalent of $[HBQ(TFEOH)_4(TFEO)]^{2-}$, which is structurally equivalent to the product of **Eq (5.4.4)**.[27]

$$2[BQ(TFEOH)_m]^- \overset{E_5^0}{\rightleftharpoons} [BQ]^0 + [HBQ(TFEOH)_4(TFEO)]^{2-} + (2m-4)TFEO^- \qquad \textbf{Eq (5.11.12)}$$

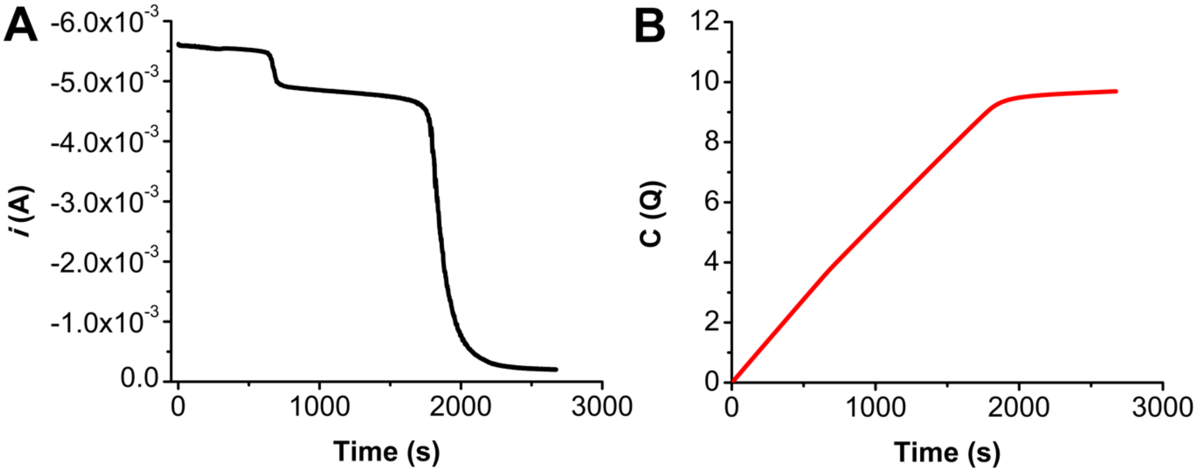

Figure S5.3.1. Coulometry experiment with 2.5 mM BQ in an MeCN solution under N_2 saturation conditions. The analyte solution volume was 25 mL, containing a total of 6.25 x 10^{-5} moles of BQ and passing a total of 9.7 C of charge. Conditions: 0.1 M $TBAPF_6$/MeCN; Carbon cloth (Plain Carbon Cloth 1071 from FuelCellStore) working and counter electrodes; Ag/AgCl pseudoreference electrode. Applied potential of –2.1 V vs. Fc^+/Fc.

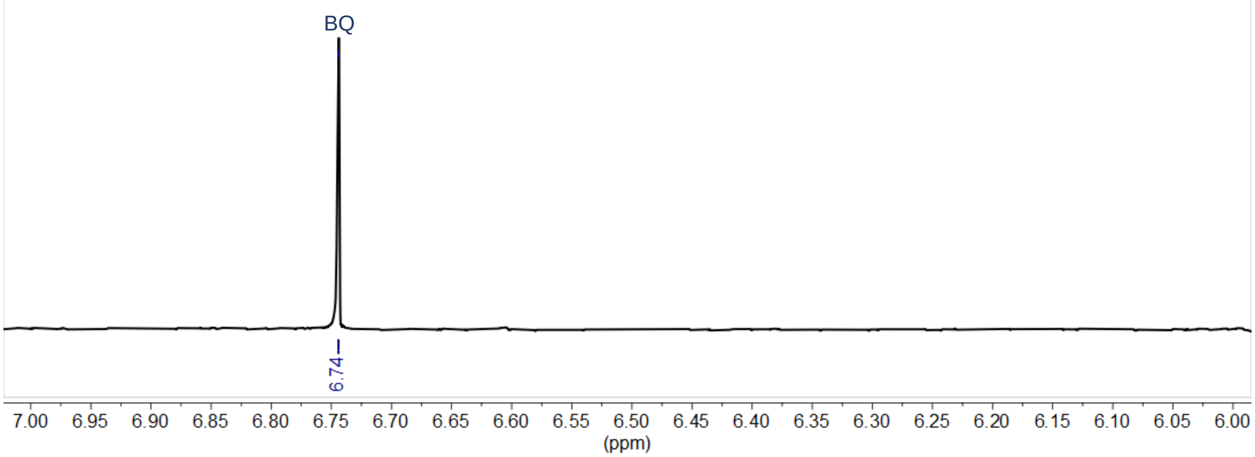

Figure S5.3.2. ^{1}H NMR of an authentic BQ sample taken prior to coulometry experiment in **Figure S5.3.1** under an atmosphere of N_2. The ^{1}H NMR sample was prepared from a 3:1 mixture of coulometry experiment solution and CD_3CN, respectively. The aromatic peak at 6.74 ppm corresponds to BQ under aprotic and inert conditions.

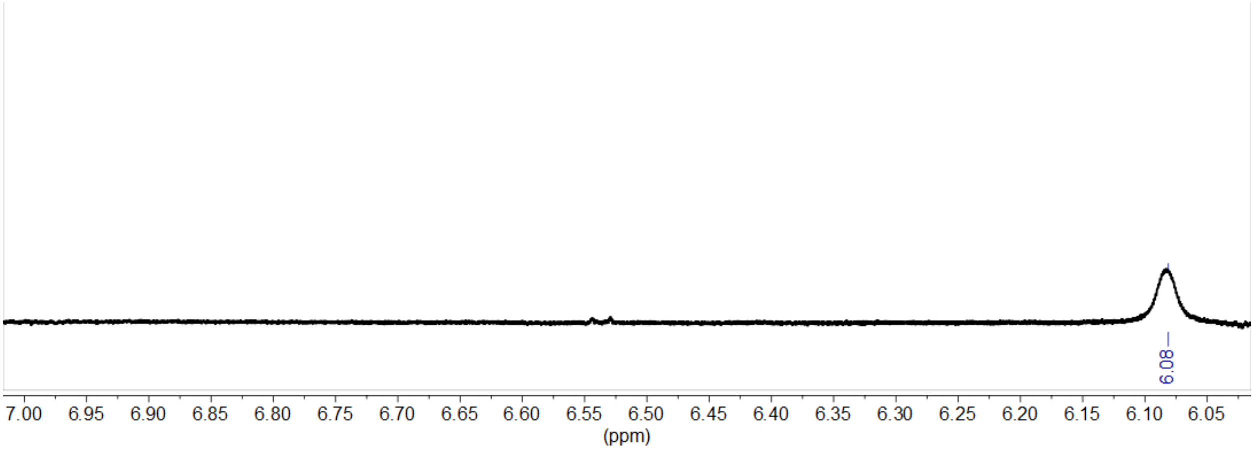

Figure S5.3.3. ^{1}H NMR spectrum of an authentic $[BQ]^{2-}$ sample taken after coulometry experiment in **Figure S5.3.1** under an atmosphere of N_2. ^{1}H NMR solution was prepared from a 3:1 mixture of coulometry experiment solution and CD_3CN, respectively. The peak at 6.08 ppm corresponds to the two-electron reduced product of BQ under aprotic and inert conditions. Additionally, the absence of a peak at 6.74 ppm corresponding to BQ indicates complete substrate consumption from the coulometry experiment in **Figure S5.3.1**.

Table S5.3.1. Data from variable TFEOH concentration CV data with 0.5 mM BQ (**Figure 5.3.2A**).

[TFEOH(M)]	**$E_{1/2}$ (V vs. Fc^+/Fc)**	**ΔE_p (V)**
0.0000	-0.891	0.0736
0.00130	-0.889	0.0728
0.00260	-0.887	0.0738
0.00400	-0.886	0.0756
0.00530	-0.885	0.0718
0.00660	-0.884	0.0738
0.0264	-0.870	0.0776
0.0528	-0.850	0.0838
0.132	-0.801	0.0985
0.198	-0.769	0.117
0.264	-0.742	0.151
1.37	n/a	n/a

*Potential values in table correspond to data for the most positive BQ reduction potential, which has been characterize as a two-electron redox process when TFEOH is present as illustrated in coulometry experiments.

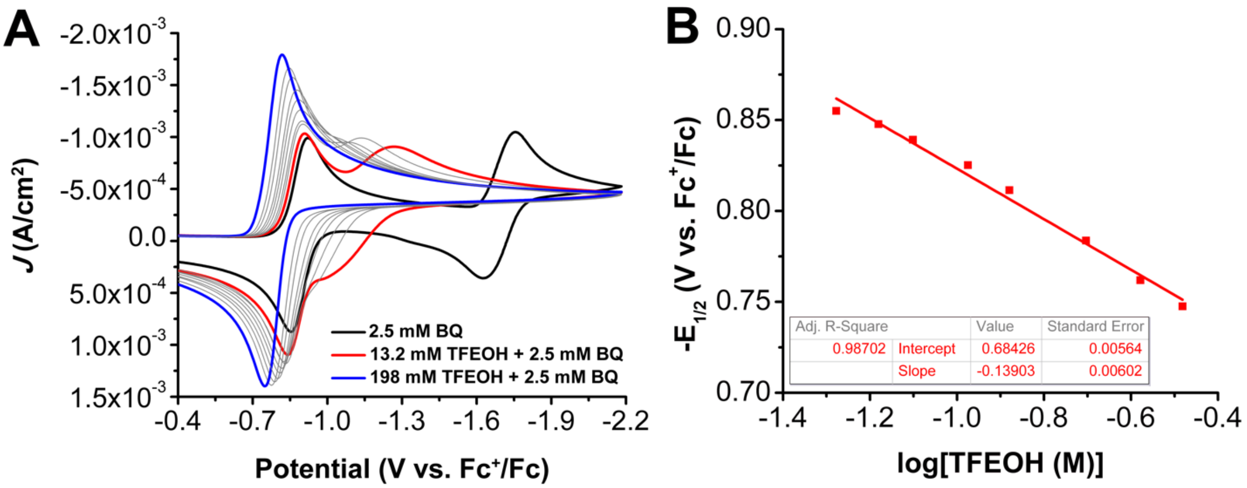

Figure S5.3.4. (**A**) CVs of TFEOH titration with 2.5 mM BQ obtained under Ar saturation conditions. (**B**) Linear fit of -$E_{1/2}$ versus log[TFEOH (M)] for the two-electron BQ reduction feature observed between –0.75 and –0.86 V vs. Fc$^+$/Fc obtained from CV titration data in (**A**). Conditions: 0.1 M $TBAPF_6$/MeCN; glassy carbon working electrode, glassy carbon counter electrode, Ag/AgCl pseudoreference electrode; 100 mV/s scan rate; referenced to internal ferrocene standard.

Table S5.3.2. Data from variable TFEOH concentration CV data with 2.5 mM BQ (**Figure S5.3.2**).

[TFEOH(M)]	$E_{1/2}$ (V vs. Fc$^+$/Fc)	ΔE_p (V)
0.0000	-0.888	0.0675
0.0132	-0.876	0.0675
0.0264	-0.867	0.0714
0.0396	-0.862	0.0725
0.0528	-0.855	0.0755
0.0660	-0.848	0.0756
0.0792	-0.839	0.0777
0.106	-0.825	0.0706
0.132	-0.812	0.0704
0.198	-0.783	0.0694

*Potential values in table correspond to data for the most positive BQ reduction potential, which has been characterize as a two-electron redox process when TFEOH is present as illustrated in coulometry experiments.

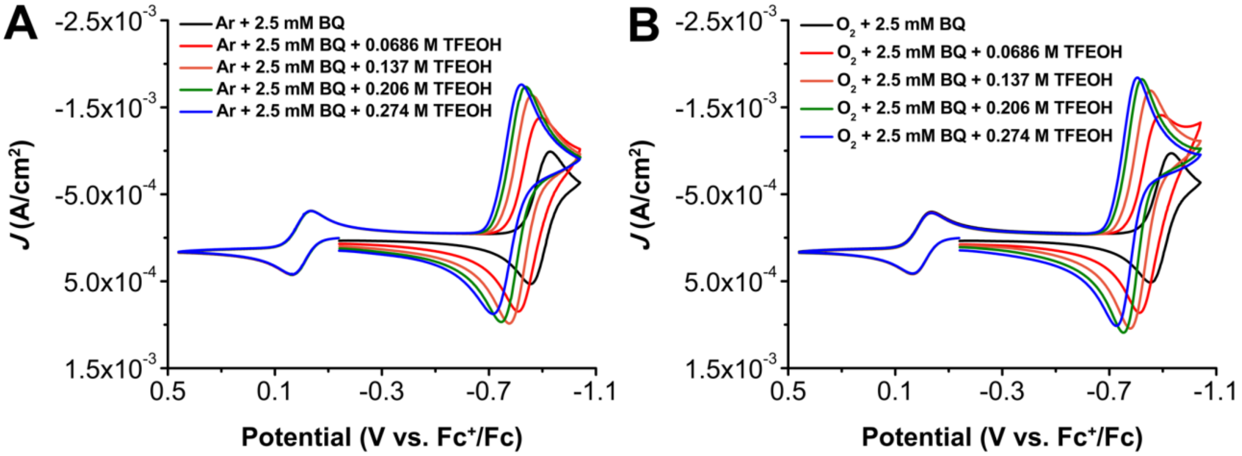

Figure S5.3.5. CVs with 2.5 mM BQ with variable TFEOH concentration under Ar (**A**) and O_2 (**B**) saturation conditions. Conditions: 0.1 M $TBAPF_6$/MeCN; glassy carbon working electrode, glassy carbon counter electrode, Ag/AgCl pseudoreference electrode; 100 mV/s scan rate; referenced to internal ferrocene standard.

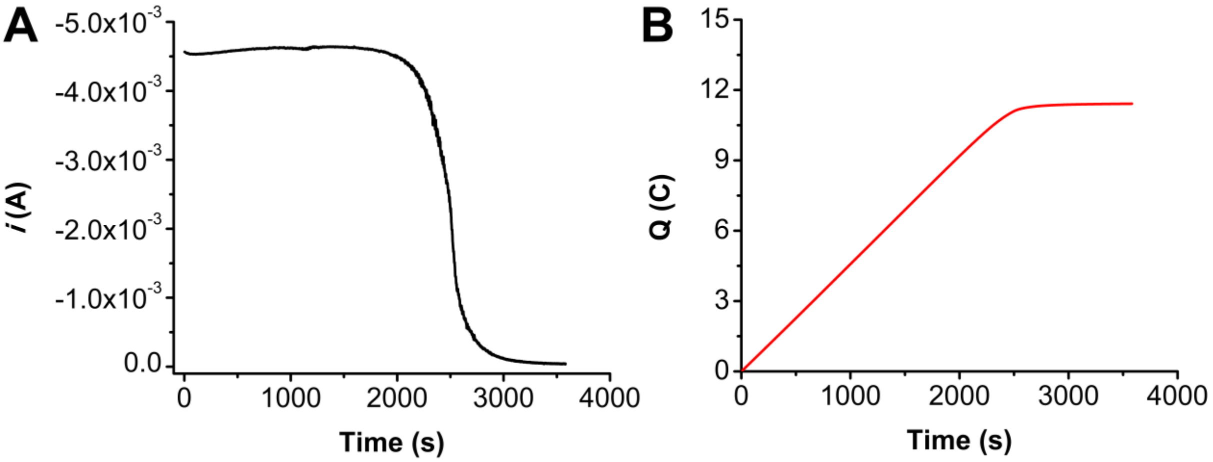

Figure S5.4.6. Coulometry experiment with 2.5 mM BQ and 1.37 M TFEOH in an MeCN solution under N_2 saturation conditions. Conditions: 0.1 M $TBAPF_6$/MeCN; Carbon cloth (Plain Carbon Cloth 1071 from FuelCellStore) working and counter electrodes; Ag/AgCl pseudoreference electrode. Applied potential of –1.1 V vs. Fc^+/Fc. The solution for this experiment contained 6.30×10^{-5} moles of BQ and a total of 11.42 C of charge was passed indicating 1.88 electrons were transferred.

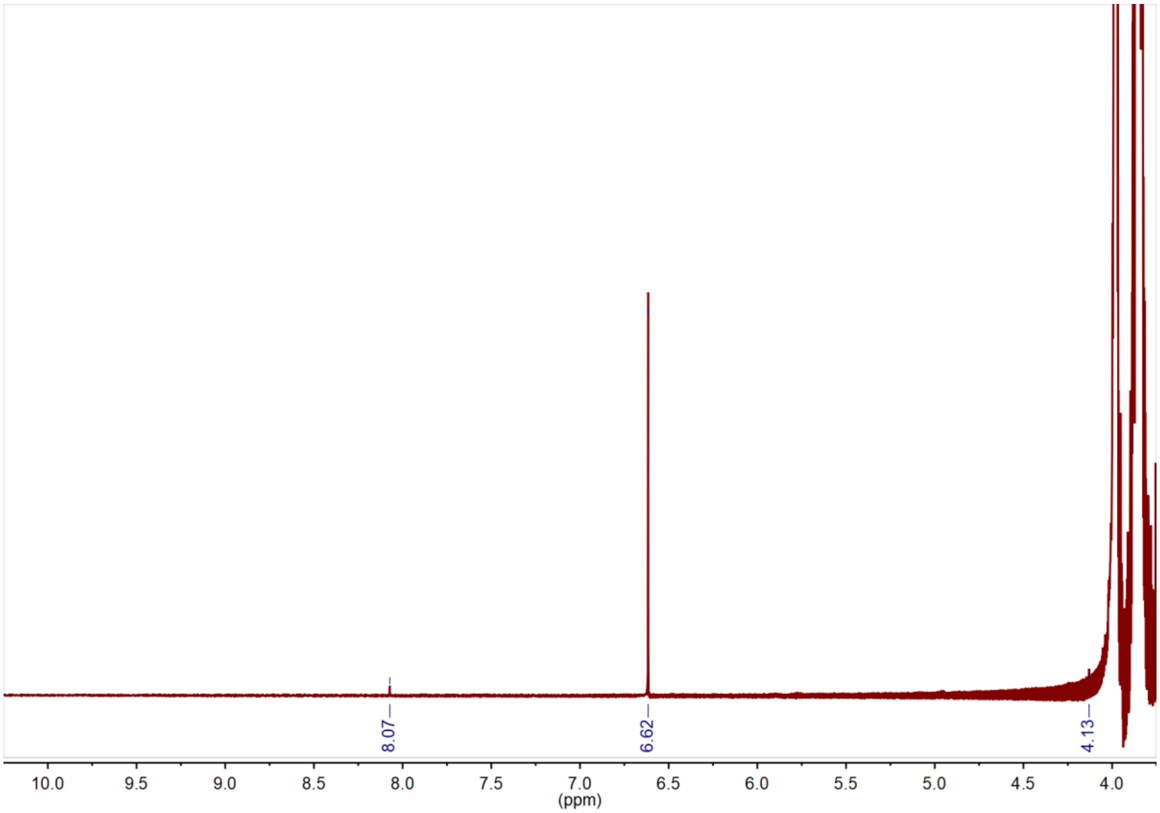

Figure S5.4.7. ^{1}H NMR taken after coulometry experiment with 2.5 mM BQ and 1.37 M TFEOH under an atmosphere of N_2. ^{1}H NMR solution was prepared from a 5:1 mixture of coulometry experiment solution and CD_3CN, respectively.

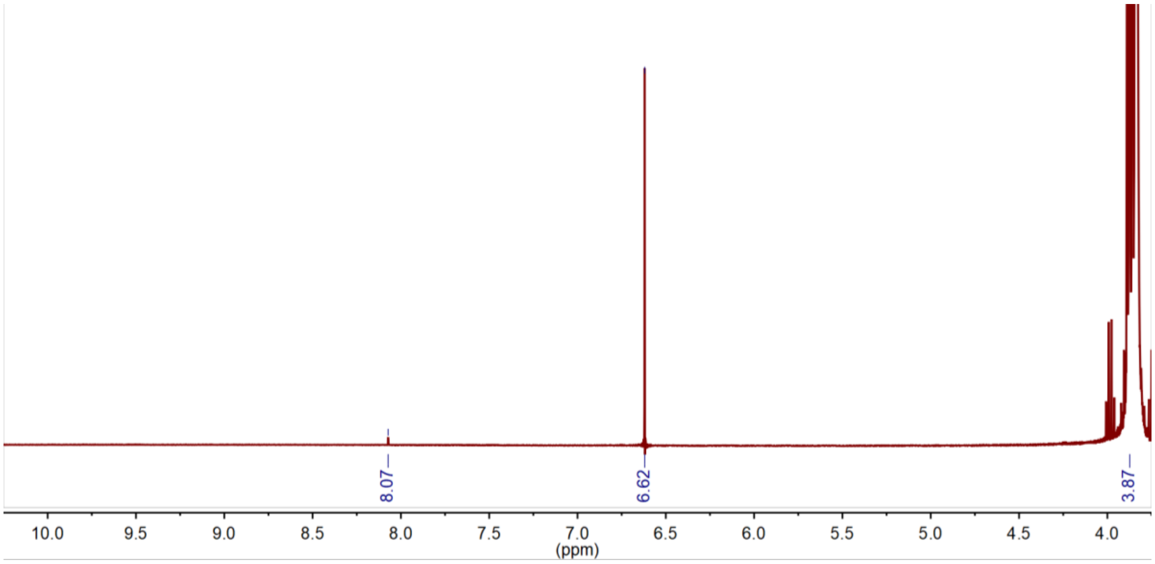

Figure S5.4.8. ^{1}H NMR taken of a solution with 2.5 mM H_2Q and 1.37 M TFEOH under an atmosphere of N_2. ^{1}H NMR solution was prepared from a 5:1 mixture of the MeCN experiment solution and CD_3CN, respectively.

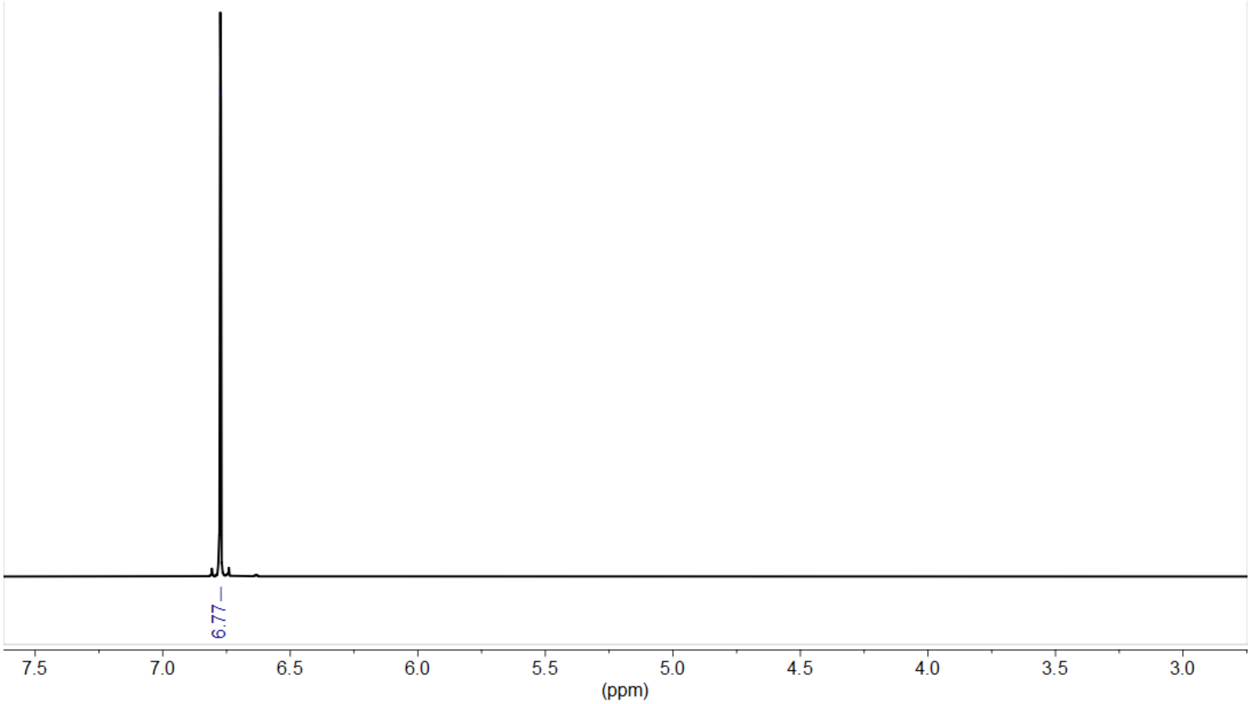

Figure S5.4.9. Control ^{1}H NMR of BQ in CD_3CN under an N_2 atmosphere.

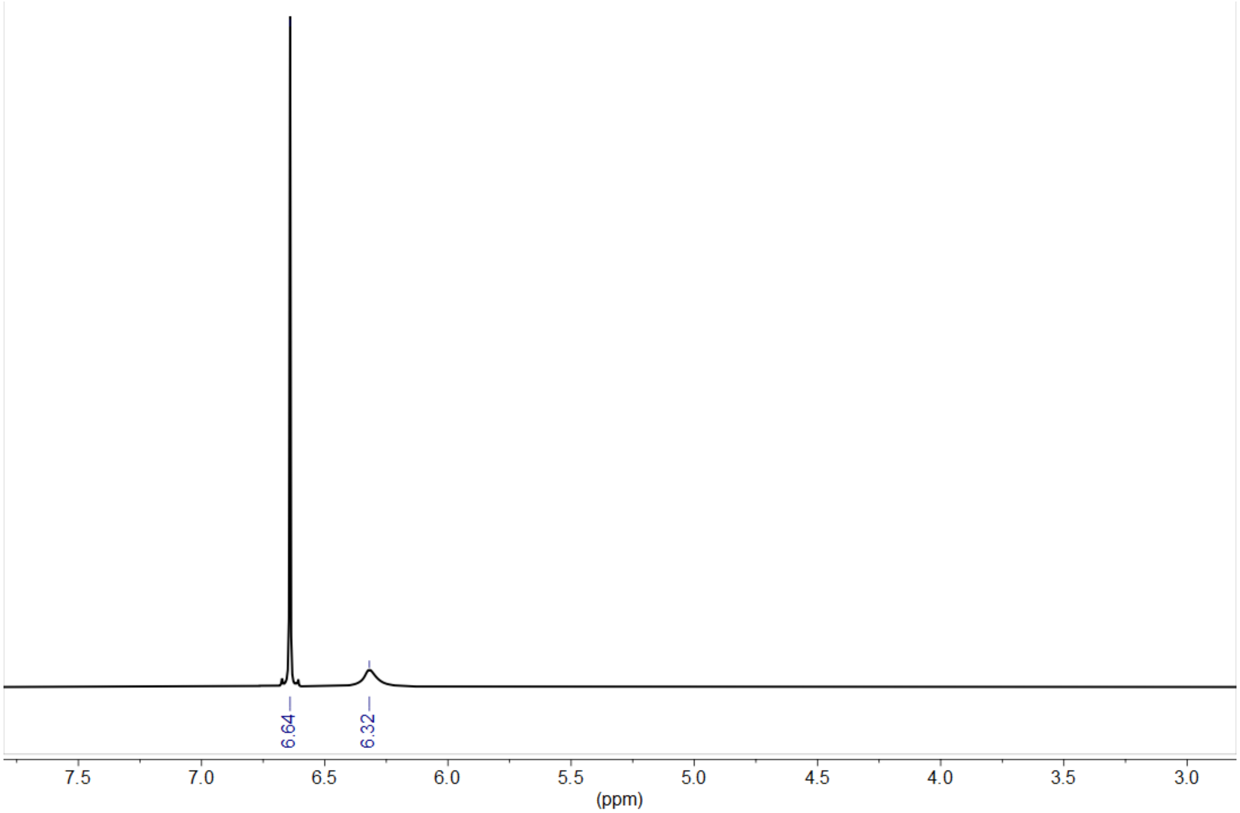

Figure S5.4.10. Control ^{1}H NMR of H_2Q in CD_3CN under an N_2 atmosphere.

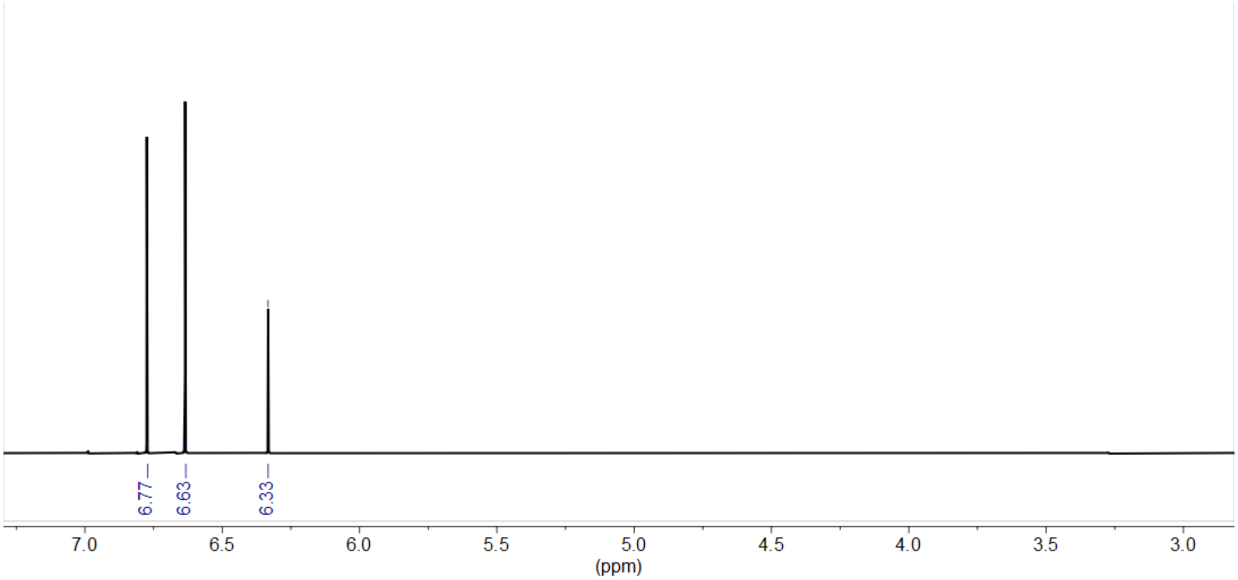

Figure S5.4.11. Control ^{1}H NMR of quinhydrone in CD_3CN under an N_2 atmosphere.

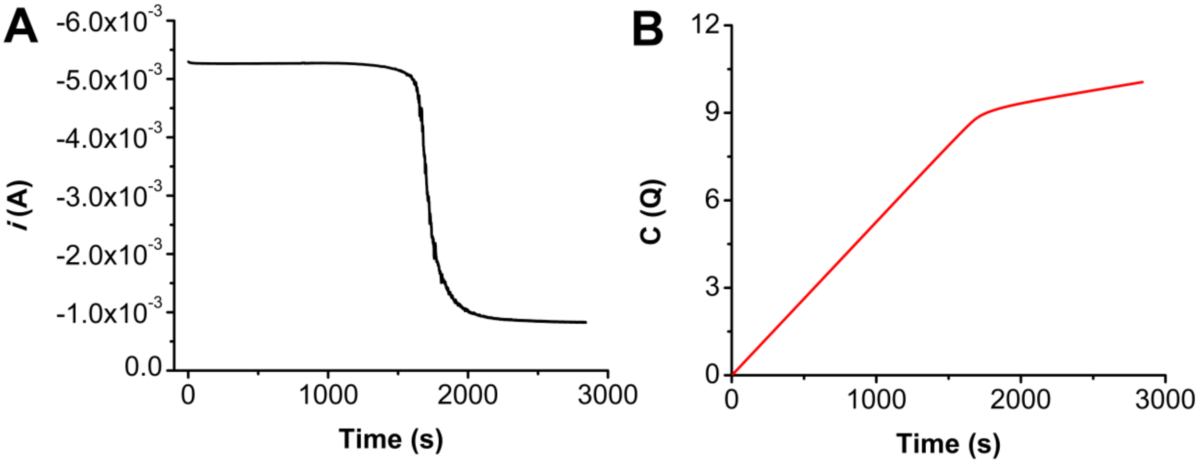

Figure S5.4.12. Coulometry experiment with 2.6 mM BQ and 1.37 M acetic acid in an MeCN solution under N_2 saturation conditions. Conditions: 0.1 M $TBAPF_6$/MeCN; Carbon cloth (Plain Carbon Cloth 1071 from FuelCellStore) working and counter electrodes; Ag/AgCl pseudoreference electrode. Applied potential of –1.1 V vs. Fc^+/Fc. The solution for this experiment contained 6.57 x 10^{-5} moles of BQ and a total of 10.06 C of charge was passed indicating 1.59 electronswere transferred.

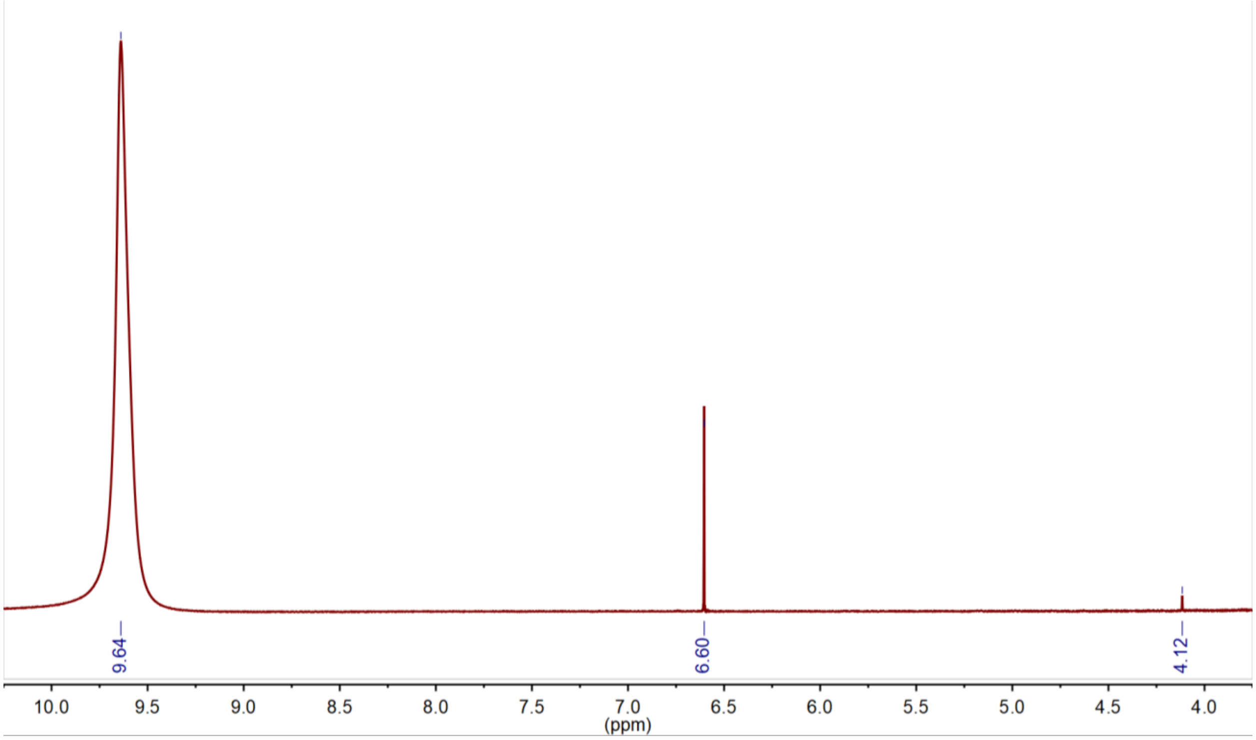

Figure S5.4.13. ^{1}H NMR taken after coulometry experiment with 2.6 mM BQ and 1.37 M acetic acid under an atmosphere of N_2. ^{1}H NMR solution was prepared from a 5:1 mixture of coulometry experiment solution and CD_3CN, respectively. The peak at 9.64 corresponds to acetic acid.

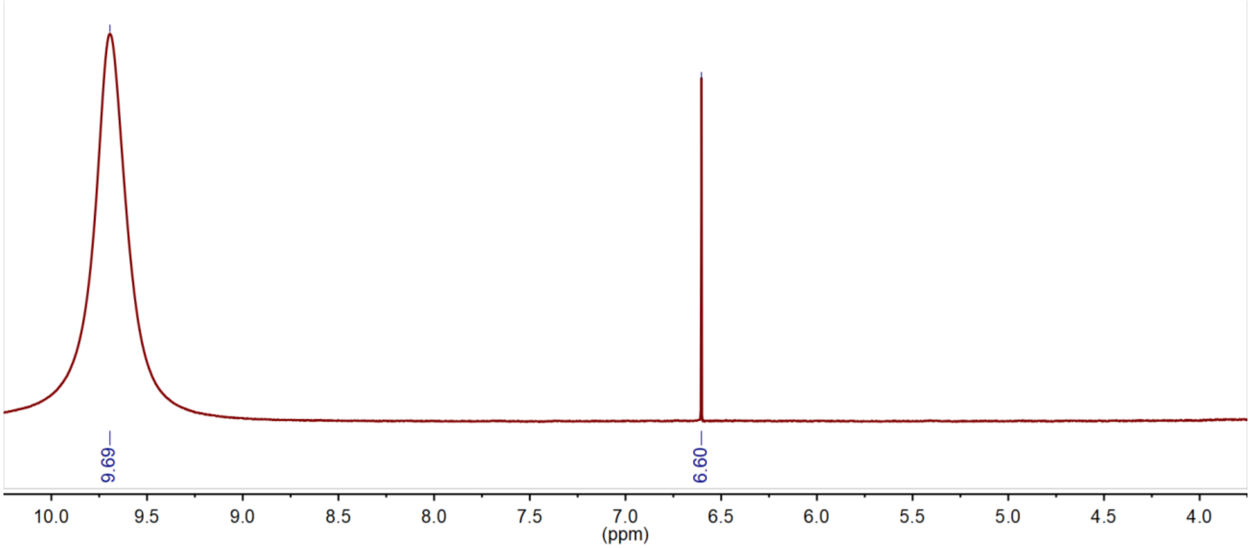

Figure S5.4.14. ^{1}H NMR taken of a solution with 2.5 mM H_2Q and 1.37 M acetic acid under an atmosphere of N_2. ^{1}H NMR solution was prepared from a 5:1 mixture of the MeCN experiment solution and CD_3CN, respectively. The peak at 9.69 is assigned to acetic acid.

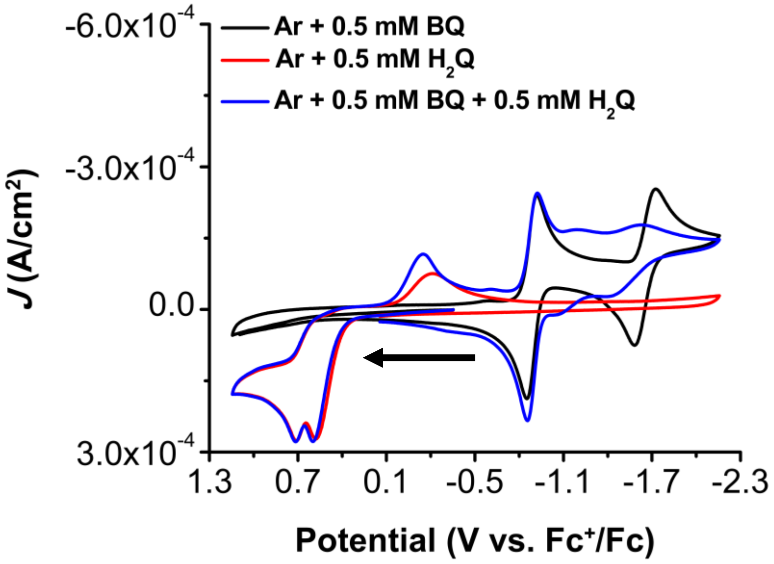

Figure S5.4.15. CV data comparing the individual responses of 0.5 mM H_2Q (red) and 0.5 mM BQ (black) relative to when they are both present in situ (blue). Conditions: 0.1 M $TBAPF_6$/MeCN; glassy carbon working electrode, glassy carbon counter electrode, Ag/AgCl pseudoreference electrode; 100 mV/s scan rate; referenced to internal ferrocene standard. Arrow designates the direction of the CV trace.

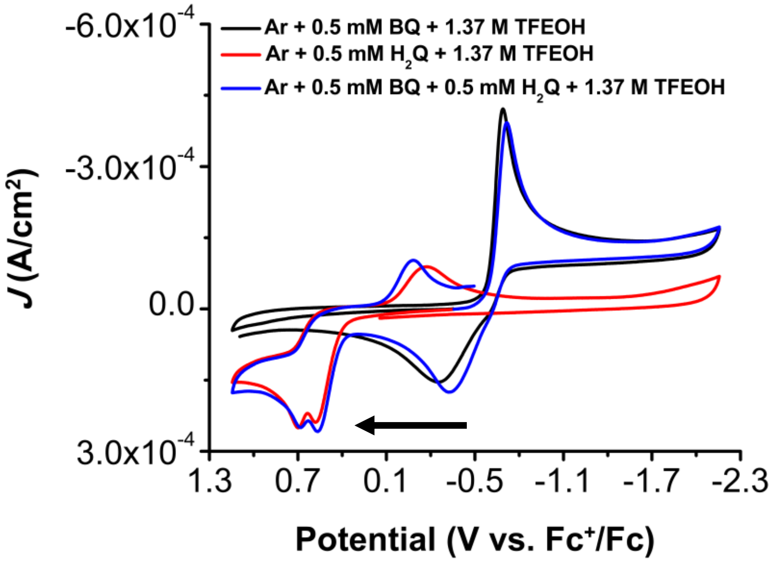

Figure S5.4.16. CV data with 1.37 M TFEOH comparing the individual responses of 0.5 mM H_2Q (red) and 0.5 mM BQ (black) relative to when they are both present in situ (blue). Conditions: 0.1 M $TBAPF_6$/MeCN; glassy carbon working electrode, glassy carbon counter electrode, Ag/AgCl pseudoreference electrode; 100 mV/s scan rate; referenced to internal ferrocene standard. Arrow designates the direction of the CV trace.

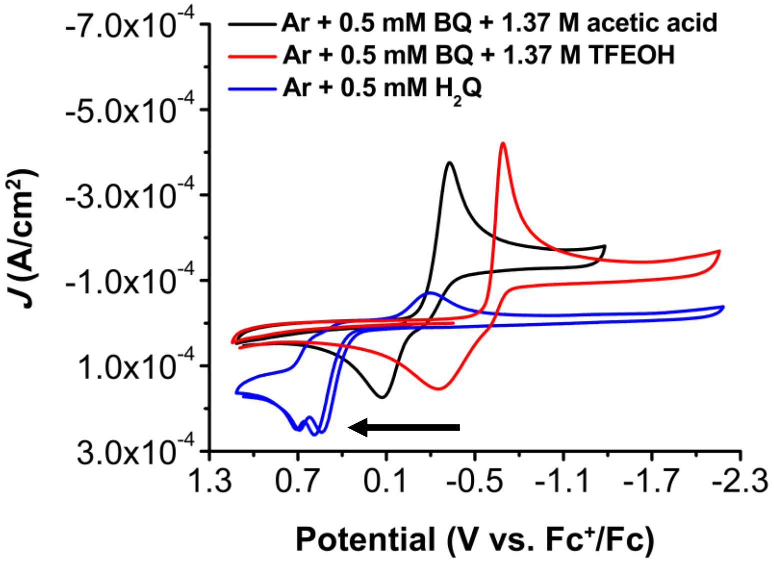

Figure S5.4.17. CV data under argon saturation conditions comparing 0.5 mM BQ with 1.37 M TFEOH (red) and 1.37 M acetic acid (black) with the redox response of 0.5 mM H_2Q under aprotic conditions (blue). Conditions: 0.1 M $TBAPF_6$/MeCN; glassy carbon working electrode, glassy carbon counter electrode, Ag/AgCl pseudoreference electrode; 100 mV/s scan rate; referenced to internal ferrocene standard. Arrow designates the direction of the CV trace. We note that the observed BQ reduction features do not align with H_2Q oxidation, with or without either TFEOH or acetic acid present. For acetic acid specifically, this has previously been attributed to non-covalent interactions between H_2Q generated in situ and the associated acetate ions.[54-55]

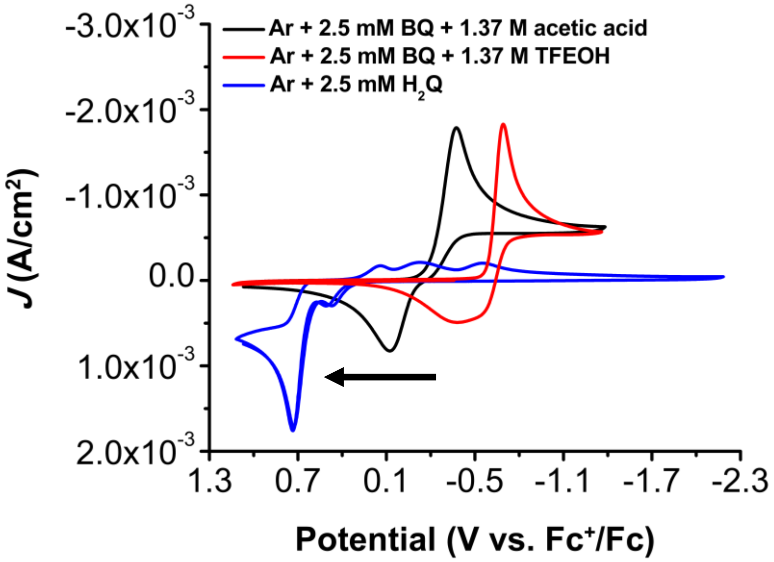

Figure S5.4.18. CV data under argon saturation conditions comparing 2.5 mM BQ with 1.37 M TFEOH (red) and 1.37 M acetic acid (black) with the redox response of 2.5 mM H_2Q under aprotic conditions (blue). Conditions: 0.1 M $TBAPF_6$/MeCN; glassy carbon working electrode, glassy carbon counter electrode, Ag/AgCl pseudoreference electrode; 100 mV/s scan rate; referenced to internal ferrocene standard. Arrow designates the direction of the CV trace. We note that the observed BQ reduction features do not align with H_2Q oxidation, with or without either TFEOH or acetic acid present. For acetic acid specifically, this has previously been attributed to non-covalent interactions between H_2Q generated in situ and the associated acetate ions.[54-55]

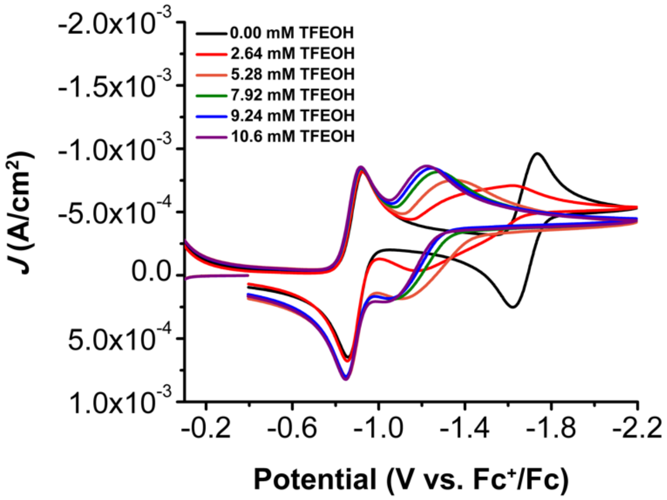

Figure S5.5.19. (**A**) CVs of TFEOH titration with 2.5 mM BQ obtained under Ar saturation conditions focusing on the one-electron BQ reduction feature at –1.69 V vs. Fc^+/Fc obtained from CV titration data in (**A**). Conditions: 0.1 M $TBAPF_6$/MeCN; glassy carbon working electrode, glassy carbon counter electrode, Ag/AgCl pseudoreference electrode; 100 mV/s scan rate; referenced to internal ferrocene standard.

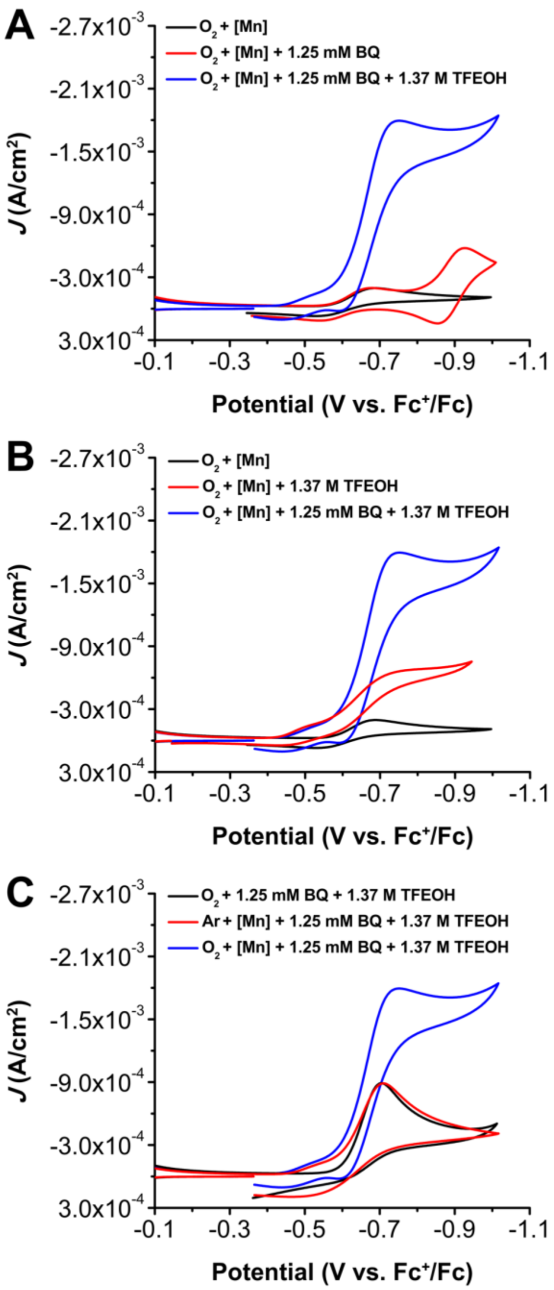

Figure S5.6.20. (**A**) CVs comparing 0.5 mM of Mn(^{tbu}dhbpy)Cl **1**, with 1.25 mM BQ both with (blue) and without (red) 1.37 M TFEOH under O_2 saturation conditions. (**B**) CVs comparing 0.5 mM of Mn(^{tbu}dhbpy)Cl **1**, with 1.37 M TFEOH both with (blue) and without (red) 1.25 mM BQ. (**C**) CVs comparing 0.5 mM Mn(^{tbu}dhbpy)Cl **1**, with 1.37 M TFEOH and 0.125 mM BQ under Ar (red) and O_2 (blue) saturation conditions compared to a control CV in the absence of Mn(^{tbu}dhbpy)Cl **1** (black). Conditions: 0.1 M $TBAPF_6$/MeCN; glassy carbon working electrode, glassy carbon counter electrode, Ag/AgCl pseudoreference electrode; 100 mV/s scan rate; referenced to internal ferrocene standard.

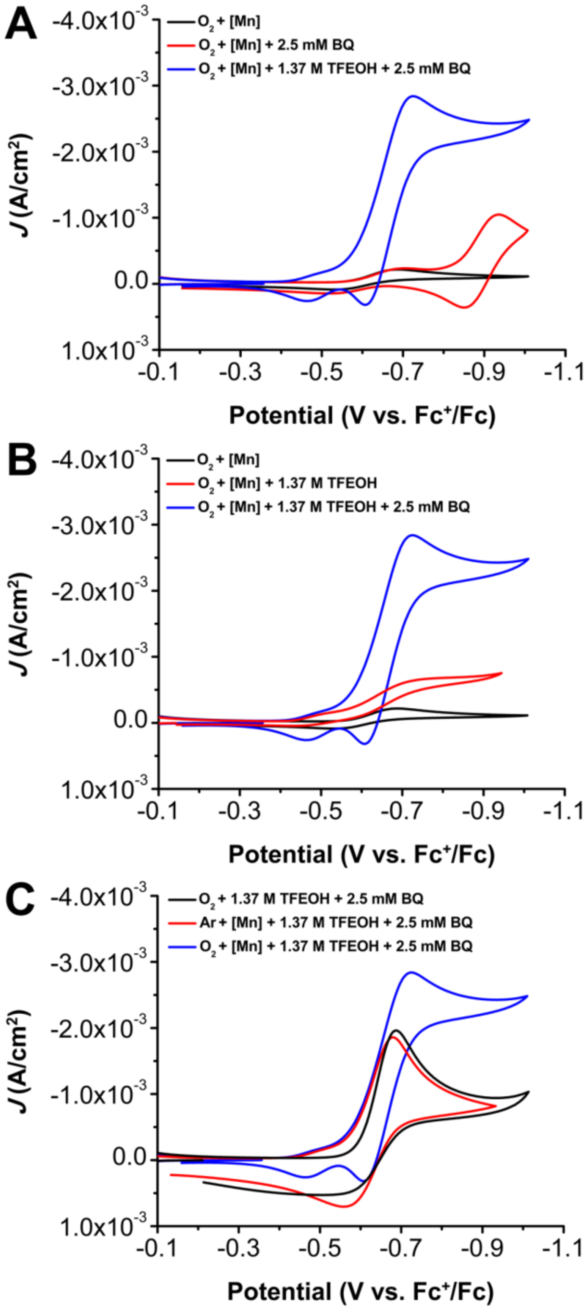

Figure S5.6.21. (**A**) CVs comparing 0.5 mM of Mn(^{tbu}dhbpy)Cl **1**, with 2.5 mM BQ both with (blue) and without (red) 1.37 M TFEOH under O$_2$ saturation conditions. (**B**) CVs comparing 0.5 mM of Mn(^{tbu}dhbpy)Cl **1**, with 1.37 M TFEOH both with (blue) and without (red) 2.5 mM BQ. (**C**) CVs comparing 0.5 mM Mn(^{tbu}dhbpy)Cl **1**, with 1.37 M TFEOH and 2.5 mM BQ under Ar (red) and O$_2$ (blue) saturation conditions compared to a control CV in the absence of Mn(^{tbu}dhbpy)Cl **1** (black). Conditions: 0.1 M TBAPF$_6$/MeCN; glassy carbon working electrode, glassy carbon counter electrode, Ag/AgCl pseudoreference electrode; 100 mV/s scan rate; referenced to internal ferrocene standard.

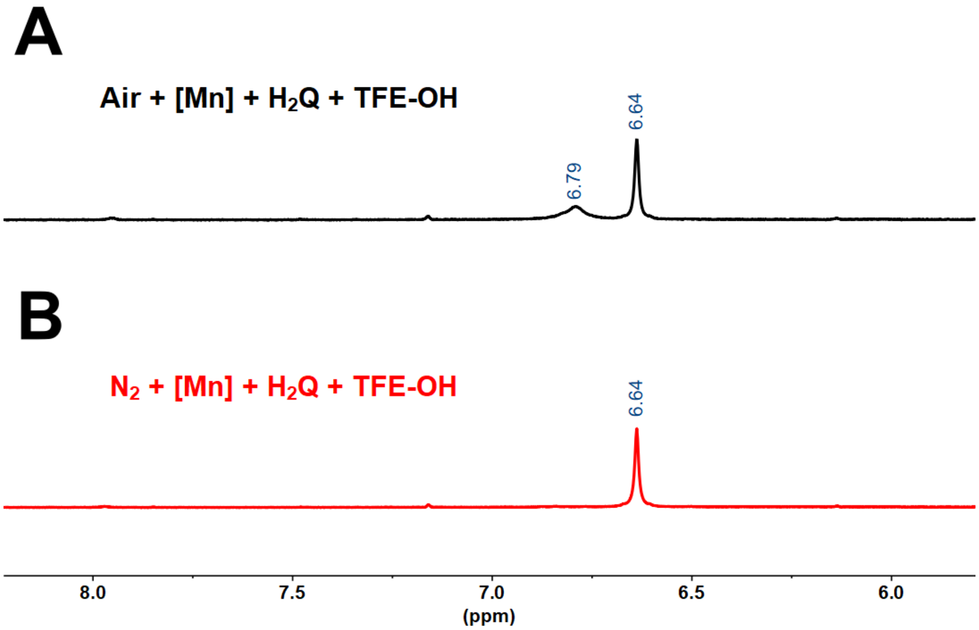

Figure S5.6.22. Overlay of ^{1}H NMR aromatic region from experiment with 2.5 mM H_2Q, 0.274 M TFEOH, and 0.5 mM Mn(^{tbu}dhbpy)Cl **1** in CD_3CN under an atmosphere of N_2 (B, red) versus an atmosphere of air (A, black). [Mn] = Mn(^{tbu}dhbpy)Cl **1**.

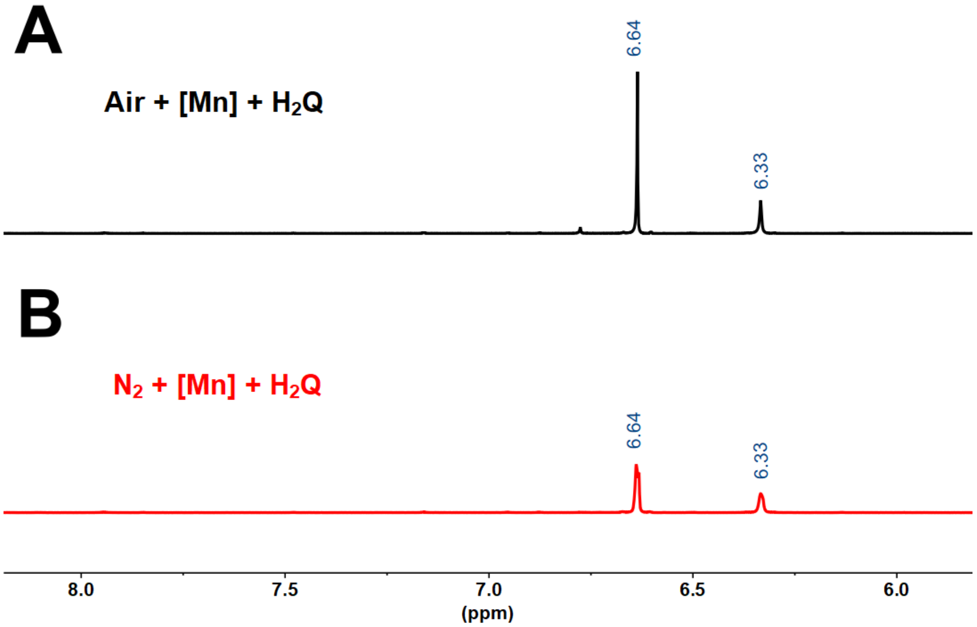

Figure S5.6.23. Overlay of ^{1}H NMR aromatic region from experiment with 2.5 mM H_2Q and 0.5 mM Mn(^{tbu}dhbpy)Cl **1** in CD_3CN under an atmosphere of N_2 (B, red) versus an atmosphere of air (A, black). [Mn] = Mn(^{tbu}dhbpy)Cl **1**.

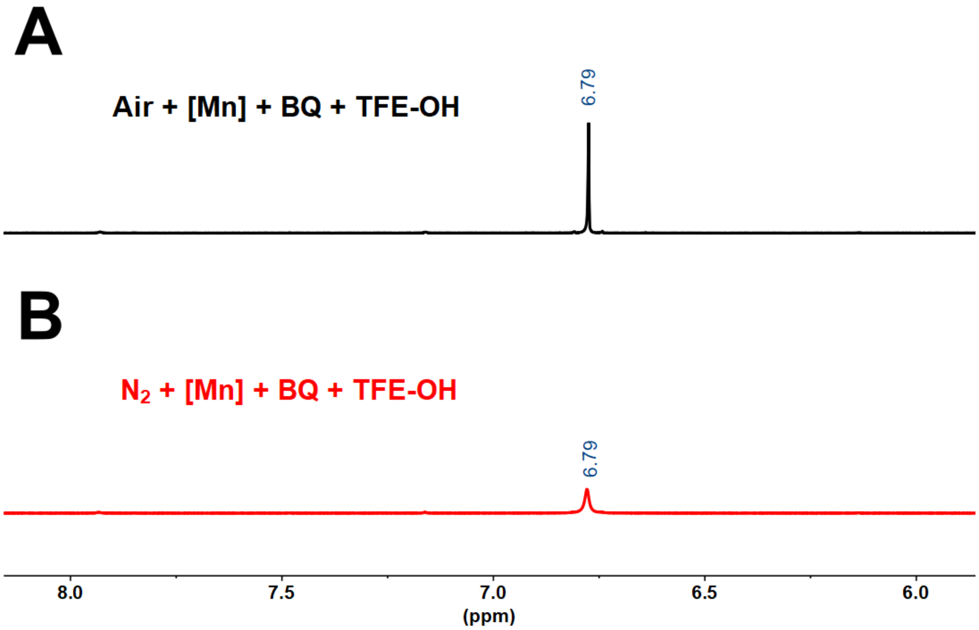

Figure S5.6.24. Overlay of ^{1}H NMR aromatic region from experiment with 2.5 mM BQ, 0.274 M TFEOH, and 0.5 mM Mn(^{tbu}dhbpy)Cl **1** in CD_3CN under an atmosphere of N_2 (B, red) versus an atmosphere of air (A, black). [Mn] = Mn(^{tbu}dhbpy)Cl **1**.

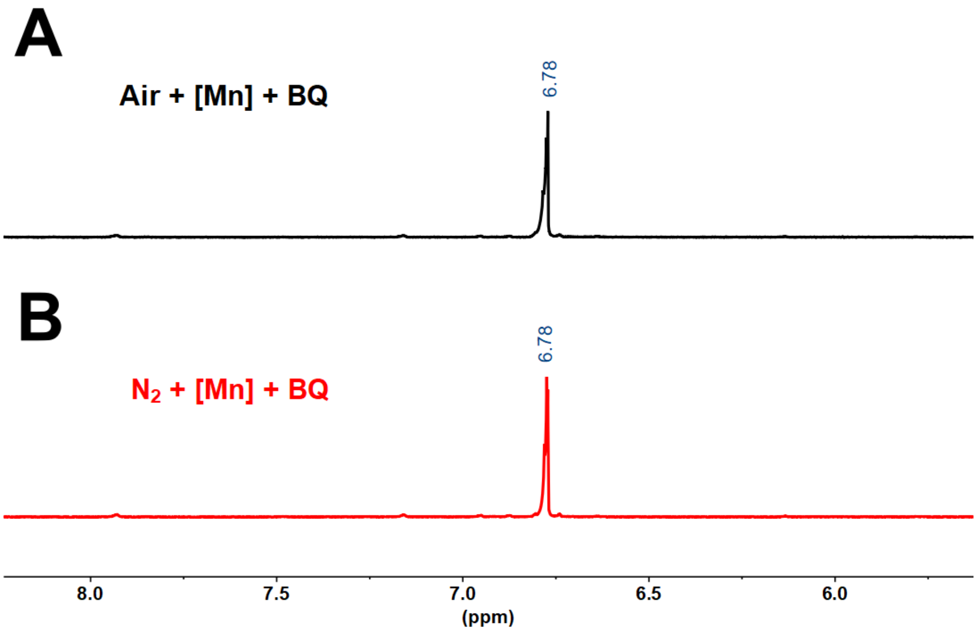

Figure S5.6.25. Overlay of ^{1}H NMR aromatic region from experiment with 2.5 mM BQ and 0.5 mM Mn(^{tbu}dhbpy)Cl **1** in CD_3CN under an atmosphere of N_2 (B, red) versus an atmosphere of air (A, black). [Mn] = Mn(^{tbu}dhbpy)Cl **1**.

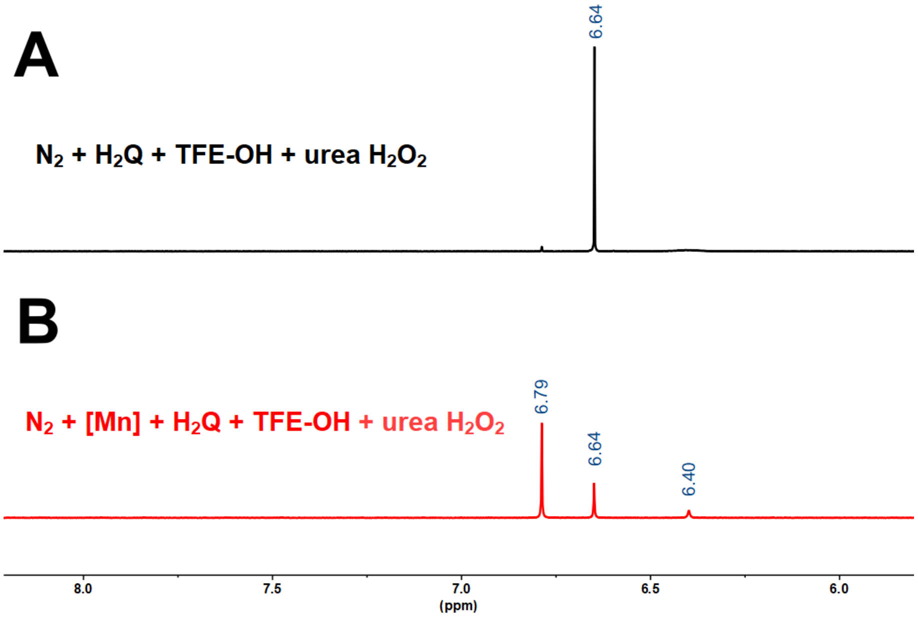

Figure S5.6.26. Overlay of ^{1}H NMR aromatic region from experiment with 0.5 mM H_2Q, 0.5 mM urea•H_2O_2, 0.274 M TFEOH in CD_3CN under an N_2 atmosphere with 0.5 mM Mn(^{tbu}dhbpy)Cl **1** present (B, red) and in the absence of Mn(^{tbu}dhbpy)Cl **1** (A, black). [Mn] = Mn(^{tbu}dhbpy)Cl **1**.

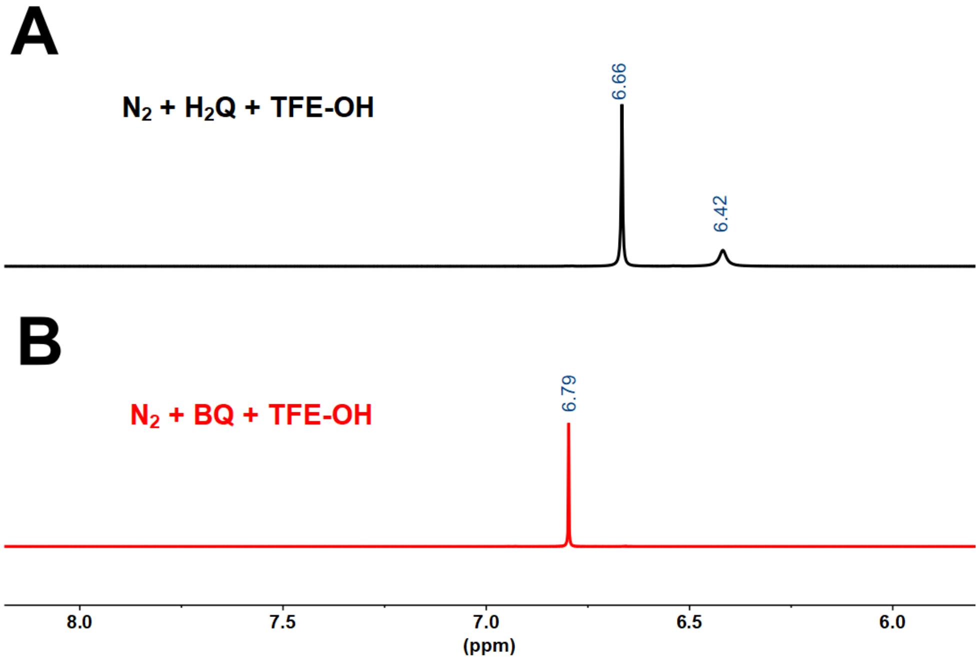

Figure S5.6.27. Aromatic region of control ^{1}H NMRs of 0.274 M TFEOH with 2.5 mM BQ (A, black) versus 2.5 mM H_2Q (B, red) in CD_3CN under an N_2 atmosphere.

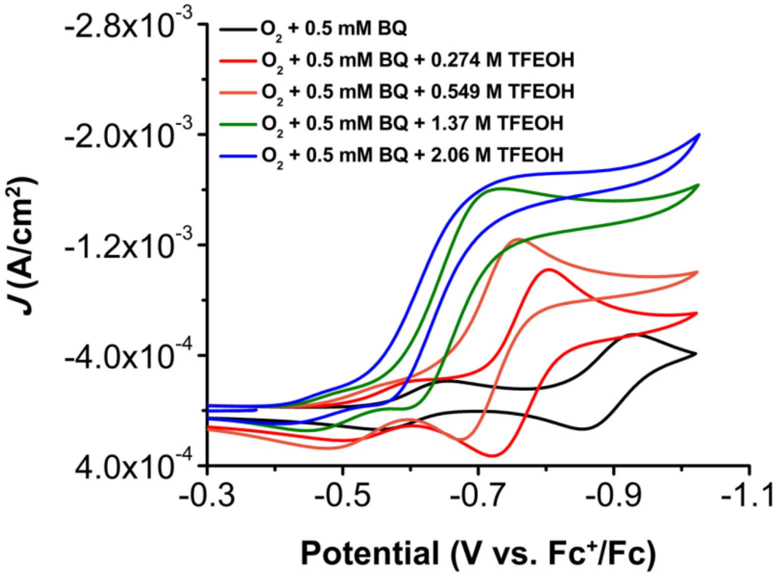

Figure S5.7.28. CVs of 0.5 mM Mn(^{tbu}dhbpy)Cl **1**, and 0.5 mM BQ obtained under O_2 saturation conditions with variable TFEOH concentration. Conditions: 0.1 M $TBAPF_6$/MeCN; glassy carbon working electrode, glassy carbon counter electrode, Ag/AgCl pseudoreference electrode; 100 mV/s scan rate; referenced to internal ferrocene standard.

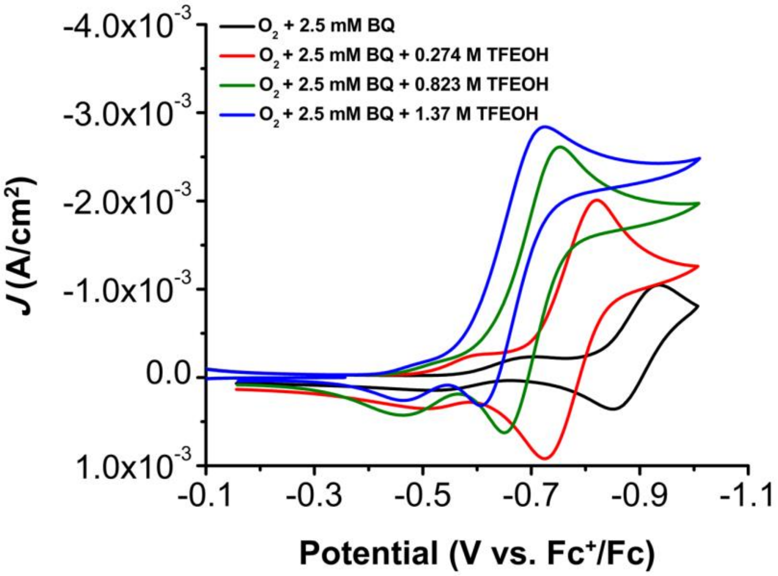

Figure S5.7.29. CVs of 0.5 mM Mn(^{tbu}dhbpy)Cl **1**, and 2.5 mM BQ obtained under O_2 saturation conditions with variable TFEOH concentration. Conditions: 0.1 M $TBAPF_6$/MeCN; glassy carbon working electrode, glassy carbon counter electrode, Ag/AgCl pseudoreference electrode; 100 mV/s scan rate; referenced to internal ferrocene standard.

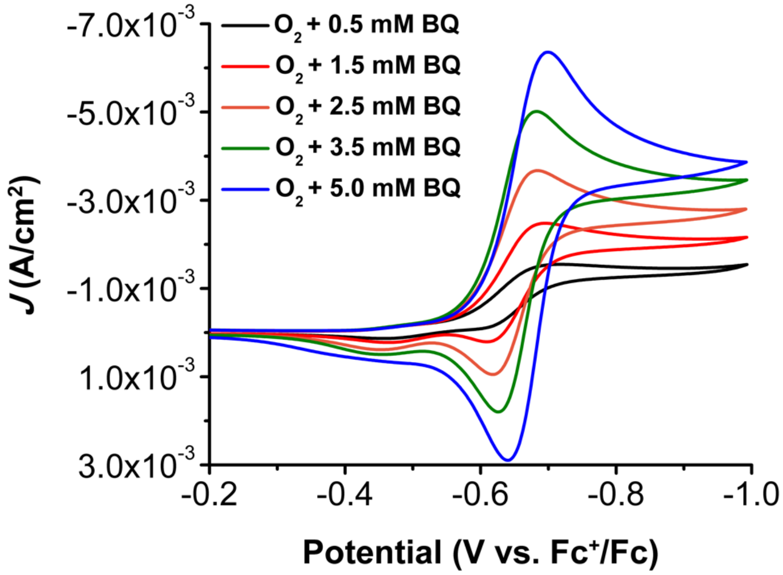

Figure S5.7.30. CVs of 0.5 mM Mn($^{\text{tbu}}$dhbpy)Cl **1**, and 1.37 M TFEOH obtained under O_2 saturation conditions with variable BQ concentration. Conditions: 0.1 M $TBAPF_6$/MeCN; glassy carbon working electrode, glassy carbon counter electrode, Ag/AgCl pseudoreference electrode; 100 mV/s scan rate; referenced to internal ferrocene standard.

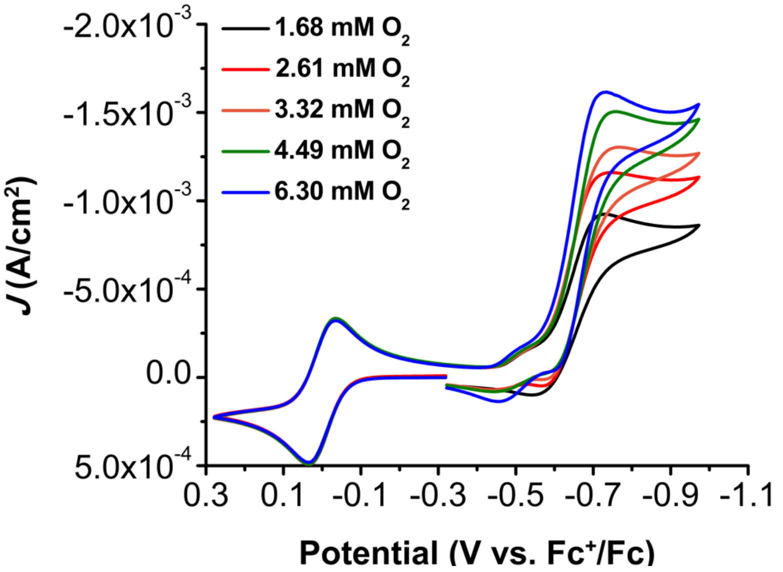

Figure S5.7.31. CVs of 0.5 mM Mn($^{\text{tbu}}$dhbpy)Cl **1**, 0.5 mM BQ, and 1.37 M TFEOH with variable O_2 concentration. Conditions: 0.1 M $TBAPF_6$/MeCN; glassy carbon working electrode, glassy carbon counter electrode, Ag/AgCl pseudoreference electrode; 100 mV/s scan rate; referenced to internal ferrocene standard.

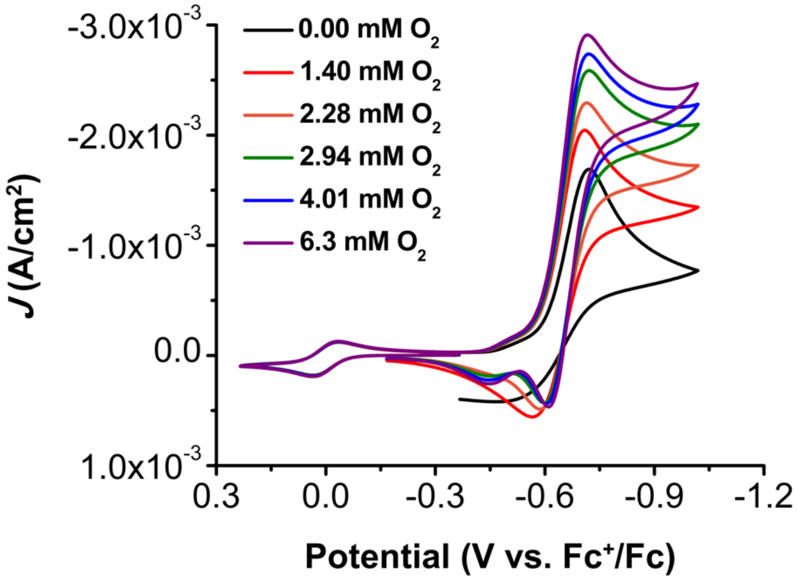

Figure S5.7.32. CVs of 0.5 mM Mn(^{tbu}dhbpy)Cl **1**, 2.5 mM BQ, and 1.37 M TFEOH with variable O_2 concentration. Conditions: 0.1 M $TBAPF_6$/MeCN; glassy carbon working electrode, glassy carbon counter electrode, Ag/AgCl pseudoreference electrode; 100 mV/s scan rate; referenced to internal ferrocene standard.

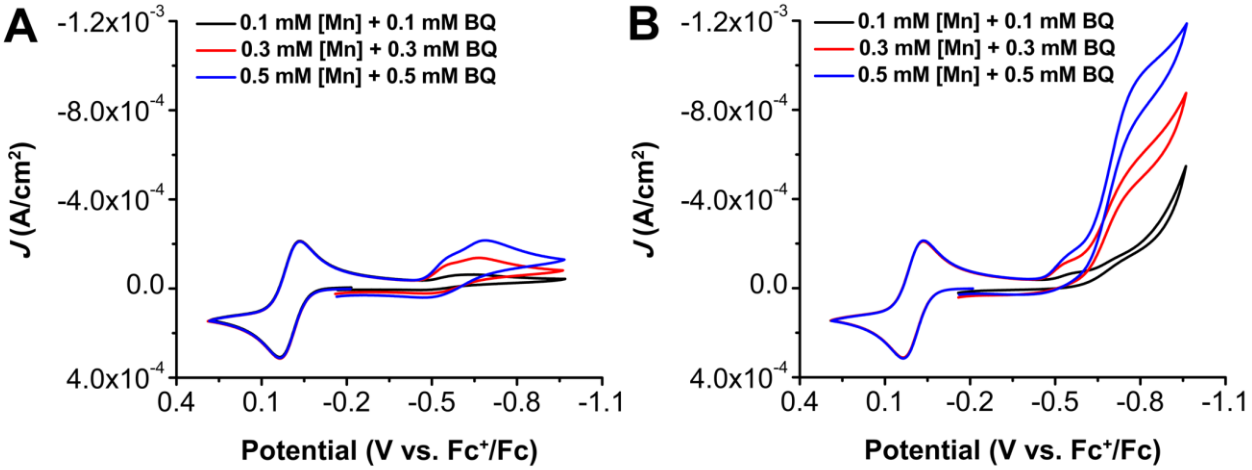

Figure S5.7.33. CVs with 1.37 M TFEOH under Ar (**A**) and O_2 (**B**) saturation conditions with variable Mn(^{tbu}dhbpy)Cl **1** and BQ concentration. Conditions: 0.1 M $TBAPF_6$/MeCN; glassy carbon working electrode, glassy carbon counter electrode, Ag/AgCl pseudoreference electrode; 100 mV/s scan rate; referenced to internal ferrocene standard.

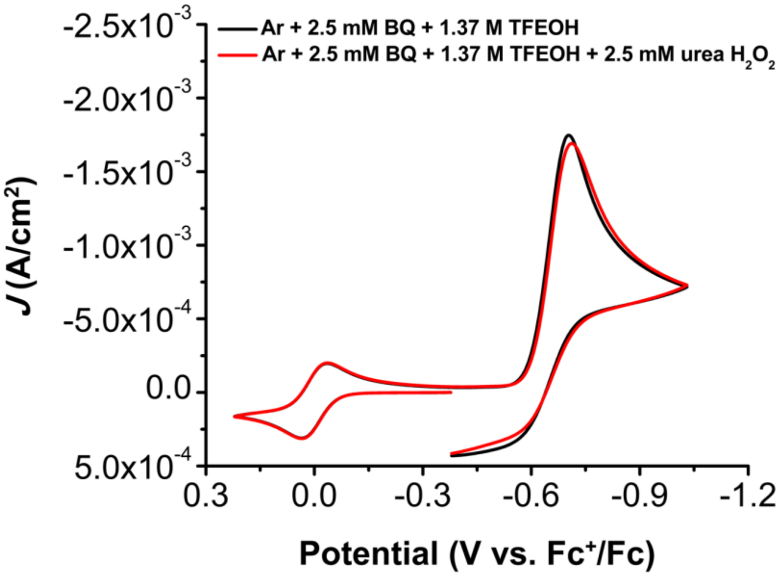

Figure S5.7.34. Control CVs of 2.5 mM BQ with 1.37 M TFEOH and 2.5 mM urea H_2O_2 under Ar saturation conditions to illustrate that no significant reactivity occurs between BQ and free H_2O_2 in the presence of a proton source. Conditions: 0.1 M $TBAPF_6$/MeCN; glassy carbon working electrode, glassy carbon counter electrode, Ag/AgCl pseudoreference electrode; 100 mV/s scan rate; referenced to internal ferrocene standard.

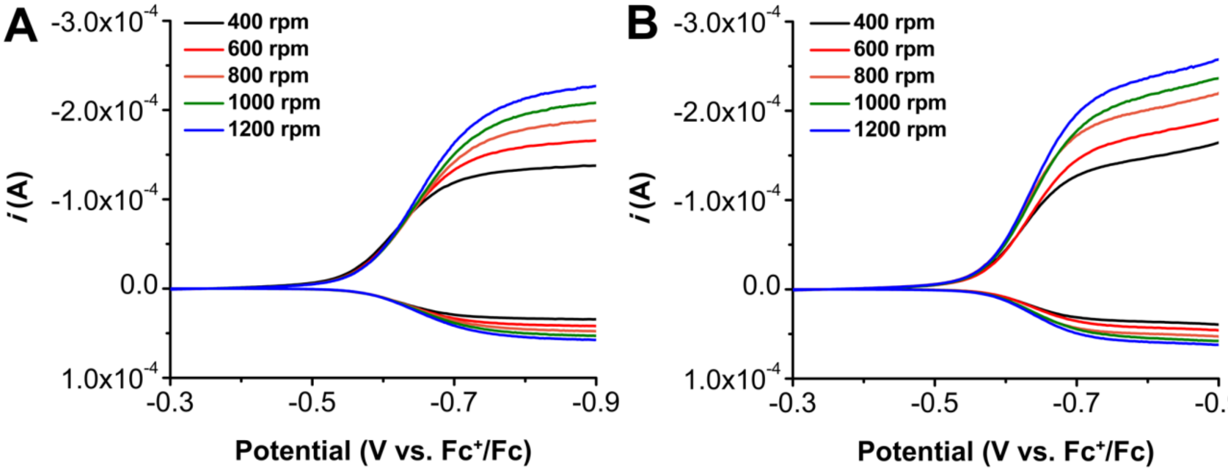

Figure S5.8.35. Linear Sweep Voltammograms of RRDE experiment with 0.5 mM BQ and 1.37 M TFEOH at various rotation rates under Ar (**A**) and O_2 (**B**) saturation conditions; ring potential = 0.85 V vs Fc^+/Fc. Conditions: glassy carbon working electrode/Pt ring working electrode, glassy carbon rod counter electrode, Ag/AgCl pseudoreference electrode; scan rate 0.02 V/s.

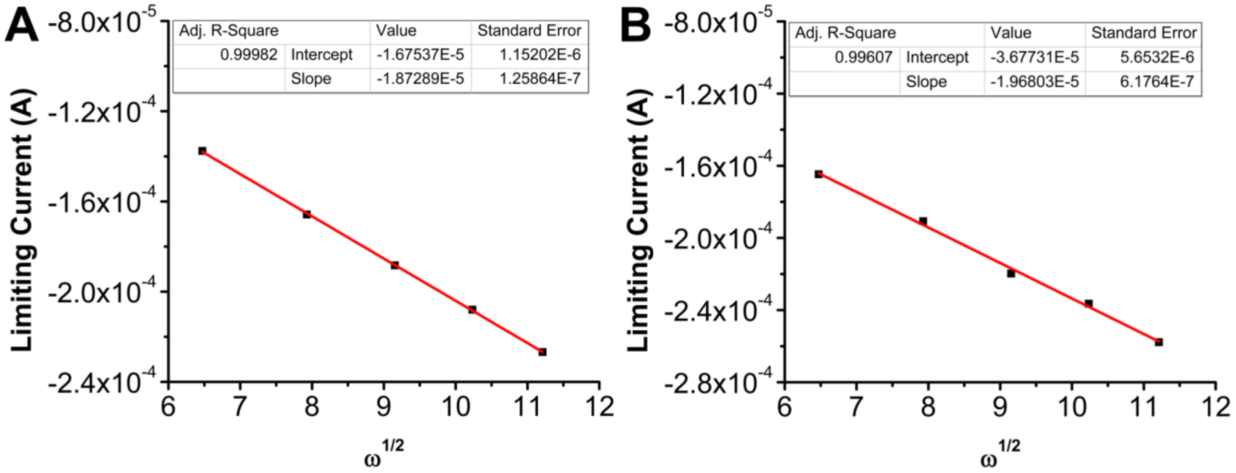

Figure S5.8.36. Levich plots from data obtained from Linear Sweep Voltammograms of BQ (0.5 mM) by RRDE with 1.37 M TFE under Ar (**A**) and O_2 (**B**) saturation conditions at various rotation rates; ring potential = 0.85 V vs Fc^+/Fc.

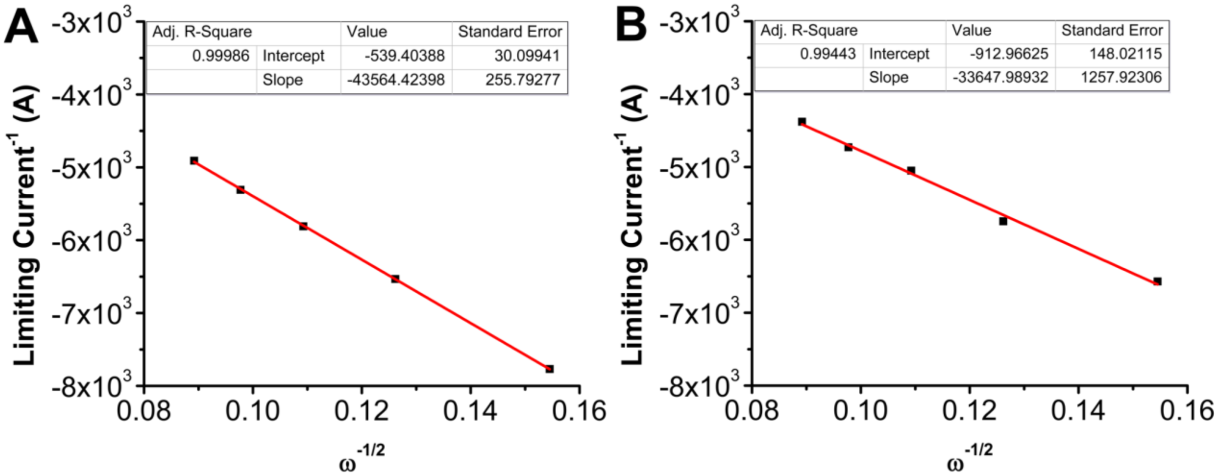

Figure S5.8.37. Koutecky-Levich plots from data obtained from Linear Sweep Voltammograms of BQ (0.5 mM) by RRDE with 1.37 M TFE under Ar (**A**) and O_2 (**B**) saturation conditions at various rotation rates; ring potential = 0.85 V vs Fc^+/Fc.

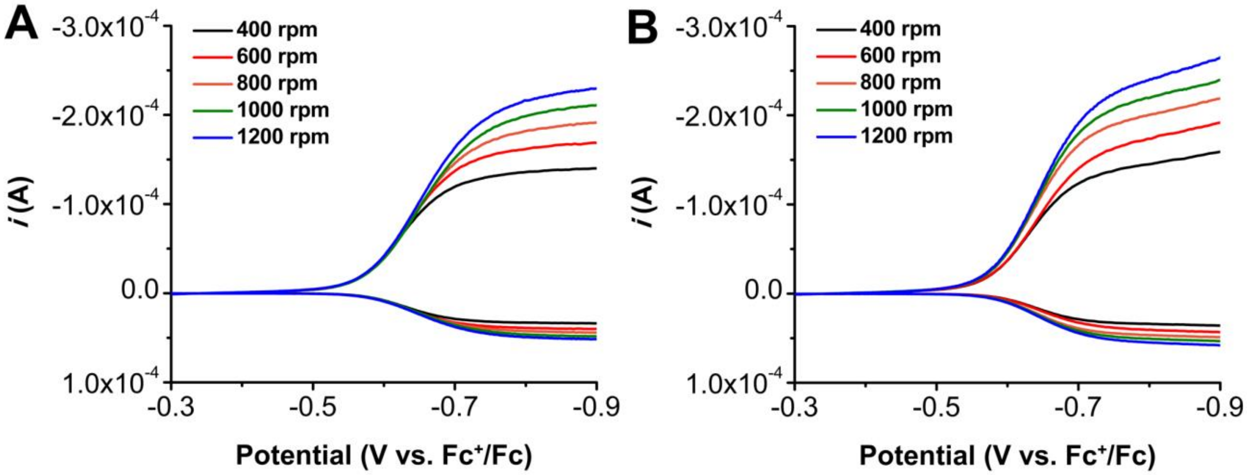

Figure S5.8.38. Linear Sweep Voltammograms of RRDE experiment with 0.5 mM BQ and 1.37 M TFEOH at various rotation rates under Ar (**A**) and O_2 (**B**) saturation conditions; ring potential = 0.4 V vs Fc^+/Fc. Conditions: glassy carbon working electrode/Pt ring working electrode, glassy carbon rod counter electrode, Ag/AgCl pseudoreference electrode; scan rate 0.02 V/s.

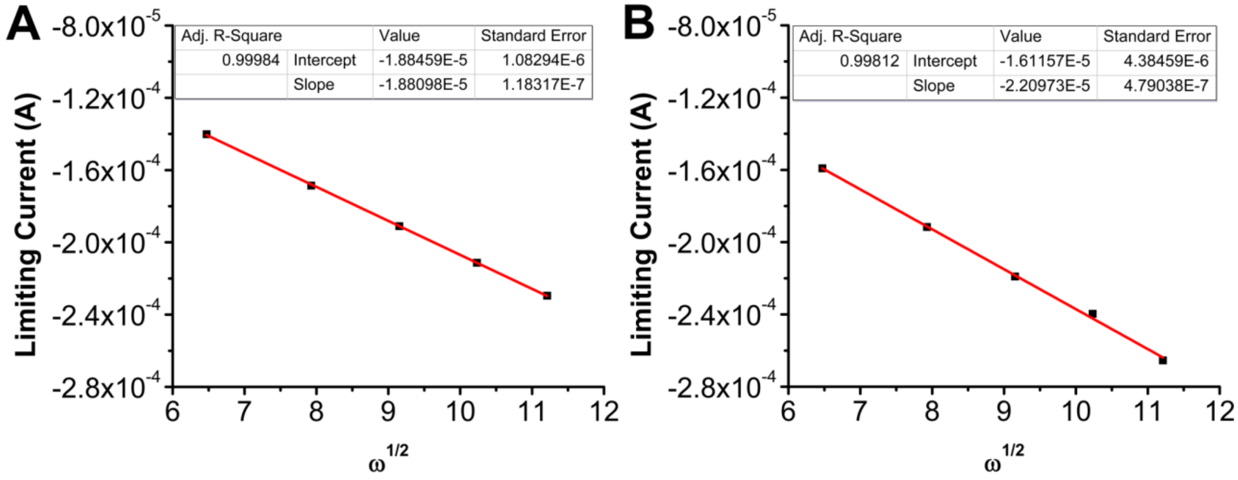

A

Adj. R-Square		Value	Standard Error
0.99984	Intercept	-1.88459E-5	1.08294E-6
	Slope	-1.88098E-5	1.18317E-7

B

Adj. R-Square		Value	Standard Error
0.99812	Intercept	-1.61157E-5	4.38459E-6
	Slope	-2.20973E-5	4.79038E-7

Figure S5.8.39. Levich plots from data obtained from Linear Sweep Voltammograms of BQ (0.5 mM) by RRDE with 1.37 M TFE under Ar (**A**) and O_2 (**B**) saturation conditions at various rotation rates; ring potential = 0.4 V vs Fc^+/Fc.

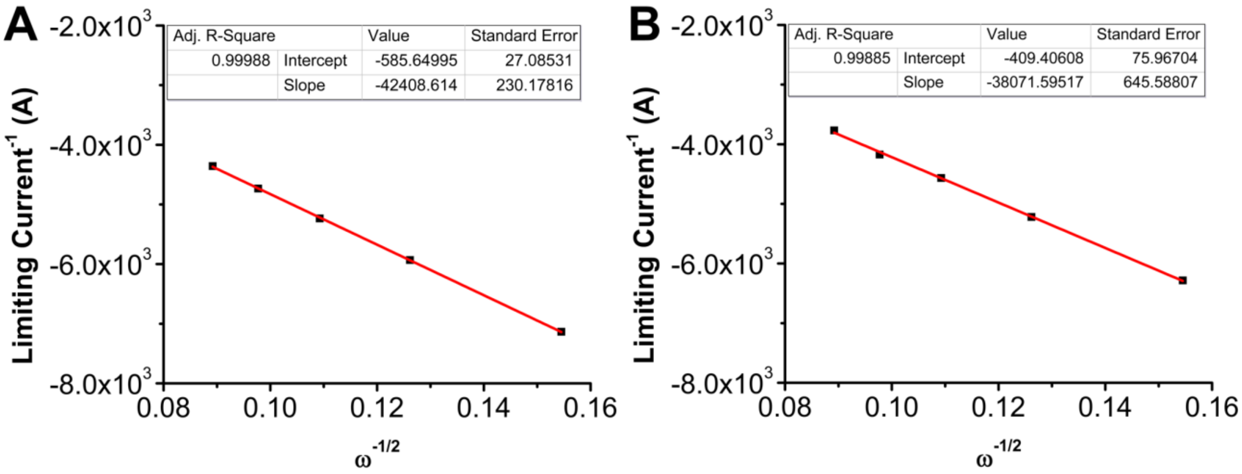

Figure S5.8.40. Koutecky-Levich plots from data obtained from Linear Sweep Voltammograms of BQ (0.5 mM) by RRDE with 1.37 M TFE under Ar (**A**) and O_2 (**B**) saturation conditions at various rotation rates; ring potential = 0.4 V vs Fc^+/Fc.

Table S5.8.3. Summary of O_2 Reduction Product Ananlysis Quantified from RRDE Experiments

Conditions	**% Selectivity for H_2O_2**	**% Selectivity for H_2O**
0.5 mM BQ + TFEOH[a]	10 (±23)%	n/a
0.5 mM Mn + TFEOH[b]	68 (±13)%	32 (±13)%
0.5 mM Mn + 0.5 mM BQ + TFEOH[c]	69 (±0.3)%	31 (±0.3)%
0.5 mM Mn + 1.25 mM BQ + TFEOH[c]	55 (±4)%	45 (±4)%
0.5 mM Mn + 2.5 mM BQ + TFEOH[c]	96 (±0.5)%	4 (±0.5)%

*-[a] denotes where selectivity was calculated across all rotation rates. -[b] denotes where selectivity was calculated at catalyst $E_{1/2}$ (-0.63 V vs. Fc^+/Fc). -[c] denotes where selectivity was calculated at the rotation rate of 400 rpm

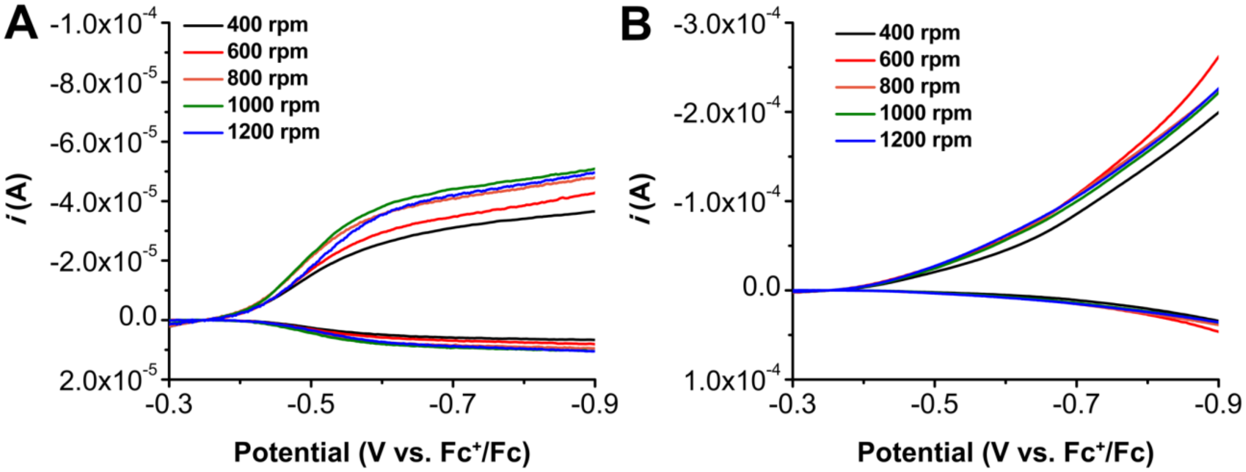

Figure S5.8.41. Linear Sweep Voltammograms of RRDE experiment with 0.5 mM Mn(^{tbu}dhbpy)Cl **1** and 1.37 M TFEOH at various rotation rates under Ar (**A**) and O_2 (**B**) saturation conditions; ring potential = 0.85 V vs Fc$^+$/Fc. Conditions: glassy carbon working electrode/Pt ring working electrode, glassy carbon rod counter electrode, Ag/AgCl pseudoreference electrode; scan rate 0.02 V/s.

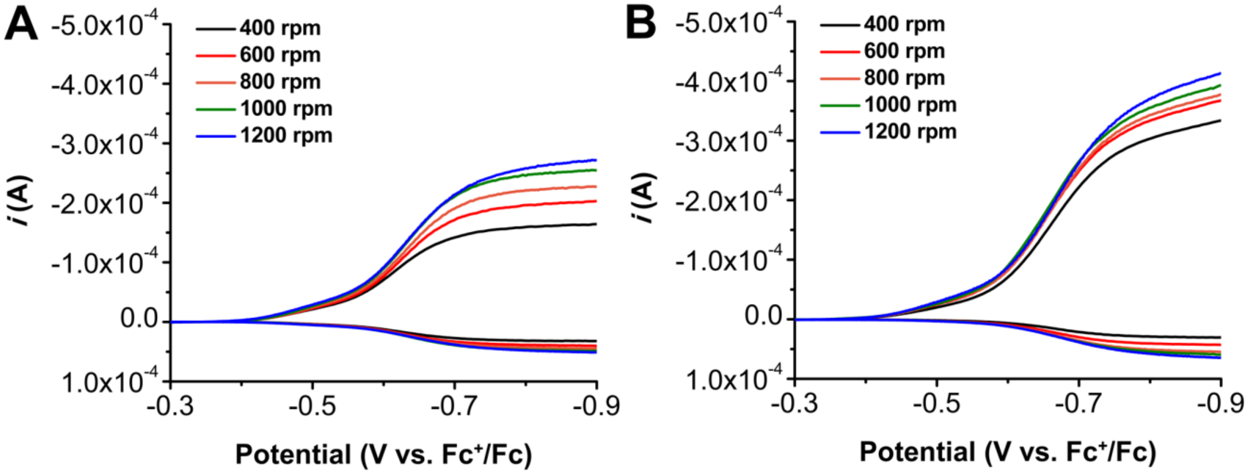

Figure S5.8.42. Linear Sweep Voltammograms of RRDE experiment with 0.5 mM Mn(^{tbu}dhbpy)Cl **1**, 0.5 mM BQ and 1.37 M TFEOH at various rotation rates under Ar (**A**) and O_2 (**B**) saturation conditions; ring potential = 0.4 V vs Fc$^+$/Fc. Conditions: glassy carbon working electrode/Pt ring working electrode, glassy carbon rod counter electrode, Ag/AgCl pseudoreference electrode; scan rate 0.02 V/s.

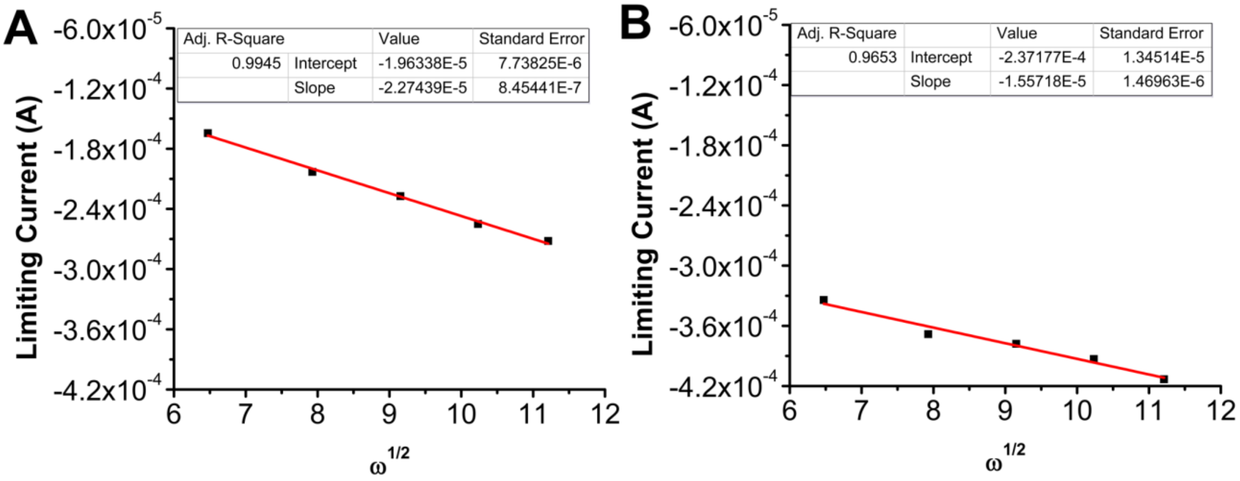

Figure S5.8.43. Levich plots from data obtained from Linear Sweep Voltammograms of 0.5 mM Mn(^{tbu}dhbpy)Cl **1** and 0.5 mM BQ by RRDE with 1.37 M TFE under Ar (**A**) and O_2 (**B**) saturation conditions at various rotation rates; ring potential = 0.4 V vs Fc$^+$/Fc.

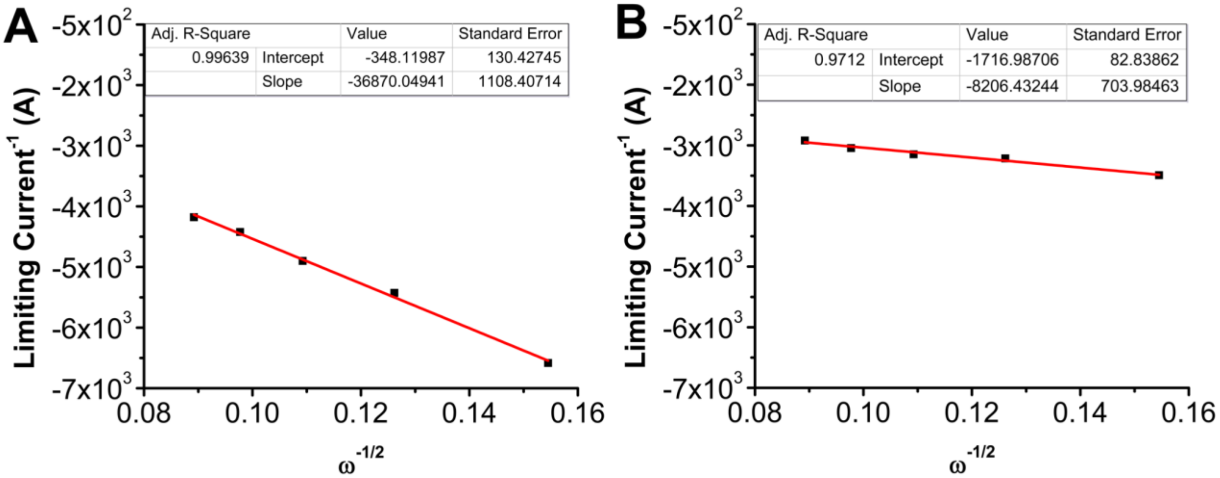

Figure S5.8.44. Koutecky-Levich plots from data obtained from Linear Sweep Voltammograms of 0.5 mM Mn(^{tbu}dhbpy)Cl **1** and 0.5 mM BQ by RRDE with 1.37 M TFE under Ar (**A**) and O_2 (**B**) saturation conditions at various rotation rates; ring potential = 0.4 V vs Fc$^+$/Fc.

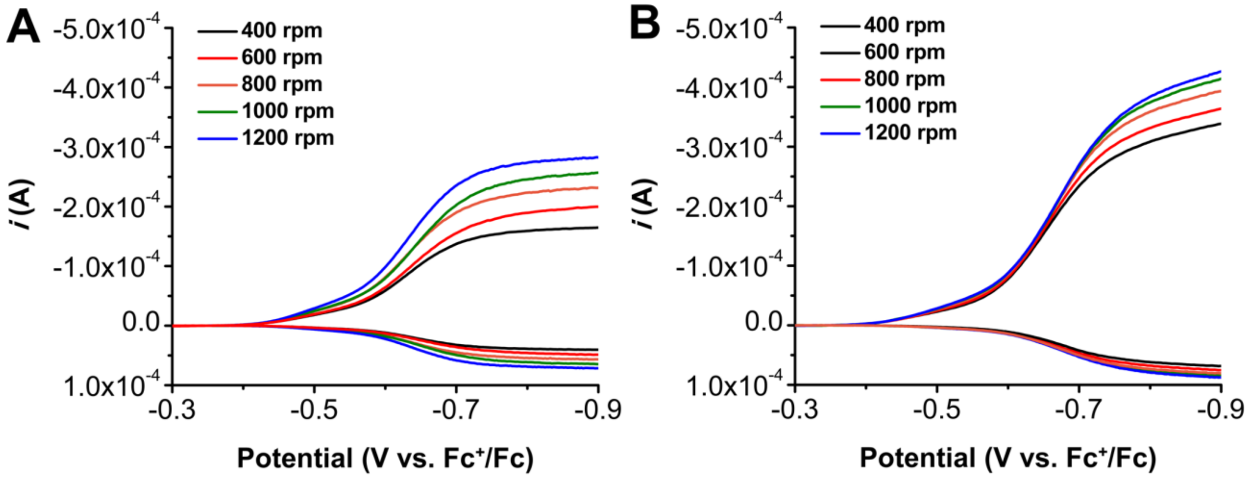

Figure S5.8.45. Linear Sweep Voltammograms of RRDE experiment with 0.5 mM Mn(^{tbu}dhbpy)Cl **1**, 0.5 mM BQ and 1.37 M TFEOH at various rotation rates under Ar (**A**) and O_2 (**B**) saturation conditions; ring potential = 0.85 V vs Fc^+/Fc. Conditions: glassy carbon working electrode/Pt ring working electrode, glassy carbon rod counter electrode, Ag/AgCl pseudoreference electrode; scan rate 0.02 V/s.

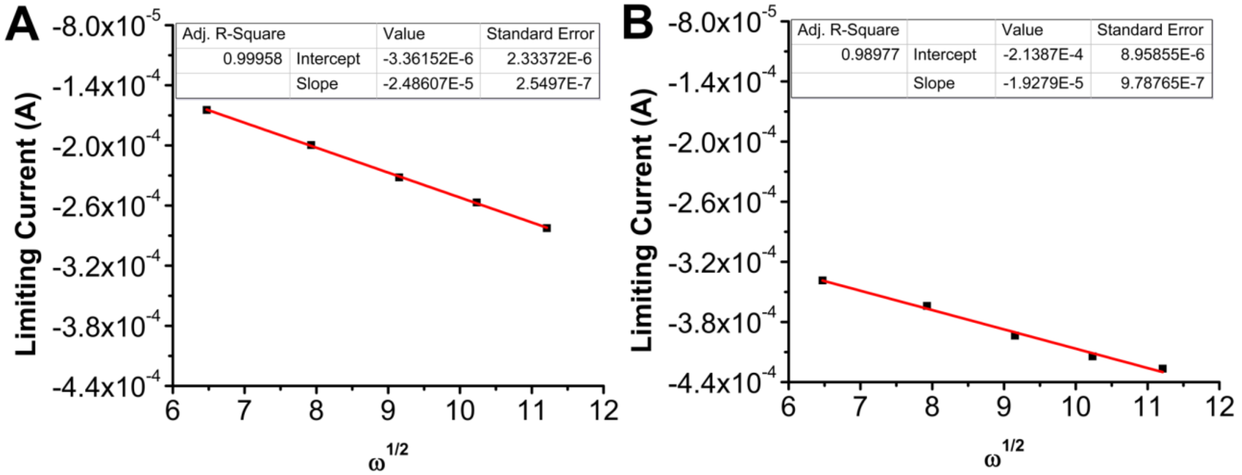

A

Adj. R-Square		Value	Standard Error
0.99958	Intercept	-3.36152E-6	2.33372E-6
	Slope	-2.48607E-5	2.5497E-7

B

Adj. R-Square		Value	Standard Error
0.98977	Intercept	-2.1387E-4	8.95855E-6
	Slope	-1.9279E-5	9.78765E-7

Figure S5.8.46. Levich plots from data obtained from Linear Sweep Voltammograms of 0.5 mM Mn(^{tbu}dhbpy)Cl **1** and 0.5 mM BQ by RRDE with 1.37 M TFE under Ar (**A**) and O_2 (**B**) saturation conditions at various rotation rates; ring potential = 0.85 V vs Fc^+/Fc.

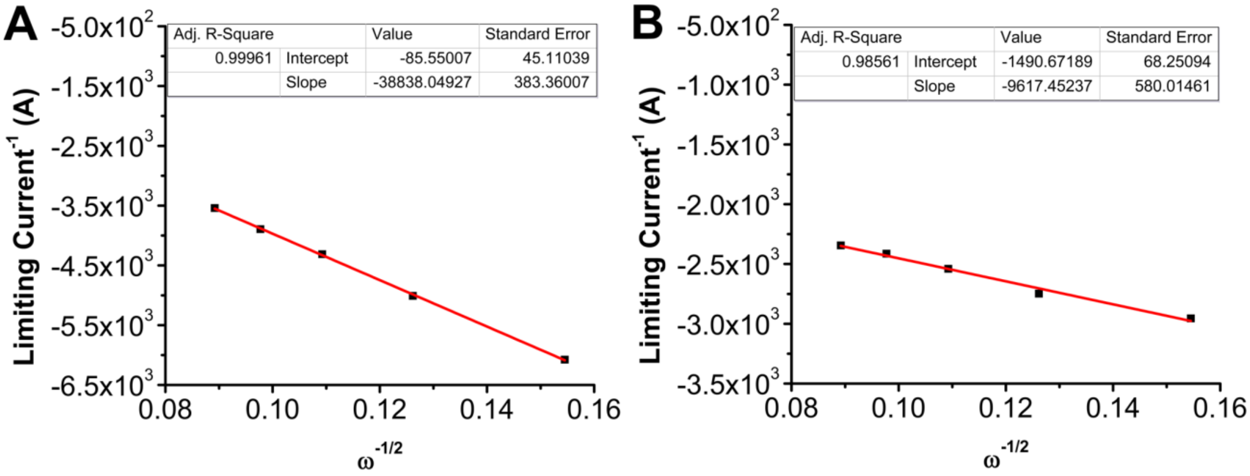

Adj. R-Square		Value	Standard Error
0.99961	Intercept	-85.55007	45.11039
	Slope	-38838.04927	383.36007

Adj. R-Square		Value	Standard Error
0.98561	Intercept	-1490.67189	68.25094
	Slope	-9617.45237	580.01461

Figure S5.8.47. Koutecky-Levich plots from data obtained from Linear Sweep Voltammograms of 0.5 mM Mn(^{tbu}dhbpy)Cl **1** and 0.5 mM BQ by RRDE with 1.37 M TFE under Ar (**A**) and O_2 (**B**) saturation conditions at various rotation rates; ring potential = 0.85 V vs Fc$^+$/Fc.

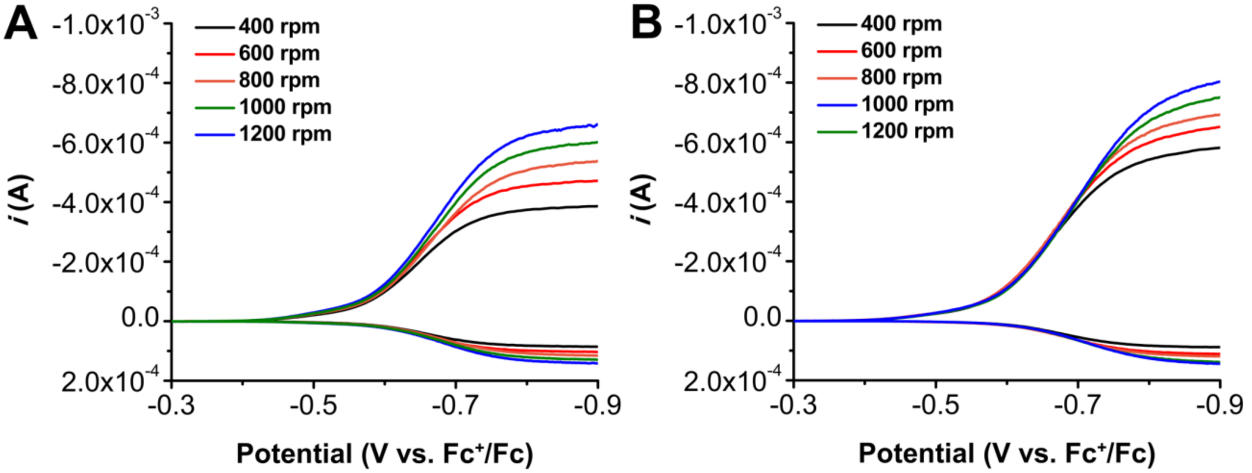

Figure S5.8.48. Linear Sweep Voltammograms of RRDE experiment with 0.5 mM Mn(^{tbu}dhbpy)Cl **1**, 1.25 mM BQ and 1.37 M TFEOH at various rotation rates under Ar (**A**) and O_2 (**B**) saturation conditions; ring potential = 0.4 V vs Fc$^+$/Fc. Conditions: glassy carbon working electrode/Pt ring working electrode, glassy carbon rod counter electrode, Ag/AgCl pseudoreference electrode; scan rate 0.02 V/s.

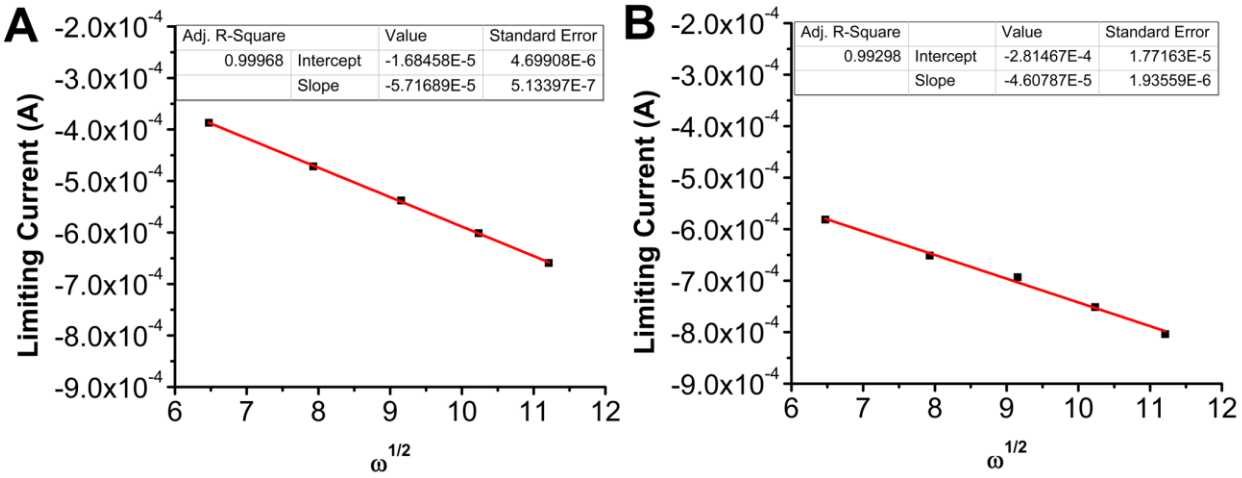

A

Adj. R-Square		Value	Standard Error
0.99968	Intercept	-1.68458E-5	4.69908E-6
	Slope	-5.71689E-5	5.13397E-7

B

Adj. R-Square		Value	Standard Error
0.99298	Intercept	-2.81467E-4	1.77163E-5
	Slope	-4.60787E-5	1.93559E-6

Figure S5.8.49. Levich plots from data obtained from Linear Sweep Voltammograms of 0.5 mM Mn(^{tbu}dhbpy)Cl **1** and 1.25 mM BQ by RRDE with 1.37 M TFE under Ar (**A**) and O_2 (**B**) saturation conditions at various rotation rates; ring potential = 0.4 V vs Fc^+/Fc.

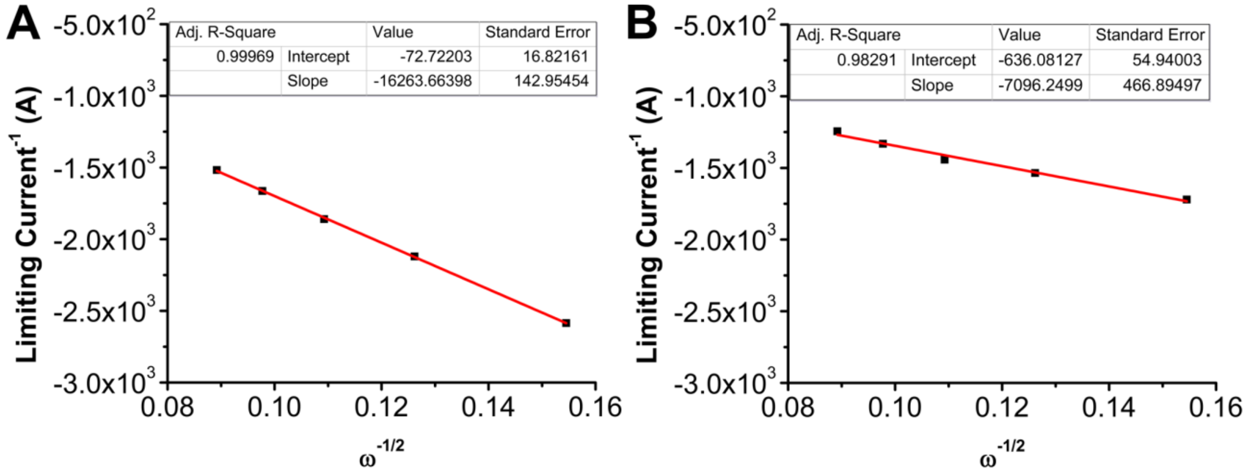

A

Adj. R-Square		Value	Standard Error
0.99969	Intercept	-72.72203	16.82161
	Slope	-16263.66398	142.95454

B

Adj. R-Square		Value	Standard Error
0.98291	Intercept	-636.08127	54.94003
	Slope	-7096.2499	466.89497

Figure S5.8.50. Koutecky-Levich plots from data obtained from Linear Sweep Voltammograms of 0.5 mM Mn(^{tbu}dhbpy)Cl **1** and 1.25 mM BQ by RRDE with 1.37 M TFE under Ar (**A**) and O_2 (**B**) saturation conditions at various rotation rates; ring potential = 0.4 V vs Fc^+/Fc.

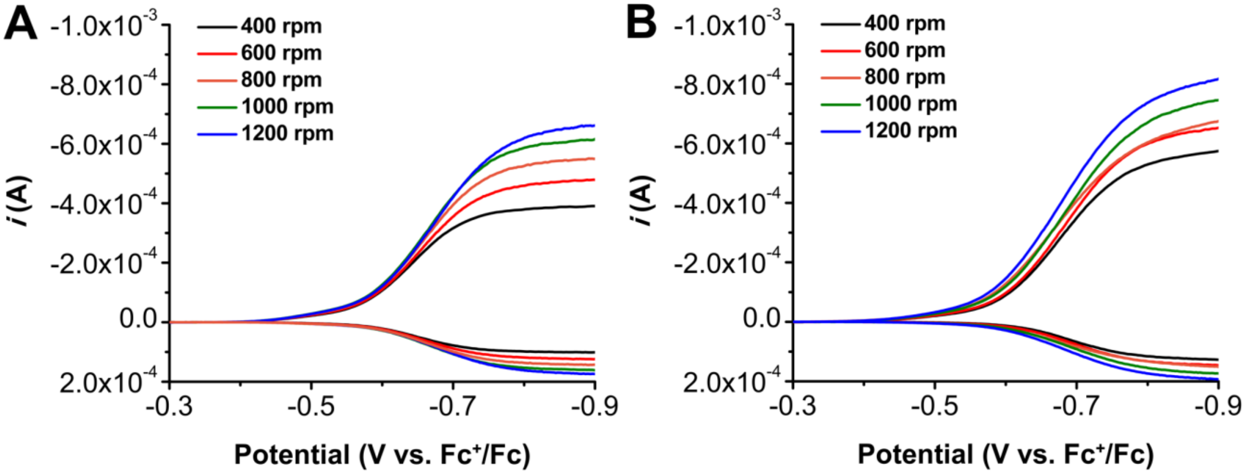

Figure S5.8.51. Linear Sweep Voltammograms of RRDE experiment with 0.5 mM Mn(^{tbu}dhbpy)Cl **1**, 1.25 mM BQ and 1.37 M TFEOH at various rotation rates under Ar (**A**) and O$_2$ (**B**) saturation conditions; ring potential = 0.85 V vs Fc$^+$/Fc. Conditions: glassy carbon working electrode/Pt ring working electrode, glassy carbon rod counter electrode, Ag/AgCl pseudoreference electrode; scan rate 0.02 V/s.

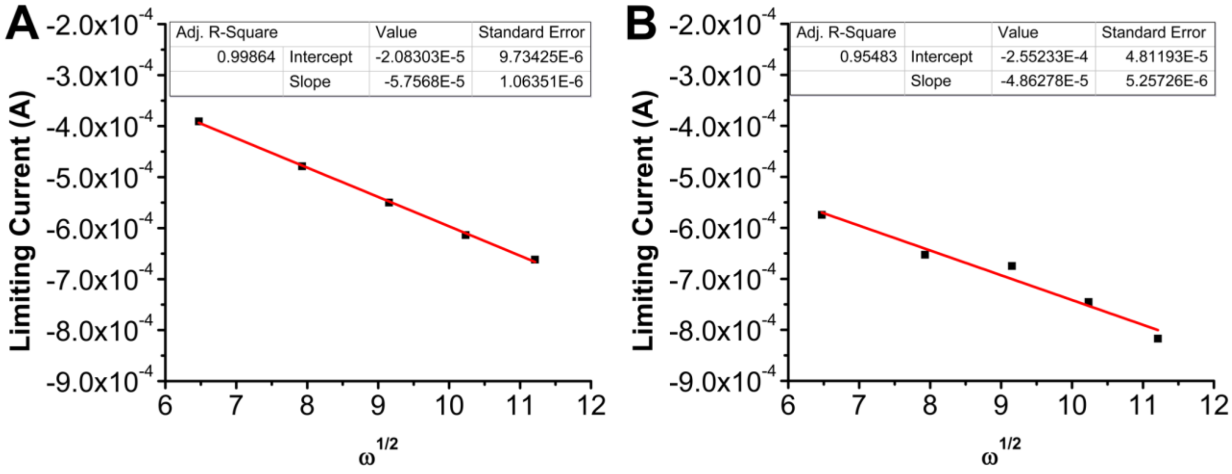

Figure S5.8.52. Levich plots from data obtained from Linear Sweep Voltammograms of 0.5 mM Mn(^{tbu}dhbpy)Cl **1** and 1.25 mM BQ by RRDE with 1.37 M TFE under Ar (**A**) and O$_2$ (**B**) saturation conditions at various rotation rates; ring potential = 0.85 V vs Fc$^+$/Fc.

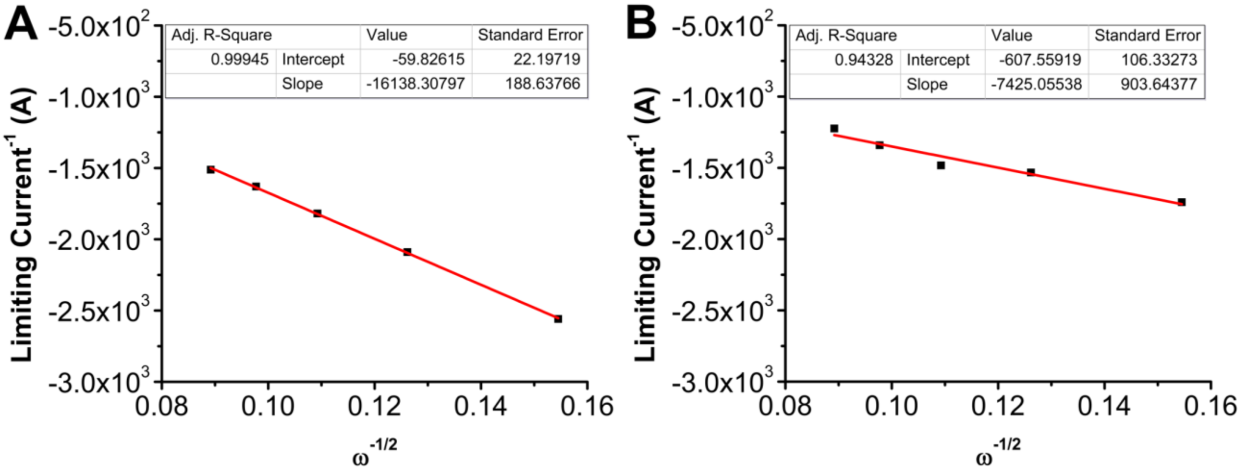

Figure S5.8.53. Koutecky-Levich plots from data obtained from Linear Sweep Voltammograms of 0.5 mM Mn(^{tbu}dhbpy)Cl **1** and 1.25 mM BQ by RRDE with 1.37 M TFE under Ar (**A**) and O_2 (**B**) saturation conditions at various rotation rates; ring potential = 0.85 V vs Fc^+/Fc.

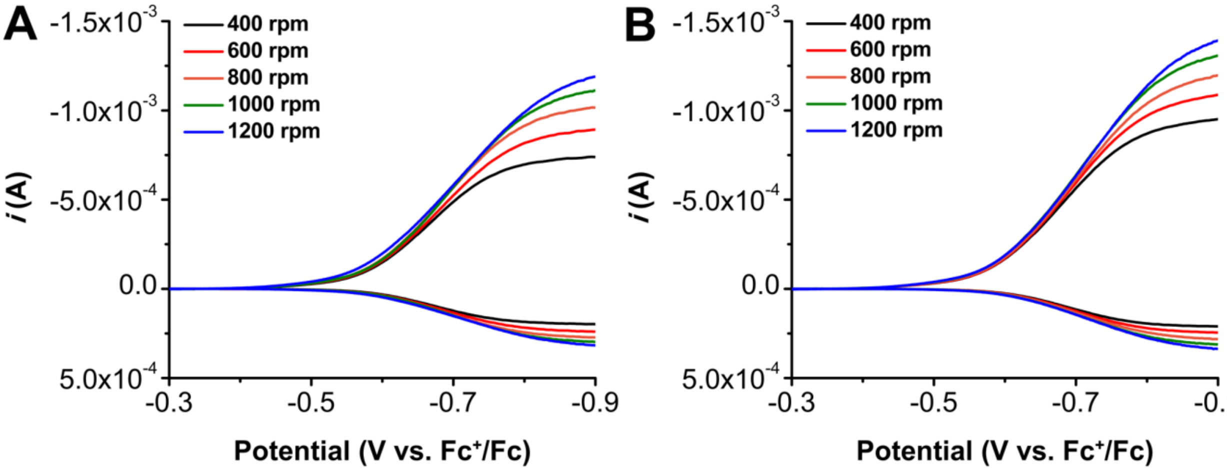

Figure S5.8.54. Linear Sweep Voltammograms of RRDE experiment with 0.5 mM Mn(^{tbu}dhbpy)Cl **1**, 2.5 mM BQ and 1.37 M TFEOH at various rotation rates under Ar (**A**) and O_2 (**B**) saturation conditions; ring potential = 0.85 V vs Fc^+/Fc. Conditions: glassy carbon working electrode/Pt ring working electrode, glassy carbon rod counter electrode, Ag/AgCl pseudoreference electrode; scan rate 0.02 V/s.

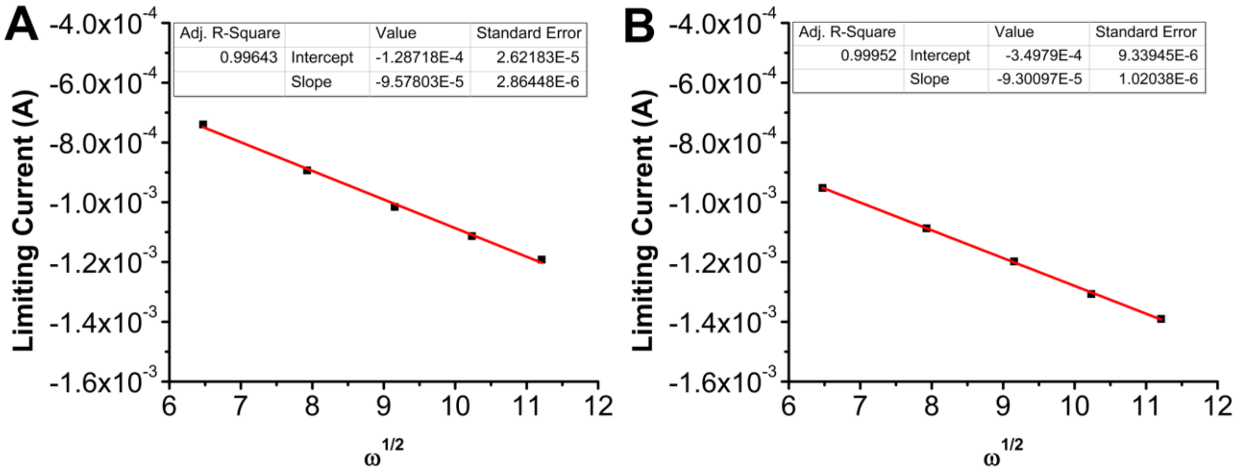

Figure S5.8.55. Levich plots from data obtained from Linear Sweep Voltammograms of 0.5 mM Mn(^{tbu}dhbpy)Cl **1** and 2.5 mM BQ by RRDE with 1.37 M TFE under Ar (**A**) and O$_2$ (**B**) saturation conditions at various rotation rates; ring potential = 0.85 V vs Fc$^+$/Fc.

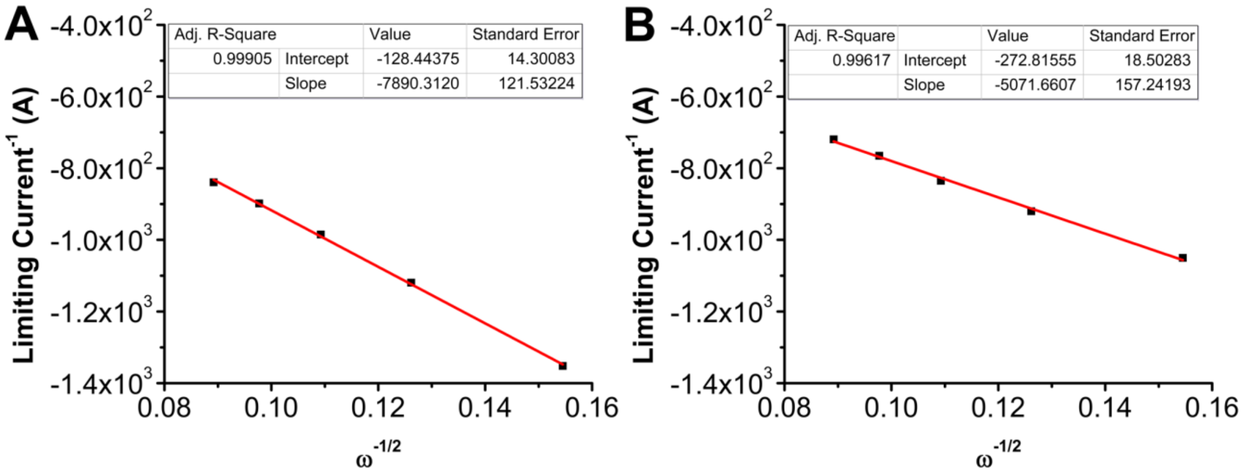

Figure S5.8.56. Koutecky-Levich plots from data obtained from Linear Sweep Voltammograms of 0.5 mM Mn(^{tbu}dhbpy)Cl **1** and 2.5 mM BQ by RRDE with 1.37 M TFE under Ar (**A**) and O$_2$ (**B**) saturation conditions at various rotation rates; ring potential = 0.85 V vs Fc$^+$/Fc.

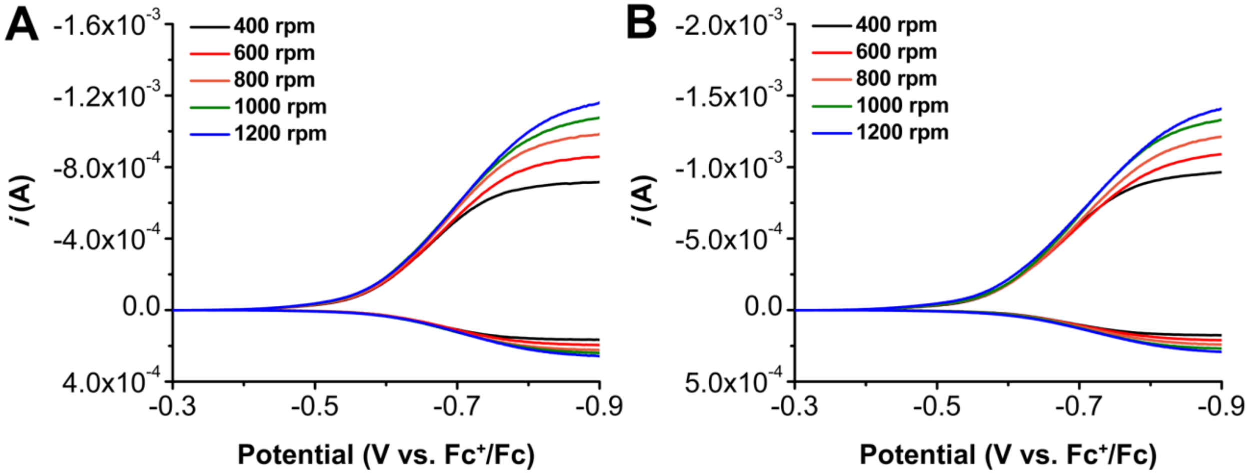

Figure S5.8.57. Linear Sweep Voltammograms of RRDE experiment with 0.5 mM Mn(^{tbu}dhbpy)Cl **1**, 2.5 mM BQ and 1.37 M TFEOH at various rotation rates under Ar (**A**) and O_2 (**B**) saturation conditions; ring potential = 0.4 V vs Fc$^+$/Fc. Conditions: glassy carbon working electrode/Pt ring working electrode, glassy carbon rod counter electrode, Ag/AgCl pseudoreference electrode; scan rate 0.02 V/s.

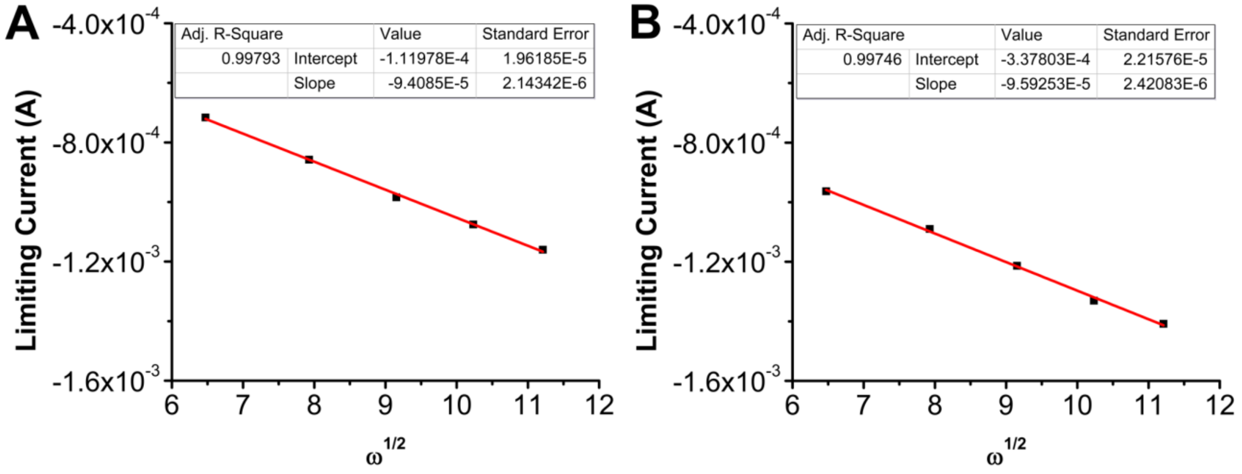

Figure S5.8.58. Levich plots from data obtained from Linear Sweep Voltammograms of 0.5 mM Mn(^{tbu}dhbpy)Cl **1** and 2.5 mM BQ by RRDE with 1.37 M TFE under Ar (**A**) and O_2 (**B**) saturation conditions at various rotation rates; ring potential = 0.4 V vs Fc$^+$/Fc.

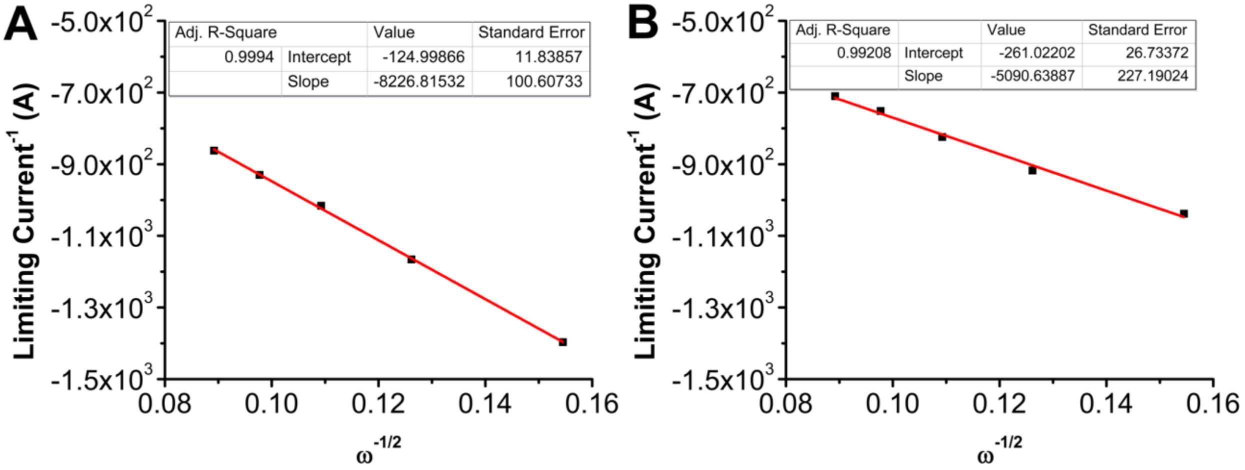

Figure S5.8.59. Koutecky-Levich plots from data obtained from Linear Sweep Voltammograms of 0.5 mM Mn(^{tbu}dhbpy)Cl **1** and 2.5 mM BQ by RRDE with 1.37 M TFE under Ar (**A**) and O_2 (**B**) saturation conditions at various rotation rates; ring potential = 0.4 V vs Fc^+/Fc.

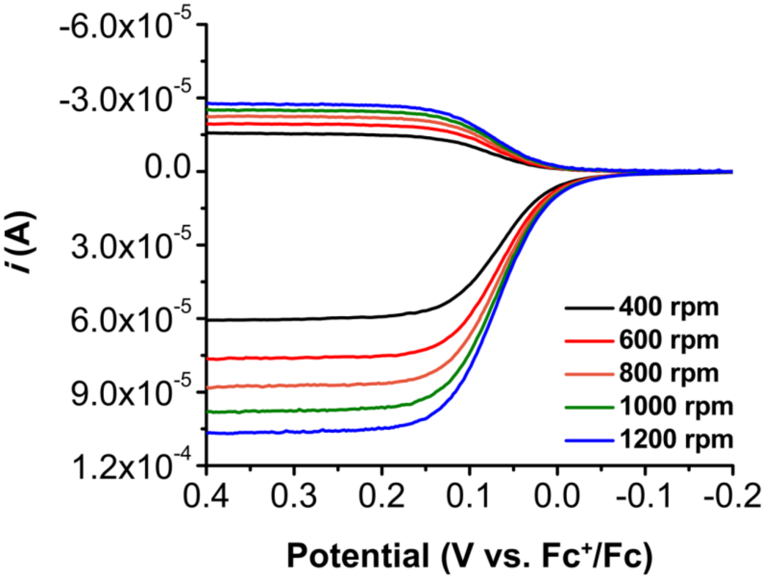

Figure S5.11.60. Linear Sweep Voltammograms of RRDE experiment with 0.5 mM ferrocene at various rotation rates under Ar saturation conditions; ring potential = 0.85 V vs Fc^+/Fc. Conditions: glassy carbon working electrode/Pt ring working electrode, glassy carbon rod counter electrode, Ag/AgCl pseudoreference electrode; scan rate 0.02 V/s.

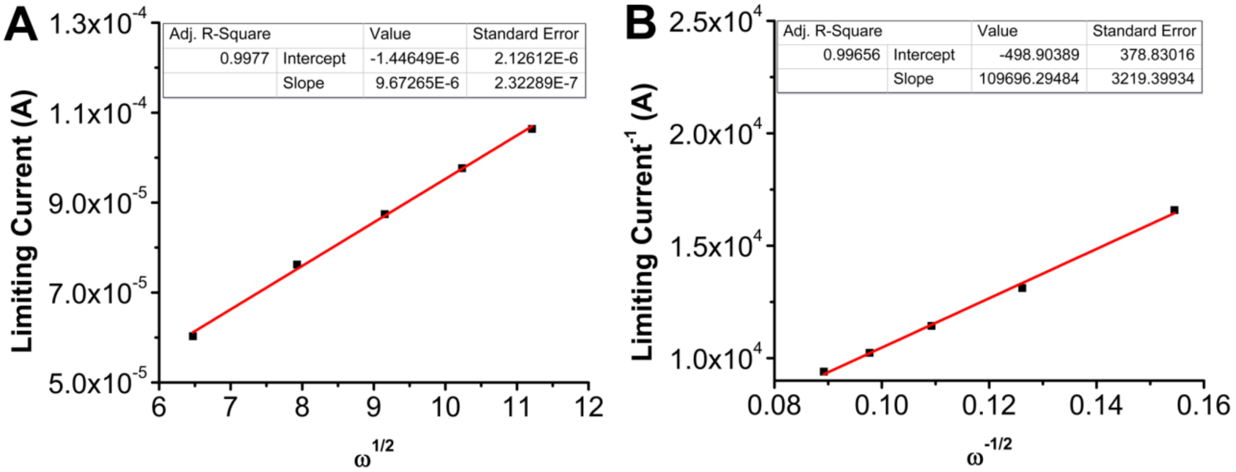

Adj. R-Square		Value	Standard Error
0.9977	Intercept	-1.44649E-6	2.12612E-6
	Slope	9.67265E-6	2.32289E-7

Adj. R-Square		Value	Standard Error
0.99656	Intercept	-498.90389	378.83016
	Slope	109696.29484	3219.39934

Figure S5.11.61. Levich (**A**) and Koutecky**-**Levich (**B**) plots from data obtained from Linear Sweep Voltammograms of 0.5 mM ferrocene by RRDE under Ar saturation conditions at various rotation rates; ring potential = 0.85 V vs Fc$^+$/Fc.

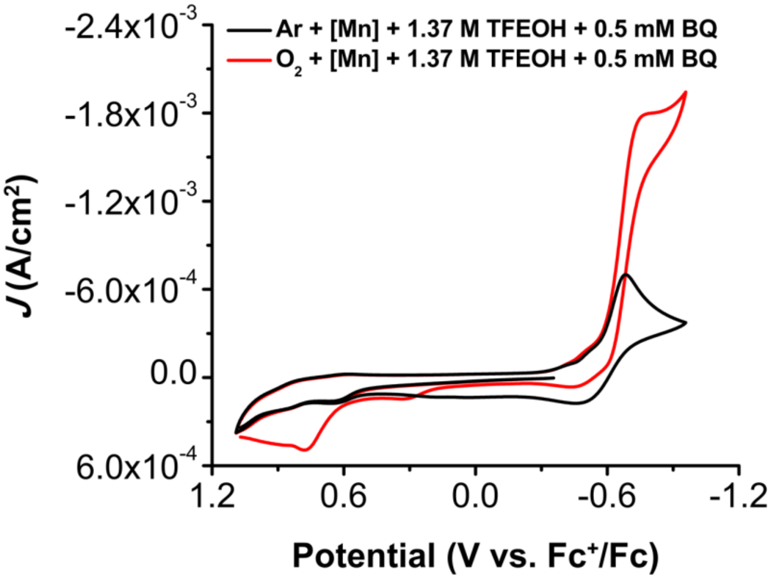

Figure S5.11.62. CVs of 0.5 mM Mn(^{tbu}dhbpy)Cl **1**, and 0.5 mM BQ obtained under Ar (black) and O_2 (red) saturation conditions with 1.37 M TFE-OH. Conditions: 0.1 M $TBAPF_6$/MeCN; glassy carbon working electrode, glassy carbon counter electrode, Ag/AgCl pseudoreference electrode; 100 mV/s scan rate; referenced to internal ferrocene standard.

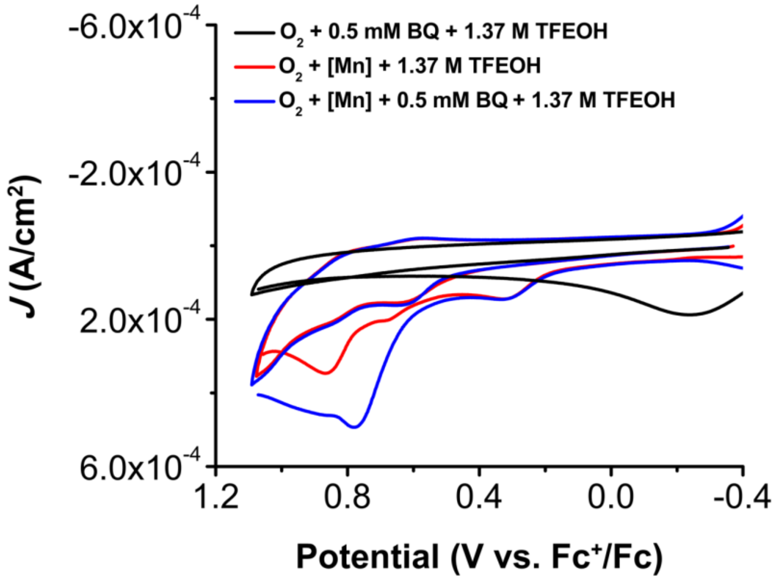

Figure S5.11.63. CVs of oxidative regions; all CV sweeps start at –0.35 V and proceed to an initial switching potential at +1.2 V, then to a second switching potential at –1.0 V, before sweeping to an ending potential of +1.2 V. Conditions: 0.1 M TBAPF$_6$/MeCN; glassy carbon working electrode, glassy carbon counter electrode, Ag/AgCl pseudoreference electrode; 100 mV/s scan rate; referenced to internal ferrocene standard.

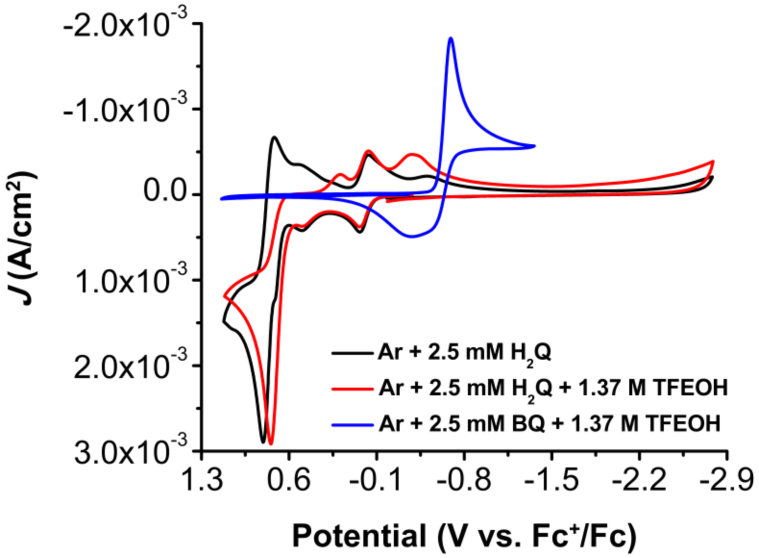

Figure S5.11.64. CVs of 2.5 mM H_2Q with (red) and without (black) TFEOH under Ar saturation conditions and comparable data under O_2 with BQ (blue). For all traces, the arrow indicates the initial sweep direction; the blue trace sweeps to positive potentials twice, before and after reducing potentials. Conditions: 0.1 M $TBAPF_6$/MeCN; glassy carbon working electrode, glassy carbon counter electrode, Ag/AgCl pseudoreference electrode; 100 mV/s scan rate; referenced to internal ferrocene standard. Arrow designates the direction of the CV trace.

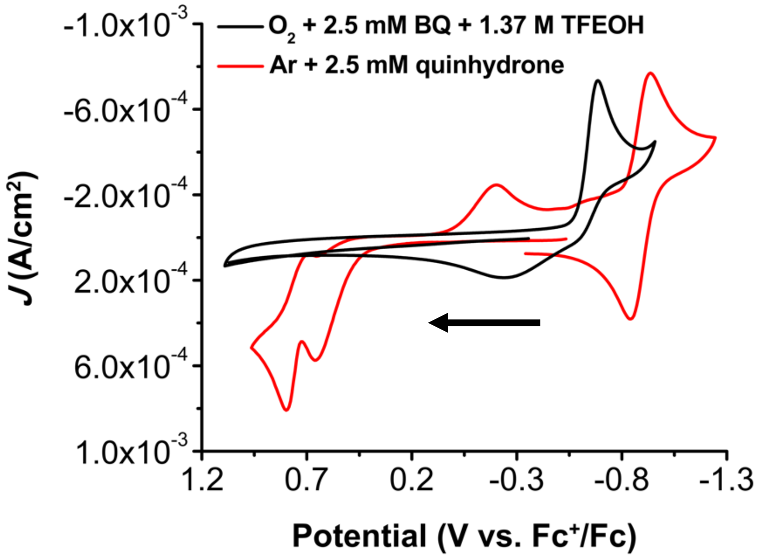

Figure S5.11.65. CVs with 2.5 mM quinhydrone under Ar saturation conditions (red) and 2.5 mM BQ with 1.37 M TFEOH under Ar saturation conditions (black). For all traces, the arrow indicates the initial sweep direction; the black trace sweeps to positive potentials twice, before and after reducing potentials. Conditions: 0.1 M TBAPF$_6$/MeCN; glassy carbon working electrode, glassy carbon counter electrode, Ag/AgCl pseudoreference electrode; 100 mV/s scan rate; referenced to internal ferrocene standard. Arrow designates the direction of the CV trace.

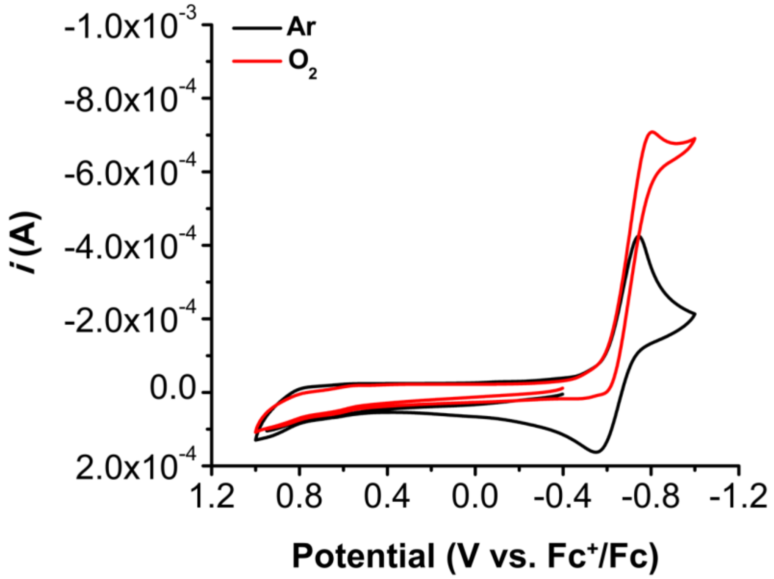

Figure S5.11.66. CVs obtained with the RRDE electrode used in this study with 0.5 mM Mn(^{tbu}dhbpy)Cl **1**, 2.5 mM BQ and 1.37 M TFEOH under Ar (black) and O_2 (red) saturation conditions. Conditions: 0.1 M $TBAPF_6$/MeCN; glassy carbon working electrode, glassy carbon counter electrode, Ag/AgCl pseudoreference electrode; 100 mV/s scan rate; referenced to ferrocene standard.

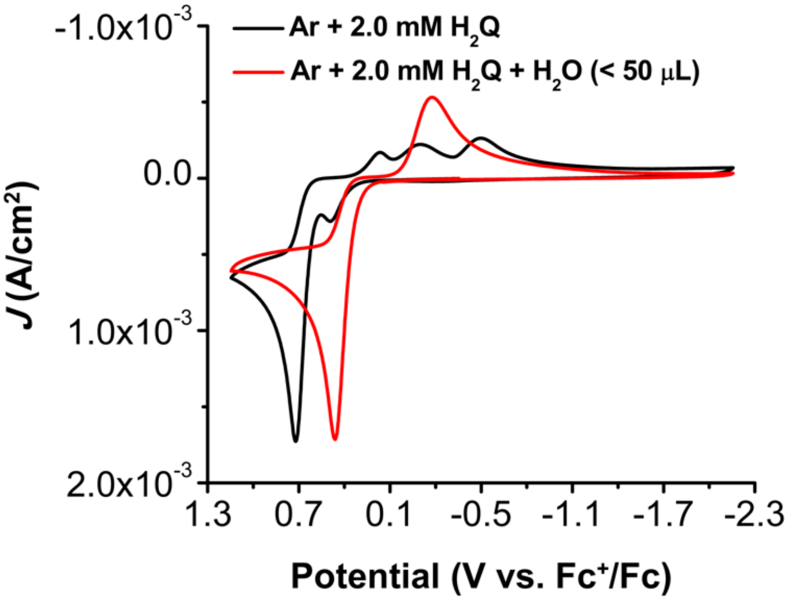

Figure S5.11.67. CVs of 2.5 mM H_2Q with (red) and without (black) added water under Ar saturation conditions. The data with added water closely match those reported for related studies by others,[55-56] who reported using solvent as received and did not recrystallize electrolyte. This indicates that the divergence we observe from these prior results in our own data is the result of residual water in the samples studied by others. Conditions: 0.1 M $TBAPF_6$/MeCN; glassy carbon working electrode, glassy carbon counter electrode, Ag/AgCl pseudoreference electrode; 100 mV/s scan rate; referenced to internal ferrocene standard.

5.12 Acknowledgments C.W.M. conceived and supervised the experiments; all experiments were carried out by S.L.H.; E.N.C. and A.G.R. assisted in developing adequate experimental procedures specific to this manuscript. The authors thank Dr. Michael L. Pegis for helpful discussion concerning the RRDE quantification of non-Levich behavior by molecular electrocatalysts. The authors also thank Spenser Simpson for assistance and advice in NMR methods.

5.13 References:

1. Savéant, J.-M., *Chem. Rev.* **2008,** *108*, 2348–2378.
2. Savéant, J.-M., *Angew. Chem., Int. Ed.* **2019,** *58*, 2125-2128.
3. Warren, J. J.; Tronic, T. A.; Mayer, J. M., *Chem. Rev.* **2010,** *110*, 6961-7001.

4. McEvoy, J. P.; Brudvig, G. W., *Chem. Rev.* **2006,** *106*, 4455-4483.

5. Kok, B.; Forbush, B.; McGloin, M., *Photochem. Photobiol.* **1970,** *11*, 457-475.

6. Mailloux, R. J., *Redox Biol.* **2015,** *4*, 381-398.

7. Hammarström, L.; Styring, S., *Philos. Trans. R. Soc. Land. B. Biol. Sci.* **2008,** *363*, 1283-1291.

8. Pegis, M. L.; Wise, C. F.; Martin, D. J.; Mayer, J. M., *Chem. Rev.* **2018,** *118*, 2340-2391.

9. Fontecave, M.; Mansuy, D., *Tetrahedron* **1984,** *40*, 4297-4311.

10. Murahashi, S.-I.; Naota, T.; Komiya, N., *Tet. Lett.* **1995,** *36*, 8059-8062.

11. Seo, M. S.; Kim, J. Y.; Annaraj, J.; Kim, Y.; Lee, Y.-M.; Kim, S.-J.; Kim, J.; Nam, W., *Angew. Chem., Int. Ed.* **2007,** *46*, 377-380.

12. Haber, J.; Mlodnicka, T.; Poltowicz, J., *J. Mol. Cat.* **1989,** *54*, 451-461.

13. Tohru, Y.; Kiyomi, I.; Takushi, N.; Teruaki, M., *Bull. Chem. Soc. Jpn.* **1994,** *67*, 2248-2256.

14. Anson, C. W.; Ghosh, S.; Hammes-Schiffer, S.; Stahl, S. S., *J. Am. Chem. Soc.* **2016,** *138*, 4186-4193.

15. Anson, C. W.; Stahl, S. S., *J. Am. Chem. Soc.* **2017,** *139*, 18472-18475.

16. Izutsu, K.; *Commission on Electroanalytical Chemistry International Union of Pure Applied Chemistry: Acid-base dissociation constants in dipolar aprotic solvents*. Blackwell Scientific Publications Oxford: 1990; Vol. 35.

17. Huynh, M. T.; Anson, C. W.; Cavell, A. C.; Stahl, S. S.; Hammes-Schiffer, S., *J. Am. Chem. Soc.* **2016,** *138*, 15903-15910.

18. Gupta, N.; Linschitz, H., *J. Am. Chem. Soc.* **1997,** *119*, 6384-6391.

19. Costentin, C., *Chem.Rev.* **2008,** *108*, 2145-2179.

20. Quan, M.; Sanchez, D.; Wasylkiw, M. F.; Smith, D. K., *J. Am. Chem. Soc.* **2007,** *129*, 12847-12856.

21. Staley, P. A.; Lopez, E. M.; Clare, L. A.; Smith, D. K., *J. Phys. Chem. C* **2015,** *119*, 20319-20327.

22. Evans, D. H., *Chem. Rev.* **2008,** *108*, 2113-2144.

23. Evans, D. H.; René, A., *Phys. Chem. Chem. Phys.* **2012,** *14*, 4844-4848.

24. Macías-Ruvalcaba, N. A.; Evans, D. H., *.J. Phys.Chem. B* **2006,** *110*, 5155-5160.

25. René, A.; Evans, D. H., *J. Phys. Chem. C* **2012,** *116*, 14454-14460.

26. Uno, B.; Okumura, N.; Goto, M.; Kano, K., *J. Org. Chem.* **2000,** *65*, 1448-1455.

27. Macías-Ruvalcaba, N. A.; Okumura, N.; Evans, D. H., *J. Phys. Chem. B* **2006,** *110*, 22043-22047.

28. Shalev, H.; Evans, D. H., *J. Am. Chem. Soc.* **1989,** *111*, 2667-2674.

29. Shi, R. R. S.; Tessensohn, M. E.; Lauw, S. J. L.; Foo, N. A. B. Y.; Webster, R. D., *Chem. Comm.* **2019,** *55*, 2277-2280.

30. Baglia, R. A.; Zaragoza, J. P. T.; Goldberg, D. P., *Chem. Rev.* **2017,** *117*, 13320-13352.

31. Balamurugan, M.; Saravanan, N.; Ha, H.; Lee, Y. H.; Nam, K. T. J. N. C., *Nano Convergence* **2018,** *5*, 18.

32. Masa, J.; Ozoemena, K.; Schuhmann, W.; Zagal, J. H., *J. Porphyrins Phthalocyanines* **2012,** *16*, 761-784.

33. Zagal, J.; Páez, M.; Tanaka, A. A.; dos Santos, J. R.; Linkous, C. A., *J. Electroanal. Chem.* **1992,** *339*, 13-30.

34. Zagal, J. H.; Griveau, S.; Silva, J. F.; Nyokong, T.; Bedioui, F., *Coord. Chem. Rev.* **2010,** *254*, 2755-2791.

35. Zagal, J. H.; Javier Recio, F.; Gutierrez, C. A.; Zuñiga, C.; Páez, M. A.; Caro, C. A., *Electrochem. Comm.* **2014,** *41*, 24-26.

36. Flyagina, I. S.; Hughes, K. J.; Pourkashanian, M.; Ingham, D. B., *Int. J. Hydrogen Energ.* **2014,** *39*, 21538-21546.

37. Masa, J.; Schuhmann, W., *Chem. Eur. J.* **2013,** *19*, 9644-9654.

38. Schöfberger, W.; Faschinger, F.; Chattopadhyay, S.; Bhakta, S.; Mondal, B.; Elemans, J. A. A. W.; Müllegger, S.; Tebi, S.; Koch, R.; Klappenberger, F.; Paszkiewicz, M.; Barth, J. V.; Rauls, E.; Aldahhak, H.; Schmidt, W. G.; Dey, A., *Angew. Chem. Int. Ed.* **2016,** *55*, 2350-2355.

39. McGuire Jr, R.; Dogutan, D. K.; Teets, T. S.; Suntivich, J.; Shao-Horn, Y.; Nocera, D. G., *Chem. Sci.* **2010,** *1*, 411-414.

40. Pegis, M. L.; McKeown, B. A.; Kumar, N.; Lang, K.; Wasylenko, D. J.; Zhang, X. P.; Raugei, S.; Mayer, J. M., *ACS Cent. Sci.* **2016,** *2*, 850-856.

41. Passard, G.; Ullman, A. M.; Brodsky, C. N.; Nocera, D. G., *J. Am. Chem. Soc.* **2016,** *138*, 2925-2928.

42. Wasylenko, D. J.; Rodríguez, C.; Pegis, M. L.; Mayer, J. M., *J. Am. Chem. Soc.* **2014,** *136*, 12544-12547.

43. Nagao, K.; Hiroshi, S.; Tetsuo, O., *Chem. Lett.* **1985,** *14*, 1917-1920.

44. Passard, G.; Dogutan, D. K.; Qiu, M.; Costentin, C.; Nocera, D. G., *ACS Catal.* **2018**.

45. Hooe, S. L.; Rheingold, A. L.; Machan, C. W., *J. Am. Chem. Soc.* **2018,** *140*, 3232-3241.

46. Hooe, S. L.; Machan, C. W., *J. Am. Chem. Soc.* **2019,** *141*, 4379-4387.

47. Pegis, M. L.; Wise, C. F.; Martin, D. J.; Mayer, J. M., *Chem. Rev.* **2018,** *118*, 2340-2391.

48. Astudillo, P. D.; Valencia, D. P.; González-Fuentes, M. A.; Díaz-Sánchez, B. R.; Frontana, C.; González, F. J., *Electrochim. Acta* **2012,** *81*, 197-204.

49. Gamboa-Valero, N.; Astudillo, P. D.; González-Fuentes, M. A.; Leyva, M. A.; Rosales-Hoz, M. d. J.; González, F. J., *Electrochim. Acta* **2016,** *188*, 602-610.

50. Uno, B.; Okumura, N.; Goto, M.; Kano, K., *J. Org. Chem.* **2000,** *65*, 1448-1455.

51. Alligrant, T. M.; Hackett, J. C.; Alvarez, J. C., *Electrochim. Acta* **2010,** *55*, 6507-6516.

52. Aguilar-Martinez, M.; Macias-Ruvalcaba, N. A.; Bautista-Martinez, J. A.; Gomez, M.; Gonzalez, F. J.; Gonzalez, I., *Curr. Org. Chem.* **2004,** *8*, 1721-1738.

53. Savéant, J.-M.; Costentin, C., *Elements of Molecular and Biomolecular Electrochemistry: An Electrochemical Approach to Electron Transfer Chemistry*. Wiley: 2019.

54. Gonzalez, F. J.; Astudillo, P. D.; Magali, S.; Macías-Ruvalcaba, N. A.; Bautista Martinez, J. A. A.; Aguilar-Martinez, M.; Gómez, M.; Frontana, C. E.; Gonzalez, I., *ECS Transactions* **2019,** *3*, 25-36.

55. Astudillo, P. D.; Tiburcio, J.; González, F. J., *J. Electroanal. Chem.* **2007,** *604*, 57-64.

56. Alligrant, T. M.; Alvarez, J. C., *J. Phys. Chem. C* **2011,** *115*, 10797-10805.

Chapter 6

Dibenzothiophene-5,5-dioxide as a Co-Catalyst to Enhance the Electrocatalytic Reduction of CO_2 to CO by a Molecular Cr Complex

Chapters 6 contains material for upcoming publications and have been incorporated with consent of all current contributing authors. These authors include Juanjo J. Moreno, Emma N. Cook, Amelia G. Reid, and Charles W. Machan. The work in this chapter was published in preprint form and is available at https://doi.org/10.26434/chemrxiv.14165951.v1

6.1 Abstract

The electrocatalytic reduction of CO_2 is an appealing method for converting renewable energy sources into value-added chemical feedstocks. We report a co-electrocatalytic system for the reduction of CO_2 to CO comprised of a molecular Cr complex and dibenzothiophene-5,5-dioxide (DBTD) as a redox mediator which achieves high activity (1.51-2.84 x 10^5 s^{-1}) and quantitative selectivity. Under aprotic or protic conditions, DBTD produces a co-electrocatalytic response with **1** by coordinating *trans* to the site of CO_2 binding and mediating electron transfer from the electrode with quantitative efficiency for CO. This assembly is reliant on through-space electronic conjugation between the π frameworks of DBTD and the bpy fragment of the catalyst ligand, with contributions from dispersion interactions and weak sulfone coordination. The resulting interaction stabilizes a key intermediate in a new aprotic catalytic pathway and lowers the energy of the rate-determining transition state under protic conditions.

6.2 Introduction

Concerns over increasing energy demands and climate change have led to continued interest in molecular electrocatalysis.[1-3] The conversion of CO_2 to value-added products, as part of a carbon neutral (or negative) cycle, is an attractive strategy for addressing the challenges associated with the rising atmospheric CO_2 concentration.[4-9] The electrocatalytic reduction of CO_2 to CO could significantly alter the emissions impact of industrial processes related to Fischer-Tropsch chemistry and syngas, if hydrogen from renewable sources is used.[10-13]

The reduction of CO_2 to CO by molecular electrocatalysts requires the sequential transfer of two electrons and an oxo acceptor (e.g. $2H^+$ or CO_2).[14-15] The general paradigm is for a catalyst to accept electrons from the electrode prior to substrate binding. During energy conversion in living cells, chemical bonds are modified by synergistic systems, like the electron transport chain, which achieve high energy efficiency and selectivity by pairing redox-active moieties with metal centers to direct the flow of reducing equivalents.[16] Analogous reactivity has been translated to only one example of homogenous co-electrocatalytic CO_2 reduction,[17] while similar reactivity is known for other electrocatalytic reactions.[18-21] An alternative mechanism for directing electron transfer is through-space electronic conjugation (TSEC), a mechanism of electronic communication between stacked π systems which enables efficient energy and charge transport which has found application in optoelectronic materials and for studying conductance in molecular junctions (**Figure 6.2.1**).[22-26]

Intrigued by the notion that TSEC could enhance catalytic activity in catalyst-mediator assemblies, we sought to identify a suitable redox mediator (RM) and transition metal complex. We selected dibenzothiophene-5,5-dioxide (DBTD) as the RM (**Figure 6.2.1**), which is derived from a petroleum contaminant[27] and has well-defined electrochemical properties at reducing potentials,[28] to pair with a Cr-based catalyst developed in our lab, Cr(^{tbu}dhbpy)Cl(H_2O) (**Figure 6.2.1**).[29-30] Herein, we report to our knowledge the only example where TSEC has been used as a key component in a homogeneous co-electrocatalytic system with an inner-sphere mechanism. DBTD functions in part to drive electron transfer in an analogous way to RMs used in dye-sensitized solar cells or bioelectrocatalysis.[31-32] However, the interaction between the Cr catalyst and DBTD also modifies the potential energy surface of the reaction, altering the mechanism of protic and aprotic CO_2 reduction and enhancing kinetic activity. This co-catalytic behavior is the combined result of weak sulfone coordination to the Cr center, dispersive forces, and TSEC between the RM and ligand backbone of the catalyst.

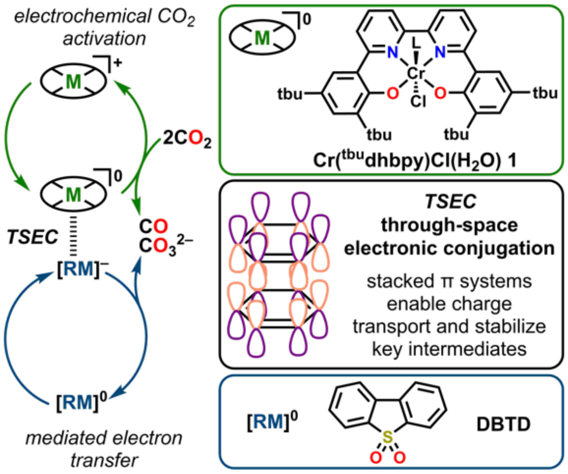

Figure 6.2.1. Overview of co-electrocatalytic system with inner-sphere electron transfer based on TSEC between DBTD and Cr(^{tbu}dhbpy)Cl(H_2O) **1**.

6.3 Experimental Results

Cyclic voltammetry (CV) experiments were carried out in 0.1 M tetrabutylammonium hexafluorophosphate ($TBAPF_6$) with *N,N*-dimethylformamide (*N,N*-DMF) as the solvent. Under argon (Ar) saturation conditions, DBTD displays a reversible redox feature with an $E_{1/2} = –2.25$ V versus the ferrocenium/ferrocene (Fc^+/Fc) internal standard (**Figure S6.3.1**). Control CVs show minimal reactivity with CO_2 or phenol (PhOH) on the CV timescale**.** CV analysis under aprotic conditions established that this redox feature is a one-electron process, in agreement with a pervious report [33](**see 6.6 Supporting Information**). A control electrolysis experiment was performed with DBTD under CO_2 saturation conditions and again with added PhOH (**Figures S6.3.2-S6.3.3**): CO and H_2 were detected with low Faradaic efficiencies (FEs) and less than one turnover was achieved based on [DBTD] in both cases (**Table 6.3.1**). Under aprotic CO_2 saturation conditions, **1** does not achieve a single turnover of CO production in electrolysis experiments and no co-products were detected.

The addition of DBTD (2.5 mM) to a solution of **1** (1.0 mM) under Ar saturation conditions suggests no interaction occurs at the $DBTD^{0/–}$ reduction under inert conditions (**Figures S6.3.4**). Conversely, under CO_2 saturation conditions this mixture generates a large irreversible increase in current at the $DBTD^{0/–}$ couple, suggestive of a catalytic process (**Figure 6.3.2**, blue).[34] *This reactivity is not intrinsic to either component in control reactions*: **1** and DBTD do not individually possess electrocatalytic activity for aprotic CO_2 reduction. Because the Cr catalyst does not present an intrinsic reduction feature near –2.25 V vs Fc^+/Fc, this suggests that DBTD does not act simply as an outer-sphere RM, but rather that the one-electron reduction of DBTD results in the formation of a new adduct that modifies the electronic structure of **1**, enabling co-electrocatalytic CO_2 reduction. It is also worth noting that sulfones are poor ligands with few reports on their coordination chemistry, suggesting that the molecular interaction cannot be ascribed to a strong dative covalent bond between sulfone and Cr.[35-36]

Importantly, no co-electrocatalytic activity is observed in control experiments with decamethylcobaltocene and **1**, further confirming that outer-sphere electron transfer alone cannot achieve co-electrocatalytic behavior (**Figure S6.3.8**). While experiments with the related sulfoxide dibenzothiophene-5-oxide showed current increases under aprotic co-electrocatalytic conditions, this mediator reacted with CO2 in the absence of **1** (**Figure S6.3.9**).

Bulk electrolysis experiments with **1** and DBTD at –2.3 V vs Fc^+/Fc show 91±10% efficiency for CO, with carbonate confirmed as the co-product by NMR, indicating that the reductive disproportionation of CO_2 is occurring (**Table 6.3.1** and **S6.3.3**; **Figure S6.3.10**).[37] Variable concentration studies were carried out via CV (**Figures S6.3.11-S6.3.13**), indicating that the catalytic current has a dependence on [DBTD] and [**1**]. Comparable experiments with CO_2 showed a first-order concentration dependence. Since the overall reaction requires two equivalents of CO_2, this observation suggests that one of the CO_2 binding steps is kinetically invisible under catalytic conditions. while varying the concentration of a fixed ratio of DBTD to **1** showed consistent increases in current with sustained irreversibility at the DBTD reduction potential (**Figure S6.3.14**). We note that the complexity of the proposed reaction pathway and overlapping current responses precludes the accuracy of more detailed analyses, but emphasize that in all cases the catalytic current is proportional to the concentration of all components.

When 0.1 M PhOH is added to **1** and DBTD under CO_2 saturation, minimal difference compared to identical conditions in the absence of DBTD is observed until ca. −2.10 V vs Fc^+/Fc[29] (**Figure 6.3.2**). A comparison of all catalytic conditions indicates that the increase in current density at −2.25 V vs Fc^+/Fc does not correspond to a simple overlay of the independent catalytic responses: PhOH and **1** produce 0.542 mA/cm^2 catalytic current density under CO_2 saturation, **1** and DBTD generate 1.39 mA/cm^2, and the combination of PhOH, DBTD and **1** yield 2.23 mA/cm^2. Bulk electrolysis experiments at –2.3 V vs Fc^+/Fc with **1**, DBTD, and PhOH present 102±14% efficiency for CO (**Figure S6.3.4**, **Table 6.3.1**). Variable concentration studies were subsequently analyzed to establish kinetic relationships between **1**, DBTD, PhOH, and CO_2 (**Figures S6.3.15-S18**). These data again show that the catalytic current is proportional to the concentration of **1**, DBTD, and the combination of the two, as well as PhOH and CO_2.

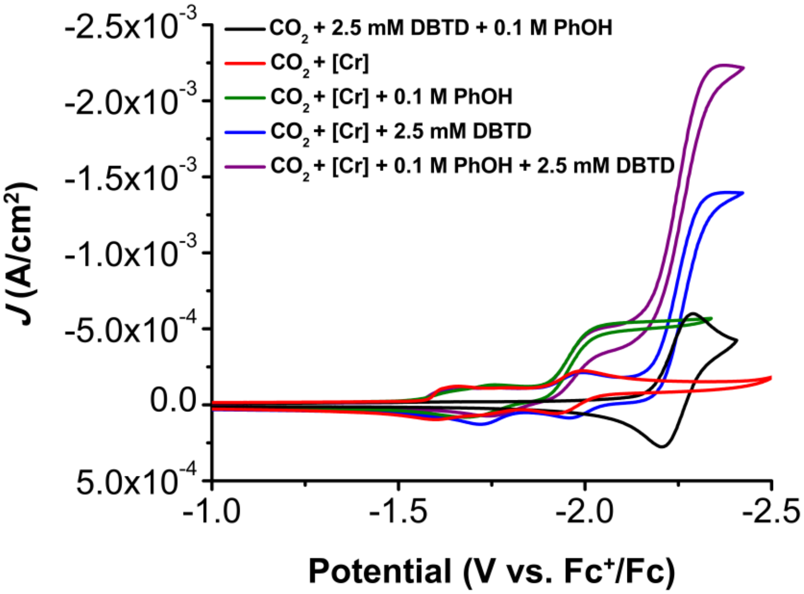

Figure 6.3.2. CVs comparing the reactivity of Cr(^{tbu}dhbpy)Cl(H_2O) **1** (1.0 mM) and DBTD under aprotic and protic conditions; 100 mV/s, 0.1 M $TBAPF_6$/DMF.

Table 6.3.1. Results from CPE experiments under CO_2 saturation conditions.

Conditions	Potential (V vs Fc^+/Fc)	FE_{CO} (%)	TOF_{CPE} s^{-1}	η (V)	TON_{CO} (w.r.t [1])	TON_{CO} (w.r.t [DBTD])
[Cr]	-2.7	57±3	-	-	0.81	-
[Cr]	-2.3	0	-	-	-	-
DBTD	-2.3	32±1	-	-	-	0.90
[Cr] + DBTD	-2.3	91±10	1.51×10^5	0.69	16	3.1
DBTD + PhOH	-2.3	28±1	-	-	-	0.52
[Cr] + PhOH[a]	-2.1	96±8	1.79×10^4	0.11	15[a]	-
[Cr] + PhOH	-2.3	111±14	3.10×10^4	0.11	11.4	-
[Cr] + PhOH + DBTD	-2.3	102±14	2.84×10^5	0.41	29	5.8

* –[Cr] = $Cr(^{tbu}dhbpy)Cl(H_2O)$ **1**. PhOH = 0.6 M [PhOH]. Turnovers correspond to moles of electrons passed in coulometry studies divided by two to account for CO formation. [a] – previously reported results.[29]

6.4 Discussion

From these experimental results, we propose a mechanism for this reactivity as illustrated in **Figure 6.4.3**, where starting from the one-electron reduced species of *v*, subsequent reduction by one electron generates the overall two-electron reduced species of *v* which binds CO_2 to form either the Cr–CO_2 adduct in the aprotic pathway or the carboxylate adduct in the protic pathway.[38-39] Upon the generation of $[DBTD]^{\bullet-}$ at more reducing potentials, we hypothesized that $[DBTD]^{\bullet-}$ binds to the Cr metal center in the axial position, trans to the site of CO_2 binding. CO_2 binding likely occurs first, since we have experimentally and computationally established that a highly reversible binding interaction at Cr occurs at potentials ~150 mV more positive than the one-electron reduction of DBTD.[38-39] We postulated that the driving force for assembly arises in part from dispersive interactions between the bpy and DBTD scaffolds, over-coming repulsive Coulombic interactions between the anionic Cr complex and $DBTD^{\bullet-}$.

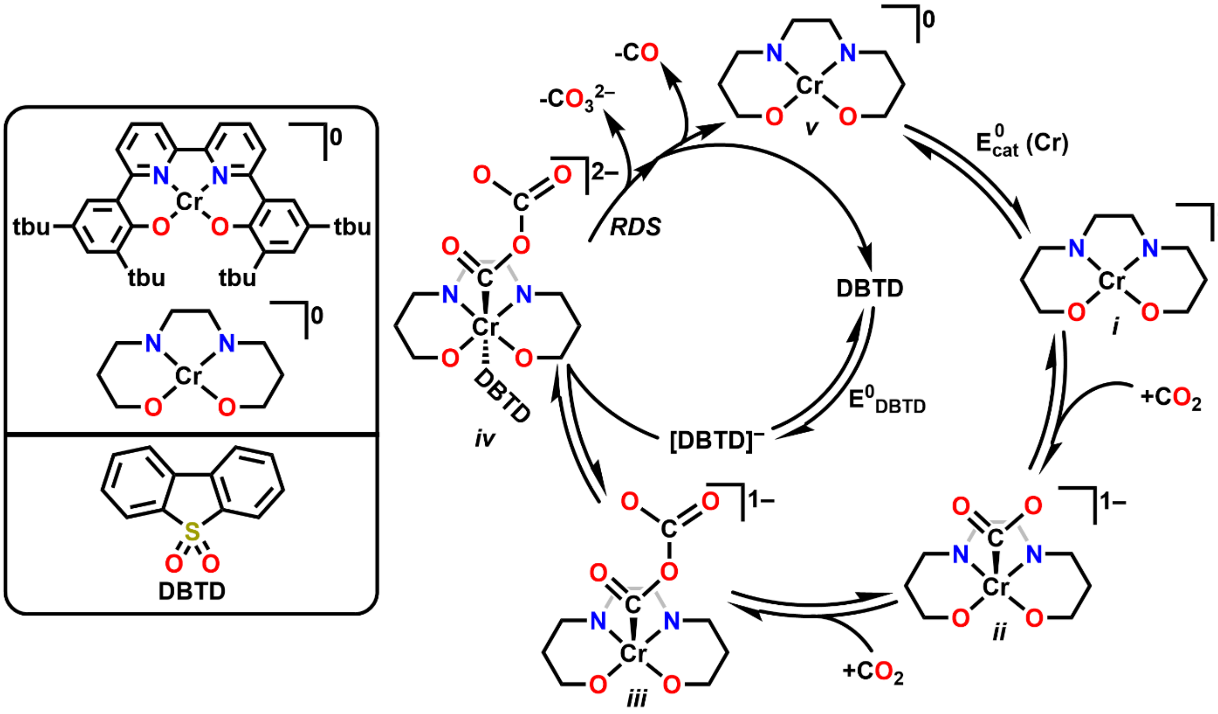

Scheme 6.4.3. Proposed mechanism for the co-electrocatalytic CO_2 reduction by **2** and DBTD under aprotic and protic (grey brackets) conditions.

6.5 Conclusion

In conclusion, we report what is, to the best of our knowledge, the only example of the coordination chemistry-driven assembly of a redox mediator and a transition metal complex to generate a co-catalytic enhancement of CO_2 electroreduction. The addition of DBTD demonstrates nascent electrocatalytic CO_2 reduction activity under aprotic conditions, at potentials where *v* has minimal intrinsic catalytic response in its absence. Computational and experimental studies to develop new redox mediator and catalyst combinations and expand the mediator scope are currently underway.

6.6 Supporting Information

Materials and Methods

General.

All chemicals and solvents (ACS or HPLC grade) were commercially available and used as received unless otherwise indicated. Cr(^{tbu}dhbpy)Cl(H_2O) was prepared according to our previous report.[38] For all air-sensitive reactions and electrochemical experiments, HPLC-grade solvents were obtained as anhydrous and air-free from a PPT Glass Contour Solvent Purification System. Gas cylinders were obtained from Praxair (Ar as 5.0; O_2 as 4.0) and passed through activated molecular sieves prior to use. Gas mixing for variable concentration experiments was accomplished using a gas proportioning rotameter from Omega Engineering. UV-vis absorbance spectra were obtained on a Cary 60 from Agilent. An Anton-Parr Multiwave Pro SOLV, NXF-8 microwave reactor was used for microwave syntheses.

Electrochemistry.

All electroanalytical experiments were performed using a Metrohm Autolab PGSTAT302N potentiostat. Glassy carbon working (⌀ = 3 mm) and non-aqueous silver/silver chloride pseudoreference electrodes behind PTFE tips were obtained from CH Instruments. The pseudoreference electrodes were obtained by depositing chloride on bare silver wire in 10% HCl at oxidizing potentials and stored in a 0.1 M tetrabutylammonium hexafluorophosphate/acetonitrile solution in the dark prior to use. The counter electrode was a glassy carbon rod (⌀ = 3 mm). All CV experiments were performed in a modified scintillation vial (20 mL volume) as a single-chamber cell with a cap modified with ports for all electrodes and a sparging needle. Tetrabutylammonium hexafluorophosphate ($TBAPF_6$) was purified by recrystallization from ethanol and dried in a vacuum oven before being stored in a desiccator. All data were referenced to an internal ferrocene standard (ferricenium/ferrocene reduction potential under stated conditions) unless otherwise specified. All voltammograms were corrected for internal resistance. Ferrocene was purified by sublimation prior to use.

Bulk Electrolysis.

Bulk electrolysis experiments were performed in a glass Pine H-cell with two compartments separated by a glass frit. A 60 mL stock solution of DMF with 0.1 M $TBAPF_6$ was prepared for each bulk electrolysis experiment. Approximately 25 mL of the stock solution was added to each half of the H-cell. One side of the H-cell contained the $Cr(^{tbu}dhbpy)Cl(H_2O)$ **2** catalyst, any additional substrate, such as PhOH, and a glassy carbon rod working electrode. The other side of the H-cell contained approximately 0.075 M ferrocene as a sacrificial reductant along with a graphite rod counter electrode and a Ag/AgCl pseudoreference electrode. The electrolysis experiment was referenced by taking a CV of the side of the H-cell that contained the ferrocene solution. The H-cell was sealed with two septa that were connected by a piece of PTFE tubing which aided to maintain equal pressure between each half of the cell during the electrolysis. Before starting the electrolysis experiment, both sides of the H-cell were sparged with the desired gas for 20 minutes and the sealed cell was allowed to equilibrate for 30 minutes. The resistance between the two halves of the H-cell was measured using the i-interrupt procedure available in the NOVA software provided by Metrohm.

Bulk Electrolysis Product Analysis.

During bulk electrolysis experiments, either 50 or 250 µL GC injections of the headspace were periodically taken for the detection and quantification of any gaseous products produced. After each bulk electrolysis experiment, the total volume of solution was measured. The total volume of the sealed H-cell was also measured to account for the total headspace volume for accurate quantification of gaseous products. A calibration curve for CO and H_2 was used to quantify gaseous products produced during electrolysis experiments in the same manner as we previously reported.[38] For liquid product detection of bicarbonate, see **Figure S6.3.6**.

Overpotential Calculations.

CO_2 Reduction with PhOH Present.

The calculation of the overpotential η for CO_2 reduction by **1** under conditions with PhOH present was performed according to reported methods.[40] The following equation was used for the determination of the reaction standard potential in V with respect to the Fc^+/Fc couple:

$$E_{CO2/CO} = 0.73\,V - 0.059(pK_a)$$

The pK_a for PhOH in DMF is reported as 18.8[41]:

$$E_{CO2/CO}(PhOH) = -1.84\,V\ vs\ Fc^+/Fc$$

The $E_{cat/2}$ determined experimentally for **1** is –1.95 V vs Fc^+/Fc, therefore the overpotential η is:

$$\eta = \left|E_{cat/2} - E_{CO2/CO}\right| = |-1.95\,V - (-1.84\,V)| = 110\,mV$$

This assumes no contribution from homoconjugation of the acid. We note that the homoconjugation constant (HA_2^-) for PhOH in DMF has been reported as $\log(K_{HA_2^-})$ =

3.8.[42] Therefore, we emphasize that the described overpotential calculated above for PhOH is the lower-limit approximation, as homoconjugation is expected to alter the effective overpotential. The overpotential equation can be modified to account for homoconjugation:

$$E_{CO2/CO} = 0.73\,V - 0.059(pK_a) - \frac{-2.303RT}{nF}\log\left(mK_{HA_2^-}\right)$$

Where n = number of electrons (2) and m = number of proton transfers (2). The modified equation provides a value of $E^0_{CO2/CO}$ = –1.72 V and η **=** 230 mV. This value does not account for the possible thermodynamic contributions of the water coordinated to the pre-catalyst, the equimolar quantities of water produced for each equivalent of CO generated, or any adventitious H_2O present in the CO_2, solvent, or electrolyte. Under CO_2 saturation, any water present can form carbonic acid, pK_a(DMF) 7.37[43], and generate new equilibria involving CO_2 and bicarbonate. The role of carbonic acid (and the general hydration of CO_2 in non-aqueous solvent systems) in altering the overall thermodynamics combined with the effects of homoconjugation has been assessed by Matsubara.[44] Considering the role of water, Matsubara obtained a standard potential for CO_2 reduction to CO of –1.70 V versus Fc$^+$/Fc for PhOH in DMF with 10 mM water present (see below). Note the same value is obtained considering 10 mM water only.

For 10 mM H_2O in DMF, where AH = PhOH[44]:

$$3CO_{2(g)} + H_2O_{(sol,x)} + 2e^- \rightleftharpoons CO_{(g)} + 2HCO^-_{3\,(sol)} \qquad E^0 = -1.70\,V\ vs.Fc^+/Fc$$

$$CO_{2(g)} + 2AH_{(sol)} + 2e^- \rightleftharpoons CO_{(g)} + 2A^-{}_{(sol)} + H_2O_{(sol,x)} \qquad E^0 = -1.96\,V\ vs.Fc^+/Fc$$

$$CO_{2(g)} + 4AH_{(sol)} + 2e^- \rightleftharpoons CO_{(g)} + 2HA^-_{2\,(sol)} + H_2O_{(sol,x)} \qquad E^0 = -1.70\,V\ vs.Fc^+/Fc$$

CO_2 Reduction Under Aprotic Conditions (Reductive Disproportionation).

To our knowledge, no solution for the aprotic reduction of CO_2 in DMF has been reported. As an estimate, we used a previously reported framework[45] to derive a value, developing the following expression to solve for the standard potential of the reductive disproportionation of two equivalents of CO_2 into one each of CO and CO_3^{2-}.

$$E^0_{2CO_2\rightarrow CO,DMF,CO_3^{2-}} = E_{L,DMF} + E^0_{2CO_2\rightarrow CO,H_2O,CO_3^{2-}} - \frac{RT}{2F}\ln\left(\frac{K_{CO(DMF)\rightarrow CO(g)}}{K_{CO(aq)\rightarrow CO(g)}} x(2) \frac{K_{CO_2(aq)\rightarrow CO(g)}}{K_{CO_2(DMF)\rightarrow CO(g)}}\right) - \frac{\left(-\Delta G^0_{t,CO_3^{2-},(DMF)\rightarrow(aq)}\right)}{2F}$$

The following values are known[45]: $E_{L,DMF}$ = 0.141 V vs. SHE; $K_{CO(DMF)\rightarrow CO(g)}$ = 400; $K_{CO(aq)\rightarrow CO(g)}$ = 1040; $K_{CO_2(aq)\rightarrow CO(g)}$ = 29; $K_{CO_2(DMF)\rightarrow CO(g)}$ = 5.

The value of $E^0_{2CO_2\rightarrow CO,H_2O,CO_3^{2-}}$ was estimated using Gibbs free energies determined at 298 K using the following thermochemical data.[46]

Compound$_{(phase)}$	**ΔH kJ/mol**	**ΔS J/mol•K**
$CO_{2\ (aq)}$	-413.26	119.36
$CO_{(g)}$	-110.53	197.66
$CO_3^{2-}{}_{(aq)}$	-675.23	-50

Using the Nernst equation ($\Delta G^0 = -nFE^0$; where n = 2, F = 96485 C/mol), these thermodynamic data gave a value of –0.352 V vs SHE for the following reaction:

$$2CO_{2\ (aq)} + 2e^- \rightleftharpoons CO_{(g)} + CO_{3\ (aq)}^{2-}$$

To convert all substrates to the same phase, the previously established equilibrium constant ($K_{CO(aq)\rightarrow CO(g)}$ = 1040) was applied to the equilibrium expression above, producing a value of –0.441 V vs SHE for the following reaction:

$$2CO_{2\ (aq)} + 2e^- \rightleftharpoons CO_{(aq)} + CO_{3\ (aq)}^{2-}$$

To complete the analysis, a final conversion was needed to estimate $\Delta G^0_{t,CO_3^{2-},(DMF)\rightarrow(aq)}$. We estimated this value using the known data for sulfate (SO_4^{2-}; $\Delta G^0_{t,SO_4^{2-},(aq)\rightarrow(DMF)} = 105$ kJ/mol[47]), a dianion for which a value for H_2O to DMF is known. We note that this assumption is comparable to a previous one made for the bicarbonate monoanion.[45]

This produces a final value of $E^0_{2CO_2\rightarrow CO,DMF,CO_3^{2-}}$= –0.863 V vs SHE. Using known conversion factors (Fc^+/Fc = +0.45 V vs SCE in DMF[48]; SCE = +0.244 V vs SHE[49]), a final value of –1.56 V vs Fc^+/Fc is obtained. We emphasize that this value is likely to produce a lower limit for overpotential, given that residual H_2O is often present in electrochemical working solutions (carbonic acid formation is anticipated under CO_2 saturation, pK_a(DMF) = 7.37) and the carbonate dianion is a strong base.

Determination of TOF from Preparative Electrolysis[50]

The integrated expression of current for a homogeneous electrocatalytic response (considering an application of steady-state conditions to the substrate) has been solved previously[45]:

$$\frac{i}{FA} = \frac{n^{\sigma}_{cat}[cat]\sqrt{(k_{obs}C^0_A D_{cat})}}{1 + \exp\left[\frac{F}{RT}\left(E_{app} - E_{1/2}\right)\right]}$$

where i is the average current (Amps) specific to the reaction product of interest, F is Faraday's constant (96485 C mol^{-1}), A is the area of the electrode (cm^2), n^{σ}_{cat} is the number of electrons in the catalytic process (2) with σ = 1 under the assumption that all electrons are delivered to the catalyst by the electrode[51] (σ = 0.5 corresponds to the case where homogeneous electron transfer occurs between catalyst molecules in solution), $[cat]$ is the concentration of the catalyst (mol cm^{-3}), k_{obs} is the apparent turnover frequency (s^{-1}), C_A^0 is the concentration of CO_2 saturated in DMF (mol cm^{-3}), D_{cat} is the diffusion coefficient of the catalyst (cm^2 s^{-1}), R is the ideal gas constant (Joule mol^{-1} K^{-1}), T is the temperature (K), E_{app} is the applied potential during preparative electrolysis (V), and $E_{1/2}$ is the standard potential of the catalyst (V).

$$\frac{i}{A} = J = CO\ specific\ current\ density$$

Substituting and rearranging the first expression to solve for k_{obs}

$$k_{obs} = \frac{J^2 \left(1 + \exp\left[\frac{F}{RT}\left(E_{app} - E_{1/2}\right)\right]\right)^2}{F^2 (n_{cat}^{\sigma}[cat])^2 C_A^0 D_{cat}}$$

with k_{obs} in hand, the TOF can be expressed for a given potential according to the following relationship

$$TOF = \frac{k_{obs}}{1 + \exp\left[\frac{F}{RT}\left(E_{app} - E_{1/2}\right)\right]}$$

Previously reported (data from Ref[2]) parameters for electrocatalysis mediated by Cr(^{tbu}dhbpy)Cl(H_2O) in DMF with 0.62 M PhOH under CO_2 saturation:

- $E_{1/2}$ catalyst: −1.95 V vs Fc^+/Fc
- Temperature: 298.15 K
- [CO_2]: 2.3×10^{-4} mol cm^{-3}
- Catalyst diffusion coefficient: $2 \cdot \times 10^{-6}$ cm^2 s^{-1}

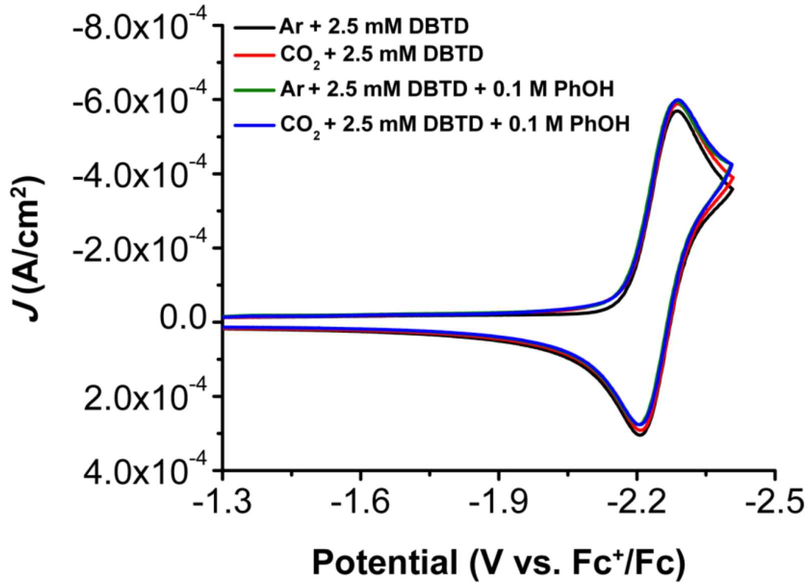

Figure S6.3.1. CVs of 2.5 mM DBTD both with and without 0.1 M PhOH obtained under Ar and CO_2 saturation conditions. Conditions: 0.1 M $TBAPF_6$/*N,N*-DMF; glassy carbon working electrode, glassy carbon counter electrode, Ag/AgCl pseudoreference electrode; 100 mV/s scan rate; referenced to internal ferrocene standard.

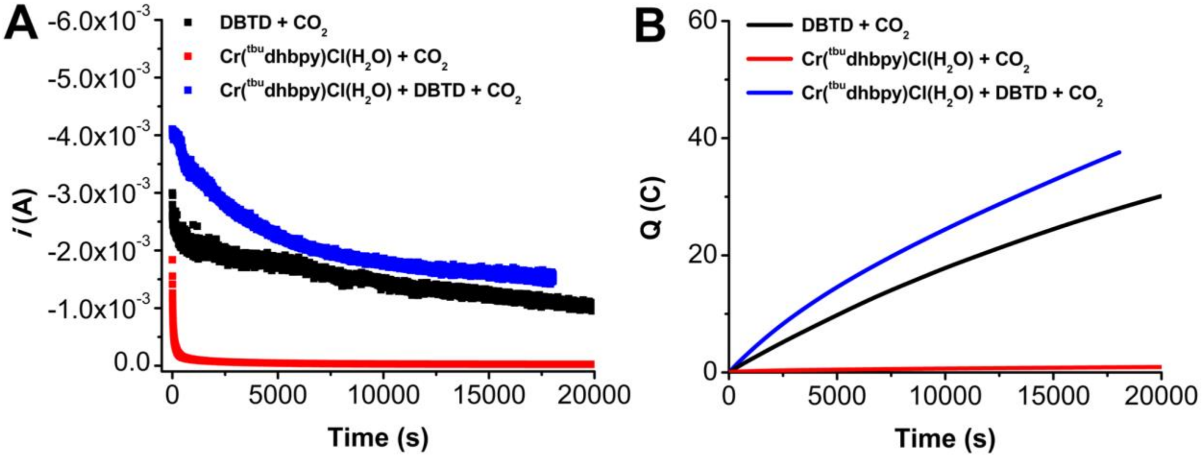

Figure S6.3.2. (**A**) Current versus time trace from bulk electrolysis experiment. (**B**) Charge passed versus time for the bulk electrolysis experiment shown in (**A**). Conditions were 0.5 mM Cr(^{tbu}dhbpy)Cl(H_2O) **1** and 2.5 mM DBTD under a CO_2 atmosphere at either –2.1 (red) or –2.3 (blue and black) V vs Fc^+/Fc in 0.1 M $TBAPF_6$/*N,N*-DMF; working electrode was a glassy carbon rod, counter electrode was a graphite rod, and the reference was a nonaqueous Ag/AgCl pseudoreference electrode; 0.075 M Fc was used as sacrificial oxidant.

Table S6.3.1. Results from CPE experiment in **Figure S6.3.2**, black.

Time (s)	Charge (coulombs)	moles (e^-)	Moles of CO	FE_{CO}
*37814	44.5	1.17 x 10^{-4}	7.06 x 10^{-5}	30.62
*37814	44.5	3.16 x 10^{-4}	7.53 x 10^{-5}	32.64
*37814	44.5	3.90 x 10^{-4}	7.79 x 10^{-5}	33.78

-* indicates a triplicate series of injections carried out upon completion of electrolysis

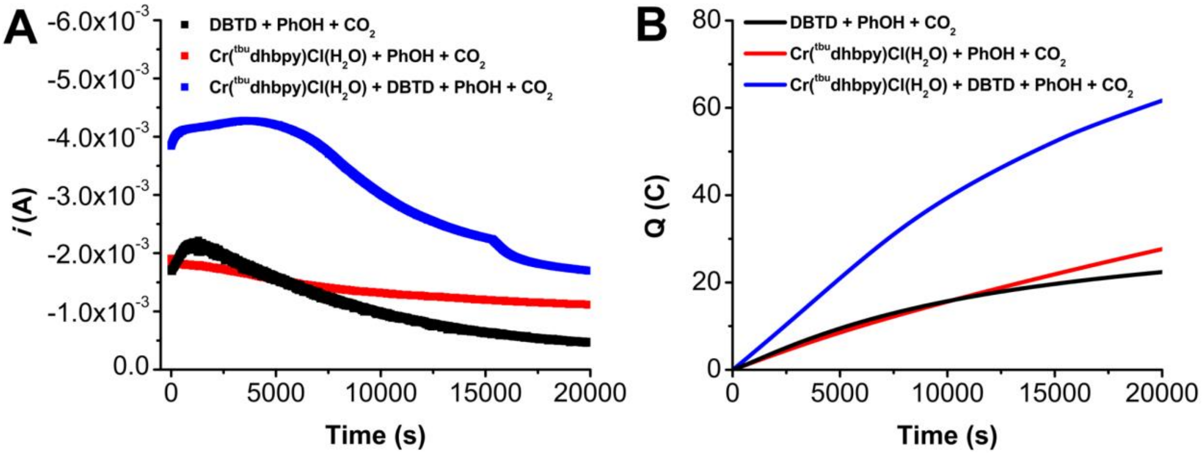

Figure S6.3.3. (**A**) Current versus time trace from bulk electrolysis experiment. (**B**) Charge passed versus time for the bulk electrolysis experiment shown in (**A**). Conditions were 0.5 mM Cr(^{tbu}dhbpy)Cl(H_2O) **1**, 0.48 M PhOH, and 2.5 mM DBTD under a CO_2 atmosphere at –2.3 V vs Fc^+/Fc in 0.1 M $TBAPF_6$/*N,N*-DMF; working electrode was a glassy carbon rod, counter electrode was a graphite rod, and the reference was a nonaqueous Ag/AgCl pseudoreference electrode; 0.075 M Fc was used as sacrificial oxidant.

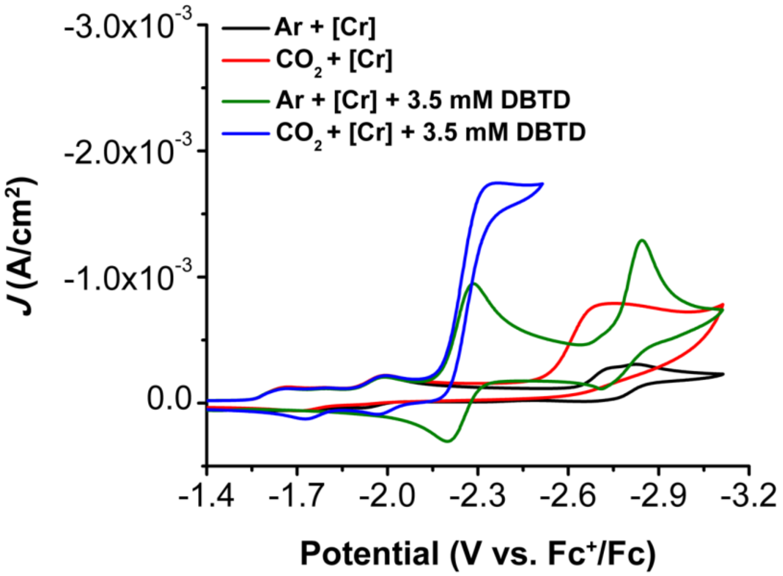

Figure S6.3.4. CVs comparing the reactivity of Cr($^{\text{tbu}}$dhbpy)Cl(H_2O) **1** and DBTD under aprotic conditions. Conditions: 0.1 M TBAPF$_6$/*N,N*-DMF; glassy carbon working electrode, glassy carbon counter electrode, Ag/AgCl pseudoreference electrode; 100 mV/s scan rate; referenced to internal ferrocene standard. [Cr] = Cr($^{\text{tbu}}$dhbpy)Cl(H_2O) **1** (1.0 mM)

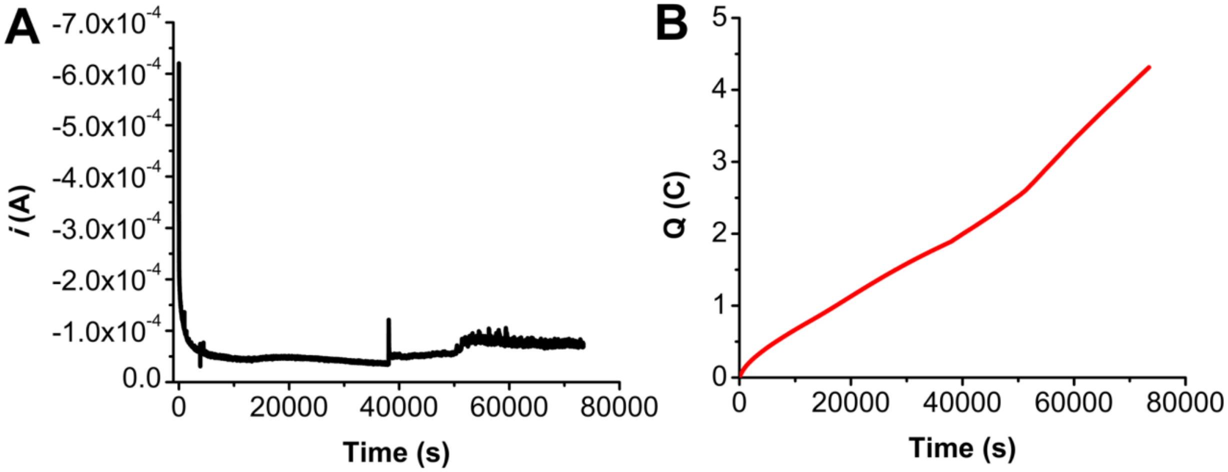

Figure S6.3.5. (**A**) Current versus time trace from bulk electrolysis experiment. (**B**) Charge passed versus time for the bulk electrolysis experiment shown in (**A**). Conditions were 0.58 mM Cr($^{\text{tbu}}$dhbpy)Cl(H_2O) **1** under a CO_2 atmosphere at –2.7 V vs Fc$^+$/Fc in 0.1 M TBAPF$_6$/*N,N*-DMF; working electrode was a glassy carbon rod, counter electrode was a graphite rod, and the reference was a nonaqueous Ag/AgCl pseudoreference electrode; 0.075 M Fc was used as sacrificial oxidant.

Table S6.3.2. Results from CPE experiment in **Figure S6.3.5**.

Time (s)	Charge (coulombs)	moles (e^-)	Moles of CO	FE_{CO} (%)
*73439	4.31	1.17×10^{-4}	1.36×10^{-5}	60.76
*73439	4.31	3.16×10^{-4}	1.22×10^{-5}	54.36
*73439	4.31	3.90×10^{-4}	1.27×10^{-5}	55.30

-* indicates a triplicate series of injections carried out upon completion of electrolysis

Table S6.3.3. Results from CPE experiment in **Figure S6.3.2**, blue.

Time (s)	Charge (coulombs)	moles (e^-)	Moles of CO	FE_{CO} (%)
3620	11.28	1.17×10^{-4}	4.23×10^{-5}	72.42
13550	30.47	3.16×10^{-4}	1.57×10^{-4}	99.66
*18050	37.59	3.90×10^{-4}	1.75×10^{-4}	89.77
*18050	37.59	3.90×10^{-4}	1.90×10^{-4}	97.59
*18050	37.59	3.90×10^{-4}	1.90×10^{-4}	97.54

-* indicates a triplicate series of injections carried out upon completion of electrolysis

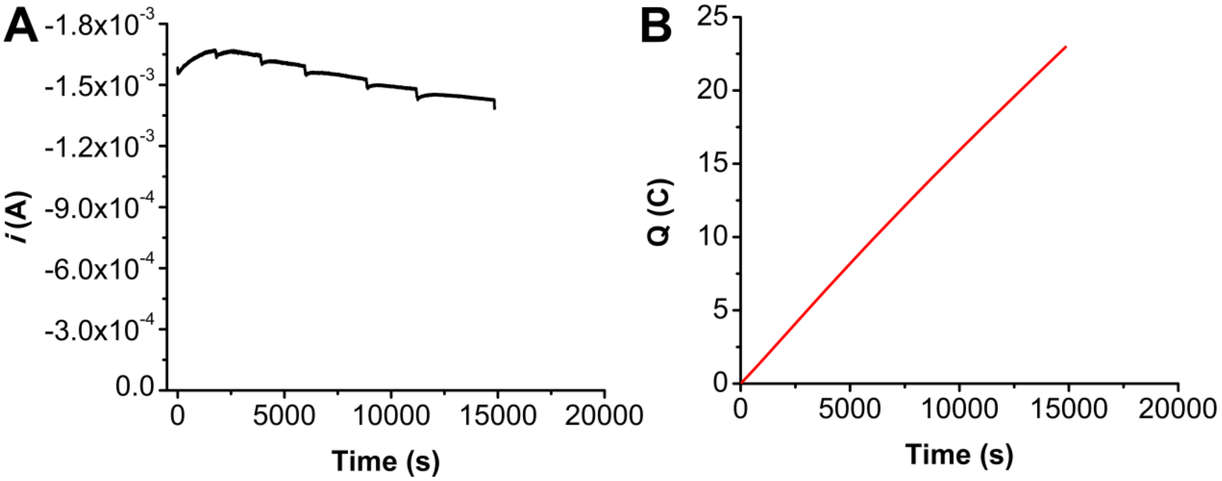

Figure S6.3.6. (**A**) Current versus time trace from bulk electrolysis experiment. (**B**) Charge passed versus time for the bulk electrolysis experiment shown in (**A**). Conditions were 0.5 mM Cr(^{tbu}dhbpy)Cl(H_2O) **1** under a CO_2 atmosphere with 0.6 M PhOH at –2.3 V vs Fc^+/Fc in 0.1 M $TBAPF_6$/*N,N*-DMF; working electrode was a glassy carbon rod, counter electrode was a graphite rod, and the reference was a nonaqueous Ag/AgCl pseudoreference electrode; 0.075 M Fc was used as sacrificial oxidant.

Table S6.3.4. Results from CPE experiment in **Figure S6.3.6**.

Time (s)	Charge (coulombs)	moles (e^-)	Moles of CO	FE_{CO} (%)
6000	9.78	1.01×10^{-4}	4.16×10^{-5}	82.25
8850	14.19	1.47×10^{-4}	8.18×10^{-5}	111.3
11200	17.69	1.83×10^{-4}	1.02×10^{-4}	111.6
*14855	22.96	2.38×10^{-4}	1.40×10^{-4}	117.5
*14855	22.96	2.38×10^{-4}	1.47×10^{-4}	123.9
*14855	22.96	2.38×10^{-4}	1.43×10^{-4}	120.3

-* indicates a triplicate series of injections carried out upon completion of electrolysis

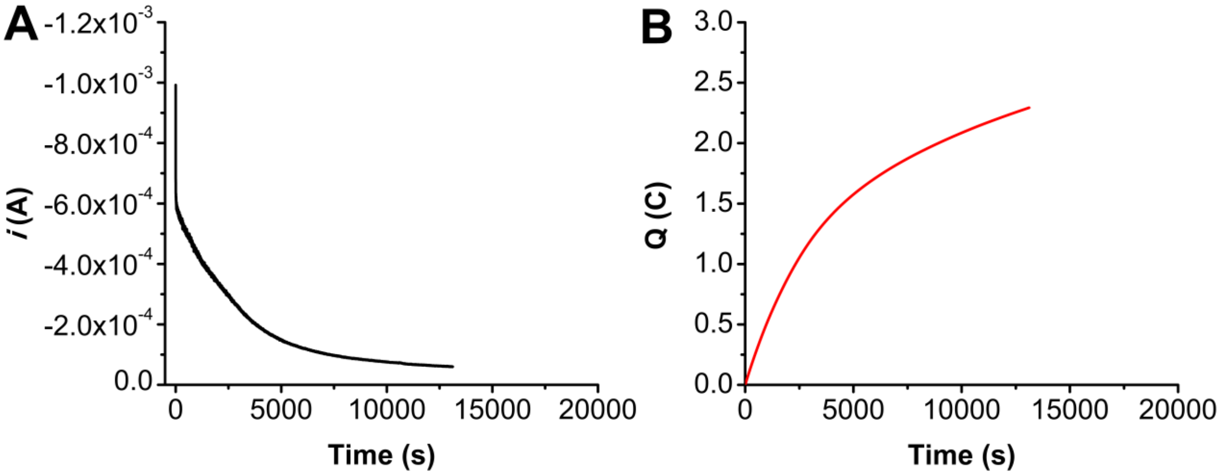

Figure S6.3.7. (**A**) Current versus time trace from bulk electrolysis experiment. (**B**) Charge passed versus time for the bulk electrolysis experiment shown in (**A**). Conditions were 0.5 mM Cr(^{tbu}dhbpy)Cl(H_2O) **1** under a CO_2 atmosphere at –2.3 V vs Fc^+/Fc in 0.1 M $TBAPF_6$/*N,N*-DMF; working electrode was a glassy carbon rod, counter electrode was a graphite rod, and the reference was a nonaqueous Ag/AgCl pseudoreference electrode; 0.075 M Fc was used as sacrificial oxidant.

*Note no CO was detected by GC product analysis in this experiment.

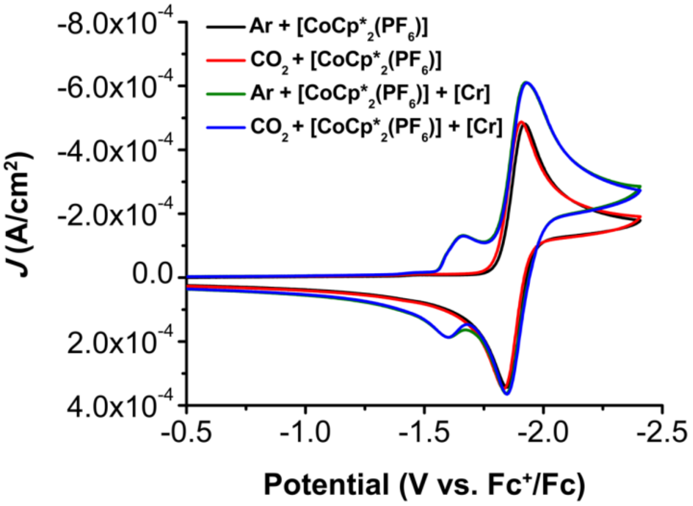

Figure S6.3.8. CVs evaluating the aprotic CO_2 reduction activity of Cr(^{tbu}dhbpy)Cl(H_2O) **1** and decamethylcobaltocene Cp^*_2Co under aprotic conditions. Conditions: 0.1 M $TBAPF_6$/*N,N*-DMF; glassy carbon working electrode, glassy carbon counter electrode, Ag/AgCl pseudoreference electrode; 100 mV/s scan rate; referenced to internal ferrocene standard. [Cr] = Cr(^{tbu}dhbpy)Cl(H_2O) **1** (1.0 mM).

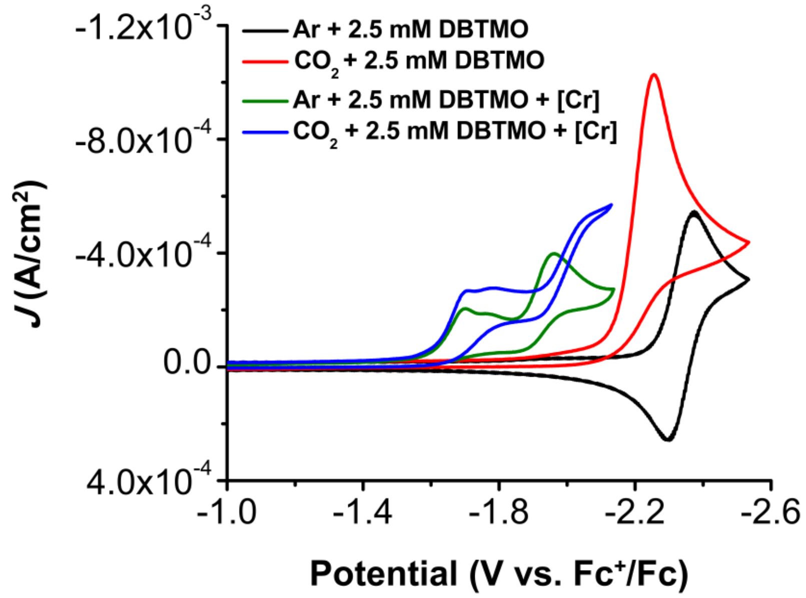

Figure S6.3.9. CVs evaluating the aprotic CO_2 reduction activity of Cr(^{tbu}dhbpy)Cl(H_2O) **1** and dibenzothiophene-5-oxide (DBTMO). Conditions: 0.1 M $TBAPF_6$/*N,N*-DMF; glassy carbon working electrode, glassy carbon counter electrode, Ag/AgCl pseudoreference electrode; 100 mV/s scan rate; referenced to internal ferrocene standard. [Cr] = Cr(^{tbu}dhbpy)Cl(H_2O) **1** (1.0 mM).

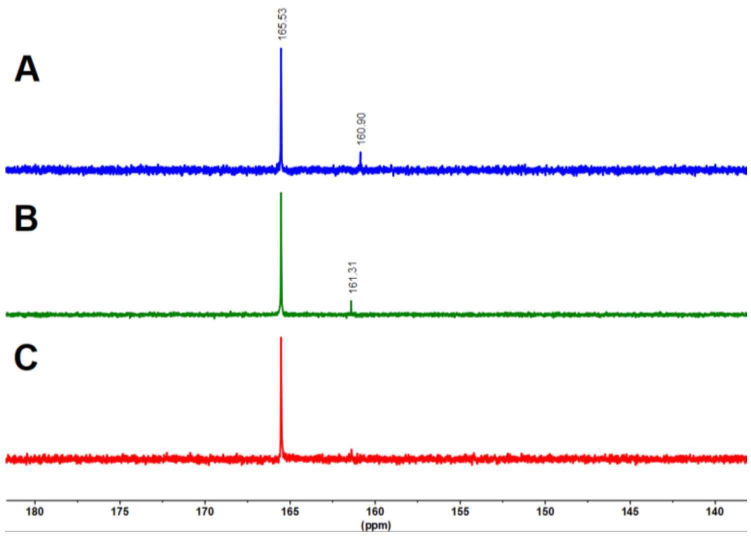

Figure S6.3.10. $^{13}C\{^1H\}$ NMRs in D_2O for product analysis of bulk electrolysis solutions. (**A**) $^{13}C\{^1H\}$ NMR in D_2O from prepared sample of $TBA^+[HCO_3]^-$ that was synthesized according to reported procedures.[52] (**B**) $^{13}C\{^1H\}$ NMR in D_2O from the post electrolysis solution of Cr(^{tbu}dhbpy)Cl(H_2O) **1** and DBTD under a CO_2 atmosphere at –2.3 V vs. Fc^+/Fc (**Figure S6.3.2**, blue). (**C**) $^{13}C\{^1H\}$ NMR in D_2O from the post electrolysis solution of DBTD under a CO_2 atmosphere at –2.3 V vs. Fc^+/Fc (**Figure S6.3.2**, black). For (**B**) and (**C**) the sample was prepared from a 50/50 mixture of the electrolysis solution and D_2O. For (**B**)

N,N-DMF was added as an internal reference (δ 165.53) to the sample that was dissolved in D_2O. Peak at δ 160.9 is assigned to HCO_3^-.

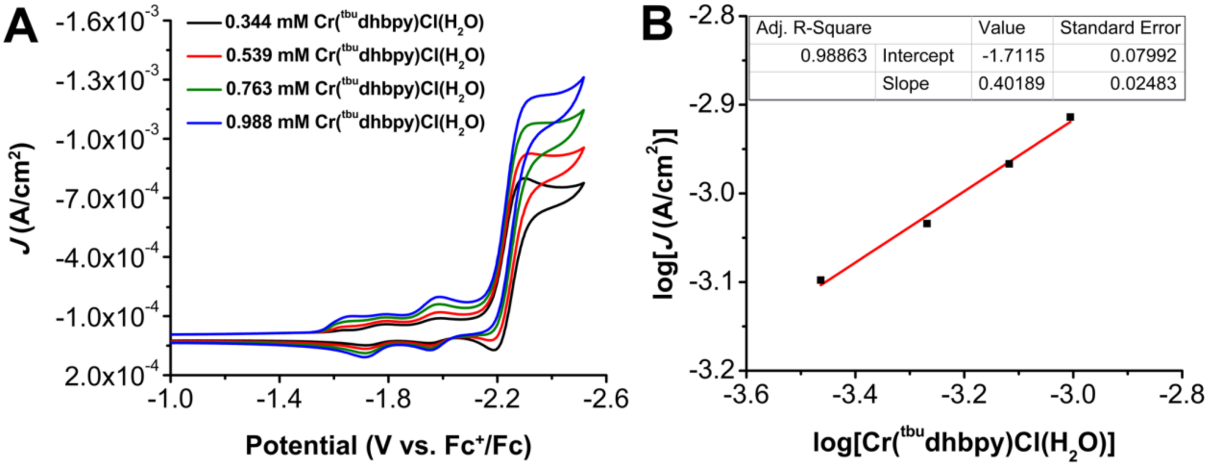

Figure S6.3.11. (**A**) CVs of Cr(^{tbu}dhbpy)Cl(H_2O) **1** at variable concentrations, obtained under CO_2 saturation with 2.5 mM DBTD. Conditions: 1.0 mM analyte with 0.1 M $TBAPF_6$/*N,N*-DMF; glassy carbon working electrode, glassy carbon counter electrode, Ag/AgCl pseudoreference electrode; 100 mV/s scan rate; referenced to internal ferrocene standard. (**B**) Log-log plot from data obtained from CVs of Cr(^{tbu}dhbpy)Cl(H_2O) **1** under variable concentration conditions with 2.5 mM DBTD under CO_2 saturation.

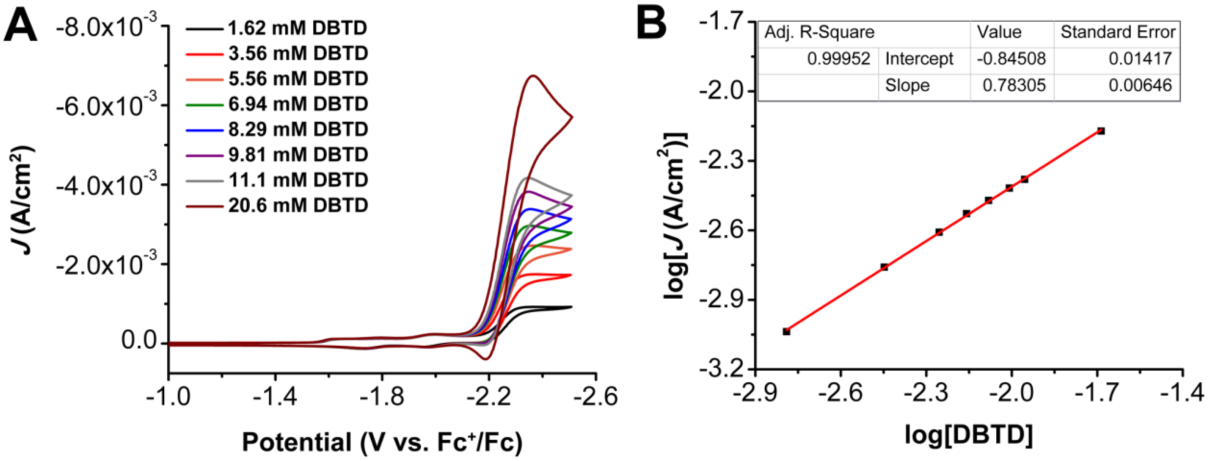

Figure S6.3.12. (**A**) CVs of DBTD at variable concentrations, obtained under CO_2 saturation with 1.0 mM Cr(^{tbu}dhbpy)Cl(H_2O) **1**. Conditions: 0.1 M $TBAPF_6$/*N,N*-DMF; glassy carbon working electrode, glassy carbon counter electrode, Ag/AgCl pseudoreference electrode; 100 mV/s scan rate; referenced to internal ferrocene standard. (**B**) Log-log plot from data obtained from CVs of DBTD under variable concentration conditions with 1.0 mM Cr(^{tbu}dhbpy)Cl(H_2O) **1** under CO_2 saturation.

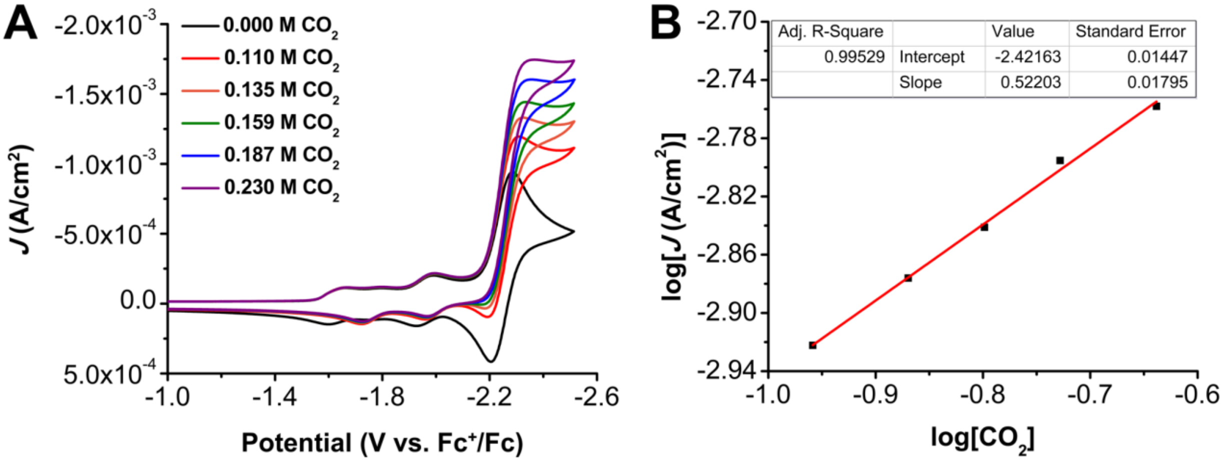

Figure S6.3.13. (**A**) CVs of 1.0 mM Cr(^{tbu}dhbpy)Cl(H_2O) **1** with 3.5 mM DBTD at variable CO_2 concentrations. Conditions: 0.1 M $TBAPF_6$/*N,N*-DMF; glassy carbon working electrode, glassy carbon counter electrode, Ag/AgCl pseudoreference electrode; 100 mV/s scan rate; referenced to internal ferrocene standard. (**B**) Log-log plot from data obtained from CVs of 1.0 mM Cr(^{tbu}dhbpy)Cl(H_2O) **1** with 3.5 mM DBTD at variable CO_2 concentrations.

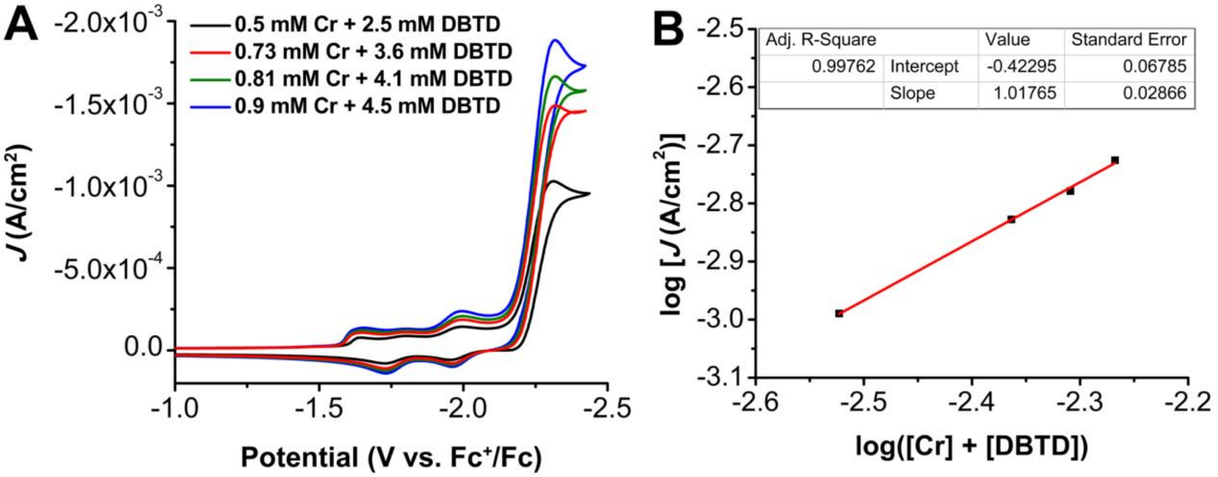

Figure S6.3.14. (**A**) CVs where the concentrations of Cr(^{tbu}dhbpy)Cl(H_2O) **1** and DBTD were varied at a fixed 1:5 ratio of **1**:DBTD under CO_2 saturation conditions. Conditions: 0.1 M $TBAPF_6$/*N,N*-DMF; glassy carbon working electrode, glassy carbon counter electrode, Ag/AgCl pseudoreference electrode; 100 mV/s scan rate; referenced to internal ferrocene standard. (**B**) Log-log plot from data in (**A**) at 2.36 V vs Fc$^+$/Fc. For the x-axis, a log of the total concentration, taken as the sum of the concentration of Cr and DBTD, was used.

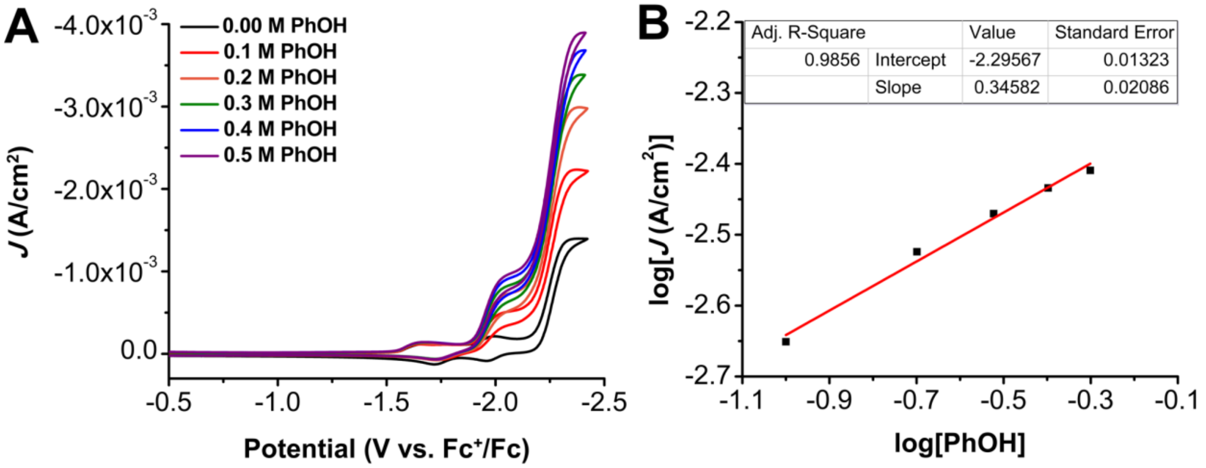

Figure S6.3.15. (**A**) CVs of PhOH at variable concentrations, obtained under CO_2 saturation with 1.0 mM Cr(^{tbu}dhbpy)Cl(H_2O) **1** and 2.5 mM DBTD. Conditions: 0.1 M $TBAPF_6$/*N,N*-DMF; glassy carbon working electrode, glassy carbon counter electrode, Ag/AgCl pseudoreference electrode; 100 mV/s scan rate; referenced to internal ferrocene standard. (**B**) Log-log plot from data obtained from CVs of PhOH at variable concentrations with 1.0 mM Cr(^{tbu}dhbpy)Cl(H_2O) **1** and 2.5 mM DBTD under CO_2 saturation. Current density at -2.38 V vs Fc+/Fc was used in the loglog plot analysis.

Table S6.3.5. Results from CPE experiment in **Figure S6.3.3**, blue.

Time (s)	Charge (coulombs)	moles (e^-)	Moles of CO	FE_{CO} (%)
5100	21.40	2.22×10^{-4}	1.40×10^{-4}	126.4
*23736	67.70	7.02×10^{-4}	3.24×10^{-4}	92.38
*23736	67.70	7.02×10^{-4}	3.33×10^{-4}	94.78
*23736	67.70	7.02×10^{-4}	3.27×10^{-4}	93.25

-* indicates a triplicate series of injections carried out upon completion of electrolysis

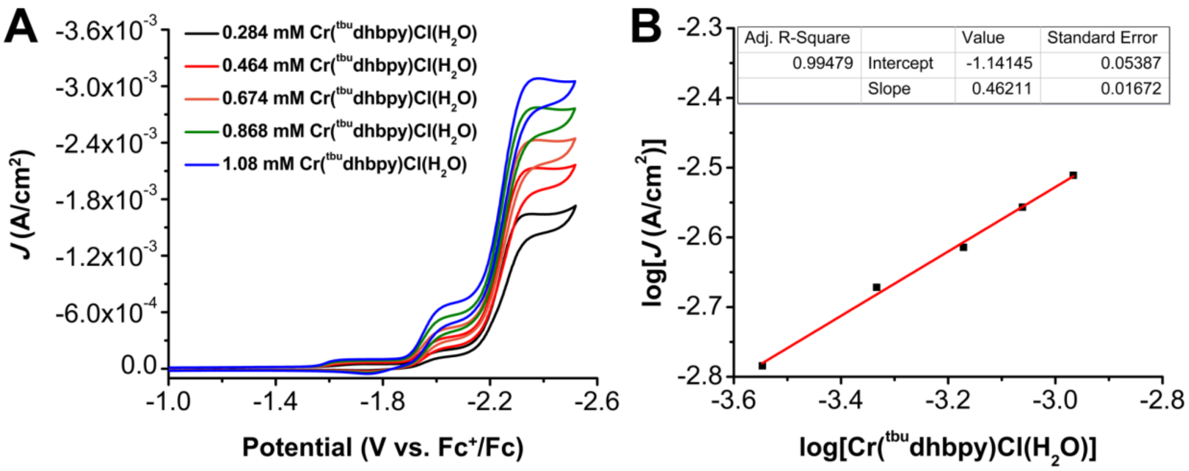

Adj. R-Square		Value	Standard Error
0.99479	Intercept	-1.14145	0.05387
	Slope	0.46211	0.01672

Figure S6.3.16. (**A**) CVs of Cr(^{tbu}dhbpy)Cl(H_2O) **1** at variable concentrations, obtained under CO_2 saturation with 2.82 mM DBTD and 0.325 M PHOH. Conditions: 1.0 mM analyte with 0.1 M $TBAPF_6$/*N,N*-DMF; glassy carbon working electrode, glassy carbon counter electrode, Ag/AgCl pseudoreference electrode; 100 mV/s scan rate; referenced to internal ferrocene standard. (**B**) Log-log plot from data obtained from CVs of Cr(^{tbu}dhbpy)Cl(H_2O) **1** under variable concentration conditions with 2.5 mM DBTD and 0.325 M PhOH under CO_2 saturation.

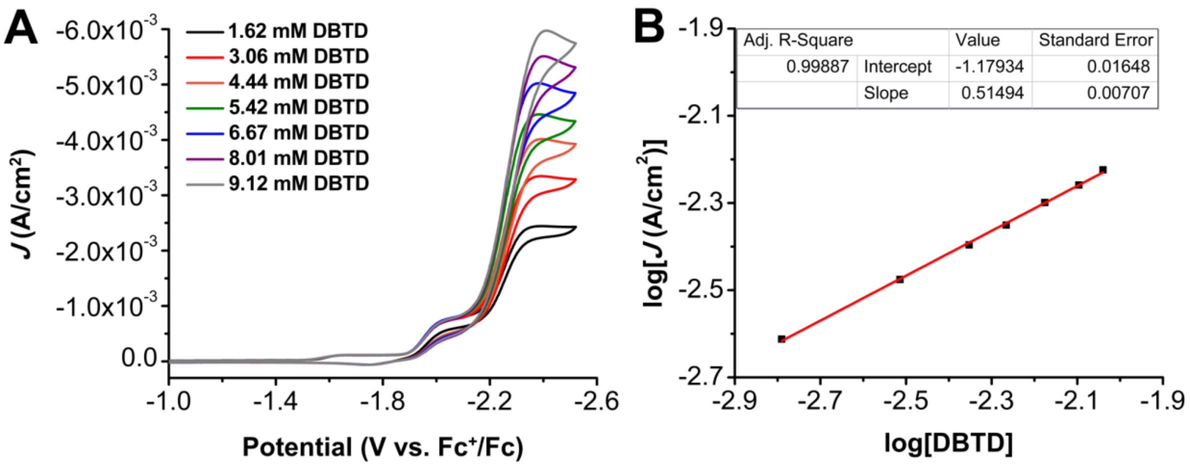

Adj. R-Square		Value	Standard Error
0.99887	Intercept	-1.17934	0.01648
	Slope	0.51494	0.00707

Figure S6.3.17. (**A**) CVs of DBTD at variable concentrations, obtained under CO_2 saturation with 1.0 mM Cr(^{tbu}dhbpy)Cl(H_2O) **1** and 0.325 M PhOH. Conditions: 0.1 M $TBAPF_6$/*N,N*-DMF; glassy carbon working electrode, glassy carbon counter electrode, Ag/AgCl pseudoreference electrode; 100 mV/s scan rate; referenced to internal ferrocene standard. (**B**) Log-log plot from data obtained from CVs of DBTD under variable concentration conditions with 1.0 mM Cr(^{tbu}dhbpy)Cl(H_2O) **1** and 0.325 M PhOH under CO_2 saturation.

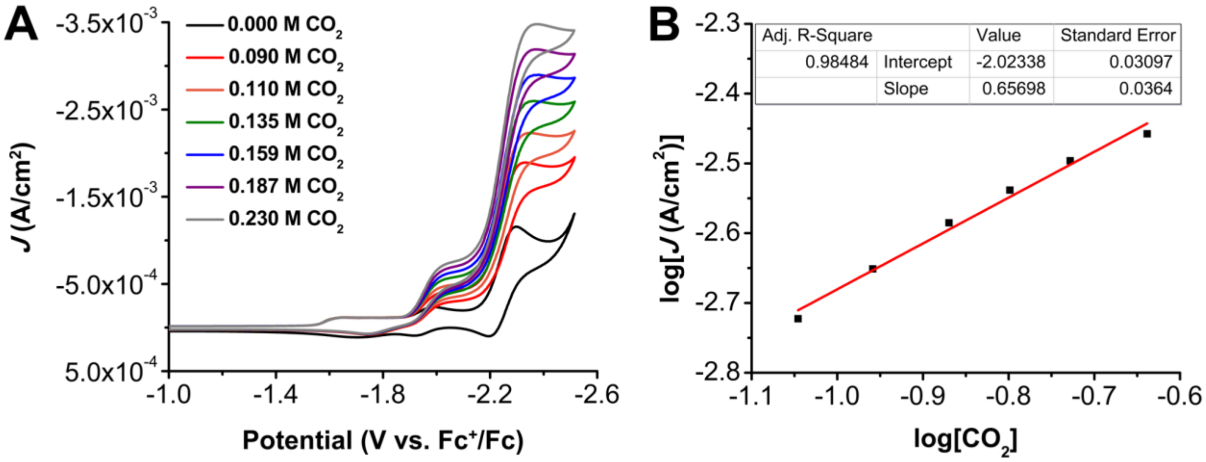

Adj. R-Square		Value	Standard Error
0.98484	Intercept	-2.02338	0.03097
	Slope	0.65698	0.0364

Figure S6.3.18. (**A**) CVs of 1.0 mM Cr(^{tbu}dhbpy)Cl(H_2O) **1** with 3.5 mM DBTD and 0.239 M PhOH at variable CO_2 concentrations. Conditions: 0.1 M $TBAPF_6$/*N,N*-DMF; glassy carbon working electrode, glassy carbon counter electrode, Ag/AgCl pseudoreference electrode; 100 mV/s scan rate; referenced to internal ferrocene standard. (**B**) Log-log plot from data obtained from CVs of 1.0 mM Cr(^{tbu}dhbpy)Cl(H_2O) **1** with 3.5 mM DBTD and 0.239 M PhOH at variable CO_2 concentrations.

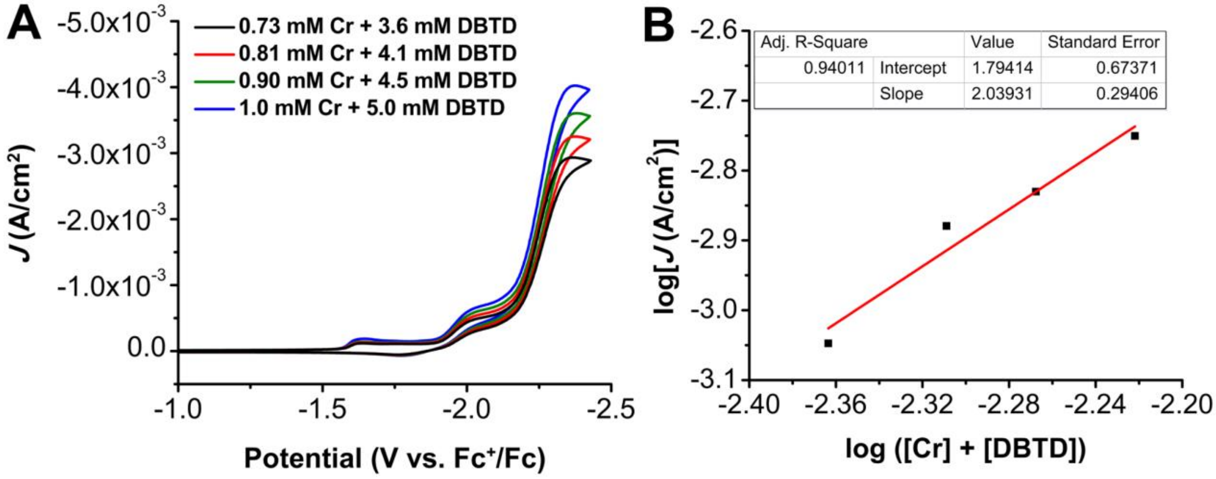

Adj. R-Square		Value	Standard Error
0.94011	Intercept	1.79414	0.67371
	Slope	2.03931	0.29406

Figure S6.3.19. (**A**) CVs where the concentrations of Cr(^{tbu}dhbpy)Cl(H_2O) **1** and DBTD were varied at a fixed 1:5 ratio of **1**:DBTD under CO_2 saturation conditions with 0.2 M PhOH. Conditions: 0.1 M $TBAPF_6$/*N,N*-DMF; glassy carbon working electrode, glassy carbon counter electrode, Ag/AgCl pseudoreference electrode; 100 mV/s scan rate; referenced to internal ferrocene standard. (**B**) Log-log plot from data in (**A**) at 2.38 V vs Fc⁺/Fc. For the x-axis, a log of the total concentration, taken as the sum of the concentration of Cr and DBTD, was used.

6.7 Acknowledgments. C.W.M. conceived and supervised the experiments; all experiments were carried out by S.L.H.; all computational work was carried out by S.L.H. and J.J.M.; E.N.C. and A.G.R. assisted in developing adequate experimental procedures specific to this manuscript.

6.8 References:

1. DuBois, D. L., *Inorg. Chem.* **2014,** *53*, 3935-3960.
2. Das, B.; Thapper, A.; Ott, S.; Colbran, S. B., *Sustain. Energy Fuels* **2019,** *3*, 2159-2175.
3. IPCC *Global Warming of 1.5°C. An IPCC Special Report*; World Meterological Organization: Geneva, Switzerland, 2018.
4. Appel, A. M.; Bercaw, J. E.; Bocarsly, A. B.; Dobbek, H.; DuBois, D. L.; Dupuis, M.; Ferry, J. G.; Fujita, E.; Hille, R.; Kenis, P. J. A.; Kerfeld, C. A.; Morris, R. H.; Peden, C. H. F.; Portis, A. R.; Ragsdale, S. W.; Rauchfuss, T. B.; Reek, J. N. H.; Seefeldt, L. C.; Thauer, R. K.; Waldrop, G. L., *Chem. Rev.* **2013,** *113*, 6621–6658.
5. Aresta, M.; Dibenedetto, A.; Angelini, A., *Chem. Rev.* **2014,** *114*, 1709-1742.
6. Morris, A. J.; Meyer, G. J.; Fujita, E., *Acc. Chem. Res.* **2009,** *42*, 1983–1994.
7. Francke, R.; Schille, B.; Roemelt, M., *Chem. Rev.* **2018,** *118*, 4631-4701.
8. Kinzel, N. W.; Werlé, C.; Leitner, W., *Angew. Chem., Int. Ed.* **2021**, https://doi.org/10.1002/anie.202006988.
9. Kinzel, N. W.; Werlé, C.; Leitner, W., *Angewandte Chemie*, https://doi.org/10.1002/ange.202006988.
10. Jacobs, G.; Davis, B. H., Chapter 5 Conversion of Biomass to Liquid Fuels and Chemicals via the Fischer–Tropsch Synthesis Route. In *Thermochemical*

Conversion of Biomass to Liquid Fuels and Chemicals, The Royal Society of Chemistry: 2010; pp 95-124.

11. Seh, Z. W.; Kibsgaard, J.; Dickens, C. F.; Chorkendorff, I.; Nørskov, J. K.; Jaramillo, T. F., *Science* **2017,** *355*, eaad4998.
12. Alper, E.; Yuksel Orhan, O., *Petroleum* **2017,** *3*, 109-126.
13. Agarwal, A. S.; Rode, E.; Sridhar, N.; Hill, D., Conversion of CO2 to Value-Added Chemicals: Opportunities and Challenges. In *Handbook of Climate Change Mitigation and Adaptation*, Chen, W.-Y.; Suzuki, T.; Lackner, M., Eds. Springer New York: New York, NY, 2014; pp 1-40.
14. Qiao, J.; Liu, Y.; Hong, F.; Zhang, J., *Chem. Soc. Rev.* **2014,** *43*, 631-675.
15. Benson, E. E.; Kubiak, C. P.; Sathrum, A. J.; Smieja, J. M., *Chem. Soc. Rev.* **2009,** *38*, 89-99.
16. Melin, F.; Hellwig, P., *Chem. Rev.* **2020,** *120*, 10244-10297.
17. Smith, P. T.; Weng, S.; Chang, C. J., *Inorg. Chem.* **2020,** *59*, 9270–9278.
18. Anson, C. W.; Ghosh, S.; Hammes-Schiffer, S.; Stahl, S. S., *J. Am. Chem. Soc.* **2016,** *138*, 4186-4193.
19. Landa-Medrano, I.; Lozano, I.; Ortiz-Vitoriano, N.; Ruiz de Larramendi, I.; Rojo, T., *J. Mat. Chem. A* **2019,** *7*, 8746-8764.
20. Liang, Z.; Lu, Y.-C., *J. Am. Chem. Soc.* **2016,** *138*, 7574-7583.
21. Anson, C. W.; Stahl, S. S., *J. Am. Chem. Soc.* **2017,** *139*, 18472-18475.
22. Li, J.; Shen, P.; Zhao, Z.; Tang Ben, Z., *CCS Chemistry 1*, 181-196.
23. Morisaki, Y.; Chujo, Y., *Polym. Chem.* **2011,** *2*, 1249-1257.

24. Bai, M.; Liang, J.; Xie, L.; Sanvito, S.; Mao, B.; Hou, S., *J. Chem. Phys.* **2012,** *136*, 104701.

25. Morisaki, Y.; Chujo, Y., *Angew. Chem., Int. Ed.* **2006,** *45*, 6430-6437.

26. Morisaki, Y.; Chujo, Y., *Angew. Chem.* **2006,** *118*, 6580-6587.

27. Breysse, M.; Djega-Mariadassou, G.; Pessayre, S.; Geantet, C.; Vrinat, M.; Pérot, G.; Lemaire, M., *Catal. Today* **2003,** *84*, 129-138.

28. Oka, K.; Kato, R.; Oyaizu, K.; Nishide, H., *Adv. Funct. Mat.* **2018,** *28*, 1805858.

29. Hooe, S. L.; Dressel, J. M.; Dickie, D. A.; Machan, C. W., *ACS Catal.* **2020,** *10*, 1146-1151.

30. Moreno, J. J.; Hooe, S. L.; Machan, C. W., *Inorg. Chem.* **2020**, DOI:10.1021/acs.inorgchem.0c03136.

31. Chen, H.; Simoska, O.; Lim, K.; Grattieri, M.; Yuan, M.; Dong, F.; Lee, Y. S.; Beaver, K.; Weliwatte, S.; Gaffney, E. M.; Minteer, S. D., *Chem. Rev.* **2020,** *120*, 12903-12993.

32. Boschloo, G.; Hagfeldt, A., *Acc. Chem. Research* **2009,** *42*, 1819-1826.

33. Tsai, E. W.; Throckmorton, L.; McKellar, R.; Baar, M.; Kluba, M.; Marynick, D. S.; Rajeshwar, K.; Ternay, A. L., *J. Electroanal. Chem. Interf. Electrochem.* **1986,** *210*, 45-67.

34. Savéant, J.-M.; Costentin, C., *Elements of Molecular and Biomolecular Electrochemistry: An Electrochemical Approach to Electron Transfer Chemistry*. Wiley: 2019.

35. Dikarev, E. V.; Becker, R. Y.; Block, E.; Shan, Z.; Haltiwanger, R. C.; Petrukhina, M. A., *Inorg. Chem.* **2003,** *42*, 7098-7105.

36. Cotton, F. A.; Felthouse, T. R., *Inorg. Chem.* **1981,** *20*, 2703-2708.

37. Nichols, A. W.; Chatterjee, S.; Sabat, M.; Machan, C. W., *Inorg. Chem.* **2018,** *57*, 2111-2121.

38. Hooe, S. L.; Dressel, J. M.; Dickie, D. A.; Machan, C. W., *ACS Catal.* **2020,** *10*, 1146-1151.

39. Moreno, J. J.; Hooe, S. L.; Machan, C. W., *ChemRxiv* **2020,** *DOI: 10.26434/chemrxiv.12363356.v1*.

40. Pegis, M. L.; Wise, C. F.; Martin, D. J.; Mayer, J. M., *Chem. Rev.* **2018,** *118*, 2340-2391.

41. Pegis, M. L.; Roberts, J. A. S.; Wasylenko, D. J.; Mader, E. A.; Appel, A. M.; Mayer, J. M., *Inorg. Chem.* **2015,** *54*, 11883-11888.

42. Nielsen, M. F. H., Ole, *Acta Chemica Scandinavica* **1992**, 883-896.

43. Roy, S.; Sharma, B.; Pécaut, J.; Simon, P.; Fontecave, M.; Tran, P. D.; Derat, E.; Artero, V., *J. Am. Chem. Soc.* **2017,** *139*, 3685-3696.

44. Matsubara, Y., *ACS Energy Lett.* **2019,** *4*, 1999-2004.

45. Costentin, C.; Drouet, S.; Robert, M.; Savéant, J.-M., *J. Am. Chem. Soc.* **2012,** *134*, 11235-11242.

46. CRC Handbook of Chemistry and Physics. 101st ed.; Rumble, J. R., Ed. CRC Press, Taylor & Francis Group, an Informa Group Company: 2020. (accessed 01/11/2021).

47. Ion Solvation in Neat Solvents. In *Ions in Solution and their Solvation*, 2015; pp 107-155.

48. Connelly, N. G.; Geiger, W. E., *Chem. Rev.* **1996,** *96*, 877-910.

49. Sawyer, D. T.; Sobkowiak, A.; Roberts, J. L., *Electrochemistry for Chemists*. 2nd ed.; John Wiley & Sons, Inc.: New York, 1995.

50. Moreno, J. J.; Hooe, S. L.; Machan, C. W., *Inorg. Chem.* **2021**, 10.1021/acs.inorgchem.0c03136.

51. Cometto, C.; Chen, L.; Lo, P.-K.; Guo, Z.; Lau, K.-C.; Anxolabéhère-Mallart, E.; Fave, C.; Lau, T.-C.; Robert, M., *ACS Catal.* **2018,** *8*, 3411-3417.

52. Cheng, S. C.; Blaine, C. A.; Hill, M. G.; Mann, K. R., *Inorg. Chem.* **1996,** *35*, 7704-7708.

Chapter 7

Summary and Outlook

7.1 Overview of Completed Research

The first portion of the research detailed in this thesis was focused on the use of a molecular manganese catalyst for the oxygen reduction reaction. The synthesis and electrocatalytic reduction of dioxygen by a molecular manganese (III) complex with a tetradentate dianionic bipyridine-based ligand, Mn(^{tbu}dhbpy)Cl, was initially investigated. Electrochemical characterization suggests that upon reduction to Mn(II), the coordinated phenolate moieties of the ligand are protonated with a Nernstian dependence on the added proton source, allowing protons and electrons to be incorporated into the overall complex. The parent species is competent for the electrocatalytic reduction of dioxygen to H_2O_2 with 81±4% Faradaic efficiency. Mechanistic studies suggest that the catalytically active species has been generated through phenol acting as a proton donor to the Mn complex following a single-electron reduction of the parent species, generating a neutral species with a vacant coordination site at the metal center. As a consequence, the active catalyst has a pendent proton source in close proximity to the active site for subsequent intramolecular reactions.[1]

Spectrochemical stopped-flow analyses with this Mn(^{tbu}dhbpy)Cl catalyst utilized decamethylferrocene as a reductant and uncovered a change in mechanism based on the nature of the reductant, although H_2O_2 is still generated when a homogeneous reductant is used. Mechanistic studies under buffered conditions in acetonitrile (MeCN) suggest that when a homogeneous reductant is used, a disproportionation pathway occurs that does not demonstrate an acid pK_a dependence.[2] Additional studies with the Mn(^{tbu}dhbpy)Cl catalyst have utilized *p*-benzoquinone as a mediator to alter catalyst selectivity to H_2O over H_2O_2.

Studies on the molecular electrocatalytic reduction of CO_2 began with the first molecular chromium (Cr) electrocatalyst, Cr(^{tbu}dhbpy)Cl(H_2O) where 6,6′-di(3,5-di-*tert*-butyl-2-phenolate)-2,2′-bipyridine = [^{tbu}dhbpy]$^{2-}$, for the selective reduction of CO_2 to CO and H_2O with quantitative efficiencies. It was found that an added proton donor, phenol (PhOH), was required for catalysis. However, under CO_2 saturation conditions with an added proton donor, the Cr(^{tbu}dhbpy)Cl(H_2O) catalyst was able to achieve turnover frequencies of 5.7 ± 0.1 s^{-1} with a high Faradaic efficiency for CO (FE_{CO} = 96 ± 8) at an overpotential of 110 mV. Variable concentration electrochemical analyses experimentally determined the reaction to be first order with respect to PhOH, CO_2, and Cr(^{tbu}dhbpy)Cl(H_2O).[3] A mechanism was proposed from the experimental and computational studies and the rate determining step was suggested to be the C-OH bond cleavage of the carboxylate intermediate.[3-4]

Additional experimental studies with this Cr complex have involved the use of an organic mediator, dibenzothiophene-5,5-dioxide, as an additive to enhance the previously reported catalysis and enable new reactivity under aprotic conditions. Both experimental and computational analyses are were carried out for this system and computational studies have shown the importance of dispersion and electronic coupling between the organic mediator and the bipyridine backbone of the catalyst ligand framework.

7.2 Extensions Beyond the Completed Research

The completed research described herein has laid the groundwork for numerous potential expansions based on these initial results. One possible expansion of interest has been the alteration of the ligand framework (**Figure 7.2.1**). While modification of the phenolate moieties of the ^{tbu}dhbpy ligand has been done,[5] the most noteworthy success has been observed experimentally via modification of the bipyridine backbone (**Figure 7.2.1 A**). The use and modification of a phenanthroline backbone in place of the bipyridine in the ligand backbone is also being analyzed (**Figure 7.2.1 B and C**). Water-soluble versions of the ligand framework offer a novel expansion of this research in terms of applicability and the ability to gain mechanistic insight based on a more clearly defined pK_a for these systems.

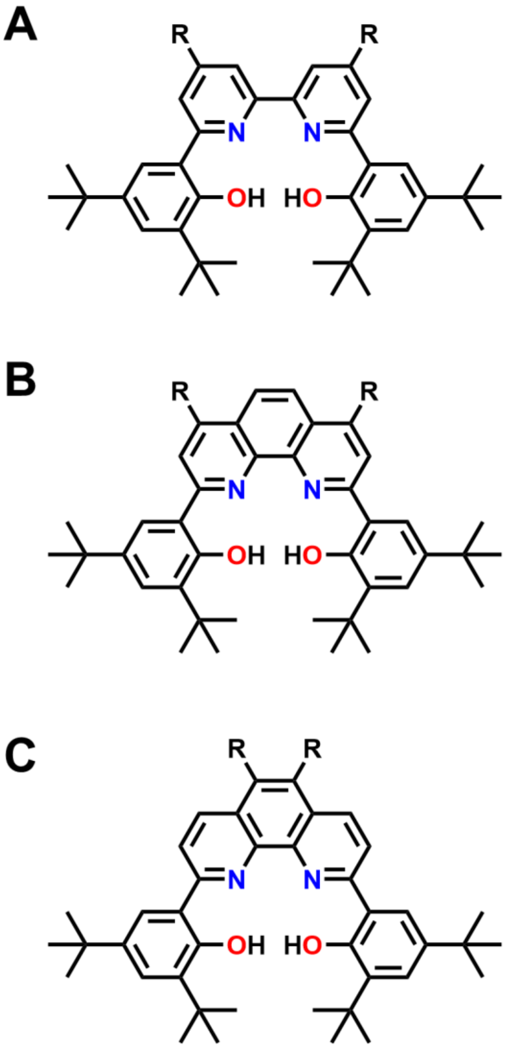

Figure 7.2.1. Noteworthy potential expansions of the $^{\text{tbu}}$dhbpy ligand framework where R indicates functional group tolerance and modification.

Another area of expansion beyond the catalyst ligand framework includes the modification of the added organic mediator. This can be carried out by modifying the reduction potential, steric profile, or proton donating ability of the added mediator. However, it is important to note that it is likely the case that a well-understood mechanism must be elucidated before iterative optimization strategies of the organic mediator can be achieved.

7.3 Outlook on the Field – ORR and CO2RR Catalysis

In the field of ORR and CO2RR catalysis there are two areas which have gained increasing interest over recent years and will likely guide the focus of future research within the field. The first includes the use of organic mediators as a way to incorporate additional protons and electrons into a catalyst system. This area of research has gained interest in electrochemical ORR and CO2RR systems but is still currently not well understood and developed.[6-9] Future research in the field will lead to additional mechanistic insight into the role of the added mediator as well as the development of iterative optimization strategies for modification of the added mediator.

The second area of research in the field that will likely guide the focus of future research is that related to the development of linear free energy relationships (LFERs) for catalytic systems. While LFERs are not new to the field, the manner in which they are understood and developed has gained increasing amounts of interests over recent years. For any given catalyst system, the rate of the reaction is dependent on the rate-limiting step of the reaction. The ability to understand how to scale and manipulate the rate-limiting step of a mechanism has become a paramount method for the development of iterative optimization strategies in catalyst systems.[10-14] Additionally, the ability to understand and control broken scaling relationships in both catalytic ORR and CO2RR systems will continue to motivate research in this area.

7.4 References

1. Hooe, S. L.; Rheingold, A. L.; Machan, C. W., *J. Am. Chem. Soc.* **2018,** *140*, 3232-3241.
2. Hooe, S. L.; Machan, C. W., *J. Am. Chem. Soc.* **2019,** *141*, 4379-4387.
3. Hooe, S. L.; Dressel, J. M.; Dickie, D. A.; Machan, C. W., *ACS Catal.* **2020,** *10*, 1146-1151.
4. Moreno, J. J.; Hooe, S. L.; Machan, C. W., *ChemRxiv* **2020,** *DOI: 10.26434/chemrxiv.12363356.v1*.
5. Nichols, A. W.; Hooe, S. L.; Kuehner, J. S.; Dickie, D. A.; Machan, C. W., *Inorg. Chem.* **2020,** *59*, 5854-5864.
6. Lee, K. J.; Lodaya, K. M.; Gruninger, C. T.; Rountree, E. S.; Dempsey, J. L., *Chem. Sci.* **2020,** *11*, 9836-9851.
7. Anson, C. W.; Ghosh, S.; Hammes-Schiffer, S.; Stahl, S. S., *J. Am. Chem. Soc.* **2016,** *138*, 4186-4193.
8. Anson, C. W.; Stahl, S. S., *J. Am. Chem. Soc.* **2017,** *139*, 18472-18475.
9. Smith, P. T.; Weng, S.; Chang, C. J., *Inorg. Chem.* **2020,** *59*, 9270-9278.
10. Martin, D. J.; Wise, C. F.; Pegis, M. L.; Mayer, J. M., *Acc. Chem. Research* **2020**.
11. Pegis, M. L.; Wise, C. F.; Koronkiewicz, B.; Mayer, J. M., *J. Am. Chem. Soc.* **2017,** *139*, 11000-11003.
12. Wang, Y.-H.; Pegis, M. L.; Mayer, J. M.; Stahl, S. S., *J. Am. Chem. Soc.* **2017,** *139*, 16458-16461.

13. Wang, Y.-H.; Schneider, P. E.; Goldsmith, Z. K.; Mondal, B.; Hammes-Schiffer, S.; Stahl, S. S., *ACS Cent. Sci.* **2019,** *5*, 1024-1034.

14. Azcarate, I.; Costentin, C.; Robert, M.; Savéant, J.-M., *J. Am. Chem. Soc.* **2016,** *138*, 16639-16644.

Curriculum Vitae – Shelby Lane Hooe

Current Address

Department of Chemistry
University of Virginia
McCormick Road
PO Box 400319
Charlottesville, VA 22904-4319
Phone: (804)-517-7636
E-mail: slh3bf@virginia.edu

Personal

Born: July 28; Louisville, KY.

Education and Training

University of Virginia	Inorganic Chemistry and Electrocatalysis	Ph.D. (2016-present; IP)
Gardner-Webb University	Chemistry	B.A. (2016)

Summary of Professional Experience

University of Virginia (2016-present)	Teaching Assistantships -General Chemistry I (Fall 2016) -General Chemistry II (Spring 2017 and 2018) Doctoral Candidate, Chemistry Department -Advisor: Charles W. Machan. Research Specialization: Inorganic Chemistry and Electrocatalysis.

Chemistry Awards and Honors:

2018	2nd Place Winner for Metrohm Young Chemist Award
2018	Travel Award; 3rd International Conference on Proton-Coupled Electron Transfer
2019	Double Hoo Research Grant Recipient with Julia M. Dressel
2019	1st Place Winner of University of Virginia-Dept. of Chemistry 3rd Year Poster Session
2019	Recipient of the ACS Women Chemist Committee/Eli Lily Travel Award

Presentations:

June 11th, 2018	Poster at 3rd International Conference on Proton-Coupled Electron Transfer (Title: Electrocatalytic Reduction of Dioxygen to Hydrogen Peroxide by a Molecular Manganese Complex)
April 30th, 2019	University of Virginia Departmental Colloquium Honoring Winners of Annual 3rd Year Poster Session (Title: Electrocatalytic Reduction of Dioxygen to Hydrogen Peroxide by a Molecular Manganese Complex)
August 25th, 2019	ACS San Diego Poster Presentation (Title: Electrocatalytic Reduction of Dioxygen to Hydrogen Peroxide by a Molecular Manganese Complex with a bipyridine-containing Schiff base ligand)

August 26th, 2019	ACS San Diego SciMix Poster Session (Title: Electrocatalytic Reduction of Dioxygen to Hydrogen Peroxide by a Molecular Manganese Complex with a bipyridine-containing Schiff base ligand)
August 27th, 2019	ACS San Diego Oral Presentation (Title: Electrocatalytic Reduction of Dioxygen to Hydrogen Peroxide by a Molecular Manganese Complex with a bipyridine-containing Schiff base ligand)
November 15th, 2019	Invited Speaker for the Applications of Chemistry Seminar Series at Gardner-Webb University (Title: Electrocatalytic Reduction of Dioxygen and Carbon Dioxide by Molecular Transition Metal Catalysts)

Publications (# = equal contribution):

1) Hooe, S.L.; Rheingold, A.L.; Machan, C.W. "Electrocatalytic Reduction of Dioxygen to Hydrogen Peroxide by a Molecular Manganese Complex with a Bipyridine-Containing Schiff Base Ligand" *J. Am. Chem. Soc.* 2018, DOI: 10.1021/jacs.7b0902.
2) Heyer, A.J.; Shivokevich, P.J.; Hooe, S.L.; Welch, K.D.; Harman, W.D.; Machan, C.W. "Reversible modulation of the redox characteristics of acid-sensitive molybdenum and tungsten scorpionate complexes" *Dalton Trans.* 2018, DOI: 10.1039/C8DT00598B.
3) Hooe, S.L.; Machan, C.W. "Dioxygen Reduction to Hydrogen Peroxide by a Molecular Mn Complex: Divergence between Homogeneous and Heterogeneous Reductants" *J. Am. Chem. Soc.* 2019, DOI: 10.1021/jacs.8b13373.
4) Huelsenbeck, L.D. #; Hooe, S.L.#; Ghorbanpour A.; Conley, A.; Heinrich, H; Machan, C.W., Giri, G. "Metal-Organic Frameworks as Porous Templates for Enhanced Cobalt Oxide Electrocatalyst Performance" *ACS Appl. Energy Mater.* 2019, DOI: 10.1021/acsaem.9b00127
5) Lieske, L.E.; Hooe, S.L.; Nichols, A.W.; Machan, C.W. "Electrocatalytic Reduction of Oxygen by Mn(III) meso-Tetra(N-methyl-4-pyridyl) Porphyrin in Universal Buffer" *Dalton Trans.* DOI: 10.1039/C9DT01436E
6) Hooe, S.L.; Machan, C.W. "Catalytic Reduction of O_2 to H_2O_2 via a Mn Complex" *Trends in Chemistry* 2019, DOI: 10.1016/j.trechm.2019.09.002
7) Hooe, S.L.; Machan, C.W. "Highly Efficient Electrocatalytic Reduction of CO_2 to CO by a Molecular Chromium Complex" *ACS Catalysis* 2019*,* DOI: 10.1021/acscatal.9b04687
8) Nichols, A.W.; Hooe, S.L., Kuehner, J.; Dickie, D.A.; Machan, C.W. "Electrocatalytic CO_2 Reduction to Formate with Molecular Fe(III) Complexes Containing Pendent Proton Relays" *Inorg. Chem.* 2020*,* DOI: 10.1021/acs.inorgchem.9b03341.
9) Moreno, J.J.; Hooe, S.L.; Machan, C.W. "A DFT Study of the Electrocatalytic Reduction of CO_2 by a Molecular Chromium Complex" *Inorg. Chem.* 2021, DOI: 10.1021/acs.inorgchem.0c03136